

Society of Automotive Engineers
of China (SAE-China)
International Federation
of Automotive Engineering Societies (FISITA)
Editors

Proceedings of the FISITA 2012 World Automotive Congress

Volume 3: Future Automotive
Powertrains (I)



Lecture Notes in Electrical Engineering

Volume 191

For further volumes:
<http://www.springer.com/series/7818>

Society of Automotive Engineers of China
(SAE-China) · International Federation of
Automotive Engineering Societies (FISITA)
Editors

Proceedings of the FISITA 2012 World Automotive Congress

Volume 3: Future Automotive
Powertrains (I)



 Springer

The Springer logo, consisting of a stylized chess knight piece (horse) facing left, positioned to the left of the word 'Springer' in a serif font.

Editors
SAE-China
Beijing
People's Republic of China

FISITA
London
UK

ISSN 1876-1100
ISBN 978-3-642-33776-5
DOI 10.1007/978-3-642-33777-2
Springer Heidelberg New York Dordrecht London

ISSN 1876-1119 (electronic)
ISBN 978-3-642-33777-2 (eBook)

Library of Congress Control Number: 2012948289

© Springer-Verlag Berlin Heidelberg 2013

This work is subject to copyright. All rights are reserved by the Publisher, whether the whole or part of the material is concerned, specifically the rights of translation, reprinting, reuse of illustrations, recitation, broadcasting, reproduction on microfilms or in any other physical way, and transmission or information storage and retrieval, electronic adaptation, computer software, or by similar or dissimilar methodology now known or hereafter developed. Exempted from this legal reservation are brief excerpts in connection with reviews or scholarly analysis or material supplied specifically for the purpose of being entered and executed on a computer system, for exclusive use by the purchaser of the work. Duplication of this publication or parts thereof is permitted only under the provisions of the Copyright Law of the Publisher's location, in its current version, and permission for use must always be obtained from Springer. Permissions for use may be obtained through RightsLink at the Copyright Clearance Center. Violations are liable to prosecution under the respective Copyright Law. The use of general descriptive names, registered names, trademarks, service marks, etc. in this publication does not imply, even in the absence of a specific statement, that such names are exempt from the relevant protective laws and regulations and therefore free for general use.

While the advice and information in this book are believed to be true and accurate at the date of publication, neither the authors nor the editors nor the publisher can accept any legal responsibility for any errors or omissions that may be made. The publisher makes no warranty, express or implied, with respect to the material contained herein.

Printed on acid-free paper

Springer is part of Springer Science+Business Media (www.springer.com)

Contents

Part I Alternative Fuel and New Engine

Experimentation Investigate of Gasoline Engine Emergency Alternative Fuel	3
F2012-B01-003 Lianling Ren, Changfa Liu, Xingwang Wang and Rui Ge	
Analytical Assessment of C2–C8 Alcohols as Spark-Ignition Engine Fuels	15
F2012-B01-004 Thomas Wallner, Andrew Ickes and Kristina Lawyer	
Improvement of the Automotive Spark Ignition Engine Performance by Supercharging and the Bioethanol Use	27
F2012-B01-007 Constantin Pana, Niculae Negurescu and Alexandru Cernat	
Theoretical and Experimental Investigations on the LPG Fuelled Diesel Engine	37
F2012-B01-009 Niculae Negurescu, Constantin Pana and Alexandru Cernat	
The Research Development in Direct Injection Spark-Ignition Natural Gas Engine.	51
F2012-B01-010 Jianjun Zheng, Xiaodong Chen, Tiegang Hu and Zhangsong Zhan	

Experimental Results Using Ammonia Plus Hydrogen in a S.I. Engine	65
F2012-B01-015 Stefano Frigo, Roberto Gentili, Giacomo Ricci, Giuseppe Pozzana and Massimiliano Comotti	
Dual Fuel H2-Diesel Heavy Duty Truck Engines with Optimum Speed Power Turbine	77
F2012-B01-018 Alberto Boretti	
Well-to-Wheel Analyses for Energy Consumption and Greenhouse Gas Emissions of Electric Vehicles Using Various Thermal Power Generation Technologies in China	101
F2012-B01-022 Wei Shen and Weijian Han	
Effects of Fuel Thermo-Physical Properties on Spray Characteristics of Biodiesel Fuels	117
F2012-B01-023 Xinwei Cheng, Harun M. Ismail, Kiat Hoon Ng, Suyin Gan and Tommaso Lucchini	
System Design for a Direct-Boost Turbocharged SI Engine Using a Camshaft Driven Valve	127
F2012-B01-024 Christoph Voser, Christopher Onder and Lino Guzzella	
Exploring the Potential of Dual Fuel Diesel-CNG Combustion for Passenger Car Engine	139
F2012-B01-025 David Serrano and Lecointe Bertrand	
Sustainable Mobility: Lithium, Rare Earth Elements, and Electric Vehicles	155
F2012-B01-026 Timothy J. Wallington, Elisa Alonso, Mark P. Everson, Frank R. Field, Paul G. Gruber, Gregory A. Keoleian, Stephen E. Kesler, Randolph E. Kirchain, Pablo A. Medina, Emily K. Kolinski Morris, Rich Roth and Andrew M. Sherman	

Controller Design and Emission Improvement for Lean-Burn CNG Engine Based on UEGO Controller 167
 F2012-B01-031
 Xiaojian Mao, Junhua Song, Du Wang, Junxi Wang, Hangbo Tang and Bin Zhuo

Biogas as a Fuel for City Buses 179
 F2012-B01-037
 Jerzy Merkisz and Wojciech Gis

High-Concentration Ethanol Fuels for Cold Driving Conditions 193
 F2012-B01-040
 Juhani Laurikko, Nils-Olof Nylund, Jari Suominen and Mika P. A. Anttonen

The Effects of Intake Valve Closing Timing on Engine Performance and Emissions in a DME Compression Ignition Engine at Low Load Cold Start Condition 211
 F2012-B01-044
 Jaeheun Kim and Choongsik Bae

Environmental Performance of Diesel Fuels Containing Oxygenated Additive Packages 227
 F2012-B01-045
 Miłosław Kozak, Jerzy Merkisz, Piotr Bielaczyc and Andrzej Szczotka

A Study of Dual-Diluted Control Strategy for NG Engine 239
 F2012-B01-049
 Yanchun Chen, Chao Wang, Dongxu Hua and Changbo Fu

Research and Development of Heavy-Duty NG Engine and its Key Technologies of Combustion 251
 F2012-B01-050
 Huili Dou, Jun Li, Zhongshu Wang, Xiaocao Yu, Zhongchang Liu and Jingxue Li

Part II Advanced Hybrid Electric Vehicle

Development of CHS Hybrid System for City Bus 265
 F2012-B02-006
 Guangkui Shi, Renguang Wang, Hongtao Chen and Zhiguo Kong

Optimization of an Extended-Range Electric Vehicle	275
F2012-B02-009	
Haitao Min, Dongjin Ye and Yuanbin Yu	
Driving Intention Identification Method for Hybrid Vehicles Based on Fuzzy Logic Inference.	287
F2012-B02-015	
Qingnian Wang, Xianzhi Tang and Lei Sun	
The Control Technologies of PMSM for FAW-TMH System.	299
F2012-B02-016	
Cheng Chang, Huichao Zhao, Xiuhui Dong and Yandong Wen	
Modeling and Simulation of Power Train System for Extended-Range Electric Vehicle Using Bond Graphs	313
F2012- B02-017	
Ke Song and Tong Zhang	
Optimization of Hybrid Strategies with Heuristic Algorithms to Minimize Exhaust Emissions and Fuel Consumption	323
F2012-B02-023	
Michael Planer, Thorsten Krenek, Thomas Lauer, Zahradnik Felix, Bernhard Geringer and Michael Back	
Development for Control Strategy of ISG Hybrid Electric Vehicle Based on Model	333
F2012-B02-025	
Hongtao Peng, Zheng Li, Bin Chen, Jieyu Wu, Zhenglan Zhao, Yuehong Shu and Junjun Lei	
Development of New Hybrid Transaxle for Front-Wheel Drive (FWD) 2.5-Liter Class Vehicles	343
F2012-B02-026	
Kunihiro Kobayashi, Takahisa Yashiro, Hiroshi Takekawa and Kazuhiro Fujita	
Key Items for Future Hybrid Applications: Energy Storage and Power Electronics for Micro Hybrids up to Full Hybrids and EVs	355
F2012-B02-027	
Peter Willemsen, Feng Ji and Marc Nalbach	

Direct-Computation-Based Traction Motor Control for Dynamic Performance Improvement in Electric Vehicles 365
 F2012-B02-033
 Xi Zhang and Chengliang Yin

Energy Optimization for the Mild Hybrid Electric Vehicle with CVT Under Driving Conditions 375
 F2012-B02-036
 Yongxia Zheng, Feng Zhao, Yugong Luo and Keqiang Li

Development of Plug-in Hybrid System for Midsize Car 387
 F2012-B02-037
 Shinichi Matsumoto, Hiroaki Takeuchi and Kenji Itagaki

Study on System Efficiency and Power Flow Optimization for Dual-Mode Hybrid Electric Vehicle 401
 F2012-B02-038
 Lijin Han, Changle Xiang, Weijing Yan, Yun-long Qi and Ran Liu

Development of Commercial Hybrid Vehicle Automatic Transmission System 417
 F2012-B02-040
 Chiaki Umemura, Kazumi Ogawa, Toshinori Murahashi and Yasutoshi Yamada

A Dynamic Coordinated Control Strategy for Mode-Switch of Hybrid Electric Vehicle Based on the Effect Control 427
 F2012-B02-043
 Na Zhang, Feng Zhao and Yugong Luo

‘Commercial Vehicle Electrification’ Challenges in Dimensioning and Integration in the Entire Vehicle 439
 F2012-B02-054
 Winter Martin

Plug-In Hybrid Vehicle with a Lithium Iron Phosphate Battery Traction Type 449
 F2012-B02-062
 Danut Gabriel Marinescu, Ion Tabacu, Florin Serban, Viorel Nicolae, Stefan Tabacu and Ionel Vieru

Design and Simulation of Air Cooled Battery Thermal Management System Using Thermoelectric for a Hybrid Electric Bus	463
F2012-B02-065	
Vahid Esfahanian, Saber Ahmadi Renani, Hassan Nehzati, Nima Mirkhani, Mohsen Esfahanian, Omid Yaghoobi and Ali Safaei	
Analysis of Rotor’s Magnetic Bridge and Yoke Design to EM’s Performance Influence	475
F2012-B02-069	
Ming Han, Wenxiang Huang and Pingliang Luo	
HyBoost: An Intelligently Electrified Optimised Downsized Gasoline Engine Concept	483
F2012-B02-070	
Jason King, Matthew Heaney, James Saward, Andrew Fraser, Mark Criddle, Thierry Cheng, Guy Morris and Paul Bloore	
Development of B70HEV and B50PHEV Based on Faw-TMH Powertrain	497
F2012-B02-073	
Jun Li, Minghui Liu, Dongqin Liu, Ziliang Zhao and Xingwang Yang	
The Research of Electromagnetic Fields During Testing of a Hybrid Powerplant and a Hybrid Car Prototype	509
F2012-B02-074	
Elena Teriaeva	
Research on the Efficiency of the Dual-Mode Hybrid Vehicle	519
F2012-B02-075	
Weijing Yan, Changle Xiang, Lijin Han and Donghao Zhang	
Power Transmission Properties of Dry Hybrid V-Belt with Protuberant Tension Member on Contact Surfaces of Blocks: It’s Effect with Respect to Speed Ratio.	531
F2012-B02-076	
Hirotoishi Kawakami, Kazuya Okubo, Toru Fujii, Hiroyuki Sakanaka and Ryuichi Kido	
A Comparative Analysis of Optimization Strategies for a Power-Split Powertrain Hybrid Electric Vehicle	541
F2012-B02-077	
Jackeline Rios and Pierluigi Pisu	

Part III Plug-in Electric Vehicle

Development of a Compact-Class Range Extended Electric Vehicle Demonstrator 553
 F2012-B03-004
 Michael Bassett, Jonathan Hall, John Powell, Simon Reader, Marco Warth and Bernd Mahr

Modeling of the Lithium Battery Cell for Plug-In Hybrid Electric Vehicle Using Electrochemical Impedance Spectroscopy. 563
 F2012-B03-005
 Hyun-sik Song, Tae-Hoon Kim, Jin-Beom Jeong, Dong-Hyun Shin, Baek-Haeng Lee, Byoung-Hoon Kim and Hoon Heo

On-Board Powerplant Numerical Optimization of Internal Combustion Engines in Series Hybrid-Powertrains. 573
 F2012-B03-007
 Thorsten Krennek, Thomas Lauer, Bernhard Geringer and Bacher Christopher

Torque-Vectoring Driveline for Electric Vehicles 585
 F2012-B03-009
 Bernd-Robert Hoehn, Karsten Stahl, Philipp Gwinner and Ferdinand Wiesbeck

Plug-In Hybrid Vehicle Powertrain Design Optimization: Energy Consumption and Cost 595
 F2012-B03-012
 João P. Ribau, João M. C. Sousa and Carla M. Silva

Simulation-Based Energy Flow Study of Purely Electric-Drive Vehicles 615
 F2012-B03-014
 Bin Wang, Mian Li, Min Xu and Jianhua Zhou

Design of Auxiliary Electric Driving System in Rear Wheels of Vehicles 631
 F2012-B03-015
 Hongzan Xu, Quan Sun, Xufeng Wu, Qiqian Jin, Yi You and Fuquan Zhao

Study on the Relationship Between EV Cost and Performance 639
 F2012-B03-018
 Pupeng Wan, Zhiqiang Du, Qiqian Jin, Yi You and Fuquan Zhao

Hil Validation of Extended-Range Electric Vehicle Control Unit Based on Orthogonal Test 647
 F2012-B03-022
 Haibo He, Qiqian Jin, Tingting Dong and Fuquan Zhao

Development of a Control System of Hybrid Power System Based on the XPC Target for Electric Vehicles 655
 F2012-B03-024
 Yaming Zhang and Rui Xiong

A Study on Effective Thermal-Shock Test Improvement of Battery Packs for PHEVs 667
 F2012-B03-025
 Byoung-Hoon Kim, Hong-Jong Lee, Jin-Beom Jeong, Baek-Haeng Lee, Dong-Hyun Shin, Hyun-Sik Song, Tae-Hoon Kim and Ji-Yoon Yoo

Challenges in NVH for Electric Vehicles 675
 F2012-B03-029
 Benjamin Meek, Herman Van der Auwear and Koen De Langhe

Study on New Concept Powertrain for Range-Extended Electric Vehicles 687
 F2012-B03-032
 Minghui Liu, Ziliang Zhao, Xingwang Yang, Chuan Li and Guopeng Luo

Parameters Optimization of PHEV Based on Cost-Effectiveness from Life Cycle View in China 697
 F2012-B03-037
 Jiuyu Du, Hewu Wang and Minggao Ouyang

Approach of Gasoline Hybrid Technology for “95G CO2/KM” Emissions Regulation. 705
 F2012-B03-038
 Jun Li, Ziliang Zhao, Yihong Zheng, Minghui Liu and Heqi Liang

Part IV Advanced Battery Technology

Study on Drive Battery High Voltage Safety System for Hybrid Electric Vehicle 721
 F2012-B04-002
 Xingfeng Fu, Sijia Zhou, Yingjun Zheng and Chengjiao Tu

Automaker Energy Storage Needs for Electric Vehicles 729
 F2012-B04-005
 Alvaro Masias, Kent Snyder and Ted Miller

Design of the Experimental Procedures for Analysis of Thermal and Electrical Properties of a Prismatic LiFeYPO₄ Battery in a Modified Electric Car 743
 F2012-B04-007
 Chayangkun Sanguanwatana, Chadchai Srisurangkul, Monsak Pimsarn and Shoji Tsushima

Intelligent BMS Solution Using AI and Prognostic SPA 755
 F2012-B04-008
 Subrahmanyam Sista and Avinash Sista

Thermal Modeling and Effects of Electrode Configuration on Thermal Behaviour of a LifePO₄ Battery 765
 F2012-B04-013
 Cheng Ruan, Kun Diao, Huajie Chen, Yan Zhou and Lijun Zhang

Thermal Behavior and Modeling of Lithium-Ion Cuboid Battery 779
 F2012-B04-020
 Hongjie Wu and Shifei Yuan

Application of Battery-Ultracapacitor Hybrid System in the Hybrid Electric Vehicles 785
 F2012-B04-021
 Huanli Sun, Xiaojuan Pei, Lichao Xu, Hemin Wang, Yi Sheng and Yuanbin Yu

A Lithium-Ion Battery Fractional Order State Space Model and its Time Domain System Identification 795
 F2012-B04-023
 Hongjie Wu, Shifei Yuan and Chengliang Yin

Optimizing BMS Operating Strategy Based on Precise SOH Determination of Lithium Ion Battery Cells. 807
 F2012-B04-024
 Karsten Mueller, Daniel Tittel, Lars Graube, Zecheng Sun and Feng Luo

Part V Hydrogen Fuel Cell Vehicle

**Novel Concept of Long-Haul Trucks Powered
by Hydrogen Fuel Cells 823**

F2012-B05-002

Bahman Shabani, John Andrews, Aleksandar Subic and Biddyut Paul

Practical Research on Hydrogen Safety of Fuel Cell Vehicles 835

F2012-B05-004

Yong He, Bing Wu, Honghu Wang, Pengcheng Zhao and Yachao Li

Modeling and Analysis of a Fuel Cell Hybrid Vehicle 847

F2012-B05-005

Mircea Nicolae Glazer, Ioan Mircea Oprean and Marius Valentin Băţăuş

**Optimal Battery Discharging Strategy for a Range Extended
Fuel Cell City Bus 859**

F2012-B05-008

Liangfei Xu, Minggao Ouyang, Jianqiu Li,
Fuyuan Yang and Languang Lu

Part VI Charging Infrastructure and Smart Grid Technology

**EV Charging Through Wireless Power Transfer:
Analysis of Efficiency Optimization and Technology Trends 871**

F2012-B06-001

Heri Rakouth, John Absmeier, Andrew Brown Jr., In-Soo Suh,
Miller John M., Randy Sumner and Richard Henderson

Part VII Demonstration of Electric Vehicles in Cities

**Development and Performance Evaluation of an Electric
Mini Bus Equipped with an Inductive Charging System 887**

F2012-B07-002

Thomas Pontefract, Kimiyoshi Kobayashi, Yuto Miyasaka,
Kento Tanaka, Yushi Kamiya, Yasuhiro Daisho
and Shunsuke Takahashi

**The Study of Re-construction Method of EV Business Model
Based on Value Chain Analysis 899**

F2012-B07-003

Qiang Ye and Hewu Wang

Part VIII Other

Research on Parameter Matching and Fuzzy Logic Control Strategies of EMT Hybrid Energy Storage System 911
 F2012-B08-008
 Changle Xiang, Yanzi Wang, Weida Wang, Lijin Han and Donghao Zhang

Cost-Effectiveness Analysis of CO₂ Reduction with Future Automobile Technologies in the Japanese Automotive Sector 923
 F2012-B08-009
 Shuichi Kanari

The Small-Signal Model Stability Analysis of Full-Bridge Buck Converter with Compensation Network 937
 F2012-B08-014
 Lin Zhang, Dengmeng Fu and Haoxing Liu

The HV Safety Management Design of Battery System in Electric Vehicle 951
 F2012-B08-016
 Tao Yan, Qi qian Jin and Fuquan Zhao

The Free Piston Stirling Principle as Prime Mover for Alternant Hydraulic Propulsion Systems. 957
 F2012-B08-020
 Horia Abaitancei, Cristi Irimia, Gabriel Carciumaru, Ionut Tudor Soare and Sebastian Radu

Design and Analysis of a Dual Power Supply with Super-Capacitor for EV 969
 F2012-B08-021
 Ye Lu, Fen Liu, Xiaoyu Jia and Xiao Liang

An Electrically Driven Chassis System Concept for Sub-Compact Vehicles with Integrated Close-to-Wheel Motors 979
 F2012-B08-022
 Shih-Jen Yeh, Ingo Albers and Stephan Pollmeyer

Future Commercial Vehicle Powertrains: Contributions to Sustainable Transportation 987
 F2012-B08-024
 Heimo Schreier and Lukas Walter

Part I
Alternative Fuel and New Engine

Experimentation Investigate of Gasoline Engine Emergency Alternative Fuel

Lianling Ren, Changfa Liu, Xingwang Wang and Rui Ge

Abstract This paper has integrated various methods such as engine bench test and actual road test, etc. to conduct a feasibility study on the emergency alternative fuel of gasoline by mixed jet fuel and gasoline. The research is divided into three parts. The first step is to mix the jet fuel and gasoline in different proportions and to analysis physicochemical properties. The study shows that both the evaporation and anti-knock quality decrease after mixing jet fuel with gasoline. The second step is to make bench test on the external characteristics and load characteristics with CA20 made use of so as to study the influences of the jet fuel to the dynamic performance and economical efficiency of the engine. The result shows that while the mixing proportion increases, the engine power decreases and the fuel consumption increases gradually. When the proportion reaches 40 %, the engine power drops by 5.3 to 11.7 %, the fuel consumption rises by an average of 3.8 %,The third step is to make a test on actual use for 1,000 km in order to study the adaptability of the jet fuel to the gasoline cars making use of blending fuel with 40 % jet fuel mixed in. The result shows that the lubricating oil dilution and exhaust emissions of engine become worse. All of the above studies show that as for the gasoline engine, the mixed oil can only be used as emergency alternative fuel due to its harm to the engine.

F2012-B01-003

L. Ren (✉)

Research fields: fuel additive and alternative fuel,
POL Research Institute of Beijing, Beijing, China
e-mail: rll-1119@163.com

C. Liu

Beijing Aviation Logistics Oil Supply Agent, Beijing, China

X. Wang · R. Ge

Military Representative Office in Dalian Refinery, Dalian, China

Keywords Automobile · Kerosene · Jet fuel · Emergency alternative · Engine · Gasoline

1 Introduction

The working conditions of the gasoline cars are closely related to the physical and chemical properties of gasoline. To make the engine operate, the fuel of the gasoline engine has to meet the following requirements [1, 2]: (1) Good anti-detonation quality. The gasoline should have an appropriate high octane number. And when it is injected into the combustion chamber, it can be quickly ignited with stable burning and no detonation so as to make the engine reach the maximum power. (2) Suitable evaporability. After vaporized in the carburetor or the intake port, the gasoline should be mixed with air in certain proportion to form mixed gas before burning in the cylinders. Therefore, the evaporability of the gasoline directly affects the combustion velocity and combustion completeness of gasoline, which consequently affects the power and economical efficiency of engine. (3) Good oxidation stability. If the oxidation stability of gasoline is poor, the gums generated by oxidation will block the fuel filters, destroys the normal supply of fuel, creates carbon deposition and increases the tendency of the occurrence of detonation.

Both the jet fuel and auto gasoline are petroleum products, with the closest distillation range. If the mixture of jet fuel and auto gasoline can meet the minimum requirement of engine fuel—to make cars normally operate, it will relieve the difficulty of oil usage in the emergency conditions to some extent. This paper analyses the properties of the mixed fuel and its influences to the engine performance when jet fuels and auto gasoline are mixed in different proportions.

2 Experimentation

2.1 Samples

A series of samples are made by mixing gasoline and jet fuel in different proportions. After mixing, the proportions of the jet fuel to the samples (calculated by volume fraction) are respectively as following: 0, 10, 20, 30, 40, 50, 60, 70, 80, 90 and 100 %. The measurement results of the physical and chemical properties of the samples have been listed in Table 1.

Table 1 Physical and chemical properties of the samples

Items	Proportions of jet fuel										
	Auto gasoline	10 %	20 %	30 %	40 %	50 %	60 %	70 %	80 %	90 %	Jet fuel
Serial number	M00	M10	M20	M30	M40	M50	M60	M70	M80	M90	M100
Existent gum (mg•100 ml ⁻¹)	24.6	21.8	20.2	14.1	16.0	11.9	10.1	9.1	5.4	2.8	0.5
	0.4	0.3	0.5	0.1	0.3	0.1	0.3	0.1	0.2	0.1	0.2
Saturated vapor pressures (kPa)	49.5	44.5	39.5	37.5	34.0	30.5	28.5	18.0	14.0	10.0	4.5
Initial boiling point (°C)	42	45	49.5	45	55	56	59	56	59	75	153
10 % distil-off temperature (°C)	61	63	68	69	80	85	96	111	133	154	170
50 % distil-off temperature (°C)	109	114	126	138	151	160	166	175	180	182	184
90 % distil-off temperature (°C)	173.5	183	191	197	201	202	204	205	208	209	209
Final boiling point(°C)	208	218	223	227	234	234	237	239.5	237	241.5	241
Research octane number	91.4	87.5	82.8	76.0	69.0	-	-	-	-	-	-

Table 2 Main parameters of the engine used for test

Project		Parameters
Cylinder numbers		Inline 4-cylinders
Cylinder diameters	mm	86
Compression ratio		10:1
Max. piston air leakage	L/min	28
Ignition sequence		1-3-4-2
Cooling methods		Forced water cooled
Lubrication methods		Combined pressure and splashing

Table 3 Main equipments

Serial number	Type of equipments	Service
1	Electric eddy current dynamometer of CW160 type	To test power and torque
2	Engine CA20 and associated measurement control device	To control engine condition
3	FCZ210Z intelligent oil consumption measurement device	To measure fuel consumption ratio

2.2 Methods

2.2.1 Bench Test Research

According to GB 1105-87 Performance Test Methods for Reciprocating Internal Combustion Engine and GB 3847-83 Measurement Methods for the Emission Smoke at Full Load from the Auto Diesel Engine, four fuels of M00, M20, M30 and M40 are selected, with engine CA20 made use of, to make bench test on the external characteristics and load characteristics so as to study the influences of the jet fuel to the dynamic performance and economical efficiency of the engine. For the technical parameters of the engine and the main equipments used, please see Tables 2 and 3 respectively.

2.2.2 Actual Driving Test Research

M40 with 40 % jet fuel mixed in has been used in 5 gasoline cars to make a test on actual use for 1,000 km in order to study the adaptability of the jet fuel to the gasoline cars. Cold start, dynamic performance, performance variation of engine oil and off gas emission are mainly tested to analyze the adaptability of the jet fuel. For the main parameters of the test cars, please see Table 4.

Table 4 Conditions of the test gasoline cars

Car model	Number of cylinders	Compression ratio	Odometer scale	Car conditions
CA141	6	7.4	56,000	Good
Cherokee Model 7250	4	8.6	34,000	Good
Beijing Jeep Model 2020	4	7.6	16,000	Good
Santana 2000	4	9.5	152,000	Good
Jetta	4	9.3	3,000	Good

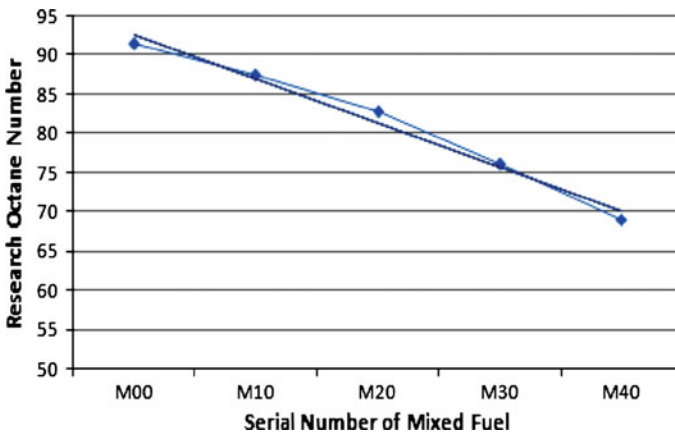


Fig. 1 Relationship between addition of jet fuel and anti-detonation quality

3 Results and Discussions

3.1 Analysis on the Anti-Detonation Quality of the Mixture of Gasoline and Jet Fuel

For the fuel of the gasoline engine, the octane number, as significant index of the combustion performance of fuel, determines if the engine can normally work. If the octane number is too low, it will be difficult to ignite the engine and the detonation will be easy to happen. By measuring the octane numbers of M00, M10, M20, M30, M40, we can know from Fig. 1: Firstly, line charts are made with the octane numbers got. From Fig. 1 we can see that the decrease margin of the octane number forms a linear relationship with the proportion of jet fuel mixed: $R^2 = 0.984$. They have a good correlation with each other. Secondly, the octane number of the mixed fuel has reduced as the proportion of the jet fuel mixed has increased. When the mixed amount increases from 0 to 40 %, the octane number reduces from 91.4 of M00 to 69.0 of M40, which has exceeded the minimum requirement of the petroleum

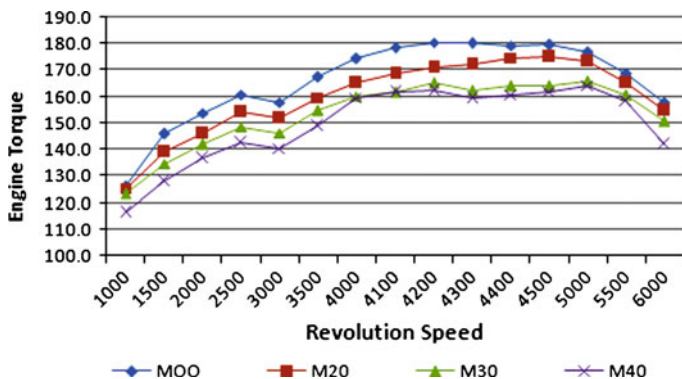


Fig. 2 Contrast of engine torque

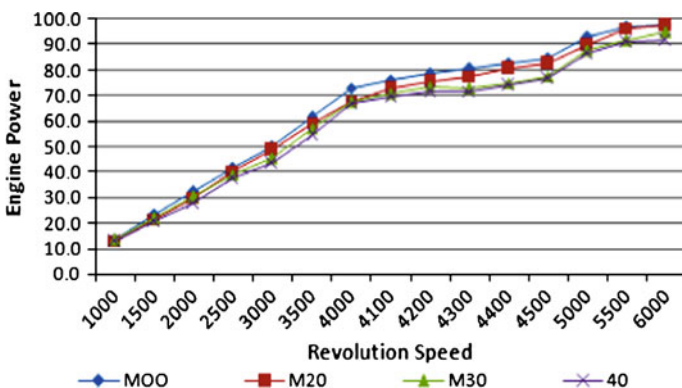


Fig. 3 Contrast of engine power

Table 5 Data of cold start test

Fuel	Auto. gasoline	M20	M30	M40
Times needed for successful start (s)	1~2	1~3	2~4	2~4
Max. number needed for successful start	1	1	1	2

products’ quality. Therefore, as the proportion of jet fuel mixed increases, the anti-detonation quality of the engine gradually becomes poor. If the mixing proportion increases further, the octane value would continue to decrease, which may cause the unstable performance of the engine. Consequently, this article does not use the fuel whose mixing proportion is over 40 % for test when carrying on the study of the jet fuel’s influence to the engine performance.

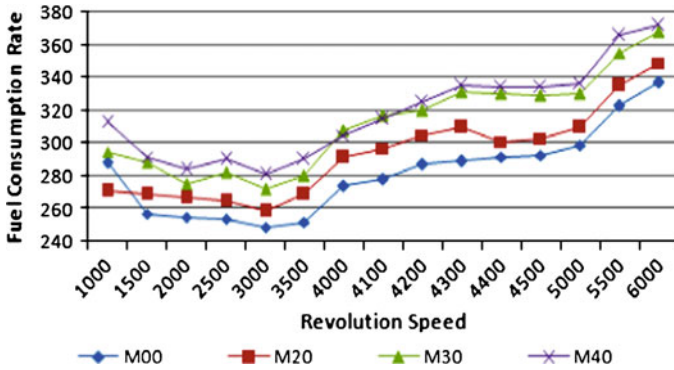


Fig. 4 Contrast of FCR during external characteristics test

3.2 Influences to Engine Performance When Jet Fuel is Mixed in

3.2.1 Dynamic Property

Figures 2 and 3 respectively show the external characteristics data of torque and power of the engine when using the four fuels. Based on the data, it is easy to find that the variation trends of torque and power when the mixed fuel is burnt is in conformity with that when car gasoline is burnt. As the pictures show, all the maximum torque points appear around 4,200 r/min. With the raise of the revolution speed, power gradually increases. When the revolution speed reaches 4,000 r/min, the increasing level of the power begins to reduce. When the revolution speed reaches 5,500–6,000 r/min, the maximum power is reached. But both the torque and power reduce as the proportion of jet fuel mixed increases. Compared with car gasoline, the torque’s decline range of M20 is 0.9~5.6 %, with power decline range being 0.1~7.4 %. For M30, the decline range is 2.6~9.9 % and 0~9.8 % respectively. For M40, the decline range is 6.2~12.5 % and 5.3~11.7 % respectively.

Table 5 shows the cold start conditions of engine when respectively using M20, M30 and M40. Under the indoor engine bench test temperature of $15 \pm 2 \text{ }^\circ\text{C}$, cold start performance test has been made. The addition of the jet fuel has made an adverse impact on the cold start performance. Compared with car gasoline, the cold start time becomes longer and the number of cold start also increases when the mixed fuel is used as the engine fuel. Therefore, long time usage of the mixed fuel will damage the engine.

The engine has a set of spark plug ignition system to accurately control the discharge time of the spark plug and the spark energy generated. After the mixed gas of fuel and air goes into the cylinder, it will be ignited by the spark plug when the compression of it closes to the end so as to ensure the normal working of the gasoline engine. After the mixed gas of fuel and air goes into the cylinder, two

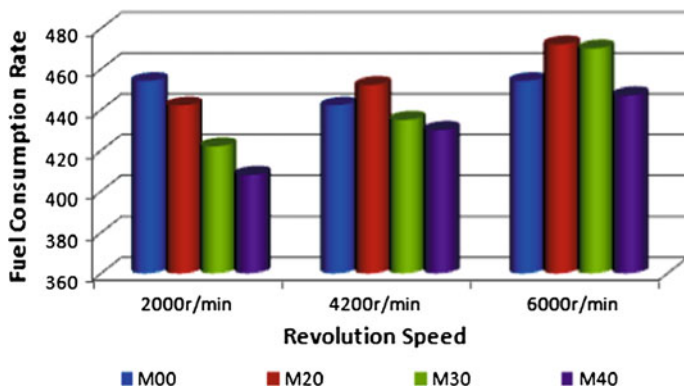


Fig. 5 Contrast of FCR at low power during load-characteristic test

problems will appear at the original ignition advance angle. One is that it is not the best time for spark plug to discharge, since the decreased combustion propagation speed of the fuel and the reduced explosion pressure both cut down the combustion efficiency of diesel and influences the effective power. The other is that it is not the optimum state for spark energy. Due to the heavier fraction of jet fuel compared with that of gasoline, the self-ignition point of fuel reduces while the ignition point rises correspondingly, which makes it difficult for spark energy to ignite the mixed gas but easy for the variation of start to occur. Thus, the car gasoline mixed with jet fuel will make an impact on the cold start and dynamic performance of the engine.

3.2.2 Economical Efficiency of Fuel

From the data of external characteristics test shown in Fig. 4, all the four fuels present a regulation as following: the fuel consumption rates, dropping before rising, all reach the lowest at 3,000 r/min. Thus, it could be said that 3,000 r/min is the most economical point for engine. Under each speed condition of engine, the fuel consumption rate goes up as the increase of the proportion of the jet fuel mixed. In the whole speed range, compared with car gasoline, the increase of the fuel consumption rate of M20 is $-5.9 \sim 7.3\%$ with an average increase of 4.2% ; the increase of the fuel consumption rate of M30 is $2.4 \sim 14.5\%$ with an average increase of 10.7% ; the increase of the fuel consumption rate of M40 is $8.7 \sim 15.9\%$ with an average increase of 12.9% . Meanwhile, M30 and M40 share almost the same fuel consumption rate, with an average gap of each being within 2.0% .

Figures 5 and 7 show the fuel consumption rate of the four fuels in the load-characteristic test. From them, it is easy to see that the oil consumption rate rises as the revolution speed increases. Under each revolution speed, fuel consumption rate at high power is less than that at low power. Under the relatively low power, fuel consumption rate reduces as the proportion of jet fuel mixed increases, that is

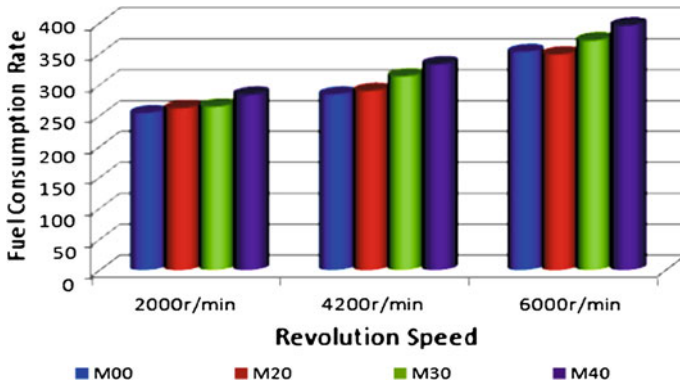


Fig. 6 Contrast of FCR at high power during load-characteristic test

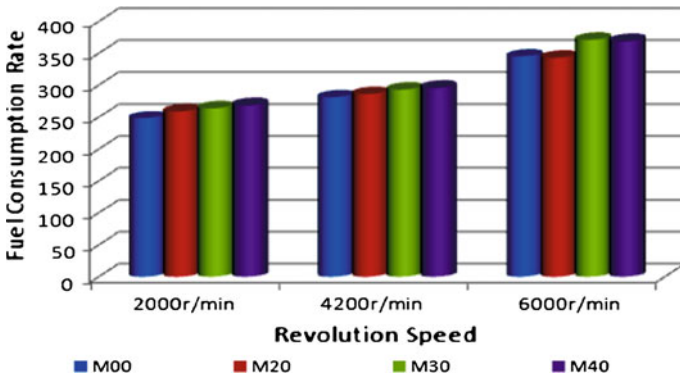


Fig. 7 Contrast of lowest FCR during load-characteristic test

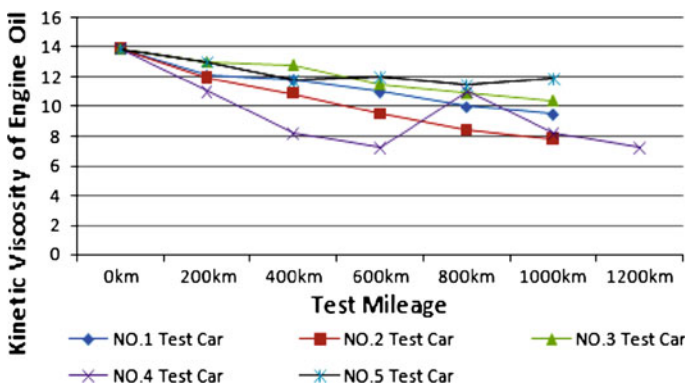


Fig. 8 Change of kinetic viscosity of engine oil during driving test

Table 6 Variation of splash lights of engine oil before and after test

Car No.	No. 1	No. 2	No. 3	No. 4	No. 5	Testing methods
Splash light before test (°C)	230	230	230	230	230	ASTM D92-02
Splash light after test (°C)	172	168	178	156	196	
Reduction ratio of splash light (%)	25.2	27.0	22.6	32.2	14.8	

M20 > M30 > M40. While it is completely different under the high power, the fuel consumption rate presents that M20 < M30 < M40. But seen from the whole, the addition of the jet fuel still has adverse effects on the economic efficiency of the fuel. For example, the fuel consumption rate of M20, M30 and M40, compared with that of car gasoline, respectively has an increase of 1.3, 2.9, 3.8 % (Fig. 6).

3.3 Influences to the Actual Use When the Jet Fuel is Mixed in

No failure has occurred to the 5 cars during the test. All of them can be normally cold started at 20 °C. Both the No. 1 truck and No. 3 jeep need to be accelerated at the beginning of the start for 2 ~ 3 min before the normal idle speed. While the rest three have no obvious abnormal conditions occurred during cold start. While the cars are running in the smooth road, the dynamic performance and acceleration, compared with the combustion of the car gasoline, have no obvious abnormal conditions. However, while the cars are climbing the lane, the dynamic performance of each car has been found to decline. From this we can see that under heavy duties, the addition of the jet fuel has a relatively great impact on the dynamic performance.

Figure 8 shows the test data of kinetic viscosity of the engine oil during driving test. From the picture, it is easy to see that NO. 5 car has the best performance with the reduction ratio of kinetic viscosity being 14.4 %. The variation ratio of kinetic viscosity of NO. 3 car is 25.1 %. While the viscosity of NO. 4 car, with the worst performance, has reduced to 7.2 mm²/s when the car has run for 600 km. In order to avoid abnormal wears, even the “scuffing of cylinder bore and bush-burning”, the oil of NO. 4 car has been changed while it has run for 600 km before it goes on the 1,000 km driving test. When the test is completed, the viscosity once again drops to 7.2 mm²/s.

When the jet fuel is added into the gasoline, the fraction increases. After the mixed fuel is injected into the engine, it is not easy to be homogeneously mixed, which will lead to the incomplete combustion. The unburnt fuel will infiltrate into the oil tank along the inner wall of the cylinder, which will result in the reduction of the oil density and thus aggravate the wear of the piston. Due to the 152,000 km running and serious wear to the pistons before the test, the NO. 4 car, with a relatively poor condition, has the most serious dilution of engine oil. This can also be proven by the variation of the flashing points in Table 6. From the above analysis, it is obvious to see that the jet fuel will dilute the engine oil to some extent, but the dilution degree is closely related to the engine conditions.

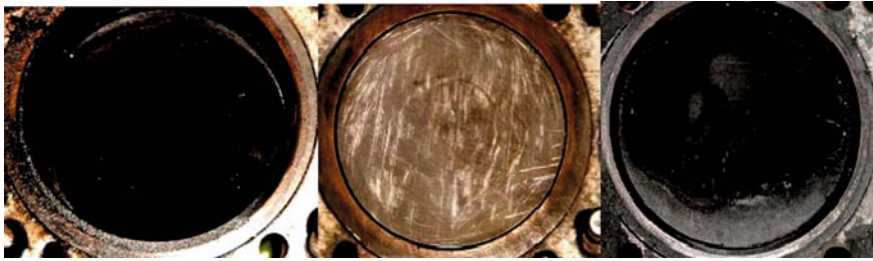


Fig. 9 Contrast of the carbon deposit on the top of piston (carbon deposit conditions before the test, carbon deposit conditions after the carbon deposit is cleared before the test, carbon deposit conditions after the test)

Table 7 The influence of the jet fuel to the exhaust emissions of the engine

Car No.	Project	Fuel	HC (ppm)	CO ₂ (%)	λ
1	Before the test	Car gasoline	503	11.1	1.226
	After 1,000 km	+40 % jet fuel	592	10.5	1.156
	After the test	Car gasoline	486	11.8	1.229
2	Before the test	Car gasoline	637	8.7	1.420
	After 1,000 km	+40 % jet fuel	884	7.6	1.514
	After the test	Car gasoline	448	9.1	0.958
3	Before the test	Car gasoline	327	12.7	0.961
	After 1,000 km	+40 % jet fuel	391	11.8	0.925
	After the test	Car gasoline	204	12.9	0.914

NO. 3 car has been used to analyze the influence of the jet fuel to carbon deposit generation. The car has undertaken an overhaul inspection, with the carbon deposit on the tope of the piston and in the cylinder head being cleared, before the test. A contrastive analysis has been made, as shown in Figs. 9, on the carbon deposit conditions before and after the test. After M40 is used to make the 1,000 km driving test, the carbon deposit generated in the engine is not much different from that before the test, which shows that the carbon deposit is within an acceptable range.

In order to study the influence of the jet fuel to the auto off gas, the author has used exhaust emission analyzer of MRU-OPTRANS1600 model to make a contrastive inspection to the exhaust emissions of the test cars of NO. 1, 2 and 3. For the inspection result, please see Table 7. Through the data analysis, it is easy to see that after M40 is used to make the 1,000 km test, the HC content, compared with that before the test, has risen, while the CO₂ content has reduced. After the test is completed, another inspection is made to test the exhaust emissions with M40 being replaced with car gasoline. There is a returning trend shown in the test data. This shows that the addition of the jet fuel has affected the complete combustion of gasoline. As a result, the incomplete combustion increases, which is also proven by the data of combustion efficiency (λ).

4 Conclusions

For gasoline engine, if the mixed fuel is burnt, it will make a relative great impact on the power, torque and fuel consumption rate, which will eventually lead to the drop of the dynamic performance and the reduction of the economical efficiency of the fuel. Long time use of the mixed fuel will lead to serious wear and dilution. Auto. gasoline with certain proportion of jet fuel mixed in can be used as the emergency fuel of the gasoline engine, but not for long-time use. Besides, the mixed proportion cannot be too big, otherwise, it will cause a relative huge damage to the engine.

References

1. Xiong Y, Xu SH (2008) Oil application and management. China Petrochemical Press, Beijing
2. He XL, Zan YH (2004) Fuels for internal-combustion engine. China Petrochemical Press, Beijing

Analytical Assessment of C2–C8 Alcohols as Spark-Ignition Engine Fuels

Thomas Wallner, Andrew Ickes and Kristina Lawyer

Abstract The U.S. Renewable Fuel Standard (RFS2) requires a drastic increases in production of advanced biofuels up to 36 billion gallons over the next decade while corn-based ethanol will be capped at 15 billion gallons. Currently ethanol is the predominant alternative fuel and is widely distributed at 10 vol % blends in gasoline (E10). However, certain properties of ethanol make it less desirable as a blending agent in particular at higher blend levels. Therefore the engine- and vehicle-related properties of longer chain alcohols are evaluated in comparison to gasoline to determine their suitability as blending agents for spark-ignition engine fuels. This analytical study aims at providing comprehensive property data for a range of alcohol isomers with a carbon count up to C8. Relevant physical property data is used to determine the general suitability of longer chain alcohol isomers as blending agents based on factors such as melting point and boiling. Based on initial findings the scope of the study was narrowed down to alcohols in the C2–C6 range. It was determined that the engine- and combustion-relevant information is missing from the literature for a wide range of longer chain isomers. Thus fuel testing for engine-relevant properties such as lower heating value, knock resistance (RON, MON) and Reid Vapour Pressure (RVP) for alcohols up to C6 was performed as part of this study. Data suggests that the melting point of alcohols

F2012-B01-004

T. Wallner (✉) · A. Ickes · K. Lawyer
Argonne National Laboratory, DuPage County, Illinois, USA
e-mail: twallner@anl.gov

A. Ickes
e-mail: aickes@anl.gov

K. Lawyer
Michigan Technological University, Houghton, Michigan, USA
e-mail: klawyer@anl.gov

increases with increasing carbon count and all C7 and C8 isomers exhibit melting points in excess of $-40\text{ }^{\circ}\text{C}$ making their use as vehicle fuel questionable. Boiling points increase with increasing carbon count and *n*-structures generally have slightly higher boiling points than their respective *iso*-structures. Latent heat of vaporization decreases with carbon count, the mass-specific value for ethanol is triple that of gasoline, the energy specific ratio increases to a factor of 5. Alcohol fuels generally have a significantly lower RVP than gasoline, RVP decreases with increasing carbon count. Stoichiometric air demand and fuel energy content increase with carbon count. Knock resistance expressed as Research Octane Number (RON) and Motor Octane Number (MON) decreases significantly with increasing carbon count, *iso*-structures show increased knock resistance compared to their respective *n*-structures. This study is limited to analytical results as well as fuel property testing according to ASTM standards. Only properties of neat alcohols are evaluated in comparison to gasoline certification fuel, gasoline blend stock for ethanol blending and E10. The analysis of the reported properties is further focused on spark-ignition engine applications only. Future phases of this project will include the assessment of properties of multi-component blends as well as efficiency, performance and emissions testing on a modern direct-injection engine. While data for a limited number of commonly used alcohols such as ethanol and *iso*-butanol is available in the literature, little or no data is available for a majority of other alcohols and their isomers. In addition, engine-related data published in the past occasionally disregards the significant differences between alcohol isomers of the same chain length. This study offers a comprehensive review of physical properties of alcohols and their common isomers in the C2–C8 range as they relate to in-vehicle use and spark-ignition combustion engine application. Data presented in this paper suggests that higher alcohols have certain physical properties that might be desirable for blending with gasoline. Due to their oxygen content all alcohols have an inherent disadvantage in terms of energy content compared to non-oxygenated fuels. While this disadvantage becomes less pronounced with increasing carbon count, other less desirable properties such as a low RVP and reduced knock resistance become more dominant with longer chain length alcohols. In addition to merely evaluating properties, the selection of promising alcohols and blend levels will ultimately depend on the introduction scenario and target properties.

Keywords Alcohol fuels · Spark-ignition engine · Physical properties · Combustion · Knock resistance · RON · MON · RVP

1 Background

In the United States ethanol is the predominant alternative fuel for spark ignition engine applications and is widely used in blends of 10 vol % in gasoline (E10). Further, the U.S. Environmental Protection Agency (EPA) recently granted a

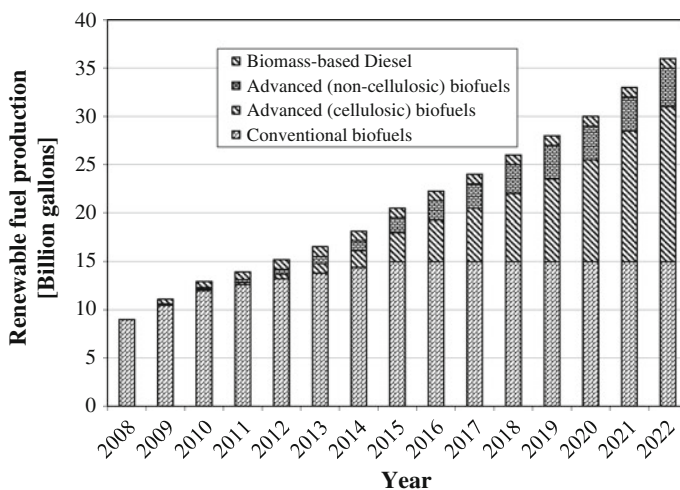


Fig. 1 Production targets according to the U.S. renewable fuel standard (RFS2) [7]

waiver for use of blends of 15 vol % of ethanol in vehicles starting from model year 2001 [1]. Although more than 10 Mio vehicles on the road today are Flex Fuel vehicles capable of operating on E85, only a small fraction of these vehicles are actually fueled on the high-level ethanol blend. At the same time, the U.S. Renewable Fuel Standard (RFS2) calls for a dramatic increase in production of alternative fuels until 2022 (see Fig. 1). Other alcohols beyond ethanol may possess properties which make them suitable for vehicle use, providing opportunities for further petroleum displacement.

A research project with the working hypothesis that a certain blend of gasoline with ethanol as well as higher alcohols could provide a fuel with properties superior to those of traditional gasoline-ethanol blends is currently underway at Argonne National Laboratory. In addition to ethanol, which is already widely used in blends with gasoline (E10) in the US market, alcohols with up to eight carbon atoms (C8—octanol) were considered for this study. Three groups of criteria were identified as critical to selecting suitable higher alcohols blends; (1) fuel properties, (2) production process, and (3) Emissions and Performance. The scope of the initial phase of the project, which is summarized here, focuses exclusively on the fuel properties of these higher alcohols. Other aspects which will be covered in later phases include the production process and potential synergies of certain mixed alcohols as well as the impact of alcohol fuels on engine performance and emissions characteristics. The final selection of promising alcohol fuel blends will be based on several sub-criteria within the three main groups with targets for near term, mid-term and long-term scenarios.

Table 1 Overview of C1–C8 alcohols

Common name	Carbon count	Chemical composition	Oxygen content (mass %)
Methanol	1	CH ₄ O	49.9
Ethanol	2	C ₂ H ₆ O	34.7
Propanol	3	C ₃ H ₈ O	26.6
Butanol	4	C ₄ H ₁₀ O	21.6
Pentanol	5	C ₅ H ₁₂ O	18.1
Hexanol	6	C ₆ H ₁₄ O	15.7
Heptanol	7	C ₇ H ₁₆ O	13.8
Octanol	8	C ₈ H ₁₈ O	12.3

2 Overview of Alcohol Fuels

Table 1 shows an overview of the alcohols with carbon counts from one to eight. Alcohols are characterized as organic compounds with a hydroxyl functional group (–OH) bound to a carbon atom. The table shows the common name of alcohols up to eight carbon counts together with their chemical composition. Alcohols contain oxygen as part of the hydroxyl group and the oxygen content is one of the main differentiating factors and will be used alternately with carbon count to distinguish between the different alcohols. For alcohols with a carbon count of 3 or higher, isomers exist that can be differentiated by their structure and the locating of the hydroxyl group. The straight chain isomer with the hydroxyl group connected to the terminal carbon is commonly referred to as *n*-isomer or *l*-isomer (e.g. *n*-butanol or *l*-butanol). The branched isomer with the OH-group at the terminal carbon is called *iso*-structure.

The properties of certain alcohol isomers with the same carbon count differ significantly based on structural differences. Also, there are significant limitations in the availability of property data especially for many of the less common isomers of longer-chain alcohols. Current production levels of the most common alcohol isomers, such as methanol, ethanol, *iso*-propanol, *n*-butanol and *iso*-butanol each exceed 1 billion lbs per year.

3 Physical Properties

This section covers the analytical assessment of alcohol fuels based on physical properties relevant to engine and vehicle operation. The melting point of a substance is critical to ensure that the fuel stays liquid regardless of region and season. Figure 2a shows the melting points of a large range of alcohol isomers as a function of carbon count with *l*- and *iso*-structures highlighted were applicable. Although there are several outliers, a general trend of increasing melting temperature with longer carbon chain length can be observed. Using –40 °C as a realistic upper limit shows that several hexanol and octanol isomers are close or

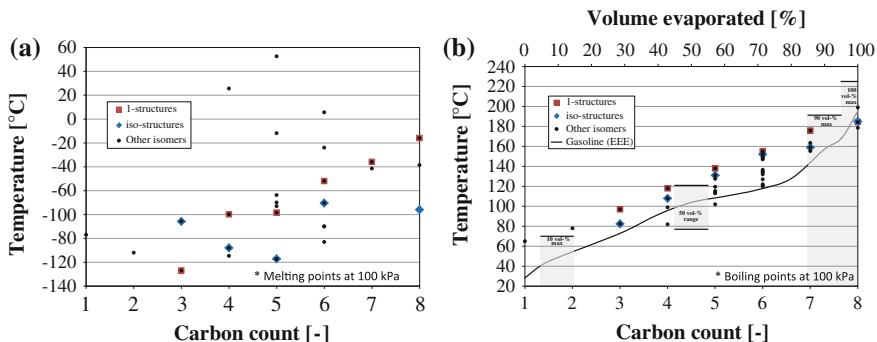


Fig. 2 a Melting points b boiling points of alcohols and distillation curve of gasoline

even exceed this threshold. It is also worth noting that *tert*-butanol far exceeds the threshold with a melting point of 25.5 °C.

Fuel evaporative behavior is critical to ensure proper engine cold start as well as hot operation. Since alcohols are single components, they have a boiling point rather than an evaporation curve typical for multi-component fuels such as gasoline. ASTM standard D4814 specifies certain points in the evaporative curve of gasoline fuels, specifically the point at which 10 vol % are evaporated at a maximum of 70 °C, 50 vol % between 77 and 121 °C and 90 vol % at a 190 °C maximum. The end point is limited to a 225 °C maximum. Figure 2b shows the boiling point of a range of alcohol fuels as a function of carbon count for *I*- and *iso*-structures as well as other isomers. A clear trend of increasing boiling temperature with increasing carbon chain length can be observed for the alcohols investigated in this study. In addition the *I*-structures show a slightly increased boiling point compared to the respective *iso*-structures. Boiling temperatures for the considered range of C1–C8 alcohols ranges from 65 °C for methanol to almost 200 °C for certain octanol isomers. Figure 2b also includes a distillation curve for certification gasoline (Tier II EEE U.S. Federal Emission Certification Fuel) displaying volume evaporated as a function of temperature (X-axis on the top). The fact that alcohols evaporate at a defined boiling point versus the distillation range typical for gasoline results in an extension of the gasoline curve at the boiling point of the alcohol if blended. Therefore, the boiling point is critical in influencing the evaporative behavior in particular when longer chain alcohols are used or when targeting higher blends levels.

Latent heat of vaporization is another critical factor influencing in-cylinder mixture preparation in engines. Heat of vaporization results in a temperature reduction inside the engine intake system for port fuel injection and in-cylinder for direct-injection engines since energy taken from the intake air is required to evaporate the fuel. Increased heat of vaporization is desirable particularly for direct injection engines because it can significantly reduce in-cylinder process temperatures thus reducing NOx emissions formation as well as knock propensity. As shown in Fig. 3a, mass-specific latent heat of vaporization decreases with

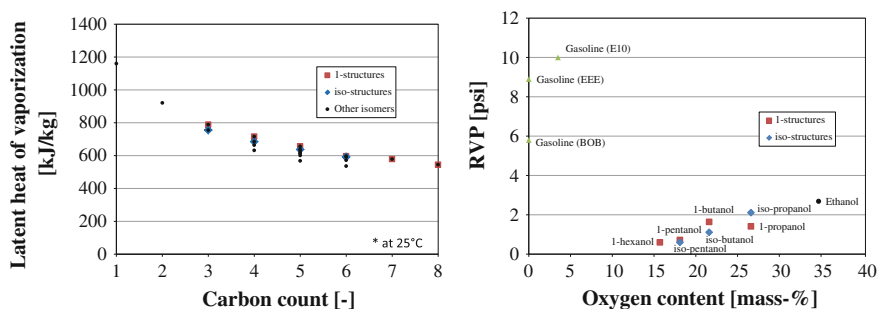


Fig. 3 a Latent heat of vaporization b Reid Vapor Pressure (RVP) for various alcohols

increasing carbon count. The differences in heat of vaporization within a group of alcohols are limited compared to the significant differences between different chain length alcohols. The energy needed to evaporate 1 kg of ethanol (921 kJ) is almost triple that of *iso*-octanol (350 kJ). For comparison, the latent heat of vaporization of gasoline is around 300 kJ/kg.

Vapor pressure is used to determine the volatility of gasoline and other spark-ignition engine fuels. The Standard Test Method for Vapor Pressure of Petroleum Products (Mini Method) according to ASTM 5191 was used to compare Reid Vapor Pressure (RVP) for the fuels considered in this study. This test method is suitable for testing samples with boiling points above 0 °C that exert a vapor pressure between 7 and 130 kPa (1.0 and 18.6 psi) at 37.8 °C. Based on comparative tests it was also determined that this method is applicable for gasoline/ethanol blends [1]. The RVP values for a range of gasoline fuels as well as alcohol isomers as a function of oxygen content are shown in Fig. 3b. While all tested fuels meet the boiling point requirements of 0 °C (see Fig. 2b), the two pentanol isomers as well as *l*-hexanol fall outside the specified vapor pressure range. The results show a clear trend of decreasing RVP with decreasing oxygen content for the alcohol fuels, while all tested alcohols display RVP values significantly below those of gasoline. ASTM D4814 specifies the maximum RVP for gasoline fuels with 9.0 psi as the maximum in “volatility attainment areas” and 7.8 psi in “volatility non-attainment areas”. In addition a 1 pound waiver was granted for gasoline/ethanol blends with at least 9 vol % and no more than 10 vol % of ethanol practically increasing the maximum to 10 psi. This is significant since low level ethanol blends (as well as methanol and propanol) show near-azeotropic behavior with an increase in RVP at low blend levels when mixed with gasoline [1]. In general, blending gasoline with higher alcohols (C4 and higher) is expected to decrease Reid Vapor Pressure regardless of blend levels. While lower RVP is desirable from an evaporative emissions point of view, too low an RVP can cause cold start issues and related increase in hydrocarbon emissions.

The stoichiometric air demand describes the mass ratio of air to fuel that is required to create a stoichiometric mixture. Assuming that the amount of air inside an engine is approximately constant for a given load, a decrease in stoichiometric

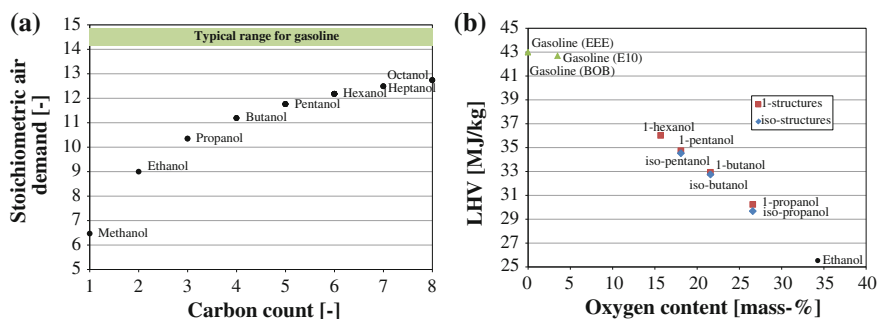


Fig. 4 a Stoichiometric air demand b Lower Heating Value (LHV) for alcohol fuels

air demand suggests that an increased amount of fuel is required to create a stoichiometric mixture. Figure 4a shows the stoichiometric air demand for the range of C1–C8 alcohols as a function of carbon count. Since air demand does not depend on molecular structures, there is no difference in air demand among isomers. However, as alcohols are characterized by an OH functional group, the fuel itself already contains oxygen (see Table 1). The impact of the single OH group on air demand decreases with increasing carbon count reflected in increased stoichiometric air demand. For reference the typical range of stoichiometric air demand for gasoline fuels (~ 14.5) is also shown in Fig. 4a.

Mass-specific fuel energy content, characterized by lower heating value (LHV) for several gasoline types and a range of alcohol isomers is shown in Fig. 4b as a function of fuel oxygen content. As can be clearly seen, increasing oxygen content of the fuel almost linearly reduces the lower heating value from approx. 42 to 43 MJ/kg for gasoline to approx. 26 MJ/kg for ethanol. This almost 40 % reduction in mass-specific energy content can be reduced with longer-chain alcohols such as butanol with a LHV penalty compared to gasoline of approx. 23 % or hexanol with a respective penalty of only 16 %. However, due to their oxygen content the energy per unit mass is still significantly reduced compared to the gasoline baseline. Among the alcohol isomers, *1*-structures show slightly higher lower heating values compared to their respective *iso*-structures.

Other relevant factors when evaluating the suitability of alcohol fuels for engine combustion include physical properties such as solubility in water and combustion-related factors such as laminar flame speeds and ignitability limits. Solubility of alcohols in water decreases with increasing carbon count; C1–C3 alcohols are fully miscible, miscibility decreases from C4–C8 alcohols and higher alcohols are immiscible with water. Solubility is particularly relevant because it influences transportability in pipelines [2]. The flammability limits of short-chain alcohols are similar to those of gasoline. At increasing chain length the upper flammability limit decreases while the more relevant lower flammability limits remains constant. Limited data is available to suggest trends in terms of laminar burning velocity of longer-chain alcohol fuels. Data available for C1–C4 alcohols suggests decreasing laminar flame speeds with increasing carbon chain length.

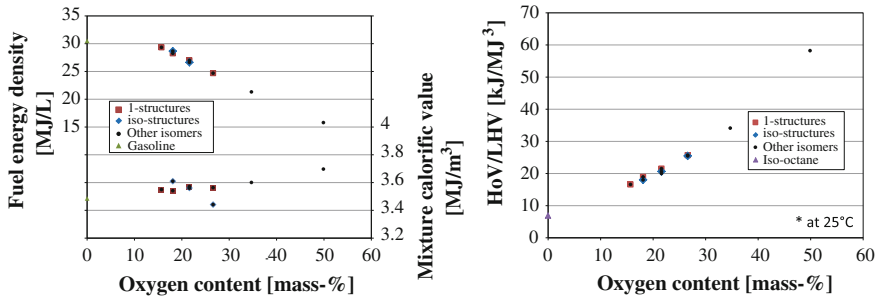


Fig. 5 a Energy content b energy-specific heat of vaporization of various alcohols

4 Engine-Related Properties

In addition to relevant physical properties of alcohols compared to gasoline discussed in the previous chapter, there are several critical engine-related properties that need to be considered when selecting alcohol fuels for blending with gasoline. While the lower heating value as a metric for mass-specific energy content is relevant when comparing fuels, the volumetric energy content of a fuel directly affects injection duration when used in an engine. This is particularly relevant since typical engine calibrations utilize injection duration as a metric for the amount of energy introduced to the engine and changes in injection duration influence the mixture formation process in particular for direct injection engines. The top portion of Fig. 5a shows the fuel energy density of gasoline as well as several alcohol isomers as a function of fuel oxygen content. Due to the increased density of alcohol fuels ($\sim 790\text{--}830\text{ kg/m}^3$) compared to gasoline ($\sim 740\text{ kg/m}^3$) the difference in volumetric energy content is not as pronounced as the gravimetric energy density (compare Fig. 4b). Nonetheless the volumetric energy content of ethanol ($\sim 21.3\text{ MJ/l}$) is still more than 30 % below that of gasoline ($\sim 31.6\text{ MJ/l}$) while that of *iso*-pentanol (28.3 MJ/l) is only approx. 10 % below the gasoline benchmark. The lower portion of Fig. 5a shows the mixture calorific value (right axis) for gasoline and alcohols versus oxygen content. The mixture calorific value is a metric for the energy content of a certain volume of stoichiometric air/fuel mixture; it is assumed that the fuel is introduced directly into the combustion chamber in which case the mixture calorific value is calculated based on lower heating value, stoichiometric air demand and air density [1]. The mixture calorific value for gasoline is approx. 3.5 MJ/m^3 , while the values for alcohols are slightly higher with approx. 3.55 MJ/m^3 for propanol, butanol and hexanol, 3.6 MJ/m^3 for ethanol and almost 3.7 MJ/m^3 for methanol. Assuming constant engine efficiencies and constant volumetric efficiency for the different fuels, an advantage in mixture calorific value directly translates into an improvement in engine torque.

Considerations analogous to the gravimetric versus volumetric energy content are the basis of determining the latent heat of vaporization per unit energy. The mass specific latent heat of vaporization shown in Fig. 3a is a useful metric to

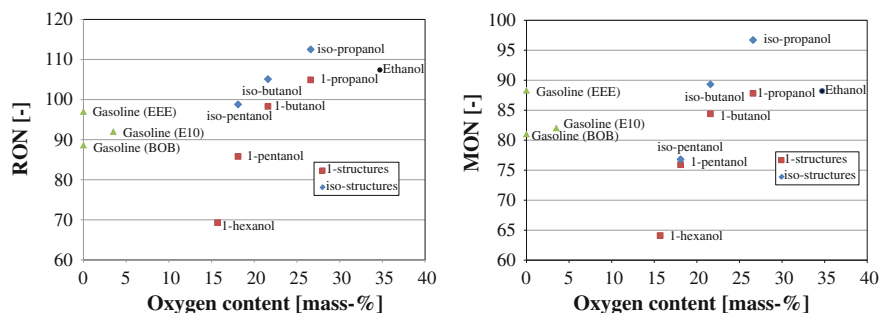


Fig. 6 a Research Octane Number (*RON*) b Motor Octane Number (*MON*) for gasoline and various alcohol fuels

compare fuels, the result in the engine is a cooling effect. This charge cooling effect is particularly pronounced for direct injection engines and can significantly improve the knock resistance [3–5]. Therefore, the engine-relevant metric would be the latent heat of vaporization normalized by the amount of fuel energy delivered to the engine. The quantification of this fuel-energy-specific heat of vaporization is shown in Fig. 5b as a function of fuel oxygen content. The latent heat of evaporation value of *iso*-octane (representative for gasoline) is approx. 7 kJ/MJ of fuel energy. For alcohols the value increases linearly with oxygen content and reaches a maximum for methanol. For comparison, the fuel-energy-specific latent heat of vaporization of ethanol is approx. 34 kJ/MJ which is almost a five-fold increase compared to gasoline (the mass-specific latent heat only increased by a factor of three as discussed earlier).

While the heat of vaporization potentially improves the knock behavior, the traditional measure for knock resistance is the octane number. Spark-ignition engine fuels are classified based on Research Octane Number (*RON*) according to ASTM D2699 and Motor Octane Number (*MON*) according to ASTM D2700. Although the applicability of *RON* and *MON* in modern, downsized, turbo-charged engines has been widely discussed [3–6], the values are still a commonly used benchmark for fuel characterization. Both, *RON* and *MON* are determined by comparing a fuel’s knock behavior to that of a mix of primary reference fuels using a single-cylinder CFR engine. Both, engine speed and operating temperatures are higher for *MON* determination compared to *RON*.

Figure 6a shows the measured *RON* values for a range of gasoline fuels as well as several alcohol isomers. Gasoline EEE has a higher *RON* value (~ 98) compared to both, a blend stock for ethanol blending (BOB at *RON* ~ 87) as well as a 10 vol % blend of BOB with ethanol (E10 at *RON* ~ 92). Alcohol fuels span a wide range of Research Octane Numbers with a general trend of decreasing *RON* with decreasing oxygen content. *iso*-structures generally have higher *RON* values than the respective *n*-structures. This difference accounts for approx. 7 points for propanol and butanol and increases to 13 points for pentanol. *iso*-propanol exhibits the highest *RON* of all tested fuels at ~ 112.5 , while *1*-hexanol has a *RON* of only

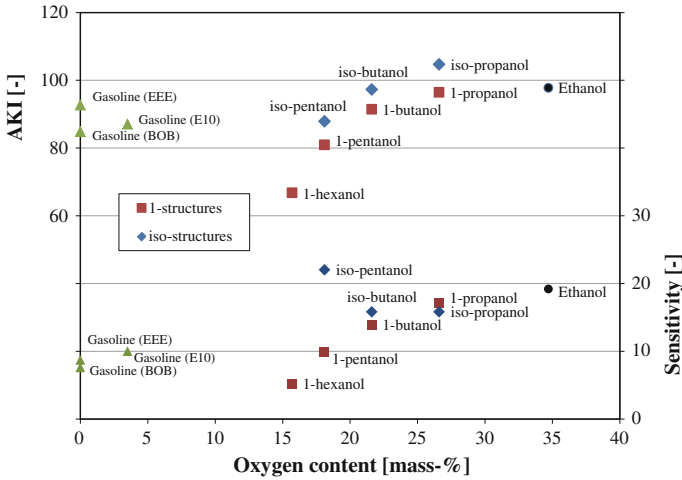


Fig. 7 AKI and sensitivity for gasoline and various alcohol fuels

69.3. It is also worth noting that Research Octane Numbers do not scale linearly when blending gasoline and alcohols as shown in [5].

Due to the higher test speed and operational temperatures, Motor Octane Numbers are typically lower than Research Octane Numbers. Figure 6b shows measured MON for the same range of gasoline and alcohol fuels. EEE features a MON of 88, BOB has a MON of 81 and E10 has a MON of 82. A trend in terms of decreasing MON with increasing alcohol chain length similar to RON behavior can be observed. Also, *iso*-structures display increased knock resistance compared to *n*-structures. However, while the RON difference increased with longer chain length, the advantage in MON of *iso*-structures over *n*-structures decreases from approx. 9 points for propanol to 5 for butanol and less than one point for pentanol.

Other widely used fuel characteristics derived from RON to MON values are the Anti-Knock Index ($AKI = (RON + MON) / 2$) and knock sensitivity ($RON - MON$). Figure 7 shows AKI and sensitivity as a function of oxygen content for gasoline and the range of alcohol fuels considered in this study. The AKI for E10 turns out to be 87 $[(82 + 92)/2]$ which is typical for regular pump gasoline (containing up to 10 vol % ethanol). *Iso*-propanol with a value of approx. 105 exhibits the highest AKI of all tested fuels. The previously identified trends of decreasing knock values with increasing chain length as well as improved values of *iso*-structures over *n*-structures remain unchanged. The advantage in AKI of *iso*-structures over *n*-structures remains almost constant with approx. 6–8 points regardless of chain length. This is due to the fact that sensitivity of *n*-structures decreases with increasing chain length while it increases for *iso*-structures as shown in the bottom of Fig. 7. Sensitivity of gasoline fuels is in the range of 8–10 which is considerable lower than most alcohols except for the longer chain *n*-structures of pentanol and hexanol.

5 Conclusions

An analytical assessment of the properties of alcohols up to C8 was performed to determine their suitability as fuels for spark ignition engines. While some, mainly shorter chain alcohols that are produced in quantities of more than 1 billion gallons annually are well characterized, little to no relevant property specifications are available for certain longer chain isomers. The following general trends can be derived based on increasing carbon chain length or decreasing oxygen content respectively. Specific differences between common structures, in particular *n*- and *iso*-structures are noted where applicable:

- The melting point of alcohols increases with increasing carbon count and several C7 and C8 isomers exhibit melting points in excess of $-40\text{ }^{\circ}\text{C}$ making their use as vehicle fuels questionable
- Boiling points increase with increasing carbon count and *n*-structures generally have slightly higher boiling points than their respective *iso*-structures
- Latent heat of vaporization decreases with carbon count, the mass-specific value for ethanol is triple that of gasoline, the energy specific ratio increases to a factor of 5
- RVP decreases with increasing carbon count and alcohol fuels generally have a significantly lower RVP than gasoline
- Stoichiometric air demand and fuel energy content increase with carbon count
- Knock resistance expressed as Research Octane Number (RON) and Motor Octane Number (MON) decrease significantly with increasing carbon count, *iso*-structure show increased knock resistance compared to their respective *n*-structures.

Overall, the Renewable Fuel Standard (RFS2) requires a significant increase in production of advanced, cellulosic and non-cellulosic biofuels. Longer-chain alcohols might turn out to be an interesting alternative to ethanol due to their properties which more closely resemble gasoline.

Acknowledgments This work was funded by the Iowa Corn Promotion Board as part of a project to determine properties of multi-component alcohol gasoline blends. The authors wish to thank Rodney Williamson and David Ertl of Iowa Corn Promotion Board/Iowa Corn Growers Association for their support and the valuable discussions. The submitted manuscript has been created by UChicago Argonne, LLC, Operator of Argonne National Laboratory (“Argonne”). Argonne, a U.S. Department of Energy Office of Science laboratory, is operated under Contract No. DE-AC02-06CH11357. The U.S. Government retains for itself, and others acting on its behalf, a paid-up nonexclusive, irrevocable worldwide license in said article to reproduce, prepare derivative works, distribute copies to the public, and perform publicly and display publicly, by or on behalf of the Government.

References

1. Environmental Protection Agency (EPA) (2011) Partial grant of clean air act waiver application submitted by growth energy to increase the allowable ethanol content of gasoline to 15 percent. Federal Register Vol. 76, No. 17. 2011
2. Whims S (2002) Pipeline considerations for ethanol. Department of agricultural economics. Kansas State University
3. Pischinger R, Klell M, Sams T (2002) Thermodynamics of internal combustion engines (in German: Thermodynamik der verbrennungskraftmaschine). Springer, Wien. ISBN 3-211-83679-9
4. Stein R, Polovina D, Roth K, Foster M et al (2012) Effect of heat of vaporization, chemical octane, and sensitivity on knock limit for ethanol–gasoline blends. SAE Int J Fuels Lubr 5(2):823–843. doi:[10.4271/2012-01-1277](https://doi.org/10.4271/2012-01-1277)
5. Kasseris E, Heywood J (2012) Charge cooling effects on knock limits in SI DI engines using gasoline/ethanol blends: part 1-quantifying charge cooling, SAE Technical Paper 2012-01-1275, doi:[10.4271/2012-01-1275](https://doi.org/10.4271/2012-01-1275)
6. Kasseris E, Heywood J (2012) Charge cooling effects on knock limits in si di engines using gasoline/ethanol blends: part 2-effective octane numbers. SAE Int J Fuels Lubr 5(2):844–854. doi:[10.4271/2012-01-1284](https://doi.org/10.4271/2012-01-1284)
7. ASTM standard ASTM D5191–10b (2007) Standard test method for vapor pressure of petroleum products (mini method). ASTM international, West conshohocken, PA, doi:[10.1520/D5191-10B](https://doi.org/10.1520/D5191-10B), www.astm.org
8. Andersen VF, Anderson JE, Wallington TJ, Mueller SA, Nielsen OJ (2010) Vapor pressures of alcohol-gasoline blends. Energy Fuels 24:3647–3654
9. Mittal V, Heywood J (2008) The relevance of fuel RON and MON to knock onset in modern SI engines. SAE Technical Paper 2008-01-2414, 1(1):1366–1380 doi: [10.4271/2008-01-2414](https://doi.org/10.4271/2008-01-2414)
10. Mittal V, Heywood J (2010) The shift in relevance of fuel RON and MON to knock onset in modern SI engines over the last 70 Years. SAE Int J Engines 2(2):1–10. doi:[10.4271/2009-01-2622](https://doi.org/10.4271/2009-01-2622)
11. Kalghatgi G (2001) Fuel anti-knock quality—part I. engine studies. SAE Technical Paper 2001-01-3584, doi:[10.4271/2001-01-3584](https://doi.org/10.4271/2001-01-3584)
12. Kalghatgi G (2001) Fuel anti-knock quality—part II. Vehicle studies—how relevant is motor Octane Number (MON) in modern engines? SAE Technical Paper 2001-01-3585, 2001, doi:[10.4271/2001-01-3585](https://doi.org/10.4271/2001-01-3585)
13. Section 201–202 Renewable Fuel Standard (RFS) Energy Independence and Security Act of 2007 (Pub. L. 110–140, originally named the CLEAN Energy Act of 2007)

Improvement of the Automotive Spark Ignition Engine Performance by Supercharging and the Bioethanol Use

Constantin Pana, Nicolae Negurescu and Alexandru Cernat

Abstract The general objective of this paper is application of the supercharging method and bioethanol use at the spark ignition engine for improving performance of power and torque, improving engine efficiency, decrease of the emissions level and increases of the engine specific power. The paper brings an important contribution to pollution problems solving in large urban areas, the solution can being easily implemented on spark ignition engines in running, even on the old designs which can be converted to fit the current rules of pollution. A modern method to increase efficiency and specific power of the spark ignition engines is supercharging. Supercharging is common for diesel engines, but for SI engines becomes restrictive because of the main disadvantages represented by abnormal combustion phenomena with knock, exhaust gases temperature increasing, engine thermal and mechanical stresses increasing. By using modern control methods of the combustion, supercharging becomes an efficient method even for SI engine. The theoretical and experimental investigations were performed on a 1.5L aspirated spark ignition engine with MP injection which was supercharged. The supercharged engine was fuelled with gasoline-bioethanol blends. The use of bioethanol at supercharged SI engine assures an efficient cooling effect of the intake air due to its higher heat of vaporization. The intake air cooling effect leads to a volumetric efficiency increasing

F2012-B01-007

C. Pana (✉) · N. Negurescu · A. Cernat
Department of Thermotechnics, Engines, Thermal Equipments and Refrigeration
Installations, University Politehnica of Bucharest, Bucharest, Romania
e-mail: constantinpana@yahoo.com

N. Negurescu
e-mail: nnegurescu@yahoo.com

A. Cernat
e-mail: cernatalex@yahoo.com

and the knock appearance risk is reduced. For to achieve of the research objectives the following methodology was used: modelling of the thermo-gas-dynamics processes inside engine cylinder for the theoretical evaluation of engine energetic performance; experimental investigations carrying out on the test bed of the SI engine in two versions: aspirated engine and supercharged engine fuelled with gasoline- bioethanol blends, respectively. For to achieve of the research objectives the following methodology was used: modelling of the thermo-gas-dynamics processes inside engine cylinder for the theoretical evaluation of energetic and pollution performance for aspirated engine and also for of the supercharged engine fuelled with gasoline-bioethanol blends in order to decrease the experimental investigations volume; experimental investigations carrying out on the test bed of the SI engine in two versions: aspirated engine and supercharged engine fuelled with gasoline-bioethanol blends, respectively; the interfacing of the electronic control units for the supercharged spark ignition engine fuelled with gasoline- bioethanol blends. The obtained results of the research are: development of a physic-mathematical model to simulate thermo-gas-dynamics processes inside engine cylinder; determining the bioethanol influences on the engine cylinder filling; determining the bioethanol influences on the supercharged spark-ignition engine combustion process; engine efficiency increasing by up to 10 %, specific power increasing by up to 33 %, pollutant emission levels reduction (was obtained a reduction of 20 % for NO_x emissions, a 10 % reduction of CO emission and a 13 % reduction of HC emission); establishing the optimal correlation between dosage—electric spark advance—boost pressure—exhaust gases temperature—coefficient of excess air on one hand and functional regime of the engine on the other hand. The abnormal combustion phenomena with knock study in this paper were not developed. As a research novelty is the solution for use of gasoline- bioethanol blends at the supercharging SI engine. Original elements of the research are: application of the supercharging procedure to an aspirated car spark ignition engine; use of gasoline- bioethanol blends as an injected fuel in blower downstream with effect of cooling the compressed air. The SI engine supercharging and use of gasoline- bioethanol blends is a good method to efficiency and power performance increasing. The pollutant emissions level decreases due to the improvement of the combustion processes. Bioethanol can be considered as an efficient anti-knock agent.

Keywords Supercharged engine · SI engine · Downsizing · Knock

1 Introduction

An efficient method to increase thermal efficiency and specific power of the spark ignition engines is supercharging [1, 2]. Supercharging is common for diesel engines, but for SI engines becomes restrictive because of the main disadvantages represented by abnormal combustion phenomena with knock, exhaust gases

temperature increasing, engine thermal and mechanical stresses increasing [3]. Supercharging is a significant method for the specific power increasing of the spark ignition engine which can be assured by the increase of indicated mean effective pressure. This efficient method allows the use of the downsizing and down speeding concepts which applied at the SI engines represent modern solutions for a lower displacement engines development (compact gauge and low costs), with a lower speed for maximum power/maximum torque comparative to aspirated engines (for the same or higher power/torque values), with favourable influences on engine thermal and mechanical stress, thermal efficiency, pollutant emissions and wear. Supercharging was considered a common method used for IMEP increase for diesel engine only. The main issues of spark ignition engine supercharging are represented by possibility of knocking phenomena appears, exhaust gases temperature increases, engine thermal–mechanical stress increases.

Nowadays modern management of SI engine running allows the supercharging use also for the spark ignition engines. Thus, the engine operation electronic control can assure every time an optimal correlation between supercharging pressure—compression ratio—spark ignition timing—supercharging air temperature—dosage-exhaust gases temperature that can allows the spark ignition engine operation without knocking combustion and with remarkable energetically and polluting performance. For example, at the supercharging use the engine thermal efficiency could be increased by 20 %, the specific power could be increased by up to 20 %, and the pollutants emission level could be reduced (is estimated to obtain a reduction of over 5 % for NO_x emissions, a 15 % reduction of CO emission and a considerable reduction in CO₂ emission) [4].

During the last time the supercharging of SI engines became the most efficient method of increasing their performance from the point of view of energetically and polluting terms [5, 6].

Due to sever national and international pollutant regulations for automotive SI engine, especially for CO₂, the research programs are leaded for alternative fuels use and for engine thermal efficiency improvement which is directly related to CO₂ emission. Among the alternative fuels used for automotive SI engine bioethanol represents a viable fuel due to its unlimited manufacturing sources. The use of bioethanol at supercharged SI engines assures an efficient intake air cooling effect due to its higher heat of vaporization. The intake air cooling effect leads to a volumetric efficiency improvement and reduces the knock risk developed. The higher bioethanol octane number (RON 106-114) increases the auto-igniting resistance of the end-gas and it may be considered as an efficient antiknock agent. The good burning properties of the bioethanol comparative with the gasoline (greater burning speed, smaller carbon content and larger oxygen content at molecular level) assure the combustion efficiency increases. These advantages of the bioethanol use are added at the supercharged SI engine typically distinguished advantages: thermal efficiency and specific power increase and pollutant emissions decrease.

In order to use bioethanol as alternative fuel for a supercharge SI engine the following methods can be use [7, 8]:

1. The engine can be fuelled with bioethanol- gasoline blends by:
 - (a) intake manifold bioethanol-gasoline blends injection (MP injection)
 - (b) in-cylinder direct bioethanol-gasoline blends injection
2. The injection of bioethanol in the intake manifold after compressor (an intense local cooling effect of the compressed air is achieved) and a separately injection of gasoline in the intake manifold in intake valve port or direct injection in cylinder.

The paper objectives are the increase of the specific power, of the thermal efficiency and the decrease of the pollutants emissions level for an automotive spark ignition engine by supercharging method and bioethanol fuelling. The authors have the goal to apply supercharging method to a serial automotive aspirated spark ignition engine. The SI engine supercharged was fuelled with ethanol- gasoline blend (E20) by MP injection.

1.1 Engine In-Cylinder Thermo-Gas Dynamic Processes Simulation

Engine in-cylinder processes simulation was developed for a 1.5 l engine. In order to define the energetically performance and the cycle performance parameters, a zero dimensional and unizonal physic-mathematical model was developed [9]. There have been considered the following hypothesis:

- (a) The motor fluid is treated as a perfect gas.
- (b) The system is thermodynamically homogenous, thus its every point has the same temperature and pressure.
- (c) The entire combustion developers neglecting the chemical reactions that leads to intermediate reaction products.

The model takes into consideration the local cooling effect produced by ethanol vaporisation and relieves the influence of this parameter on cylinder filling and engine performances. The model uses a Vibe combustion formal law and takes into consideration the heat transferred to the walls, which has been calculated with Woschni formula (1994).

For knock avoiding, the combustion duration was established shorter than end-gas auto ignition delay, parameters being evaluated by Douaud and Evzat equation [2]. For program calibration the experimental investigations results were used and the considered model hypotheses were verified. The modelling processes was developed for the aspirated engine and for the supercharged engine designed and built in the laboratories of the Department of Thermotechnics, engines, thermal equipments and refrigeration installations from University Politehnica of Bucharest at different engine operating regimens. Different supercharging pressures, p_s —absolute pressure—and temperatures, T_s , of the blower exhaust cooled air were taken into consideration.

For knock avoiding the reach dosages in the area $\lambda = 0.8-1$ and cooling of the inlet air were used. For each operation regime, the spark ignition timing was set up for knock avoiding. The modelling results for full load and speed of 2,500 rpm are shown in Figs. 2, 3, 4.

2 Experimental Investigations

The experimental researches were carried on an automotive SI engine 1.5 L. The engine mounted on a test bench (Fig. 1) was equipped with the next necessary instruments for measuring operations: AVL ALPHA 160 eddy current dynamometer equipped with throttle actuator that work in parallel with the dynamometer in order to operate the throttle, real time AVL data acquisition system for processing and storage of measured data's, AVL in-cylinder pressure transducer line, AVL gas analyzer, Khrone Optimass mass flow meter, engine inlet air flow meter, thermo resistances for engine cooling liquid temperature, engine oil and air intake temperatures and thermocouples for exhaust gas temperature, manometer for air pressure from engine intake manifold. All instrumentation was calibrated prior to engine testing. The experimental investigations were carried out on the aspirated engine and also the supercharged engine. In this paper the experimental investigation results for a turbocharged E20 fuelled engine are shown. (The supercharge system is equipped in this first stage with a variable-geometry turbine [10]. As novelty character of the research, in the next research stage the engine will be equipped with a compressor mechanically actuated with variable transmission ratio for supercharge pressure modification. The bioethanol will be injected into the compressed air in order to assure an efficient cooling).

Experimental research's carried out to obtain fuel consumption characteristics for different speeds and engine full load and to determinate the energetically and pollutant engine performance. At each engine operating regime for maximum pressure limitation and knock avoiding, the dosage, spark ignition timing and supercharge pressure were modified. Thus, an optimal correlation between supercharge pressure-compression ratio- dosage-spark timing-exhaust gases temperature was establish. Based on fuel consumption characteristics were obtained some graphic representations for different parameters such as: effective power, indicated specific fuel consumption (ISFC), maximum pressure, pollutants emissions level (HC, CO, and NO_x) versus air-fuel ratio λ , at different boost pressure values and engine operation regimes.

3 Theoretical and Experimental Investigations Results

The results of theoretical and experimental investigations presented in Figs. 2, 3, 4 show good correlation between them.

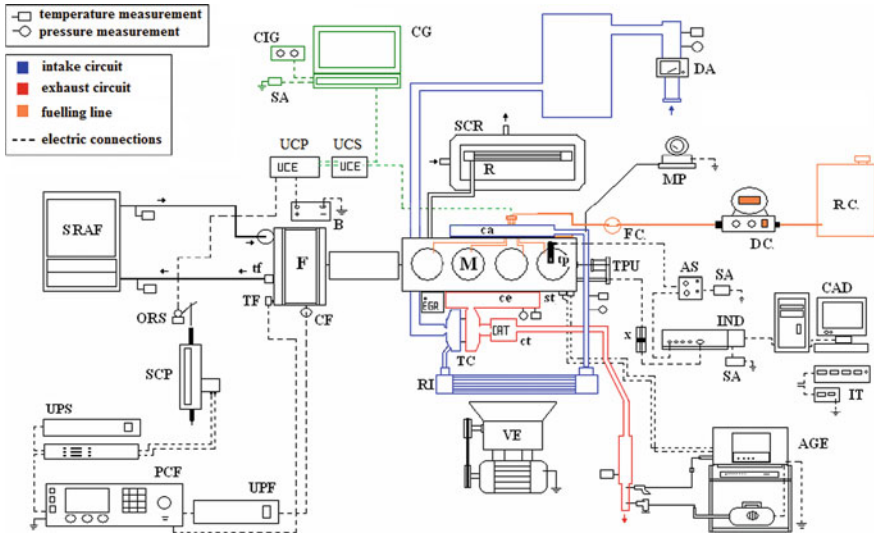
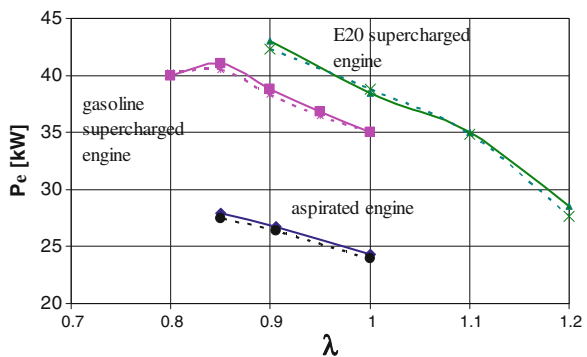


Fig. 1 Test bed schema. AGE exhaust gas analyzer; AS charge amplifier; B battery; ca intake manifold; CAD data acquisition computer; ce intake manifold; CF dyno power cell; CG fuelling system computer; CIG injectors actuation; ct three way catalyst; DA air flowmeter; DC fuel flowmeter; EGR exhaust gas recirculation valve; F eddy current dyno; FC fuel filter; IND Indimodul 621 data acquisition unit; IT temperature indicators; M Daewoo 1.5 spark ignition engine; MP supercharging pressure manometer; ORS throttle; PCF dyno command panel; R engine cooler; RI intercooler; RC fuel reservoir; SA power supply; SCF throttle actuator servomotor; SRAAF dyno cooling system; st gas analyzer speed sensor; TC turbo compressor; tf dyno cooling water temperature sensor; TF dyno speed transducer; tp cylinder pressure transducer; TPU angle encoder; UCP principal electronic control unit; UCS secondary electronic control unit; UPF dyno power unit; UPS throttle actuator servomotor power unit; VE cooling electric fan for intercooler; x electronic emitter–receptor

Fig. 2 Engine power versus air–fuel ratio at full load and 2,500 rpm—1.4 bar boost pressure



Supercharging pressures used are in the range of 1.3–1.8 bar. Comparative to the aspirated engine, the maximum pressure increases with almost 100 % for a supercharging pressure (p_s) of 1.8 bar at engine full load and 4,800 rpm (speed of

Fig. 3 ISFC versus air–fuel ratio at full load and 2,500 rpm—1.4 bar boost pressure

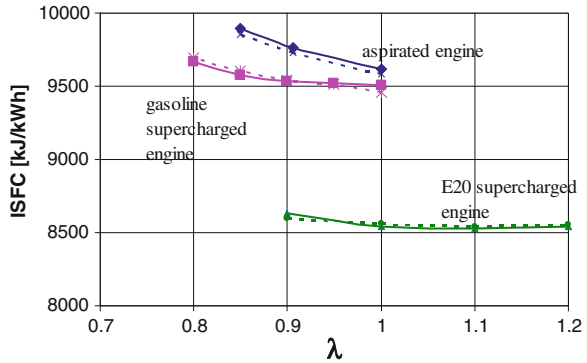
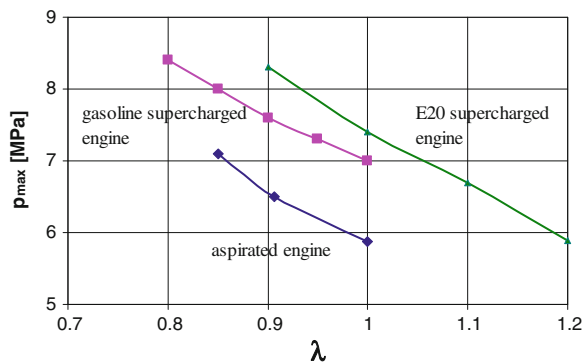


Fig. 4 Maximum pressure versus air–fuel ratio at full and 2,500 rpm—1.4 bar boost pressure



maximum power). High value of maximum pressure leads to the limitation of supercharging pressure at 1.4 bar when the increases of maximum pressure value (~with 50 % comparative to classic solution) is acceptable for the engine reliability. For this supercharging pressure, the engine maximum power increases with 33 % (from 65 kW for aspirated engine to 86 kW for supercharged engine). In order to avoid the knocking and to limit the maximum pressure, the ignition angle value optimization was achieved. The results of the theoretical and experimental investigations are presented in the Figs. 2, 3, 4, 5, 6, 7. The maximum torque value of the aspirated engine obtained at 3,000 rpm is establish at 2,500 rpm for the supercharge engine and the maximum power at 3,700 rpm comparative to 4,800 rpm for aspirated engine. Thus, by supercharging use the down speeding concept can be applied and the mechanical stresses and engine wear are reduced.

The theoretical and experimental results at full load regime and 2,500 rpm for the aspirated engine and also for the supercharged one (1.4 bar boost pressure) are presented in Figs. 2–7.

Thus, a good correlation between the theoretical and measure results is observed from the Figs. 2, 3 (continuous line-measured results; discontinuous line-calculated results).

Fig. 5 CO emission versus air–fuel ratio at full load full load and 2,500 rpm—1.4 bar boost pressure

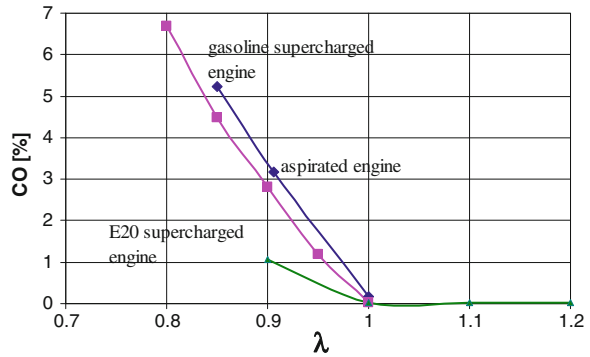
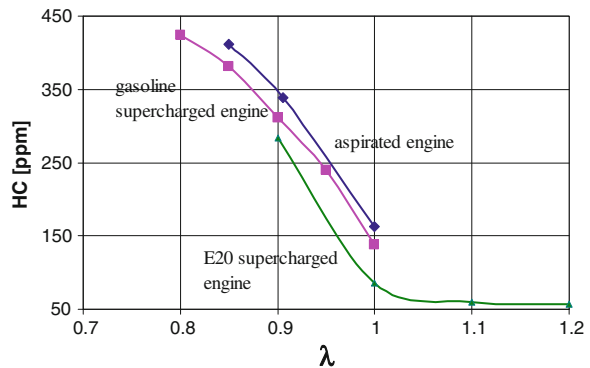


Fig. 6 HC emission versus air–fuel ratio at full load 2,500 rpm—1.4 bar boost pressure



By supercharging the engine power increases with $\sim 55\%$ for all air-fuel ratios, Fig. 2, engine efficiency being improved, Fig. 3. For stoichiometric dosage, the ISFC decreases with $\sim 3\%$ by supercharging for gasoline fuelling and with $\sim 10\%$ for E20 fuelling. For knock avoiding at supercharged engine much reach dosages were used ($\lambda = 0.8-1$). At the same dosage, for bioethanol E20 use the power of the supercharged engine increases with $\sim 10\%$ comparative to the supercharged gasoline fuelled engine due to the cooling effect produced by bioethanol vaporisation and to the combustion improvement.

Bioethanol fuelling allows engine operation at much leaner mixtures without knocking running, the power for stoichiometric dosage of the supercharge engine being obtained for a much leaner dosage, $\lambda = 1.1$, but for a 10% lower specific fuel consumption. The supercharging method also leads to the increase of the maximum gas pressure with unfavourable influences on mechanical stresses. For maximum gas pressure limitations, the authors limits the supercharging pressure at 1.4 bar (the theoretical and experimental investigations were developed for a wide area of supercharging pressures, 1.1–1.8 bar) for which, at stoichiometric dosage and also for reach dosages, the maximum pressure rises with 18% for gasoline fuelling and with 23% for E20 fuelling. In the area of lean dosages, $\lambda = 1.2$, for E20 fuelling, the supercharged engine in-cylinder maximum pressure is at the same level comparative

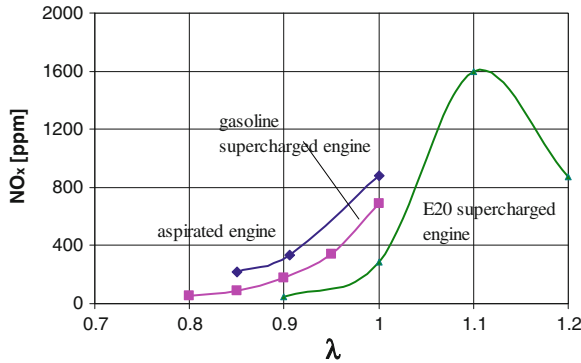


Fig. 7 NO_x emission versus air–fuel ratio at full load and 2,500 rpm—1.4 bar boost pressure

to gasoline engine. Authors appreciate that at these levels of maximum pressure values, the engine thermo-mechanical stresses are not critical and engine design major modifications are not required. The improvement of the combustion process by supercharging use at spark ignition engine leads to the favourable effect of CO and HC emissions level decreases for gasoline fuelled engine (with 10 and 13 %, respectively, at stoichiometric dosage and more significantly for reach dosages). For E20 the reduction of those two emissions is more accentuated, due to a lower C content and better combustion properties for bioethanol.

Regarding the NO_x emission a reduction of 20 % is assured at stoichiometric dosage and reaches dosages, at gasoline and also much more at E20 fuelling, because of the local cooling effect produced by bioethanol vaporisation. Instead, in the area of much leaner dosages, the NO_x concentration pronounced increases, over the level established for aspirated gasoline engine, because of the oxygen content increases. In terms of theoretical investigations, authors appreciates that thru the extension of the lean dosages area, $\lambda = 1.2$, the NO_x emission concentration significantly decreases, with the effect of supercharged engine power reduction (power that always remains bigger comparative to the aspirated engine).

4 Conclusions

From the theoretical and experimental investigations results analyze the following conclusions can be formulated:

1. SI engine supercharging is a method to obtain engine efficiency and specific power/torque performance increasing.
2. At bioethanol use a supplementary increase of the engine efficiency and power/torque is obtained.
3. The utilisation of the supercharge method for SI engine allows the significant reduce of the CO and HC emissions.

4. At bioethanol use for supercharge engine the reduction of CO and HC emissions are more significant due to much better combustion properties of bioethanol that allows lean dosages use.
5. SI engine supercharging method use leads to a significant decrease of NO_x for gasoline supercharged engine, in the area of stoichiometric and reach dosages.
6. For bioethanol use at supercharged engine the reduction of NO_x is more important in the area of $\lambda > 1.1$ dosages, were the strategy of engine load qualitative adjustment can be applied.
7. The thermo-mechanical stresses of the supercharged engine are much higher comparative to the aspirated engine and can be controlled by supercharging pressure limitation, without engine design major modification.
8. Knock is the most important limiting factor of the supercharging engine. An optimum correlation establish between air boost pressure-air boost temperature—compression ratio-dosage-spark ignition advance-exhaust gas temperature-brake mean effective pressure, brake specific fuel consumption leads to the avoiding of knocking phenomena.
9. Supercharging represents an efficient method of he engine downsizing and down speeding concepts use.
10. Bioethanol can be defined as an efficient agent for knock avoiding.

References

1. Heywood JB (2005) Engine research center—2005 Symposium, University of Madison, Wisconsin, 8–9 June 2005
2. Heywood JB (1988) Internal combustion engines fundamentals. McGraw-Hill Book Company, New York
3. Khiar D, Lauber J, Guerra TM, Floquet T, Colin G, Chamaillard Y (2008) Turbocharged spark ignition engine modelling and control strategy. *Int J Veh Des* 48(3–4)
4. Wang LS, Yang S (2006) Turbo-cool turbo charging system for spark ignition engines. *Proc Inst Mech Eng, Part D: J Automob Eng* 220(8)
5. Ibrahim A, Bari S (2010) An experimental investigation on the use of EGR in a supercharged natural gas. *Fuel* 89(7):1721–1731
6. Novatil J, Polasek M, Vitek O, Macek J, Baumrnek P (2003) Simulation of supercharged and turbocharged small spark ignition engine. *Mecca* 3
7. Negurescu N, Pana C, Popa MG, Cernat A, Soare D (2006) Aspects of using ethanol in SI engines. In: FISITA Congress, Yokohama
8. Pana C, Negurescu N, Popa MG, Cernat A, Soare D (2007) Aspects of the use of ethanol in spark ignition engine, paper no. JSAE 20077271 (SAE 2007-01-2040) 2007 JSAE/SAE International Fuels and Lubricants Meeting, Kyoto, Japan, CD, ISBN 978-4-915219-92-4
9. Dragomir C, Pana C, Negurescu N, Cernat A (2012) Theoretical and experimental investigations of the engine turbocharging. *Buletin Institut Politehnic Iasi, Tom LVII(LXI), Fasc. 2*
10. Pana C, Negurescu N, Popa MG, Cernat A (2010) Investigations regarding the use of the turbocharging and bioethanol at SI engines. *Buletin Institut Politehnic Iasi, Tom LVI(LX), Fasc. 4*

Theoretical and Experimental Investigations on the LPG Fuelled Diesel Engine

Niculae Negurescu, Constantin Pana and Alexandru Cernat

Abstract For energetically performance improvement and pollution level decreases of diesel engine different methods were applied, as the modifying of the energetically solution, exhaust gases after-treatment and some alternative fuel use (ethanol, methanol, biodiesel, DME, CNG, LPG e.g.) in different fuelling solution as direct injection or intake fuelling. Thought, the available information's in the trade literature for a complete analyse of alternative fuel diesel engine performances are insufficient. This happens also because of the operating and design particularities of the diesel engines used for experimental researches. In the paper the authors show the results of an theoretically and experimental investigations achieved on a 1.5 L common rail diesel engine dual fuelled with LPG and diesel fuel by diesel-gas method. The diesel-gas method is simple and can be applied with minimal modifications also for the engines in use. Is very difficult to use only LPG at the diesel engine because it has an auto ignition high endurance ($CN = -2$ to -3), different fuelling methods being use. By diesel-gas method the LPG is injected in the inlet manifold and forms with the air a homogeneous mixture, ignited by a diesel fuel pilot, the combustion being developed thru the homogeneous mixture from the combustion chamber. The general objective of this paper is the reduction of the diesel engine pollutant emissions by LPG use, without affecting the energetically performances. The specific objectives of this research are the establishment of the optimal LPG cycle dose and setup of the diesel engine optimal adjustments for all engine operating regimes.

F2012-B01-009

N. Negurescu (✉) · C. Pana · A. Cernat
Department of Thermotechnics, Engines, Thermal Equipments and Refrigeration
Installations, University Politecnica of Bucharest, Bucharest, Romania
e-mail: nnegurescu@yahoo.com

C. Pana
e-mail: constantinpana@yahoo.com

Keywords Alternative fuel · Diesel engine · Smoke · LPG

1 Introduction

The LPG use for diesel engine is limited by its higher autoignition resistance. From this point of view the LPG can't be use on diesel engines as single fuel without some special additives in order to obtain a fuel with an acceptable cetane number and a stable autoignition. As cetane number improvement additives were used DTBP (Di-Tertiary-Butyl-Peroxide), 2EHN (2-ethyl-hexyl-nitrate) or DME (dimethyl ether), [1]. The additive use implies a serial of exploitation difficulties regarding safety issues and expensive cost price. Another method of diesel engine conversion into a spark ignition engine implies important disadvantages as engine major design modifications (compression ratio reductions and the adapting of an ignition system) and reduction of the engine efficiency comparative to the classic diesel engine.

From practical reasons the most common method for engine fuelling with gaseous fuels, LPG type, is the formation of the mixture outside the engine cylinder. The air-gaseous fuel mixture has a higher homogeneity rate and because of that the mixture repartitions between the engine cylinders is more uniform. This particularity offers advantages in efficiency and pollution level, [2–6]. However, intake system LPG fuelling method brings as disadvantage the reduction of inlet air quantity [7–11]. For normal aspirated engines this leads to the reduction of the engine power. For supercharged engines the increases of supercharging pressure eliminate this issue. For diesel-gas method, the ignition of the LPG-air homogeneous mixture assured by a diesel fuel pilot injected into combustion chamber is followed by high speed flame propagation thru the air-LPG mixture, mixture defined by a significant homogeneous state.

LPG knock resistance is higher comparative to gasoline, defined by an octane number bigger with ~ 15 units. This fact allows the running of the LPG fuelled engine at higher compression ratio, specific to diesel engines, using sufficiently lean air-LPG mixtures. For the establishing of dosage area that provide engine normal running, the inlet LPG quantity is limited from the consideration of knock, brutal running avoiding, pressure rate limitation and occurrence of flame incomplete propagation (flame extinction into the gas volume).

The LPG injectors are mounted on the engine inlet manifold and actuated by a second electronic control unit connected back tot back with the engine ECU. The dual fuelling system is very flexible one and offers the multiple possibilities for the modification of different parameters such as: diesel fuel injection timing and duration, LPG injection duration, e.g. The engine power performance was maintained at the same level comparative to the classic solution. Thus the operating regimes setup implies the decrease of the diesel fuel quantity at the increases of LPG cycle dose.

2 Experimental Investigations

The experimental researches were carried on an automotive diesel engine, type K9K –1.5 dci, 50 kW/4,000 rpm equipped with a LPG injection system, at different engine operating regimens and for different substitution percents of the diesel fuel with LPG. The experimental engine was mounted on a test bench, Fig. 1, equipped with the next necessary instruments for measuring operations: Schenck E90 eddy current dynamometer equipped with throttle actuator that work in parallel with the dyno in order to operates the control lever of the injection pump, real time AVL data acquisition system for processing and storage of measured data's, AVL in-cylinder pressure transducer line, AVL gas analyzer and opacimeter for Diesel engines, Khrono Optimass mass flow meters, engine inlet air flow meter, thermo resistances for engine cooling liquid temperature, engine oil and air intake temperatures and thermocouples for exhaust gas temperature, manometer for air pressure from engine intake manifold, LPG gas detector for test bad cell. All instrumentations were calibrated prior to engine testing. Experimental research's carried out to obtain fuel consumption characteristics for different speeds and engine full load and to determine the energetically and pollutant engine performances. Based on fuel consumption characteristics were obtained some graphic representations for different parameters such as: brake specific fuel consumption (BSFC), pollutants emissions level (HC, CO₂, NO_x, smoke) versus to LPG substitute ratio, x_c . In order to study the in-cylinder combustion process, the influence of diesel fuel substitution by LPG dose, 50 pressure diagrams form successive cycles were register.

The engine power could increases at the LPG fuelling but in order to not affect engine reliability and to improve engine running by maintaining or improving its efficiency and to decrease the emissions level, the authors choose to maintain the standard engine power value. The fuelling system for LPG uses an injectors unit connected to engine intake manifold and controlled by a LPG electronic control unit in order to establish the LPG cycle dose for every operating regime.

The LPG electronic control unit works in parallel with the main ECU of the engine and is connected to a computer which allows the modification of the injectors opening duration. Thus is achieved the reduction of diesel fuel cycle quantity at the increase of LPG dose and the maintaining of the engine power at the same level.

3 Experimental and Theoretical Results

The experimental investigations were developed at different engine running regimes for diesel fuel and LPG dual fuelling at different diesel fuel substitute ratios, energetically defined x_c .

Figure 2 shows the p - α variation pressure diagrams, averaged and smoothed, at 100 % load and 4,000 rpm speed for different diesel substitute ratios by LPG, x_c .

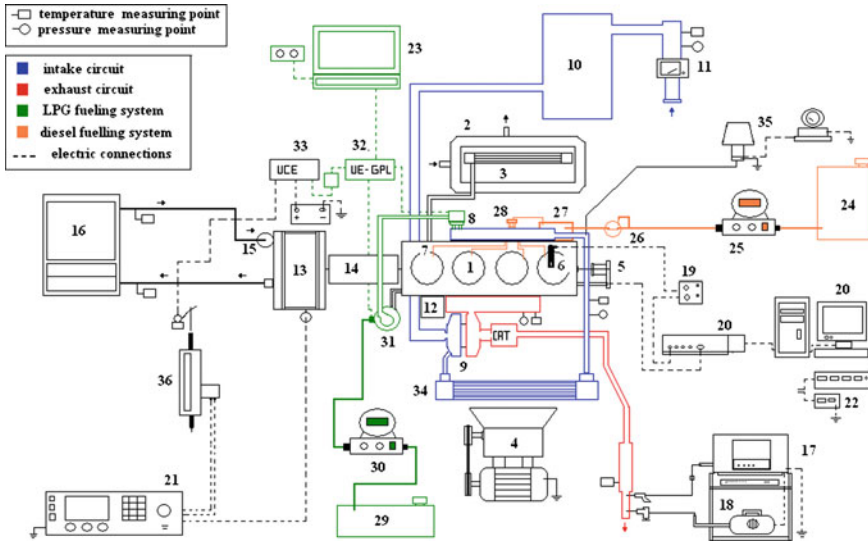


Fig. 1 Test bed schema 1 1.5 dci diesel engine, 2 engine cooling system, 3 engine water cooler, 4 intercooler fan, 5 engine angular encoder, 6 AVL piezoelectric pressure transducer, 7 diesel fuel injector, 8 LPG injector, 9 Turbocharger, 10 intake air drum, 11 intake air flow meter, 12 exhaust gas recirculation, 13 Schenck E90 dyno, 14 dyno-engine coupling, 15 Schenck E 90 dyno cooling water pump, 16 dyno cooling system, 17 AVL Dicom 4000 gas analyser, 18 AVL Dicom 4000 Opacimeter, 19 AVL charge amplifier, 20 PC + AVL data acquisition system, 21 Schenck E 90 dyno controller, 22 temperatures displays: **a** exhaust gas, **b** intake air, **c** engine oil, **d** engine cooling liquid, **e** engine oil pressure, 23 diesel fuel and LPG injection control Laptop, 24 diesel fuel tank, 25 diesel fuel mass flowmeter, 26 fuel filters, 27 high pressure pump for common Rail, 28 Common Rail, 29 LPG tank, 30 LPG mass flowmeter, 31 LPG vaporizer, 32 LPG ECU, 33 diesel engine ECU, 34 intercooler, 35 supercharge pressure measuring system, 36 throttle actuator

The experimental investigations mark out the influence of LPG substitute ratio on efficiency, maximum pressure, maximum pressure rate and pollutant emissions. The variation of this parameters versus LPG substitute dose, x_c , at full load and speed of 4,000 rpm operating regime are presented in the Figs. 3, 4, 5, 6, 7 and 8.

At full load and 4,000 rpm regime the BSFC slightly decrease until $x_c = 18\%$ LPG substitute ratio comparative to classic solution, Fig. 3. Forward increases of x_c lead to the increases of BSFC comparative to the diesel fuelling: with 2.5 % at $x_c = 29.5\%$ and with 3.6 % for $x_c = 40\%$. Thus, following the efficiency criteria, at the dual fuelling the LPG substitute ratio must be limited at $x_c \sim 20\%$. This tendency in variation of BSFC versus x_c was also registered for other investigated operating regimes of the dual fuelled engine by diesel gas oil method.

The maximum pressure and the maximum pressure rate increase when the diesel substitute ratio also increases, Figs. 4 and 5, influence explained by the combustion intensification of the LPG-air homogeneous mixture during the rapid burning phase comparative to the phase of pilot burning. The values of averaged cycles, the minimal and the maximum values from the individual cycles are also

Fig. 2 Diagrams of $p-\alpha$, averaged and smoothed, 100 % load and 4,000 rpm speed

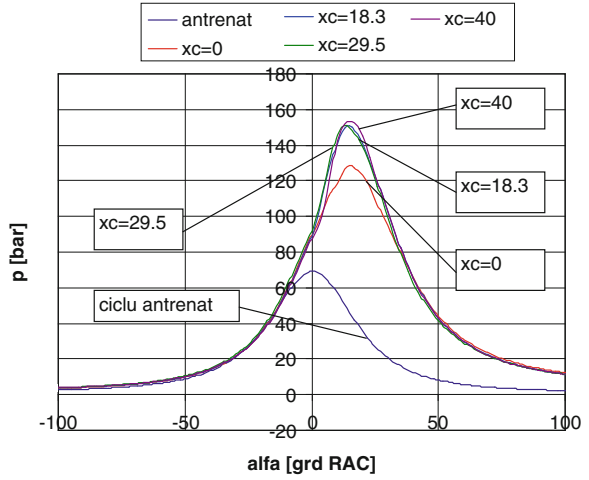


Fig. 3 BSFC- x_c , for 100 % load and 4,000 rpm speed

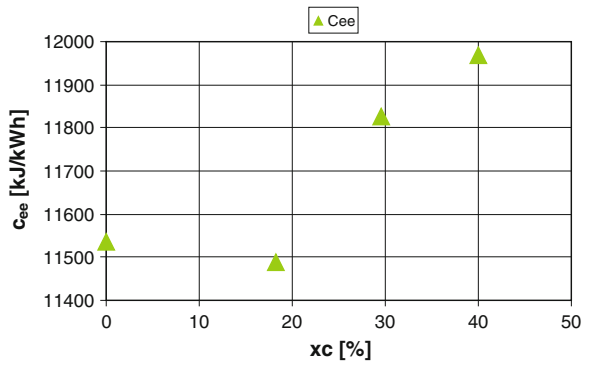


Fig. 4 $p_{max}-x_c$ at 100 % load and 4,000 rpm

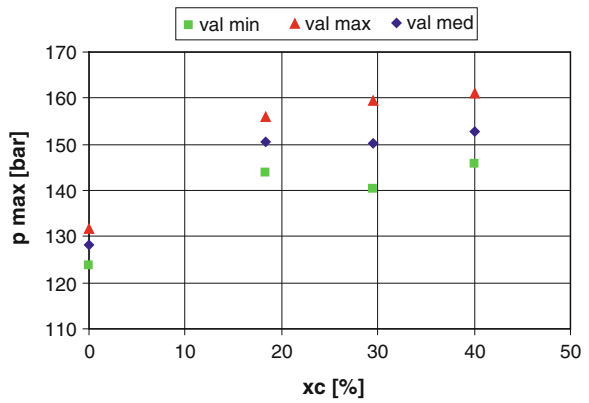


Fig. 5 $(dp/d\alpha)_{\max-x_c}$ at 100 % load and 4,000 rpm

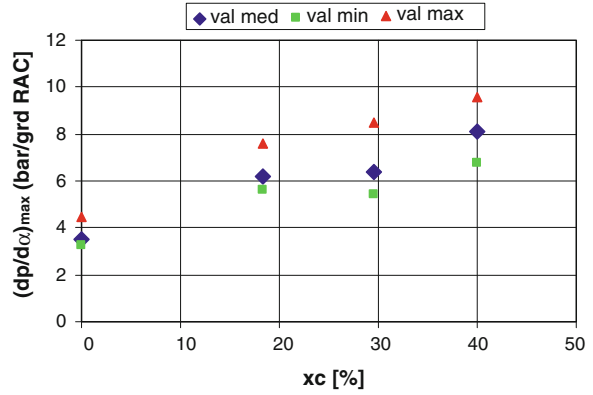


Fig. 6 $HC-x_c$ at 100 % load and 4,000 rpm

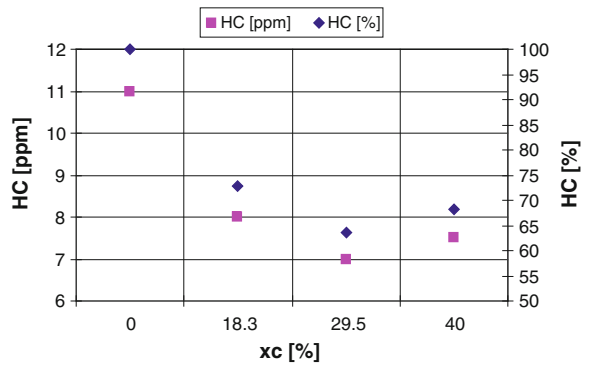
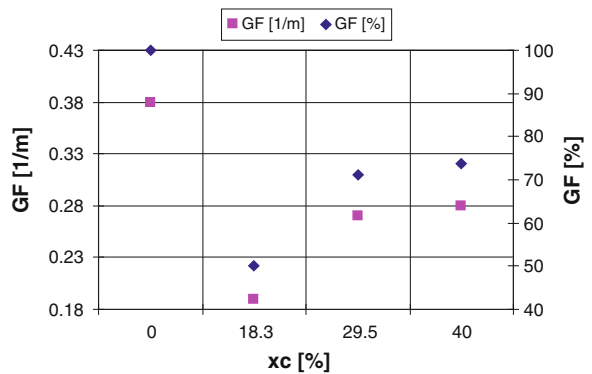
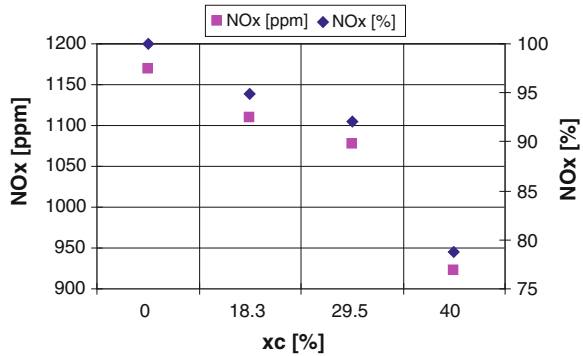


Fig. 7 $K-x_c$ at 100 % load and 4,000 rpm



represented. The increase in maximum pressure is 23 % for $x_c = 40$ % comparative to the reference solution for full load and speed of 4,000 rpm. Reached values of 16 MPa in maximum pressure for some cycles implies the limitation of the substitution ratio in order to maintain the engine reliability.

Fig. 8 NO_x-x_c at 100 % load and 4,000 rpm



From $x_c = 20\%$ the dispersion in values of maximum pressure and maximum pressure angle increase, Fig. 4. The value for the coefficient of cycle variability $(COV)_{p_{max}}$ increases when the substitute ratio also increases, but doesn't exceed 3 % and is no reason for x_c limitation. A much pronounced increases of $(COV)_{p_{max}}$ at $x_c > 20\%$ is observed, [13].

Maximum pressure rate rises with the substitute ratio increase, Fig. 5 shows an increase of 130 % at $x_c = 40\%$ for the maximum pressure rate, reaching values of 8–10 bar/CA deg. Taken into consideration the increase of dispersion in $(dp/dz)_{max}$ values, Fig. 5, and the value of $(COV)_{(dp/dz)_{max}}$ which increases from 6.64 % at $x_c = 18.3$ to 9.21 % for $x_c = 29.5\%$, the maximum substitute ratio must be limited at $x_c \sim 20\%$. In this way the coefficient in cycle variability for IMEP $(COV)_{pi}$ can also be take into consideration because its values continuous rise with the increases of substitute ratio x_c , registering values of 8 % for $x_c = 18.3\%$, 11.8 % for $x_c = 29.5\%$ and 3.2 % for $x_c = 40\%$, almost 13 times higher comparative to the reference regime, $x_c = 0$, [13]. If the accepted limit is $(COV)_{pi} < 10\%$, [12], then the substitution ratio must be limited at $x_c \sim 25\%$. In this conditions the values for maximum pressure and the maximum pressure rate are limited at $p_{max} = 15$ MPa and $(dp/dz)_{max} = 6$ bar/CA deg. and are in normal limits for the investigated engine.

The increase of the cycle variability coefficients can be explained by the in-cylinder state achieved before pilot injection. Before diesel fuel injection the air-LPG homogenous mixture formed in the intake manifold and admitted inside the cylinder is very lean. The global dosage of the mixture situated in front of the flame becomes leaner and influences the combustion process also in terms of cycle to cycle variability. For $x_c = 18.5\%$ the air-fuel ratio before diesel injection is $\lambda = 7.3$, $\lambda = 5.10$ for $x_c = 29.5\%$ and $\lambda = 3.6$ for $x_c = 40\%$. At diesel fuelling the values for the coefficients in cycle variability are 1.3 % in maximum pressure and 1 % for IMEP. Because the combustion starts in different conditions of leaner mixtures for dual fuelling, the coefficients in cycle variability rise with 46 at 1.9 % for p_{max} and with 700 at 8 % for IMEP even for small LPG quantities, $x_c = 18.3\%$, comparative to the classic solution. The increase of cycle variability can be assigned to the lean mixtures existed inside the cylinder before the combustion starts and influences the rapid burning phase.

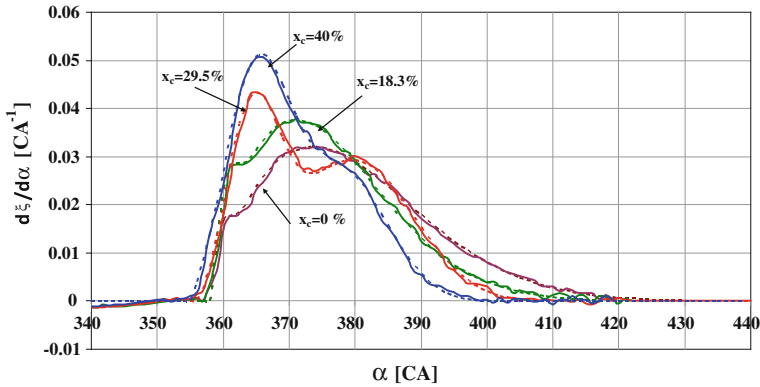


Fig. 9 $d\xi/d\alpha-\alpha$, at 100 % load and 4,000 rpm (continuous line-by processing of pressure diagram p- discontinuous line-by Vibe functions)

HC emission decreases with 36 % comparative to the reference regime for $x_c = 29.5\%$ at full load and 4,000 rpm speed and slightly increases at $x_c = 40\%$, Fig. 6. Important reductions of 30–50 % for HC emission were obvious also for other investigated operating regimes of the diesel-gas LPG fuelled engine, [6, 13]. This decrease is explained by the improvement of the combustion process in terms of high homogeneity of the LPG-air mixture. Smoke emission from the exhaust gases, evaluated by K coefficient, significantly decreases for LPG running in dual system. At 100 % load and speed of 4,000 rpm, the smoke emission decreases with $\sim 50\%$ for $x_c = 18.3\%$, Fig. 7, followed by a more reduced decrease of $\sim 40\%$ when the substitute ratio increase till $x_c = 40\%$.

NO_x emission level significantly decreases at the increase of diesel substitute ratio x_c , Fig. 8, being 21 % at $x_c = 40\%$. A similar variation tendency for the NO_x emission versus substitute ratio was registered also for other operating regimes, [6, 13]. The reduction of the NO_x emission when the diesel fuel is substituted by LPG is explained by the reduction tendency of the available oxygen and the decrease of the gases temperature at the combustion of the LPG-air lean homogenous mixtures, evaluated as a global temperature defined by the state equation. At LPG fuelling by diesel-gas method the increase of substitute ratio x_c the air-fuel ratio is reduced because the quantity of inlet air decreases and because for 1 kg of LPG the theoretically air quantity is bigger comparative to quantity required for 1 kg of diesel fuel. For the investigated operating regimes the burning laws was determined from indicated diagrams editing, Fig. 9.

Because of the physical and chemical phenomena's complexity from the combustion process, for simplification, in the calculus model the following hypothesis was considered:

- physical and chemical properties of the motor fluid in each calculus point and any moment are uniform;
- the motor fluid is a perfect gases homogenous mixture;

- temperature and pressure gradients in the combustion chamber are neglected;
- the chemically species are in chemical equilibrium;
- the dissociate phenomena is neglected;
- the blow-by is neglected, which in normal conditions has a reduce ponderosity without exceeding 2–2.8 %,
- convection heat transfer thru the walls is calculated with Woschni equation;
- the specific heats were calculated taken into consideration the instantaneous composition and temperature of the in-cylinder motor fluid.

From the energetically balance equation the heat release rate is obtained, $\frac{d\zeta}{d\alpha}$:

$$\frac{d\zeta}{d\alpha} = \left[\frac{V}{\gamma - 1} \cdot \frac{dp}{d\alpha} + \frac{\gamma}{\gamma - 1} \cdot \frac{dV}{d\alpha} + \frac{dQ_w}{d\alpha} \right] \cdot \frac{1}{m_{DFDF} + m_{GPLGPL}}$$

where γ is the specific heats ratio, V, p and T—volume, pressure and instantaneous cylinder temperature, m_{DF} , m_{GPL} and H_{DF} , H_{GPL} —cycle fuel doses and LPG and diesel fuel low caloric heat, respectively, Q_w - heat transferred to the walls by convection.

Based on pressure diagrams registered on each operating regime, for different diesel fuel substitute ratio by LPG, by application of the calculus model the heat release rate $d\zeta/d\alpha - \alpha$ was determined. The physic-mathematical model for thermo-gas-dynamic inside engine cylinder processes simulation was calibrated by experimental results.

Thus, in the Fig. 9 for full load and speed of 4,000 rpm the heat release rates $d\zeta/d\alpha - \alpha$ are shown. Based on these determinations other parameters useful for analysing and interpretation of some particularly phenomena's regarding the influence of LPG substitute ratio on combustion process can be obtained. For these interpretations, maximum heat release rate and angular fractions of 5, 10, 50 and 90 % from the reaction heat were determinate.

Heat release rate, Fig. 9, has the characteristic shape for an engine with pilot injection, showing that at the beginning of the combustion a phase with a restrain increase for heat release exists and is characteristic to diesel pilot dose. This aspect is specific only to the curves related to the diesel running, $x_c = 0$. For LPG running in dual system by diesel-gas method, the LPG-air homogenous mixture ignites from the diesel pilot and the heat release rate, during the initial burning phase which includes the pilot burning, also increases. LPG amplifies the quantity of heat release by preformed mixture burning. Heat release maximum rate increases with the increase of diesel fuel substitute ratio by LPG, Fig. 10, in accordance with the variation of maximum pressure and maximum pressure rate.

The LPG participation during the first phase of combustion direct influences the positioning versus TDC of the moments 5, 10, 50 and 90 % of the reaction heat. The angles on which the same fraction of reaction heat is release are moved earlier comparative to diesel fuelling, when the substitute ratio increases, Figs. 11, 12, 13, 14.

Fig. 10 $(dQ/d\alpha)_{\max}$ at 100 % load and 4,000 rpm

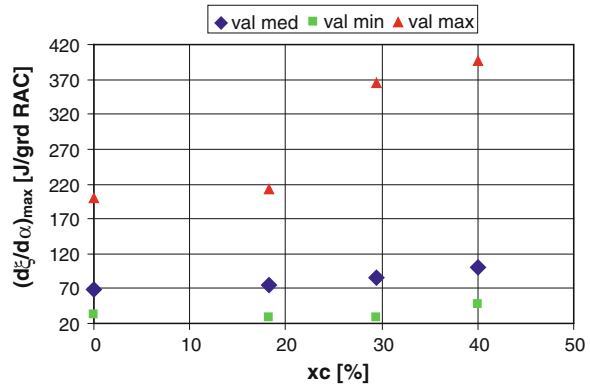
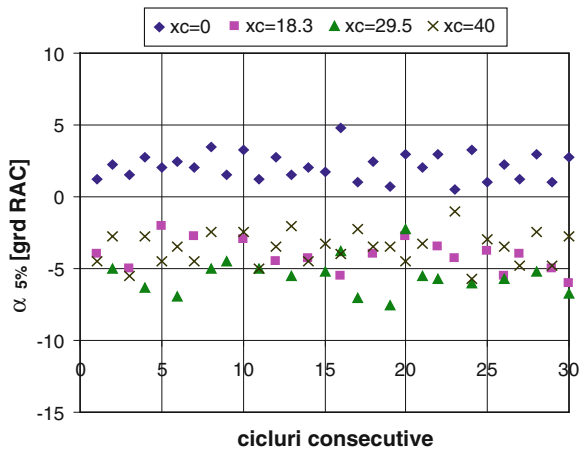


Fig. 11 Angle of 5 % from heat release, ξ_5 %, in consecutive cycles, at 100 % load and 4,000 rpm



The obtained burning laws from the indicated diagrams at full load and speed of 4,000 rpm can be explained by a burning formal law defined by two Vibe functions, definitive for diesel engines.

$$\frac{d\xi}{d\alpha} = 6,9 \cdot R_c \cdot \frac{m_p + 1}{\Delta\alpha_r} \cdot \left(\frac{\alpha - \alpha_d}{\Delta\alpha_r}\right)^{m_p} \cdot \exp\left[-6,9 \cdot \left(\frac{\alpha - \alpha_d}{\Delta\alpha_r}\right)^{m_p+1}\right] + 6,9 \cdot (1 - R_c) \cdot \frac{m_d + 1}{\Delta\alpha_a} \cdot \left(\frac{\alpha - \alpha_d}{\Delta\alpha_a}\right)^{m_d} \cdot \exp\left[-6,9 \cdot \left(\frac{\alpha - \alpha_d}{\Delta\alpha_a}\right)^{m_d+1}\right]$$

where: $\Delta\alpha_r$, and $\Delta\alpha_a$ respectively, rapid burning duration and combustion duration; α_d combustion start; m_p , and m_d respectively—shape factors for preformatted mixture burning, and diffusive burning, respectively; R_c —factor of heat repartition during the rapid burning phase.

Fig. 12 Angle of 10 % from heat release, ξ_{10} % in consecutive cycles, at 100 % load and 4,000 rpm

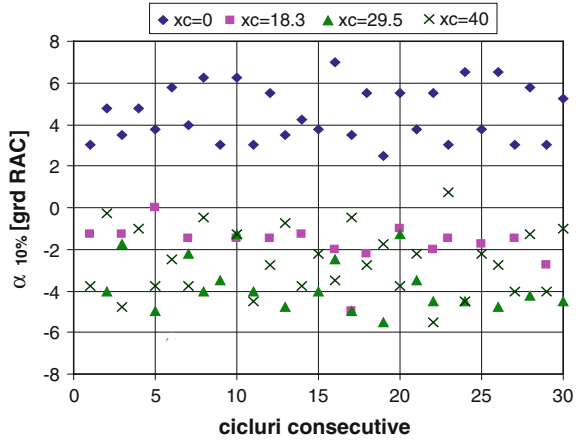


Fig. 13 Angle of 50 % from heat release, ξ_{50} % in consecutive cycles, at 100 % load and 4,000 rpm

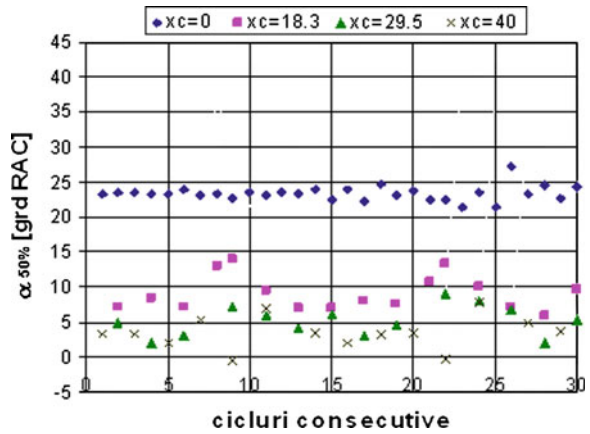


Fig. 14 Angle of 90 % from heat release in ξ_{90} % consecutive cycles, at 100 % load and 4,000 rpm

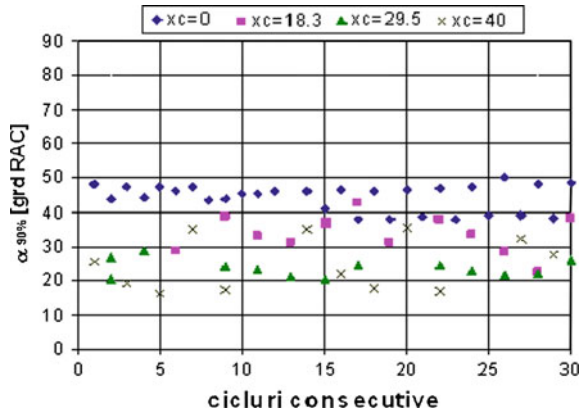


Table 1 The values of the parameters

Parameter	Substitute ratio x_c (%)				
	0	18.3	29.5	40	
m_p	1.12	1.15	1.6	1.8	
m_d	0.8	0.8	2.1	2.8	
$\Delta\alpha_r$ (CA)	6	8	23	25	
$\Delta\alpha_a$ (CA)	72	60	54	44	
R_c	0.02	0.04	0.35	0.48	

In Fig. 9, the discontinuous line curves shows the heat release rate obtained by using formal burning laws with Vibe functions, for substitute ratio $x_c = 0, 18.3, 29.5$ and 40% at full load and $4,000$ rpm. In Table 1 the values of the parameters used for the heat release rate calculus, with two Vibe functions, are presented.

Is observed that when the substitute ratio increases, the factor of heat repartition during the rapid burning phase R_c and $\Delta\alpha_r$ duration also increase, the heat quantity released from the preformatted mixture combustion being significantly increased. Thus, the quantity of heat released during the diffusive phase decreases because the diesel dose, which preponderant burns during this stage, is reduced at the increasing of the substitute ratio. The total combustion duration $\Delta\alpha_a$ decreases when the x_c increase, because of the rapid burning of the LPG-air homogeneous mixture and of the reduction of the diesel dose, that burns preponderant during the diffusive phase, and the maximum rate of heat release increases and is achieved sooner on the cycle. In generally, when the substitute ratio increases, the shape factors m_p and m_d also increase, but their values are relative reduced in order to simulate a much faster heat release during the respective burning periods.

4 Conclusions

The combustion process and engine performance are significantly influenced by the LPG cycle dose that substitutes the diesel fuel. The theoretical and experimental results show important decreases of emissions level ($HC \sim 36\%$, smoke $\sim 50\%$, $NO_x \sim 17\%$ at full engine load and $4,000$ rpm) in the same operating regimes of the engine, in conditions maintaining or lowering break specific fuel consumption.

The potential benefits of using LPG in diesel engines are on economical and environmental side because is composed from simple hydrocarbons, doesn't contain sulphur and has a lower carbon content comparative to diesel fuel. The increasing of the diesel fuel substitute ratio by LPG leads to a increase in maximum pressure and maximum pressure rate comparative to reference regime of diesel running and represents criteria's of limitation for the substitute ratio. Thus, for the full load regime and $4,000$ rpm speed, x_c was limited at $\sim 25\%$.

Comparative to diesel fuelling, the partial substitution of the diesel fuel by LPG implies the increase of reaction heat release rate during the rapid combustion phase.

The study of combustion process at different substitute's ratios allows the establishment of some correlations between the burning laws edited from indicated pressure diagrams and formal burning laws with two Vibe functions, suitable for diesel engines. The factor of heat repartition during the rapid burning phase, R_c , and the shape factors, m_p and m_d , increases with the x_c substitute ratio increase, but their values are relative reduced in order to simulate a the faster heat release development during the respective combustion periods.

References

1. Goto S, Daeyup L (1999) Development of an LPG DI diesel engine using cetane number enhancing additives. *Alternative Fuels 1999*, SAE Inc., USA, ISBN 0-7680-0493-4, pp 205–214
2. Pana C, Negurescu N, Popa MG, Cernat AL, Despa P, Bujgoi FL (2008) Aspects of the LPG use in diesel engine by diesel-gas method. *FISITA World Congress*, Munchen, 2008
3. Pana C, Negurescu N, Popa MG, Boboc G, Cernat AL (2008) Reduction of NO_x, smoke and BSFC in a diesel engine fueled with LPG. In: *MECCA Journal of middle European construction and design of cars*, vol III. No. 4, pp 37–43, Dec 2005, Praha, Czech Republic, ISSN 1214-0821
4. Pana C, Negurescu N, Popa MG, Racovitza AL, Boboc G, Cernat AL (2005) Performance of a diesel engine fueled by LPG. In: *5th International colloquium fuels 2005*, Technische Akademie Esslingen, Germany, pp 143–148, 12–13 Jan 2005, ISBN 3-924813-59-0
5. Pana C, Negurescu N, Popa MG, Racovitza AL (2003) Performance of LPG fuelled diesel engine using DMI method. In: *4th International colloquium fuels 2003*, Technische Akademie Esslingen, Germany, pp 451–460, 15–16 Jan 2003 ISBN 3-924813-51-5
6. Pana C, Negurescu N, Popa MG, Cernat AL, Soare D, Despa P, Bujgoi FL (2006) Dual fuelling system with alternative fuels for ecological automotive diesel engine. Research contract no. X2C10/2006, University Politehnica Bucharest, Romania
7. Ayhan V, Parlak A, Cesur I, Boru B, Kolip A (2011) Performance and exhaust emission characteristics of a diesel engine running with LPG. *International Journal of the Physical Sciences*, vol. 6(8). ISSN 1992–1950 ©2011 Academic Journals, Turkey, pp 1905–1914
8. Qi DH, Bian YZH, Ma ZHY, Zhang CHH, Liu SHQ (2007) Combustion and exhaust emission characteristics of a compression ignition engine using liquefied petroleum gas-diesel blended fuel. *Energy Conver Manage* 48(2):500–509
9. Vijayabalan P, Nagarajan G (2007) Performance, emission and combustion of LPG diesel dual fuel engine using glow plug. In <http://jjmie.hu.edu.jo>
10. Thirupathi Reddy K, Ram Reddy P, Ramana Murthy PV (2008) Experimental investigations on the dual fueled diesel engine. *Asian J Sci Res* 1(4):429–436, ISSN 1992-1454
11. Rao GA, Raju AVS, Govinda Rajulu K, Mohan Rao CV (2010) Performance evaluation of a dual fuel engine (Diesel + LPG). *Indian J Sci Technol* 3(3) (Mar 2010) ISSN: 0974- 6846
12. Heywood JB (1988) *Internal combustion engine fundamentals*. McGraw-Hill, NY
13. Cernat A (2010) Contributions to the study of a diesel engine running on diesel fuel and liquid petroleum gas. Doctoral Dissertation, University Politehnica of Bucharest

The Research Development in Direct Injection Spark-Ignition Natural Gas Engine

Jianjun Zheng, Xiaodong Chen, Tiegang Hu and Zhangsong Zhan

Abstract Natural gas is thought to be one of the most promising alternatives to traditional vehicle fuels. Nowadays, the natural-gas-fueled engine has been realized in both the spark-ignition engine and the compression-ignition engine. Due to the complicated fueling systems in dual fuel mode and the loss in volumetric efficiency in port injection mode, direct injection spark-ignition natural gas engine can be utilized to avoid these defects and its mixture preparation flexibility will improve the fuel economy. The ability to increase the compression ratio can improve the engine performance. In addition, natural gas direct injection combustion can avoid smoke emission from gasoline direct injection combustion. Due to the high injection pressure requirement, special gas injector should be developed to match the injection and flow characteristics. Meanwhile, the arrangement of spark plug and fuel injector is very sensitive to the engine performance and emissions. The injection timings and ignition timings are very important operating parameters and the control of these parameters will determine the mixture concentration distribution in the cylinder and thus the combustion characteristics. Natural gas direct injection combustion can realize high combustion stability with less cycle-by-cycle variation and the lean burn limit can be extended compared with that of the port injection mode, and also the HC emission can be reduced based on appropriate charge stratification and gas flow condition. However, the particle number concentration and NO_x emission will increase with the improvement of combustion status. Adding hydrogen into direct injection natural gas engine is expected to improve the engine performance and decrease engine

F2012-B01-010

J. Zheng (✉) · X. Chen · T. Hu · Z. Zhan
Powertrain R&D Center of Changan Automobile Co Ltd, Changan,
People's Republic of China
e-mail: sunqiemail@163.com

emissions. By using the swirl injection system, this engine can realize the increase of brake thermal efficiency and the reduction of the brake NO_x , HC, CO and CO_2 emission simultaneously, when the hydrogen fraction exceeds 10 %. Nevertheless, further research in spark-ignition system and fuel injection system should be conducted before the product stage of this kind of engine.

Keywords Research development · Natural gas · Direct injection · Spark-ignition · Engine

1 Introduction

Natural gas is thought to be one of the most promising alternatives to traditional vehicle fuels for engines since it has cleaner combustion characteristics and plentiful reserves. Nowadays, natural gas is widely used in taxis and city buses all over the world and the natural-gas-fueled engine has been realized in both the spark-ignition engine and the compression-ignition engine. In addition, its high-octane value and good anti-knock property permits high compression ratio which will lead to higher thermal efficiency. Previous studies showed low emissions by using natural gas. Engines fuelled with natural gas emit less carbon monoxide (CO) and non-methane hydrocarbons (NMHC) compared with gasoline engines [1, 2].

Currently, there are mainly two kinds of operating mode for engines fueled with natural gas in practical application. In the first mode (homogeneous charge mode), the homogeneous mixture of natural gas and air is ignited by a spark plug as in the conventional port fuel injection (PFI) petrol engines. As natural gas occupies a larger fraction of intake charge, it has the demerit of lower volumetric efficiency, and this will decrease the amount of fresh air into the cylinder, leading to a lower power output compared with that of gasoline engine [3]. In addition, the homogeneous charge combustion makes it difficult to burn the lean mixture, for the narrow flammability limit of natural gas. Furthermore, these engines have a lower thermal efficiency due to engine knock restriction and unavoidable throttling at the intake at partial load. In the second operating mode (dual fuel mode), the homogeneous natural gas is ignited by pilot injection of the diesel fuel before the top-dead-center (TDC). This needs two sets of separate fuel supply systems and makes the system complicated. In addition, HC emissions still remain high at light loads [3]. So-called homogeneous lean combustion engines have appeared. This can realize a higher thermal efficiency due to the lower pumping loss, the lower heat loss and the increase in the specific heat ratio, but the NO_x emissions keep higher level due to the ineffectiveness of the existing catalyst. Also, the large cycle-by-cycle variation restricts the lean operation limit of this type of homogeneous mixture engines [4–8].

In recent years, a gasoline direct injection (GDI) engine has entered into the stage of production for modern two and four stroke petrol engines. The major

advantages of a GDI engine are the increase in the fuel efficiency. The charge stratification formed by fuel injection and turbulence in the combustion chamber permits extremely lean combustion without high cycle-by-cycle variations, leading to a high combustion efficiency and low emissions at small load [9–11]. In addition, there is no throttling loss in some GDI engines, which greatly improves the volumetric and thermal efficiencies. Moreover, the charge cooling due to fuel evaporation, reducing the occurrence of knocking, and this allows utilization of an increased compression ratio to improve engine performance and thermal efficiency.

An effective method to exploit or combine the advantages of natural gas and fuel direct injection technology is the development of the direct injection spark-ignition natural gas engine (DISINGE). This type of engine can be utilized to avoid the loss in volumetric efficiency, as natural gas is directly injected into the cylinder. It is flexible in mixture preparation because of forming a stratified mixture in the cylinder at low loads, and improving the fuel economy. The ability to increase the compression ratio can improve the engine performance. In addition, natural gas direct injection combustion can avoid smoke emission from GDI combustion [12–15].

During the past decades, several studies were conducted on natural gas direct injection combustion by using a rapid compression machine (RCM) as well as real research engines [15–25]. Among these works, the effect of adjusting nozzle geometry, fuel injection pressure, arrange of injector, spark plug, the shape of piston crown, fuel injection timing, ignition timing as well as compression ratio, and even adding some fraction of hydrogen into natural gas on engine performance and exhaust emissions characteristics was studied experimentally and numerically. Therefore, a detailed understanding of these research achievements and the latest status is required to improve the engine performance and exhaust emissions of this type of engine further. Based on this background, this chapter reviews the past work achievements and the recent research status of the DISINGE.

2 The Fundamentals of Direct Injection Spark-Ignition Natural Gas Engine

It is very important to acquire an ideal mixture distribution in the combustion chamber of DISINGE. Therefore, the arrangement of fuel injector and spark plug, piston shape, fuel injection pressure, injection timing, spark ignition timing and compression ratio will have a great influence on the performance, combustion and emission characteristics of the engine. Due to limited space, the related interpretations are showed in this section briefly.

2.1 The Effect of Compression Ratio

Due to the usage of natural gas and direct injection pattern, the possibility of knocking occurrence will be greatly decreased and an increased compression ratio can be used to improve the engine performance and thermal efficiency. Zheng et al. [25] compared the effect of compression ratio on performance, combustion and emission characteristics of DISINGE experimentally, the results showed that a compression ratio of 12 is the compromise optimum value both for performance and emissions of a DISINGE. Therefore, the new DISINGEs with a higher compression ratio of 12~14 were developed these years [26–30]. Kalam et al. [26] developed a new DISINGE with an elevated compression ratio of 14 and modified ignition system, this engine can get more brake power and better NO_x emission properties than that of the original gasoline engine with the same displacement volume.

2.2 The Effect of Nozzle Geometry and Fuel Injection Pressure

The natural gas injector should be designed to deliver a precisely metered fuel quantity with a highly repeatable spray characteristics under the same operating condition. Mainly, there are two types of gas injector used for DISINGEs in the literature, multi-hole injector and swirl injector [18, 28]. Due to the swirl injectors with a single exit orifice have a lower flow rate, the advance injection timings are required to get the engine power output, while multi-hole injectors with a reasonable tumble flow level can also acquire better mixture formation in-cylinder. It is considered that the orientation of the nozzle hole, the hole distribution and the cone angle of individual spray plumes are critical parameters for the engine to acquire ideal spray structure, reliable flame propagation and thus good engine performance. Unfortunately, there is few literature refers to it and further research on gas fuel injection system is needed.

The fuel injection pressure requirement of DISINGEs are much higher than that of PFI spark-ignition natural gas engine [7, 15, 18]. Usually, the injection pressure of port fuel injection engine is around 0.5 MPa. On the contrary, the injection pressure of DISINGE is above 8 MPa [31]. This is due to high fuel injection pressure is required to overcome the cylinder ambient pressure during late stage of intake and/or compression stroke, and to realize an ideal mixture distribution in the cylinder. Due to the high injection pressure requirement, special gas injector should be developed to match the injection and flow characteristics. However, the adopt of high injection pressure makes the structure of the system complicated and increases the requirement to the seal and lubrication of the valves as well as the

system reliability. Some researchers developed new DISINGEs with relative lower injection pressure such as 2 MPa [26, 27]. With increased compression ratio and modified ignition system, this engine can acquire slightly higher brake power than original gasoline engine with the same displacement volume.

2.3 The Arrangement of Injector, Spark Plug and the Shape of Piston Crown

As the flammability range of natural gas is narrower than that of gasoline and stratified charge mixture pattern is used in the DISINGEs at low and medium loads, the mixture concentration around the spark plug at ignition timing should have better flammability to realize a stable ignition. Therefore, the arrangement of fuel injector and spark plug as well as the shape of piston crown are important factors. The research work of Yuichi et al. [18] showed that the relative distance from injector holes to spark plug can be determined by the quasi-static spray theory, and also the usage of deep dish type piston cavity can increase the squish flow intensity to overcome the demerit of the harder mixing process between natural gas and air than the conventional fuels. In addition, unlike the GDI engine, the impingement of gas jet against cavity wall and swirl flow can improve the mixture formation process [18].

2.4 The Control of Injection Strategy

Based on the high fuel injection pressure, the common mixture formation strategy in-cylinder is summarized as that at light and median engine loads, the late injection timing or two stage injection strategy will be utilized to form a stable stratified mixture in the cylinder, which is a richer mixture formed in the vicinity of spark plug at spark ignition time ($\varphi = 1.0 \sim 1.4$), and a leaner mixture in the region apart from the spark plug. At high load, an early injection timing will be used to acquire a nearly homogeneous mixture formed in the cylinder to get more torque and decreased exhaust emissions.

It is worth to mention that due to the mixing process between natural gas and air is harder than that of the conventional fuels, sufficient time should be allowed for the mixing between fuel and air [18]. Therefore, more advanced injection timings compared with petro engines should be adopted to realize a reasonable mixture distribution in the chamber. Zeng et al.'s result showed that an optimum injection timing exists around 180 BTDC (medium engine load condition), and the thermal efficiency, maximum pressure in-cylinder, and the maximum rate of heat release can get the maximum value around this point [15]. For the more retarded injection timing, the mixing time for fuel and air is not sufficient, leading to an extreme non-

uniform mixture formed in the cylinder, and this is unfavourable for the sequential ignition and flame propagation process, resulting in the decrease of thermal efficiency and engine power output. On the contrary, for the more advanced injection timing, a relative lean uniform mixture is formed in the chamber, and it is also not benefit for the realization of the stratified mixture mode at lean condition, leading to a decreased ignition ability and flame propagation speed, which leads to the reduce of thermal efficiency. The result of Liu et al. [29] also showed that at lambda of 1.33, the engine can get maximum net IMEP at injection timing of 170° BTDC with a single hole injector and the injection pressure is 8.0 MPa. However, due to great differences exist between the injection pressure and nozzle geometry of the various injection systems, the control strategies also vary a lot in the injection timings. Yuichi et al. [18] studied the effect of injection timing on cyclic variation of maximum pressure in-cylinder, the results showed that at lambda of 2.5 and 2.3, the injection timing of 30° BTDC can get the lowest cyclic variation of maximum pressure in-cylinder; at lambda of 1.04 and 1.40, the injection timing of 90 can get the lowest cyclic variation of maximum cylinder pressure with a six hole injector and the injection pressure is 10 MPa.

2.5 The Control of Ignition Strategy

Ignition timings are very important operating parameters and the control of these parameters will determine the flame kernel initialization and development in the combustion chamber and thus the sequent combustion characteristics. As the flame speed of natural gas is lower than that of the conventional fuels at the same temperature and pressure condition, the advanced ignition timings should be utilized at low and medium engine load in DISINGEs. Huang et al. [32] studied the effect of ignition timing on combustion and emission characteristics of a DISINGE, their results showed that advanced ignition timings will lead to an increased thermal efficiency, maximum cylinder pressure, and maximum rate of heat release as well as a short combustion duration and decreased HC emission. CO emission varies insignificantly with spark timing. But the advanced ignition timing will also result in an increased NO_x emission. Usually, retarded ignition timings are adopted to decrease the NO_x emissions, but this will lead to the decrease of engine power output at high engine load [7].

2.6 Effect of Hydrogen Addition

Similar with PFI natural gas engine, adding hydrogen into natural gas has great impact on the combustion and emissions characteristics of the DISINGEs. As natural gas has the demerits of relatively narrow flammability range and slow flame propagation speed compared with conventional gasoline and diesel, it will

result in a limited lean-burn ability and larger cyclic variations occur at small engine load [33, 34]. In addition, the low flame speed will lead to lower thermal efficiency which will decrease engine power output and increase fuel consumption [2, 4]. An effective method to overcome the disadvantages of poor lean-burn ability and slow flame speed of natural gas is to blend the natural gas with the fuel which possesses wide flammability range and high flame speed. Hydrogen is considered to be the best gaseous additive to natural gas due to its wide flammability range and fast burning velocity. And adding hydrogen into natural gas is thought to greatly improve the engine performance at small engine load and decrease exhaust emissions [35, 36]. Therefore, some researchers studied the effect of adding hydrogen into natural gas on the performance and emissions characteristics in a DISINGE [14, 28, 32, 37–39]. Professor Huang and his group investigated the effect of hydrogen fraction on combustion and emission characteristics in a direct injection engine fueled with natural gas-hydrogen blends under a compression ratio of 8 and hydrogen fraction less than 20 % [14, 32, 38]. Their results showed that for the same spark timing, the brake thermal efficiency is increased and the combustion duration is decreased with increasing hydrogen fraction in the natural gas-hydrogen blends [32].

Wang et al. [39] studied the combustion and emissions characteristics of a direct injection engine fueled with natural gas-hydrogen blends at an increased compression ratio of 12 and extended hydrogen fraction range from 0 to 40 % by utilizing a single hole high pressure injector. They conducted the experiment based on the same injection timings and ignition timings for different natural gas-hydrogen blends under the specified engine speed/load conditions. Their results showed that the thermal efficiency increased with increasing the hydrogen fraction, but the NO_x emissions also increased simultaneously with increasing the hydrogen fraction, and the trend is more remarkable when hydrogen fraction exceeds 20 %. Zheng et al. [28] investigates the combustion and emissions properties of a spray guided direct injection engine fueled with natural gas-hydrogen blends with a swirl injector. The results showed that the thermal efficiency increases with increasing the hydrogen fraction at various injection timings, and also when the hydrogen fraction exceeds 10 %, the brake HC, CO and CO_2 emissions decrease with the increase of hydrogen fraction.

3 Advantages in Performance and Emission Characteristics

3.1 Lean Operating Limitation

As mentioned above, due to lean combustion and stratified mixture formed in the combustion chamber under low engine load, the lean operating limitation of DISINGEs will be greatly extended compared to PFI natural gas engine [7, 15, 21, 40, 41].

Normally, a PFI natural gas engine can acquire very lean combustion with a lambda of 1.6 and the COV of IMEP is larger than 10 %. However, if direct injection operating mode is adopted, the COV of IMEP will be less than 5 % at the same lambda condition [7]. Huang et al. [21] studied the basic behaviour of direct injection natural gas combustion by using a RCM, their results shows that comparing with homogeneous mixture case, direct injection natural gas mode can acquire extremely lean combustion at an equivalence ratio of 0.03. The research result of Shiga et al. [40] showed that the lean operating limitation of direct injection natural gas combustion depends on fuel injection timing and spark ignition timing, and the engine can realize very lean combustion with stratified mixture at optimum injection timing and spark ignition timing. Zheng et al.'s result also showed that stable combustion can be realized when the overall excess air ratio exceeds 1.6 with a compression ratio which is larger than a certain value (e.g. CR = 12) at low engine load [41]. This is due to the stratified mixture formed in the cylinder, which is relative rich mixture around the spark plug and lean mixture in the end gas region. In addition, the high pressure fuel injection also increase the mixture turbulent level in the cylinder, which will improve the ignition ability and accelerate flame propagation, leading to higher thermal efficiency and stable combustion.

3.2 Engine Performance and Emissions

Due to lower throttling loss in DISINGEs, the volumetric and thermal efficiency are greatly increased compared with PFI natural gas engines. In addition, based on the good anti-knock property of natural gas, higher compression ratio can be used to improve the combustion and thermal efficiency. Furthermore, the charge stratification and the turbulent intensified by the fuel injection also improve the combustion status and thus engine performance. Huang et al.'s result showed that direct injection natural gas combustion can get shorter combustion duration, higher pressure rise due to combustion, and higher rate of heat release compared with homogeneous mixture case [21]. The new DISINGE developed by Kalam and his colleague can acquire slightly higher brake power than original gasoline engine with the same displacement volume [26, 27]. Huang et al. [21] reported that the combustion efficiency maintains as high as 0.92 when the average equivalence ratio in the range of 0.1–0.9 due to stratification mixture formation in the direct injection natural gas combustion.

The unburned methane emissions of direct injection natural gas combustion were almost the same level as that of homogeneous mixture combustion as showed in Huang et al.'s results [21]. But the CO emission increased steeply with increasing the equivalence ratio when equivalence ratio exceeds 0.8, this is due to an over stratified mixture formed in the cylinder. Due to higher combustion temperature in the cylinder, the NO_x emission is at higher level for DISINGEs [7]. Huang et al.'s result also showed that the NO_x emission get its maximum value at lower equivalence ratio region [21]. Therefore, retarded ignition timing strategy

are adopted to decrease the NO_x emissions in usual, but this will lead to the decrease of engine power output at high engine load [7]. But Arcoumanis et al. [42] reported that NO_x emission is lower for direct injection natural gas combustion due to an increased charge stratification. There are few literature refer to the particle number and mass distribution of DISINGEs. It is reported that particle number concentration will increase with the improvement of combustion status and the peak particle number concentration occurs at a diameter of 0.039 μm by Liu et al. [29] which is at the same level of PFI natural gas. In addition, as natural gas is gaseous fuel, there are no liquid fuel droplets distributed in the cylinder, and the local air fuel ratio distribution is not influenced by fuel impingement, wall-wetting and fuel evaporation. Therefore, the effect of mixture inhomogeneity on particle number is weaker than that of the GDI engine [29].

3.3 Cycle-by-Cycle Variations

Due to stratified mixture and fast flame propagation based on intensified turbulence produced by the high pressure fuel injection at light load, DISINGEs can acquire better ignition ability and realize stable combustion. Huang et al. [24] studied the cyclic variations of natural gas direct injection combustion by using a RCM. Their results showed that natural gas direct injection combustion can realize high combustion stability with less cycle-by-cycle variation in the maximum cylinder pressure, the maximum rate of pressure rise and maximum rate of heat release at the given equivalence ratio. In addition, Huang et al. [16] also studied the cyclic variations of natural gas direct injection combustion on a single cylinder research engine (SCRE). The results also showed that the DISINGE has a better lean burn capability, and the misfire and partial burn cycles only occurs when the equivalence ratio is below 0.4. Zheng et al. [41] investigated the effect of compression ratio on cyclic variations in a DISINGE and to analyze the cause of cycle-by-cycle variations in the direct injection natural gas combustion. Their result shows that a compromise compression ratio exists for the DISINGE to acquire the stable engine operation and low cycle-by-cycle variations. Their results also showed that cyclic variations of the DISINGEs are resulted from the fluctuations in flame development duration and late combustion durations, which is different from PFI engine in which cycle-by-cycle variations mainly result from fluctuations at the initial stage of combustion. Professor Sen et al. [43] investigated the dynamics of cycle-to-cycle variations in a DISINGE by using continuous wavelet transform and cross wavelet transform method. The results reveal that the cyclic variations exhibit multiscale dynamics as fluctuations occurs at different timescales, and the spectral power of cyclic variations for compression ratio of 12 was found to be significantly reduced at the various timescales compared to the cyclic variations at other compression ratios. Their results also proved Zheng et al.'s results that strong interdependence exists between the IMEP and main combustion duration as well as total combustion duration over a wide range of frequencies and engine cycles [41].

4 Future Development

4.1 Spark-Ignition System

As natural gas has the disadvantages of relatively narrow flammability range and slow flame propagation speed compared with conventional fuels, the DISINGE also suffers from poor lean-burn ability and remarkable cyclic variations at small engine load when over lean combustion (no throttle case) mode was used [33, 34]. And under the over lean combustion mode, the current commercial spark ignition system is harder to achieve stable ignition for all operating conditions, especially when more residual gas exists in the combustion chamber and large cyclic variations of fuel concentration occurs in the vicinity of the spark plug. Therefore, further effort in spark-ignition system development should be conducted before the product stage of DISINGEs and the ultra high energy spark ignition system with special design is expected to be introduced in the future product of DISINGEs.

4.2 Fuel Injection System

In the DISINGEs, without the consideration on fuel spray and atomization, usually natural gas is directly injected in the cylinder by electromagnetic injector, and the fuel injection systems should have wide range of setting variations for injection control such as valve open timing and duration under high fuel feed pressure. For the high pressure electromagnetic injector, normally the ratio of fuel-feed pressure and in-cylinder pressure is more than the critical pressure ratio, the chock flow condition is kept during the fuel injection, the amount of fuel injected is almost proportion to the injection duration [14, 18, 25, 28]. However, due to an ideal stratified or homogenous mixture is expected to formed in cylinder in various DISINGEs, the fuel injector should be designed specially to consider the interaction of fuel jet, air flow, chamber shape. Therefore, further research in fuel injection system should be conducted later.

5 Summary and Conclusions

This chapter reviews the past research development in DISINGEs briefly, the remarkable conclusions are as follows:

The compression ratio, nozzle geometry, fuel injection pressure, arrangement of fuel injector, spark plug and shape of piston is extremely critical to the engine performance and emissions. Meanwhile, the injection timings and ignition timings are very important operating parameters and the control of these parameters will determine the mixture concentration distribution in the cylinder and thus the

combustion characteristics. Adding hydrogen into DISINGE is expected to improve the engine performance and decrease engine emissions.

Natural gas direct injection combustion can realize high combustion stability with less cycle-by-cycle variation and the lean burn limit can be extended compared with that of the port injection mode. The HC emission can be reduced based on appropriate charge stratification and gas flow condition. However, the particle number concentration and NO_x emission will increase with the improvement of combustion status.

Due to great differences exist between the injection pressure and nozzle geometry of the various injection systems, special gas injector should be developed to match the injection and flow characteristics. Further research in spark-ignition system and fuel injection system should be conducted before the product stage of this kind of engine.

Acknowledgments The authors express their thanks to all the colleague in Engine CFD Analysis Department in Powertrain R&D Center of Changan Automobile Co Ltd for their great help during the manuscript preparation.

References

1. Weaver CS (1989) Natural gas vehicles—a review of the state of the art. SAE paper 892133
2. Rousseau S, Lemoult B, Tazerout M (1999) Combustion characteristics of natural gas in a lean burn spark-ignition engine. Proc Inst Mech Eng Part D 213(5):481–489
3. Yamamoto Y, Sato K, Matsumoto S (1994) Study of combustion characteristics of compressed natural gas as automotive fuel. SAE paper 940761
4. Ben L, Dacros NR, Truquet R, Charnay G (1999) Influence of air/fuel ratio on cyclic variation and exhaust emission in natural gas SI engine. SAE paper 992901
5. Hassaneen AE, Varde KS, Bawady AH, Morgan AA (1998) A study of the flame development and rapid burn durations in a lean-burn fuel injected natural gas SI engine. SAE paper 981384
6. Ramesh A, Corre O, Tazerout M (2002) Experimental investigation on cycle by cycle variations in a natural gas fueled spark ignition engine. In: Proceedings of the 2nd international SAE India mobility conference, Chennai, India, 10–12 Jan 2002, pp 145–152
7. Choa HM, He BQ (2007) Spark ignition natural gas engines—a review. Energy Convers Manage 48(2):608–618
8. Corbo P, Gambino M, Iannaccone, S, Unich A (1995) Comparison between lean-burn and stoichiometric technologies for CNG heavy-duty engines. SAE paper 950057
9. Brehob DD, Stein RA, Haghgoie M (1998) Stratified-charge engine fuel economy and emission characteristics. SAE paper 982704
10. Kano M, Saito K, Basaki M (1998) Emissions and fuel economy of a 1998 Toyota with a direct injection spark ignition engine. SAE paper 981462
11. Iwamoto Y, Noma K, Nakayama O, Yamauchi T, Ando H (1997) Development of gasoline direct injection engine. SAE paper 970541
12. Willi ML, Richards BG (1995) Design and development of a direct injected, glow plug ignition-assisted, natural gas engine. J Eng Gas Turbines Power 117(4):799–803
13. Meyers DP, Bourn GD, Hedrick JC, Kubesh JT (1997) Evaluation of six natural gas combustion systems for LNG locomotive applications. SAE paper 972967

14. Huang ZH, Wang JH, Liu B, Zeng K, Yu JR, Jiang DM (2006) Combustion characteristics of a direct injection engine fueled with natural gas-hydrogen mixtures. *Energy Fuels* 20(2):540–546
15. Zeng K, Huang ZH, Liu B, Liu LX, Jiang DM, Ren Y, Wang JH (2006) Combustion characteristics of a direct injection natural gas engine under various injection timings. *Appl Therm Eng* 26(8–9):806–813
16. Huang ZH, Liu LX, Jiang DM, Ren Y, Liu B, Zeng K, Wang Q (2008) Study on cycle-by-cycle variations of combustion in a natural-gas direct injection engine. *Proc Inst Mech Eng Part D* 222(9):1657–1667
17. Honjo F, Miura A, Nakamura A, Tsuchiya T (2004) CNG in-cylinder direct injection engine system. *Proc JSAE Annu Congr* 118(04):13–16
18. Yuichi G (1999) Mixture formation and ignition in a direct injection natural gas engine. *JSME Int J B Fluids Therm Eng* 42(2):268–274
19. Hill PG, Douville B (2000) Analysis of combustion in diesel engines fueled by directly injected natural gas. *J Eng Gas Turbines Power* 122(1):141–149
20. Douville B, Ouellette P, Touchette A, Ursu B (1998) Performance and emissions of a two stroke engine fueled using high-pressure direct injection of natural gas. *SAE Trans* 107(3):1727–1735
21. Huang ZH, Shiga S, Ueda T, Jingu N, Nakamura H, Ishima T, Obokata T, Tsue M, Kono M (2002) A basic behavior of CNG DI combustion in a spark-ignited rapid compression machine. *JSME Int J B Fluids Therm Eng* 45(4):891–900
22. Huang Z, Shiga S, Ueda T, Nakamura H, Ishima T, Obokata T, Tsue M, Kono M (2003) Combustion characteristics of natural-gas direct injection combustion under various fuel injection timings. *Proc Inst Mech Eng Part D* 217(5):393–401
23. Huang Z, Shiga S, Ueda T (2003) Effect of fuel injection timing relative to ignition timing on the natural-gas direct injection combustion. *J Eng Gas Turbines Power* 125(3):783–790
24. Huang Z, Shiga S, Ueda T, Nakamura H, Ishima T, Obokata T, Tsue M, Kono M (2003) Study of cycle-by-cycle variations of natural gas direct injection combustion using a rapid compression machine. *Proc Inst Mech Eng Part D* 217(1):53–61
25. Zheng JJ, Wang JH, Wang B, Huang ZH (2009) Effect of the compression ratio on the performance and combustion of a natural-gas direct injection engine. *Proc Inst Mech Eng Part D* 223(1):85–98
26. Kalam MA, Masjuki HH, Mahlia TMI, Fuad MA, Halim K, Ishak A, Khair M, Yusoff A, Shahrir A (2009) Experimental test of a new compressed natural gas engine with direct injection. *SAE paper* 2009-01-1967
27. Hassan MH, Kalam MA, Mahlia TMI, Aris I, Nizam MK, Abdullah S, Ali Y (2009) Experimental test of a new compressed natural gas direct injection engine. *Energy Fuels* 23(10):4981–4987
28. Zheng JJ, Hu EJ, Huang ZH, Ning DZ, Wang JH (2011) Combustion and emission characteristics of a spray guided direct injection spark-ignition engine fueled with natural gas-hydrogen blends. *Int J Hydrogen Energy* 36(17):11155–11163
29. Liu YF, Liu B, Liu L, Zeng K, Huang ZH (2010) Combustion characteristics and particulate emission in a natural-gas direct injection engine: effects of the injection timing and the spark timing. *Proc Inst Mech Eng J Automobile Eng* 224(8):1071–1080
30. Liu YF, Liu B, Zeng K, Huang ZH, Zhou L, Sun J (2012) Performance and emission characteristics of a hydrogen-enriched compressed natural gas direct injection spark ignition engine diluted with exhaust gas recirculation. *Proc Inst Mech Eng J Automobile Eng* 226(1):123–132
31. Korakianitis T, Namasivayam AM, Crookes RJ (2011) Natural-gas fueled spark-ignition (SI) and compression-ignition (CI) engine performance and emissions. *Prog Energy Combust Sci* 37(1):89–112
32. Huang ZH, Wang JH, Liu B, Zeng K, Yu JR, Jiang DM (2007) Combustion characteristics of a direct injection engine fueled with natural gas-hydrogen blends under different ignition timings. *Fuel* 86(3):381–387

33. Bauer CG, Forest TW (2001) Effect of hydrogen addition on the performance of methane-fueled vehicles. Part I: effect on S.I. engine performance. *Int J Hydrogen Energy* 26(1):55–70
34. Ma FH, Wang Y, Liu HQ, Li Y, Wang JJ, Ding SF (2008) Effects of hydrogen addition on cycle-by-cycle variations in a lean burn natural gas spark-ignition engines. *Int J Hydrogen Energy* 33(2):823–831
35. Akansu SO, Dulger Z, Kahraman N, Veziroglu TN (2004) Internal combustion engines fueled by natural gas-hydrogen mixtures. *Int J Hydrogen Energy* 29(14):1527–1539
36. Dimopoulos P, Bach C, Soltic P, Boulouchos K (2008) Hydrogen–natural gas blends fuelling passenger car engines: combustion, emissions and well-to-wheels assessment. *Int J Hydrogen Energy* 33(23):7224–7236
37. Li HL, Karim GA (2005) Exhaust emissions from an SI engine operating on gaseous fuel mixtures containing hydrogen. *Int J Hydrogen Energy* 30(13–14):1491–1499
38. Huang ZH, Wang JH, Liu B, Zeng K, Yu JR, Jiang DM (2006) Combustion characteristics of a direct injection engine fueled with natural gas-hydrogen blends under various injection timings. *Energy Fuels* 20(4):1498–1504
39. Wang JH, Huang ZH, Fang Y, Liu B, Zeng K, Miao HY, Jiang DM (2007) Combustion behaviors of a direct injection engine operating on various fractions of natural gas-hydrogen blends. *Int J Hydrogen Energy* 32(15):3555–3564
40. Shiga S, Ozone S, Machacon HTC, Karasawa T, Nakamura H, Ueda T, Jingu N, Huang ZH, Tsue M, Kono M (2002) A study of the combustion and emission characteristics of compressed-natural-gas direct injection stratified combustion using a rapid compression machine. *Combust Flame* 129(1–2):1–10
41. Zheng JJ, Huang ZH, Wang JH, Wang B, Ning DZ, Zhang YJ (2009) Effect of compression ratio on cycle-by-cycle variation in a natural gas direct injection engine. *Energy Fuels* 23(11):5357–5366
42. Arcoumanis C, Flora H, Kim JW, Xu HM (2000) Injection natural gas engine for light duty applications. In: International conference on 21st century emissions technology, London, England. 04–05 Dec 2000
43. Sen AK, Zheng JJ, Huang ZH (2011) Dynamics of cycle-to-cycle variations in a natural gas direct injection spark-ignition engine. *Appl Energy* 88(7):2324–2334

Experimental Results Using Ammonia Plus Hydrogen in a S.I. Engine

Stefano Frigo, Roberto Gentili, Giacomo Ricci, Giuseppe Pozzana and Massimiliano Comotti

Abstract In the prospective to reduce greenhouse gas emission from vehicles, the use of hydrogen as fuel represents a possible solution. However, if proper engine running with hydrogen has been widely demonstrated, hydrogen storage onboard of the vehicle is a major problem. A promising solution is storing hydrogen in the form of ammonia that is liquid at roughly 9 bar at environmental temperature and therefore involves relatively small volumes and requires light and low-cost tanks. Moreover, liquid ammonia contains 1.7 times by volume as much hydrogen as liquid hydrogen itself. It is well known that ammonia can be burned directly in I.C. engines, however a combustion promoter is necessary to support combustion especially in the case of high-speed S.I. engines. As a matter of fact, the best (and carbon-free!) promoter is hydrogen, which has very high combustion velocity and wide flammability range, whereas ammonia combustion is characterised by low flame speed, low flame temperature, narrow flammability range (combustion is impossible if mixture is just slightly lean), high ignition energy and high self-ignition temperature.

F2012-B01-015

S. Frigo (✉) · R. Gentili
Dipartimento di Ingegneria dell'Energia e dei Sistemi, Università di Pisa, Pisa, Italy
e-mail: s.frigo@ing.unipi.it

R. Gentili
e-mail: r.gentili@ing.unipi.it

G. Ricci
EDI Progetti e Sviluppo, Pontedera, Italy
e-mail: g.ricci@ediprogetti.it

G. Pozzana
Pont-Tech S.C.R.L, Pontedera, Italy

M. Comotti
Acta S.p.A, Crespina, Italy

The experimental activity shown in the paper was aimed at determining proper air-ammonia-hydrogen mixture compositions for the actual operating conditions of a twin-cylinder 505 cm³ S.I. engine. Hydrogen and ammonia are separately injected in the gaseous phase. The experimental results confirm that it is necessary to add hydrogen to air-ammonia mixture to improve ignition and to speed up combustion, with ratios that depend mainly on load and less on engine speed. This activity is correlated with a larger-scale project, founded by Tuscany Region, in which a partnership of research and industry entities has developed a fully-working plug-in hybrid electric vehicle equipped with a range-extending 15 kW IC engine fuelled with hydrogen and ammonia. Hydrogen is obtained from ammonia by means of on-board catalytic reforming.

Keywords Ammonia engine · Hydrogen engine · Alternative fuels · Carbon-free fuels · Ammonia reforming

Abbreviations

AIT	Auto ignition temperature
AMIE	Absolute minimum ignition energy
BTDC	Before top dead centre
CA	Crank angle
CNG	Compressed natural gas
COV	Coefficient of variation
DI	Direct injection
EBTE	Engine brake thermal efficiency
ECU	Electronic control unit
EC	Energy content (stoichiometric mixt)
EGR	Exhaust gas recirculation
FL	Flammability limits (gas in air)
HAER	Hydrogen-ammonia energy ratio
IC	Internal combustion
LFV	Laminar flame velocity
LHV	Lower heating value
IMEP	Inlet mean effective pressure
MBT	Maximum best torque
RPM	Revolution per minute
ON	Octane number
SCR	Selective catalytic reactor
SI	Spark ignition
ST	Stoichiometric
TDC	Top dead centre
UEGO	Universal exhaust gas oxygen
WOT	Wide open throttle
ρ	Density

1 Introduction

The main problem of electric vehicles is poor driving range due to low battery capacity. This drawback is enhanced by power requirement for lights and heating in winter.

Therefore in many cases range extenders are required, which use fuel to produce electricity when necessary [1–4]. Almost all present range extenders are based on conventional S.I. or C.I. engines, which are reliable and not expensive, but produce large green house gas emissions.

To produce carbon-free emissions, hydrogen can be employed as fuel in the range-extender engine (I.C. engine running ability with hydrogen has been widely demonstrated), but it reduces the range extending capacity, due to the scarce amount of hydrogen that can be stored on board. Moreover, as underlined by other authors [5], actually there is no existing infrastructure for hydrogen delivery and over 90 % of hydrogen production is still from reforming of fossil fuels such as natural gas, with the accompanying CO₂ emissions.

A solution to overcome this problem consists in storing hydrogen in the form of ammonia, which, at environmental temperature, is liquid at roughly 9 bar at environmental temperature and therefore involves relatively small volumes and requires light and low-cost tanks. Moreover, liquid ammonia contains 1.7 times by volume as much hydrogen as liquid hydrogen itself [6, 7].

Roughly 85 % of world ammonia production is based on steam reforming of natural gas using the well known Haber–Bosch process [8], but ammonia can be produced also electrochemically, or organically, or biologically, or by renewable sources: biomass energy, wind energy, solar energy, geothermal energy, hydro-electric energy can be used to electrolyse hydrogen from water and produce ammonia. These methods provide a number of scalable manufacturing routes that can be developed and employed in accordance with evolving market demand and economy.

The possibility to use ammonia as direct gasoline replacement has been concretely discussed since mid-1960s [9–12], even if previous attempts and a patent of 1938 attest the possibility of using a mixture of hydrogen, ammonia and nitrogen as fuel in internal combustion engines [13, 14]. Some experiences show that lone ammonia can be burned in IC engines. However, due to low flame temperature, low laminar burning velocity and high ignition energy, it is practical to use ammonia together with other fuels used as combustion catalysts. Some investigations attest [15–19] that the best one is hydrogen, showing that a small amount, added to air-ammonia mixture, is effective to speed combustion up.

The opposed and potentially complementary properties of hydrogen and ammonia give new prospective in engine combustion control. As aforesaid, ammonia is characterized by low flame speed (also with respect to gasoline) and narrow flammability range (combustion is impossible even with low excess air), high ignition energy and high auto-ignition temperature. On the other side,

Table 1 Combustion properties of ammonia, hydrogen and gasoline [21]

Properties	Ammonia	Hydrogen	Gasoline
LHV (MJ/kg)	18.8	120	44.5
FL (vol. %)	15–28	4.7–75	0.6–8
LFV (m/s)	0.015	3.51	0.58
AIT (°C)	651	571	230
AMIE (mJ)	8.0	0.018	0.14
ON (RON)	>130	>100	90–98
ρ (25 °C, 1 bar) (g/L)	0.703	0.082	740
ST (air/fuel) (mass)	6.04	34.3	~ 14.5
EC (st. mixt.) (MJ/kg)	2.8	3.3	2.7

hydrogen displays low ignition energy, high combustion velocity and wide flammability range that allows the engine to operate with very high air–fuel ratios.

A comparison of combustion properties of ammonia, hydrogen and gasoline are given in Table 1 [17–20].

Extensive analyses of ammonia production cost and of energy per unit of storage tank volume, in comparison with other conventional fuels (gasoline, compressed natural gas CNG, liquefied petroleum gas LPG, methanol, hydrogen) has been conducted by other authors [20]. The study shows that ammonia is the least expensive fuel in terms of cost per GJ stored onboard, while in terms of GJ/m³ ammonia becomes the third, after gasoline and LPG. Moreover, ammonia is the cheapest fuel per 100 km driving range.

It is noteworthy resuming some data, shown in Table 2, related to a comparison of ammonia and hydrogen storage and driving range characteristics on a prototype vehicle based on a Ford Focus. Some of the original data were recalculated taking into consideration the Italian law that imposes 200 bars as maximum storage pressure on board. The power-train performance is characterized by 1.19 MJ/km shaft power and the efficiency of the ammonia engine has been taken the same as of the hydrogen engine. As it can be noted, the driving range of the NH₃ vehicle is much longer and hence less expensive (for ammonia it was assumed a cost of \$0.30/kg and for hydrogen an average cost of \$4/kg). Moreover, the tank of the ammonia car is about 6 times more compact.

Some additional advantages of ammonia in respect of hydrogen are commercial availability and viability, global distribution network, easy handling experience, etc., while the problem of its toxicity that can easily be overcome with the current control and storage technologies.

The experimental activity displayed in this paper was mainly aimed at developing a simple electronic hydrogen-ammonia injection system and determining appropriate air-ammonia-hydrogen mixture composition for each actual operating condition of a prototype engine and therefore at establishing the proper technical characteristics of the injection system.

This activity is correlated with a larger scale project, focused on a range-extended electric vehicle (briefly presented at the end of the paper) involving the

Table 2 Ammonia and hydrogen storage characteristics

Parameter	Unit	Ammonia	Hydrogen
Tank volume	Liter	60	200
Storage pressure	Bar	10	200
Energy on-board	MJ	814	393
Estimated driving range	km	340	165
Tank compactness	L/100 km	18	121

Table 3 Experimental engine specifications

Model	Lombardini LGW 523 MPI
Displacement	505 cm ³
Stroke	62 mm
Bore	72 mm
Compression ratio	10.7:1
Cooling system	Water cooled
Valves	2 per cylinder
Max power (gasoline)	21 kW @ 6,000 rpm
Max torque (gasoline)	39 Nm @ 2,200 rpm
Engine velocity at idle	1,100 rpm
Mass	49 kg

ammonia-plus-hydrogen I.C. engine and where the necessary flow of hydrogen comes from a special catalytic ammonia cracker (purposely realized within the project) that is heated by engine exhaust gases. No production of greenhouse gases occurs since ammonia does not contain carbon.

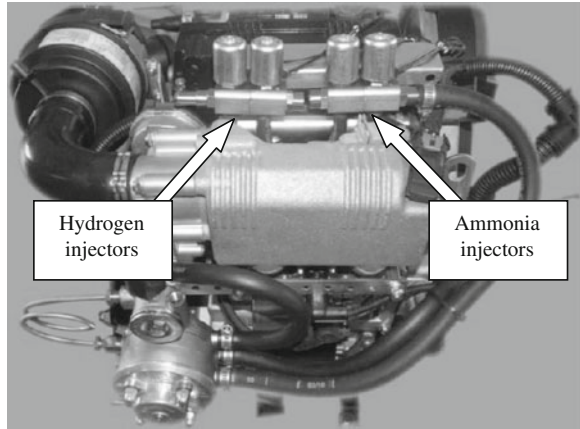
2 Engine Experimental Setup

The prototype engine derives from a 505 cm³ Lombardini twin-cylinder S.I. engine, whose specifications are reported in Table 3. Hydrogen and ammonia are separately injected in the gaseous phase. Accordingly, the original intake manifold was modified to add electro-injectors for hydrogen and for ammonia to the original ones for gasoline. This is the only mechanical modification the original engine underwent.

As a whole, six electro-injectors are now located on the intake manifold (three for each duct). The injectors for ammonia and for hydrogen are conventional ones for CNG application with appropriate modifications to their inner parts.

Ammonia was stored in the liquid phase at room temperature and 9 bars. An heated vaporizer with a pressure regulator was placed before the electro-injectors. Careful attention was dedicated to the hydrogen-ammonia feeding line to avoid leakages and partial ammonia condensation before the injectors.

Fig. 1 The experimental engine with *ammonia* and *hydrogen injectors* in evidence



The original ECU was replaced with a fully-programmable one (MoTeC model M800) and set to drive the ignition system and the six electro-injectors for hydrogen, ammonia and gasoline (this last option, i.e. the use of gasoline, was kept in the prospective of a more flexible hybrid vehicle).

The engine was fully instrumented. A magnetic sensor was located on the camshaft for the correct phasing of the injection and ignition events. Thermal flow meters were adopted to measure hydrogen and ammonia consumption. Piezo-resistive pressure sensors gauged the intake and the exhaust pipes, while a special spark plug with integrated piezoelectric sensor gauged cylinder pressure. Pressure sensors were placed in the ammonia and in the hydrogen feeding lines. Thermocouples were located in the intake and exhaust pipes, as well as in the cooling and in the lubrication circuits. To measure fuel-air ratio (λ) a proportional O_2 (UEGO) sensor was placed in the exhaust pipe, while a chemiluminescence NO_x analyzer gauged the exhaust emissions. An optical encoder was placed on the frontal side of the crankshaft, while an AVL Indicom system performed data acquisition and processing. The intake air flow rate was controlled by the original motorized throttle valve.

Figure 1 shows a picture of the experimental engine with ammonia and hydrogen injectors in evidence.

3 Experimental Activity and Results

Preliminary tests were performed to verify the possibility to operate the engine with a mixture of air, ammonia and hydrogen and to determine proper injection timings and feeding line pressures of hydrogen and ammonia for suitable combustion at all speeds and loads. This first experimentation was performed mainly in view of producing hydrogen on board the vehicle by ammonia catalytic reforming, to verify whether the working temperature and the output limits in hydrogen flow

rate and pressure (roughly $1.35 \text{ Nm}^3/\text{h}$ and 0.5 bar relative pressure) of the designed catalytic reformer were compatible with engine characteristics and needs.

This performance of the catalytic reformer was separately verified by experimental tests that proved full conversion of ammonia to hydrogen and nitrogen (whose flow rate to the engine is negligible compared to nitrogen flow rate due to air intake) at the designed temperature of $500 \text{ }^\circ\text{C}$. Yet, ammonia conversion was proved to be almost complete even at as low reformer temperature as $450 \text{ }^\circ\text{C}$, allowing security margin in case of exhaust gas temperature fluctuation. The thermal energy necessary for the catalytic reaction can be obtained from the exhaust gasses whose temperature, into the operative range examined, is always higher $550 \text{ }^\circ\text{C}$. In addition, the reformer is electrically heated to overcome the problem of insufficient exhaust gas temperature during cold start transient.

Injection timings for hydrogen and ammonia were set at TDC of the passive cycle. Feeding line relative pressures for hydrogen was set at 0.4 bar, while for ammonia a relative pressure of 2.4 bar was utilised.

The next experimental activity was focused on determining the minimum hydrogen-to-ammonia energy ratios (HAER) that keep $\text{COV}_{\text{imep}} < 10 \%$. This is considered the maximum value of cyclic variation for acceptable engine behaviour [22]. Tests were performed at various speeds (from 2,500 to 5,000 rpm with steps of 500 rpm) and loads (full and half load) with stoichiometric mixtures ($\lambda = 1$), taking the operating range of the engine connected to the electric generator into account. Forthcoming tests will explore engine behaviour with lean mixtures.

Ignition advance was set at MBT at every engine speed and load and for each experimental condition 100 cycles were recorded and analysed.

The experimentation evidenced two important issues, summarized as follows:

1. With the smallest acceptable HAER, 40° to 42° BTDC ignition timing gives the best results at every engine speed and load. This spark advance is 10° to 15° larger than with gasoline and can be addressed to high ignition energy and low flame speed that characterize and protract ammonia combustion, leading to larger heat loss through cylinder walls and less residual expansion than with gasoline, with consequent less thermal efficiency.
2. Engine COV_{imep} rapidly increases as HAER falls below a certain value, as Fig. 2 proves for full load and $\lambda = 1$ at 3,000 and 4,000 rpm. In this case COV_{imep} sharp increase occurs below a HAER value of roughly 6–7 %, yet engine behaviour remains acceptable up to a HEAR value of roughly 5 %.

Conservatively, the HAER below which engine COV_{imep} rapidly increases have been considered as the “practical” minimum HAER that is given in Fig. 3 versus engine speed with $\lambda = 1$, at full and half load.

Figure 4 displays brake power vs. engine speed at WOT and $\lambda = 1$ with gasoline and with ammonia plus the above-mentioned minimal sufficient amounts of hydrogen, proving that in the second case power is roughly 10 % less at low rpm and 25 % less at high rpm. This is due to mixture poor volumetric heating value, because of the high specific volume of ammonia and hydrogen, and to ammonia low flame speed that penalizes the more, the faster the engine runs.

Fig. 2 COV_{imep} versus HEAR at 3,000 and 4,000 rpm, WOT, $\lambda = 1$

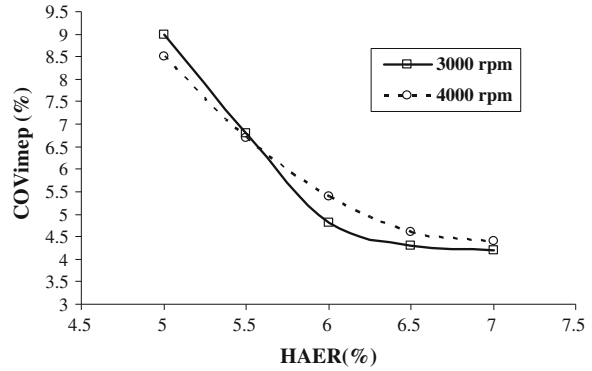


Fig. 3 Minimum HEAR versus engine speed at full and half load, $\lambda = 1$

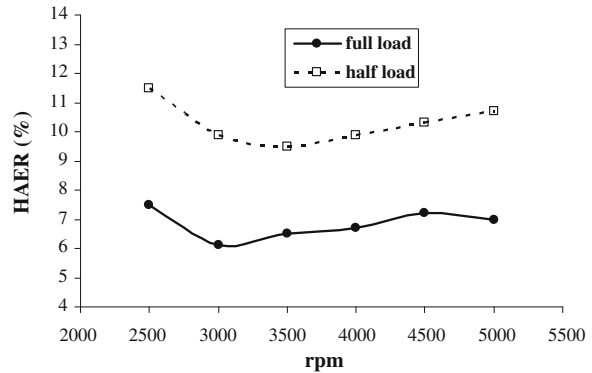
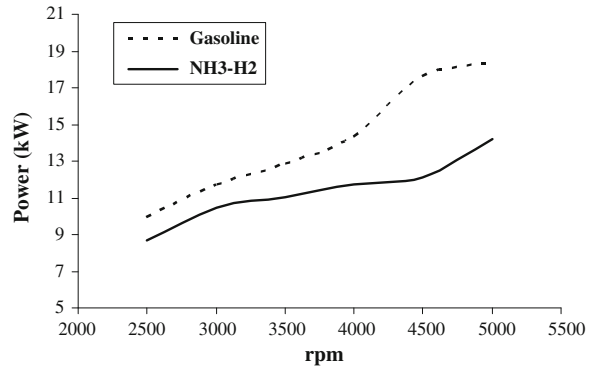
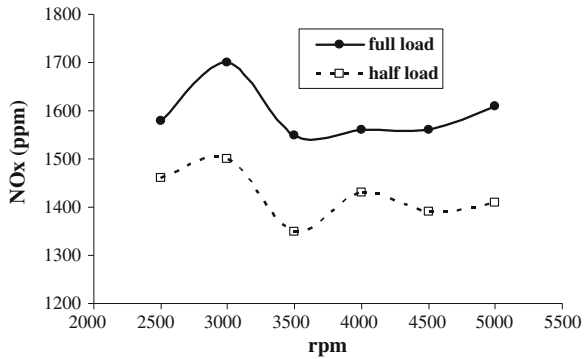


Fig. 4 Brake power versus engine speed with gasoline and with ammonia plus hydrogen at WOT, $\lambda = 1$



NO_x is the only meaningful pollutant found in the exhaust emissions (unburned hydrocarbons from lubricant are negligible and the presence of ammonia in the exhaust gas was not measured). Figure 5 displays NO_x emission vs. engine speed with the minimum HEAR at full and half load, keeping $\lambda = 1$. At full load, NO_x maximum emission is 1,700 ppm at 3,000 rpm. Due to the lower combustion temperatures, NO_x emission is always lower at half load, with a maximum of

Fig. 5 NO_x versus engine speed with ammonia plus hydrogen at full and half load, $\lambda = 1$



1,500 ppm, still located at about 3,000 rpm. Yet, NO_x emission is not a problem, since, in the case of stoichiometric mixture, NO_x can be effectively abated by a normal reducing catalyst and, in the case of lean mixture, the use of a SCR is eased by the presence of ammonia onboard.

3.1 Cold Start Procedure

Hydrogen-to-ammonia ratio must be considerably increased to guarantee correct engine cold start, as data on Table 4 prove. Cold start feeding conditions must be kept for few seconds after starting, with the engine at idle (1,800 rpm, quite high idle speed in respect of around 1,100 rpm with gasoline). Then hydrogen-to-ammonia ratio is progressively reduced and engine speed increased to reach the required operating conditions.

Since hydrogen flow rate is higher than the one provided by the catalytic reformer, a suitable amount of hydrogen must be stored in a tank that will be recharged during engine normal running. Solutions are being studied to reduce the cold-start requirement of hydrogen flow rate to the level provided by the catalytic reformer. Among them, high engine compression ratio (allowed by very high ammonia octane number) and special solutions for ignition are worth mentioning.

4 The Range-Extended Electric Vehicle

The ammonia-hydrogen engine was installed on prototype range-extended electric vehicle that derives from Effedi Gasolone 35, a small commercial vehicle conceived for garbage collection, originally equipped with a Diesel engine.

This vehicle displays two important features:

1. It has a flexible chassis that is suitable for the transformation to hybrid (several new devices must be installed on board, such as all the electric and electronic devices, the hydrogen generator, the ammonia tank, etc.);

Table 4 Cold start feeding conditions

H ₂ flow rate	2.6 Nm ³ /h
H ₂ feeding line relative pressure	0.4 bar
NH ₃ flow rate	0.54 Nm ³ /h
NH ₃ feeding line relative pressure	2.1 bar
HAER	360 %

Fig. 6 Final assembly of the vehicle, ready for road test

- It is a typical example of vehicle for city use; as a matter of fact it is the smallest available one with 3.5 t capacity and it is characterized by high manageability.

Range-extended electric vehicles for garbage collection are especially suited for city centres where noise and pollution are very important issues and where these vehicles can work in pure electrical mode (sometimes garbage is collected during the night), restricting the use of the I.C. engine to the transfer travels.

The prototype is a series hybrid: the vehicle is driven by the electric motor with no mechanical connection to the I.C. engine that only runs a generator to recharge the batteries.

All the components of the power train, i.e. the I.C. engine, the generator, the electric motor, the electronic controls and devices, etc. were expressly studied, designed and realised.

Because of the toxicity of gaseous ammonia, a suitable monitoring system was integrated into the vehicle. It is based on a modular architecture, which allows the integration of several sensors in a scalable plug-an-play structure and provides data pre-elaboration.

Three ammonia sensors are located in different places of the vehicle: one is placed inside the cockpit, for the safety of the driver; another sensor is placed near both the ammonia tank and the catalytic reactor, to monitor possible ammonia leakages, and the last one is at the exit of the tailpipe to detect the presence of unburned ammonia. The system alarms were settled on a threshold of 20 ppm of ammonia for inside the vehicle and of 100 ppm for outside.

The final assembly of the vehicle, ready for road test, is showed on Fig. 6.

5 Conclusions

Ammonia represents a hydrogen carrier and can be effectively utilized as fuel in IC engines, provided that a small percentage of other fuels is added as combustion catalyst. Among them, the best one is hydrogen, which can be obtained directly from ammonia on board the vehicle by means of a catalytic reformer.

In this experimental activity a simple electronic fuel injection system, that injects ammonia and hydrogen in the gaseous phase, was designed and implemented on a 505 cm³ twin-cylinder S.I. engine that was mechanically modified only as concerns the intake manifold, to host the electro-injectors for ammonia and hydrogen.

The final aim of the study is the design and construction of an electric vehicle, where the ammonia-plus-hydrogen engine is employed as range extender and hydrogen is obtained from ammonia by on-board catalytic reforming.

The experimental results confirm the need to speed combustion up by adding hydrogen to air-ammonia mixture, with ratios that mainly depend on load. The minimum HAER to get correct engine behaviour (i.e. $COV_{imep} < 10\%$) is roughly 6–7 % at full load and 10–11 % at half load.

Keeping $\lambda = 1$ on the whole, engine stability increases increasing the HAER, as expected.

NO_x is the only meaningful pollutant found in the exhaust emissions (unburned hydrocarbons from lubricant are negligible), with a maximum of 1,700 ppm at full load and 3,000 ppm.

The presence of ammonia in the exhaust gas was not measured at test bench. However, an ammonia sensor is placed at the exit of the exhaust pipe on the vehicle for the next road testing activity.

No meaningful mechanical inconvenience occurred during the described experimental activity. Nevertheless, long-time reliability of the injection system for ammonia and for hydrogen has to be verified.

Acknowledgments The authors are pleased to acknowledge the financial support granted by Regione Toscana within “Progetto SAVIA”, which is part of the Regional Operative Program co-financed by the European Community.

References

1. Klostermann A (2011) Future of automotive powertrains. Trends and developments in range extender technology. Automotive Technology Centre, 2011
2. Ribau J, Silva C, Brito FP, Martins J (2012) Analysis of four-stroke, Wankel, and microturbine based range extenders for electric vehicles. *Energy Convers Manage* 58:120–133

3. Varnhagen S, Same A, Remillard J, Park JW (2011) A numerical investigation on the efficiency of range extending systems using Advanced Vehicle Simulator. *J Power Sources* 196:3360–3370
4. Tate ED, Harpster MO, Savagian PJ (2008) The electrification of the automobile: from conventional hybrid, to plug-in hybrids, to extended-range electric vehicles. *SAE Paper 2008-01-0458*
5. Lan R, Irvine JTS, Tao S (2012) Ammonia and related chemicals as potential indirect hydrogen storage materials. *Int J Hydrogen Energy* 37:1482–1494
6. Thomas G, Parks G (2006) Potential roles of ammonia in a hydrogen economy—a study of issues related to the use ammonia for on-board vehicular hydrogen storage. World Wide Web location, 2006 (http://www.hydrogen.energy.gov/pdfs/nh3_paper.pdf)
7. Agosta V (2003) *The Ammonia Economy*. ASME, 2003
8. Rafiqul I, Weber C, Lehmann B, Voss A (2005) Energy efficiency improvements in ammonia production—perspectives and uncertainties. *Energy* 30:2487–2504
9. Cornelius W, Huellmantel LW, Mitchell HR (1966) Ammonia as an engine fuel. *SAE Transaction*, p 300
10. Starkman ES, Newhall HK, Sutton R, Maguire T, Farbar L (1966) Ammonia as a spark ignition engine fuel: theory and application. *SAE Paper 660155*
11. Gray Jr JT, Demitroff E, Meckel NT, Quillian Jr. RD Ammonia Fuel Engine Compatibility and Combustion. *SAE Paper 660156*, 1066
12. Pearsall J, Garabedian C (1967) Combustion of anhydrous ammonia in diesel engines. *SAE Paper 670947*, 1967
13. Kroch E (1945) Ammonia—A fuel for motor buses. *J Inst Petrol* 31:213–223
14. Zavka M (1938) Device for operating internal combustion engines with mixtures of Ammonia, Hydrogen and Nitrogen prepared from Ammonia. Patent # 2,140,254, Patented 13 Dec 1938
15. Arora N, Gupta DCP (1970) Ammonia as S.I. engine fuel. *Metals and mineral review*—January 1970
16. Mørch CS (2007) Performance of ammonia/hydrogen mixtures in SI engines. Master's thesis. Department of Mechanical Engineering, Technical University of Denmark, Danish language (July 2007)
17. Mørch CS, Bjerre A, Gøttrup MP, Sorenson SC, Schramm J (2011) Ammonia/hydrogen mixtures in an SI-engine: engine performance and analysis of a proposed fuel system. *Fuel* 90, Elsevier, Amsterdam, pp 854–864
18. Ciccarelli G, Jackson D, Verreault J (2006) Flammability limits of NH₃–H₂–N₂–air mixtures at elevated initial temperatures. *Combustion and Flame* 144, Elsevier, Amsterdam, pp 53–63
19. Lee JH, Kim JH, Park JH, Kwon OC (2010) Studies on properties of laminar premixed hydrogen-added ammonia/air flames for hydrogen production. *International Journal of Hydrogen Energy*, vol 35. Elsevier, Amsterdam, pp 1054–1064
20. Zamfirescu C, Dincer I (2009) Ammonia as a green fuel and hydrogen source for vehicular applications. *Fuel Process Technol* 90:729–737
21. H2ICE Ford Focus proves the viability of hydrogen internal combustion technology, internet source, 2008 (http://media.ford.com/article_display.cfm?article_id=16375)
22. Heywood JB (1988) *Internal combustion engine fundamentals*. McGraw-Hill, NY

Dual Fuel H2-Diesel Heavy Duty Truck Engines with Optimum Speed Power Turbine

Alberto Boretti

Abstract The turbocharged direct injection lean burn Diesel engine is the most efficient engine now in production for transport applications with full load brake engine thermal efficiencies up to 40–45 % and reduced penalties in brake engine thermal efficiencies reducing the load by the quantity of fuel injected. The secrets of this engine's performances are the high compression ratio and the lean bulk combustion mostly diffusion controlled in addition to the partial recovery of the exhaust energy to boost the charging efficiency. The major downfalls of this engine are the carbon dioxide emissions and the depletion of fossil fuels using fossil Diesel, the energy security issues of using foreign fossil fuels in general, and finally the difficulty to meet future emission standards for soot, smoke, nitrogen oxides, carbon oxide and unburned hydrocarbons for the intrinsically “dirty” combustion of the fuel injected in liquid state and the lack of maturity the lean after treatment system. Renewable hydrogen is a possible replacement for the future of the Diesel that is free of carbon dioxide and other major emissions, with the only exception of nitric dioxides. In this paper, a Diesel engine is modelled and converted to run hydrogen retaining the same of Diesel full and part load efficiencies. The conversion is obtained by introducing a second direct fuel injector for the hydrogen. The dual fuel engine has slightly better than Diesel fuel efficiencies all over the load range and it may also permit better full load power and torque outputs running closer to stoichiometry. The development of novel injectors permitting multiple

F2012-B01-018

A. Boretti (✉)

Missouri University of Science and technology, Rolla, USA
e-mail: a_boretti@yahoo.com

A. Boretti
University of Ballarat, Ballarat, Australia

injections shaping as in modern Diesel despite the extremely low density of the hydrogen fuel is indicated as the key area of development of these engines.

Keywords Heavy duty trucks · Hydrogen · Internal combustion engines · Power turbine

Abbreviations

BDC	Bottom dead centre
CNG	Compressed natural gas
CVT	Continuously variable transmission
EGR	Exhaust gas recirculation
EVO	Exhaust valve opening
EVC	Exhaust valve closure
HPDI	High pressure direct injection
IVO	Intake valve opening
IVC	Intake valve closure
LHV	Lower heating value
TC	Turbocharged
TDC	Top dead centre

1 Dual Fuel H2ICE

Apart from few remarkable experiences of the past, the most part of the hydrogen internal combustion engines (H2ICE) have been built in the last 20 years and in almost the totality of the cases starting from a gasoline-fuelled power plant. Many traditional gasoline engines have been modified for manifold or port injection of hydrogen with combustion controlled by a spark discharge and load controlled by throttling the intake. Direct injection of hydrogen has proved to be effective in improving the performances of these gasoline-like H2ICEs both experimentally and computationally [1, 2]. Diesel-like applications have also been proposed [3–6]. Computationally, it has been demonstrated that a dual fuel pilot Diesel and hydrogen main direct injection permits similar to Diesel only operation and efficiencies both full and part load [3]. Experimentally, it has been demonstrated that direct injection of hydrogen only by using today's best single fuel injectors may permit similar to Diesel efficiencies continuously operating a glow plug providing surface ignition of the hydrogen and air mixture [4–6].

Single fuel direct injection injectors for compression ignition engine applications with hydrogen are proposed by Westport [7] and Hoerbiger [8]. The Westport injector has been already adopted in a large number of engine applications but with Compressed Natural Gas (CNG) and ignition forced by either a hot surface or a spark. With hydrogen, these off-the-shelf injectors are not able to deliver the

amount of fuel needed to large displacement heavy duty truck (HDT) engine cylinders within acceptable time frames.

Three properties of hydrogen are particularly relevant for the use as a fuel for a compression ignition engine. Hydrogen has a very low density, therefore delivery of quantities large enough within time frames small enough may be an issue. Hydrogen has a wide ignition limits of mixtures with air, from $\lambda = 0.14$ to $\lambda = 10$ homogeneous. This permits the load control throttle-less typical of the Diesel. Hydrogen has auto ignition temperatures in air of about 850 K much larger than the Diesel. This requires much higher in-cylinder temperatures or the assisted start of combustion to produce Diesel-like combustion processes.

With reference to Diesel, hydrogen has also the advantage to be delivered into the combustion chamber in its gaseous form. When the hydrogen jets penetrate the combustion chamber, then they mix with the surrounding air and the hydrogen is heated up. There is no need to vaporize the liquid droplets, and combustion may proceed much faster with hydrogen after the more troublesome start-up phase also thanks to the faster combustion properties of the hydrogen versus the Diesel vapour made up of various hydrocarbon vapours.

Two compression ignition hydrogen engines ideas have been developed recently, one working with hydrogen only but requiring a surface ignition, and one working with a pilot Diesel injection preceding the main hydrogen injection. Both experiences are very far from production standards with [3] probably much easier to be translated in a real product than [4–6]. Auto-ignition of hydrogen is also studied in [9].

In the surface system ignition of [4–6] working with a single fuel injection pulse, the hydrogen is first ignited following impingement on the continuously operated glow plug. This surface ignition occurs 0.4 ms after the injector needle opens, immediately after the impinging of the hydrogen on the glow plug and the mixing with the surrounding air. The combustion evolution then sharply raises the chamber pressure and temperature, and once better auto-ignition conditions are globally reached within the chamber, then all of the hydrogen jets emerging from the multi holes injector ignite just following the mixing with air [4–6]. Assuming adequate glow plug surface temperature, combustion starts as soon as one of the hydrogen jets reaches the glow plug. Knock is avoided by the then quick combustion of the hydrogen already available in the chamber. After the combustion start-up phase, the injection of hydrogen in high temperatures gases produces a combustion rate basically controlled by the rate of injection for the hydrogen that then burns almost instantaneously following mixing with air and temperature heating up.

The conversion is obtained here by introducing a second direct fuel injector for the hydrogen. A sketch of the combustion chamber is shown in Fig. 1.

The computational results proposed in [3] with a pilot Diesel preceding a main hydrogen injection have shown that as soon as the main injection of hydrogen occurs in an environment with temperatures high enough and within the same injection duration of the main diesel injection, then the fuel conversion efficiency can be made even higher both full and part load and thanks also to the ability to run richer λ than the Diesel both the power and torque outputs may also be increased.

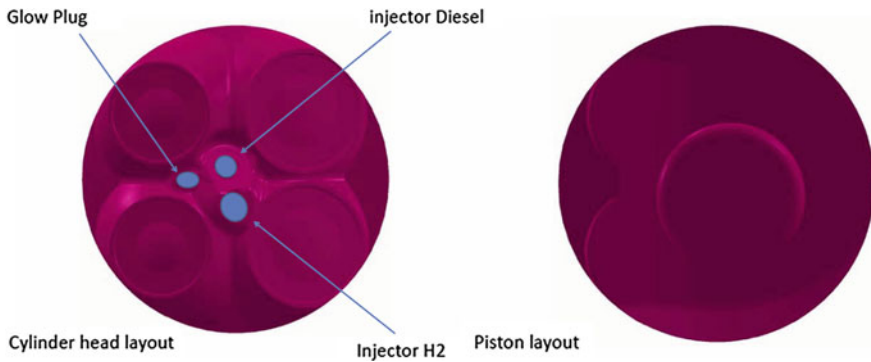


Fig. 1 Diesel igniting fuel design—main combustion chamber. The main chamber multi fuel injector introduces the most part of the fuel. The Diesel injection may occur prior, simultaneously or after the multi fuel injection

2 Optimum Speed Power Turbine

The engine considered as the baseline is a Diesel engine having a power turbine. Internal combustion engines have a maximum theoretical fuel conversion efficiency that is similar to that of fuel cells and considerably higher than the mid-40 % peak values seen today. To be precise, this is a true statement only at high temperatures, because at low temperatures the fuel cell has a much better theoretical efficiency, but this does not make too much difference for the typical operating conditions of heavy duty truck engines. The primary limiting factors to approaching these theoretical limits of conversion efficiency start with the high irreversibility in traditional premixed or diffusion flames, but include heat losses during combustion and expansion, untapped exhaust energy, and mechanical friction. One area where there is large potential for improvements in ICE efficiency is losses from the exhaust gases [10, 11]. Exhaust losses are being addressed by analysis and development of compound compression and expansion cycles achieved by variable valve timing, variable stroke use of turbine expanders, regenerative heat recovery, and application of thermoelectric generators. Employing such cycles and devices, it has been claimed to have the potential to increase engine efficiency by 10 % [10, 11]. Of all these technologies, the more mature is the use of two turbines in series; one waste gated driving the upstream compressor, and one to producing additional power to the driveline, historically known as turbo compound.

The use of turbo compounding goes back quite a long way. The concept was originally used back in the late 1940 and 1950s on two notable aircraft engines [12, 13]. Its promise of low fuel consumption was soon overtaken by the rapid development of the turboprop engine. For automotive diesel engines, the introduction of a power turbine downstream of the turbocharger generates more work by re-using the exhaust gases from the conventional turbocharger [14–23]. The

work generated by the power turbine is then fed back into the engine crankshaft via an advanced transmission. A gear is fitted to the power turbine shaft. To assist the power turbine, the turbine for the conventional turbocharger is designed for a reduced expansion ratio. This small turbocharger gives another system advantage to the turbo compound engine, providing better transient response and higher boost pressure for improved low speed torque. The behaviour of the two turbines in series—turbocharger and power turbine—offers a dynamic response across the engine speed and air flow range. However, it requires optimum matching of the turbines.

In traditional turbo compounding applications, the turbo compound includes a downstream axial flow power turbine plus the speed reduction gears, the fluid coupling and the final gear reduction to crankshaft to supplement crankshaft power. In the mechanical transmission made up of a gear train and a hydraulic coupling, the turbine is running with maximum speeds of up to 70,000 rpm. The gear ratio from the exhaust turbine to the turbo compound intermediate shaft is around 6:1, and the gear ratio from the intermediate shaft to the crankshaft is around 5:1 for an overall gear ratio of about 30:1. Torsional vibrations caused from the internal combustion engine process would be increased by the overall gear ratio exceeding 30:1 and could possibly destroy the turbine. To reduce torsional vibrations the turbo compound intermediate shaft is equipped with a hydrodynamic coupling with a slip inside the coupling that is normally around 2 %.

Despite few truck manufacturers claim better efficiency and increased power output as a result of the additional power turbine, this solution has not encountered so far the favour of the vast majority of truck and the totality of car manufacturers. Because the amount of energy available downstream of the turbocharger turbine is small and the complexity to add a second power turbine geared to the crankshaft is high, turbo compound is expected in principle to provide limited advantages in a limited area of operation of the engine at high costs in terms of design, control, packaging and weight. Engine manufacturers that have had or will have Turbo compound Engines include Volvo, Iveco (off-highway) and Scania. Detroit Diesel, Cummins, CAT, Mercedes, and International have also considered the technology.

In the Diesel engine considered as the baseline for the hydrogen conversion, the traditional gear train coupling of the power turbine is replaced by a constant variable transmission (CVT). A by-pass of the power turbine is also included. This permits to narrow the range of speeds where the turbine operates producing more power than the power loss for back pressures while permitting temperatures to the downstream after treatment system high enough.

The principle of adding a power turbine in a configuration with a clutch, a continuously variable transmission and a by-pass is a novelty. The very well know fixed gear ratio connection of a power turbine always operational to the crankshaft is also very well know to produce more downfalls then benefits, and as a matter of fact, almost every car maker has studied this opportunity then dropping the solution for non adequate cost-to-benefit ratio (Fig. 2).

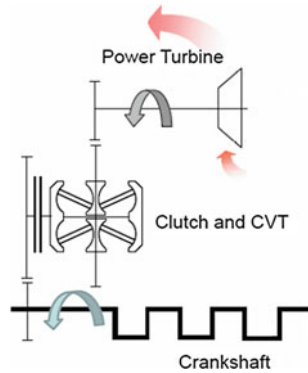


Fig. 2 Sketch of the novel power turbine layout. With reference to the arrangement previously proposed with just a gear in between the crankshaft and the power turbine shaft, this design now include a clutch and a continuously variable transmission to disconnect the power turbine when bypassed by the exhaust gases and to operate the power turbine at the most favourable speed

Table 1 12.8 l in-line six cylinder turbo charged directly injected Diesel engine

Displacement per cylinder (l)	2.13
Number of cylinders	6
Engine layout	I-6
Compression ratio	18
Bore (mm)	131
Stroke (mm)	158
Connecting rod length (mm)	300
Wrist pin offset (mm)	0
Clearance volume (l)	0.125
Engine type	C.I.
Number of intake valve per cylinder	2
Intake valve diameter (mm)	46.3
Intake valve maximum lift (mm)	12.1
Number of exhaust valve per cylinder	2
I VO (deg)	314 (-46)
I VC (deg)	602 (+62)
Exhaust valve diameter (mm)	41.5
Exhaust valve maximum lift (mm)	13.4
E VO (deg)	100 (-80)
E VC (deg)	400 (+40)

3 Engine Details

Engine performance simulations are performed for a 12.8 l in-line six cylinder turbo charged directly injected HDT Diesel engine converted to hydrogen. The engine geometry (baseline) is presented in Table 1. A power turbine downstream of the turbocharger is used to recover a percentage of the thermal energy that

would normally be lost through the engine's exhaust. A by-pass of the power turbine is also included. This permits to operate the power turbine when this turbine produces more power than the power loss for the back pressures while permitting temperatures to the downstream after treatment system high enough. A constant variable transmission (CVT) permits operation of the power turbine at the more efficient speeds.

The Diesel engine has a target performance of 2,600 Nm torque 1,000–1,450 rpm, and of about 400 kW of power 1,450–1,900 rpm, with BSFC values around 190 g/kWh, corresponding to brake fuel conversion efficiencies of 44 %. The Diesel engine is compliant with EURO-5 emission standards. The additional cooling of the exhaust gases through the power turbine may in principle reduce the effectiveness of the exhaust after treatment systems. However, using the power turbine for high loads and speeds only, this is not an issue, because temperatures for these loads and speeds will be otherwise much higher than those of medium to low loads and speeds. Operating with hydrogen, only the NO_x system is a concern and the other after treatment device is then removed. With hydrogen, the temperatures to the power turbine are larger, with the subsequent opportunity to further increase the exhaust energy recovered.

4 Non-predictive Combustion Modelling

The proposed designs may permit operation Diesel-like, gasoline-like and mixed Diesel/gasoline-like. Their analysis in engine performance codes may only follow drastic assumptions about the injection and combustion evolution. Diesel-like and gasoline-like operations with different fuels may be modeled by using non-predictive Wiebe functions only.

For the Diesel-like operation (M1), the pilot Diesel direct injection occurs before the main chamber multi fuel is injected. This mode of combustion assumes that the most part of the main chamber multi fuel is injected after proper conditions are created for the main chamber multi fuel injection combustion to occur place diffusion controlled.

The main injection combustion is modeled with the GT-POWER DI Wiebe model [24]. This model imposes the burn rate using a three-term Wiebe function (the superposition of three normal Wiebe curves). These Wiebe curves approximate the "typical" shape of a DI compression ignition burn rate. The purpose of using three functions is to make it possible to model pre-ignition (the large initial spike) and larger tail. The injection profile does not influence the burn rate except if, at any instant, the specified cumulative combustion exceeds the specified injected fuel fraction. The inputs of the Wiebe equations are *SOI* = Start of Injection, *ID* = Ignition Delay, *DP* = Premix Duration, *DM* = Main Duration, *DT* = Tail Duration, *FP* = Premix Fraction, *FT* = Tail Fraction, *EP* = Premix Exponent, *EM* = Main Exponent, *ET* = Tail Exponent and *CE* = Fraction of Fuel Burned (also known as "Combustion Efficiency"). The calculated constants of these equations are *FM* = Main Fraction, *WCP* = Wiebe Premix Constant,

WCM = Wiebe Main Constant and WCT = Wiebe Tail Constant given by equation below:

$$F_M = (1 - F_P - F_T) \quad (1)$$

$$WC_P = \left[\frac{D_P}{2.302^{1/(E_P+1)} - 0.1051^{1/(E_P+1)}} \right]^{-(E_P+1)} \quad (2)$$

$$WC_M = \left[\frac{D_M}{2.302^{1/(E_M+1)} - 0.1051^{1/(E_M+1)}} \right]^{-(E_M+1)} \quad (3)$$

$$WC_T = \left[\frac{D_T}{2.302^{1/(E_T+1)} - 0.1051^{1/(E_T+1)}} \right]^{-(E_T+1)} \quad (4)$$

With θ = Instantaneous Crank Angle, the burn rate is finally given by the equation below:

$$\begin{aligned} \text{Combustion}(\theta) = & (CE) \cdot (F_P) \cdot \left[1 - e^{-(WC_P)(\theta - SOI - ID)^{(E_P+1)}} \right] \\ & + (CE) \cdot (F_M) \cdot \left[1 - e^{-(WCM)(\theta - SOI - ID)^{(E_M+1)}} \right] + (CE) \cdot (F_T) \cdot \left[1 - e^{-(WC_T)(\theta - SOI - ID)^{(E_T+1)}} \right] \end{aligned} \quad (5)$$

The cumulative burn rate is calculated, normalized to 1.0. Combustion starts at 0.0 (0.0 % burned) and progresses to 1.0 (100 % burned). The values of the model inputs may be obtained using the excel worksheet accompanying the software from a recorded pressure trace. With pressure traces recorded at different loads and speeds, then the model inputs can be made a tabular function of speed and load for all the inputs.

For the operation gasoline-like (M3), the Diesel post injection occurs after the main chamber multi fuel is injected. The main injection combustion is modeled with the GT-POWER SI Wiebe model [24]. This model can be used with any type of injection, but if the fuel is injected directly into the cylinder, the start of injection must precede the start of combustion so that there is fuel in the cylinder to burn when combustion starts. At any instant, the specified cumulative burned fuel fraction must not exceed the specified injected fuel fraction. The inputs of the Wiebe equations are: AA = Anchor Angle; D = Duration; E = Wiebe Exponent; CE = Fraction of Fuel Burned (also known as ‘‘Combustion Efficiency’’); BM = Burned Fuel Percentage at Anchor Angle; BS = Burned Fuel Percentage at Duration Start; BE = Burned Fuel Percentage at Duration End. The calculated constants of these equations are Burned Midpoint Constant BMC, Burned Start Constant BSC, Burned End Constant BEC, Wiebe Constant WC and Start of Combustion SOC given by equation below with θ the Instantaneous Crank Angle, $BMC = -\ln(1 - BM)$, $BSC = -\ln(1 - BS)$, $BEC = -\ln(1 - BE)$:

$$WC = \left[\frac{D}{BEC^{1/(E+1)} - BSC^{1/(E+1)}} \right]^{-(E+1)} \quad (6)$$

$$SOC = AA - \frac{(D) \cdot (BMC)^{1/(E+1)}}{BEC^{1/(E+1)} - BSC^{1/(E+1)}} \quad (7)$$

$$Combustion(\theta) = (CE) \cdot \left[1 - e^{-(WC)(\theta - SOC)^{(E+1)}} \right] \quad (8)$$

The cumulative burn rate is calculated, normalized to 1.0. Combustion starts at 0.0 (0.0 % burned) and progresses to 1.0 (100 % burned). The Wiebe constants may be matched to an apparent burn rate that has been calculated from measured cylinder pressure [13]. With pressure traces recorded at different loads and speeds, then the model inputs can be made a tabular function of speed and load [13] for all the inputs.

In mixed Diesel/gasoline modes of operation (M2), the Diesel injection occurs in the main chamber after only part of the main chamber multi fuel is injected. The engine then operates mixed Diesel-like/gasoline-like.

Homogeneous Charge Compression Ignition operation (M4) is obviously also theoretically possible without any igniting Diesel. Being HCCI quite difficult to be controlled and limited to a very narrow window of operating conditions, an HCCI assisted operation is made possible by the post injection of the Diesel approaching top dead centre in M3.

The novel designs permit complicated strategies coupling premixed and diffusion combustions within the main chamber, but unfortunately these strategies cannot be modeled with the available Wiebe function approach. An experimental campaign is certainly the best option available to address all the issues and fully explore the capabilities of the systems.

5 Simulation Results

Engine performance simulations have been performed with the GT-POWER code [24]. Figure 3 presents the volumetric efficiency and the compressor pressure ratio versus the engine speed and load for the Diesel engine operating with and without the power turbine. The maximum load BMEP, torque and power curves are also shown. With the power turbine, the engine generally works with a reduced compressor pressure ratio and with a reduced volumetric efficiency for the same BMEP, because the power turbine supplements the in-cylinder power supply when the power turbine is operational.

Figures 4, 5, 6, and 7 presents the BMEP and the fuel conversion efficiency with Diesel and hydrogen fuels operating in diffusion Diesel-like combustion mode. A $\lambda = 1.45$ is always considered for the Diesel, where both $\lambda = 1.45$ and $\lambda = 1.35$ are considered for the hydrogen fuel. The operation with hydrogen and

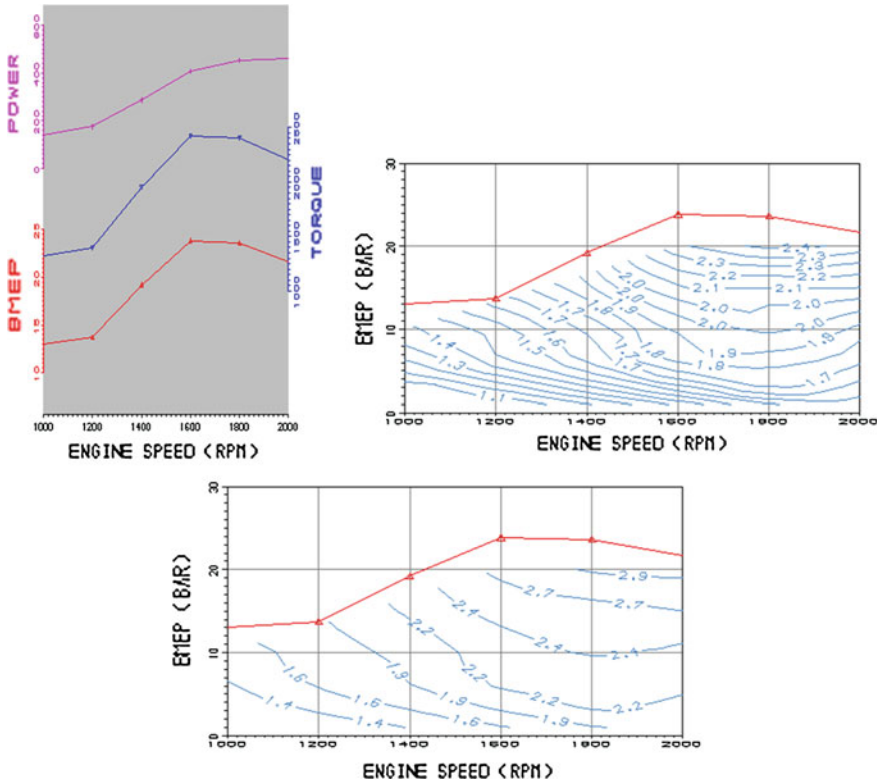


Fig. 3 **a** Volumetric efficiency (*top*) and compressor pressure ratio (*bottom*) versus engine speed and load for the Diesel engine operating without the power turbine. Full load $\lambda = 1.45$ BMEP (bar), torque (Nm) and power (kW) versus engine speed also shown. **b** Volumetric efficiency (*top*) and compressor pressure ratio (*bottom*) versus engine speed and load for the Diesel engine operating with the power turbine. Full load $\lambda = 1.45$ BMEP (bar), torque (Nm) and power (kW) versus engine speed also shown

Diesel is compared with same $\lambda = 1.45$. Then, because hydrogen permits much richer mixtures (the Diesel is a mixture of complex, liquid hydrocarbons much more difficult to burn closer to stoichiometry) a $\lambda = 1.35$ is considered for hydrogen.

The gaseous fuel has the opportunity to increase both power and torque outputs and efficiency. The operation with same λ permits much higher BMEP with hydrogen than Diesel (5 bar more on average). The operation with same λ also permits much higher fuel conversion efficiencies with hydrogen than Diesel (2–3 % points on average). The Diesel fuel has a lower heating value of 43.25 MJ/Kg and a stoichiometric air-to-fuel ratio of 14.33. This translates in 2.82 MJ of energy per kg of stoichiometric mixture of Diesel and air. The hydrogen fuel has a lower heating value of 119.9 MJ/Kg and a stoichiometric air-to-fuel ratio of 34.04. This translates in 3.42 MJ of energy per kg of stoichiometric mixture of hydrogen

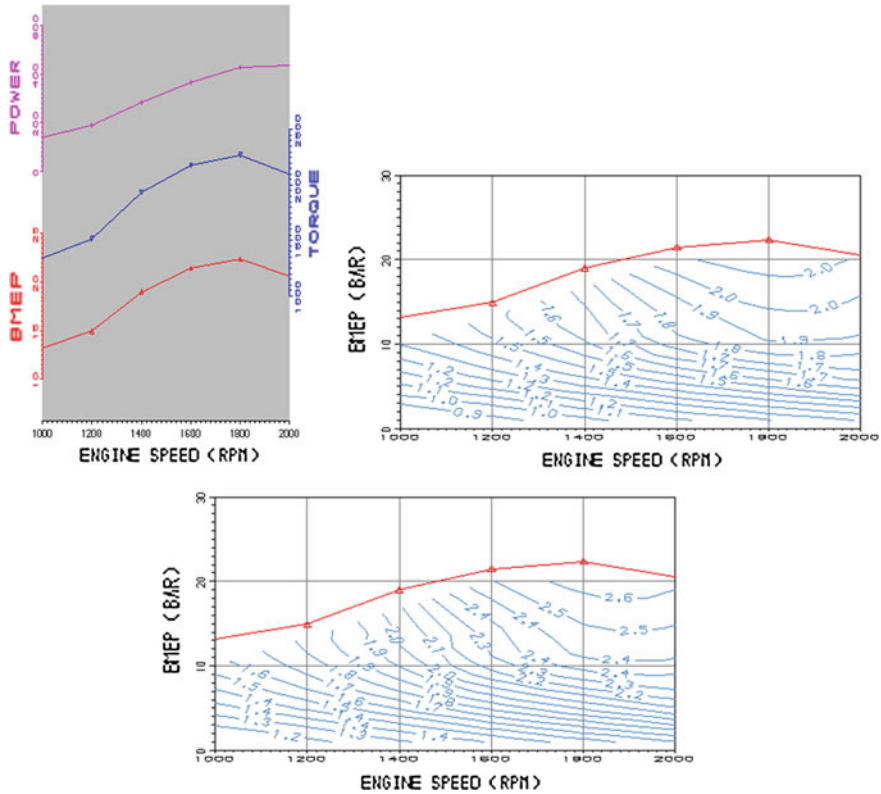
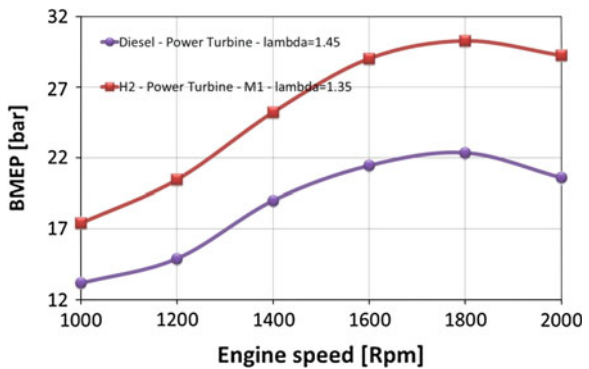


Fig. 3 continued

Fig. 4 BMEP of the engine operating $\lambda = 1.45$ with Diesel or $\lambda = 1.35$ with hydrogen, with Diesel-like combustion mode M1 when fuelled with hydrogen and power turbine supplementing the power output of the crankshaft operational



and air. Clearly, running with hydrogen at similar fuel conversion efficiencies of the Diesel, the same BMEP is obtained with much leaner mixtures. Worth of mention is that the assumption of similar burning rates for the Diesel and the hydrogen at same percentage of maximum load produces a larger heat release rate with the hydrogen.

Fig. 5 Fuel conversion efficiency of the engine operating $\lambda = 1.45$ with Diesel or $\lambda = 1.35$ with hydrogen, with Diesel-like combustion mode M1 when fuelled with hydrogen and power turbine supplementing the power output of the crankshaft operational

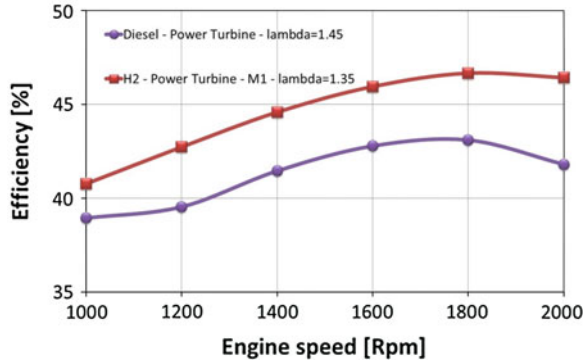


Fig. 6 BMEP of the engine operating $\lambda = 1.45$ with Diesel and hydrogen, with Diesel-like combustion mode M1 when fuelled with hydrogen and power turbine supplementing the power output of the crankshaft operational

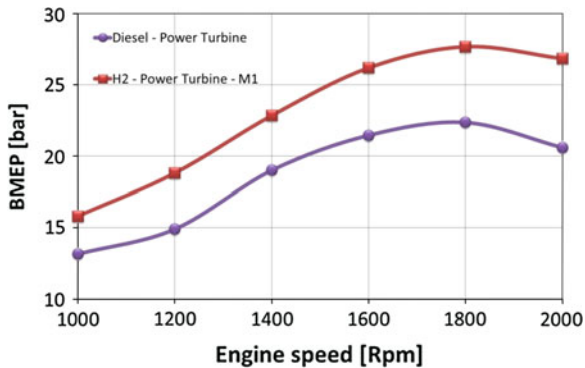


Fig. 7 Fuel conversion efficiency of the engine operating $\lambda = 1.45$ with Diesel or hydrogen, with Diesel-like combustion mode M1 when fuelled with hydrogen and power turbine supplementing the power output of the crankshaft operational

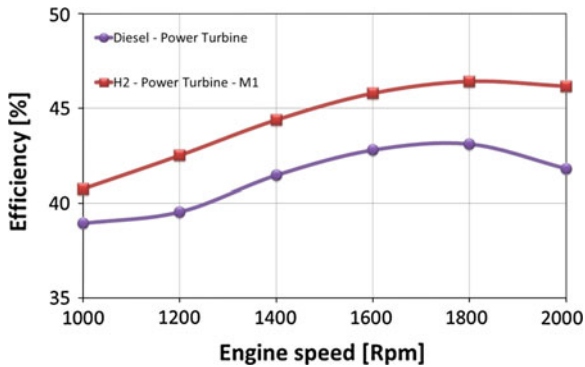
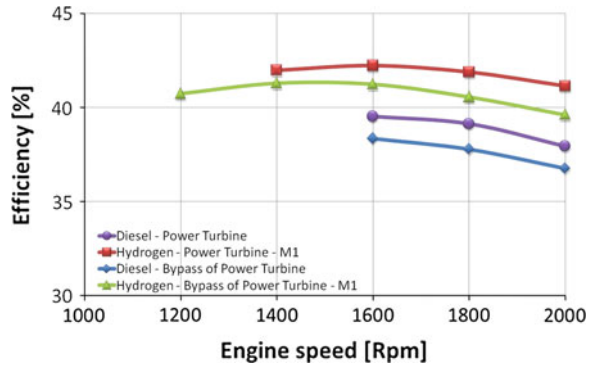


Figure 8 presents the fuel conversion efficiency of the engine operating with Diesel or hydrogen at 20 bar BMEP, with Diesel-like combustion mode when fuelled with hydrogen and power turbine supplementing the power output of the crankshaft operational or bypassed and disconnected. With Diesel the average working λ is 1.5–1.55 with or without power turbine, while with hydrogen the working λ is 1.73–1.85 with or without power turbine. With the power turbine, the

Fig. 8 Fuel conversion efficiency of the engine operating at 20 bar BMEP with Diesel or hydrogen, with Diesel-like combustion mode M1 when fuelled with hydrogen and power turbine supplementing the power output of the crankshaft operational bypassed and disconnected



power produced in-cylinder decreases less than the power produced in the power turbine, and the efficiency of the fuel conversion process increases. With hydrogen, the engine works more fuel energy efficiently than with the Diesel. Some points are missed in the speed range because at these speeds the engine delivers less than the listed BMEP.

Figure 9 presents the fuel conversion efficiency of the engine operating with Diesel or hydrogen fuel at 15 bar BMEP, with Diesel-like combustion mode when fuelled with hydrogen and power turbine supplementing the power output of the crankshaft operational or bypassed and disconnected. With Diesel the average working λ is 1.79–1.77 with or without power turbine, while with hydrogen the working λ is 1.94–1.98 with or without power turbine. Operating with hydrogen in the mode of HCCI/gasoline like premixed combustion the maximum pressure within the cylinder would be 204–210 bar with or without power turbine. This operation is therefore not shown. At 15 bar, the benefits of the power turbine are almost cancelled. The power turbine is producing a power marginally larger than the power lost within the cylinder for the increased back pressure. With hydrogen, the engine works more fuel energy efficiently than with the Diesel.

Figure 10 presents the fuel conversion efficiency of the engine operating with Diesel or hydrogen fuel at 10 bar BMEP, with Diesel-like injection and combustion mode Diesel-like or HCCI/gasoline-like when fuelled with hydrogen and power turbine supplementing the power output of the crankshaft operational or bypassed and disconnected. With Diesel the average working λ is 2.14–2.17 with or without power turbine, while with hydrogen the working λ is 2.53–2.61 in combustion mode Diesel-like and 2.35–2.60 in combustion mode HCCI/gasoline-like with or without power turbine. At 10 bar, the benefits of the power turbine are lost. The power turbine is producing a power smaller than the power lost within the cylinder for the increased back pressure. With hydrogen, the engine works more fuel energy efficiently than with the Diesel. Replacing the Diesel-like operation with the operation HCCI/gasoline-like the fuel conversion efficiency increases. Improvements of efficiency are 1–3 % points. Intermediate results are expected operating the engine in the mixed Diesel/gasoline-like mode increasing the amount of main chamber fuel injected before the injection in the jet ignition pre-chamber.

Fig. 9 Fuel conversion efficiency of the engine operating at 15 bar BMEP with Diesel or hydrogen, with Diesel-like combustion mode M1 when fuelled with hydrogen and power turbine supplementing the power output of the crankshaft operational bypassed and disconnected

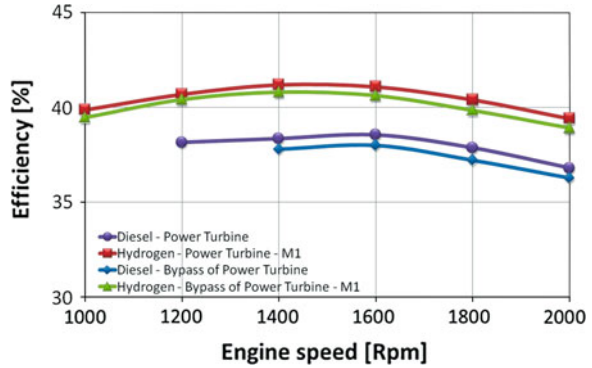


Fig. 10 Fuel conversion efficiency of the engine operating at 10 bar BMEP with Diesel or hydrogen, with Diesel-like combustion mode M1 or HCCI/gasoline-like combustion modes M3-4 when fuelled with hydrogen and power turbine supplementing the power output of the crankshaft operational bypassed and disconnected

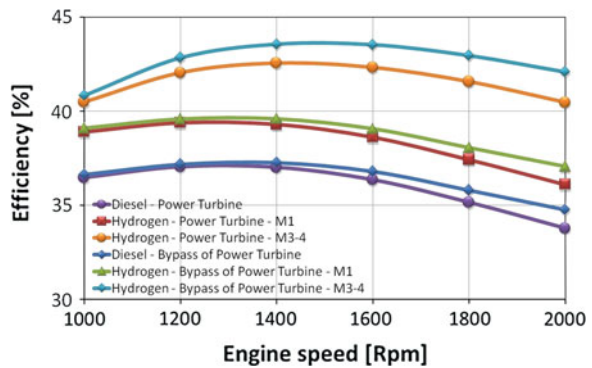


Figure 11 presents the fuel conversion efficiency of the engine operating with Diesel or hydrogen fuel at 5 bar BMEP, with Diesel-like combustion mode or HCCI/gasoline-like combustion modes when fuelled with hydrogen and power turbine supplementing the power output of the crankshaft operational or bypassed and disconnected. With Diesel the average working λ is 2.98–3.49 with or without power turbine, while with hydrogen the working λ is 3.64–4.18 in combustion mode Diesel-like and 3.48–4.21 in combustion mode HCCI/gasoline-like with or without power turbine. At 5 bar, the power turbine has no benefits. With hydrogen, the engine works more fuel energy efficiently than with the Diesel. Replacing the Diesel-like operation with the operation HCCI/gasoline-like the fuel conversion efficiency increases. Improvements of efficiency are 1 % point. Intermediate results are expected operating the engine in the mixed Diesel/gasoline-like mode increasing the amount of main chamber fuel injected before the injection in the jet ignition pre-chamber.

Figure 12 presents the fuel conversion efficiency of the engine operating with Diesel or hydrogen fuel at 2.5 bar BMEP, with Diesel-like or HCCI/gasoline-like combustion modes when fuelled with hydrogen and power turbine supplementing the power output of the crankshaft operational or bypassed and disconnected. With Diesel the average working λ is 3.98–4.90 with or without power turbine, while

Fig. 11 Fuel conversion efficiency of the engine operating at 5 bar BMEP with Diesel or hydrogen, with Diesel-like combustion mode M1 or HCCI/gasoline-like combustion modes M3-4 when fuelled with hydrogen and power turbine supplementing the power output of the crankshaft operational bypassed and disconnected

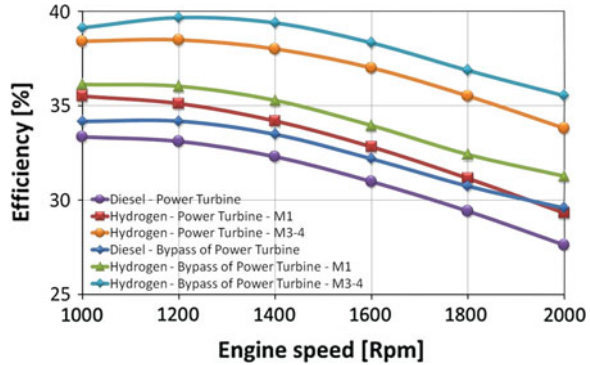
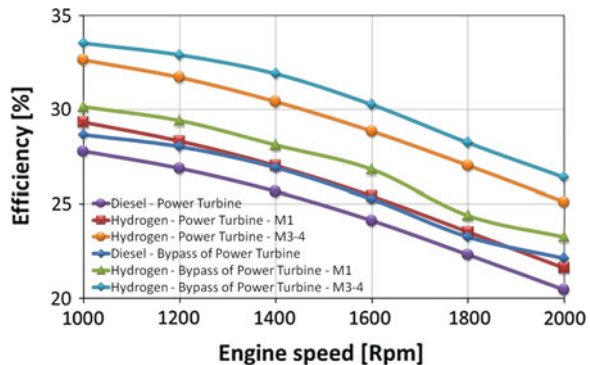


Fig. 12 Fuel conversion efficiency of the engine operating at 2.5 bar BMEP with Diesel or hydrogen, with Diesel-like combustion mode M1 or HCCI/gasoline-like combustion modes M3-4 when fuelled with hydrogen and power turbine supplementing the power output of the crankshaft operational bypassed and disconnected



with hydrogen the working λ is 4.88–5.99 in Diesel-like operation and 4.98–6.11 in operation HCCI/gasoline-like with or without power turbine. Comments on fuel efficiency with hydrogen or Diesel, with or without power turbine and with different modes using hydrogen are same as above for 5 bar.

Figure 13 finally presents the fuel conversion efficiency of the engine operating with Diesel or hydrogen fuel at 1 bar BMEP, with Diesel-like combustion mode when fuelled with hydrogen and power turbine supplementing the power output of the crankshaft operational or bypassed and disconnected. With Diesel the average working λ is 5.46–6.75 with or without power turbine, while with hydrogen the working λ is 6.67–8.21 with or without power turbine. With hydrogen in operation HCCI/gasoline-like the working λ would be 7.13–8.72 with or without power turbine and these points are omitted because it is not expected that combustion may occur rapidly at these λ . Comments on fuel efficiency with hydrogen or Diesel, with or without power turbine are same as above, even if differences are smaller because of the much larger importance of friction losses.

Figure 14 finally presents the maximum efficiency versus BMEP at different speeds with mode of combustion Diesel-like and power turbine engaged and fluxed, while Fig. 15 presents the maximum efficiency versus BMEP at different speeds with different modes of combustion—Diesel-like or mixed HCCI/gasoline-like—and

Fig. 13 Fuel conversion efficiency of the engine operating at 1 bar BMEP with Diesel or hydrogen, with Diesel-like combustion mode M1 when fuelled with hydrogen and power turbine supplementing the power output of the crankshaft operational bypassed and disconnected

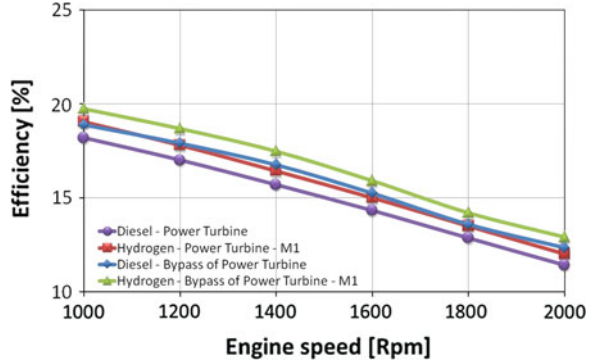
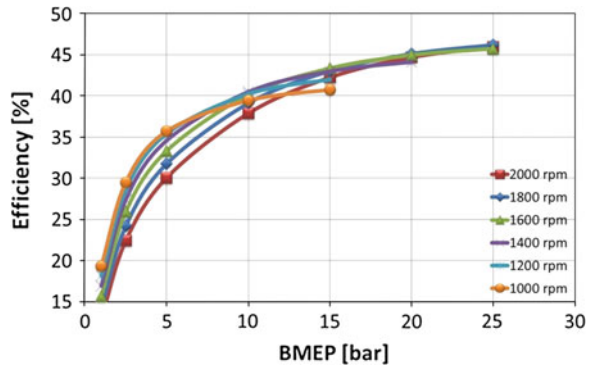


Fig. 14 Maximum efficiency versus BMEP at different speeds with mode of combustion M1 and power turbine operational

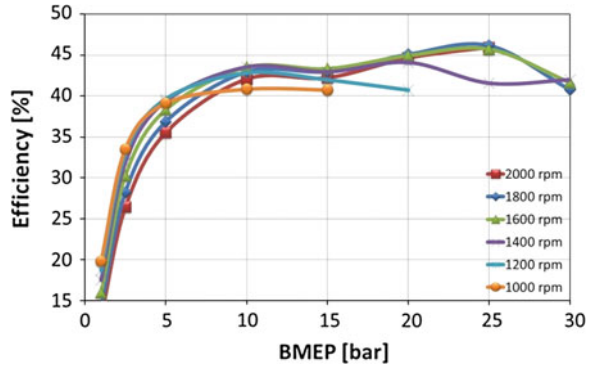


power turbine operational or bypassed and disconnected. The mixed HCCI/gasoline-like mode is only allowed at BMEP values of 2.5–10 bar. The largest BMEP are obtained without the power turbine. The power turbine helps at high loads to improve the fuel conversion efficiency. These figures give the trends of fuel conversion efficiency versus the load.

Reducing the engine speed for a given BMEP, the maximum in the fuel conversion efficiency is clearly shifting to the left to lower engine speeds. This is mostly the result of a friction component of BMEP weakly dependent on the load but linearly and quadratically dependent on the speed. The friction mean effective pressure FMEP is computed through the Chen and Flynn correlation [30]. The correlation has a constant term (for accessory friction), a term which varies with peak cylinder pressure, a third term linearly dependent on mean piston velocity (for hydrodynamic friction) and a fourth term quadratic with mean piston velocity (for windage losses). The equation used to calculate the Friction Mean Effective Pressure (FMEP) is given below:

$$FMEP = A_{cf} + \frac{1}{ncyl} \sum_{i=1}^{ncyl} \left[B_{cf} \cdot (P_{cyl})_i + C_{cf} \cdot (S_{fact})_i + Q_{cf} \cdot (S_{fact})_i^2 \right] \quad (9)$$

Fig. 15 Maximum efficiency versus BMEP at different speeds with different modes of combustion—M1 or M3-4—and power turbine operational or disengaged and bypassed. The M3-4 mode is only allowed at BMEP values of 2.5–10 bar. The largest BMEP are obtained without the power turbine



with: $S_{\text{fact}} = \frac{1}{2} \cdot \text{RPM} \cdot S$, A_{cf} , B_{cf} , C_{cf} and Q_{cf} user inputs, P_{max} the maximum cylinder pressure, RPM the cycle-average engine speed and S the cylinder stroke. Each cylinder has its own contribution to the total engine friction based upon its own maximum cylinder pressure and stroke (folded into the speed factor, S_{fact}). A_{cf} is the constant portion of the Chen-Flynn friction correlation, B_{cf} the term which varies linearly with peak cylinder pressure, C_{cf} the term accounting for hydrodynamic friction in the power cylinder which varies linearly with the piston speed and Q_{cf} the term which varies quadratically with the piston speed and accounts for windage losses in the power cylinder. As soon as the load is reduced, being $\text{BMEP} = \text{IMEP} - \text{FMEP}$, with IMEP the indicated mean effective pressure resulting from the in cylinder pressure work, the operation at higher engine speeds clearly result to be less efficient.

6 SRM Detailed Chemistry Simulations

The SRM (Stochastic Reactor Model) suite [26] is a sophisticated engineering tool for carrying out computations of fuels, combustion and emissions formation in an IC engine context. The software has five major features that distinguish it from conventional 1 or 3D fluid dynamics approaches. It can solve for in-cylinder in-homogeneities (in contrast to 1D codes), enabling to deal with composition/thermal stratification. On account of its unique approach, the code is faster than 3D CFD, enabling to carry out model parameter and design optimizations. It includes detailed combustion chemistry, enabling to solve for fuels, combustion characteristics, emissions and engine performance. The gaseous emissions of NO_x , CO and HCs are computed based on their formation starting as a fuel molecule, during combustion and expansion. Soot emissions can also be computed using a detailed soot model, which solves for soot particle dynamics providing information such as particle size distribution including composition and morphology of soot aggregates. SRM is either and both a 1 or 3D code. The code combines the features from both approaches, the speed of 1D and mostly of the predictive capabilities of 3D, but with the addition of detailed combustion chemistry.

The stochastic term means combustion is modeled as a process involving a sequence of observations each of which is considered as a random sample from a probability distribution. Stochastic fluctuations are inherent to any internal combustion engine operation and need to be accounted in engine models. Each element of the probability distribution is termed a stochastic particle. In a way a stochastic particle represents the air–fuel parcel. Depending on the application, between 50 and 500 stochastic particles are typically required to properly sample in-cylinder processes. IN the simulations performed here after, 250 parcels are used. The SRM Suite uses a probability density function (PDF) based approach that simplifies many of the most computationally expensive fluid-dynamic processes whilst maintaining much of the predictive capability of the 3D CFD codes. This is achieved by down sampling the required number of grid points associated with CFD from tens-of-thousands down to a few hundred stochastic particles which best represent the in-cylinder mixture composition states. The method retains most of the spatial information required to achieve a predictive model without incurring the computational overhead. The ensemble of the stochastic particles approximates the distribution of the in-cylinder properties such as the composition of chemical species and the temperature. The model is then solved to account for the influence of the processes such as fuel injection, combustion kinetics, turbulent mixing, piston motion and convective heat loss on the multi-dimensional PDF. The approach thus accounts for in homogeneities in composition and temperature in the engine cylinder.

Unfortunately, the SRM direct injection of the fuel permits multiple injection events but is limited to a single composition fuel, i.e. to a fuel having same prescription of mass fractions for all the injections. Furthermore the direct injection occurs from a single injector location. Within these limitations, the SRM software is used to improve the understanding of the detailed chemical kinetics for the unconventional multi fuel, multi injector, Diesel injection ignition system as described below.

Simulations are performed from intake valve closure 120 crank angle degrees (cad) before top dead center (BTDC) to exhaust valve opening 100 crank angle degrees (cad) after bottom dead center (ABDC) starting from the intake valve closure conditions of the 25 bar, 1,900 rpm operating point. The initial pressure is 2.6 bar and the temperature is 344 K. EGR internal or external is neglected for sake of simplicity. The mass of air is 4620 mg. Simulations are performed lean of stoichiometry with different fuels using the same amount of fuel energy rather than the same fuel-to-air equivalence ratio to compare their behaviors.

7 Multi Mode Combustion with Diesel Ignition

These simulations consider the option to directly inject the main chamber fuel with a specific injector in addition to the Diesel injector and to control the about TDC ignition with the Diesel injection ignition. The glow plug is retained.

The SRM detailed PRF mechanism chemistry is now used [26]. Despite this mechanism includes all the major hydrocarbon components, the fuel composition is limited to a mixture of $\text{N-C}_7\text{H}_{16}$ and $\text{I-C}_8\text{H}_{18}$ surrogate of Diesel and gasoline. The SRM detailed PRF mechanism [26] includes 208 different species. However, simulations with H_2 , CH_4 , C_3H_8 , and NH_3 are not possible because the fuel composition may only be $\text{I-C}_8\text{H}_{18}$ or $\text{N-C}_7\text{H}_{16}$.

The simulations will be limited to the reference $\text{N-C}_7\text{H}_{16}$ pilot plus main injection combustion, plus two conditions where the top dead center ignition is obtained auto igniting the $\text{I-C}_8\text{H}_{18}$ injected early during compression (homogeneous charge compression ignition mode). In a first case, no further injection of $\text{I-C}_8\text{H}_{18}$ is made during expansion. This is basically a particular gasoline-like mode. In a second case, the early compression injection of $\text{I-C}_8\text{H}_{18}$ is followed by a second injection of $\text{I-C}_8\text{H}_{18}$ during the expansion, as in the mixed Diesel/gasoline-like mode. The Diesel-like operation with pilot $\text{N-C}_7\text{H}_{16}$ and then $\text{I-C}_8\text{H}_{18}$ is not investigated because of the multi fuel issue. Similarly, the support of the auto ignition process of $\text{I-C}_8\text{H}_{18}$ injecting $\text{N-C}_7\text{H}_{16}$ at top dead center is not analyzed.

Results are presented in Fig. 16, with the same fuel energy input of the previous paragraph in case of $\text{I-C}_8\text{H}_{18}$ of Fig. 16a and $\text{N-C}_7\text{H}_{16}$ of Fig. 16b. The figure presents in-cylinder pressure, temperature, heat release rate and cumulative heat release rate. The fuel input of $\text{I-C}_8\text{H}_{18}$ of Fig. 16c is one half of the total of Fig. 16a or b. The simulations are performed for same pressure, temperature and composition at intake valve closure of the prior paragraph. The injection of 100 mg of liquid $\text{I-C}_8\text{H}_{18}$ occurs -100 to -75 cad BTDC. Under these specific circumstances, no Diesel ignition is needed to start combustion, because the early injected $\text{I-C}_8\text{H}_{18}$ auto ignites before TDC, with heat release becoming significant about TDC. Then a second injection of 100 mg of liquid $\text{I-C}_8\text{H}_{18}$ occurs from TDC to 25 cad ATDC for the results of Fig. 16a, while no more fuel is injected in the case of Fig. 16c. Auto-ignition of $\text{I-C}_8\text{H}_{18}$ is quite difficult to be controlled even in simulations; therefore a pilot Diesel injection is always practically needed to make the TDC ignition stable and repeatable. Even in the simulations, small changes bring to much earlier auto ignition or not significant auto ignition.

Injection of the 200 mg of liquid $\text{I-C}_8\text{H}_{18}$ earlier during the compression stroke does not make any sense, because it would only produce huge compression work and compression pressure. With the 100 + 100 mg splitting, part of the fuel burns HCCI-like at TDC, and part of the fuel burns Diesel-like after TDC. This maximizes the pressure work for a given fuel energy within normal mechanical constraints. As previously noted, injection of a small quantity of liquid $\text{N-C}_7\text{H}_{16}$ is theoretically not needed at TDC in this particular case but practically necessary to make robust the process. This injection is needed to ensure that combustion starts about TDC. Being the auto-ignition process quite difficult to be controlled over a full speed and load map by simply adjusting the amount of $\text{I-C}_8\text{H}_{18}$ injected during compression, the TDC injection of $\text{N-C}_7\text{H}_{16}$ is what makes the TDC start of combustion stable and repeatable at any load and speed. The $\text{I-C}_8\text{H}_{18}$ injected during the compression stroke may be adjusted with the speed and load up to values that do not incur in significant auto ignitions. Then, the TDC ignition of

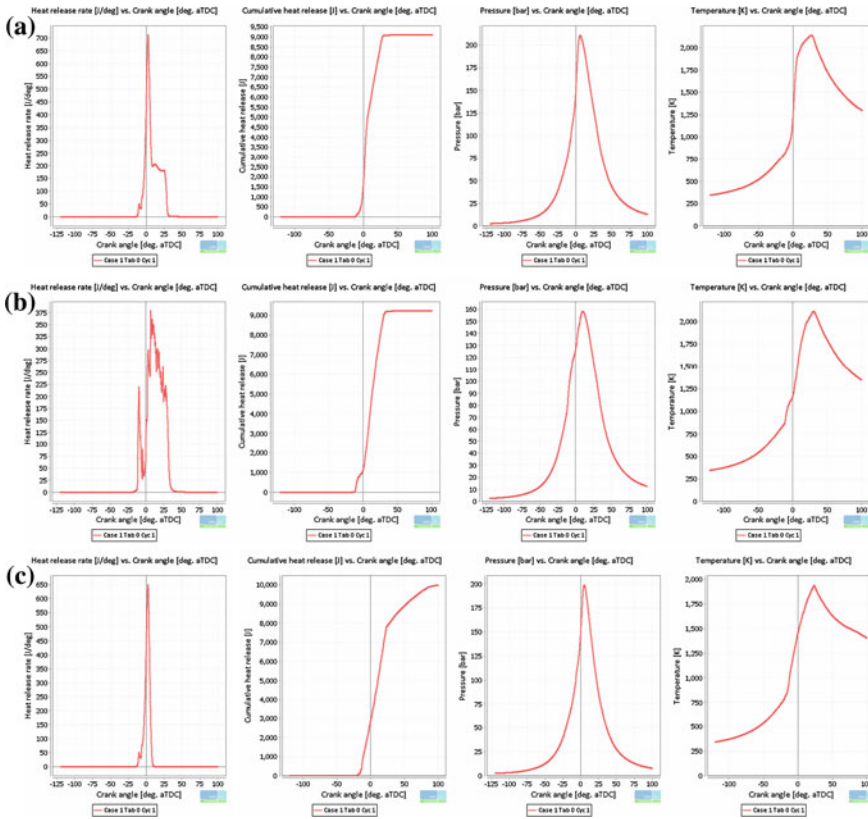


Fig. 16 Top to bottom heat release rate, cumulative heat release rate, in-cylinder pressure and temperature with 100 + 100 mg of I-C₈H₁₈ (a), 20 + 180 mg of N-C₇H₁₆ (b) and 100 mg of I-C₈H₁₈ (c)

N-C₇H₁₆ is what starts combustion. The I-C₈H₁₈ injected earlier during compression burns premixed, the I-C₈H₁₈ injected after during expansion burns diffusion.

Figure 16 presents the results with early injection of I-C₈H₁₈ 100 mg –100 to –75 cad BTDC and late injection of I-C₈H₁₈ 100 mg TDC to 25 cad ATDC (a), pilot injection of N-C₇H₁₆ 20 mg –25 to –10 cad BTDC followed by a main injection of N-C₇H₁₆ 180 mg –5 cad BTDC to 25 cad BTDC (b) and finally early injection of I-C₈H₁₈ 100 mg –100 to –75 cad BTDC (c). I-C₈H₁₈ and N-C₇H₁₆ have very close lower heating value and stoichiometric air-to-fuel ratios. Obviously the almost isochoric premixed combustion of I-C₈H₁₈ permit the best pressure distribution during the expansion stroke (positive work) versus pretty much the same pressure distribution during the compression work (negative work) during non-firing conditions thus producing the larger indicated mean effective pressure (IMEP) and therefore the larger output and the larger fuel efficiency.

These simulations demonstrated the opportunity to produce a nearly optimal pressure build up within limited maximum pressure constraints modulating the premixed and diffusion combustion events. Worth of mention is that the very high in cylinder temperatures for this mild lean of stoichiometry operation is an opportunity to further increase the fuel conversion efficiency by injecting water and expanding steam as shown in [13, 14].

To properly study all the possible combustion modes with better details, obviously a fully 3D CFD + chemical kinetic simulation is needed for the two phase, multi fuels, reacting flows but more than that a detailed experimental campaign is needed for the further engine development as well as the refinement of the models.

8 Discussion and Conclusions

Up to 20–25 % of the fuel energy in a modern heavy duty diesel is exhausted, and by adding a power turbine in the exhaust flow, theoretically up to 20 % of this exhaust energy can be recovered. In reality, only a minor part of this fuel energy can be practically recovered, first of all because of the added exhaust back pressure also increasing the pumping losses. Further limits to the use of a power turbine arise from the after treatment requiring temperatures above threshold values to operate efficiently. The increasing use of cooled EGR further limits the perspectives of this technique. Crank train coupling and power turbine add weight, complexity in design, control and service and costs, with a definitively negative trade-off in light load applications.

The additional cooling of the exhaust gases reduces the effectiveness of exhaust after treatment systems, requiring more active regenerations for particulate filter and reducing the time NOx control systems are effective. This is not an issue for the proposed application where a by-pass system avoids the cooling for expansion in the power turbine except than when useful and without implications on the after treatment. The use of external cooled EGR is negative with a turbo compound because the exhaust energy decreases due to energy extracted into cooling system reducing the energy available to turbo charger and power turbines. Space requirements of turbo compound further constrain packaging of exhaust gas recirculation and turbochargers.

Simulations performed for a 12.8 l in-line six cylinder turbo charged directly injected Diesel engine have shown the opportunity to gain up to 2 % points in efficiency at high loads and speeds where the wasted energy is relatively large. At low engine loads the converted energy available downstream of the turbine is not enough to compensate for back pressure losses and the efficiency deteriorates. The turbo compound has therefore the advantage of improved fuel conversion efficiency in applications where high engine loads are dominating, but negative impact at light load. Also worth of mention the increase in maximum power output about maximum speed, where otherwise the power output sharply reduces. These

improvements do not impact on the efficiency of the after treatment as well as on the use of cooled EGR to control the emissions, because the power turbine is by-passed when needed.

The use of a constant variable transmission to replace a gear ratio in between the power turbine and the crankshaft has the advantage of permitting operation of the power turbine within a narrow range of speeds decoupled from the speed of the crankshaft. The better efficiency of the power turbine translates in a better recovery of the exhaust energy. The idea of using a CVT and a by-pass is relatively novel and the model will certainly need further refinements. Prototyping of the solution will certainly help considerably in understanding the limits of the technology only partially addressed in this paper.

Results of simulation on a compression ignition Diesel Truck engine converted to hydrogen provide better than Diesel brake efficiencies at same BMEP outputs. The hydrogen engine also permits higher power and torque outputs running about same λ . The multi-mode operation permits to improve significantly also the part load efficiencies versus the Diesel.

In addition to the Diesel-like operation, the engine design permits a HCCI/gasoline-like mode delivering better part load efficiencies as presented here, but more than that mixed gasoline/Diesel like modes where the premixed and diffusion combustion may be finely tuned to deliver better maximum torque and power outputs as well as better full and part load efficiencies.

The practical design of these hydrogen truck engines requires the development of better fuel injectors able to deliver the mass of hydrogen requested by the large displacement cylinder within small time frames.

References

1. http://www.greencarcongress.com/2007/03/hyice_concludes.html [Internet]. [Cited 2011 May 20]
2. Boretti A (2011) Stoichiometric H₂ICE with water injection. *Int J Hydrogen Energy* 36:4469–4473
3. Boretti A (2011) Diesel-like and HCCI-like operation of a truck engine converted to hydrogen. *Int J Hydrogen Energy* 36:15382–15391
4. <http://www.greencarcongress.com/2009/03/high-pressure-d.html> [Internet]. [Cited 2011 May 20]
5. Eichlseder H, Spuller C, Heindl R, Gerbig F, Heller K (2010) Concepts for diesel-like hydrogen combustion. *MTZ worldwide Edition*: 2010-01. <http://www.atzonline.com/index.php?do=show/site=a4e/sid=7569549924dbde0eca7dd0586568901/alloc=3/id=10799> [Internet]. [Cited 2011 May 20]
6. Eichlseder H, Spuller C, Heindl R, Gerbig F, Heller K (2009) New and innovative combustion systems for the H₂-ICE: compression ignition and combined processes. *SAE P. 2009-01-1421*
7. <http://www.westport.com/core-technologies/fuel-injectors> [Internet]. [Internet]. [Cited 2011 May 20]
8. <http://www.hoerbiger.com/Niche-Automotive-Applications.10762.0.html?&L=39> [Internet]. [Cited 2011 May 20]

9. Boretti A (2010) Modelling auto ignition of hydrogen in a jet ignition pre-chamber. *Int J Hydrogen Energy* 35:3881–3890
10. Department of Energy, Energy efficiency and renewable energy, vehicle technology program (2008) FY 2008 progress report for advanced combustion engine technologies. http://www1.eere.energy.gov/vehiclesandfuels/pdfs/program/2008_adv_combustion_engine.pdf (retrieved Sep 30, 2010)
11. Department of Energy, Energy efficiency and renewable energy, vehicle technology program (2009) FY 2009 progress report for advanced combustion engine research and development. http://www1.eere.energy.gov/vehiclesandfuels/pdfs/program/2009_adv_combustion_engine.pdf (retrieved Sep 30, 2010)
12. Gerdan D, Wetzler JM (1948) Allison V-1710 compounded engine. SAE Paper 480199
13. Welsh HW Engine compounding for power and efficiency. SAE Paper 480198
14. Rowe MR (1949) Compounding the piston engine. SAE Paper 490088
15. Hazen RM (1950) The case for the turbo-prop engine. SAE Paper 500084
16. Brands MC et al Vehicle testing of cummins turbo compound diesel engine. SAE Paper 810073
17. Wilson DE The design of a low specific fuel consumption turbocompound engine. SAE Paper 860072
18. Tennant DWH, Walsham BE (1989) The turbocompound diesel engine. SAE Paper 890647
19. Assanis DN, Heywood J Development and use of a computer simulation of the turbocompounded diesel system for engine performance and component heat transfer studies. SAE Paper 860329
20. Greszler A (2008) Diesel turbo-compound technology. Paper presented to the ICCT/NESCCAF workshop improving the fuel economy of heavy-duty fleets II, San Diego, CA. http://www.nescaum.org/documents/improving-the-fuel-economy-of-heavy-duty-fleets-1/greszler_volvo_session3.pdf/ (retrieved Sep 29, 2010)
21. Brockbank C (2009) Application of a variable drive to supercharger & turbo compounder applications. SAE Paper 2009-01-1465
22. Ishii M (2009) System optimization of turbo-compound engine (first report: compressor and turbine pressure ratio). SAE Paper 2009-01-1940
23. Wagner R et al (2010) Investigating potential light-duty efficiency improvements through simulation of turbo-compounding and waste-heat recovery systems. SAE Paper 2010-01-2209
24. http://www.gtisoft.com/applications/a_Engine_Performance.php [Internet]. [Cited 2011 May 20]
25. Chen S, Flynn P (1965) “Development of a Single Cylinder Compression Ignition Research Engine,” SAE Technical Paper 650733. doi:10.4271/650733
26. CMCL innovations, “SRM suite”. www.cmclinnovations.com/html/srmsuite.html [Internet]. [Cited 2012 April 26]

Well-to-Wheel Analyses for Energy Consumption and Greenhouse Gas Emissions of Electric Vehicles Using Various Thermal Power Generation Technologies in China

Wei Shen and Weijian Han

Abstract Since majority of electricity in China is generated from coal and natural gas, the study carried out WTW analyses for battery electric vehicles (BEVs) using China's various thermal power generation technologies and compare their total energy use and GHG emissions against gasoline or diesel internal combustion engine vehicles (ICEVs), as well as hybrid electric vehicles (HEVs). The WTW analyses of BEVs, HEVs and ICEVs were conducted using the GREET (Greenhouse gases, regulated emissions, and energy use in Transportation) model developed by Argonne National Lab combined with a localized database of Chinese domestic data. A 2011 mid-size gasoline car is used as a baseline. Two types of BEV assumed in this study: Common BEVs and High-efficient BEVs. Common BEV pathways will save up to 99 % petrol consumption. However, comparing to that of HEV pathway, WTW energy consumption of all Common BEV pathways will be increased, with a maximum of 71 %. WTW energy consumption of High-efficient BEVs will be 2–29 % less than the WTW energy in the HEV pathway. GHG emissions of Common BEVs depend on differences in power generation technologies. Without CCS, the WTW GHG emissions of Common BEVs using coal-fired electricity are 11–77 % higher than the WTW GHG emissions of the baseline. When USC and IGCC generation technologies are

F2012-B01-022

W. Shen (✉)

APA Research, Ford Motor Company, Unit 4901, Tower C, Beijing Yintai Center.No. 2 Jianguomenwai Street, 100022 Chaoyang District, Beijing, China
e-mail: wshen5@ford.com

W. Han

APA Research, Ford Motor Company, 1317 RIC, 2101 Village Road, Dearborn, MI 48121, USA
e-mail: whan1@ford.com

equipped with CCS, the WTW GHG emissions of High-efficient BEVs are 79–83 % less than that of the baseline, and 69–75 % less than the hybrid pathway. This is the first time that a WTW analysis in China at this magnitude was completed with a fully localized fuel-cycle database. Outcomes of the study provide more relevance and accuracy for both the government and industry to develop strategies and policies in China. The model and database developed in this study can be used for analysis both at national and regional levels. This study did not include the energy use and GHG emissions in vehicle manufacturing stage. Although it is a small portion in the analysis, it could provide understanding of the difference in vehicle manufacturing process between EVs and traditional gasoline vehicles. This paper shows that the Common BEVs currently demonstrated are not a silver bullet for attacking energy consumption challenges and GHG emissions. In China context, full HEVs seem more attractive than Common BEVs to deal with energy security and GHG reduction challenge today. In order to achieve GHG reduction targets through vehicle electrification, China must promote CCS technology to help USC and IGCC power plants deliver low-carbon transportation energy on supply side. At the same time, High-efficient BEVs have to be set as the highest priority of automotive technology development.

Keywords Electric vehicle • Well-to-Wheel Analysis • GHG emissions • Thermal power generation • China

1 Introduction

China's economy has undergone fast and sustained growth in the past three decades. In 2010, China sold a record high—18 million vehicles and became the largest auto market in the world. China's vehicle parc reached 78 million [1], which consumed more than 150 million tons of gasoline and diesel [2]. A total of 430 million tons of crude oil were used to meet the growth of energy in transportation, of which 55 % were imported oil [3]. It is projected that China's vehicle parc will be 550–730 million in 2050 [4]. To fuel such a big number of vehicles, China faces significant challenges in energy security. At the same time, China is the largest CO₂ emitter in the world and contributed 23.6 % of the world's total CO₂ emissions from fuel combustion in 2009 [5]. At the Climate Change Summit of United Nations in 2009, the Chinese government promised to reduce by 40–45 % carbon intensity per GDP in 2020 from 2005 levels.

Vehicle electrification is viewed an effective solution to both energy security and GHG reduction by the Chinese government. In 2009 the government launched a “new-energy vehicle” (NEV) program to demonstrate plug-in hybrid vehicles (PHEVs), battery electric vehicles (BEVs) and fuel cell vehicles (FCVs). The demo program extended to 25 cities with 6000 NEVs, 4500 charging poles and 100 charging/battery swap stations by the end of 2011 [6]. Recently, the State

Council approved the “Energy Saving and New Energy Vehicle Industry Development Plan (2012–2020)” that targeted development of PHEVs and BEVs as strategy for transforming the Chinese automotive industry. According to the plan, sales of PHEVs and BEVs will reach a half million units by 2015 and 5 million units by 2020. In China’s Twelfth Five-Year-Plan (FYP) (2011–2015) of National Strategic Emerging Industries Development, the government promises to devote RMB 1–2 billion annually to support R&D and subsidize demonstration of NEVs in the 25 cities. In addition, the government will initiate a series of incentive policies to attract customers to NEVs, including removal of limits on license plates, tax exemptions, and reduction of electricity prices and parking fees.

The main reasons for promoting BEVs are energy conservation and GHG reduction [7, 8]. Although BEVs do not use gasoline or diesel and have zero emission of GHG in operation, the electricity they consuming is primarily generated from coal-fired power plants with high GHG emissions. It is essential to evaluate energy use and GHG emissions of BEVs during their entire life cycle. The objective of this project is to carry out WTW analyses for BEVs using various thermal power generation technologies and compare their total energy use and GHG emissions against gasoline or diesel internal combustion engine vehicles (ICEVs), as well as hybrid electric vehicles (HEVs).

2 Methodology and Data Collection

2.1 Model

The WTW analyses of BEVs, ICEVs and HEV were conducted using the GREET (Greenhouse gases, regulated emissions, and energy use in Transportation) model developed by Argonne National Lab [9] combined with a localized database of Chinese domestic data. The scope of analyses is limited to energy consumption and GHG emissions in the fuel cycle and does not cover manufacturing and infrastructure construction. The function unit is defined as 1 km traveled of a five-seat compact car. Total life-cycle energy use is a summation of fuel consumption per km travel by car, and energy use during fuel process including extraction, production, and distribution of the fuel.

GHG emissions are expressed in terms of grams CO₂-equivalent (gCO₂-eq.). The “equivalence” is based on the conventional global warming potentials (GWPs) of respective individual GHGs for a time span of 100 years. Because radiative forcings are time dependent, so are the GWPs. The GWP value provided by the Intergovernmental Panel on Climate Change for the methane (CH₄) is 25¹ [10].

¹ More recently, by incorporating gas-aerosol interactions, some researchers have indicated that the methane GWP ought to be revised upward to about 33 [11]. This revision is not considered here.

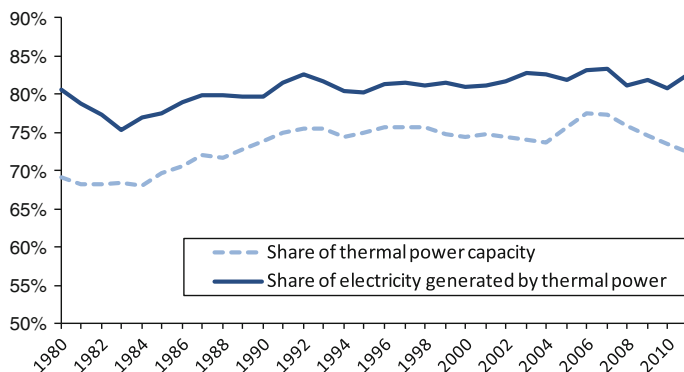


Fig. 1 Share of thermal generation capacity and electricity generated from thermal power plants in China (1980–2010)

2.2 Power Sources Mix of China's Electric Grid

Although there has been fast development of renewable and fossil-free resources, such as biomass, hydro, solar, wind, geothermal and nuclear in the past five years, the fossil fuel fired portion in the China's electric grid remains high. As the working hours of renewable power plants is less than fossil-fired counterpart and the China's total demand of electricity grew very sharply, the proportion of electricity coming from fossil fuels has nearly not changed, as shown in Fig. 1. Half of China's coal consumption is used to generate about 77 % of the nation's electricity, less than 5 % of which is presently based on clean-coal technology (such as ultra-supercritical pulverized coal combustion and integrated gasification combined cycle—IGCC). Hydro-electricity contributes a little more than 16 % of China's electricity. Nuclear contributes 1.8 %, while natural gas also accounts for 1.8 %. Fuel-oil power has greatly reduced in the past two decades, from 7.0 % in the 1990s to less than 2 % in 2010 [3]. As the hike of fuel oil price and government's action to shut down small generation units, existing oil-fired units are usually used as backup power source for big enterprises and mostly do not connect with grid [12].

There have been several studies that project the future mix of electric grid in China [12–15]. All studies indicate that coal-fired power will continue to dominate China's electricity in the near and mid-term future. Integrating information from some authoritative sources [16–18], our projections of China's electricity grid are illustrated in Table 1.

In the past few decades the unit capacity of coal-fired and gas-fired power plants has increased to get better efficiency. As summarized in Table 2 [19], generation units below 200 MW were mainstream and accounted for 75 % of thermal power plants in 1985, while units equal to and above 300 MW were only 8 %. In 2000, these percentages changed to 45 and 38 %. Between 2005 and 2010, mainstream technologies for new thermal power plants were 600 MW and above supercritical (SC) units, ultra-supercritical (USC) units, and 350–400 MW natural

Table 1 The Chinese electricity supply mix in 2010 and 2020

	Coal (%)	NG (%)	Oil (%)	Nuclear (%)	Biomass (%)	Hydro (%)	Wind and Others (%)
2010	76.9	1.7	1.7	1.8	0.5	16.2	1.2
2020 projection	71.0	3.0	–	8.0	1.0	14.5	2.5

Table 2 China's thermal power generation unit share by unit capacity

	1985 (%)	2000 (%)	2004 (%)	2010 (%)
≥1000 MW				50
600–999 MW		7	11	32
300–599 MW	8	31	33	36
200–299 MW	16	17	14	7
100–199 MW	27	15	15	9
≤100 MW	49	30	27	110

Source CEC

gas combined cycle (NGCC) units. In 2010, the percentage of generation units equal to and greater than 600 MW accounted for 37 % of total thermal power generation units, while proportion of generation units with less than 200 MW reduced to 20 %.

2.3 Coal-Fired Power Generation

Coal-fired power in China comes primarily from conventional pulverized coal-fired power plants.² These pulverized coal-fired units can be classified as high pressure (HP), very high pressure (VHP), subcritical, SC and USC based on parameters of boilers and turbines. The temperature and pressure for different coal-fired units are listed in Table 3.

China started to produce HP units in the 1950s. The first 125 MW VHP unit was built in 1969. The majority of 50–100 MW HP units and 125–200 MW VHP units which are still in operation were built in the 1990s or early this century. The average net coal consumption per kilo-watt hours (kWh) of electricity generated in 50–100 MW units is 417 grams standard coal equivalent (gce). For 125–150 MW VHP units, this indicator is 371 gce per kWh with a maximum of 396 gce per kWh. For 200 MW VHP units, the average net coal consumption is 365 gce per kWh with a maximum of 386 gce per kWh [20].

² In order to use coal gangue and low quality lignite, China also built a number of power plants with circulating fluidized bed technology, currently about seventeen 300 MW units and one 600 MW unit, 1 % in total thermal power capacity. In addition, there is a 250 MW IGCC demonstration unit located in Tianjin.

Table 3 Mainstream parameters of thermal power generation unit

	HP	VHP	Subcritical	SC	USC
Temperature (°C)	535	535	538	566	600
pressure (MPa)	8.8	12.2	16.7	24.2	25–27

China started to import 300 and 600 MW subcritical units in the 1980s. The first 600 MW SC unit was imported in 1992. Domestically made 600 MW SC units were put into operation in 2004. Installation of 600 and 1000 MW USC units began in 2006. By 2010, there were more than 700 units of 300 MW, about 400 units of 600 MW, and 32 units of 1000 MW power generation system in operation. The average net coal consumption per kWh of electricity generated in 300 MW level subcritical units is 334 gce. For 600 MW subcritical units, this indicator improves to 322 gce. When USC technology is employed, the average net coal consumption is 312 and 290 gce per kWh for 600 and 1000 MW units, respectively [21].

In addition to design parameters, operation management, and maintenance, some external factors, such as ambient temperature and coal type, will also change the power supply efficiency in the real world. The greatest impact often comes from actual capacity factor (CF) which can not be controlled by the power plant operators. Some studies have proved that net coal consumption rate will largely higher than design value which is caused by much higher turbine heat loss and service power rate and lower boiler efficiency when real CF is less than 75 % [22–24]. The average CF of Chinese coal-fired units was 60 % in 2011, a little higher than that of 2010 [19]. Relatively low CF will have negative impact on the unit performance, including net coal consumption rate. Our survey shows that the worst net coal consumption rate of 300 and 600 MW subcritical units can reach 366 and 349 gce per kWh, respectively. For 600 MW SC unit and 1000 MW USC unit, worst net coal consumption rate reached 323 and 313 gce per kWh, respectively. These data are substantially higher than the average level of different types of units announced by the CEC.

China constructed a clean coal power generation system in 2009 to demonstrate CO₂ capture and sequestration (CCS) technology. The CCS equipment has a capacity of 120 kt/yr, serving for two 600 MW SC units. Integrated Gasification Combined Cycle (IGCC) is considered a more advanced clean coal technology to match CCS. When IGCC is coupled with CCS, the net coal consumption rate could only increase 20 % comparing with that of original IGCC system. This incremental energy consumption percentage is only half of that of newly built pulverized power plant with CCS and one third of that in existing pulverized power plant adding CCS [25, 26]. The five major state owned utility companies in China initiated nine 200–400 MW IGCC plants from 2005 to 2006. However, only one 250 MW IGCC plant was put into demo operation by 2011 as there are some concerns in generating cost, actual efficiency and equivalent available factor (EAF). The power supply efficiency of this demo plant is not available. The actual power supply efficiency of 250 MW level IGCC plants demonstrated in North America and Europe is in a range of 37–43 % [27].

To reduce air pollution in big cities, some existing coal-fired units are replaced with gas-fired units in thermal power plants near the city. Newly built coal-fired power plants are in remote locations. Electricity is transmitted long distances to urban customers. Data released by the State Electricity Regulatory Commission (SERC) indicates that in 2010 there was a 6.5 % loss of electricity during the long distance transmission, comparable to US rates for 2007 [28].

2.4 Natural Gas Fired Power Generation

In order to meet the challenge of reducing carbon intensity per GDP, China is planning to increase NG consumption in next five years to 250 billion cubic meters, more than double the current level. In 2010 NG used for power generation accounted for 17 % of overall NG consumption. Large growth of NG-fired power generation is part of an aggressive plan to increase NG consumption to 12 % of primary energy use in China by 2020 [29].

The total capacity of NG-fired power generation in China was 33 GW in 2011 [19]. Typical gas-fired power generation technologies deployed in China are 180 MW natural gas combined cycle (NGCC) and fast growing 350 MW NGCC in the past five years. Among 119 NG-fired power plants surveyed nationwide, 64 units were 350 MW NGCC and 46 units were 180 MW NGCC. These 18 and 350 MW NGCC units accounted for 98 % of gas-fired power generation capacity in China. The theoretical power supply efficiencies of 180 and 350 MW NGCC plant could reach 50 and 55 % respectively. However, statistical data shows that the real CF of most of Chinese gas-fired units were only in a range of 30–50 % in recent years [30]. The average CF of gas-fired units nationwide was only 37 % in 2011 [19]. Some researchers have proved that gas-fired power generation units have an 20–31 % increase in heat loss when they operated at 30–40 % load rate [31]. Another study showed that power supply efficiency would be reduced from 51 to 42 % when CF decreased from 100 to 45 % and then slipped to 40 % when CF further fell to 30 % [32].

2.5 Coal Mining, Processing and Transportation

China's proved coal reserve is about 114,500 million tones at the end of 2011. As China consumes more than three billion tones of coal each year, the reserve-production ratio (R/P ratio) is 33 years, less than one-third of world average. Sub-surface mining dominates the industry, accounting for 95 % of coal extraction in China. Mining one tone of coal consumes 34 kWh electricity and 27 kg raw coal [33]. Furthermore, for each tone of coal excavated, there is an accompanying emission of roughly 7–8 cubic meters of methane [34, 35], 6 cubic meters of CO₂ [33], and trace amounts of SO₂ and oxides of nitrogen. About 25 % of the coal

Table 4 Key parameters of coal long-distance transportation

	Waterway	Railway		Truck
Mode Share (%)	15	45		40
Distance (km)	1,500	640		500
Fuel type	Fuel oil	Diesel	Electricity	Diesel
Energy intensity (kJ/t km)	257	203	78	1,480

produced in China was cleaned and sorted in 2010 [3]. For each tone of coal cleaned and sorted, 3 kWh electricity was consumed. There is about 10 % of gangue eliminated during the process that has a total energy efficiency of 95 % [33].

For power plants, coal transport is comprised of 45 % railway, 40 % highway and 15 % waterway. The average transport distance is 640 km for railway and 1500 km for waterway (coal for power generation is transported by barge from ports in North China to the 7 southeast provinces) [36]. There is no statistical data available and we estimate the highway transportation distance is 500 km. Some key parameters of long-distance transportation is showed in Table 4. The energy consumed for the return trip of the empty vehicle and vessel after delivery has been considered.

2.6 NG Recovery, Processing and Transportation

Besides a few inland NG-fired power plants that can use local NG resources, the majority of NG-fired power generation units are located in southeast coastal areas to which NG is delivered either by long distance pipeline from west China, or LNG ocean tanker. About 40 % of China's imported LNG came from Australia in 2010 [37]. Two cases are assumed in this study: The first is NG pipeline from Xinjiang to the east coast at a distance of 4,000 km; and the second is LNG ocean tanker of 147,000 cubic meters from Dampier port, Australia, to Shanghai Yangshan port at a distance of about 6,000 km. Energy efficiency for NG liquefaction is generally 85–93 % [38, 39]. NG transportation and distribution parameters for the two cases are shown in Table 5.

2.7 Vehicle Technologies

We compared BEV with the conventional gasoline car, diesel car, and hybrid electric car in terms of total energy use and GHG emissions. Our baseline is a MY2011 mid-size³ gasoline car with a gross vehicle weight (GVW) of 1,280–

³ According to definition from U.S. EPA, mid-size car is pointed to the car with a total passenger & cargo volume from 110 to 119 cubic feet.

Table 5 Key parameters of NG transportation and distribution

	Pipeline	Ocean tanker (LNG)
Distance (km)	4,000	6,000
Fuel type	NG and electricity	LNG and fuel oil
Energy intensity (kJ/t km)	1,435	66

1,430 kg, 1.8 l engine with port-injection spark-ignition (PISI), and five-speed automatic transmission. The baseline car uses RON 93 gasoline and meets China Stage IV emission standards. The baseline car has a fuel consumption of 8.0 l/100 km under New European Drive Cycle (NEDC). Although actual fuel consumption could be 20–30 % higher for driving in big cities, like Beijing and Shanghai [40], for convenience and consistency, we use fuel consumption in NEDC test to compare the different pathways.

A diesel car with direct-injection compression-ignition (DICI) could save 20 % of the energy consumed by the baseline vehicle (about 30 % saving if counted in fuel volume). If direct-injection is applied to a gasoline car, with turbocharging system, fuel consumption could be reduced 10–15 %; while a full HEV could deliver more than 30 % fuel consumption savings. There are no official fuel consumption data under NEDC for BEVs in China. Some reports indicate that the currently demonstrated BEVs consumed 20–27 kWh/100 km [41, 42]. Our field survey in demo taxi fleet showed a even higher electricity consumption—sometimes more than 30 kWh/100 km. There are some international brands of BEVs that have fuel consumption in a range of 14–17 kWh/100 km. We assumed two cases in this study: The first is the Common BEV and the second, the High-efficient BEV. Their fuel consumptions are 24 and 16 kWh/100 km respectively. The charging loss of BEV is estimated to a range of 7–15 %.

3 Results and Discussion

We conducted WTW analyses for 20 fuel/vehicle systems, including 16 electric vehicle pathways. WTW energy results of Common BEVs and High-efficient BEVs using different power generation technologies are summarized in Figs. 2 and 3. The WTW petroleum consumption for each pathway is marked in darker color. Each solid bar denotes an average value with upper and lower bounds. Thus each pathway represents a range due to differences in technologies and operational conditions in energy feedstock recovery, transportation, and storage, fuel production, transportation and distribution, and electricity generation, transmission and charging, including efficiencies difference among power generation units.

The WTW energy consumption of the baseline PISI gasoline car is 3.34 MJ/km. The gasoline direct-injection plus turbo pathway (DISI) will cut 15 % of the baseline WTW energy consumption, while the dieselization pathway can reduce the WTW energy consumption to 2.60 MJ/km. The WTW energy consumption of

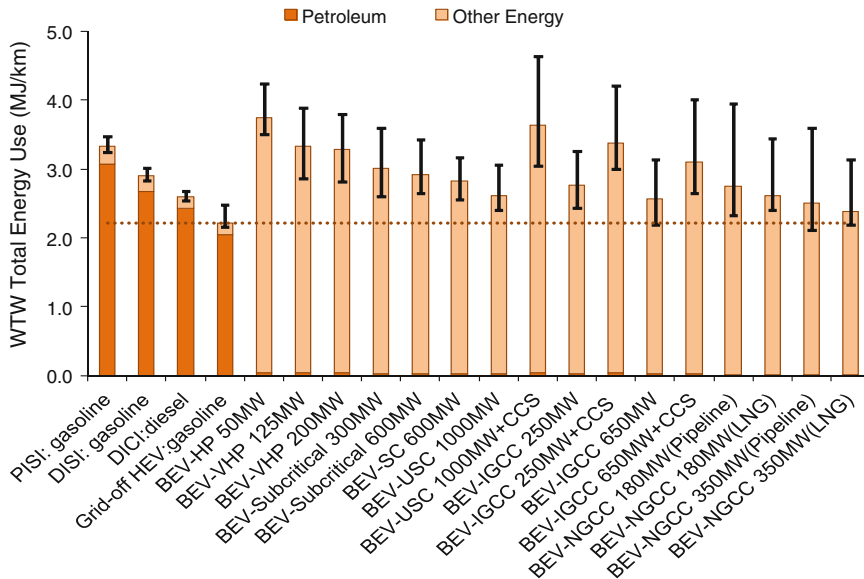


Fig. 2 WTW total energy use and petroleum replacement of common BEV pathways

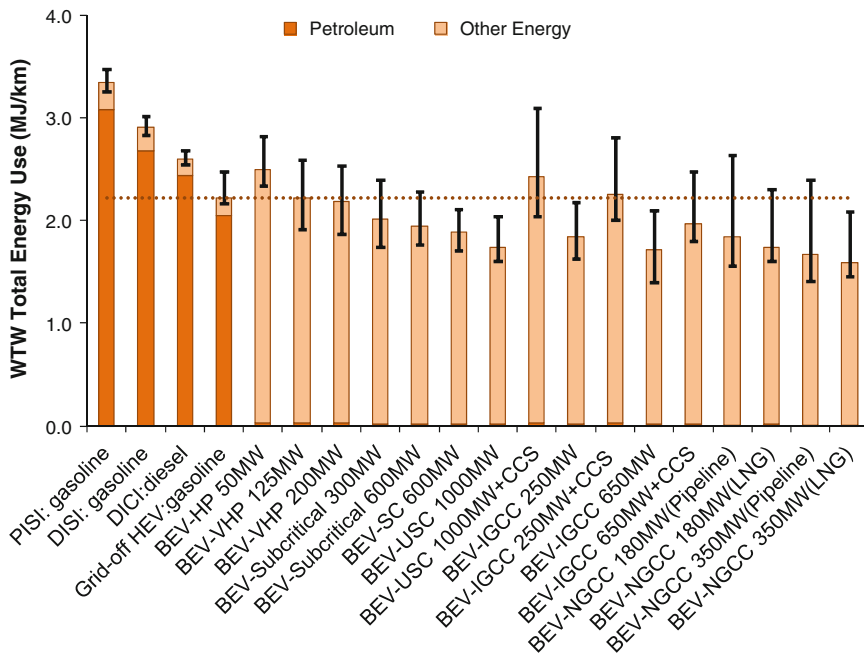


Fig. 3 WTW total energy use and petroleum replacement of high-efficient BEV pathways

the hybrid pathway can be further reduced to 2.22 MJ/km without increase in PM_{2.5} emission.

As shown in Fig. 2, all Common BEVs can reduce petroleum consumption no matter whether electricity is generated from coal or NG. WTW petroleum consumption for EVs is less than 2 % of the petroleum used in the baseline gasoline car. Even compared to the HEV pathway, BEVs can save up to 99 % of petroleum. The little petroleum consumed in the BEV pathways is from fuel used in transport of coal to power plants.

In the vehicle operation stage, energy consumption of Common BEVs on per 100 km basis is only 25 % of that in the DISI pathway, and it is 66 % lower than the HEV pathway. However, WTW total energy analysis tells a total different story. When Common BEVs use electricity from coal-fired power plants with generation units less than 600 MW (which occupies 60 % of coal-fired power generation units in 2010), the WTW energy consumption of Common BEVs will increase 4–40 % compared to the baseline. Compared to the HEV pathway, WTW energy of Common BEVs will increase 7–60 % for NG-fired electricity generation and 17–71 % coal-fired electricity generation.

The High-efficient BEV is equipped with an advanced motor, regenerative braking system, and battery package with high energy density. WTW energy consumption of High-efficient BEVs is 2.22 MJ/km when electricity is from 125 MW VHP generation units, which is equal to WTW energy of the HEV pathway. If electricity is from more efficient generation units, such as 200 MW VHP, 300 MW subcritical, 600 MW SC and 1000 MW USC units, the WTW energy consumptions of High-efficient BEVs are 2, 9, 15 and 22 % less than the WTW energy consumption in the HEV pathway. If electricity is from NG-fired generation units, WTW energy consumption of High-efficient BEVs will be 17–29 % less than the WTW energy in the HEV pathway.

The WTW GHGs emission of the baseline PISI gasoline car is 249 gCO₂-eq./km. The DISI plus turbo pathway will cut 15 % of the baseline WTW GHG emissions, while the hybrid pathway can reduce the WTW GHG emissions to 167 gCO₂-eq./km. In the vehicle operation stage, there is no GHG emission of Common BEVs. Therefore WTW GHG emissions of BEVs depend on differences in power generation technologies. As shown in Fig. 4, when electricity comes from HP and VHP generation units, WTW GHG emissions of all Common BEVs are above 350 gCO₂-eq./km, with a maximum of 440 gCO₂-eq./km. If electricity is generated from mainstream generation units today and in future, such as 300 MW subcritical, 600 MW SC and 1000 MW USC units, the WTW GHG emissions of Common BEVs are still 28, 20, and 11 % higher than the WTW GHG emissions of the baseline gasoline pathway and much higher than that of HEV pathway. CCS technology must be employed for coal-fired power plants to meet GHGs emission reduction tasks. When USC and IGCC are equipped with CCS, the WTW GHG emissions of Common BEVs can be reduced to 78 and 63 gCO₂-eq./km respectively. However, as a trade-off, the pathways with CCS technology will

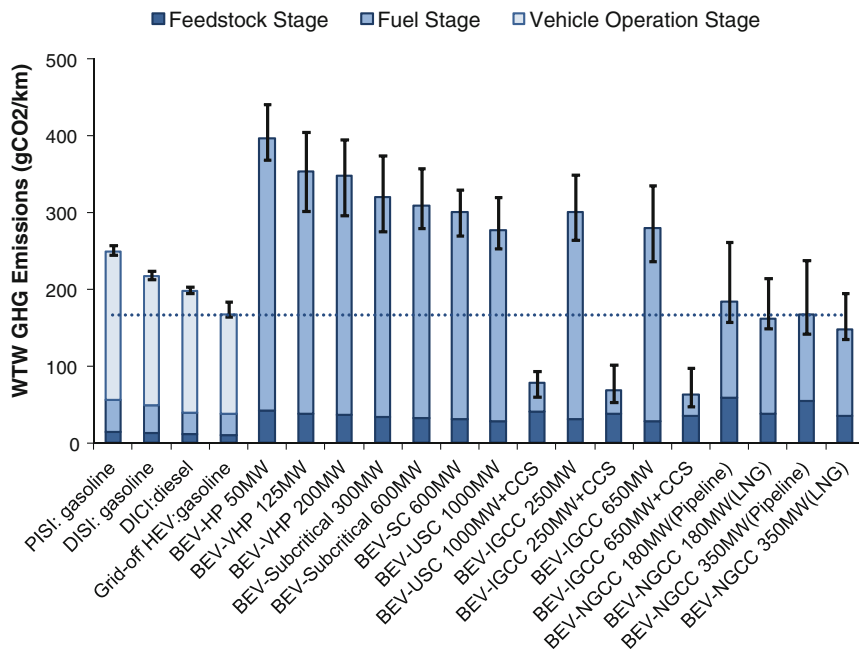


Fig. 4 WTW GHG emissions of common BEV pathways

consume more energy in the whole fuel-cycle. If electricity is generated by NG-fired 350 MW units using NG piped from Xinjiang Province, the WTW GHG emissions of Common BEVs are similar to that of the HEV pathway. With electricity generated by LNG fired NGCC, the WTW GHG emissions of Common BEVs are 12 % less than that of HEV pathway. The difference is caused by the higher energy consumption in processing and transport of long-distance pipeline NG compared to LNG from overseas.

WTW GHG emissions of High-efficient BEV powered by electricity from different coal-fired units are 10–59 % higher than the HEV pathway. However, WTW GHG emissions of High-efficient BEV using electricity from any 300 MW or larger generation units are less than that of the advance gasoline pathway—DISI. When USC and IGCC are equipped with CCS, the WTW GHG emissions of High-efficient BEVs are 79–83 % less than that of the baseline, and 69–75 % less than that of the HEV pathway. WTW GHG emissions of High-efficient BEVs using electricity from NGCC units are 51–60 % less than that of the baseline, and 27–41 % less than that of the HEV pathway (Fig. 5).

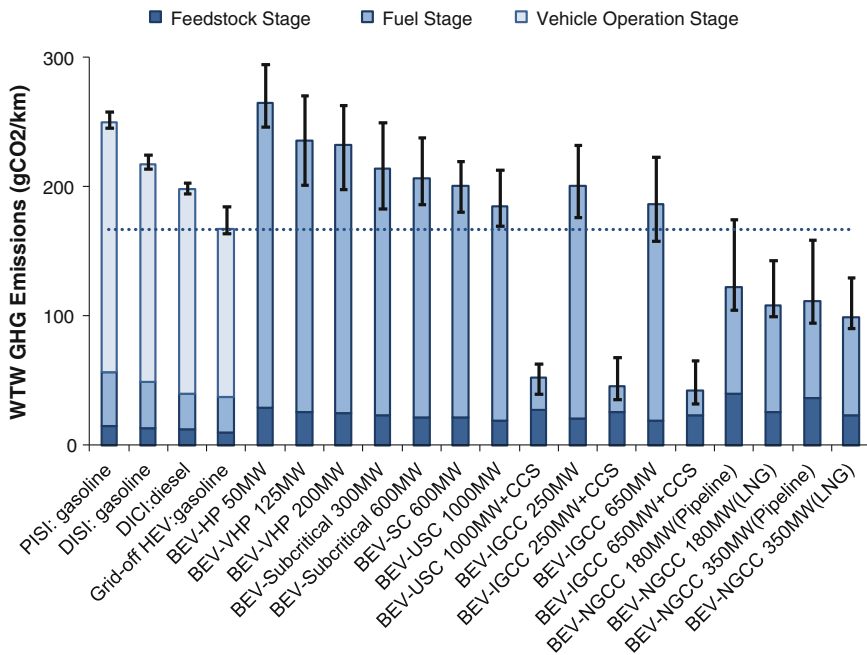


Fig. 5 WTW GHG emissions of high-efficiency BEV pathways

4 Conclusions and Implications

The WTW analyses indicates that Common BEVs currently demonstrated are not a silver bullet for attacking energy consumption challenges and GHG emissions in China. The electric grid in China will be dominated by coal-fired power generation through the next few decades. Although electrification of China’s vehicle fleet could reduce dependence on petroleum, it will not realize the targets of conservation of energy and reduction of GHG emissions. Considering China was a net importer of some 144 Mt coal in 2010 [3], the energy conservation concern also needs to be kept in mind, as responsibility to global warming mitigation.

With electricity from 300 MW or larger coal-fired generation units, WTW GHG emissions of High-efficient BEVs are lower than that of the advanced DISI gasoline pathway, but still higher than that of the hybrid pathway. Only with electricity generated from NGCC units, or coal-fired units with CCS, is High-efficient BEV pathway more attractive than the hybrid pathway in GHGs reduction.

With a coal-fired dominant grid in near and mid-term future, in order to achieve GHG reduction targets through vehicle electrification, China must promote CCS technology to help USC and IGCC power plants to deliver low-carbon transportation energy in supply side. At the same time, High-efficient BEVs have to be set as the highest priority of automotive technology development.

References

1. National Bureau of Statistics of China (NBS) (2011) China statistical yearbook. China Statistics Press, Beijing
2. Sinopec (2012) China's diesel supply and quality upgrading. In: Prepared for workshop of China's vehicle dieselization, MIIT, Beijing
3. National Energy Administration (2011) China energy statistical yearbook. China Statistics Press, Beijing
4. Huo H, Wang M, Johnson L, He D (2007) Projection of Chinese motor vehicle growth, oil demand, and CO₂ emissions through 2050. *Transp Res Rec* 2038:69–77
5. International Energy Agency (IEA) (2011) IEA statistics: CO₂ emissions from fuel combustion—Highlights, 2011 Edition. (<http://www.iea.org/co2highlights/co2highlights.pdf>)
6. Qian M (2011) Progress of China's new energy vehicles (NEVs) demonstration program. In: Prepared for EU-China workshop on NEV energy consumption assessment, Beijing, Dec 7 2011
7. Ministry of Industry and Information Technology (2012) Energy saving and new energy vehicle industry development plan (2012–2020). MIIT, Beijing (<http://zbs.miit.gov.cn/n11293472/n11295142/n11299123/14559272.html>)
8. Ministry of Science and Technology (MoST) (2012) 12th five-year special plan on electric vehicle technologies development. MoST, Beijing (www.most.gov.cn/tztg/201204/W020120420547632346015.pdf)
9. Wang, M (1999) GREET 1.5-transportation fuel-cycle model volume 1: methodology, development, use, and results, ANL/ESD-39. Argonne National Laboratory, Chicago
10. Intergovernmental Panel on Climate Change (2007) Climate change 2007: the physical science basis. Contribution of working group I to the fourth assessment report of the intergovernmental panel on climate change. Cambridge University Press, Cambridge
11. Shindell DT, Faluvegi G, Koch DM, Schmidt GA, Unger N, Bauer SE (2009) Improved attribution of climate forcing to emissions. *Science* 326:716–718
12. Zhao J, Zhao M (2005) Review and prospective of China's thermal power structure optimization and technical upgrading. China Power Engineering Consulting Group Corporation, Beijing
13. Energy Information Administration (2011) International energy outlook 2011, EIA, DoE, Washington, DC (<http://www.eia.gov/forecasts/ieo/>)
14. International Energy Agency (2011) World Energy Outlook 2011. IEA, Paris
15. Development Research Center of the State Council of China, Energy Research Institute of National Development and Reform Commission of China, Institute of Nuclear and New Energy Technology at Tsinghua University (2009) 2050 China energy and CO₂ emissions report. Science Press, Beijing
16. National Development and Reform Commission (2007) Mid- and long-term development plan of renewable energy. Beijing, NDRC
17. National Development and Reform Commission (2007) Mid- and long-term development plan of nuclear power generation. Beijing, NDRC
18. China Electricity Council (2010) Target and glidepath of energy saving and GHG reduction in the power industry during the 12th five-year plan. In: Prepared for summit of China energy 2010. Beijing
19. China Electricity Council (2012) Statistical databook of china power industry 2011. Beijing, CEC
20. State Electricity Regulatory Commission (2008–2011) Power industry energy saving report. SERC, Beijing
21. China Electricity Council (2011) 300 and 600 MW thermal power generation energy efficiency investigation. Beijing, CEC
22. Liu F, Jiang X, Li Z (2008) Investigation on affects of generator load on coal consumption rate in fossil power plant. *Power Syst Eng* 24(4):47–49

23. Sun W, Sun Y (2012) The influence of instantaneously variable load on coal consumption rate in ultra-supercritical unit. *Electric Power* 45(1):20–24
24. Zhang Y, Zhu B, Lei Z (2007) Study on load under economic operation of ultra-supercritical units. *Thermal Power Gener* 11:1–3
25. Intergovernmental Panel on Climate Change (2005) Special report on carbon dioxide capture and storage: summary for policymakers and technical summary. Cambridge University Press, Cambridge
26. National Energy Technology Laboratory (2007) Fossil energy power plant desk reference: IGCC plants with and without CCS. DOE/NETL-2007/1282. NETL, Washington, DC
27. Jiao S (2009) Review and prospect on development of IGCC technology. *Electric Power Constr* 30(1):1–7
28. State Electricity Regulatory Commission, National Development and Reform Commission, Ministry of Environment Protection, National Energy Administration (2011) Energy saving and emission reduction of power industry in 2010 and 11th five-year term. Beijing
29. Hu W (2012) Introduction of China's natural gas 12th five-year plan. International Energy Club, Beijing
30. State Electricity Regulatory Commission (2010) Capacity factor report of grid connected power generation units from Guangdong electricity dispatching center. Guangzhou, SERC
31. Ye J (2011) Operation optimization and energy-saving Retrofit for a 109FA gas-steam combined cycle unit. *Power Equip* 25(2):121–124
32. Zhou X, Zhai M (2009) Analysis of cycle efficiency of new NGCC power station. *Thermal Power Technol* 1:9–12
33. Chinese Coal Research Institute (2006) Report to NDRC on energy efficiency, emissions and cost of coal mining and washing. Beijing, CCRI
34. Zheng S (2002) Coal bed methane emission inventory in China. *China Coal* 28(5):37–40
35. Ma Z, Pan Z, He H (1999) Greenhouse gas emission factor for coal power chain in China and the comparison with nuclear power chain. *Chin J Nucl Sci Eng* 19(3):268–274
36. China Communication and Transportation Association (2011) China transportation statistical yearbook. China Transportation Statistics Press, Beijing
37. British Petroleum (2012) Statistical review of world energy. BP, London (<http://www.bp.com/bodycopyarticle.do?categoryId=1&contentId=7052055>)
38. Bennett P (2006) Private communication. BP China, Beijing
39. Sinopec (2008) Low energy consumption NG liquefaction unit design and test. Report from Chengdu NG chemical plant. Sinopec, Chengdu
40. Huo H, Yao Z, He K, Yu X (2011) Fuel consumption rates of passenger cars in China: labels versus real-world. *Energy Policy* 39(11):7130–7135
41. SINA (2012) DM II model vehicle in Beijing auto show. SINA, Beijing (<http://auto.sina.com.cn/car/2012-04-16/0919953747.shtml>)
42. Greencarcongress (2012) BYD introduce new dual-mode qin. GCC, Detroit (<http://www.greencarcongress.com/2012/04/denza-20120423.html#more>)

Effects of Fuel Thermo-Physical Properties on Spray Characteristics of Biodiesel Fuels

Xinwei Cheng, Harun M. Ismail, Kiat Hoon Ng, Suyin Gan
and Tommaso Lucchini

Abstract The main emphasis of this study is to examine the effects of biodiesel thermo-physical properties on the fuel spray development using CFD modelling. A complete set of 12 thermo-physical properties is estimated for PME, SME and CME. The methods employed for this as reported here are generic as the methods are dependent on the chemical compositions and temperature. Sensitivity analysis is performed by integrating the estimated fuel properties into CFD modelling. Variations in spray development such as mass of fuel evaporated and liquid and vapour axial penetration length of biodiesel fuels are found to be different from fossil diesel due to the difference in thermo-physical properties. A total of five biodiesel properties are identified to have profound impacts on fuel spray development, which are liquid density, liquid viscosity, liquid surface tension, vapour pressure and vapour diffusivity. Nevertheless, only liquid surface tension and vapour pressure are the most sensitive fuel properties to the fuel spray

F2012-B01-023

X. Cheng (✉) · H. M. Ismail · Kiat HoonNg
Department of Mechanical, Manufacturing and Materials Engineering, The University of Nottingham Malaysia Campus, Jalan Broga, 43500 Semenyih, Selangor, Malaysia
e-mail: chem_ph@hotmail.com

H. M. Ismail
e-mail: keyzhi@exmail.nottingham.edu.my

Kiat HoonNg
e-mail: hoonkiat.ng@nottingham.edu.my

S. Gan
Department of Chemical and Environmental Engineering, The University of Nottingham Malaysia Campus, Jalan Broga, 43500 Semenyih, Selangor, Malaysia

T. Lucchini
Department of Energy, Politecnico Di Milano, Milan, Milano, Italy

development. The work has provided better representation of biodiesel properties, which improve the in-cylinder CFD simulation of reacting spray jet for the fuel.

Keywords Biodiesel · CFD · Fuel spray · Thermo-physical properties

1 Introduction

Despite the widespread use of biodiesel in conventional diesel engine, there is a need for more comprehensive research work to conclusively determine the benefits and drawbacks of biodiesel [1, 2]. One such effort is the utilisation of computational fluid dynamics (CFD) techniques to better understand and improve biodiesel fuel spray, combustion and emission characteristics in compression ignition (CI) engines.

For accurate in-cylinder CFD simulations of biodiesel spray combustion process, the most important element is the spray and vapour structures of fuel as these structures dictate the fuel vaporisation rate and the subsequent ignition, combustion and pollutant formation processes. Since fuel spray and vapour structures are primarily governed by the fuel thermo-physical properties, it is imperative to understand the effects of these properties of different biodiesel fuels in comparisons to fossil diesel. Nevertheless, there are limited studies on developing and establishing the impacts of thermo-physical properties of biodiesel fuels [1–3]. Moreover, most of the fuel properties were developed based on the mixture compositions of soybean [1–3] or based on approximated single component molecule, for example methyl oleate ($C_{19}H_{36}O_2$) that represents rapeseed methyl ester [4]. Thus, fuel spray modelling using the approximated generic biodiesel fuel properties inherently result in a certain level of inaccuracy in the predictions.

In line with the discussion above, the reported work here is based on palm methyl ester (PME), soybean methyl ester (SME) and coconut methyl ester (CME) to represent biodiesel fuels with low, moderate and high degree of unsaturation, respectively. The fuel properties of PME, SME and CME are first developed due to limited comprehensive validated thermo-physical properties of biodiesel fuels available. Then, a set of numerical experiments are performed to investigate the sensitivity of individual fuel properties under constant volume combustion. Fuel spray characteristics of biodiesel fuels and fossil diesel are the main interest of comparisons for the sensitivity analysis of fuel properties.

2 Development of Biodiesel Thermo-Physical Properties

There is a total of 12 pertinent biodiesel thermo-physical properties excluding critical properties. The evaluation of biodiesel properties is done using empirical methods available in the literature. The selection of appropriate methods of evaluation is

Table 1 Average FAME compositions of PME, SME and CME based on mole fraction

FAME	Fuel types			Critical property		
	PME	SME	CME	Temperature (K)	Pressure (bar)	Volume (ml/mole)
Laureate (C ₁₃ H ₂₆ O ₂)	–	–	0.53	695.330	14.210	789.500
Myristate (C ₁₃ H ₃₀ O ₂)	0.011	–	0.20	724.110	14.210	901.500
Palmitate (C ₁₇ H ₃₄ O ₂)	0.410	0.080	0.12	767.050	14.210	1013.500
Stearate (C ₁₉ H ₃₈ O ₂)	0.042	0.040	0.065	775.590	14.210	1125.500
Oleate (C ₁₉ H ₃₆ O ₂)	0.429	0.250	0.085	774.400	14.080	1105.500
Linoleate (C ₁₉ H ₃₄ O ₂)	0.108	0.550	–	798.460	13.950	1085.500
Linolenic	–	0.080	–	801.680	13.830	1065.500
Critical temperature (K)	773.455	789.209	721.202			
Critical pressure (bar)	13.993	13.000	15.304			
Critical volume (ml/mol)	1063.814	1084.644	884.839			

assessed through the applicability of these methods over a wide range of temperature. In order to reduce the complexity in the evaluation of fuel properties, the chemical compositions of fatty acid methyl ester (FAME) components for each biodiesel in this study, PME, SME and CME are maintained to five distinct components as listed in Table 1. Fuel properties of fossil diesel, represented by tetradecane (C₁₄H₃₀) are used as the basis of comparisons for the estimated biodiesel properties.

In the estimation of biodiesel thermo-physical properties, the critical properties, critical pressure, critical volume and critical temperature of each FAME component are first evaluated using Lydersen's method [5] as listed in Table 2. Then, Lee-Kesler mixing rule [5] is imposed according to respective biodiesel chemical compositions to obtain the critical properties of PME, SME and CME. These critical properties are vital as any biodiesel properties beyond these properties will cease to be valid. The estimated critical properties of FAME components in this study are validated against those in literature [3]. Approximately 20 % of error is obtained for critical pressure, whereas less than 0.6 % of error is found for the estimated critical temperature and critical volume. Besides that, Lydersen's method [5] is proven accurate with reasonable error margin of only 10 % [6]. Therefore, the estimated critical properties for other biodiesel fuels are reasonably accurate as the critical properties are evaluated based on the respective chemical compositions of FAME components.

Figures 1a–l displays the estimated thermo-physical properties of PME, SME and CME, as well as the fossil diesel properties. The liquid densities of PME, SME and CME are predicted using Rackett equation modified by Spencer and Danner [5]. Less than 10 % of deviation is obtained when the estimated liquid densities of

Table 2 Methods of evaluation for the thermo-physical properties of biodiesel fuels

Thermo-physical property	Method of analysis	References
Critical properties	Joback modification of Lydersen's method	[5]
Liquid density	Rackett equation	[5]
Liquid surface tension	Correlation proposed by Allen et al.	[7]
Liquid viscosity	Orrick and Erbar method, Letsou and Stiel method	[5] [5]
Liquid heat capacity	van Bommel correlation	[8]
Liquid thermal conductivity	Method of Robbins and Kingrea	[5]
Vapour pressure	Antoine equation	[9]
Latent heat of vaporisation	Pitzer acentric correlation	[5]
Vapour viscosity	Correlation by Chung et al.	[10]
Vapour thermal conductivity	Correlation by Chung et al.	[11]
Vapour diffusivity	Method of Wilke and Lee	[12]
Vapour heat capacity	Method of Rihani and Doraiswamy	[5]
Second virial coefficient	Method of Tsonopolous	[5]
Mixing rules	Lee-Kesler equation, Simple mixing rule, Nissan and Grunberg method	[5] [5] [5]

SME across the interested temperature range are compared to the estimated properties of SME by Yuan et al. [3]. Since the trends and range of estimated liquid densities of PME and CME are similar to SME, the estimated liquid densities of PME and CME are proven accurate. Based on Fig. 1a, the liquid densities of PME, SME and CME are 20 % higher than diesel at lower temperatures and linearly decrease with increasing temperatures. Thus, the vaporisation rates of biodiesel fuels are lower than fossil diesel. Liquid surface tensions of PME, SME and CME are predicted using equation proposed by Allen et al. [7]. Liquid surface tensions of PME, SME, CME and fossil diesel are presented in Fig. 1b. The validation of liquid surface tensions is done by comparing the estimated liquid surface tension of SME against predicted value by Allen et al. [7] at 40 °C. The estimated surface tension value at 40 °C for SME in this study is 30.2 mN/m, is approximately 7 % higher than measured value of 28.2 mN/m by Allen et al. [7]. Comparatively, the liquid surface tensions of the biodiesel fuels are 14 % higher than diesel. Thus, the fuel spray break-up and vaporisation rates of biodiesel fuels are expected to be lower than fossil diesel.

Low temperature liquid viscosities of FAME components of PME, SME and CME are computed using Orrick and Erbar method [5] up to reduced temperature (ratio of temperature to critical temperature) of 0.7. Grunberg and Nissan method [5], a mixing rule specifically for liquid viscosity is then used to compute the liquid viscosities of PME, SME and CME. For liquid viscosity at reduced temperature higher than 0.7, Letsou and Stiel method [5] is utilised. The estimated values of SME seen in Fig. 1c are validated against those measured by Tat and van Gerpen [5] with the largest relative error of 18 % at 0 °C and the least error of 7 % at 100 °C as seen in Table 3. The error is observed to be reduced with increasing

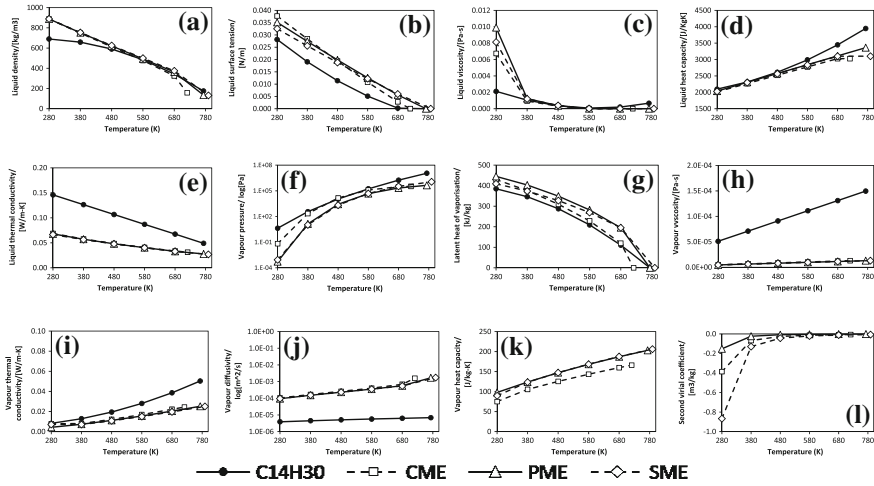


Fig. 1 Thermo-physical and transport properties of PME, SME and CME as compared to C₁₄H₃₀ for **a** liquid density, **b** liquid surface tension, **c** liquid viscosity, **d** liquid heat capacity, **e** liquid thermal conductivity, **f** vapour pressure, **g** latent heat of vaporisation, **h** vapour viscosity, **i** vapour thermal conductivity, **j** vapour diffusivity, **k** vapour heat capacity, and **l** second virial coefficient

Table 3 Comparisons between predicted and measured liquid viscosities of SME

Temperature (°C)	Predicted liquid viscosity (mPa s)	Measured liquid viscosity ^a (mPa s)	Relative error (%)
0	9.89	12.07	18.09
20	6.00	6.4	6.33
40	3.87	3.89	0.40
60	2.64	2.63	0.34
80	1.88	1.92	2.22
100	1.39	1.49	7.03

^a Values obtained from Tat and Van Gerpen [14]

temperatures. Therefore, the estimated liquid viscosity values for SME seen in Fig. 1c are relatively accurate as do the estimated liquid viscosity values of PME and CME as the correlations used are dependent on temperature and chemical compositions. It is expected that the break-up processes of fuel droplets will be affected by liquid viscosities since the estimated liquid viscosities of biodiesel fuels are higher than fossil diesel especially at lower temperatures.

The liquid heat capacities of PME, SME and CME are estimated using correlation by van Bommel et al. [8] and simple mixing rules [5]. The trends of estimated liquid heat capacities of PME, SME and CME are compared to fossil diesel. Here, similar trend is found where the estimated liquid heat capacities of biodiesel fuels displayed in Fig. 1d are 25 % lower than fossil diesel at higher temperatures. This implies that fuel droplets of biodiesel fuels are heated up faster

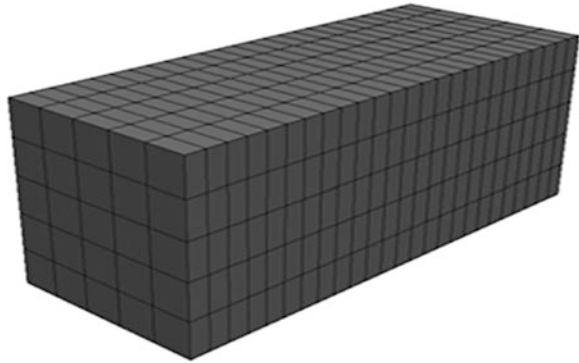
than fossil diesel and consequently the vaporisation rate of fuel droplets is enhanced. The liquid thermal conductivities of individual FAME components are predicted using the method of Robbins and Kingrea [5]. After that, Li's equation [5] is employed to determine the liquid thermal conductivities of PME, SME and CME. Based on Fig. 1e, the estimated biodiesel liquid thermal conductivities are compared to fossil diesel as a result of the limited validation data. Liquid thermal conductivity is required to compute heat transfer across the fuel droplets, where a transient temperature distribution is assumed [9].

Vapour pressure is one of the key thermo-physical properties as it affects the vaporisation process of fuel spray. Vapour pressure of each FAME component is evaluated using Antoine equation [9] and then simple mixing rule [5] is applied to obtain the vapour pressure of PME, SME and CME. Based on Fig. 1f, the estimated vapour pressures for PME, SME and CME remained low from 280 up to 580 K. But the vapour pressures of biodiesel fuels increase to maximum value at their respective critical temperature right after 580 K. The validation of estimated vapour pressures is done by comparing the trends of estimated vapour pressures of PME, SME and CME seen in Fig. 1f against the predicted and measured vapour pressure values of SME [3]. Satisfactory agreement of less than 10 % is found. Latent heat of vaporisation at normal boiling point is estimated using Pitzer acentric factor correlation [5]. Compared to fossil diesel, the latent heat of vaporisations of the biodiesel fuels are 13 % lower along the temperature range as seen in Fig. 1g. Thus, the fuel droplets of biodiesel fuels will be heated up quickly during the vaporisation process.

Vapour viscosities and vapour thermal conductivities are calculated by employing the Chapman-Enskog kinetic theory [5] as proposed by Chung et al. [10, 11]. Both vapour viscosities and thermal conductivities of PME, SME and CME are fairly accurate when vapour viscosity and thermal conductivity of fossil diesel are taken as the baseline case for validation. Vapour viscosities of the PME, SME and CME are comparatively lower than fossil diesel as seen in Fig. 1h. From Fig. 1i, vapour thermal conductivities of biodiesel fuels are also lower than fossil diesel. Hence, it is important to investigate the rate of break-ups of vapour fuel droplets and the heat transfers across the combustion chamber as these two phenomena are affected by vapour viscosity and thermal conductivity.

Vapour diffusivity defines the speed of movements of fuel vapours in the combustion chamber. The estimated vapour diffusivities of PME, SME and CME are presented in Fig. 1j and are evaluated using Wilke and Lee method [12]. Good agreement is obtained when the trends of estimated vapour diffusivities of PME, SME, CME and fossil diesel are compared. Meanwhile, values of vapour heat capacity are predicted using the method of Rihani and Doraiswamy [5] as presented in Fig. 1k. The transient heat transfer of surrounding gas to the fuel droplet surface depends on the vapour heat capacity of fuel. Vapour heat capacity is also required to predict the vapour viscosities and vapour thermal conductivities of the PME, SME and CME. On the other hand, second virial coefficient is a coefficient used in gas equation expansion. The second virial coefficients of FAME

Fig. 2 Computational mesh of constant volume combustion chamber



components are computed using the method of Tsonopoulos [5]. The Lee-Kesler mixing rule [5] is then applied to determine the second virial coefficient of PME, SME and CME, as presented in Fig. 11.

3 Numerical and Experimental Operating Conditions

In-cylinder constant volume combustion is simulated using OpenFOAM to examine the sensitivity of individual biodiesel properties to the fuel spray development. The constant volume combustion chamber utilised displayed in Fig. 2 with a total volume of 2 L is built based on Chalmer's high-pressure, high-temperature spray rig [13]. The operating conditions for the constant volume combustion are listed in Table 4, where a vertically aligned and single-hole injector operating at 313.15 K temperature and 1200 bar pressure is used [13]. In order to examine the effects of individual properties on the fuel spray characteristics, the properties of PME are set as base properties. Then, each individual fuel property is varied to that of fossil diesel. The main results of interest here are the development of fuel spray, liquid and vapour axial penetration length, mass of fuel evaporated and Sauter Mean Diameter (SMD). Due to limited experimental data available for SME and CME, the sensitivity analysis in this study is only conducted for PME.

4 Sensitivity Analysis of Biodiesel Thermo-Physical Properties Under Constant Volume Combustion

Only 5 out of the 12 thermo-physical properties of PME have been identified as significant properties since profound changes on the biodiesel spray analysis are found as shown in Fig. 3. The five significant properties include liquid density, liquid surface tension, liquid viscosity, vapour pressure, and vapour diffusivity.

Table 4 Numerical and experimental operating conditions for the constant volume combustion chamber

Chalmer’s high-pressure, high-temperature constant volume combustion chamber [15]	
Volume	2 Litre
Pressure	50 bar
Temperature	830 K
Nozzle diameter	0.14 mm
Injection duration	3.5 ms

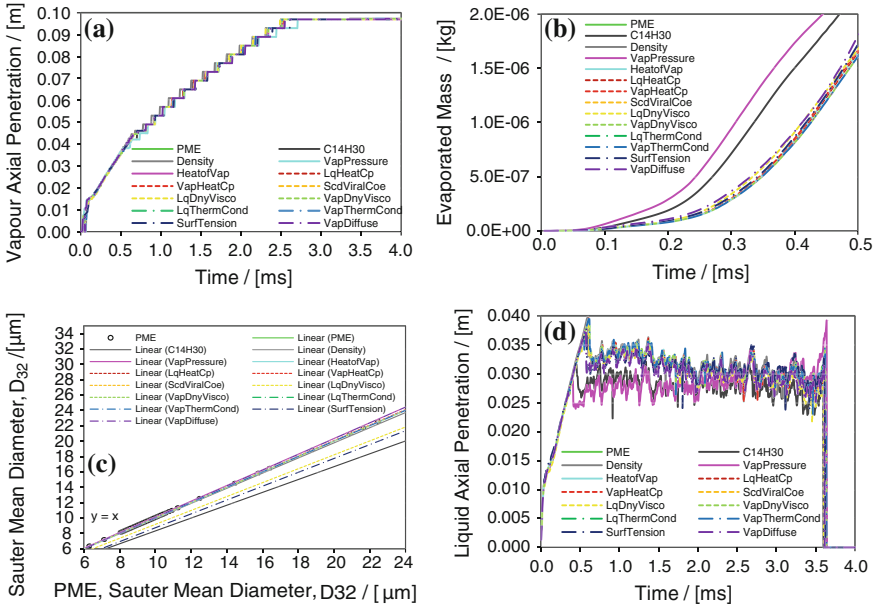


Fig. 3 Constant volume sensitivity analysis of reacting spray jets by examining the effects of individual fuel properties on **a** vapour axial penetration length, **b** evaporated mass, **c** sauter mean diameter, and **d** liquid axial penetration length

Among the identified five significant properties, vapour pressure has the largest impact based on the changes on fuel spray structures as seen in Figs. 3a–d. The reason for this is due to the notable difference in biodiesel properties as illustrated in Fig. 1f, where vapour pressure of PME is lower than fossil diesel. Hence, the vaporisation rate of fuel droplets is higher. In Fig. 3b, vapour pressure has the largest influence to the vaporisation rate amongst other fuel properties. Besides that, the liquid axial penetration for vapour pressure is also one of the lowest, which implies that the vaporisation rate of the fuel droplet is the fastest.

Apart from vapour pressure, liquid surface tension is also observed to have noticeable effects on the spray structure. Larger liquid surface tension value of PME than fossil diesel is found as displayed in Fig. 1b proves that the break-ups and

atomisation rates of fuel droplets into smaller particles are slower. Thus, the liquid axial penetration length of liquid surface tension is comparatively longer than other fuel properties due to larger fuel droplets formed with high momentum to penetrate across the combustion chamber as seen in Fig. 3d. Liquid viscosity, liquid density and vapour diffusivity have marginal effects on the spray structure such as the mass of fuel evaporated and SMD as compared to vapour pressure and liquid surface tension. This is presented in Fig. 3b and c. Based on Fig. 3a–d, liquid heat capacity, liquid thermal conductivity, latent heat of vaporisation, vapour viscosity, vapour thermal conductivity, vapour heat capacity and second virial coefficient are deemed to be less important since only marginal effects are observed.

In short, biodiesel thermo-physical properties are shown to affect the fuel spray development. In particular, liquid density, liquid viscosity, liquid surface tension, vapour pressure and vapour diffusivity are distinguished as determined as the most influential fuel properties based on the observation of fuel spray development and structures. It is imperative to accurately determine all the required fuel properties for different biodiesel fuels for in-cylinder CFD simulation in order to accurately describe the fuel spray characteristics.

5 Conclusion

A set of thermo-physical properties for biodiesel using generic methods is developed here, where the methods employed is suitable for biodiesel produced from various feedstocks. From the sensitivity analysis, liquid density, liquid surface tension, liquid viscosity, vapour pressure and vapour diffusivity exert the most significant influences on biodiesel fuel spray development. Larger fuel droplet and longer fuel spray axial penetration are found as a result of the higher values in liquid density, liquid viscosity and lower vapour pressure for biodiesel. Subsequently, poorer vaporisation rate of the biodiesel fuel spray results, which affect the air-fuel mixture preparation process. The key conclusion drawn from this study is that the thermo-physical properties of biodiesel play an important role in defining the fuel spray development, which subsequently gives rise to its distinct combustion and emission behaviours from fossil diesel combustion. For accurate in-cylinder CFD simulation for biodiesel spray combustion, the thermo-physical properties of biodiesel must be determined appropriately.

References

1. Chakravarthy K, McFarlane J, Daw SC, Ra Y, Reitz RD (2007) Physical properties of soy bio-diesel and implications for use of bio-diesel in diesel engines. SAE paper
2. Ra Y, Reitz RD, McFarlane J, Daw SC (2008) Effects of fuel physical properties on diesel engine combustion using diesel and bio-diesel fuels. SAE paper

3. Yuan W, Hansen AC, Zhang Q (2003) Predicting the physical properties of biodiesel for combustion modelling. *Trans ASAE* 6(46):1487–1493
4. Junfeng Y, Golovitchev VI (2009) Construction of combustion models for rapeseed methyl ester bio-diesel fuel for internal combustion engine applications. *Biotechnology Advances* 27:641–655
5. Reid RC, Prausnitz JM, Sherwood TK (1987) *The properties of gases and liquids*. McGraw Hill, New York
6. Anand K, Sharma RP, Mehta PS (2011) A comprehensive approach for estimating thermo-physical properties of biodiesel fuels. *Appl Therm Eng* 31:235–242
7. Allen CW, Watts KC, Ackman RG (1999) Predicting the surface tension of biodiesel fuels from their fatty acid composition. *J Am Oil Chem Soc* 76(3):317–323
8. Van Bommel MJ, Oonk HAJ, Van Miltenberg JC (2004) Heat capacity measurements of 13 methyl esters of n-carboxylic acids from methyl octanoate to methyl eicosanoate between 5 and 350 K. *J Chem Eng Data* 49:1036–1042
9. Ceriani R, Meirelles AJA (2004) Predicting vapour-liquid equilibria of fatty systems. *Fluid Phase Equilib* 215(2):227–236
10. Chung TH, Lee LL, Startling KE (1984) Applications of kinetic gas theory and multiparameter correlation for prediction of dilute gas viscosity and thermal conductivity. *Ind Eng Chem Fundam* 23:8–13
11. Chung TH, Ajlan M, Lee LL, Startling KE (1988) Generalized multiparameter correlation for nonpolar and polar fluid transport properties. *Ind Eng Chem Res* 27:671–679
12. Poling BE, Prausnitz JM, O'Connell JP (2001) *The properties of gases and liquids*. McGraw Hill, New York
13. Ochoterena R, Larsson M, Andersson S, Denbratt I (2008) Optical studies of spray development and combustion characterization of oxygenated and Fischer-Tropsch fuels. SAE paper
14. Tat ME, Van Gerpen JH (2000) The specific gravity of biodiesel and its blends with diesel fuel. *J Am Oil Chem Soc* 77(2):115–119
15. Tat ME, Van Gerpen JH (1999) The kinematic viscosity of biodiesel and its blends with diesel fuel. *J Am Oil Chem Soc* 76(12):1511–1513

System Design for a Direct-Boost Turbocharged SI Engine Using a Camshaft Driven Valve

Christoph Voser, Christopher Onder and Lino Guzzella

Abstract Downsizing and turbocharging for retaining the maximal power is a common approach to improve the fuel economy of SI internal combustion engines. Due to the additional turbocharger dynamics, small engines suffer from a significant time lag of the torque build-up. The injection of pressurized air into the combustion chamber during the compression phase, also called direct-boost, can recover the driveability. Thus far, expensive and complex fully variable valve-trains have been proposed for the air exchange between the air tank and the combustion chamber. In this paper, a direct-boost system using a camshaft driven valve is designed. An appropriate control strategy is presented. The transient performance of the complete system and the feasibility of the control strategy are demonstrated on a modified 0.75 l turbocharged two-cylinder test bench engine.

Keywords Downsizing · Turbocharging · Turbo lag · Driveability · Direct-boost

1 Introduction

Downsizing and turbocharging for retaining the maximal power is a common approach to improve the fuel economy of SI internal combustion engines [1, 2].

F2012-B01-024

C. Voser · C. Onder (✉) · L. Guzzella
Institute for Dynamic Systems and Control, ETH Zürich, Zurich, Switzerland
e-mail: onder@idsc.mavt.ethz.ch

C. Voser
e-mail: voserc@ethz.ch

L. Guzzella
e-mail: lguzzella@ethz.ch

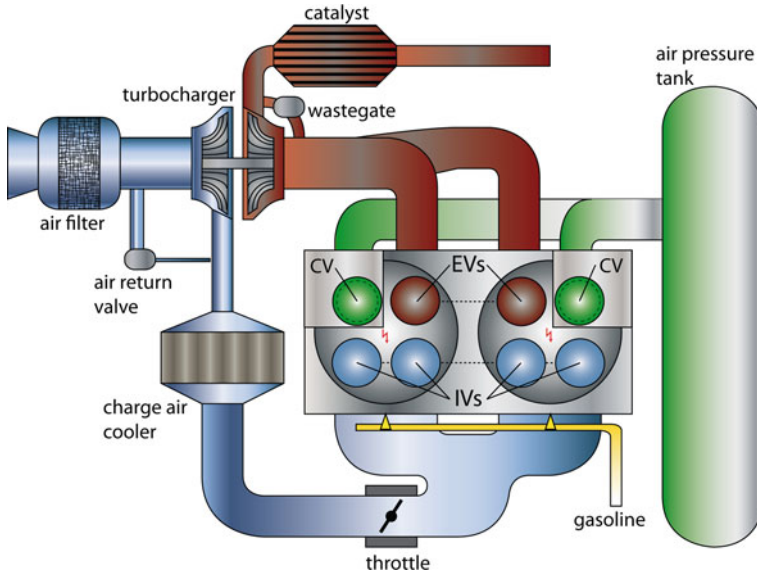


Fig. 1 Schematic of the downsized and turbocharged SI engine with direct-boost. Charge valve (CV), exhaust valve (EV), intake valve (IV)

Due to the additional turbocharger dynamics, small engines suffer from a significant time lag of the torque build-up. The injection of pressurized air into the combustion chamber during the compression phase, also called direct-boost, can recover the driveability. Figure 1 shows the resulting engine structure. Thus far, expensive and complex fully variable valve-trains have been proposed for the air exchange between the air tank and the combustion chamber. Fully variable valves are rather complex devices that demand an additional power supply, e.g., electric, hydraulic and pneumatic.

In this paper, a direct-boost system using a camshaft driven valve with fixed valve timing, called charge valve (CV), is designed. The valve actuation has to be equipped with an on/off capability only. The introduction of a camshaft driven, deactivatable CV makes the system much more cost-effective and thus more attractive for a realization. The loss of variability in the valve-train results in the demand of a sophisticated control strategy to achieve a fast and smooth torque response.

First, a model is presented for the air mass transferred through a camshaft driven CV. This model is then implemented in a mean value model (MVM) of a 0.75 l turbocharged two-cylinder SI engine. Validation measurements of the mean value model are shown. The mean value model is then used to study the performance of the torque build-up for various CV sizes. A procedure for the choice of the valve size and the respective camshaft profile is presented. To achieve a smooth torque response a control strategy is derived. The high dynamic of the ignition variation ideally complements the on/off actuation of the CV. A compromise between air and fuel

Table 1 Data of modified engine

Displacement	0.751
No. of cylinders	2
Rated power	61 kW
Rated torque	131 Nm
Compression ratio	9

demand arises. Since a small air tank has significant advantages concerning packaging and cost, the minimal-air control strategy is analyzed and experimentally verified on the test bench engine.

2 Model

According to [3], the air mass transferred through a camshaft driven CV m_{CV} is calculated as

$$m_{CV} = \mu_{CV}/\omega_e,$$

where ω_e is the engine speed. The variable μ_{CV} is called the CV mass flow. It depends on the tank pressure, the diameter and the lift curve of the CV. The air mass transferred per engine cycle through the camshaft driven CV is inversely proportional to the engine speed. Thus, the effect of the direct-boost is largest at low engine speeds. This ideally compensates the turbo lag, which is most prominent at low engine speeds.

To study the dynamic performance of a turbocharged (TC) SI port-fuel injected engine with direct-boost a standard mean value model is extended with the capability to simulate the injection of air through a camshaft driven CV. The engine used for this analysis is a modified 0.75 l two-cylinder engine where one exhaust valve was replaced by a fully variable camless valve that is actuated by an electro-hydraulic valve-train system (EHVS). Details on the modification are given in [4]. The main parameters of the engine are given in Table 1. A specially designed controller for the EHVS allows the injection of a defined amount of air through the CV. This functionality allows an emulation of the behaviour of a camshaft driven CV in terms of the mass transferred instead of the lift curve.

Figure 2 shows the simulated and measured trajectories of the mean effective pressure with and without boosting at an engine speed of 2000 rpm. The solid lines show the case with direct-boost for a CV mass flow of $\mu_{CV} = 34$ g/s, i.e., $m_{CV} = 0.167$ g at 2000 rpm. At $t = 0$ s, the throttle is fully opened and the direct-boost is activated. It remains active in the time frame shown. The engine torque is measured with a torque flange sensor which is located between the dynamometer and an elastic shaft that is connected to the engine. The measured torque signal is post-processed with a non-causal filter over one engine revolution. The oscillations

Fig. 2 Comparison of measurement and simulation data of the mean effective pressure p_{me} for $\mu_{CV} = 34.9$ g/s and 2000 rpm. *Dashed curves* without boost, *solid curves* with boost

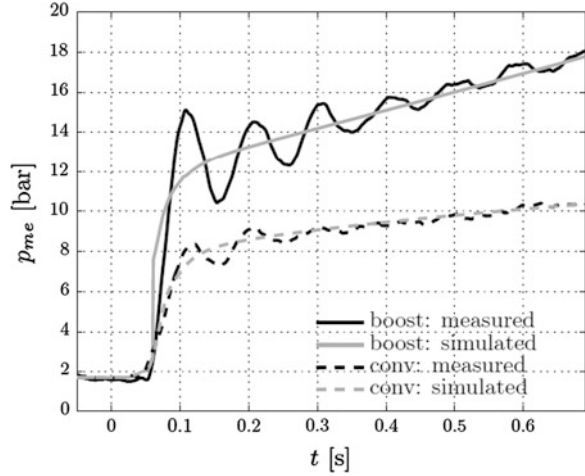
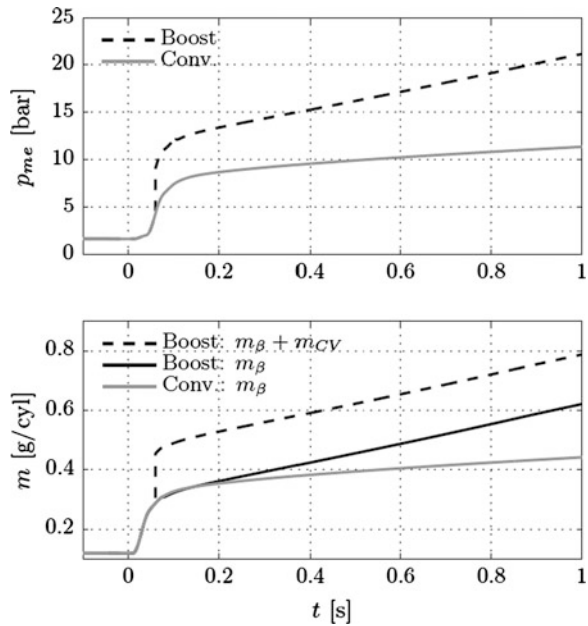


Fig. 3 Simulation-based comparison of the transient response of the conventional and the boosted engine at 2000 rpm



present after the torque step result from the unmodelled elasticity of the shaft. Since the engine is port-fuel injected, the torque does not immediately rise after the tip-in. The delay from injection update to torque center is approximately one engine cycle. The dashed lines show the situation without boosting where the throttle is fully opened at $t = 0$ s.

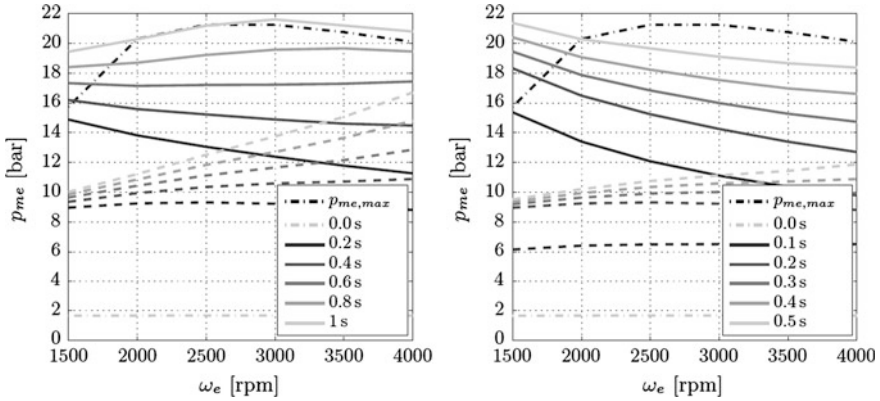


Fig. 4 Build-up of the mean effective pressure at constant engine speeds: The *dashed lines* show the performance of the TC SI engine without boost. The *solid lines* depict the performance with boost. The *gray dash-dot line* indicates the engine torque before the throttle step and the direct-boost activation. *Left* $\mu_{CV} = 34.9$ g/s. *Right* $\mu_{CV} = 55$ g/s (Note the differing legend)

The good agreement between the simulation and the measurement confirm that the MVM approximates the dynamic behaviour sufficiently well. It is therefore suited for the subsequent performance analysis.

3 System Performance

In the model validation shown in Fig. 2 it was already noticeable that the direct-boost substantially accelerates the torque build-up. The fastest torque build-up is achieved if the throttle is fully opened and the direct-boost is activated. In this way, the maximal amounts of air and consequently fuel enter the cylinder. The injection of compressed air affects the transient response in two ways: In addition to an instantaneously higher torque due to the higher in-cylinder air mass, the exhaust enthalpy flow is substantially increased, which leads to a much faster TC acceleration. In Fig. 3 the transient performance of the conventional and the direct-boosted engine are shown. The upper plot shows the mean effective pressure while the lower plot shows the various air mass per cylinder. As a result of the faster TC acceleration, the intake air mass per cylinder m_β increases considerably faster with direct-boosting. On top of that air from the tank is injected which leads to the high torque.

Figure 4 shows the torque build-up at constant engine speed for two different CV sizes, i.e., values of μ_{CV} . Prior to the activation of the boost mode and before the opening of the throttle is initiated, the engine is operated at a mean effective pressure p_{me} of 1.7 bar. The solid lines show the torque development with direct-boost. The dashed lines show the performance without direct-boost.

The left plot in Fig. 4 shows the engine performance resulting from a CV design with $\mu_{CV} = 34.9$ g/s. The maximum stationary torque $p_{me, max}$ is reached

within one second for every engine speed. At low engine speeds the turbo lag is eliminated completely as a result of the inverse proportionality of the CV air mass to the engine speed. The right plot shows the performance for $\mu_{CV} = 55$ g/s (note the differing legend). As a result of the higher value of μ_{CV} , the torque rise with direct-boost is faster, of course, due to the increased CV air mass. In this case the maximum stationary torque for every engine speed is reached within approximately 0.6 s or less.

The performance without the direct-boost activation is significantly slower. Especially at low engine speeds, the turbo lag is well noticeable. Figure 4 clearly shows that the direct-boost substantially improves the response behaviour at low engine speeds. For high engine speeds the responsiveness can be improved also, but to a smaller extent.

3.1 CV Sizing: Determination of the CV Mass Flow

An appropriate value for the CV mass flow μ_{CV} can be derived by formulating a performance criterion that has to be reached, e.g., torque step from 1.7 to 20 bar p_{me} in 0.5 s at 2000 rpm. This performance would require a CV mass flow of $\mu_{CV} = 55$ g/s (see Fig. 4, right).

3.2 CV Design

According to [1], the CV mass flow μ_{CV} is a function of the tank pressure, the CV diameter and its valve lift curve. The relevant design variables are the CV opening (CVO), the CV closing (CVC), the CV acceleration, the CV diameter and the minimal tank pressure.

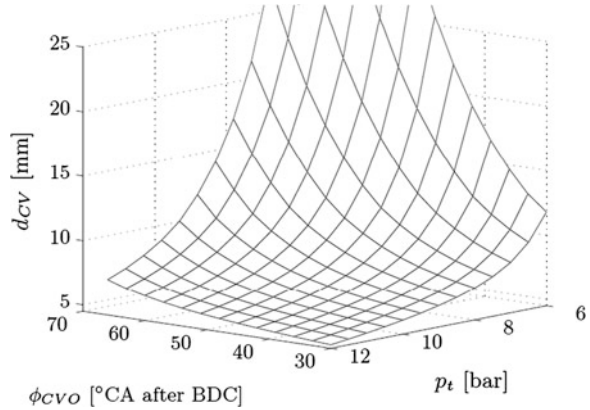
$$\mu_{CV} = f(\phi_{CVO}, \phi_{CVC}, a_{CV}, d_{CV}, p_t)$$

The derivation of the CV design variables is underdetermined since there is one equation for five variables. Additional constraints reduce the feasible design space. In the following the most important constraints are discussed.

3.2.1 Spatial Constraint

Adding a CV to the cylinder head might reduce the area available for intake valves (IVs) and exhaust valves (EVs). If the fitting of the CV requires the downsizing of the IVs and/or the EVs, the volumetric efficiency of the conventional combustion mode might be deteriorated, possibly reducing the peak power capability. However, depending on the cylinder head design the downsizing might not be necessary, resulting in an unaltered volumetric efficiency.

Fig. 5 CV diameter as a function of the tank pressure p_t and the CV opening angle ϕ_{CVO} : $\mu_{CV} = 34.9$ g/s



3.2.2 Valve Timing Constraint

The earliest opening of the CV is possible around IV closing (IVC). An overlap of several degrees is acceptable, but blowing charge out through the IVs has to be avoided because pressurized air would be wasted. Hence, shifting IVC in favour of the CV opening has an impact on the gas exchange performance in the conventional combustion mode.

3.2.3 Safety Constraint

Any flow of air/fuel mixture from the cylinder to the tank has to be avoided. Hence, throughout the opening period of the CV, the cylinder pressure has to be smaller than or equal to the tank pressure. A minimal value for the tank pressure can be found which should never be underrun in order to guarantee a safe operation in the entire operating range.

3.2.4 Results

All variable configurations shown in Fig. 5 correspond to the same $\mu_{CV} = 34.9$ g/s. It can be concluded that

- a higher tank pressure allows a smaller CV diameter, and
- an earlier CV opening also allows a smaller CV diameter.

Recall that the CV mass can only take on the values zero and m_{CV} due to the on/off capability. Hence, the activation or deactivation of the direct-boost always leads to a step in the cylinder air mass. In the following section a control strategy is presented which results in a smooth torque response.

4 Control Strategy

According to [5], when tipping in, the driver expects a good driveability and comfort. For the discussion of these requirements Fig. 6 is used. Good driveability is characterized by as much torque as possible as fast as possible. Hence, the torque request has to be met in minimal time t_{step} . This goal is achieved if the direct-boost u_{CV} is activated and the throttle u_{th} is fully opened, i.e., the exhaust enthalpy and consequently the TC acceleration are maximized. In addition to a fast torque build-up, the driver wants a smooth and predictable torque development when tipping in, i.e., the torque trajectory has to remain constant once the desired torque is reached. Consequently, the direct-boost cannot be switched off immediately after the desired torque is reached at t_{step} because it would lead to a drop of the air mass in the cylinder m_a to the value of the intake air mass m_β , which is below the desired value $m_{a,des}$. Thus, the torque would drop, too. Consequently, the direct-boost has to remain active which results in excessive charge in the cylinder, i.e., $m_a > m_{a,des}$. To keep the torque at the desired level, the spark timing has to be retarded. The deactivation of the direct-boost occurs when the intake air mass is equal to the desired air mass, i.e., at $t_{b, off}$.

As a result of the spark retardation the efficiency of the engine e_{ign} is reduced and more fuel is used. Alternatively, the throttle could be closed to reduce the amount of excess charge and thus improving the efficiency. However, the exhaust enthalpy and the TC acceleration are decreased which leads to a longer duration with air injection and thus to a higher air consumption. Figure 7 shows the resulting trade-off between the consumption of compressed air Δm_a and extra fuel Δm_f for a load step from 1.7 bar to 16.7 bar p_{me} at 2000 rpm. The trade-off has thoroughly been analyzed in [6].

The minimal amount of air is used if the throttle remains fully open until the intake air mass reaches the desired value. However, the excessive charge and hence the extra fuel mass are maximal. This strategy is called minimal-air control strategy. Its resulting air and extra fuel consumptions are indicated by the dot most to the right in Fig. 7. The minimal-fuel control strategy, indicated by the dot most to the left, requires 65 % less extra fuel than the minimal-air control strategy. However, the amount of air required is 60 % higher. Thus, for the same number of boosts without refilling, the tank volume has to be 60 % larger. Accordingly, the requirements for the packaging are substantially relaxed if the minimal-air control strategy is applied. For a vehicle that consumes 4 l of gasoline on 100 km on the MVEG-95 drive cycle, the fuel consumption increases by 0.4 % if there are 18 turbo lag compensations (i.e., after every gear shift-up and in every acceleration phase) and if the minimal-air control strategy is used (77 mg fuel per boost). A more fuel efficient control strategy lowers the fuel consumption increase on the MVEG-95 drive cycle to 0.15 %. These calculations show that the fuel consumption increase due to the direct-boost is very small. These analyses lead to the conclusion that the substantially relaxed space requirements of the minimal-air control strategy clearly exceed the marginal fuel consumption increase associated with it.

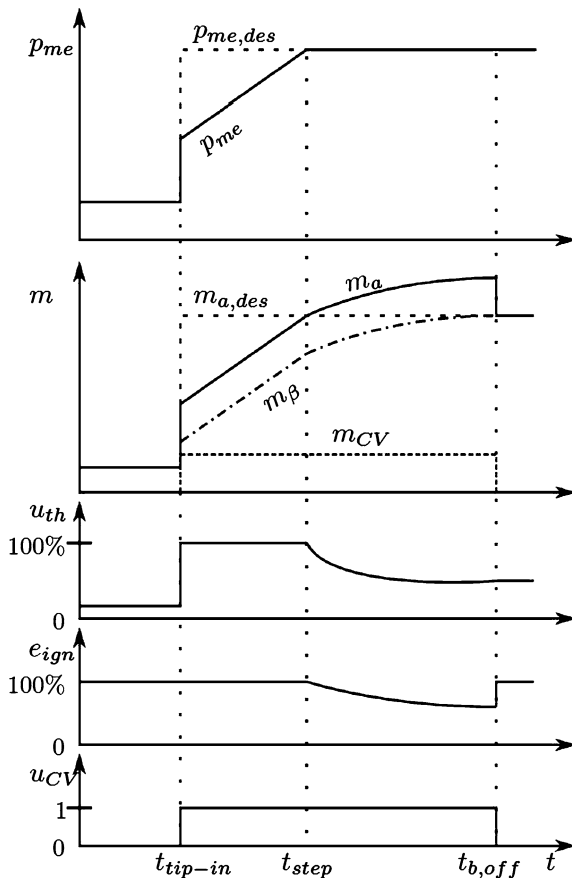


Fig. 6 Schematic representation of the torque control inputs during a transient with turbo lag compensation

Figure 8 shows the air and extra fuel consumption data for steps from 1.7 bar p_{me} to various loads and at various engine speeds with the minimal-air control strategy. The air consumption, which is depicted in the left plot, decreases with increasing engine speed because the boost time is shorter as a result of the higher exhaust enthalpy. To reach a higher torque more air is used because of the longer boost time. The plot on the right shows the amount of extra fuel for various torque steps and engine speeds. At constant engine speed, the amounts of extra fuel are very similar for all torque steps considered. For increasing engine speeds the amount of extra fuel decreases, which is due to the smaller CV air mass per cycle and the faster TC acceleration, which in turn is due to the increased exhaust enthalpy flow.

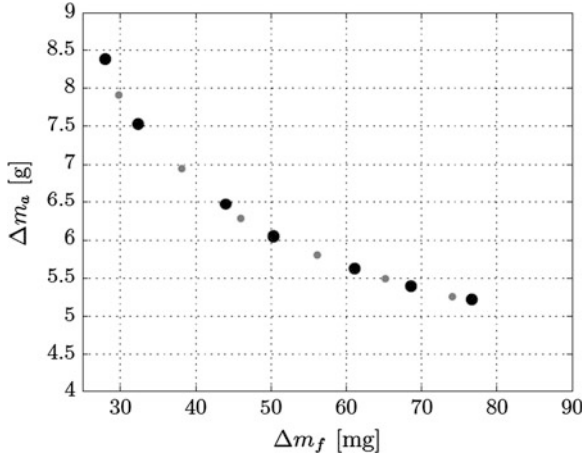


Fig. 7 Trade-off between the consumption of extra fuel Δm_f and compressed air Δm_a for a load step from 1.7 bar to 16.7 bar p_{me} at 2000 rpm with $\mu_{CV} = 34.9$ g/s

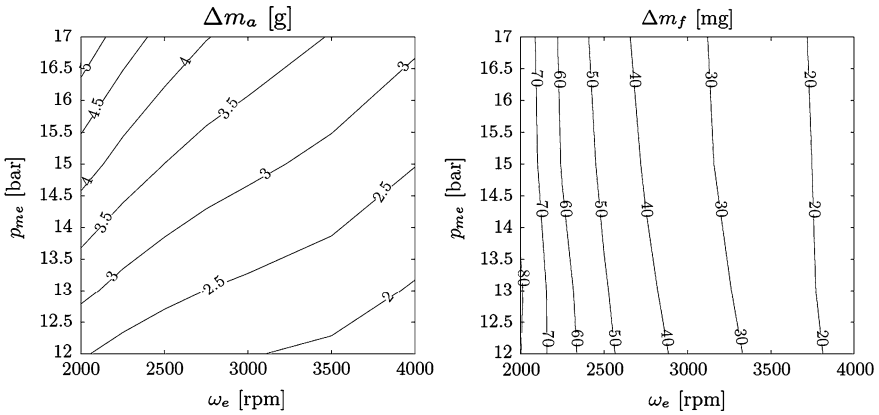


Fig. 8 Simulated values for Δm_a and Δm_f for various loads and engine speeds with the minimal-air control strategy

5 Experiments

In this section, the feasibility of the minimal-air control strategy is verified in experiments for a CV mass flow of $\mu_{CV} = 34.9$ g/s. Figure 9 shows two measured turbo lag compensations. The mean effective pressure p_{me} and the intake air mass m_β trajectories are compared with the corresponding simulation results.

The left plots in Fig. 9 show the measurement results of a turbo lag compensation at 2000 rpm. The mean effective pressure of 16.7 bar is reached within approximately 0.57 s. This value matches the result shown in Fig. 4. The

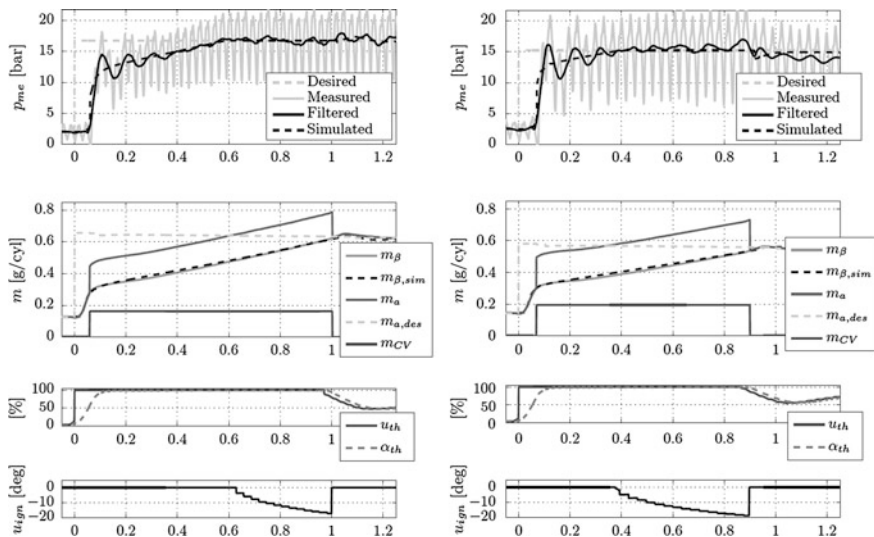


Fig. 9 Measured turbo lag compensations. *Left* at 2000 rpm from 1.7 bar to 16.7 bar p_{me} . *Right* at 1700 rpm from 1.7 bar to 15.2 bar p_{me}

Table 2 Number of boosted combustion cycles and the amount of compressed air used in simulation (Sim) and in experiments (Meas)

Data set (rpm)	No. of boosts		Δm_a		
	Sim	Meas	Sim (g)	Meas (g)	Error (%)
2,000	32.0	31	5.22	5.05	-3.2
1,700	23.9	23	4.64	4.46	-3.9

measured and the simulated trajectories of the mean effective pressure match well, and so do the trajectories of the simulated and the estimated intake air masses m_β and $m_{\beta,sim}$. The third subplot shows the demanded and the actual throttle positions u_{th} and α_{th} , which are fully open during the turbo lag compensation. In the third subplot the ignition retardation u_{ign} is depicted. At $t = 0.57$ s, the air mass in the cylinder m_a is larger than the desired value $m_{a,des}$. Consequently the spark timing is retarded. Table 2 lists the number of boosted combustion cycles, the measured air consumption and the simulated air consumption. Due to the reciprocating behaviour of an engine, the number of boosted combustion cycles and the air mass used Δm_a can only take on discrete values. In each boosted combustion cycle, 0.167 g of air is injected. This value corresponds to the discretization of Δm_a . The error resulting from one additional boosted combustion for this experiment is 3.3 %. Accordingly, the deviation between simulation and experiment given in Table 2 is in the order of one boosted combustion cycle. In the MVM simulation the reciprocating nature is neglected and, hence, the value of Δm_a and the number of boosted combustion cycles are continuous.

The right plots in Fig. 9 shows the measurement results of a turbo lag compensation at 1700 rpm. In this case the desired mean effective pressure of 15.2 bar can be reached within approximately 0.4 s as a result of the higher CV air mass. Due to the smaller engine speed the enthalpy flow is smaller and the duration with retarded spark timing is relatively long. Note that once the boost mode is deactivated, the desired torque cannot be held since it is larger than the maximal steady-state torque. Hence, the engine was overboosted. As above, the deviation between simulation and experiment in the total CV air mass is in the order of one boosted combustion cycle.

6 Conclusion

Direct-boost with a deactivatable camshaft driven CV is a cost-effective way to improve the driveability of strongly downsized and turbocharged SI engines. The effect of the direct-boost is largest at low engine speeds. Thus, it ideally complements the use of a conventional turbocharger who predominately restricts the driveability at low engine speeds.

A simple but effective control strategy for the throttle, the ignition and the boost activation has been proposed which leads to a fast and smooth torque response. The control strategy has been analyzed in simulation and verified with experiments on an engine test bench.

Direct-boost with a camshaft driven CV is a promising technology for the future in automobile markets which are cost sensitive and/or demand an excellent driveability.

References

1. Guzzella L, Wenger U, Martin R (2000) IC-engine downsizing and pressure-wave supercharging for fuel economy, SAE paper 2000-01-1019
2. Berns S, Hammer J, Benninger K, Klenk M, Frei R (2010) Reduction of CO₂-emissions while maintaining good driveability: suggestions for overall powertrain optimization, 31st international Vienna motor symposium
3. Voser C, Dönitz C, Ochsner G, Onder C, Guzzella L (2012) In-cylinder boosting of turbocharged spark-ignited engines. Part 1: model-based design of the charge valve, IMechE part D: J Automobile Eng
4. Dönitz C, Vasile I, Onder C, Guzzella L (2009) Realizing a concept for high efficiency and excellent driveability: the downsized and supercharged hybrid pneumatic engine, SAE paper 2009-01-1326
5. Frei S (2004) Performance and driveability optimization of turbocharged engine systems. PhD thesis no. 15510, ETH Zurich
6. Voser C, Ott T, Dönitz C, Onder C, Guzzella L (2012) In-cylinder boosting of turbocharged spark-ignited engines. Part 2: control and experimental verification, IMechE part D: J Automobile Eng

Exploring the Potential of Dual Fuel Diesel-CNG Combustion for Passenger Car Engine

David Serrano and Lecointe Bertrand

Abstract The concept of dual fuel Diesel-CNG is well known in heavy duty applications as the high octane number of methane allows converting easily existing CI engines without varying compression ratio, thus reducing adaptation costs. However, with this approach, Diesel fuel substitution ratio is quite limited and the benefits on CO₂ savings and on thermal efficiency are not exploited. The objective of this paper is to highlight experimentally the potential of a different approach for dual fuel Diesel/CNG combustion applied to smaller passenger car engines. The objective of this concept is to maximize CO₂ savings compared to traditional Diesel fuel operation by using the optimal amount of Diesel fuel and optimizing engine efficiency. The study was based on experiments carried out on a CI single cylinder engine modified for allowing dual fuel operation with methane port fuel injection. A first part of the study investigates the behaviour of dual fuel combustion process at different equivalence ratios. Then a second part described how the combustion mode needed to be adapted to the engine load: for example, lean dual fuel with EGR mode and stoichiometric dual fuel mode were addressed depending on the engine operating point. Special attention was given at the results at stoichiometric full load. Indeed, in these conditions, the dual fuel combustion is optimal compared to conventional Diesel operation: less noise, no smoke, faster end of combustion. This study demonstrated that optimizing an engine for dual fuel Diesel-CNG combustion is a challenging task. The control of Diesel fuel autoignition delay is crucial to enhance thermal engine efficiency at low load. THC emissions need to be drastically reduced to comply with stringent emissions

F2012-B01-025

D. Serrano (✉) · L. Bertrand
Rond-point de l'échangeur de Solaize, IFP Energies nouvelles, BP3 69360 Solaize, France
e-mail: david.serrano@ifpen.fr
www.ifpenergiesnouvelles.fr

standards. Further studies need to be carried out to analyze in more details the combustion process in dual fuel mode.

Keywords Dual fuel • CNG • Stoichiometry • Full load • Passenger car

Glossary

ATDC/BTDC	After/Before Top Dead Center
ABDC/BBDC	After Bottom Dead Center
CA	Crank Angle Degree
CI	Compression Ignited
cISFC	corrected Indicated Specific Fuel Consumption
CNG	Compressed Natural Gas
CoV	Coefficient of Variation
DOC	Diesel Oxidation Catalyst
EGR	Exhaust Gas Recirculation
EVO/EVC	Exhaust Valve Opening/Exhaust Valve Closing
ISCO/ISHC/ISNO _x	Indicated Specific Carbon Oxide/HydroCarbons/Nitrous Oxides
HRR	Heat Release Rate
IVO/IVC	Intake Valve Opening/Intake Valve Closing
LHV	Lower Heating Value
LNT	Lean NO _x Trap
MFB	Mass Fuel Burnt
MFB50	Crank Angle Degree for 50 % Mass Fuel Burnt
MFBAI	Crank Angle Degree for Diesel AutoIgnition (0 % Mass Fuel Burnt)
PM	Particulate Matter
SCR	Selective Catalyst Reduction
SOI	Start Of Injection
SI	Spark Ignited
WHTC	World Harmonized Transient Cycle

1 Introduction and Objectives

The dual fuel concept studied in this paper consists in injecting Diesel fuel and CNG (Compressed Natural Gas) during the same engine cycle in a CI (Compression Ignited) engine. Both methane and Diesel fuel can be injected directly [1] but in our case, gas is port injected. The homogeneous carburetted mixture of air and CNG (and sometimes with EGR too) is compressed but does not autoignite because of its high autoignition temperature. The combustion is then initiated by the direct

introduction of a Diesel fuel pilot quantity which autoignites during the end of the compression stroke. The dual fuel combustion process can be divided in four distinct steps: (1) the Diesel pilot ignition delay, (2) its combustion (which can be composed by premixed and diffusion phases), (3) the CNG combustion within and around the Diesel fuel spray and finally, (4) the “multiple” flame propagations through the carburetted mixture [2]. Dual fuel combustion is possible because flammability limits are different between the two fuels and it exploits the advantages of each one. On one hand, CNG has high hydrogen over carbon ratio, thus allowing theoretically a reduction of CO₂ emissions by nearly 25 % compared to pure Diesel fuel operation. This decrease can be more significant if methane comes from a renewable source referred as biomethane [3]. Moreover, its high knocking resistance makes it compatible with CI engines that have high compression ratios (more than 14:1). On the other hand, the main advantage of Diesel fuel is the high quantity of energy released during its combustion. As a matter of fact, the spark in SI (Spark Ignited) engines delivers about 50 mJ in a very small volume whereas the combustion of 1 mg/stroke Diesel fuel pilot injection releases 10,000 times more energy distributed in a larger volume inside the combustion chamber.

However, dual fuel combustion raises major issues that need to be addressed depending on the engine load. At high loads, performances can be reduced by the occurrence of preignition and knock [4], that’s why compression ratios can be reduced by comparison to the Diesel baseline engine. At low loads, high emissions of unburned methane are emitted because of two well-known effects. First, Diesel engines have large crevices especially the high height of top ring-land crown. Then, flame extinctions or even misfires can occur if the CNG/air premixture is excessively lean. To prevent the emissions of these unburned species, the leaner fuel/air equivalence ratio limit must be determined for dual fuel combustion in order to ensure effective flame propagation in the methane/air (even EGR) premixture.

Dual fuel combustion is well known in heavy duty CI engine applications and has been an interesting subject of research since the 1980s [5–8]. The main approach consists in reducing costs by substituting an expensive fuel (Diesel fuel) by a cheaper one (CNG). Nevertheless, with this technique, the Diesel fuel substitution ratio remains quite limited: about 30–70 % [8]. The objective of this paper is to explore and develop a different approach for dual fuel engines. It consists in achieving maximum CO₂ savings compared to traditional Diesel fuel operation. In our case, the pilot injection size is reduced to the minimum, engine efficiency is enhanced and Diesel fuel is only used as a chemical high energy ignition device. The purpose is then to define the optimal combustion mode in dual fuel operation by maximizing the engine efficiency, reducing the needs for exhaust aftertreatment (deNO_x and DPF) and keeping the level of performances identical to Diesel fuel operation. Moreover, this paper focuses on passenger car engines for which little information exists in the literature for dual fuel combustion. First, investigations were carried out by exploring the effect of methane ratio on the combustion for two different Diesel fuel pilot quantities. Then, different combustion modes were tested to obtain the highest efficiency combined with lower emissions.

Table 1 Engine specifications

Engine type/baseline	Single-cylinder/PSA DW10
Bore × stroke	85 × 88 mm
Displacement	499 cm ³
Compression ratio	17:1
Connecting rod length	145
Number of valves	4
IVO/IVC	−33°ATDC/3°ABDC
EVO/EVC	−23°ABDC/17°ATDC
Diesel injection system	Bosch common rail
Diesel injection pressure	400 bar
Diesel injector	Piezoelectric bosch CRI 3.1240 cc/158° nozzle/7 holes
Gas injection	Landi renzo port fuel injection
Gas injection pressure	2 bar relative

2 Experimental Setup

2.1 Engine Technical Configuration

The tests have been carried out on a single cylinder engine with a 499 cm³ displacement previously designed for Diesel fuel operation (Table 1). Only few minor changes were made to the baseline engine in order to allow dual fuel operation. The piston was modified by changing its compression ratio and design. In fact, three different pistons were tested with different bowls at 17:1 compression ratio. The design of these pistons was done to assure compatibility with the Diesel fuel injector selected for this study: specifically for jet angle and number of holes. The cylinder head with swirl motion was not modified. Besides, port-injection of gas was implemented on the engine. One low pressure gas injector integrated in a Landi Renzo feed ramp was installed and the gas was injected just before the intake manifold. The gas fuel was pure methane and the liquid fuel was standard EN590 European Diesel fuel. The effect of intake air temperature on combustion was cancelled as temperature was regulated to 50 °C by an air heater for all the tests. A controlled exhaust throttle simulated the backpressure of the multicylinder exhaust line.

The test supervisor and control algorithms needed for the control of both Diesel fuel and gas injection systems ran on Morphee 2, whereas the high frequency acquisition system ran on Osiris. Both software were developed by D2T, an IFP Energies nouvelles subsidiary. This system allowed highly flexible engine control, specifically with dual fuel injection parameters.

2.2 Measurements

Cylinder pressure was monitored by a flush mounted Kistler 6043A60 pressure transducer. The pressure signal was acquired every 0,1 °CA and the acquisition process covered 250 complete engine cycles. The average value of these cycles

was used as pressure data for the calculation of the combustion parameters. The engine was also equipped with an AVL Noisemeter that derived combustion noise from cylinder pressure signal. Real time levels of engine-out exhaust gases (HC, CH₄, CO, CO₂, O₂ and NO_x) were recorded by a Horiba MEXA-7100DEGR analyzer. Fume Smoke Number (FSN) was measured in the exhaust line using an AVL415S Smokemeter. Concerning the fuel metering, gas consumption was measured by a MicroMotion CMF010 Coriolis type mass flow meter. The Diesel fuel consumption could be obtained through direct weighing using AVL733S Balance Unit. However as micro quantities of Diesel fuel were used in dual fuel operation for pilot injections, the weighing was not precise. Thus, Diesel fuel mass flow rate was computed based on mass air flow rate, gas consumption and equivalence ratio measures. Mass air flow was regulated and measured thanks to a set of sonic nozzles. Equivalence ratio was measured with an UEGO NGK lambda sensor. The notion of equivalence ratio is quite complex for dual fuel combustion as it takes into account the ratio of these two fuels with different thermodynamic properties. Whatever the fuel mode was (single or dual fuel), the ISFC (Indicated Specific Fuel Consumption) was corrected in order to be able to compare the different specific fuel consumptions independently of the fuel's LHV (Lower Heating Value). Therefore, the ISFC was corrected at the Diesel fuel LHV and it was referred to as cISFC.

3 Results and Discussion

3.1 First Experimental Approach: Influence of Methane Ratio and Diesel Fuel Pilot Quantity

As dual combustion process is quite complex, it was relevant to begin with simple tests for basic understanding on the influence of methane ratio and Diesel fuel pilot quantity. These tests consisted in setting the quantity, the injection pressure and timing of a Diesel fuel pilot injection and progressively port injecting methane. This methodology allowed to sweep a large range of equivalence ratios (from the minimum until reaching stoichiometry). Engine speed was regulated at 2,000 rpm but engine load varied from around 2 to 10 bar IMEP as methane was progressively injected. The engine configuration was 17:1 compression ratio. The intake pressure was set to atmospheric pressure and no EGR was used. The injection timing was set to 20 °CA BTDC and the injection pressure to 400 bar. This methodology was used for two different pilot fuel quantity:

- 6 mg/stroke corresponding to 0.16 equivalence ratio ($1/\lambda$).
- 9 mg/stroke corresponding to 0.25 equivalence ratio ($1/\lambda$).

Figure 1 presents methane oxidation rate and unburned HC emissions versus the equivalence ratio. In order to improve the analysis of the dual fuel combustion

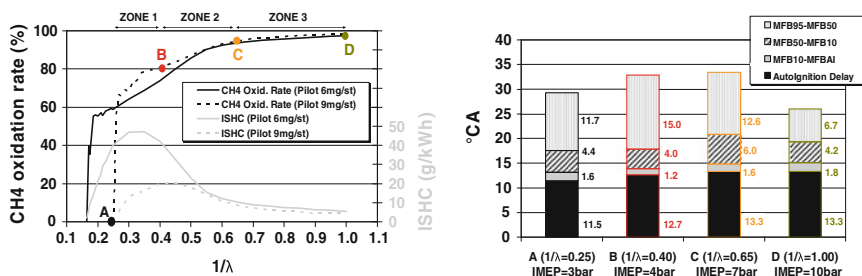


Fig. 1 CH₄ oxidation rate, ISHC emissions and combustion durations for two different Diesel fuel pilot sizes

process, the 9 mg/st pilot injection case (black dotted curve) was described taking out four specific points (referred as A, B, C and D) for which the MFB (Mass Fuel Burnt), the HRR (Heat Release Rate) and the combustion durations are shown in Figs. 1 and 2. The methane oxidation rate curve depicts that dual fuel combustion behaviour can be divided in three distinct zones.

The zone 1 is located between point A (pure Diesel fuel case) to point B (dual fuel case) on Fig. 1. Dual fuel combustion is fully controlled by the Diesel fuel pilot injection. Indeed, the Diesel fuel spray created high micro-scaled turbulence during its premixed combustion that had to be added to swirl macro-scaled motion. Thus, the methane/air premixture was entrained into this spray and methane was then oxidized. There was no flame propagation into methane/air premixture as equivalence ratio seemed to be too low even at local scale. This trend can be observed in Figs. 1 and 2 for point B that shows high duration of the combustion end phase (defined as MFB95-MFB50) and high unburned HC emissions. The ratio of methane oxidized by Diesel fuel spray increased with equivalence ratio from 60 to 80 % as more and more energy was released by Diesel fuel and methane entrained combustion. Thus, more turbulence was created and more methane could be entrained into the Diesel fuel spray. No smoke was measured whatever the equivalence ratio.

The zone 2 is located between point B to point C (Fig. 1). Dual fuel combustion was then in a transient stage. The process of the zone 1 still took place but flame propagation could barely occur in the methane/air mixture. Indeed, at point C, the last combustion phase (MFB95-MFB50) and HC emissions started to decrease. Around 90 % of the methane was burnt at point C through the combined effects of Diesel fuel spray entrainment and methane flame propagation. However, the equivalence ratio was rather low 0,65 which is close to the lean flammability limit for properly propagating a flame in a methane/air mixture. Finally, the equivalence ratio should be considered locally to understand this trend. In fact, gradients of equivalence ratios exist within the combustion chamber and particularly at the vicinity of the spray plumes.

The last zone is located between point C to point D (Fig. 1). In this zone 3, flame propagation was possible and efficient and dual fuel combustion was then controlled by both Diesel fuel pilot injection and flame propagation into methane/

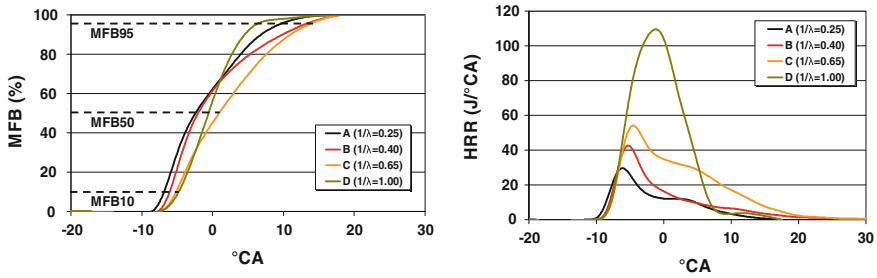


Fig. 2 MFB and HRR for 4 different equivalence ratios with 9 mg/st diesel fuel pilot

air premixture. Methane oxidation rate reached a maximum of 95 %. This maximum had to be related to the ratio of methane trapped in the combustion chamber's crevices. In fact, the volume of the different crevices represents around 4 % of the entire combustion chamber's volume. Furthermore, methane is assumed to be homogeneously distributed as it was port injected just before the intake manifold.

A focus has to be made on point D corresponding to the stoichiometry case. In these conditions, the flame propagation phase was fully efficient. Besides, the HRR evolution was significantly modified (Fig. 2). The first peak corresponding to Diesel fuel premixed combustion disappeared and only one high peak appeared on HRR curve revealing that flame propagation started just after ignition of the pilot fuel sprays. The MFB95-MFB50 duration was shorter compared to pure Diesel fuel case (point A on Fig. 1). This observation is also true for the entire combustion duration. Thus, the methane flame propagation remained faster when Diesel fuel combustion by diffusion significantly slowed down. This means that cycle efficiency for dual fuel at stoichiometry should be higher compared to pure Diesel fuel. This item will be verified in the next section. Nevertheless, CO and NO_x emissions were relatively high for stoichiometry meaning that Diesel fuel pilot size should have been optimized.

Diesel autoignition delay was slightly increased with methane ratio as depicted in Fig. 1. This trend has already been observed in the literature [9] and can be explained by the increase of both physical and chemical Diesel autoignition delay. Indeed, the diffusion of Diesel spray decelerated in a methane/air mixture and its penetration could be limited inducing an increase of physical delay. Besides, Diesel fuel pre-oxidation reactions also slowed down in presence of methane creating an increase of chemical delay [2]. The impact is visible on the MFB and the HRR evolution on Fig. 2.

The increase of pilot fuel size allowed higher methane oxidation rate in the zone 1 corresponding to methane oxidation entrained by Diesel fuel spray. Indeed, in this stage, dual fuel combustion was controlled mainly by the characteristics of Diesel fuel spray. In zones 2 and 3, methane oxidation rate was then rather the same meaning that pilot fuel injection did not affect the combustion's end represented by almost the flame propagation in methane/air mixture. Diesel fuel was then only a chemical initiator of the dual fuel combustion.

The increase of methane ratio led to an increase of engine load from 3 bar - IMEP for point A to 10 bar IMEP for point D at stoichiometry and atmospheric pressure in the intake manifold. This trend gives some clues to determine the optimal combustion modes depending on the engine load and next section is dedicated to address this item.

3.2 Second Experimental Approach: Identification of Optimal Combustion Modes

3.2.1 Methodology of Engine Load Sweep

The identification of the different combustion modes was studied by optimizing 6 steady-state points at 2,000 rpm engine speed: 4, 6, 8, 10, 22 and 26 bar IMEP. The engine configuration was 17:1 compression ratio and Diesel fuel injection pressure was set to 400 bar. No major effect on consumption or emissions were observed for higher Diesel fuel injection pressures. A low Diesel fuel injection pressure seemed to be sufficient as the injection quantities were rather small and increasing injection pressure may have caused pilot fuel vapour overmixing with methane/air premixture. The Diesel fuel mass ratio was determined in order to keep CoV (IMEP) under a 4 % level (the CoV (IMEP) represents a relative cycle-to-cycle variation of mean IMEP). For these tests, the main constraint was to stay at equal intake pressure for a same engine load. The methodology consisted, for each engine load studied, in sweeping simultaneously equivalence ratio and EGR rate at equal intake pressure compared to Diesel baseline engine. For instance, the increase of equivalence ratio at equal intake pressure was obtained by:

- air mass flow reduction that implied EGR rate increase,
- and EGR rate adaptation by closing exhaust throttle.

The result is shown on Fig. 3 with the EGR rate vs. equivalence ratio evolution. Since dual fuel combustion with methane did not produce smoke for each engine load, optimum equivalence ratio was selected by optimizing two trade-offs: IS-NO_x/cISFC and ISNO_x/ISHC as presented in Fig. 4. The implicit objective was to keep NO_x levels as low as possible and compatible with aftertreatment systems (LNT, SCR or 3-way catalyst depending on combustion mode). As a remark, for each equivalence ratio/EGR rate, optimal combustion phasing was determined by selecting the Diesel fuel pilot SOI for minimum cISFC. The whole process of optimal combustion phasing selection is not detailed on this paper but an example is given on the dual fuel lean burn mode section. Finally, for each engine load, the optimum settings appear as a bold point on the curves of Figs. 3, 4, 5, and 6.

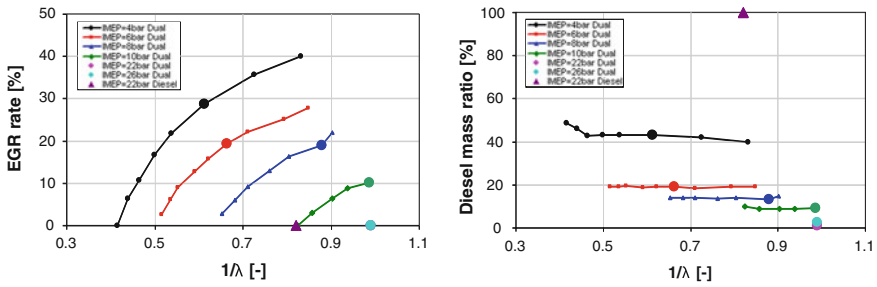


Fig. 3 EGR rate and diesel fuel mass ratio versus $1/\lambda$ for different engine loads at 2,000 rpm

3.2.2 Low to Medium Loads: Dual Fuel Lean Burn Mode

The results on Figs. 3, 4, 5, and 6 show that combustion mode depends on engine load. For low loads (4–8 bar IMEP), optimal mode was lean burn combustion with EGR. On Fig. 3, when IMEP increases, Diesel fuel mass ratio is drastically reduced: from 45 % at 4 bar IMEP to 15 % at 8 bar IMEP. Moreover, when IMEP increased, optimal equivalence ratio rose up (from 0,6 at 4 bar IMEP to 0,85 at 8 bar IMEP) and EGR rate decreased. NOx emissions were kept at levels around 2–3 g/kWh (Figs. 4, 5) compatible with traditional deNOx aftertreatment systems (LNT or SCR). However, the HC emissions reached high levels incompatible with DOC. HC emissions were composed by around 85–90 % of methane which is the more stable hydrocarbon, thus difficult to oxidize.

For each engine load in dual fuel lean burn mode, the lean limit was reached when mixture was too diluted by air to provide a stable Diesel fuel pilot autoignition. Moreover, if equivalence ratio was lower than flammability limits of methane (equivalence ratio around 0,6), flame could not properly propagate. Consequently, adding EGR gases to increase equivalence ratio should be an interesting solution. However, using too much EGR set the rich limit. In this case, flame extinctions and misfires occurred due to the over dilution of the mixture by both air and EGR gases. This fact also explained the opposite evolutions of NOx and HC emissions: NOx decreased and HC increased with equivalence ratio because of the EGR rate increase. The optima settings were found for sufficient equivalence ratio to avoid flame extinctions with methane and sufficient EGR rate to have acceptable NOx emissions (less than 3 g/kWh). Finally, HC emissions can not be significantly lowered and new injection strategies need to be studied. These trends are summarized in Fig. 4 for ISNOX/cISFC and ISNOx/ISHC trade-offs.

Noise combustion was kept around and below 85 dB which was the target of the Diesel baseline engine for this range of engine loads (Fig. 6). The optimal combustion phasing represented by MFB50 was very sensitive to engine load (−3 °CA ATDC at 4 bar IMEP to +13°CA ATDC at 8 bar IMEP). The earlier combustion phasing at 4 bar IMEP can be explained by the increase of both autoignition delay and whole combustion duration in very diluted mixtures by air or EGR (low equivalence ratio and high EGR rate at very low load).

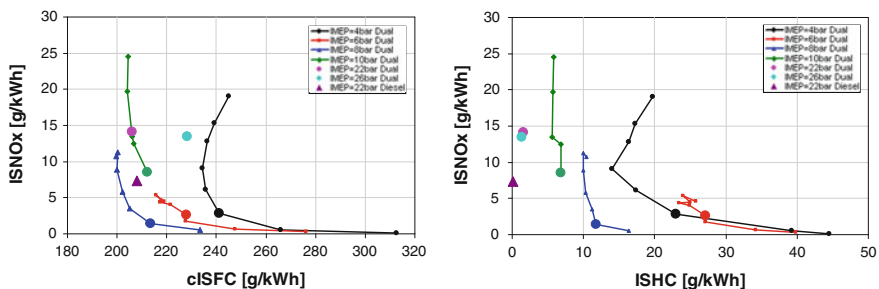


Fig. 4 ISNOx versus cISFC and ISNOx versus ISHC trades-off for different engine loads at 2,000 rpm

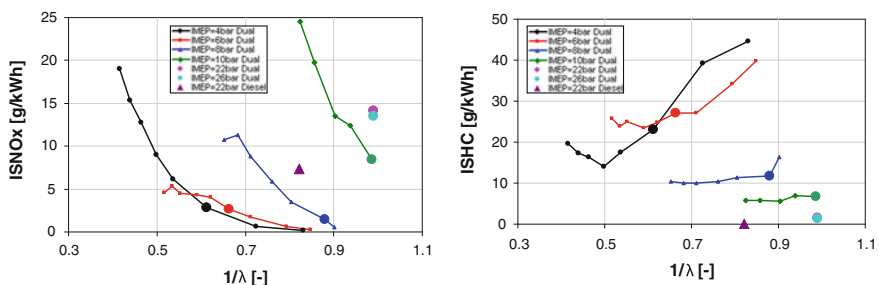


Fig. 5 Emissions of HC and NOx versus $1/\lambda$ for different engine loads at 2,000 rpm

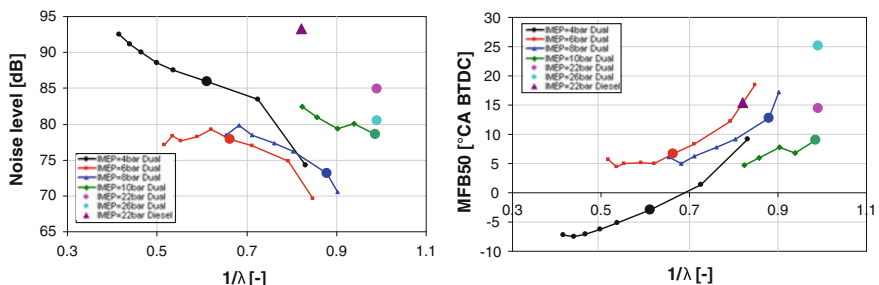


Fig. 6 Noise level and MFB50 vs. $1/\lambda$ at different engine loads at 2,000 rpm

3.2.3 Dual Fuel Lean Burn Mode: Influence of Combustion Phasing

This section focuses on the selection's process of optimal combustion phasing for optimal equivalence ratio (0.65) and optimal EGR rate (20 %) at 6 bar IMEP and 2,000 rpm engine speed. The results for fuel consumption, emissions and MFB50 are presented in Fig. 7. The earlier pilot SOI (Start Of Injection) tested was limited to 35 °CA BTDC corresponding to Diesel fuel spray targeting to remain inside the combustion chamber (for bowl-in-piston shape). It avoided problems of engine oil

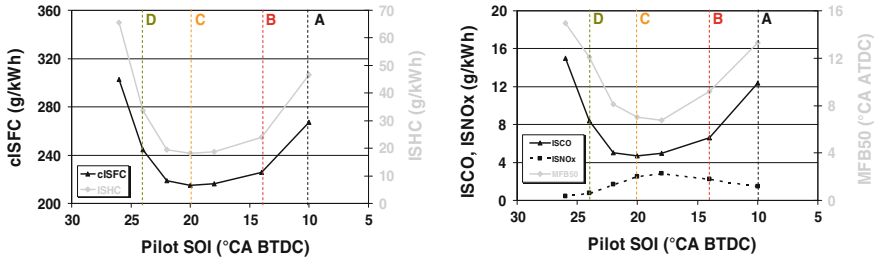


Fig. 7 Fuel consumption, emissions and MFB50 for different pilot fuel SOI at 6 bar IMEP and 2,000 rpm

dilution resulting from spray impingement onto the cylinder liner. In order to analyze the influence of combustion phasing, four different pilot SOI had been tested for which Figs. 8 and 9 depicts MFB, HRR and combustion durations: 10, 14, 20 and 24 °CA BTDC.

Fuel consumption and HC emissions had similar trends. HC and fuel consumption were minimum for pilot SOI in a range between 14–22 °CA BTDC. Then HC emissions corresponded only to crevice losses (geometry of combustion chamber) and to flame extinction as equivalence ratio might have been locally too low in some areas of the combustion chamber. The problem of HC reduction could be solved by significantly modifying the piston geometry and boosting swirl motion.

For earlier pilot SOI, HC emissions rose again as pilot fuel was injected too earlier. Indeed, the Diesel fuel autoignition delay was longer and Diesel fuel vapour had too much time to spread out in the cylinder and was then overdiluted into the methane/air premixture. Thus, the ignition was delayed and whole combustion duration was longer. The point D at 24 °CA BTDC pilot SOI in Figs. 8 and 9 is representative of this case. Furthermore, this overmixing of Diesel fuel and methane during autoignition delay is clearly noticeable on HRR curve in Fig. 8: indeed, the Diesel fuel premixed combustion peak was not visible for earlier SOI while it was amplified for later SOI.

For later pilot SOI, Diesel fuel was injected closer to the TDC and autoignition delay reached its minimum and as a consequence, combustion was retarded into the expansion stroke. Afterwards, the whole combustion duration was increased. The point A at 10 °CA BTDC pilot SOI illustrates this situation perfectly.

Concerning NOx emissions, the evolution was opposite to HC emissions and NOx emissions were maximum for minimum cISFC (Fig. 7). As combustion phasing was optimal, adiabatic flame temperature was higher than for earlier or later pilot SOI. As a result, NOx formation rate was simply higher. This trend is identical to pure Diesel fuel combustion. The optimum pilot SOI was then identified as the point C at 20 °CA BTDC that presented lower cISFC, ISHC and limited ISNOx emissions. Finally, the combustion phasing was mainly controlled the Diesel fuel autoignition delay.

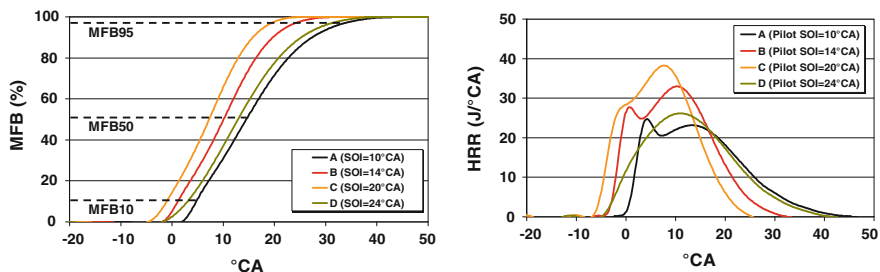
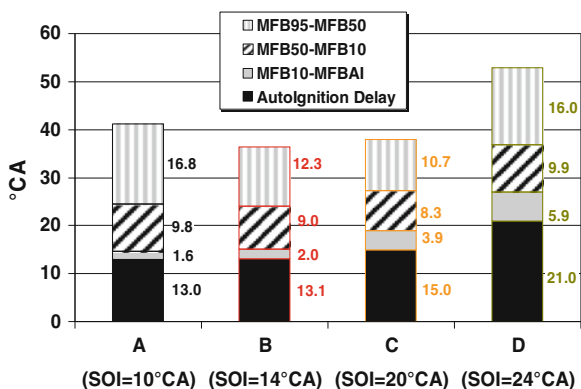


Fig. 8 MFB and HRR for 4 different pilot fuel SOI at 6 bar IMEP and 2,000 rpm

Fig. 9 Combustion durations for 4 different pilot fuel SOI at 6 bar IMEP and 2,000 rpm



3.2.4 Medium to Full Load: Dual Fuel Stoichiometry Mode

For medium to high loads (10 bar IMEP to full load), optimal mode was stoichiometry with or without EGR. Three different IMEP have been tested at stoichiometry: 10, 22 and 26 bar. The operating point at 10 bar IMEP on Figs. 3, 4, 5, and 6 showed that stoichiometry was clearly optimal compared to lean burn mode. HC emissions were constant between lean burn and stoichiometry meaning that flame propagation on methane/air premixture was efficient in this range of equivalence ratios beyond methane lean flammability limit. ISNO_x/cISFC trade-off was optimal as NO_x emissions were reduced because of the use of EGR. Moreover, EGR at stoichiometry could reduce the thermal load on the cylinder head and at the exhaust by diluting the carburetted premixture. Indeed, the dual fuel engine was derived from a Diesel baseline engine which materials and cooling system are not compatible with the high thermal constraint imposed by stoichiometric operation.

The operating point at 22 bar IMEP corresponded to full load target of the Diesel baseline engine. As neither preignition nor knock were observed for this load and as in-cylinder maximum pressure limit was not reached, it was decided to test the maximum engine load achievable while respecting mechanical engine's constraints (160 bar maximum in-cylinder pressure and 2.5 bar intake

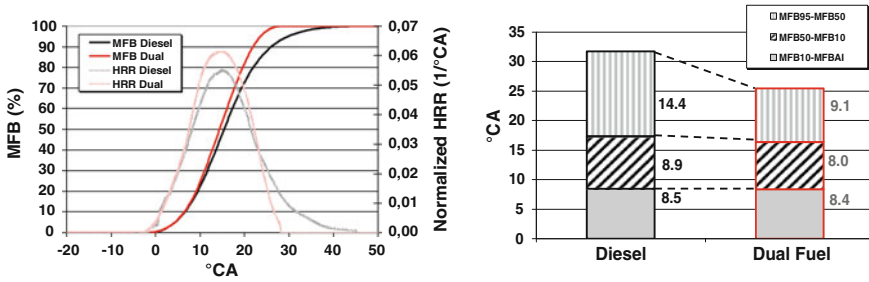


Fig. 10 MFB, HRR and combustion durations for dual fuel and pure diesel fuel at 22 bar IMEP

boost pressure). As a result, 26 bar IMEP was reached at stoichiometry without EGR. Once more, neither pre-ignition nor knock were detected for 17:1 compression ratio. In addition, noise combustion remained lower than Diesel fuel noise target (85 dB). This result could be explained by the ultra low Diesel fuel mass ratio used for this IMEP (less than 1 %) as maximum in-cylinder gradient are normally obtained during Diesel fuel premixed combustion. Generally, all the operating points at stoichiometry had ISNOx emission levels that seemed high (10–15 g/kWh) but that could be compatible with 3 way catalyst capability for NOx reduction.

3.2.5 Dual Fuel Stoichiometry Mode: Comparison Between Diesel Fuel and Dual Fuel Operation

The operating point at 22 bar IMEP corresponding to full load target of the Diesel baseline engine was also tested in pure Diesel fuel operation and compared to dual fuel operation (depicted as a triangle on Figs. 3, 4, 5, and 6). The Fig. 10 shows that Diesel fuel autoignition delay was identical between the two cases. However, the last combustion phase represented by MFB95-MFB50 duration was significantly longer for Diesel fuel operation. This means that Diesel fuel diffusion flame slowed down at the end of combustion whereas methane flame propagation kept faster. This item had already been observed during the first experimental approach.

Fuel consumption should have been reduced but it was not the case as combustion efficiency for dual fuel remained lower than the one for Diesel fuel (98.6 % for dual fuel vs. 99.6 % for Diesel fuel). Indeed, HC and CO emissions were still high for dual fuel operation at respectively 1.6 and 4.6 g/kWh. These levels can not be reduced without significantly modifying piston geometry. However, it seems relevant to remind that at same cISFC, dual fuel operation emits theoretically 25 % less CO₂ than Diesel fuel operation if Diesel fuel mass ratio is small (less than 1 %).

4 Conclusions and Perspectives

An investigation of Diesel/methane dual fuel combustion was performed using a small displacement single cylinder engine (499 cc). Most of the literature is focusing on heavy duty engines but in this study, it had been demonstrated that dual fuel operation can be used successfully on passenger car engines. A large range of IMEP (from 4 bar to 26 bar) had been tested at 2,000 rpm engine speed. The optimal combustion modes depended on engine load: lean burn with EGR for low to medium loads and stoichiometry with or without EGR for medium to full load. Neither PM emissions nor noise level were found critical. Indeed, almost no smoke was measured with dual fuel combustion. Low Diesel fuel mass ratios have been used specifically for stoichiometry (less than 1 %) meaning that CO₂ savings are high compared to pure Diesel fuel operation.

The lean burn operation range presented challenges such as the control of NO_x and HC emissions. That is why new trade-offs were considered for engine settings optimization: NO_x vs. HC and NO_x vs. fuel consumption. NO_x emissions were limited by the use of moderate levels of EGR rates. HC emissions were reduced by increasing equivalence ratio with EGR dilution. However, HC levels remained an issue. Unburned species came from both flame extinction with too lean mixtures and engine crevices (high height of top-land crown for a Diesel designed piston). In lean burn mode, combustion phasing was highly sensitive to the Diesel fuel autoignition delay.

The range of operation at stoichiometry was found really wide from 10 to 26 bar IMEP and showed interesting results in terms of emissions and fuel consumption. The main advantage is that stoichiometry allows simple and cost-effective aftertreatment using a 3 way catalyst. Full load at 26 bar was possible without preignition or knock limitations at 17:1 compression ratio with the piston geometry used in this study. This proves that Diesel/methane dual fuel combustion is compatible with high performances. Moreover, stoichiometry allowed same fuel consumption at 22 bar IMEP as Diesel fuel operation even with slight HC and CO penalties which means that improvement for better ISFC is still possible. This could be explained by the second half of the combustion that was shorter for dual fuel than for Diesel fuel operation. Therefore, methane flame propagation remains faster when Diesel fuel combustion by diffusion slows down dramatically. In addition, same fuel consumption between dual fuel and Diesel fuel with very low amounts of Diesel fuel mass ratio (<1 %) meant that the reduction of CO₂ emissions could reach around 25 % at full load. This result represents a great benefit for the upcoming WHTC (World Harmonized Transient Cycle) which requires higher engine loads compared to the NEDC cycle.

Further research needs to be carried out concerning the problem of high unburned emissions in lean burn mode by developing new innovative injection strategies and appropriate piston design. This study has shown interesting results without major engine modification. However, engine hardware optimization should be taken into account for the upcoming works such as piston design,

adaptation of swirl motion level and characteristics of Diesel fuel injector. These topics are currently addressed at IFP Energies nouvelles and will be described in upcoming papers. Moreover, other fuel combinations for dual fuel combustion can have great potential and are largely studied in the literature [10] even for passenger car or heavy-duty.

Acknowledgments Authors wish to thank Frantz Guerbet for performing the engine tests.

References

1. Scott Brown B, Rogak S, Munshi S (2009) "Multiple injection strategy in a direct-injection natural gas engine with entrained diesel". SAE paper 2009-01-1954
2. Sahoo BB, Sahoo N, Saha UK (2009) "Effect of engine parameters and type of gaseous fuel on the performance of dual-fuel gas diesel engines: a critical review". *Renew Sustain Energy Rev* 13:1151–1184
3. Lacour S, Chinese T, Alkadee D, Perilhon C, Descombes G (2012) Energy and environmental balance of biogas for dual-fuel mobile applications. *Renew Sustain Energy Rev* 16:1745–1753
4. Selim MYE (2004) Sensitivity of dual fuel engine combustion and knocking limits to gaseous fuel combustion. *Energy Convers Manage* 45(3):411–425
5. Konigsson F, Stalhammar P, Angstrom HE (2011) "Characterization and potential in a modern diesel engine". SAE paper 2011-01-2223
6. Ishiyama T. et al. (2000) "Improvement of performance and exhaust emissions in a converted dual-fuel natural gas engine". SAE paper 2000-01-1866
7. Ishiyama T, Kang J, Ozawa Y, Sako T (2011) "Improvement of performance and reduction of exhaust emissions by pilot-fuel-injection control in a lean-burning natural-gas dual-fuel engine". SAE paper 2011-01-1963
8. Fritz SG, Egbuonu RI (1993) "Emissions form heavy-duty trucks converted to compressed natural gas". SAE paper 932950
9. Selim MYE (2001) Pressure-time characteristics in diesel engine fuelled with natural gas. *Renewable Energy* 22(4):473–489
10. Duffour F, Ternel C, Pagot A (2011) "IFP Energies nouvelles approach for dual fuel diesel gasoline engines". SAE paper 2011-24-0065

Sustainable Mobility: Lithium, Rare Earth Elements, and Electric Vehicles

Timothy J. Wallington, Elisa Alonso, Mark P. Everson, Frank R. Field, Paul W. Gruber, Gregory A. Keoleian, Stephen E. Kesler, Randolph E. Kirchain, Pablo A. Medina, Emily K. Kolinski Morris, Rich Roth and Andrew M Sherman

Abstract Recognition of the importance of climate change and energy security has led to interest in electrified vehicles. Electrified vehicles contain substantial amounts of lithium and rare earth elements. There has been concern that the supplies of lithium may not be sufficient to support the development of a large scale global fleet of electric vehicles. We conducted a comprehensive analysis of the global lithium resources and compared it to an assessment of global lithium

F2012–B01-026

T. J. Wallington (✉) · M. P. Everson · R. E. Kirchain · E. K. Kolinski Morris
Systems Analytics and Environmental Sciences Department, Ford Motor Company,
Mail Drop RIC-2122, Dearborn, MI 48121-2053, USA
e-mail: twalling@ford.com

M. P. Everson
e-mail: meverson@ford.com

R. E. Kirchain
e-mail: kirchain@MIT.EDU

E. K. Kolinski Morris
e-mail: ekolinsk@ford.com

E. Alonso · F. R. Field · R. Roth · A. M. Sherman
Materials Systems Laboratory, Engineering Systems Division,
Massachusetts Institute of Technology, 77 Massachusetts Avenue, Cambridge,
MA 02139, USA
e-mail: ealonso@MIT.EDU

F. R. Field
e-mail: furd@mit.edu

R. Roth
e-mail: rroth@mit.edu

demand from 2010 to 2100 that assumes rapid and widespread adoption of electrified vehicles. We show that that even with rapid and widespread adoption of electric vehicles powered by lithium-ion batteries lithium resources are sufficient to support demand until at least 2100. The future availability of rare earth elements (REEs) is of concern due to monopolistic supply conditions, environmentally unsustainable mining practices, and rapid demand growth. We evaluated potential future demand scenarios for REEs with a focus on the issue of co-mining. In the absence of efficient reuse and recycling or the development of technologies which use lower amounts of Dy and Nd, following a path consistent with stabilization of atmospheric CO₂ at 450 ppm may lead to an increase in demand of more than 700 and 2,600 % for Nd and Dy, respectively, over the next 25 years.

Keywords Sustainability · Lithium · Rare earth elements

1 Introduction

Increasing concerns about the environmental impacts and reliability of supply of fossil fuels are motivating a global drive towards introduction of sustainable mobility technologies. The availability of materials such as lithium and rare earth elements required for these new technologies needs to be considered.

The current generation of hybrid electric vehicles (HEVs) such as the Toyota Prius and Ford Fusion Hybrid are powered by internal combustion engines with relatively small, nickel-metal hydride (Ni-MH) batteries. Lithium-ion batteries are used in plug-in hybrids (PHEVs) such as the Chevrolet Volt and the Ford C-Max Energy and battery-electric vehicles (BEVs) such as the Nissan Leaf and Ford Focus Electric. Lithium-ion (Li-ion) batteries are lighter, less bulky, more energy efficient, and are projected to be less expensive than Ni-MH batteries [1]. The use

P. W. Gruber

University of California Davis, 2028 Academic Surge, One Shields Ave, Davis,
CA 95616, USA

e-mail: pwgruber@ucdavis.edu

G. A. Keoleian · P. A. Medina

School of Natural Resources and the Environment, University of Michigan, 3504 Dana,
Ann Arbor, MI 48109-1041, USA

e-mail: gregak@umich.edu

P. A. Medina

e-mail: pmedina@umich.edu

S. E. Kesler

Earth and Environmental Sciences, University of Michigan, 2534 C.C. Little Building,
1100 North University Ave, Ann Arbor, MI 48109-1005, USA

e-mail: skesler@umich.edu

of lithium-ion batteries in vehicles is expected to increase substantially and this raises the question of whether global lithium resources will be sufficient to supply a large global fleet of electric vehicles.

Rare earth elements (REEs) are critical to clean energy technologies and have recently received much attention regarding the reliability of their supply. The International Union of Pure and Applied Chemistry (IUPAC) defines the rare earth metals as a group of 17 elements consisting of the 15 lanthanides [La, Ce, Pr, Nd, Pm, Sm, Eu, Gd, Tb, Dy, Ho, Er, Tm, Yb, Lu] plus Sc and Y. Data are mainly available for only 10 of the 17 elements, and therefore our analysis focuses on these: La, Ce, Pr, Nd, Sm, Eu, Gd, Tb, Dy and Y. REEs are important because they provide critical functionality in a wide variety of applications and are used in relatively large amounts in key technologies being developed to provide sustainable mobility and energy supply.

The availability of REEs appears to be at risk based on a number of factors, not least of which is that one country (China) controls approximately 98 % of current supply (production). Another contributor to supply risk for REEs is the fact that they are co-mined; individual REEs are not mined separately. REEs are found together in geological deposits, rendering mining of individual elements economically inefficient. The supply of any individual REE depends on the geology of the deposits, the costs of the extraction technology employed, and the price of the basket of rare earths.

In the present chapter we provide an overview of work we have performed to: (1) compare geological reserves of lithium with estimates for future global demand, and (2) evaluate future potential demand scenarios for REEs with a focus on the issue of co-mining. The supporting literature upon which we base our assumptions and details of the methods used are given elsewhere [1, 2] and not discussed here.

2 Lithium Resources

There are three types of lithium deposits: brines, pegmatite's, and sedimentary rocks. Brines are saline waters with high contents of dissolved salts. They are found naturally in the pores of rocks where lake or ocean water has undergone extreme evaporation. The most common such environment for lithium-bearing brines are playas (salt flats). Lithium is a minor but locally important constituent of these brines and is thought to have been derived from erosion of rocks surrounding the playas, and from hot springs that feed water into the playas. The brine is pumped into shallow evaporation ponds where it is evaporated under controlled conditions. Brine salt flats containing the highest concentrations of lithium are in Chile, Argentina, China, and Tibet. Brines in these deposits contain large amounts of other useful elements, including potassium and boron, which offset some of the costs of pumping and processing brines.

The average concentration of lithium in major brine resources varies from about 0.14 % at the Salar de Atacama to 0.02 % at Silver Peak, Nevada. The 3,000 km²

Table 1 World lithium resource, top 15 deposits [1]

Deposit	Country	Type	Resource (Mt Li)	Avg. concentration (% Li)
Uyuni	Bolivia	Brine	10.2	0.05
Atacama	Chile	Brine	6.3	0.14
Kings mountain belt	USA	Pegmatite	5.5	0.68
Qaidam	China	Brine	2.0	0.03
Kings valley, NV	USA	Sedimentary rock	2.0	0.27
Zabuye	China	Brine	1.5	0.07

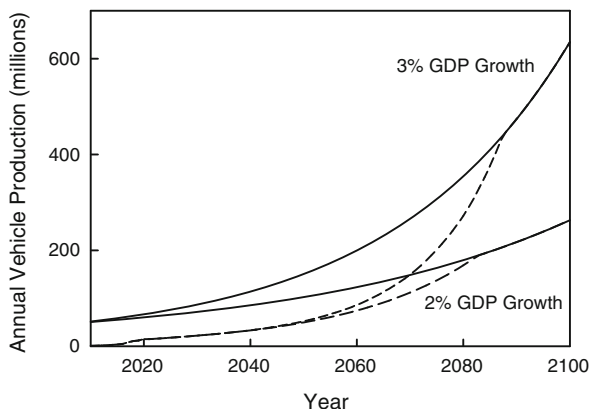
Salar de Atacama, in northern Chile, is the largest producing deposit and the world's largest producer of lithium carbonate (Li_2CO_3), with 40,000 and 25,000 tonnes of Li_2CO_3 in 2008 from operations owned by Sociedad Quimica y Minera (SQM) and Rockwood Holdings Inc., respectively. This is more than half of the world's total production of 22,800–25,400 tonnes of lithium in 2008. We estimate that Atacama has an in situ lithium resource of at least 6.3 Mt. Zabuye, in China, is the next largest producing brine deposit with an estimated lithium resource of 1.53 Mt and a production capacity of 7,500 tonnes of Li_2CO_3 (2004). Bolivia's Salar de Uyuni contains a possible total resource of 10.2 Mt of lithium, or 27 % of the world's in situ lithium resource [1].

Pegmatite deposits are coarse-grained intrusive igneous rocks that formed from the crystallization of magma at depth in the crust. Pegmatite's can contain recoverable amounts of lithium, tin, tantalum, niobium, beryllium and other elements. Lithium in pegmatite's is usually present in the mineral spodumene ($\text{LiAlSi}_2\text{O}_6$). To produce lithium carbonate from most pegmatite's, a concentrate containing the lithium-bearing mineral is obtained from the pegmatite ore, usually by flotation. The mineral concentrate is then pulverized and leached in hot solutions to release the lithium into solution, from which it is usually precipitated as lithium carbonate. The grinding, heating and dissolution steps in this process are expensive and are the reason that many pegmatite's are at a disadvantage compared to brines. Lithium is currently being extracted from at least 13 pegmatite deposits, and more deposits are under development. The largest producing spodumene pegmatite operation, in Greenbushes, Australia, has an estimated resource of 560,000 tonnes of lithium in ore with an average concentration of about 1.6 % lithium.

Lithium is also found in several different sedimentary rocks, including clay and lacustrine evaporites. In the clay deposits, lithium is a constituent of clay minerals such as smectite, from which it must be separated by processing. Hectorite [$(\text{Mg},\text{Li})_3\text{Si}_4\text{O}_{10}(\text{OH})_2$] is a type of smectite that is rich in magnesium and lithium. The best known hectorite deposit, containing 0.7 % lithium, is in Hector, California.

We estimated lithium resources from brine deposits using the relation: Lithium resource = $A \times T \times P \times D \times C$, where A = area of aquifer, T = thickness of aquifer, P = porosity of aquifer, D = density of brine, and C = concentration of Li in brine. Lithium resources from rock and mineral deposits were estimated using the relation: Lithium resource = $T \times C$, where T = tonnes of ore and C = concentration of Li in ore. We estimated that the total lithium

Fig. 1 Global annual vehicle production estimated for 2010–2100 for 2 and 3 % GDP scenarios: total vehicles are shown in *solid lines*, electric vehicles (HEVs, PHEVs, and BEVs) are shown by *dashed lines*



resource in all of the 103 deposits studied as part of this work is at least 38.3 Mt [1]. The top 6 lithium resources globally [1] are listed in Table 1.

3 Lithium Demand

The lithium demand for vehicle batteries was estimated in four steps. First, we conducted a linear regression analysis using light-duty global vehicle production for the period 1995–2008 from the Ward’s 2009 Automotive Yearbook and global GDP data; a 97 % linear correlation was found. Second, vehicle manufacturing was estimated for 2010–2100 using two GDP growth scenarios (2 and 3 %). In the 3 % GDP growth scenario the annual production of light-duty vehicles increases to approximately 630 million units in 2100. This equates to the production of 42 new vehicles per-thousand-persons per year in 2100; comparable to the current level in the US and probably an upper limit for future global production. Third, we used Credit Suisse’s projection of electric vehicle penetration from 2010 to 2030. Beyond 2030 we assumed that year-over-year electric vehicle growth remained constant in the 2 % GDP scenario and increased 0.5 % every 10 years in the 3 % GDP scenario. The projected global annual light-duty vehicle production is shown in Fig. 1. These growth projections result in 100 % EV penetration in 2083 and 2087, for 2 and 3 % GDP scenarios respectively. Fourth, battery life, vehicle life, and battery recycling were accounted for and the accumulated lithium use was estimated.

To calculate the number of batteries needed we assumed that all vehicle batteries have 10 years of useful life. The amount of lithium required per battery was calculated according to the electric range of each type of vehicle. We assumed HEVs have 2 km of electric range; PHEVs, 65 km; and BEVs, 200 km. We assumed that electric vehicles consume approximately 0.17 kWh/km and we considered a ± 20 % range around this value. Recognizing the need to avoid deep discharge and seeking to be conservative in our estimations, we added a 100 % buffer for HEV and 50 % buffer

Table 2 2010–2100 maximum expected lithium demand (in Mt, 1 Mt = one million tonnes) for electric vehicle batteries for 2 and 3 % GDP growth scenarios and recycling participation at 90 and 100 %

		Recycling = 90 (%)				Recycling = 100 (%)			
		HEV	PHEV	BEV	Total	HEV	PHEV	BEV	Total
2 %	Demanded	0.20	3.18	10.51	13.88	0.20	3.18	10.51	13.88
	Recycled	0.12	1.85	6.60	8.57	0.13	2.05	7.33	9.52
	Mined	0.08	1.33	3.92	5.32	0.06	1.12	3.18	4.37
3 %	Demanded	0.32	5.43	17.07	22.82	0.32	5.43	17.07	22.82
	Recycled	0.17	2.73	9.38	12.28	0.19	3.04	10.42	13.65
	Mined	0.15	2.70	7.69	10.54	0.13	2.40	6.65	9.18

A recovery efficiency of 90 % during the recycling process was assumed. Values differ slightly from those published previously [1] reflecting small rounding errors in the previous work

for PHEV and BEV batteries to provide adequate cycle life [1]. Lithium-ion batteries have approximately 0.114 kg Li per kWh (average for LiCoO₂, LiNiO₂, and LiMn₂O₄ cathode materials) so the lithium content of batteries in HEVs, PHEVs, and BEVs would be 0.062–0.093, 1.51–2.27, and 4.65–6.98 kg.

To account for future improvements in vehicle efficiency (e.g., weight reduction, aerodynamic and rolling resistance improvements) we assumed the per vehicle per km vehicle energy demand will decrease by a factor of two by 2100. Hence, by 2100, HEVs, PHEVs, and BEVs would contain between 0.031–0.046, 0.76–1.13, and 2.33–3.49 kg of lithium, respectively. Seeking to calculate maximum expected lithium demand, we used the upper bound of these ranges (i.e., 0.046, 1.13, and 3.49 kg) in our calculations.

Recycling of lithium from Li-ion batteries may be a critical factor in balancing the supply of lithium with future demand. The US EPA has reported that “nearly 90 % of all lead-acid batteries are recycled” and with regard to lead-acid batteries, the International Lead Association has stated that “some countries boast 100 % recycling and most others share the possibility of 100 % recyclability” [1]. We calculated total lithium demand and recycling volumes assuming two recycling participation rates (90 and 100 %) with 90 % recovery of lithium during the recycling process. The results are shown in Table 2.

An upper limit for total lithium demand for vehicle use over the period 2010–2100 of 10.5 Mt can be taken from the 3 % GDP growth case with 90 % recycling participation. This value can be combined with estimates of lithium use of 3.6 Mt in portable batteries and 3.2 Mt in non-battery uses globally through 2100 [1] to provide a total upper limit estimate of approximately 17.3 Mt. This is substantially lower than the estimate of the total global resources of 38.3 Mt [1] and we conclude that lithium availability is unlikely to constrain the electrification of the automobile industry over this century.

Table 3 Future REE demand projection scenarios [2]

Demand scenarios	Assumptions
A Aggregated evolutionary demand: overall historical production (supply) rate of growth projected into future	All RE production markets experience uniform demand growth at historical rates
B Disaggregated evolutionary demand: individual demand industry sector-level historical growth rates projected into the future	Each RE consumption market experiences demand growth at its historical rate
C Implicit revolutionary demand: market reported expectations for industry sector-level growth rates are projected into the future	Each RE consumption markets grows at rates predicted by industry experts
D Aggressive revolutionary demand: growth rate scenario B is supplemented with IEA blue map scenario for wind and automotive electrification	Aggressive automotive electrification, all wind uses permanent magnets, other RE market demand grows at historical rates
E Moderate revolutionary demand: growth rate scenario B supplemented with 2–3 % GDP growth automotive electrification scenario	Moderate automotive electrification, wind does not use permanent magnets, other RE market demand grows at historical rates

4 Rare Earth Element Demand

As with estimating future lithium demand, assessing the future global demand of rare earth elements is inherently challenging given the evolution of the underlying technological and contextual conditions. We applied two methods to project potential future demand for rare earth elements over the next 25 years [2]. The first method, evolutionary demand growth, projects commodity demand based on historic patterns of commodity use. The second method, revolutionary technology demand growth, projects demand for products within a specific market sector then maps that to commodity demand based on expected commodity use per product within that sector. For each of these methods, multiple approaches were taken to identify a range of scenarios for future rates of rare earth element demand. The different scenario assumptions examined are given in Table 3.

For Scenarios A, B, C, the demand for REEs in industry k in year T is calculated as:

$$D_{k,t=T,\text{historical/expert}} = \exp((y_T - y_0) * \ln(1 + g_{k,\text{historical/expert}}) + \ln(D_{k,t=0}))$$

where y = year and g_k is the annual growth rate for industry k . Scenarios A and B use historical trends as a predictor of future trends in RE markets and may be described as estimates for evolutionary demand growth. For Scenario C, the contribution of new technologies to growth projections is not explicitly given; rather, it is implicit in the projection which is based on expert input. We assume that industry experts consulted to define g_k for Scenario C have, to some degree, considered the evolution of individual market sectors and the technologies used by those sectors including revolutionary sectors like those explored explicitly herein. We characterize Scenario C as a form of a revolutionary demand growth based

projection. In Scenarios D and E revolutionary demand was limited to two widely discussed REE applications: automotive and renewable wind electricity generation. Other emerging clean energy applications that rely on REEs such as high efficiency lighting, solid oxide fuel cell systems, maglev trains and electric scooters could also be considered in an analogous manner, but were outside the scope of this study, in part due to lack of data.

The International Energy Agency's Blue Map/450 Greenhouse Gas (GHG) scenario was used to evaluate aggressive RE requirements for future vehicle sales and wind energy. This scenario sets out an energy pathway consistent with the goal of limiting increase in average global temperature to 2 °C. In the Blue Map scenario 80 % of new vehicles are electrified (i.e., including hybrid electric vehicles (HEV), plug-in hybrids (PHEV) and battery electric vehicles (BEV)) by 2035. In the Blue Map scenario, the wind turbine capacity additions are provided over 5 year periods; we assumed that installation occurs at a constant annual rate.

Scenario E used the vehicle production values shown in Fig. 1 to evaluate moderate revolutionary REE requirements for electric vehicles. These scenarios assume electrified vehicles increase from 6 % of total vehicle sales in 2015, to 27–35 % in 2035, and 35–48 % in 2050.

REE demand by new technology, n , was calculated as:

$$\text{Demand for REE} = D_{\text{REE}} = \sum_n \sum_j N_{nj}$$

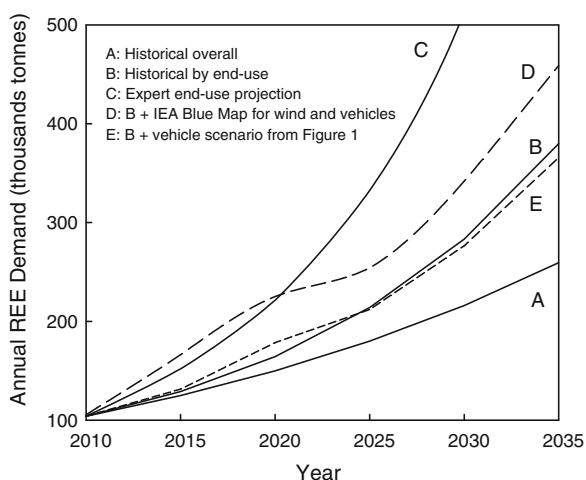
where the n th technology is either one of the different auto technologies (gasoline, diesel, BEV, HEV...) or wind and $N_{nj} = j$ th is the unit content of REEs per new car sold or wind turbine built in kilograms. The RE content per vehicle or wind turbine were assumed to be static. This is clearly a simplification. While it is expected that future technologies will likely improve their REE content performance, it is also expected that the number of applications that require RE will also increase.

The REE content of a wind turbine using a synchronous motor with a permanent magnet has been reported to be 600 kg per average 3.5 MW turbine [2]. Based on this figure, we assume an average of 171 kg of REEs per MW of built wind capacity. The portfolio of REEs in the wind turbine was assumed to follow the average magnet REE portfolio. It has been reported that wind energy capacity can also be built without permanent magnet technology, if it is too costly. The use of REEs for wind turbines could therefore also be reduced or zero. In designing the Scenario E as a moderate scenario, it was assumed that wind energy would use non-permanent magnet technology.

Our recent estimate of RE content in representative sedan vehicles with different electrification technologies [2] was used in addition to the US Department of Energy estimates for the RE content of nickel metal hydride (NiMH) batteries. NiMH batteries were assumed for HEVs up to 2020 and all other electric vehicles were assumed to contain lithium batteries (HEVs after 2020, all BEVs, PHEVs). For Scenarios D and E, total projected demand was calculated as a sum of revolutionary and evolutionary demand. The annual growth rates used for Scenarios A, B and C are presented in Table 4.

Table 4 Estimated industry-level growth rates (per annum) of key RE demand categories

Growth rates (%)	Magnets	Metal alloys	Catalysts	Polishing	Glass	Phosphors	Ceramics
Scenario A: Historical overall growth for 2006–2010	3.7						
Scenario B: Historical by industry for 2006–010 kings north 2010)	6.1	6.7	3.3	7.9	−4.1	0	6.2
Scenario C: Projections used for 2010–2015	12.5	10	4	8.5	0	8	7
Scenario C: Projections used for 2015–2035	12.5	6	4	10	0	4.5	6

Fig. 2 REE demand in scenarios A–E, see Table 3

In Scenario A, all industries would maintain the same market share over time while growing at the rate of 3.7 %/year. In Scenario B, demand for REE grows at an overall rate of 5.3 % between 2010 and 2035, which corresponds to an approximate doubling of demand between 2010 and 2025 (see Fig. 2). The modelled market shares of magnets and polishing compounds grow most, while those of automotive catalysts, petroleum catalysts and glass additives shrink.

5 Rare Earth Availability

To evaluate the implications of the projected demand growth for the REE market, we compared our projected demand with data on REE supply [2]. REE primary production for 2010 was approximately 107,000 tonnes of RE metals. The expected supply in 2015 from current mines and mines that are already being

developed is 157,000 tonnes rare earth metals, an average annual increase of 8.1 %. The portfolio of REEs mined is not expected to change significantly in the next 5 years, with Ce and La accounting for over 55 % of supply for all mines.

The USGS estimates REO total reserves are approximately 110 million tonnes. It has been reported that large amounts of RE are present in deep ocean sediments, however, the commercial feasibility of exploiting such deposits is unclear. While 50 % of RE reserves are concentrated in China, significant quantities are also found in the US and the Commonwealth of Independent States (former Soviet bloc countries). The static depletion index of REO (reserves/present production) is approximately 870 years. The known reserves for RE are therefore not expected to be constraining in the next 25 years. Moreover, at present, although RE recycling is limited to new scrap, this would be expected to change as prices rise and as applications that use concentrated amounts of RE grow in importance. Any increase in recycling would further increase the REE depletion index.

Belying their name, rare earth elements are not rare. The key concern with RE availability is not their geophysical abundance, but rather whether the RE supply base can expand at a sufficient pace to meet future demand particularly for individual RE metals. In particular, we wish to identify (a) the conditions where REEs may experience unprecedented demand growth, and (b) the implications of co-mining on RE availability under rapid demand growth in specific industries.

6 Historical Production

Global total REE production has averaged 6.5 % annual growth, but ranged between 21 and 34 % annual growth since 1970. The overall long term annual growth rate (curve fit) was 5.4 %. These rates are indicative of the strong growth in applications for REEs over the past 40 years and of the large historical fluctuations experienced in the REE market as this growth has occurred. While no guarantee can be made that future rare earth supply can grow at these historical rates, it is an indicator that growth at these rates would not be unprecedented.

Scenario D would require relatively rapid growth in total rare earth supply, 5.9 %/year, yet this rate is within 1 % of the historical overall production growth rate. Until lithium-ion batteries replace NiMH batteries in HEVs, rapid adoption of HEVs results in fast demand growth for REEs. In particular, in Scenario D, REE markets experience high growth rates relative to historical levels (8 %/year between 2010 and 2020) followed by a significant slowdown in demand (2.4 %/year between 2020 and 2025). Such changes may be accompanied by volatile prices. Satisfying the demand projected by Scenario C would require 8.6 %/year supply growth over the next 25 years, which is very challenging. While market dynamics are expected to play a role in all scenarios, Scenario C is most likely to lead to increased pressure on primary supply and, therefore, increased prices. The growth rates for Scenario E result in a lower REE demand in 2035 than Scenario B because some of the recent historical growth in rare earth demand may be

Table 5 Ratio of demand to supply for scenarios A–E

REE	T = 2010, base year= 2010	T = 2035, base year = 2010		T = 2015, base year = 2015			
	(%)	D (%)	A (%)	B (%)	C (%)	D (%)	E (%)
Ce	99	327	75	77	83	91	81
Dy	92	2630	99	111	148	332	175
Eu	95	78	86	68	97	68	68
Gd	90	145	87	71	107	83	71
La	81	249	66	68	75	82	71
Nd	106	724	87	97	124	156	105
Pr	140	669	114	128	160	170	128
Sm	99	47	83	62	92	61	61
Tb	167	249	133	116	157	125	116
Y	115	267	124	116	139	116	116
Total	98	402	80	82	96	106	87

attributed to the NiMH batteries in HEV. As projected, these batteries become substituted with lithium-ion technology and future RE demand growth is expected to slow correspondingly.

7 Limitations of Co-Mining

Even in the most aggressive growth scenarios, total RE demand growth is projected to exceed historic norms by no more than 3 %/year. However, closer examination of the results reveals significant deviation from historic norms for individual elements. REEs are co-mined and are produced in a portfolio that is determined based on the geology of RE reserves and the economics of recovery and separation technologies. When examining the future of REs, concern arises from emerging dislocations in relative demand among specific elements particularly from the imbalance between demand and supply for Dy and Nd. Vehicles and wind turbines rely very heavily on Dy, Pr and Nd. Presently exploited ores are over 70 % Ce, La and Nd.

To quantify this potential for supply constraint, we compared demand for each element in the different scenarios and divided by supply for that element (see Table 5). The percentages shown in Table 5 represent calculated demand in year T compared to current (2010) or projected (2015) supply in a base (comparison) year for the j th REE, calculated as:

$$\text{Ratio for } j\text{th element} = R_{j,T:\text{base}} = \frac{D_{j,y=T}}{S_{j,y=\text{base}}} \times 100\%$$

In the second column of Table 5, we verify our assumptions by comparing the 2010 demand estimate with the reported 2010 supply. The fact that our demand estimates for the individual elements are generally within 20 % of the reported

supply in 2010 provides confidence in the methods used. The larger discrepancies (e.g., for Pr and Tb) presumably reflect either the impact of stockpiling, or uncertainties in the literature data used in our analysis, or both.

The applications that will be most negatively affected by constraints in these REEs (i.e. increased costs) will be those dependent upon high power magnets, such as electrified vehicles and wind turbines. Applications such as petroleum refining, which depend on elements whose supply is projected to exceed demand, may be positively affected if primary producers increase overall production to meet the higher demand for specific elements. If a secondary market emerges to meet the higher demand for specific elements (i.e. recycling of magnets, but not catalysts), then, given that the portfolio of recycled REEs would be significantly different from the portfolio of primary supply, the overall supply portfolio of REEs could change significantly.

8 Conclusions

Increased electrification of the global vehicle fleet will lead to increased use of lithium and rare earth elements. We estimate the global lithium resource to be 38.3 Mt while the largest demand scenario we considered would consume approximately 17.3 Mt over the period 2010–2100. We conclude that lithium availability is unlikely to constrain the electrification of the automobile industry this century. In all scenarios of rare earth element demand that we considered, the total rare earth element demand in 2015 was within 20 % of the projected total supply. However, for some specific elements (especially Dy, Nd, and Pr) the rate of demand growth in some scenarios is challenging. In scenario D the demands for Dy and Nd exceed the projected supply by factors of approximately 3 and 2, respectively. As demand for Dy and Nd increases disproportionately relative to demands for other REE the prices of individual REE will change encouraging decreased use of Dy and Nd. This could be achieved by reduced use (e.g., materials substitution or increased efficiency), reuse, and recycling.

Acknowledgments We thank Renata Arsenault, Mike Degner, Kelly Keller, Ted Miller, and Bing Xu for helpful discussions.

References

1. Gruber PW, Medina PA, Keoleian GA, Kesler SE, Everson MP, Wallington TJ (2011) Global lithium availability: a constraint for electric vehicles? *J Ind Ecol* 15(5):760–775
2. Alonso E, Sherman AM, Wallington TJ, Everson MP, Field FR, Roth R, Kirchain RE (2012) Evaluating rare earth element availability: a case with revolutionary demand from clean technologies. *Environ Sci Technol* 46:3406–3414

Controller Design and Emission Improvement for Lean-Burn CNG Engine Based on UEGO Controller

Xiaojian Mao, Junhua Song, Du Wang, Junxi Wang, Hangbo Tang and Bin Zhuo

Abstract The configuration and driving principle of Universal Exhaust Gas Oxygen sensor (UEGO) was introduced. Based on the technology of Electronic Pressure Regulator, the system structure of Compressed Natural Gas (CNG) Engine is built. Based on the chip MPC 561 and integrate chip CJ125, the UEGO controller which include hardware design of UEGO driver and software design of Air-fuel ratio closed loop are designed. Based model and PID controller, the control strategy of Air-fuel ratio closed loop is discussed. Bench tests show that the operating temperature of UEGO is stable and the response of UEGO driver circuit is rapid and accurate, and error of steady-state is small. This system will reduce the CNG engine's fuel consumption and emission. Based of the UEGO control system, the intelligent control of engine's intake rate of air and emission could be achieved.

F2012-B01-031

X. Mao · J. Wang · H. Tang · B. Zhuo
Shanghai JiaoTong University, Shanghai, China
e-mail: xjmao@sjtu.edu.cn

J. Wang
e-mail: wjx999@163.com

H. Tang
e-mail: hb2609@163.com

B. Zhuo
e-mail: bzhuo@sjtu.edu.cn

J. Song (✉) · D. Wang
Shanghai High Energy Automotive Electronic Co., Ltd, Shanghai, China
e-mail: songjunhua203@yahoo.com.cn

D. Wang
e-mail: greenwand@163.com

Keywords CNG engine · Lean burn · UEGO · Driver · Bench test

1 Introduction

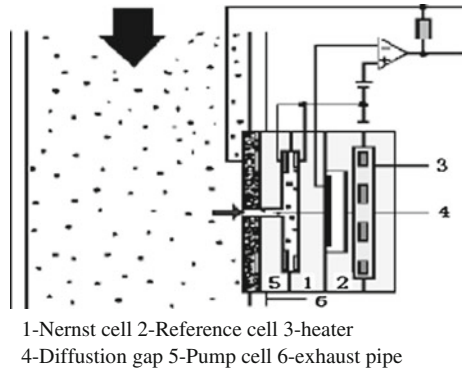
In order to save energy and protect environment, more and more strictly emission standards have been established and implemented. Therefore, energy conservation and emission control technology has become two important concerns in engine field, and the whole world is actively developing new energy resource and alternative fuels. Natural gas is considered to be one of the most promising alternative fuels, because that the storage of natural gas is rich, the main content of natural gas is CH_4 , which has high octane number, and the ability of antiknock is better. Moreover, mixer of natural gas and air is uniform. So engine power and thermal efficiency of natural gas engine are improved.

The operation of lean-burn natural gas engines can be optimized in terms of reducing engine-out emissions while maximizing efficiency through the implementation of a closed-loop fueling control system. Lean burn engines operate at an excess air/fuel ratio and, without an exhaust catalyst, are able to produce lower engine-out emissions than stoichiometric natural gas engine. A lean burn engine is designed to operate at high intake manifold pressure with an excess air ratio greater than 1. Consequently, combustion efficiency can be improved through reduced pumping losses and enhanced thermodynamic efficiency. Moreover, the leaner mixture slows down the burn, as well as decreases in-cylinder pressure and temperature, which decreases the possibility of the auto ignition of end gas and will results in lower chance of knocking and lower NO_x emissions [1]. However, with poor combustion quality, as in the case of partial burning and misfire, engine efficiency drops, and HC and CO emissions increase. So air-fuel ratio (AFR) should follow accurately the given set point, for avoiding mixtures leaner than the lean limit.

Exhaust oxygen gas sensor is one important part of electronic control system, which monitors the oxygen content of exhaust. Electric signal translated from exhaust oxygen content, was sent to ECU, which amends the actual AFR and reduces the emission [2]. Compared with the stoichiometric engine, the lean burn engine requires a special wide range or universal exhaust gas oxygen (UEGO) sensor and control algorithm to compensate for fuel composition variations. To improve the fuel economy and emission, the hardware and software design of UEGO controller should be optimized.

In this paper, a control system of CNG engine was design based on the technology of electronic pressure regulator. The technologies of lean burn and turbocharged are adopted which improve the fuel economy, power performance and emission performance of the CNG engine. The objective of the research reported in this paper is to develop a UEGO controller for lean burn natural gas engines.

Fig. 1 The structure of UEGO



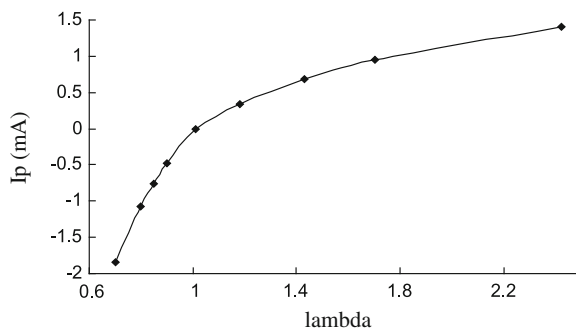
2 UEGO System

Based on working principle, exhaust gas oxygen sensor can be divided into two types: equivalent EGO and lean burn EGO. The equivalent EGO is ON/OFF type, which was applied in system of three-way catalytic converter. The other type sensor is named wide-band oxygen sensor, or universal exhaust gas oxygen sensor (UEGO).The output signal of pump current exhaust oxygen sensor is linear, so the sensor could monitor the oxygen content of exhaust continuously, and could be used in lean burn engine.

As shown in Fig. 1, this UEGO sensor consists of Nernst cell, pump cell and heater. Air and exhaust are located on both sides of pump diagram. Exhaust could reach the gap of Nernst cell and pump cell through the diffusion gas. The oxygen differential generates a certain pump current. The pump current characteristic is monotonic with positive currents in lean exhaust gases, negative in rich exhaust gases and zero at $\lambda = 1$. The Nernst cell compares the oxygen content between exhaust and reference cell, and generates a voltage to ECU. The voltage differential is 450 mV when $\lambda = 1$.The pumping current characteristic is closed loop controlled by ECU comparing the actual Nernst cell voltage with a reference voltage of 450 mV [3, 4].

LSU 4.9 of BOSCH is applied in CNG engine system, the relation curve of pump current (I_p) and excess air ratio (λ or lambda) was shown in Fig. 2 [5]. Figure 3 shows the schematic sensing mechanism. An external DC field was applied against O_2 concentration gradient during the sensor operation. In the fuel lean region, O_2 was pumped to the air reference side because the O_2 concentration gradient was small compared to the electric field. The O_2 pumping current increased at the leaner condition because O_2 could diffuse toward electrode. In contrast, in the fuel rich region, the electromotive force from O_2 concentration gradient is larger than the applied voltage. Therefore, O_2 will be pumped from the air to the exhaust side. In this case, the richer condition will pump more O_2 into the exhaust side because a larger concentration gradient will be established between

Fig. 2 The relation curve between I_p and λ



the two electrodes [6]. Therefore, the current signal can be obtained, which is proportional to the degree of fuel rich and fuel lean.

The catalytic effect of the Pt electrode in this sensor is smaller than in a conventional λ sensor because the sensor was fabricated by confirming the laminate of the ceramic green sheets at the elevated temperature (1,500 °C). Therefore, it is needed to be operated at a relatively high temperature (600–800 °C).

3 Controller Design

3.1 Hardware Design of UEGO Driver

Driver circuit of UEGO includes sensor and a control circuit which contains heating circuit, drive circuit and monitoring circuit of pump current. The heating circuit ensures the sensor remain a proper temperature and makes it enter 780 °C quickly. Heating circuit includes a temperature monitoring circuit, which monitors the temperature of sensor and takes the actual value of temperature to the sensor's temperature closed loop control. Pump current drive circuit controls the pump current. Based on the offset between 450 mV and the voltage difference, the AFR is closed loop controlled. Pump current monitoring circuit amplifies the current signal and send it to ECU, and the pump current is one important element for AFR closed loop control.

The control circuit can be designed based on discrete circuit or integrated chips. In this research, the UEGO driver circuit was shown in Fig. 4, based on the integrated chips CJ125 [7], which was developed by BOSCH semiconductor for driving the UEGO. With the integrated chip, circuit design can be simplified, reliability can be improved. The UEGO control system was designed based on a 32-bit microcontroller MPC561 [8], which integrates many intelligent modules, such as three TouCAN modules which conforms to CAN 2.0B, 32 ports queued A/D module QADC, and three timing processing unit (TPU) modules. With this microcontroller, large of periphery circuit can be saved, and the develop period can be reduced.

Fig. 3 Sensing mechanism of UEGO with simple gas diffusion barrier

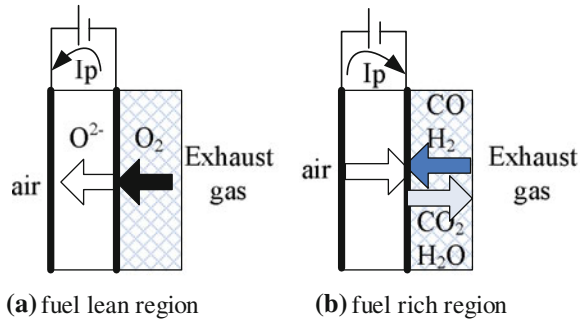
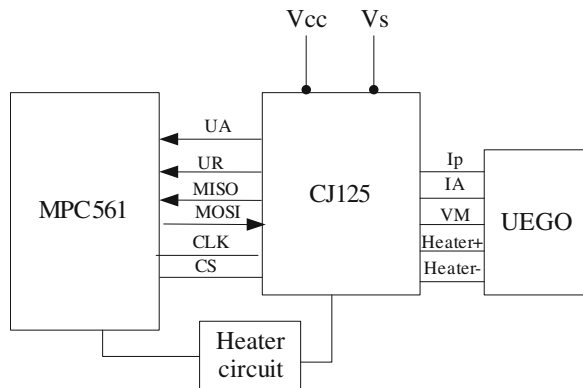


Fig. 4 The structure of UEGO drive circuit



3.2 Software Design of AFR Closed Loop

In order to control the AFR precisely of lean burn CNG engine, AFR’s voltage sampled by UEGO, and was translated to actual AFR. EPR amends the fuel according to the actual AFR. Figure 5 shows the process of AFR closed loop control. In which, V is the output voltage of UEGO driver chip and λ is access air ratio. A diagram of the AFR control principle is shown in Fig. 6. There are two nested closed loop control in A/F ratio closed control. The internal loop is fuel supply closed loop control, in which EPR adjusts the actual delta pressure to match its target value. The outside loop is A/F ratio closed loop controller, which control actual fuel to match its demand. Simplified PID model of A/F control is shown in Fig. 7. PID control and model-based are integrated in the design of A/F closed control model, which was applied in the CNG engine control system and reached a good performance.

The control cycle is discrete (control cycle is a function of engine speed) for the whole CNG control system, and there is one best control parameter (K_p , K_i , K_d) for A/F closed loop control in every control cycle. In order to improve the dynamic performance of A/F control system and to avoid larger overshoot, the variable

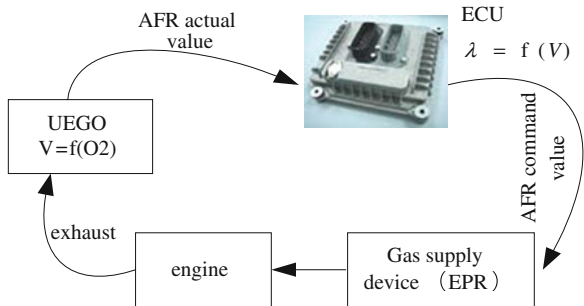


Fig. 5 AFR closed loop control process

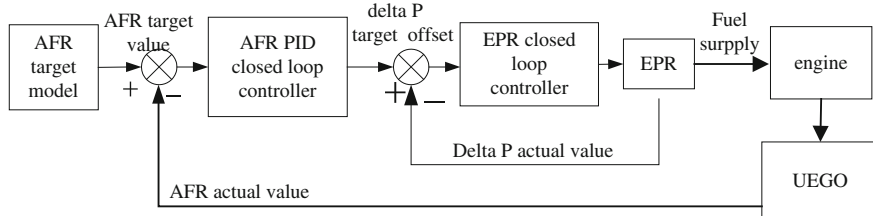


Fig. 6 The control principle diagram of AFR closed loop system for CNG engine

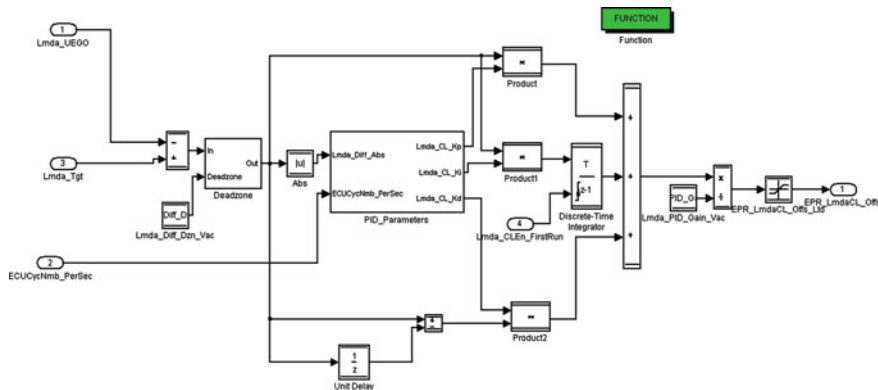


Fig. 7 Model of AFR closed loop

parameters were adopted in PID control. The functions of engine speed are selected, and the control parameters can be calibration through calibration tool, which make the stable A/F closed loop can be realized.

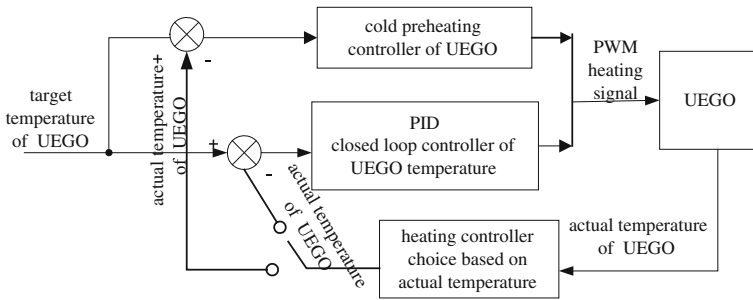


Fig. 8 The principle of UEGO heating closed loop

3.3 Closed Loop Control of UEGO Heating

The diffusion velocity of O_2 is affected by the temperature change of the UEGO sensor when the exhaust accesses the Nernst room. And the pump current is affected. So the sampling and monitoring of temperature for UEGO are very essential. The internal resistance of UEGO is changed with the temperature of the sensor, so the temperature can be monitoring through monitoring the value of internal resistance. The UEGO has very high impedance when at low temperature, and the internal resistance is 80–100 ohm when it is at normal work condition.

In order to avoid the thermal stress too large when heating is quick, the initial heating current could be not too big. And the stage was named cold preheating. After reaching the target temperature, closed loop control be carried out based on PID model. The choice of heating controller is based on the actual temperature of UEGO. The principle of heating closed loop is shown in Fig. 8.

4 Experimental Setup

The specifications of the experimental engine are listed in Table 1. Figure 9 shows the experimental setup consisting of several main subsystems, namely the CNG engine system, an electronic control system and the calibration tools, the Lambda meter and the exhaust analyzers, and a PC system equipped with calibration tools and monitoring system. The CNG engine includes a CNG bottle, electric pressure regulator, turbocharger, intercooler, electronic throttle body (ETB) and gas mixer. In this study, the technology of electronic pressure regulator (EPR) was adopted. The fuel controlled device is EPR, which is driven by a microprocessor control unit. EPR reduces the pressure of the natural gas from above 690 Kpa to the normal system pressure [9]. EPR controls the gaseous pressure to mixer through an internal pressure sensor which measures the delta pressure of fuel out of EPR and intake into mixer (shown in Fig. 10). EPR receives a command of delta pressure

Table 1 Specifications of the experimental engine

Parameter	Definition
Engine type	In-line six cylinders, spark ignition
Aspiration	Turbocharger
Intercooler	Air-to-water
Fuel type	Compressed natural gas
Bore × stroke	112 × 132 mm
Compression ratio	11
Displacement	7.8 L
Rated power/speed	191 kW/2300r/min
Maximum torque/speed	980 Nm/1400r/min

form ECU through CAN communication, and then it drives an internal diaphragm to adjust the fuel pressure. For one thing, EPR controls the actual delta pressure to match its command. For another thing, EPR feedbacks the actual delta pressure to ECU. The principle of EPR technology is similar to single injection. Gas mixture enter cylinder through inlet manifold, which makes gas mixture enter cylinders continuously and uniformly. Therefore, response performance is approved and homogeneity of each cylinder fuel can be guaranteed.

AFR closed loop was controlled by UEGO, which is stalled in the exhaust pipe to monitor the fuel supply accuracy of the engine control system. Oxygen content of exhaust was monitored by UEGO, which has a more precise manner than ON/OFF exhaust gas oxygen sensor. With the feedback signals of UEGO, fuel supply was adjusted using the closed loop control to meet fuel economy and power targets and emissions regulations.

AFR affects the emission of CNG engine directly. The emissions of HC, NO_x and CO under different excess air ratio were shown in Fig. 11. With the increase of excess air ratio, the NO_x decreases, and HC and CO increase, and HC, CO can be maintained at low levels, with the oxidation catalytic converter is installed in the exhaust pipe. Therefore, the increase of excess air ratio is beneficial to decreasing emissions [10].

5 Results and Discussion

5.1 The Control Result of UEGO's Temperature

The temperature of UEGO should be controlled in a stable value for sampling precise data. Figure 12 shows the closed loop performance of temperature control, which make UEGO to keep the desired temperature of 780 °C.

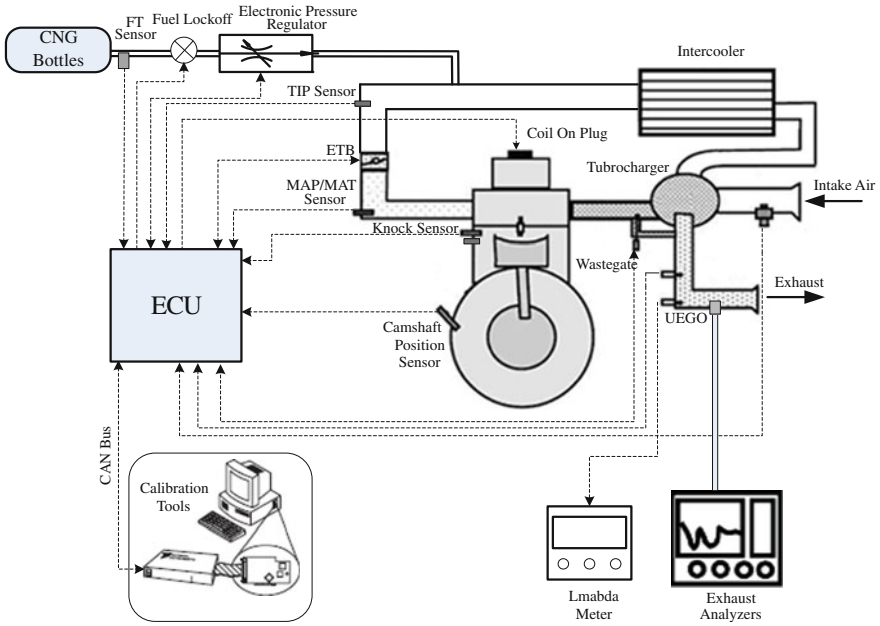


Fig. 9 The structure of CNG control system and its experimental setup

Fig. 10 The control principle of EPR

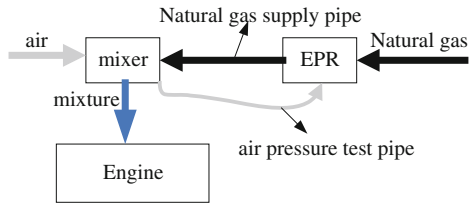
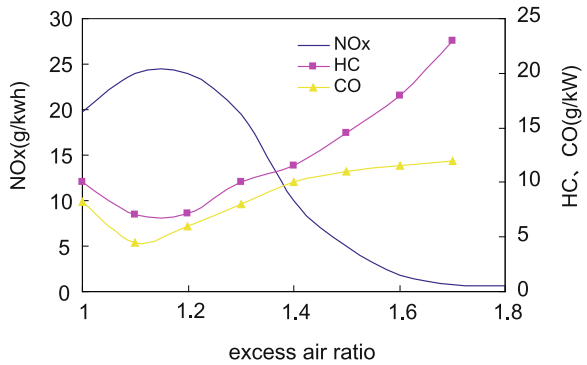


Fig. 11 The effects of excess air ratio on emissions



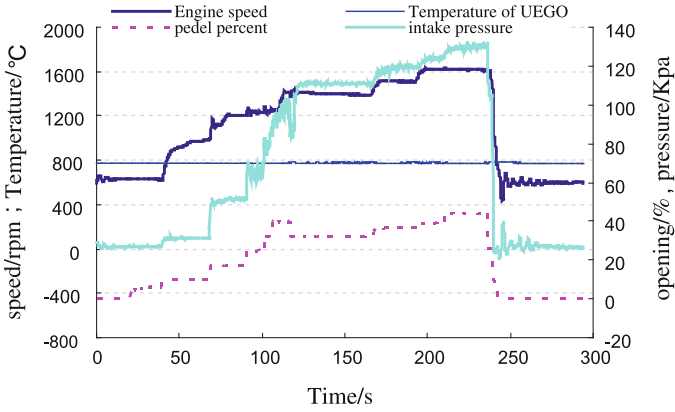


Fig. 12 The performance of UEGO's temperature control in CNG bench test

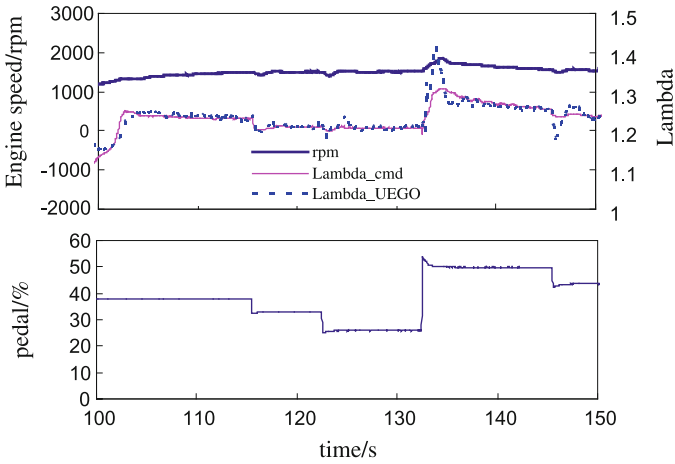


Fig. 13 The AFR closed loop performance of test bench

5.2 The Dynamic Control Performance of AFR

The desired excess air ratio of lean-burn CNG engine varies with operating condition. UEGO controller and model-based PID control for AFR control are tested in CNG engine bench. AFR closed loop control performances is showed in Figs. 13 and 14. Figure 13 shows the dynamic performance of AFR control, the overshoot is little and the match performance is well.

The AFR control performance of speed changed sudden is showed in Fig. 14. AFR closed loop control is disabled when fuel is shut off under emergency deceleration. And the closed loop is enabled, when the engine enters idle state again. The bench tests verified the model of AFR closed loop, which is reliable and efficient.

Fig. 14 AFR closed loop performance under emergency deceleration

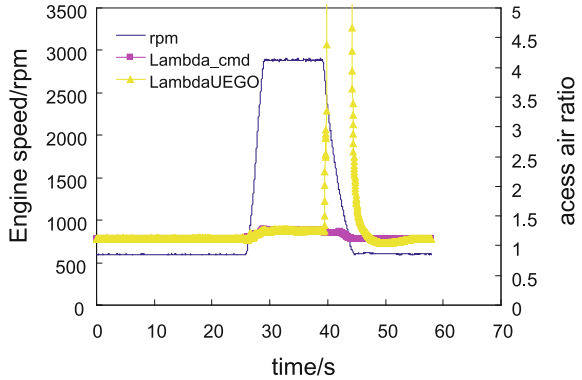


Fig. 15 Emissions of CNG engine in the bench test

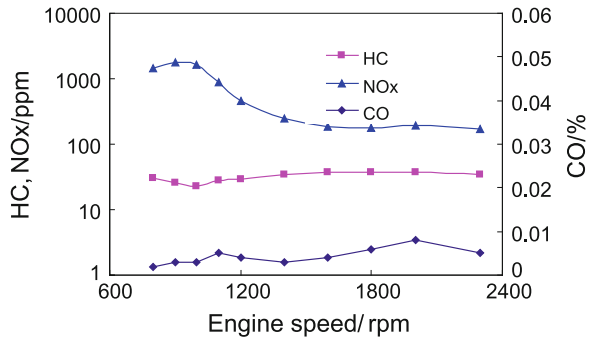
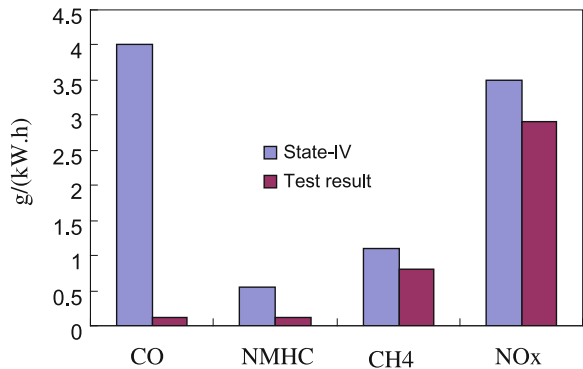


Fig. 16 The emission comparison between test result and State-IV emission standard



5.3 The Emission Performance of Lean-Burn CNG Engine Based on UEGO Controller

The emissions of CNG engine when engine is running at external characteristic for bench test is showed in Fig. 15. With the UEGO controller, the emissions of NO_x, HC and CO can be controlled within low levels. For natural gas engine, The

European Transient Cycle (ETC) test should be used to test the control effect of transient condition. Emissions performance of CNG engine can meet State-IV emission standard in china, which is showed in Fig. 16.

6 Conclusions

In this research, the UEGO controller is built for improving the accuracy of AFR closed control of CNG engine. The main conclusions can be summarized as follows:

- (1) Based on the 32-bit microcontroller and the integrated chip CJ125, the UEGO drive circuit and heater circuit were designed. The reliability of system can be improved with the methods of integrated chips.
- (2) The principle of AFR closed loop was analyzed. Based on model and PID controller, the model of AFR closed loop and temperature closed loop can be reached.
- (3) The control system of UEGO has been applied in CNG engine. The AFR closed loop tests have been verified in bench test. Theses tests show that the response of UEGO control system is rapid, accurate and steady state error is small.
- (4) When the UEGO controller is used, the emissions performance of CNG engine can reach the Stage-IV emission standard in China.

References

- Wang D, Mao X, Wang J, Zhuo B (2009) Experimental study on the operating range restrictions of lean-burn turbocharged si natural gas engine. *Energy Fuels* 23(6):3054–3062
- Riegel J, Neumann H, Wiedenmann HM (2002) Exhaust gas sensors for automotive emission control. *Solid state ionics*. Elsevier, 783–800
- Guan SX (2005) A detailed description of wide-range oxygen sensor. *J Liaoning Inst Sci Technol* 7(3):7–8
- Rui H, Guangkui L, Yaoqing S (1999) Oxygen sensors and its application in automobile. *J Transducer Technol* 18(3):1–4
- Robert Bosch GmbH (2003) Planar wide band lambda sensor. Reutlingen: Bosch, 5:1–24
- Jong-Heun L (2003) Review on zirconia air-fuel ratio sensors for automotive applications. *J Mater Sci* 38:4247–4257
- Robert Bosch GmbH (2006) Product information lambda probe interface IC-CJ125. Reutlingen: Bosch, 4:1–7
- Freescale Semiconductor(2005) MPC561/563 reference manual. Arizona: Freescale Semiconductor
- Wang JX, Song JH, Mao XJ, Wang D, Tang HB, Zhuo B Development of an electronic control unit for a compressed natural gas engine based on circuit simulation and model. In: *Proceedings IMechE Vol 223. PartD: J automobile engineering*. 1341–1350
- Mao X, Wang D, Xiao WY, Liu ZY, Wang JX, Tang HB (2009) Lean limit and emissions improvement for a spark-ignited natural gas engine through using a GPC-based Air-fuel ratio controller. *Energy Fuels* 23(12):6026–6032

Biogas as a Fuel for City Buses

Jerzy Merkisz and Wojciech Gis

Abstract *Research and/or Engineering Questions/Objective:* The road transport in Europe almost fully depends on fossil fuel. Diversification of the road transport fuels will be a key attribute for road transport in the coming years. Biogas is one of alternative renewable fuels. Actually in Poland biogas is used for generating electricity and heat. In some countries (for example in Sweden), upgraded biogas to natural gas quality (biomethane) is used as a vehicle fuel too. In this chapter estimated biogas production potential in Baltic Sea Region countries: Germany, Poland and Sweden. It is one of the purposes of European Project Baltic Biogas Bus, realized presently. *Methodology:* Authors of the paper discussed ecological results of biogas (biomethane) application for fuelling city buses. Comparative studies of exhaust emissions from city buses powered by diesel and CNG engine were carried out. The study was conducted under real traffic conditions in southern Polish city Rzeszow. Due to the lack in-service city buses with emission level Euro V in Rzeszow, comparative studies of this type of city buses powered by diesel and CNG engine was conducted in SORT I test. Determined mean values of road emissions in g/km for the city buses operated in Rzeszow. Estimated value of the total road emissions in the case that would be replaced half the fleet of city buses (40 CNG buses and about 35 % of the diesel engine powered buses, meet Euro III emission standard) by the CNG-powered (biomethane) city buses, complying with Euro V (EEV) emission standard. *Results:* It was found, inter alia, that the above-mentioned exchange half the fleet of

F2012-B01-037

J. Merkisz
Poznan University of Technology, Poznan, Poland
e-mail: merkisz@ptnss.pl

W. Gis (✉)
Motor Transport Institute, Poznan, Poland
e-mail: wojciechgis@its.waw.pl

city buses in Rzeszow for CNG-powered buses that meet Euro V (EEV) emission standard, reduced by about 10 %, first of all, the total CO₂ emissions. The reason is to use during test SORT I the bus with engine of small displacement (downsizing). Also significantly reduced the total emission of CO and NO_x (54 %) and (44 %), while THC emissions increased (70 %). Road PM emission is, as is the case in vehicles powered by CNG (biomethane), very small. The use of biomethane instead of CNG, as a fully renewable energy source, will reduce CO₂ emissions compared to diesel fuel supply very significantly, taking into account the emission from the well to the wheel. The paper presents the estimated potential of biogas in Baltic Sea Region countries: Germany, Poland and Sweden, too. *Limitations of this study:* A limitation of the study was, inter alia, lack possibilities of research in real traffic conditions in Rzeszow, exhaust pollutant emissions from city buses with the Euro V level of emissions. These buses are not operated here. The lack Portable Particulate Measurement Device (PPMD) also prevented a more accurate measurement of particulate emissions during tests city buses in Rzeszow. *What does the paper offer that is new in the field in comparison to other works of the author:* Comparative works discussed in this chapter as well as estimates of biogas potential production in above-mentioned the Baltic Sea Region countries, the authors earlier have not conducted. *Conclusion:* The new transport White Paper recommends an ambitious target of 60 % reduction of greenhouse gas emissions from transport up to 2050 in comparison to 1990. In this publication is forecasted that biomethane will be alternative road transport fuel for passenger/light duty cars, heavy duty (city) vehicles and heavy duty (long distance) vehicles in short term period (2020), mid term period (2030) and long term period (2050—only for passenger/light duty cars and heavy duty (city) vehicles). Prospect of application of biogas (biomethane) as a city fuel buses is significant.

Keywords Alternative fuels • Biogas • Biomethane • City bus transport • Ecology

1 Introduction

According to Directive 2003/30/EC [1] of the European Parliament and of the Council biogas is “a fuel gas produced from biomass and/or from the biodegradable fraction of waste, that can be purified to natural gas quality, to be used as biofuel, or wood gas”.

Feedstock for biogas production is mostly derived from agricultural, municipal and industry wastes. Biogas can be produced by the anaerobic digestion (AD) of a range of organic wastes, with the key wastes being [2]:

- sewage sludge,
- wet manure slurries from intensive styles of agriculture,
- dry manures from animal bedding, known as farm yard manure,
- waste from food processing,

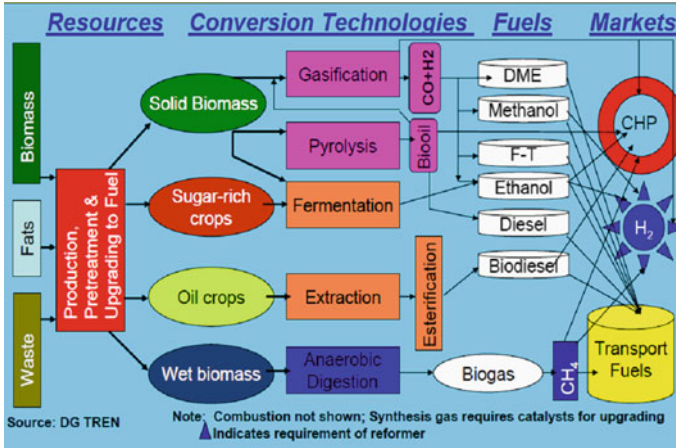


Fig. 1 Conversion technologies for production of transport fuels [3]

Table 1 Average composition of biogas in comparison for average composition of natural gas [4]

	Biogas	Landfill gas	Natural gas (Danish)
Methane (vol-%)	60-70	35-65	89
Other hydrocarbons (vol-%)	0	0	9.4
Hydrogen (vol-%)	0	0-3	0
Carbon dioxide (vol-%)	30-40	15-50	0.67
Nitrogen (vol-%)	~0.2	5-40	0.28
Oxygen (vol-%)	0	0-5	0
Hydrogen sulphide (ppm)	0-4000	0-100	2.9
Ammonia (ppm)	~100	~5	0
Lower heating value (kWh/Nm ³)	6.5	4.4	11.0

Table 2 Swedish standard for biogas as fuel for SI engines [4]

- Particles < 1 μm
- Methane $97 \pm 2 \%$
- Water < 32 mg/Nm³
- CO₂, O₂, N₂ < 5 %
- Oxygen < 1 vol %
- Sulphur < 23 mg/Nm³
- N (except for N₂) expressed as NH₃ < 20 mg/Nm³
- Odorised
- Compressed to 200 bar

For grid injection: addition of propane (around 7–9 vol %)

- food and organic waste from restaurants and other commercial operations,
- household kitchen and garden wastes.

Figure 1 presents conversion technologies for production of transport fuels [3].

Biogas can also be produced by thermal gasification, which is a process where the biomass or organic waste is heated under limited amounts of oxygen. The heat decomposes the organic material and gases as carbon dioxide, hydrogen, steam, carbon monoxide and methane are produced. Biogas produced this way is called Synthetic Natural Gas (SNG) [2].

Table 1 presents for instance average composition of landfill biogas in comparison for average composition of natural gas [4].

Biogas upgrading technologies are enabled for cleaning and removing: water, hydrogen sulfide, oxygen, nitrogen, ammonia, siloxanes, particles; increasing energy content by removing carbon dioxide; conditioning for distribution e.g.: odorization, compression; treatment of off-gas [4].

Biogas upgrading technologies are presently following: water scrubbing, Pressure Swing Adsorption (PSA), chemical absorption, membrane and cryogenic [4].

In result of these processes emerge biomethane.

Table 2 presents Swedish Standard for biogas as a fuel for SI engines [4].

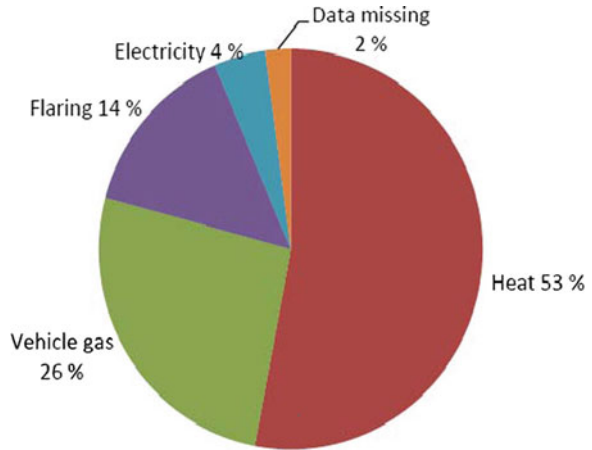
Biomethane can be used by SI engines of vehicles directly (as CBG or LBG for instance: terracastus technologies [5]) or can be injected as upgraded biogas into grid.

Figure 2 presents utilization of biogas in Sweden. Utilization share of biogas by vehicle is approximately 26 %. This type of utilization of biogas does not exist in Poland as opposite to Germany.

2 Biogas in Poland: Actual Condition and Perspective of Development

European Project Baltic Biogas Bus (BBB) stimulates the use of biogas (biomethane) as fuel of city buses aiming to reduce environmental impact.

Fig. 2 Utilization of biogas in Sweden (2008) [4]



Desk study on wider range of biogas production options and experiences including production potential scenarios for Baltic Sea Region (for Germany, Poland, Sweden etc.) is one of purpose of this project [2].

New market opportunities for the development of biogas have created a European Union Directive 2009/28/EC [6] of 5 June 2009 on promotion of renewable energy sources, requiring from Poland to achieve 15 % share of RES in final energy consumption in 2020. The construction of a new quantity target in relation to “energy consumption” offers the opportunities for biogas sector development, which can be direct or indirect used of all three end-markets of energy carriers, such as electricity, heat and transport.

Document prepared by the government titled “A Roadmap for renewable energy by 2020” as a plan for implementation of the Directive, has to specify the individual shares of energy carriers from renewable energy sources and technology in achieving the national target and their participation in general, national energy use balance. In the current year it is expected to introduce a new support system, including a new system of certification under the amendment to the Energy Law, which will determine the profitability of biogas investment in coming years.

According to the Energy Regulatory Office, on the beginning of the 2012 there were 178 biogas plants in Poland, including:

- 21 agricultural biogas plants;
- 67 biogas plants that produce biogas from sewage treatment plants;
- 89 biogas plants that produce biogas from landfills;
- 1 biogas plant that produce biogas from mixed substrate [7].

Poland received 251.8 GWh of electricity and 925 TJ of heat from biogas produced in 2008. However at the beginning of 2010 there were 124 facilities for the production of biogas with total capacity of 70.8 MW [7–12].

Production and production potential of Poland is illustrated in Table 3.

Table 3 Production and production potential of biogas in Poland

Country	Average total production potential (2010–2011) PJ	Total production (2009) PJ
Poland	52.3–115 (410.4)	4.10

So, the production of biogas is used in 3.6–7.8 % (average value 5.7 %); (1 %)

Table 4 Production and production potential of biogas in Germany

Country	Average total production potential (2010–2011) PJ	Total production (2009) PJ
Germany	414–432	176.41

So, the production of biogas is used in 40.8–42.6 % (average value 41.7 %)

3 Production Potential of Biogas in Germany

The theoretical amount of biogas possible to be obtained from biomass, waste and sewage per year is about 23–24 bn m³, which is an equivalent to the energy potential of 414–432 PJ [13]. Biogases from agricultural sector represent the highest share and in fact it takes up to about 85 % of the German biogas potential [14].

In 2006 Germany produced 22.4 bn kWh of electricity form biogas. Of this amount, approximately 49 % came from landfills and sewage treatment plants. The remaining 51 % of the biogas were produced in agricultural biogas plants using energy crops (known in Germany as “NawaRo” from the German “Nachwachsende Rohstoffe”), animal manure and waste form restaurants and slaughterhouses. Biogas production in Germany was likely to be less then 90 bn kWh in 2010, including the largest share—about 87 %—would come from agricultural biogas plants, in particular, using plants, crop residues, solid and liquid animal manure and all-season grass from pastures. In 2030 the productive potential of biogas in Germany should reach 165 bn kWh, of which 117 bn kWh of electricity will come from energy crops [15].

Production and production potential of Germany is illustrated in Table 4.

4 Production Potential of Biogas in Sweden

Sweden is a quickly developed country in the production of energy from renewable resources. Approximately 29 % of primary energy supply in the country is from renewable sources.

Biogas industry started to flourish in the years 1950–1970 in Sweden, initially to reduce the amount of sewage sludge. In 2006 in Sweden, there were 223 biogas plants: 138 municipal wastewater treatment plants, 60 plant at the landfills of municipal waste, 3 industrial wastewater treatment plants, 14 co-fermentation and 8 agricultural biogas plants. At present, in Sweden there are 229 biogas plants with

Table 5 Production and production potential of biogas in Sweden

Country	Average total production potential (2010–2011) PJ	Total production (2009) PJ
Sweden	50.4–61.2 (214.8)	4.57

So, the production of biogas is used in 7.5–9.1 % (average value 8.3 %); (2.1 %)

a total biogas production of 1.3 TWh/year. Most of these facilities, as many as 139, are located at municipal wastewater treatment plants. These plants produce almost 43 % of the Swedish biogas [16, 17].

The theoretical potential of biogas production in Sweden is about 14–17 TWh/year (50.4–61.2 PJ/year), representing more than ten times the current production of biogas. Biomasses from agriculture represent the largest part of the potential of biogas. Currently, almost 80 % of the capacity of the agricultural sector remains unused.

The total biogas production in Sweden was 1.2 TWh in 2006 [1.4 TWh (2010)].

In 2006 sewage treatment plants were characterized by the highest of biogas plants—582 GWh, as well as facilities at landfill sites—342 GWh. Co-fermentation plants produced 184 GWh of energy, industrial installations—91 GWh, while farm biogas plants—only 14 GWh.

According to the Swedish Association of Gas the production potential of biogas in Sweden is very large, and reaches of 35–40 TWh/year.

The biogas potential of about 14 TWh is produced in 50 % from crops, mainly biomass from fallow land, in 18 % from livestock manure, and in 7 % from municipal waste, including 7 % of sewage sludge and in 18 % from various other sources (industrial waste, garden waste, etc.). About 26 TWh is derived from biomass gasification of forest and agricultural production.

Production and production potential of Sweden is illustrated in Table 5.

It should be emphasized that the potential for biogas production in these countries is large, even if just for example, 20–25 % of this potential use for the production of biomethane as a fuel buses. In Germany, especially in Sweden, already in use are of this type buses. For example, in Stockholm in 2011, were in service 230 buses powered by biomethane.

5 Ecological Results of Application of Biogas (Biomethane) for Supplying City Buses

Biogas (biomethane) is similar to natural gas but renewable.

Results of research introduce in indicate that [18]:

- currently EEV certified methane buses clearly outperform EEV certified diesel vehicles for NO_x as well as PM,
- methane vehicles provide true EEV performance over time,
- all methane fuelled vehicles deliver very low PM emissions,

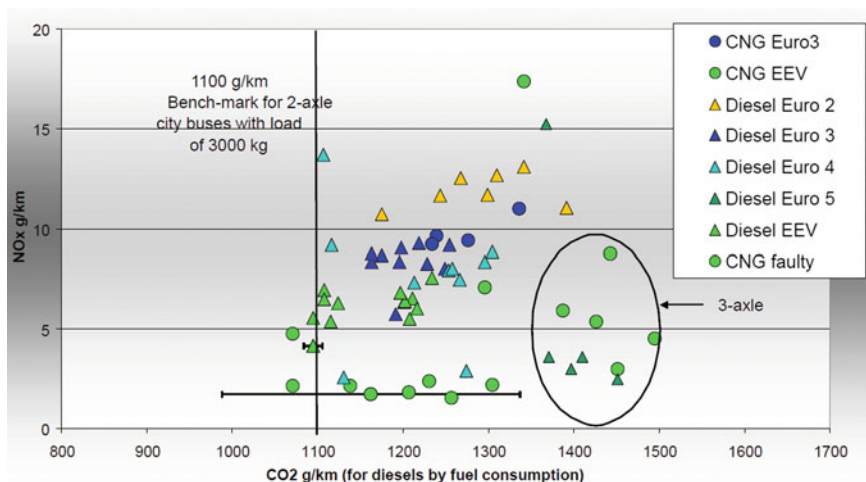


Fig. 3 NO_x and CO₂ emissions over the Braunschweig city bus—cycle [18]

- stoichiometric vehicles deliver lower NO_x and lower fuel consumption,
- clear benefit for methane also for unregulated emissions (PM numbers, aldehydes, PAH, direct NO₂ emissions etc.),
- main drawback of spark-ignited methane compared to diesel is higher energy consumption.

Table 5 presents results of above research of exhaust emissions from EEV buses (diesel and CNG) [18]. Figure 3 indicates that the best diesel and CNG buses have a tailpipe CO₂ emission of some 1,100 g/km [18]. However, it is necessary to remember that biomethane is renewable fuel and therefore CO₂ emission from well to wheel is much smaller in the case of vehicles (buses) powered by biomethane compared to diesel-powered (Table 6).

Our study of exhaust emission was conducted for city buses in Rzeszow (southern Polish city) in the real traffic conditions. Operated in Rzeszow buses (MPK Rzeszow) are characterized by exhaust emission levels not higher than Euro III. These are mainly buses powered by compression ignition (CI) engines, in the number of 148 buses, and powered by spark ignition [including diesel buses retrofitted to CNG buses (lean mixture)]. Posed the question how to change the total exhaust emissions of city buses operated in MPK Rzeszow, if in the process of replacement buses for the new to 2020, about 50 % of buses will be replace to buses powered by CNG (biomethane) engines. It is assumed that the replacement of buses, will be for new design to supply CNG (biomethane) by the manufacturer. They will by comply with the emission standards Euro IV or Euro V. Due to the lack of buses that meet such standards in MPK Rzeszow comparative study was conducted in SORT test using the buses meet Euro V-EEV. Was made comparison of exhaust emission of buses powered by diesel and spark ignition engine (powered by CNG).

Table 6 Exhaust emission from city buses [18]

City bus-cycle	CO g/km	HC g/km	CH ₄ ^a g/km	NO _x g/km	PM g/km	CO ₂ g/km	CO ₂ eqv g/km
Diesel Euro III	0.80	0.14	0.00	8.64	0.195	1189	1189
Diesel Euro IV	2.84	0.10	0.00	8.35	0.112	1194	1194
Diesel Euro V ^b	2.84	0.10	0.00	8.35	0.087	1194	1194
Diesel EEV	1.12	0.02	0.00	5.87	0.062	1116	1116
CNG Euro III	0.14	1.67	1.14	9.36	0.011	1257	1295
CNG EEV	2.27	1.04	0.87	3.18	0.007	1275	1294

^a for diesel CH₄ = 0

^b euro V emission factors are estimated by euro IV results



Fig. 4 MPK Rzeszow route No. 0 (left) and No. 30 (right)

For the evaluation of the mutual correlation of each pollutant emissions from buses powered diesel and CNG, at random were selected MPK Rzeszow bus route occurring in Rzeszow, which was conducted on assessment of pollutant emissions. Research was made on a circular route No. 0 passing direct through center of the city and on route No. 30, which is one of the longest routes of the circulation of buses in Rzeszow. The total number of MPK Rzeszow bus route is 42. The result buses pollutants emissions evaluated on other route show that above selected bus routes are representative of population of MPK Rzeszow bus route. Additionally in Bednary (near Poznan) SORT 1 driving tests were conducted on two buses, diesel and CNG powered engine.

MPK Rzeszow route No. 0 and No. 30 are illustrated in Fig. 4.

View of the on-board mounted unit's of Sensors Inc. company, SEMTECH DS (for test exhaust emission), in the vehicle with diesel engine during emission testing on route No. 0 and bus with CNG engine during testing on MPK Rzeszow bus route No. 0 are illustrated in Fig. 5.

Characteristics of nitrogen oxides emissions in the intervals speed and acceleration of the bus powered diesel engine during road test and characteristics of



Fig. 5 View of the mounted unit's of sensors Inc. SEMTECH DS, in the vehicle with diesel engine during emission testing on route No. 0 and bus with CNG engine during testing on MPK Rzeszow bus route No. 0

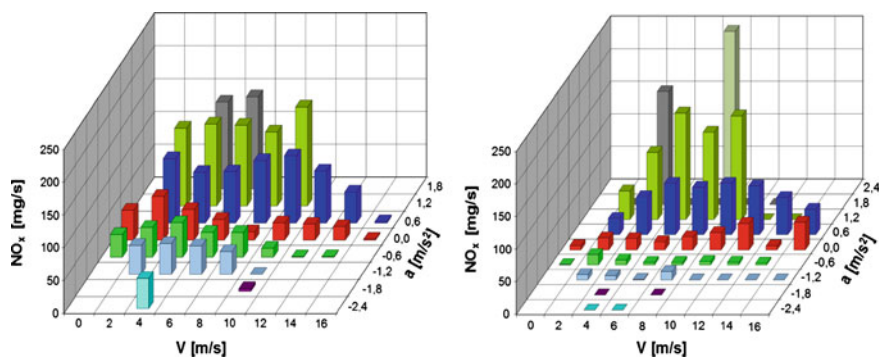


Fig. 6 Characteristics of nitrogen oxides emissions in the intervals speed and acceleration of the bus powered diesel engine during road test and characteristics of nitrogen oxides emissions in the intervals speed and acceleration of the bus powered CNG engine during road test

nitrogen oxides emissions in the intervals speed and acceleration of the bus powered CNG engine during road test are illustrated in Fig. 6.

The road emission of bus tested on MPK bus route No. 30 is illustrated in Fig. 7, however, the road emission values of tested buses in a SORT 1 test is illustrated in Fig. 8.

The highest emissions of CO and THC reached bus powered CNG engine (bus route No. 30). This was caused by work of engine on almost stoichiometric mixture due to the used in the bus three-function catalytic converter.

On the MPK bus route No. 30, bus powered diesel engine has reached the highest average value of NO_x road emissions and lowest average value of CO_2 road emissions. CNG engine powered bus has reached the highest average value of road emissions of THC, which for a bus diesel engine powered was approximately 850 %. This was due to the combustion reaction of natural gas, whose products next to the CO_2 , NMHC and CH_4 .

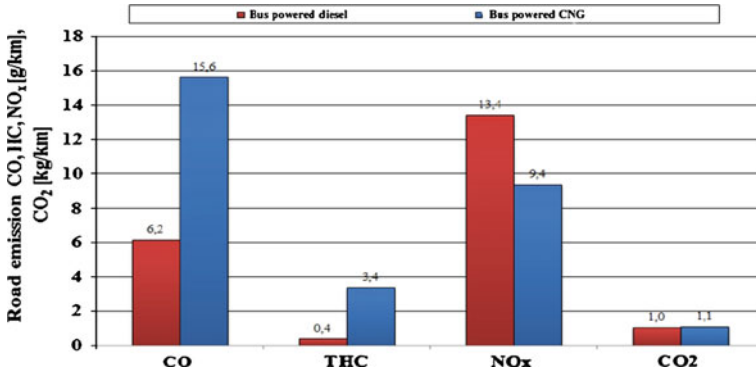


Fig. 7 The road emission of bus tested on MPK bus route No. 30

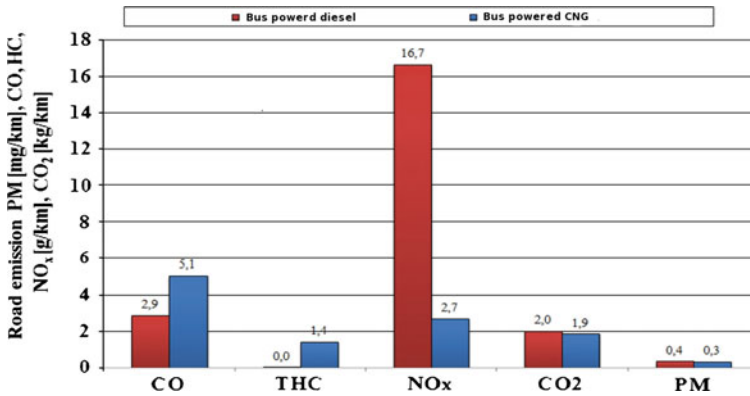


Fig. 8 The road emission values of tested buses in a SORT 1 test

Due to the lack tested buses with a length of 12 m, meet the Euro V-EEV, research in the SORT 1 test was conducted on a buses with a length of 18 m, meet the Euro V-EEV. In order to compare the mean values of road emissions of exhaust pollutants obtained in tests in Rzeszow, to the results obtained in the SORT 1 test determined correction factor, because in both types of vehicles used the same internal combustion engines. The correction factor k is the product of the ratio power/gross vehicle weight and index of resistance movement of the vehicle. The value of k was 2.04. This value was divided by the average values obtained for the road emissions of buses with a length of 18 m in the SORT 1 test.

The relative value of the total road emission of buses after the MPK Rzeszow fleet modernization (replacement of 40 buses powered spark ignition engines [CNG] and 54 buses powered diesel engines) by buses with spark ignition (CNG) complying with Euro V-EEV emission standard is illustrated in Fig. 9.

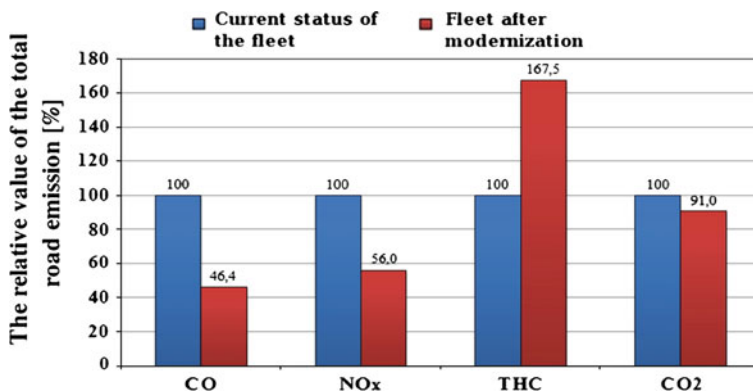


Fig. 9 The relative value of the total road emission of buses after the MPK Rzeszow fleet modernization [replacement of 40 buses powered spark ignition engines (CNG) and 54 buses powered diesel engines] by buses with spark ignition (CNG) complying with Euro V-EEV emission standard

The largest increase will occur on the total road emissions of THC (60 %). Will only reduce the total road emissions of NO_x, which will constitute approximately 90 % of the total road emissions of vehicles powered by diesel engines.

Would be most advantageous conversion of half the fleet of buses (40 buses powered spark ignition engines [CNG] meeting the Euro III emission standard and 54 buses powered diesel engines) by buses powered spark ignition engines (CNG) meeting the Euro V-EEV emission standard.

This type of upgrade would reduce the total road emission mainly CO₂ by about 10 %. Will also significantly reduced total road emissions of CO and NO_x, respectively 54 % and 44 %. However at a higher level will remain the total road emission THC, which in relation to the current status, will be about 170 %.

6 Conclusions

The EU 20-20-20 climate and energy goals can be summaries as follows:

- reduction greenhouse gas emissions at least by 20 % up to 2020,
- improving the EV's energy efficiency by 20 % up to 2020,
- increasing the share of renewable energy up to 20 % in 2020, in particular a 10 % share of renewable energy in the transport sector.

The new transport White Paper recommends an ambitions target of 60 % reduction of greenhouse gas emissions from transport up to 2050 in comparison to 1990. In this publication is forecasted that biomethane will be alternative road transport fuel for passenger/light duty cars, heavy duty (city) vehicles and heavy duty (long distance) vehicles in short term period (2020), mid term period (2030)

and long term period (2050—only for passenger/light duty cars and heavy duty [city] vehicles) [19]. Prospect of application of biogas (biomethane) as a vehicle fuel (fuel for city buses) is significant.

References

1. Directive 2003/30/EC: Official journal of the european union L123/42, 17.5.2003
2. Biernat K, Dziołak P, Gis W, Zółtowski A : Desk study on wider range of biogas production options and experiences including production potential scenarios for the Baltic Sea Region. Baltic Biogas Bus Project
3. Biernat K (2007): New technologies biocomponents and biofuels first and second generation. International conference: the quality of fuels in Poland and the European Union. Warsaw
4. Petersson A (2010): Overview of upgrading technologies. Nordic biogas conference
5. Beyer J, Brown B: Terracastus technologies. Technology for cleaning and upgrading biogas, www.businessregion.se
6. Directive 2009/28/EC: Official journal of the european union L 110/16, 5.6.2009
7. Map of renewable energy sources, developed by studies the energy regulatory office: <http://www.ure.gov.pl/uremapoze/mapa.html>
8. Ministry of agriculture and rural development (2009) Assumptions biogas development program. Program “innovative energy, agriculture energy”. Warsaw
9. Development under the title residue biomass potential inventory results (Deliverable D5.01.03) in project renewable fuels for advanced power-trains (RENEW)
10. Obtaining biogas from municipal waste, editors agroenergetyka.pl. <http://agroenergetyka.pl/?a=article&idd=149>
11. Environmental protection (2008) Central statistics office, information and statistical studies, Warsaw
12. Production of biogas from waste water treatment plants, editors aeroenergetyka.pl: <http://agroenergetyka.pl/?a=article&id=529>
13. Biogas Basisdaten Deutschland (2010), stand: Juni
14. Bundesministerium für Ernährung, Landwirtschaft und Verbraucherschutz, Fachagentur Nachwachsende Rohstoffe e.V., Biogas Basisdaten Deutschland, Stand: 2009
15. German society for sustainable biogas and bioenergy utilization GERBIO, national report on current status of biogas and biomethane production of “GasHighWay” project (IEE/08/545/SI2.528537)
16. Dahlgren S, Swedish biogas association and Swedish gas association, Biogas state of the art: Sweden
17. Avfall Sverige—Swedish waste management 2009
18. Nylund Nils-Olof (2010) Environmental benefits with biogas buses, Nordic biogas conference Oslo, 10–12
19. European alternative fuel strategy in the clean transport system interactive. JEG “transport & environmental”

High-Concentration Ethanol Fuels for Cold Driving Conditions

Juhani Laurikko, Nils-Olof Nylund, Jari Suominen
and Mika P. A. Anttonen

Abstract VTT has together with the Finnish energy company St1 tested different high-volume ethanol fuel (E85) samples in order to find the optimum composition for this fuel to perform satisfactorily in low ambient temperature driving conditions encountered in Finland quite frequently during the winter season. Altogether seven different fuel compositions were evaluated, with 70–85 % of anhydrous bioethanol, and various different mixes of regular petrol components and some specific species like ETBE, butane, iso-butanol etc. As a reference, new Euro-quality 95E10 petrol with 10 % ethanol was used. Fuel vapour pressure of each sample was adjusted according to test temperatures to match summer or winter condition and ensure effortless start-up. Test results showed that the composition of the fuel had marked influence on emissions. The lower the test temperature was, the more distinctive were the differences. Based on the results, about $-15\text{ }^{\circ}\text{C}$ would be the lower limit of operation with “straight” E85 mixture composed ethanol and petrol. On the other hand the more “engineered” fuels performed much better, and allowed starting as low as at -20 to $-25\text{ }^{\circ}\text{C}$. Cold start and driving was possible at equal level of unburned hydrocarbons and other unwanted emissions (aldehydes, ethanol) at an ambient temperature more than $10\text{ }^{\circ}\text{C}$ lower compared to “straight” E85 fuel.

Keywords E85 · Cold ambient conditions · Fuel composition · Exhaust emissions · Waste-to-fuel

F2012-E14-032

J. Laurikko (✉) · N.-O. Nylund
VTT Technical Research Centre, P.O. Box 1000FI-02044 VTT, Espoo, Finland
e-mail: juhani.laurikko@vtt.fi

J. Suominen · M. P. A. Anttonen
ST1 Biofuels Oy, P.O. Box 100FI-00381, Helsinki, Finland

1 Introduction

Use of renewable resources for transport energy supply is an opportunity to lower carbon emissions and increase energy security and diversity. However, it is by no means an easy and straightforward act, as many types of challenges need to be overcome before a successful implementation. Ethanol is today the most-used biofuel in transportation, if measured by the volume of use. Most of the ethanol is blended into regular petrol at 5–10 % concentrations depending on the market area and fuel legislation. But even 10 vol % of ethanol is less than 6 % of energy contents. Therefore, higher concentrations are needed to meet the targets.

Fuel-flexible vehicles (FFVs) present an excellent route to raise the share of ethanol amongst the petrol-fuelled fleet, as much higher ethanol concentrations are possible, up to 85 %. The technology is also quite well established and supported by multiple manufacturers. Because the rate of technical upgrade is also fairly modest compared to a regular petrol-fuelled car, the associated costs are quite marginal, as well, and in many cases an FFV option can be offered at a price equal to a regular model.

2 Target and Objectives

Blending ethanol to petrol is currently limited to 10 vol % by the current EU Fuels Quality Directive 2009/30/EC [1]. As ethanol has lower energy density than petrol, this yields only to some 6 % energy contents. When the sales started in January 2011, the share of the 95E10 fuel was estimated to reach over 70 %, based on the analysis of the compatible makes and models in the Finnish car park. However, currently only about half of the petrol cars in Finland are using the 95E10-grade. The rest use the 98E5-grade for the sake of incompatibility of the car, or because of the motorists being deterred by stories how the higher ethanol content can damage the car. Even if most of these stories are just “urban legends”, the sales volumes have not reached the anticipated levels yet, and probably will not ever meet the estimated level. Therefore, it will not be possible to reach more than 5 % energy share with low-blend grades only.

In order to raise the use of ethanol amongst petrol-fuelled cars, dedicated FFV-technology is needed. In view of creating more “surge” for the bioethanol, a Finnish energy company St1 teamed with some car importers to initiate marketing of FFV-cars in Finland. Subsequently, Ford, Volvo and Saab were the first to start selling FFV’s, and at the moment a few more marqueses have joined in, including Dacia, Chrysler, Volkswagen and Audi.

The fuel was produced by St1 using ethanol derived from special processes belonging to the company’s “Waste-to-Ethanol” concept that has a record-low carbon footprint per litre ethanol produced. The key elements are using waste and industrial side streams as feedstock, and apply new energy efficient processes and

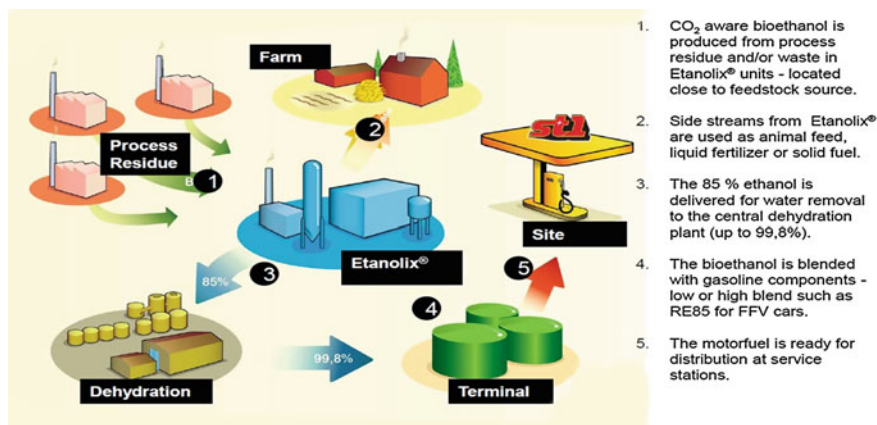


Fig. 1 Schematic overview of the Etanolix™ bioethanol production process by St1

technology, combined with small-scale initial production phase to minimise transportation of material. Figure 1 shows the schematics of this unique Etanolix™ concept with six plants now in operation. Next step was to make use of household-based bio-waste, based on a different process called Bionolix™. Those plants are slightly bigger in size, and first plant using this technology was started in 2010. However, bio-waste alone does not hold enough potential, so cellulose-based processes are needed. Development of the first Cellunolix™ plant using cardboard and other similar packaging material from household, as well as from industry and retail sector is already underway. More of this portfolio of processes can be found e.g. from an on-line article [2].

To differentiate that the ethanol for this fuel was made from renewable material, it was labelled “RE85”. For the first two years (2009–2010) fuel refilling was limited to Metropolitan Helsinki area with six stations only, but nowadays the network is expanding quite rapidly all over the country. At the moment there are over 50 stations and new ones are added each month.

Concurrent with initiating the market, a research project with VTT was started to support problem-free operation of FFV-cars using fuel with as high ethanol contents as possible. The target and objective of this research was to choose best composition for the fuel in terms of startability and exhaust emissions even at the coldest ambient conditions.

3 Test Procedures

3.1 Test Fuels and Temperatures

During the test series, altogether seven different fuel compositions were evaluated. They consisted of 70–85 % of anhydrous bioethanol, and various different mixes

Table 1 Total test matrix

Fuel	Test cell ambient temperature(°C)					Cars #	
PA1	+23	−7				3	
PA2	+23	−7				3	
PA3	+23	−7				7	
PA3T			−15	−20	−25 ^a	−25 BH ^b	3
PA5			−15	−20	−25		3
PA7		−7		−20	−25	−25 BH ^b	3
E10K	+23	−7					5
E10T		−7			−25		3
PA3w	+23	−7					2

^a Did not start

^b BH block heater for 2 h

of regular petrol components, as well as some specific species like ETBE, butane, iso-butanol etc. As a reference, new Euro-quality petrol (95E10) with 10 % ethanol was used. Fuel vapour pressure of each sample was adjusted according to test temperatures to match summer or winter condition and ensure effortless start-up.

Test matrix was composed of several ambient temperatures and selection of test cars for each fuel composition. Over 150 test runs were completed in total, producing a very in-depth and thorough material for assessing and comparing the performance of the fuels, as well as the cars, in all ambient conditions relevant to Finland and other Nordic countries.

Table 1 comprises the entire test programme, where each test run was repeated for added quality of the data. In Table 1 fuel “PA3” and “PA3T” denote the same fuel mixture with slightly different RVP for summer/winter conditions. Fuel “PA2” is a “straight-mix” with 85 % of ethanol and 15 % of regular RON95 petrol, which is the usual composition of E85 fuel around the world, where it is in use. “PA1”, “PA5” and “PA7” are mixes with 70–75 % ethanol, and were targeted towards better running in very low temperatures.

Subsequently, “E10x” were normal petrol with 10 % ethanol according to the latest EU Fuels Directive and the anticipated update in EN228 petrol standard. Again, letters “K” and “T” denoted summer and winter grades with different volatility. Table 2 gives break-down of the test fuels to their components.

4 Test Fleet

Test fleet consisted of six different fuel-flexible FFV cars. Of those four were type-approved according to Euro 4 emissions regulation, and two represented the newest technology complying with Euro 5 requirements. The Euro 4 fleet consisted of Ford Mondeo 2.0 Zetec Flexifuel, Saab 9-3 1.8t BioPower, Volvo V70 2.5 FT DRIVE and Dacia Sandero 1.6 HiFlex. The two Euro 5 compliant models were Volkswagen Passat 1.4 TSI Multifuel and Audi A4 2.0 TFSI, both with

Table 2 Composition of the tested fuel mixtures

Test fuel	PA1	PA2	PA3	PA3T	PA3w	PA5	PA7	3F95
Petrol, MK1		9.6 %	18.6 %	1.0 %	17.7 %	21.6 %	2.0 %	n/a
Ethanol	70.0 %	85.0 %	80.0 %	75.0 %	76.0 %	75.0 %	75.0 %	n/a
ETBE	25.0 %	2.0 %	1.0 %	0.0 %	1.0 %			n/a
Butane	4.6 %	3.0 %		3.0 %		3.0 %		n/a
iso-butanol	0.4 %	0.4 %	0.4 %	0.4 %	0.4 %	0.4 %	0.4 %	n/a
n-pentane							22.6 %	n/a
Water	<0.5 %	<0.5 %	<0.5 %	<0.5 %	5 %	<0.5 %	<0.5 %	n/a
Keroflux ^a (ppm-vol)	200	200	200	200	200	200	200	n/a
Colorant (ppm-vol)	20	20	20	20	20	20	20	n/a
Total	100.0 %	100.0 %	100.0 %	79.4 %	100.0 %	100.0 %	100.0 %	100.0 %

^a Denaturalizer

Table 3 Test vehicles and dynamometer settings

Make	Volvo	Saab	Ford	Dacia	Audi	VW
Model	V70	93 1.8t	Mondeo	Sandero	A4 TFSI	Passat
Model year	2009	2009	2009	2010	2011	2011
Euro level	EU4	EU4	EU4	EU4	EU5	EU5
Displacement (dm ³)	2.5	1.8	2	1.6	2	1.4
Curb weight (kg)	1,667	1,530	1496	1,111	1,570	1,557
EC combined CO ₂ (g/km)	232	177	189	170	149	144
Dynamometer settings						
Inertia (kg)	1,700	1,500	1,500	1,130	1,557	1,557
F0	33	69	8	6	61	61
F1	-0.1613	1.3505	0	0	1.596	1.596
F2	0.03588	0.02287	0.0294	0.0433	0.0223	0.0223

similar direct-injection combustion technology. The cars were 2009–2011 models, with reasonable low mileage, and were provided for this test by their importing agencies, whom we owe our gratitude. Table 3 gives some data of the cars and lists dynamometer settings used in test runs.

5 Test Set-Up and Procedures

The light-duty vehicle test facility at VTT allows the measurement of exhaust gas composition and fuel use according to regulatory procedures. In addition, determining some non-regulated emissions like aldehydes and ethanol is also possible with both on-line FTIR, as well as traditional sampling and wet chemistry route using DNPH cartridges or water impinger for sampling and HPLC for analysis. Figure 2 shows a set of these instruments.

Fig. 2 In addition to regulated emissions, measurement apparatus at the test cell allows measurements of several non-regulated emission species like aldehydes and ethanol



Subsequently, the control of the ambient temperature in the test cell is possible to $-30\text{ }^{\circ}\text{C}$. However, as quite seldom so low temperatures do occur, we limited our test series to $-25\text{ }^{\circ}\text{C}$. Notwithstanding, intermediate temperatures were also used, in particular $-7\text{ }^{\circ}\text{C}$, because with the incoming Euro 6-requirements FFV-cars need to comply also with the cold-start “Type VI” test performed at that temperature. Still today, when Euro 5 is implemented, emissions performance of an FFV-car is only tested at normal ambient conditions.

The actual testing was performed in essence by following the legislative procedure according to ECE-R83/05 regulation with the exception that ambient temperature was varied, as already mentioned. In addition, the sampling and analysis was split not only between the urban and extra-urban parts of the driving cycle, but splitting even the ECE15—cycle to two parts, where the 1st part was the first two sub-cycles, and the 2nd part was the latter two. This way we could see more accurately, how the emissions performance progressively changed over the cycle. Especially at low temperatures the domination that the cold start and subsequent one to two kilometres of driving have on the total performance is very clear.

Figure 3 depicts the test cell and shows the associated connecting tubes that needed to be properly insulated and electrically heated in order to avoid condensation of water before mixing point at low ambient temperatures. This is highly necessary, as combustion of ethanol produces a lot more water vapour than pure hydrocarbon fuels. The pictured car was not part of this test campaign, though.

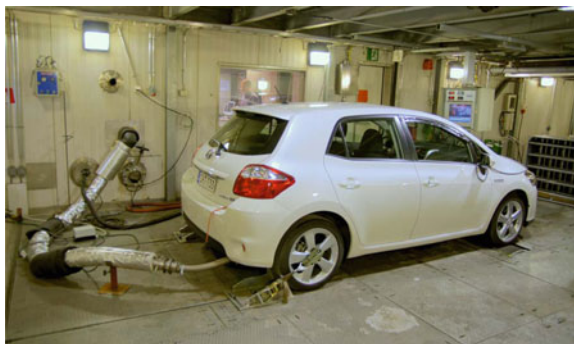


Fig. 3 Test cell at VTT allows measurements at low ambient temperatures down to $-30\text{ }^{\circ}\text{C}$. Thus, exhaust gas collection set-up with insulated and heated connecting tubes must be used to avoid condensation of the water contained in exhausts from high ethanol content fuel

5.1 Results and Discussion

5.1.1 Regulated Emissions

Tests at Normal Ambient Temperature

Figures 4, 5 and 6 depict emissions of each test car with different test fuel at normal ambient temperature, as well as an average for all the cars using that fuel.

As we can see from Fig. 4, even if those EU4 type approved cars did not need to comply with the CO limit value other than with petrol, with the RE85-formulation (“PA3”) all cars were capable of meeting this requirement. However, this was not the case with normal E85 (“PA2”). Neither was this possible with “PA1” fuel.

Notwithstanding, regarding total hydrocarbons (HC), according to Fig. 4 it was not possible for any EU4 test car to meet the limit value with any of the tested fuel compositions. However, the RE85-formulation (PA3) gave an average value about 30 % less than what was measured with normal E85. In some cars this difference was even higher in favour for RE85. Furthermore, both EU5 cars were meeting the standard also with RE85, and even if the test matrix did not include regular E85 for these cars, the margin with RE85 suggests that also with normal E85 those would pass the limit.

Clearly, according to Fig. 6 NO_x-emissions were not an issue for these FFV-cars. Only one car exceeded the limit value, and in many cases tests with RE85 resulted to smaller emissions than with petrol (E10).

Tests at Low Ambient Temperature

Since 2002 EU-legislation includes also limit values for emissions in a special cold-temperature, cold-start test called “Type VI test”. It comprises a test run at $-7\text{ }^{\circ}\text{C}$ test cell ambient, and use only the urban part (ECE15) of the European

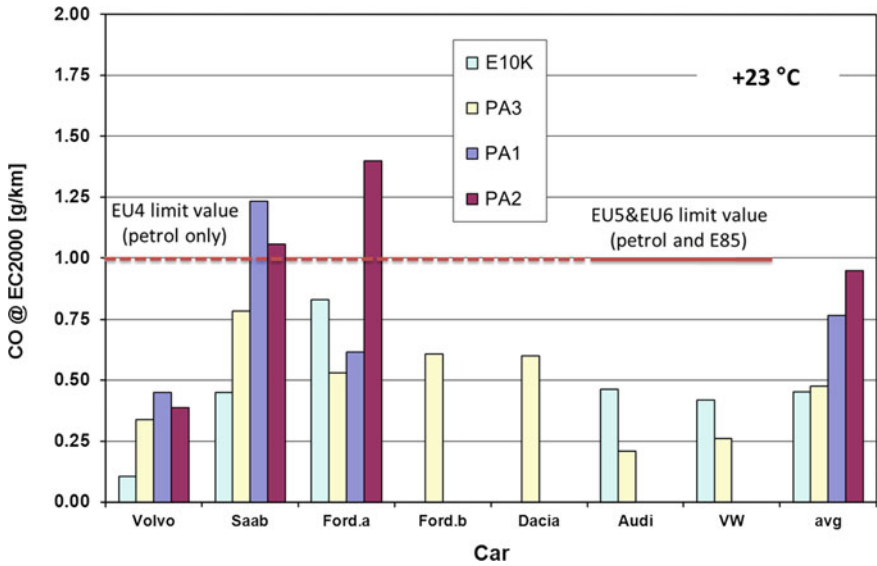


Fig. 4 CO emissions in combined EU-test at +23 °C with different cars and fuel formulations

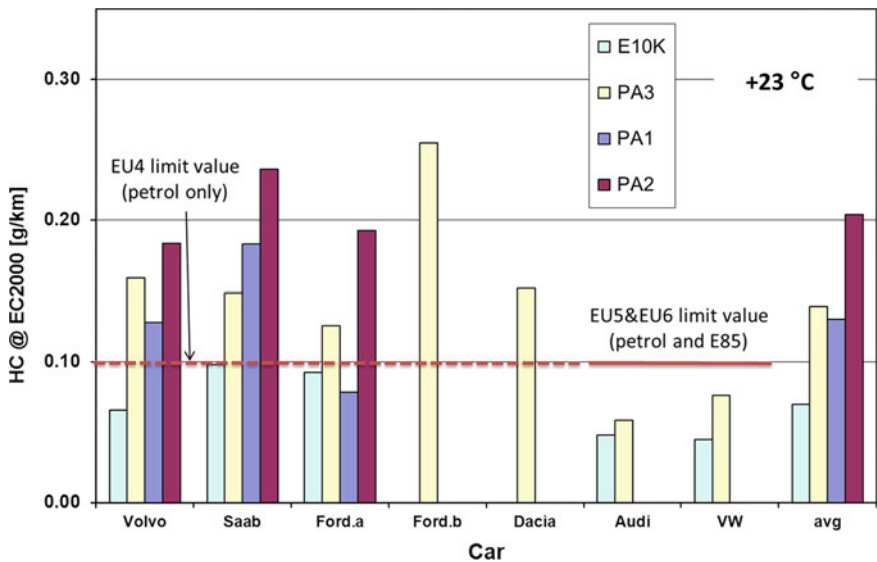


Fig. 5 HC emissions in combined EU-test at +23 °C with different cars and fuel formulations

duty cycle. Limit values are set for CO and HC, as NOx has not been seen as a matter of concern in this context.

Figures 7, 8 and 9 depict emissions measured according to this “Type VI test” procedure, even if we must bear in mind that this part of the type approval is not

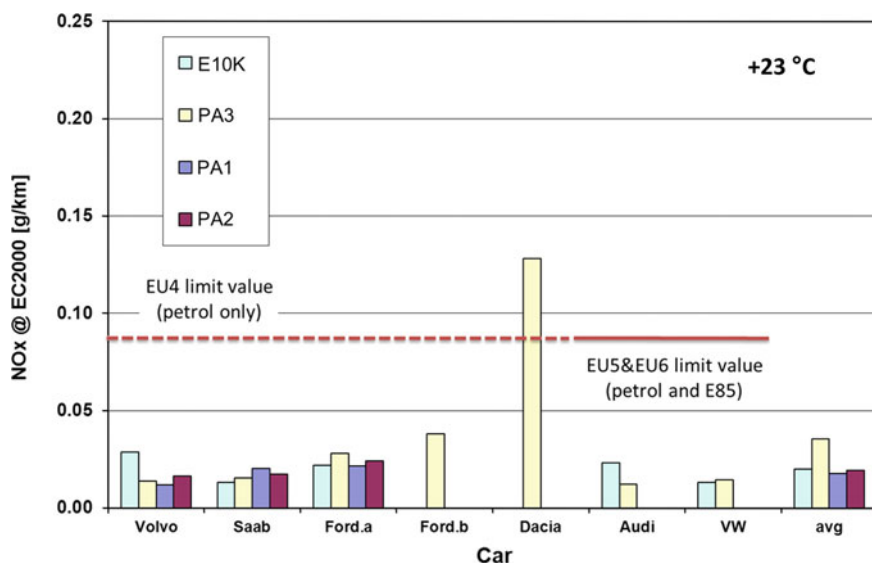


Fig. 6 NOx emissions in combined EU-test at +23 °C with different cars and fuel formulations

yet necessary for FFV-cars other than with petrol. However, it is already decided that for EU6 type approvals, FFVs need also to be tested using high ethanol content fuel, but in this application the test fuel will be limited to 75 % of ethanol and not the usual 85 %.

As Fig. 7 shows, meeting the current CO limit value (15 g/km) is not particularly hard for these FFV cars, even if this test is not yet mandatory for them. On average only one test fuel (“PA1”) resulted in emissions higher than the limit value, and mostly the responses were on par with results for normal E10-petrol.

On the other hand, Fig. 8 clearly shows that unburned hydrocarbons (HC) are a weak point of this concept. Certainly, this was no surprise, because when ambient temperature falls, fuel evaporation also becomes more difficult. Subsequently, this leads to failures in the ignition of the charge, and produces irregularities in combustion. This in turn is seen as increased HC-emissions, when the engine is still below normal running temperature. However, this phenomenon has a very the transient nature, because those high emission rates are quickly lowered, when the engine and emission control systems reach their normal running temperatures.

As a proof that this really happens, hydrocarbon emissions released during the extra-urban part (EUDC) of the complete European test are illustrated in Fig. 10. From this Figure we can clearly note that even if the emissions rates are higher for fuels having high ethanol contents, the rate is only about 10 % or less of the level encountered during the first few kilometres of driving. Unfortunately, in many cases drivers do not necessarily always continue driving for more than a few kilometres, so proportionally, emissions during the first kilometres do account more.

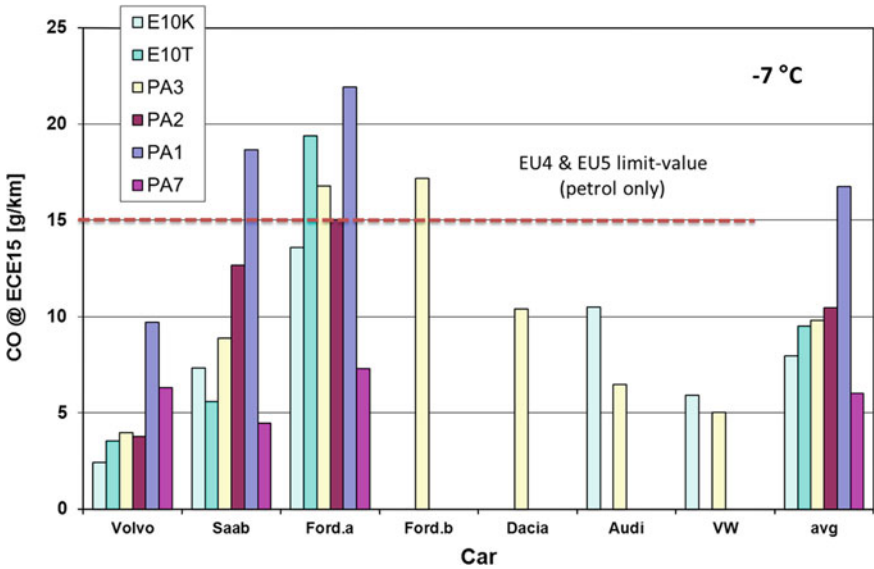


Fig. 7 CO emissions in ECE15-test at $-7\text{ }^{\circ}\text{C}$ with different cars and fuel formulations

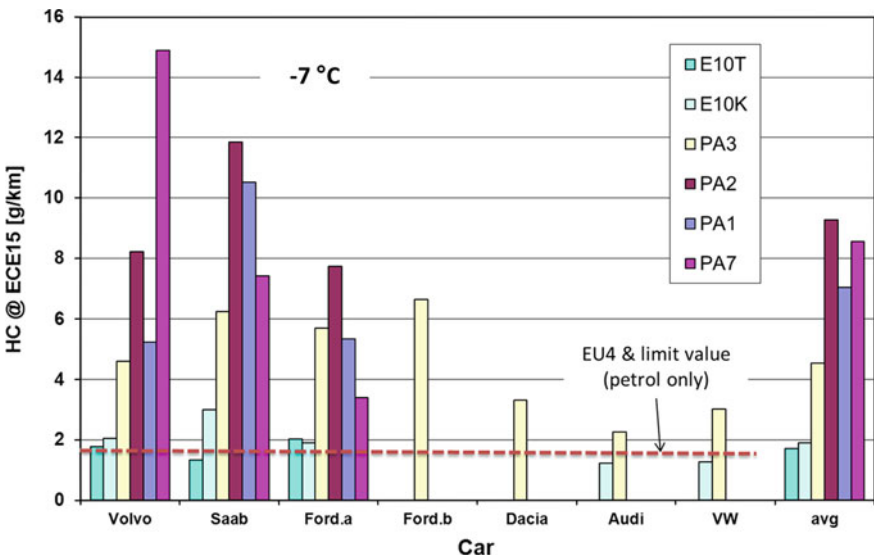


Fig. 8 HC emissions in ECE15-test at $-7\text{ }^{\circ}\text{C}$ with different cars and fuel formulations

Furthermore, it might be worth denoting that according to Fig. 9, emissions of NO_x are actually lower when using fuels with high contents of ethanol, as these two emission components seem to have almost a mirror-like behaviour.

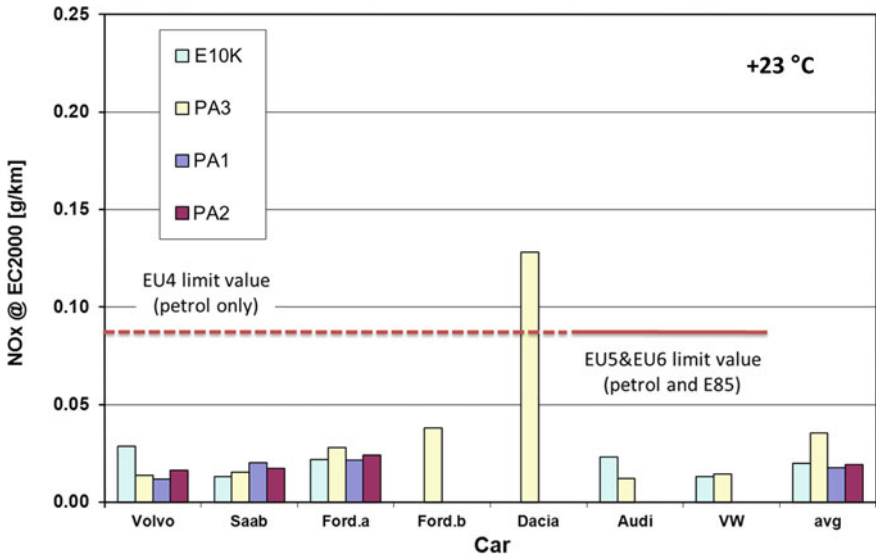


Fig. 9 NOx emissions in ECE15-test at $-7\text{ }^{\circ}\text{C}$ with different cars and fuel formulations

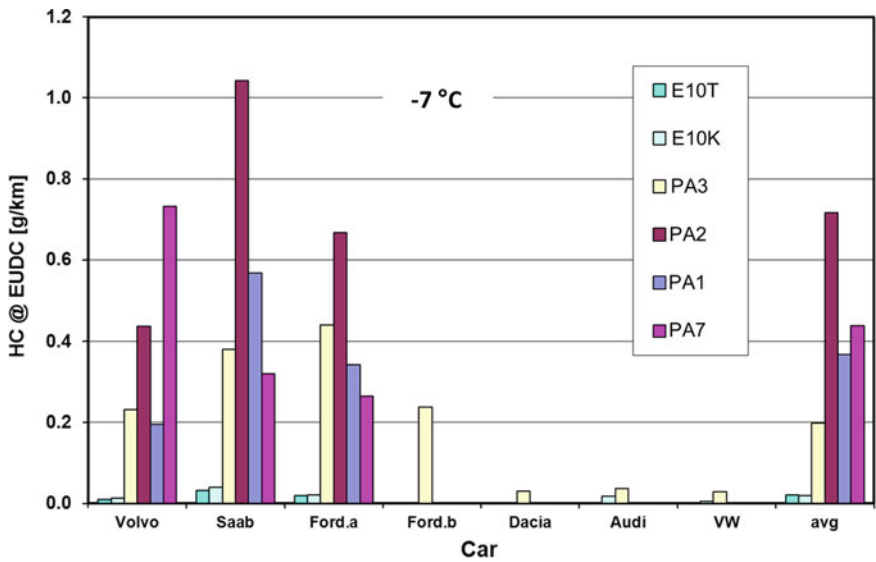


Fig. 10 HC emissions in EUDC cycle at $-7\text{ }^{\circ}\text{C}$ with different cars and fuel formulations

The Effect of Ambient Temperature on Emissions

Figures 11, 12 and 13 depict emissions released during the first two initial cycles of ECE15 as a function of ambient temperature with different fuel formulations.

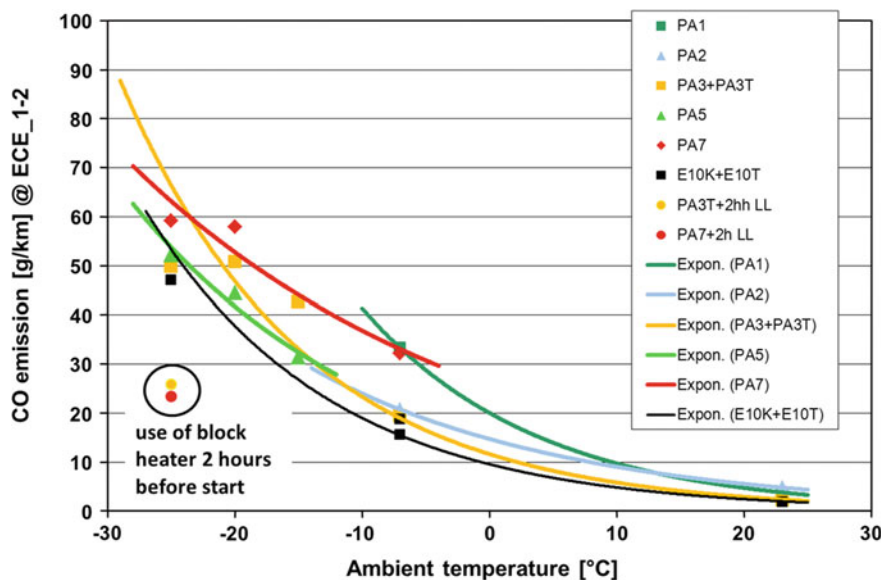


Fig. 11 Average CO emissions in first two initial cycles of ECE15 as a function of ambient temperature with different fuel formulations (2 h LL = 2 h of block heater use)

Each result is an average of two to seven cars, depending on the test fuel. In each figure, the results acquired at $-25\text{ }^{\circ}\text{C}$ using the block heater for two hours before start-up are also plotted.

As we can see from these Figures, lowering of the ambient temperature increases emissions no matter what fuel is used. With CO, depicted in Fig. 10, the increase has about the same magnitude even with normal petrol qualities that have only 10 % ethanol. However, regarding total hydrocarbon emissions, the fuel formulation has an important role to play. Compared to the normal E85 formulation (“PA2”), the optimised RE85-fuel (“PA3”) shows much lower emission rates at equal ambient temperature. Subsequently, this means that with RE85-formulation, cars can operate at lower ambient temperature, about $10\text{ }^{\circ}\text{C}$ or more, with equal HC-emissions compared to normal E85.

Furthermore, with the cold-optimised test fuels (“PA5” and “PA7”), this “leverage” is even higher. However, because those formulations had less ethanol (75 %), it was decided that commercially available RE85 fuel will have the 80 % ethanol contents most of the year, and the remainder is adjusted for good startability.

5.1.2 Non-regulated Emissions: Ethanol, Acetaldehyde and ETBE

The test procedures included also determination of some non-regulated emission species. Key components in terms of high ethanol containing fuel are probably unburned ethanol and acetaldehyde, which is its impartial combustion product,

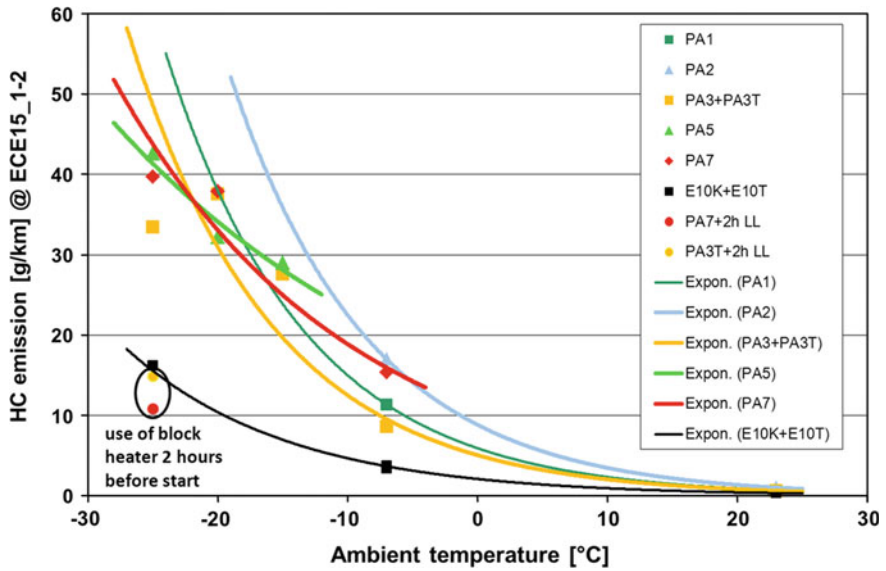


Fig. 12 Average HC emissions in first two initial cycles of ECE15 as a function of ambient temperature with different fuel formulations (2 h LL = 2 h of block heater use)

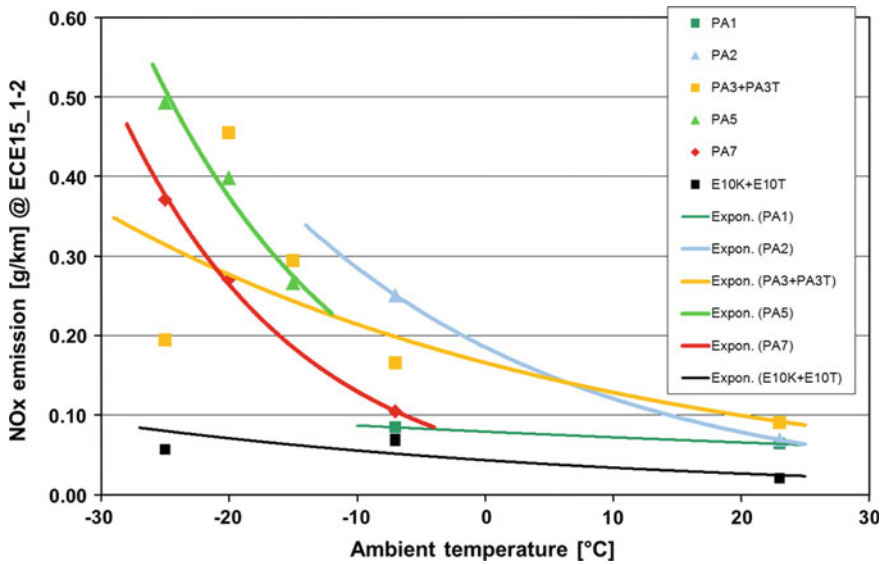


Fig. 13 Average NOx emissions in first two initial cycles of ECE15 as a function of ambient temperature with different fuel formulations

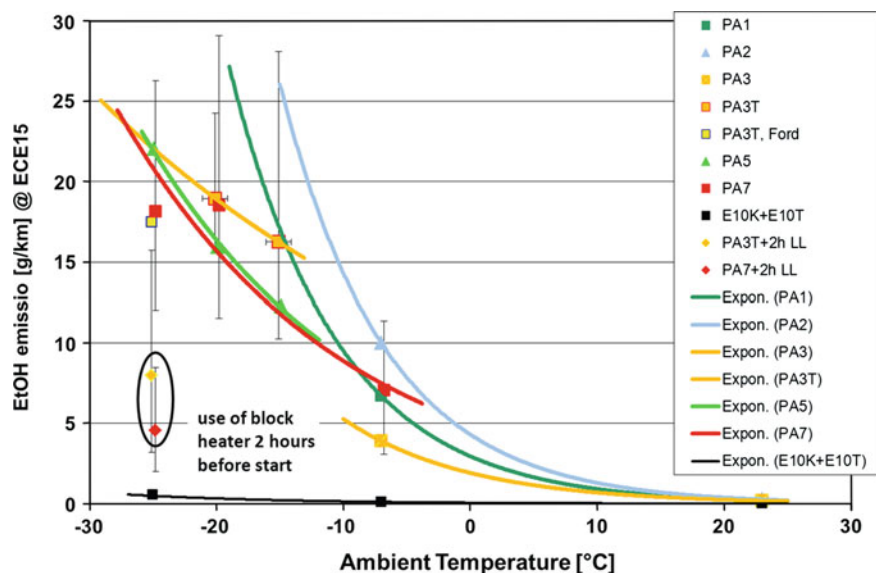


Fig. 14 Average ethanol emissions in ECE15 cycle as a function of ambient temperature with different fuel formulations

as well as ETBE, which is a major constituent in the non-ethanol part of the fuels. Figures 14, 15 and 16 depict the amounts of these emissions during the ECE15 cycle as a function of ambient temperature with different fuel formulations. Each emission vs. temperature result is an average of two to seven cars, depending on the test fuel. As an indication of the spread of results between cars, “high-low” bars are also shown for each average data point. Furthermore, in all Figures, the results acquired at $-25\text{ }^{\circ}\text{C}$ using the block heater for two hours are also plotted.

As we can see from the Figures, overall the plotted trendlines are quite similar to the corresponding trend-lines for total hydrocarbon emissions, which is quite natural. Most striking difference is probably seen in terms of ETBE, as the ETBE concentration has disproportionally high variations between test fuel formulas. Test fuel “PA1” had the highest ETBE concentration, 25 %, whereas the other test formulas did not contain any of it, or only about 1–2 %.

Admittedly, Figs. 14 and 15 show that the ethanol and acetaldehyde levels measured at ambient temperatures below $-10\text{ }^{\circ}\text{C}$ are in some cases quite high. In the “worst case” some 2.5 % of the ethanol that is fed into the engine is released unburned. But as already referred in case of total-HC emissions, this performance is highly transient, and these high concentrations are related only to the first few kilometres of driving. Of the HC release over the ECE15 cycle, typically more than 90 % is already coming from the first half of the cycle, and the same is true for ethanol and acetaldehyde, too. Thus, their impact in total emissions remains quite modest. Also those utmost low temperatures are encountered only a few days

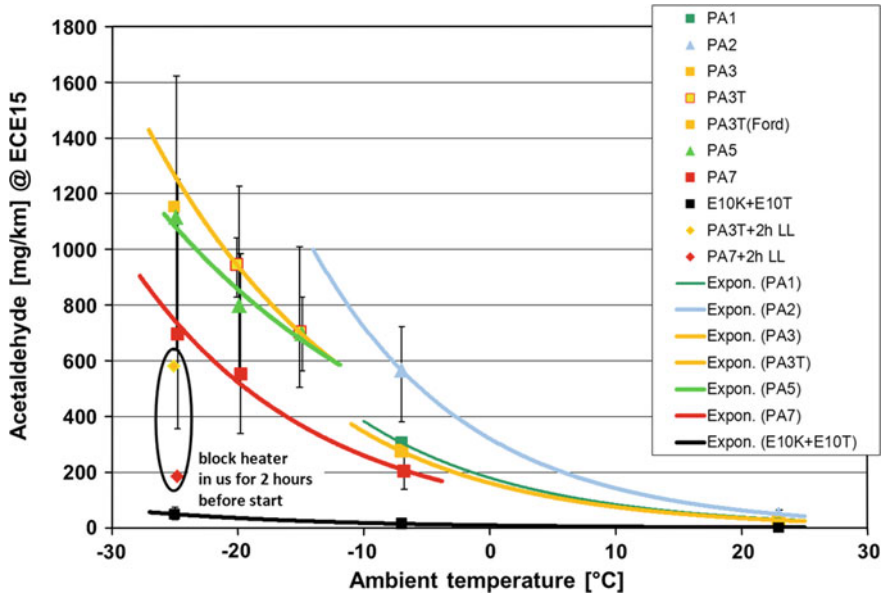


Fig. 15 Average acetaldehyde emissions in ECE15 cycle as a function of ambient temperature with different fuel formulations

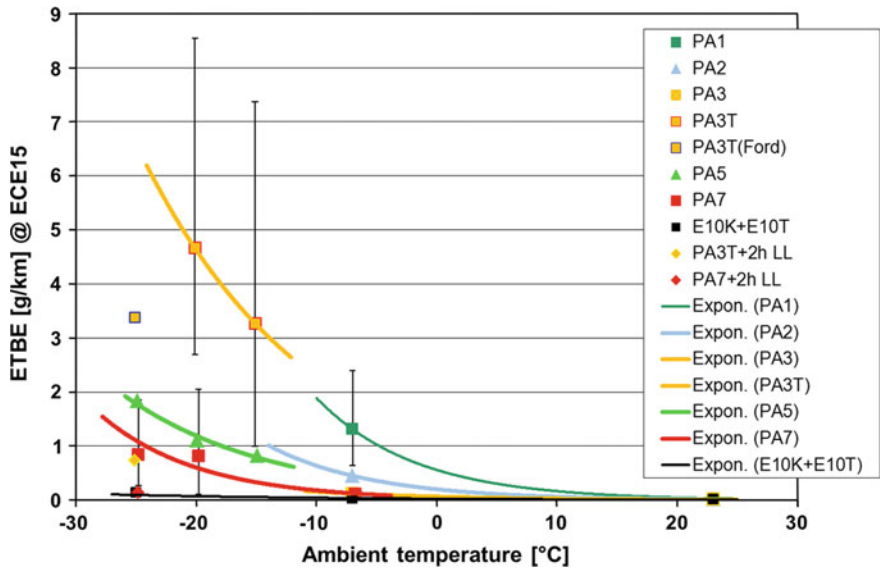


Fig. 16 Average ETBE emissions in ECE15 cycle as a function of ambient temperature with different fuel formulations

a year, at least in those southern parts of Finland, where the majority of the population living.

Our tracking of ambient temperatures around Helsinki Metropolitan Area in another research project resulted in a conclusion that roughly three months (90 days) of the year the ambient temperature in the morning is below zero. Subsequently of this period about a month (30 days) we see temperatures around or below -10 °C. Furthermore, only for a few days, less than a week, ambient temperature drops below -20 °C. We can also claim that it is not possible to drive more than 10 km of the daily driving with cold-started cold engine, even if one makes several short cold-started trips per day. Thus the total impact of these elevated emissions levels falls down to an increase that is on average less than 15 % of the annual emissions.

Our non-regulated analysis entailed also several other species of aldehydes and ketones, e.g. formaldehyde, acrolein, propionaldehyde, crotonaldehyde and methyl-ethyl-ketone. However, their concentrations remained in all cases below 5 % of the corresponding acetaldehyde level. Therefore, we have not included any further analysis of their responses in this paper.

6 Conclusions

The results from the series of tests conducted using different fuel formulations and a batch of FFV-cars showed that indeed, the composition of the fuel has an effect on the emissions output. Furthermore, we were able to substantiate that the effects are not only related to the ethanol contents of the mixture, but it is possible by choosing the composition of the “non-ethanol” portion to affect positively to the levels of emissions. Therefore, the formula chosen for the commercial fuel “RE85” resulted to better performance than the “industry-standard” formula for E85.

Even if we also demonstrated that low ambient temperatures have an increasing effect on emissions, we have also constituted that this phenomenon has a highly transient nature. High levels of emissions occur only for those first few kilometres after a cold start in cold conditions. Once the engine the warms-up and the emission control systems reach their full performance, levels of emissions drop to a low or at least reasonable level. According to our observations, this happens in two to four kilometres even at the lowest ambient temperatures included in our study (-25 °C). Therefore, the total impact of these high levels remains modest, say below 15 % on average, of the total annual emissions.

Acknowledgments This work has been conducted within the framework of “TransEco”, a Finnish national re-search programme on energy efficiency and renewable energy in transportation.

The Finnish Ministry of Trade and Employment has granted the majority of the funding, which the authors gracefully acknowledge.

The authors would like also to express their gratitude to the car importing agencies and companies that have kindly supported this work by lending vehicles for testing with no financial compensation.

Last but not least the team at VTT that has conducted the numerous experiments at sometimes very harsh cold conditions deserves our acknowledgements. So, Reijo Mikkola, Tommi Hangasmaa, Erkki Virtanen, Päivi Koponen and Pekka Piimäkorpi—your efforts are duly acknowledged.

References

1. Directive 2009/30/EC of the European Parliament and of the council <http://eur-lex.europa.eu/LexUriServ/LexUriServ.do?uri=OJ:L:2009:140:0088:0113:EN:PDF>
2. Savolainen R, Driving on waste, HighTech Finland (2010) <http://www.hightech.fi/direct.aspx?area=htf&prm1=861&prm2=article>

The Effects of Intake Valve Closing Timing on Engine Performance and Emissions in a DME Compression Ignition Engine at Low Load Cold Start Condition

Jaeheun Kim and Choongsik Bae

Abstract The effective compression ratio reduction by means of late intake valve closing (LIVC) strategy was applied in a di-methyl ether (DME) compression ignition engine to investigate its potential effects on the engine performance and emission at cold start condition. The single injection timing of the DME was varied from the beginning to the end of compression stroke. The DME was injected directly into the cylinder with an injection pressure of 60 MPa. The indicated mean effective pressure (IMEP), heat release rate and combustion duration was investigated at two different intake valve closing (IVC) conditions—base IVC of 28 degree after bottom dead center (ABDC) and LIVC of 43.9 degree ABDC. The other experimental conditions such as injection duration and the environmental temperature remained fixed. The IMEP characteristics with respect to injection timings of two different IVC timing showed similar trend at conventional combustion regime. The IMEP distribution was shifted towards advanced injection timing direction for LIVC condition. In other words, the injection timing of LIVC condition had to be advanced compared to that of base IVC timing in order to produce equal power output. The reduction in the compression ratio had resulted in lower compression pressure and the temperature, so the ignition delay was increased and the overall heat release rate was retarded to retarded crank angle. However, the combustion characteristics in terms of combustion duration and the heat release rate curve did not show great differences at early injection timings (earlier than -30 crank angle degrees ATDC (after top

F2012-B01-044

J. Kim (✉) · C. Bae

Korea Advanced Institute of Science and Technology, Yuseong, Korea
e-mail: jaeheun.kim@kaist.ac.kr

C. Bae

e-mail: csbae@kaist.ac.kr

dead center)). The NO_x emission was reduced by around 10 % due to the reduced effective compression ratio. The prolonged ignition delay which enhanced the mixture homogeneity was also considered to have contributed on the reduction of NO_x emission. The HC and CO emissions of LIVC condition were relatively higher than those of base IVC condition due to the lowered in-cylinder temperature. The smoke formation was low due to the intrinsic properties of DME. The exhaust gas temperature was higher for the LIVC timing condition. The expelled portion of the charge during the compression resulted in lower heat capacity of the working gas. The in-cylinder gas temperature increased more when the same amount of fuel energy input was delivered to the gas with lower heat capacity. It was found that, malfunction of the piezo injector occurred when applying DME fuel with inappropriate setup. It was assumed that the vaporization of the DME might occur inside the injector when the engine coolant temperature increased. The movement of the piezo stack was not able to be translated into injection events due to the gas phase inside the injector. The fuel injector was restored and able to maneuver with the injection events again when the fuel return line was pressured above the vapor pressure. In future, further experiments need to be carried out at fully warmed-up condition in order to reveal its potential of reducing effective compression ratio on improving engine performance.

Keywords DME (di-methyl ether) • Compression ignition • Late intake valve timing • Effective compression ratio

1 Introduction

Continuous efforts on improving the efficiency and reducing the hazardous emission of the internal combustion engine are being carried out by many researchers and automotive industries despite of engines' long development history. Advanced combustion such as homogeneous charge compression ignition (HCCI) and partially-premixed charge compression ignition (PCCI) are being studied on both diesel and gasoline engine to improve their efficiency [1]. Exhaust gas recirculation (EGR) and boosting are applied to control the combustion phase and achieve low NO_x emission while maintaining the engine power output. Effects of different configurations on the hardware such as injectors and piston bowl shapes are also being studied to utilize them to the advanced combustion [2]. In addition, the strategies of changing the valve events, which are widely used on the gasoline engines nowadays, are gradually being investigated on the diesel engine with an aim of improving the problems of advanced combustion in diesel engines.

There are several strategies for valve events which can be applied to diesel engines. Realization of Atkinson cycle, or Miller cycle by reducing the effective compression ratio are being studied widely. There exist a potential of reducing the NO_x emission by reducing the in-cylinder temperature and prolonging the mixing

Table 1 Theoretical efficiency comparison of different engine cycles

	Base diesel cycle	Diesel cycle with reduced compression ratio	Diesel Atkinson cycle
Compression ratio	16:1	14.8:1	14.8:1
Expansion ratio	16:1	14.8:1	16:1
Efficiency formulae	$\eta_i = 1 - \frac{1}{r_c^{\gamma-1}} \frac{\beta^\gamma - 1}{\gamma(\beta-1)}$	$\eta_i = 1 - \frac{1}{r_c^{\gamma-1}} \frac{\beta^\gamma - 1}{\gamma(\beta-1)}$	$\eta = 1 - \frac{A(\beta^\gamma A^{-\gamma} - 1) + \gamma(A-1)}{\gamma(\beta-1)r_c^{\gamma-1}}$
	β : cut off ratio (the value of “3” was used in the calculation)		
	r_c : compression ratio		
	A: Atkinson ratio (expansion ratio/compression ratio)		
	γ : specific heat ratio		
Efficiency (%)	50.14	48.85	50.12

time of the fuel and air [3]. In addition, the NOx-soot trade-off relationship can be improved by applying boosting which delivers more air for the soot oxidation [4, 5].

Di-methyl ether (DME) is one of the promising alternative fuels for the diesel engine. It is not only because of its high cetane number which is suitable for auto-ignition and its instantaneous vaporization characteristics, but also because of its high oxygen content and the absence of C–C bonds in the molecular structure which can characterize smokeless combustion [6]. The research of DME application on the diesel engine has been conducted by many researchers [7–12]. The DME engine combustion covers not only the regimes of conventional diesel combustion, but also in the advanced combustion field. It was reported that the HC and CO emissions can be reduced due to reduction of locally fuel lean or rich area thanks to the fast vaporization characteristics of DME [13]. NOx emissions showed different tendencies according to different experimental conditions, however, the NOx emission was about the same level with diesel fuel [14, 15]. Injection strategies for DME have more freedom from the conventional NOx-smoke trade-off relationship, because it can achieve smokeless combustion.

Despite all aforementioned advantages of the diesel engine technologies and DME, the research on the simultaneous application of DME alternative fuel and the valve events strategies is relatively insufficient. Further reduction of NOx emission with DME combustion is also required to fulfill the next generation emission regulations. In this study, the potential effects of the valve events on reducing the NOx emission while maintaining the same power output in a DME compression ignition engine was carried out at cold-start condition. The effective compression ratio was reduced by means of varying the intake valve closing (IVC) timing.

Prior to the experiment, a simple calculation was carried out to examine the effects on the theoretical efficiency of the cycles. The theoretical efficiency of three different engine cycles, namely diesel cycle with base compression ratio, diesel cycle with reduced compression ratio, and the diesel Atkinson cycle with only reduced effective compression ratio, were compared to observe the effects of effective compression ratio on the efficiency deterioration. The results were shown in Table 1. The theoretical efficiency value decreased as the compression ratio decreased. However, a compensation can be achieved through reducing the

Table 2 Engine specifications

Specification	Resources
Bore × Stroke (mm)	84 × 90
Compression ratio	16:1
Valves per cylinder	4 (2 intakes and 2 exhausts)
Connecting rod length (mm)	149
Displacement (cc)	499
Intake valve timing (CAD)	Open @ 10 BTDC/Close @ 28 ABDC
Exhaust valve timing (CAD)	Open @ 54 BBDC/Close @ 4 ATDC

effective compression ratio only while maintain the expansion ratio. In real engine cycle, the efficiency deterioration ratio due to the reduced compression ratio may be even smaller due to other practical factors such as combustion phase or heat transfer effect. Besides, the hazardous emissions have to be also taken into consideration in reality. It may gain some positive effect from the aspect of engine emissions. Therefore, the potential of reducing the emissions while maintaining the efficiency of the engine with reduced effective compression ratio was investigated.

2 Experimental Setup and Conditions

The experiment was conducted with a modified single-cylinder experimental engine. The specifications of the engine configuration are listed in Table 2. It has a base compression ratio of 16:1.

Figure 1 shows a schematic diagram of the experimental setup. The engine speed and load were controlled by an alternating current (AC) dynamometer. The DME with the purity of 99.9 % was used as the fuel. The DME was pressurized up to 1.5 MPa with nitrogen to supply the fuel from the fuel tank to the high pressure pump in liquid form. A pneumatic pump (Hydraulics International INC., 5L-SS-115) was used to pressurize the DME up to 60 MPa. The lubricity enhancer (Infineum, 655) of 500 ppm was added into the fuel to prevent any wear or damage to the fuel system.

The fuel was directly injected into the cylinder with a piezo-actuated injector (Bosch). The injector features a nozzle hole diameter of 0.13 mm and an injection angle of 150 degrees. The surge tanks were installed in front of the intake manifold and at the end of the exhaust manifold to reduce pressure fluctuations. The intake temperature was controlled with a pair of heater and thermocouple at the intake surge tank. The intake pressure was measured with an absolute pressure sensor (Kistler, 4045A Type).

The in-cylinder pressure was measured with a piezo-electric pressure transducer (Kistler, Type 6056A) at a sampling rate of every 0.2 crank angle degree. The pulse of 0.2 crank angle was generated by an encoder (Autonics, 1800 pulses/rev)

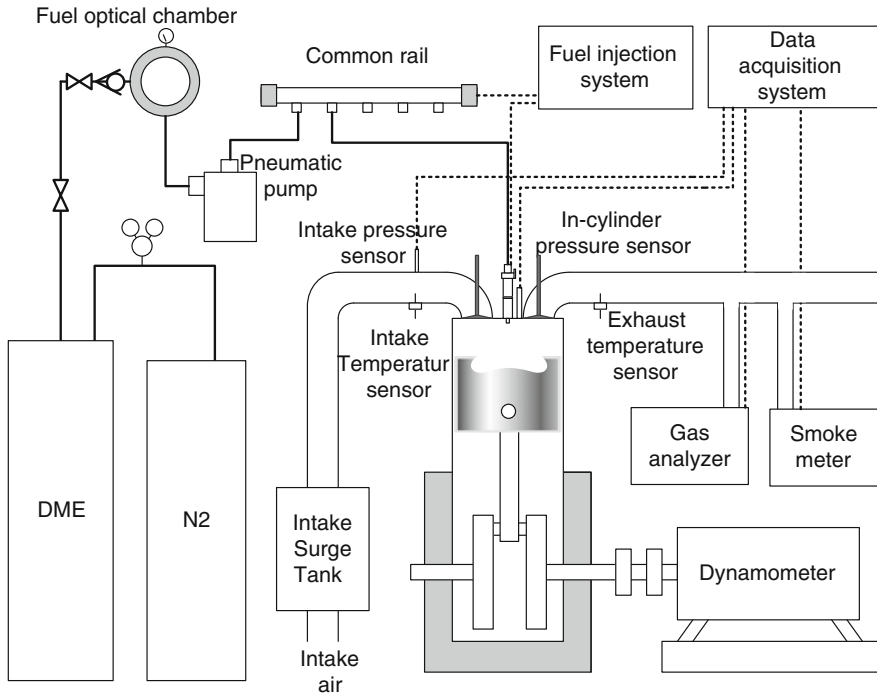


Fig. 1 Experimental setup

installed on the crankshaft. Exhaust gases were analyzed with a gas analyzer (Horiba, Mexa 1,500d) to measure the HC, NO_x, CO, and CO₂ emissions. The smoke emission was measured with a smoke meter (AVL, 415S). A data acquisition system (IOtech, Wavebook 516) was employed to acquire all engine combustion and exhaust gas data.

Table 3 shows the experimental conditions. The engine speed and the fuel quantity were fixed at 1,200 rpm and 15 mg, respectively. The single injection was adopted to investigate the preliminary results and examine the potential of reducing the effective compression ratio. The injection timing was swept over a wide range from the convention diesel combustion to the advance combustion regime. The injection pressure was fixed at 60 MPa. Two intake valve closing (IVC) settings were compared, namely 28 and 43.9 crank angle degrees (CAD) after bottom dead center (ABDC). The realization of the IVC timing is shown in Fig. 2. The intake camshaft was offset with a retardation angle of 15.9 in order to achieve the late IVC of 43.9 CAD. The naming of 'base IVC condition' and 'LIVC condition' will be used in current paper for the IVC timing of 28 and 43.9 CAD ABDC conditions, respectively, in order to enhance the understanding. The coolant temperature was set at 313 K. The detailed explanation for such low coolant temperature will be discussed in Sect. 4.

Table 3 Experimental conditions

Fuel	DME
Engine speed (rpm)	1200
Injection quantity (mg)	15
Injection timing (CAD BTDC)	100, 80, 60, 50, 40, 30, 25, 20, 15, 10, 5, 3, 0
Injection Pressure (MPa)	60
Intake valve closing (ABDC CAD)	28 (Base IVC setting), 43.9 (LIVC setting)
Compression ratio	16, 14.8
Coolant temperature (K)	313

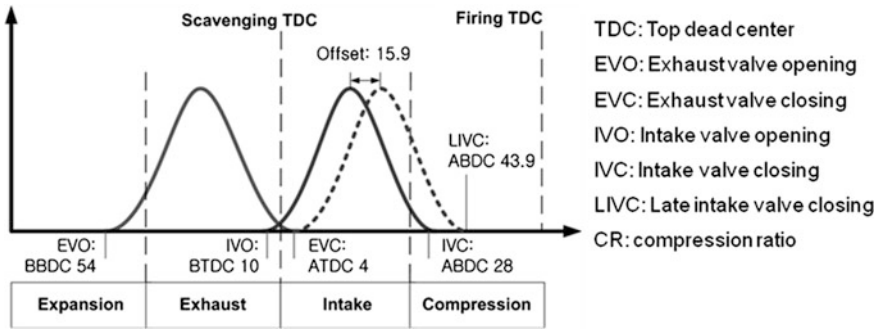


Fig. 2 Valve timing setting to realize late intake valve closing (LIVC)

The average data of 100 cycles were used to reduce the variation of the experiment results. The indicated mean effective pressure (IMEP) was derived with Eq. (1).

$$IMEP = \frac{W_{c,i}}{V_d} = \frac{\oint pdV}{V_d} \tag{1}$$

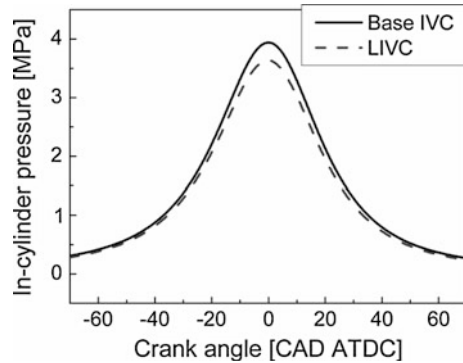
The net heat release, which does not take the heat transfer and the crevice loss into consideration, was derived with the manipulation form of first law of thermodynamics equation (Eq. (2)).

$$\frac{dQ}{d\theta} = \frac{\gamma}{\gamma - 1} p \frac{dV}{d\theta} + \frac{1}{\gamma - 1} V \frac{dp}{d\theta} \tag{2}$$

3 Experimental Results and Discussions

The in-cylinder motoring pressure was compared between base IVC and LIVC conditions, as shown in Fig. 3. The actual compression for the LIVC condition

Fig. 3 Motored in-cylinder pressure comparison between base IVC and LIVC condition at engine speed of 1200 rpm



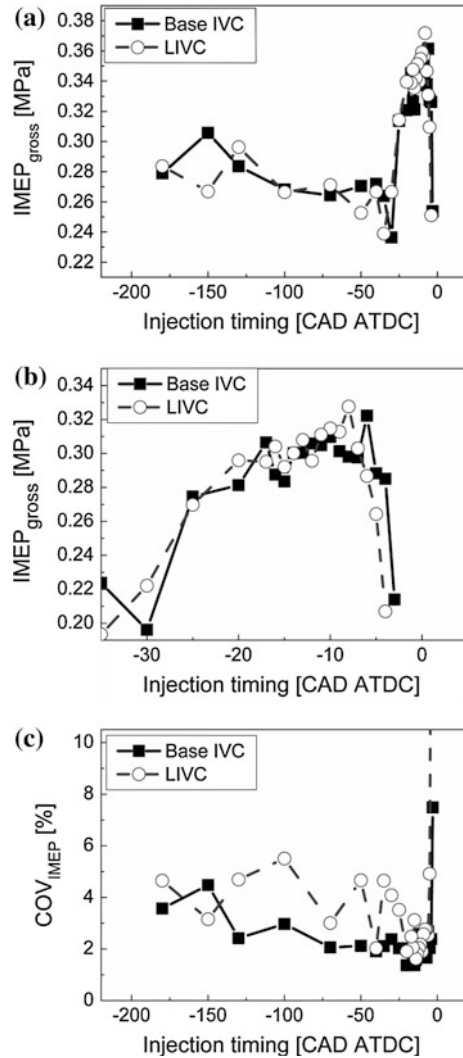
starts after the base IVC condition due to the retarded IVC timing. Therefore, the effective compression stroke reduced and resulted in lower peak motoring pressure. The effective compression ratio was reduced from original 16:1 to 14.9:1 by means of retarding the IVC timing. It implied that the peak in-cylinder gas temperature calculated from ideal gas equation was also lowered due to the reduced compression ratio.

Figure 4a shows the gross IMEP characteristics with respect to various injection timings to eliminate the effects of pumping loss difference caused by the valve timing. Figure 4b shows an expansion plot of Fig. 4a with an injection timing window from -40 to -4 CAD ATDC. The overall distribution of the IMEP values near TDC of LIVC condition was seemed to be slightly shifted towards the advanced injection timing direction compared to the base IVC condition. The IMEP decreased drastically when the injection timing was either retarded towards or advanced away from the TDC. The IMEP drop position was observed at relatively advanced injection timing for the LIVC condition compared to base IVC condition. The highest IMEP was observed at an injection timing of -6 and -8 CAD ATDC for base IVC and LIVC condition, respectively, which supported the observation of IMEP distribution shift towards advanced injection timing for LIVC condition. Detailed reasons for such phenomenon will be discussed in the latter part of the section.

The IMEP showed a lowest point with respect to the injection timing for both IVC conditions. Further advancing the injection timing into the advanced combustion regime resulted in increased IMEP, however, still lower than the injection timings of conventional combustion regime (namely the injection timings near the TDC). The lowest IMEP was attributed to the short burn duration of the DME, thus increased the negative work before the TDC. Such lowest point of IMEP was observed in both IVC conditions. Further advancing the injection timing resulted in the retardation of the onset of heat release rate due to the cooling effect of evaporated DME, thus decreased the portion of the negative work [11].

The coefficient of variation (COV) of IMEP was lower than 3% at conventional combustion regime; however, the COV increased as the injection timing entered the advanced combustion regime (Fig. 4c). Low wall temperature due to

Fig. 4 Effects of injection timing on indicated mean effective pressure (*IMEP*) and coefficient of variation (*COV*) of *IMEP*: *IMEP* of **a** Injection timing from -180 to -4 CAD ATDC, **b** Injection timing from -40 to -4 CAD ATDC, and **c** *COV* of *IMEP*



low coolant temperature and reduced effective compression ratio was considered to be the factors which had increased the *COV* of *IMEP* despite of good auto-ignitability of DME fuel.

The accumulated heat release was derived through the integration of the heat release rate with Eq. (2). The CA50 value, which is an indicator of the combustion phase and equals to the CAD where the 50 % burn of the total heat release occurs, was derived and plotted in Fig. 5. The retardation of the CA50 was observed for the LIVC condition compared to IVC condition over the entire injection timing range. The retardation value was not large due to only 15.9 degrees offset of IVC timing; however, it showed constant combustion phase retardation with the

Fig. 5 CA50 with respect to injection timing

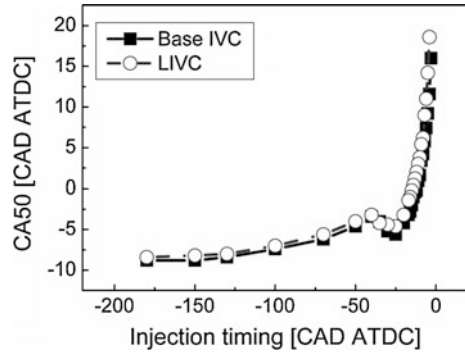
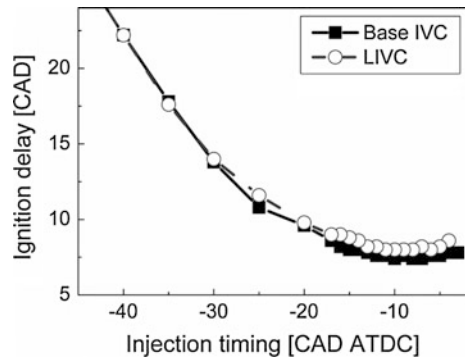


Fig. 6 Ignition delay with respect to injection timing



reduced effective compression ratio over the entire injection timings. The ignition delay was lengthened for the LIVC condition due to the reduced in-cylinder pressure and temperature, as shown in Fig. 6. The onset of heat release was retarded for the LIVC condition, therefore the CA50 was retarded. Since the CA50 value and the IMEP are closely related, the injection timing accompanied with combustion phase needed to be controlled to achieve a similar level of IMEP. A conclusion can be drawn from Fig. 5 that, at conventional combustion regime (injection timings near TDC), advancing the injection timing was required for LIVC condition to achieve similar CA50 value and IMEP value. Therefore, it explained the result of the IMEP distribution shift towards the advanced injection timing direction for the LIVC condition.

Figure 7 shows the in-cylinder pressure and heat release profile under different IVC conditions. The injection timing of conventional combustion regime (namely injection timings of -6 and -15 CAD ATDC in Fig. 7) showed great difference of heat release rate profile in amplitude and the phase under different IVC conditions. The peak heat release rate was higher and the combustion phase was more advanced for the base IVC conditions due to higher in-cylinder temperature formation at the time of injection. However, no obvious differences between two IVC conditions were observed for the early injection timings (namely injection timings

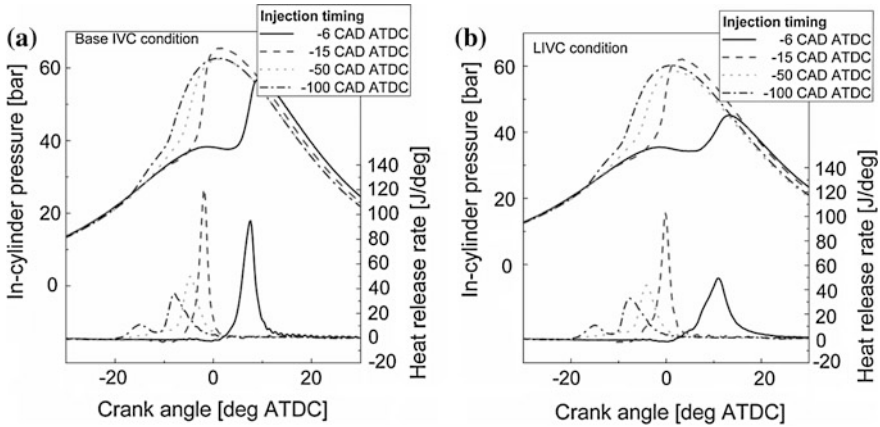
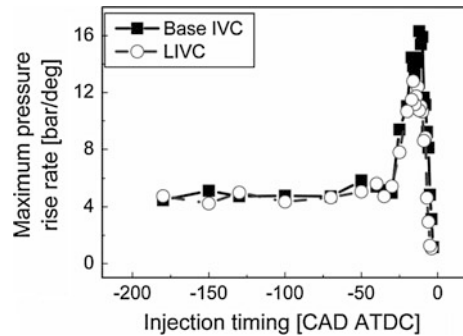


Fig. 7 In-cylinder pressure and heat release rate profile of various injection timings under different IVC conditions. **a** base IVC condition, and **b** LIVC condition

Fig. 8 Maximum pressure rise rate with respect to the injection timing



of -50 and -100 CAD ATDC in Fig. 7). The heat release of the DME showed a typical two-stage heat release, which was namely low temperature reaction (LTR) and high temperature reaction (HTR).

Figure 8 shows the maximum pressure rise rate (MPRR) with respect to the injection timing. The MPRR was reduced at conventional combustion regime under LIVC condition, while the difference between two IVC timing at early injections was small. The MPRR was reduced at conventional combustion regime due to the reduced peak heat release rate at LIVC condition. The reduced heat release rate had mitigated the sudden pressure rise during the combustion. However, the absolute value of the MPRR was still high due to the high peak heat release of the DME single injection. The value was beyond the acceptable value of 0.5 MPa/deg [16], and it was expected to be improved through adopting multiple injection strategies, which is out of the scope of the paper.

Figure 9 shows the time-averaged exhaust gas temperature acquired at the exhaust manifold. The exhaust gas temperature of the LIVC condition showed a

Fig. 9 Exhaust gas temperature with respect to the injection timing

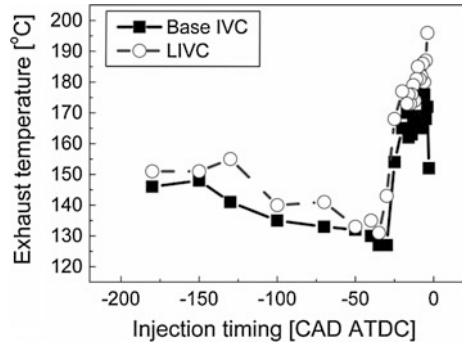
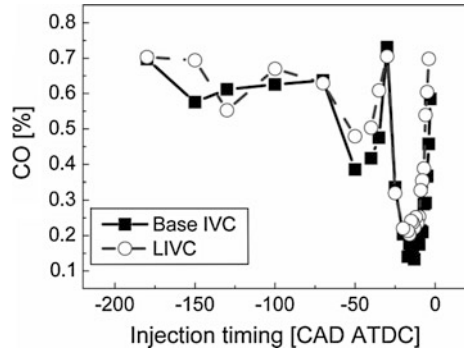


Fig. 10 CO emissions with respect to the injection timing



higher value than the IVC condition. The LIVC condition expels some portion of the charge back into the intake manifolds before it begins its compression stroke. Therefore, the trapped charge is smaller and the heat capacity of the working fluid is also smaller than that of base IVC condition. When given an equal amount of fuel quantity, which represents an equal amount of heat input under the assumption of same combustion efficiency, the temperature of the working fluid which has lower heat capacity has a higher temperature rise [4]. Thus it resulted in higher exhaust gas temperature for the LIVC condition. It was reported that the high exhaust gas temperature may enhance the light-off time of the oxidation catalyst.

The emission characteristics of different IVC conditions were analyzed. CO emissions were higher at the injection timing of conventional combustion regime due to the lower combustion temperature at LIVC condition. The peak values of CO were observed for both IVC condition at same injection timing. Further in-cylinder spray visualization may be needed to explain such phenomenon; however, it was supposed to be the point where mis-targeting between the fuel spray and the piston bowl occurred. The utilization of the air and the oxidation of the remaining CO emission were poor, thus resulted in high CO emission. The overall CO emission was relatively high compared with other works due to the low coolant temperature. Though the detailed HC emission result was not shown in the figure,

Fig. 11 a NOx and b smoke emission with respect to the injection timing

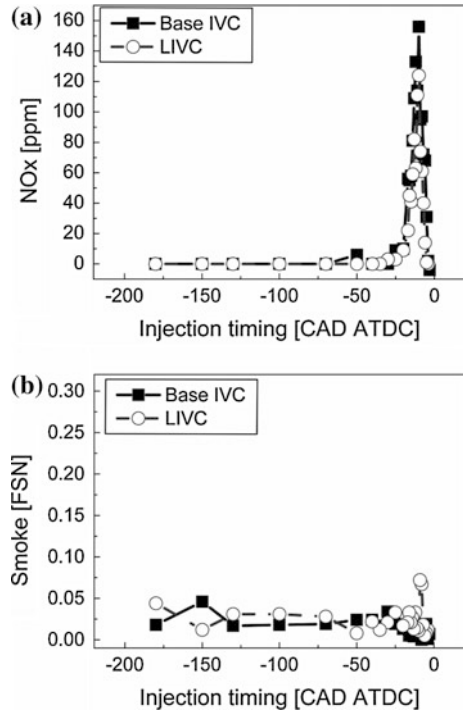


Table 4 Experimental results for same power output conditions

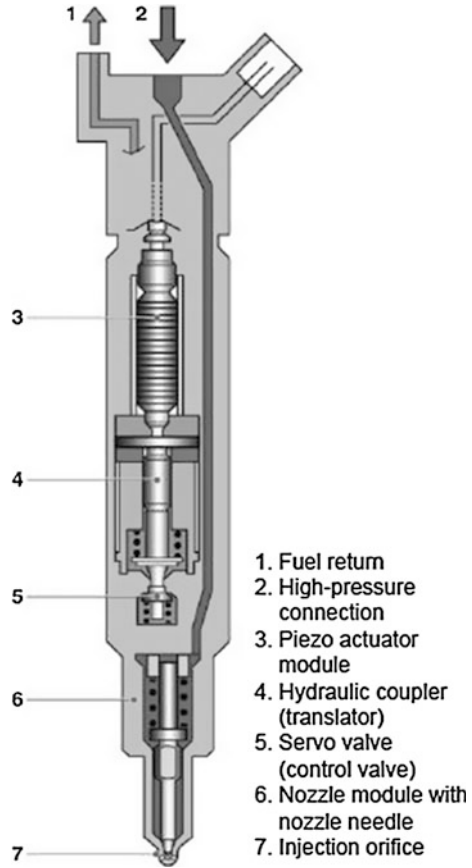
	Injection timing (CAD ATDC)	IMEP (MPa)	CO (%)	NOx (ppm)	HC (ppm)	Exhaust gas temp. (°C)
Base IVC	-6	0.32	0.2925	68	365	176
LIVC	-8	0.33	0.3541	61	273	182
Variation (%)	-	-	+21.1	-10.3	-25.2	+3.4

its tendency with respect to injection timings and IVC conditions was similar to that of CO emission (Fig. 10).

Figure 11 shows the NOx and smoke emissions. The NOx was reduced with LIVC strategies due to the reduced in-cylinder temperature at conventional combustion regimes. Early injection timings which characterize advanced combustion mode resulted in low NOx emissions for both IVC condition due to lean homogeneous mixture formation. The smoke emission was low regardless of injection timings nor the IVC conditions due to the intrinsic fuel property of smokeless combustion. Further NOx reduction can be expected with the combination of exhaust gas recirculation (EGR) strategies with more freedom from the conventional constraints of NOx-smoke trade-off relationship.

Table 4 shows the results of the highest IMEP at each IVC conditions. The NOx emission was reduced by around 10 % with the LIVC due to the reduced

Fig. 12 Construction of the piezo-inline injector [17]



in-cylinder combustion temperature. The prolonged ignition delay which enhanced the mixture homogeneity was also considered to be contributing on the reduction of NOx emission. LIVC strategy fueled with DME showed a potential to decrease NOx emissions while maintaining the same power of the engine at low load condition.

4 Limitations and the Future Scope of the Work

The experiment was conducted under relatively low coolant temperature conditions. The reason was due to the injector malfunction when applying DME as the fuel at fully warmed-up temperature (353 K) conditions. Through an analysis of the internal structure of the piezo injector, a possibility for the malfunction of the injector was analyzed.

Figure 12 shows the internal cut-away structural view of the piezo injector from Bosch [17]. Part 4 in Fig. 12 is one of the key components in the piezo injector which is called hydraulic coupler. It translates and amplifies the actuator stroke basically. It also characterizes an important function to compensate for any play between the actuator and the servo valve (e.g. caused by thermal expansion). The coupler has to be filled up with liquid diesel in order to operation well. When adopting DME to the injector, the space inside the coupler will be gradually replaced by DME. It should be reminded that the fuel return line was connected before the high pressure pneumatic pump, which had a pressure of 1.5 MPa as mentioned in the experimental setup section. The reason for the malfunction of the injector when increasing the engine coolant temperature was assumed as follows. A gradual vaporization of liquid DME occurred inside the hydraulic coupler due to the increased temperature and DME vapor pressure. When the gas portion inside the coupler increased, it was unable to deliver or translate the stroke of the piezo stack to the servo valve. The fluid path change was not able to take place, nor did the injection event occur. This kind of problem was preliminarily resolved when increasing the fuel return pressure beyond the vapor pressure of fully warmed-up coolant temperature (353 K), up to 2.5 MPa. The gas phase inside the hydraulic coupler was assumed to be replaced with liquid phase again, and the malfunctioned injector was able to be restored again. In future, further experiments need to be conducted at fully warmed-up conditions to examine the full potential of reducing effective compression ratio on the DME engine combustion.

5 Conclusions

The effective compression ratio reduction by means of late intake valve closing (LIVC) strategy was applied in a di-methyl ether (DME) compression ignition engine to investigate its potential effects on the engine performance and emission. The DME single injection timing was varied through the beginning of the compression to the end of compression stroke. Two different intake valve closing (IVC) conditions, namely base IVC of 28 deg after bottom dead center (ABDC) and LIVC of 43.9 degree ABDC, were examined.

1. The IMEP characteristics with respect to injection timings of two different IVC timings showed similar trend at conventional combustion regime, with only an IMEP distribution shift towards advanced injection timing direction. The injection timing of LIVC condition had to be advanced compared to that of base IVC timing in order to produce equal power output. The reduction in the compression ratio had resulted in lower compression pressure and temperature. Therefore, the ignition delay was increased and the overall heat release rate was retarded to the later crank angle.

2. The combustion characteristics in terms of combustion duration and heat release rate did not show great differences according to IVC timing conditions for those early injection timings which characterize advanced combustion.
3. The reduction of the effective compression ratio had brought following effects on the emissions. The NO_x emission was reduced by around 10 % due to the reduced in-cylinder combustion temperature. The prolonged ignition delay which enhanced the mixture homogeneity was also considered to have contributed on the reduction of NO_x emission. The CO and HC emissions were increased, however, due to the low oxidation rate by the low in-cylinder temperature. The smoke formation was low regardless of the IVC conditions due to the intrinsic properties of the fuel.
4. The exhaust gas temperature was higher for the LIVC timing condition. The expelled portion of the charge during the compression resulted in lower heat capacity of the working gas. It was considered that, the in-cylinder gas temperature increased more when the same amount of fuel energy input was delivered to the gas with lower heat capacity. Thus, it resulted in higher exhaust gas temperature at LIVC condition.
5. The malfunction of piezo injector occurred when applying DME fuel at fully warmed-up condition with 1.5 MPa of pressure in fuel return line. It was assumed that the vaporization of the DME may have occurred inside the injector due to the increased vapor pressure when increasing the engine coolant temperature. The pressure of the fuel-return line was then pressurized up to 2.5 MPa, which was above the vapor pressure of fully warmed-up temperature, in order to prevent vaporization. The fuel injector was restored and able to maneuver with the injection events again.

Acknowledgments This work was supported by the Energy Efficiency & Resources (2010T100100440) of the Korea Institute of Energy Technology Evaluation and Planning (KETEP) grant funded by the Korea government Ministry of Knowledge Economy.

References

1. Yao M, Zheng Z, Liu H (2009) Progress and recent trends in homogeneous charge compression ignition (HCCI) engines. *Prog Energy Combust Sci* 35(5):398–437
2. Catania AE, d'Ambrosio S, Finesso R, Spessa E, Cipolla G, Vassallo A (2009) Combustion system optimization of a low compression-ratio PCCI diesel engine for light-duty application. In: SAE 2009-01-1464
3. Xin H, Russell PD, Zongxuan S (2008) Late intake valve closing as an emissions control strategy at Tier 2 Bin 5 engine-out NO_x level. In: SAE technical paper 2008-01-0637
4. Murata Y, Nishio Y, Kusaka J, Daisho Y, Kawano D, Suzuki H, Ishii H, Goto Y (2010) Numerical analysis of Miller-premixed charge compression ignition combustion on a dynamic Φ -T map. *Int J Engine Res* 11:89–98
5. Yutaka M, Jin K, Yasuhiro D, Daisuke K, Kisakazu S, Hajime I, Yuichi G (2008) Miller-PCCI combustion in an HSDI diesel engine with VVT". SAE Technical paper 2008-01-0644

6. Arcoumanis C, Bae C, Crookes R, Kinoshita E (2008) The potential of di-methyl ether (DME) as an alternative fuel for compression-ignition engines: a review. *Fuel* 87:1014–1030
7. Sorenson SC, Mikkelsen S-E (1995) Performance and emissions of a 0.273 liter direct injection diesel engine fuelled with neat dimethyl ether. In: SAE technical paper 950064
8. Susumu S, Norimasa I (2003) Analysis of DME homogenous charge compression ignition combustion. In: SAE technical paper 2003-01-1825
9. Jang J, Bae C (2008) Effects of valve events on the engine efficiency in a homogeneous charge compression ignition engine fueled by dimethyl ether. *Fuel* 88:1228–1234
10. Yeom K, Bae C (2007) Gasoline—dimethyl ether homogeneous charge compression ignition engine. *Energy Fuels* 21(4):1942–1949
11. Jinyoung J, Kiseon Y, Kitae Y, Choongsik B, Seungmook O, Kernyong K (2008) Improvement of DME HCCI engine performance by fuel injection strategies and EGR. In: SAE technical paper 2008-01-1659
12. Yoon H, Yeom K, Bae C (2007) The effects of pilot injection on combustion in dimethyl-ether (DME) direct injection compression ignition engine. In: SAE technical paper 2007-24-0188
13. Teng H, McCandless JC, Schneyer JB (2001) Thermo-chemical characteristics of di-methyl ether—an alternative fuel for compression-ignition engines. In: SAE technical Paper 2001-01-0154
14. Egnell R (2001) Comparison of heat release and NO_x formation in a DI diesel engine running on DME and diesel fuel. In: SAE 2001-01-0651
15. Youn I, Park S, Roh H, Lee C (2011) Investigation on the fuel spray and emission reduction characteristics for dimethyl ether (DME) fueled multi-cylinder diesel engine with common-rail injection system. *Fuel Process Technol* 92:1280–1287
16. Naote H, Takahisa A, Yuichi M, Takuji I (2010) Heat release rate and NO_x formation process in two-stage injection diesel PCCI combustion in a constant-volume vessel. In: SAE technical paper 2010-01-0608
17. Bosch R GmbH (2005) Diesel-engine management. 4th edn, Bentley Publishers, London

Environmental Performance of Diesel Fuels Containing Oxygenated Additive Packages

Miłosław Kozak, Jerzy Merkisz, Piotr Bielaczyc
and Andrzej Szczotka

Abstract The application of oxygenated additives seems to be one of more promising modifications of diesel fuels in order to decrease exhaust emissions. The authors have so far tested many oxygenates, from different chemical families, but as sole fuel components. Generally speaking, these oxygenates produced favorable but different changes in exhaust emissions. The objective of this study was to investigate whether the positive effect on emissions could be maximized by the application of packages of multiple oxygenated compounds. Four different oxygenated additive packages were tested. Each package contained a combination of 2 synthetic oxygenates, which represented different chemical groups, namely: glycol ethers, maleates and carbonates. The packages were evaluated as fuel additives at a concentration of 10 % v/v in a Euro 5 diesel fuel. The New European Driving Cycle (NEDC) was selected as a representative test for this study. All the oxygenate packages were additionally tested using the US Federal Test Procedure 75 (FTP-75). This cycle was carried out in order to determine the influence of cycle conditions on oxygenated fuels' effectiveness as regards reductions in exhaust emissions. The tests were conducted on a Euro 4 passenger car equipped with a direct injection (common rail) turbocharged diesel engine. During the tests, mass emissions of CO, HC, NO_x, PM and CO₂ were measured. The influence of individual oxygenates on CO, NO_x and PM emissions is roughly additive when these oxygenates are applied together (i.e. as a package of additives). There is no such regularity for HC emissions. The research showed that the application of

F2012-B01-045

M. Kozak (✉) · J. Merkisz
Poznań University of Technology, Poznan, Poland
e-mail: milkoz@icpnet.pl

P. Bielaczyc · A. Szczotka
BOSMAL Automotive R&D Institute Ltd, Bielsko-Biala, Poland

oxygenated additives generally produces a significant reduction in PM emissions and a slight increase in NO_x emissions. An increase in CO and HC emissions was observed when maleates and carbonates were used as sole oxygenates. This increase was significantly lower when the oxygenates mentioned above were applied in a package with glycol ethers. The influence of oxygenated additive packages was different over the NEDC and FTP-75 cycles. Generally, the packages produced more favorable changes in exhaust emissions over the FTP-75 cycle, which is more transient and dynamic (stronger accelerations). The reduction in PM emissions was higher over the FTP-75 cycle. In the case of NO_x emissions, these were higher by a factor of dozen or so for oxygenated fuels than for neat diesel fuel over the NEDC, whereas over the FTP-75 they was slightly lower for oxygenated fuels than for diesel fuel. In the case of CO and HC emissions, such a clear-cut relationship between the type of driving cycle and emissions changes was not observed. Regardless of test conditions, no significant influence of oxygenated additive packages on CO₂ emissions was noted. The application of oxygenated diesel fuels containing packages of oxygenated compounds caused a significant reduction in PM and a small change in NO_x emissions, so it produced favorable changes in the PM/NO_x emissions trade-off. Favorable changes in PM/NO_x emissions produced by the application of oxygenated additive packages were, however, comparable to these achieved with use of the most effective individual oxygenates.

Keywords Diesel fuel • Oxygenates • Fuel additives • Exhaust emissions • Diesel vehicle

1 Introduction

Fuel, as the integral element of combustion in the engine has an immense effect on the composition and harmfulness of exhaust gases emitted by the engine. Changes to the EU standard requirements for diesel fuels, implemented in 2000, 2005 and 2009 were directed towards the reduction of the harmfulness of the exhaust gases emitted by engines. At present, modification of conventional properties of diesel fuel that affect emissions (cetane number, sulfur content, distillation curve, etc.) is possible only to a limited extent. Therefore, in order to take maximum advantage of the fuel's potential for exhaust emissions reduction, some more unconventional modifications of the fuel should be considered. The application of oxygenated compounds seems to be one of more promising solutions in this field. The compounds particularly affect a very troublesome component of diesel engine exhaust—i.e. particulate matter. Owing to their physical and chemical properties, groups of chemical compounds such as maleates [1–4], carbonates [5–8] and ethers [6, 7, 9–12] should be taken into consideration as potential diesel oxygenates.

Table 1 Specifications of the test vehicle

Vehicle type	Passenger car
Dry weight	950 kg
Engine type	Diesel, 4-cylinder in-line
Displacement	1.3 dm ³
Max. power	51 kW @ 4,000 rpm
Max. torque	145 Nm @ 1,500 rpm
Injection/combustion type	Direct injection common rail, turbocharged (intercooled)
Exhaust gas recirculation	Electronically controlled (closed-loop)
Emission control	Oxidation catalyst
Calibrated to	Euro 4

The authors have so far tested many oxygenates, from different chemical families, but as sole fuel components. These oxygenates produced generally speaking favorable but different changes in exhaust emissions [13–19]. The objective of this study was to investigate whether the positive effect on emissions could be maximized by application of packages of some oxygenated compounds.

The experimental results presented in the present paper were obtained within a research program investigating the effect of different synthetic oxygenates on exhaust emissions from diesel passenger cars. The objective of this study was to select the most promising oxygenate compounds as blending components in diesel fuel for further advanced testing and practical application.

2 Research Program

The tests were conducted on a Euro 4 passenger car equipped with a direct injection (Common Rail) turbocharged diesel engine. Major data on the vehicle are shown in Table 1.

The New European Driving Cycle (NEDC) was selected as a representative test for this study. The same fuels were additionally tested using the US Federal Test Procedure 75 (FTP-75). This cycle was carried out in order to determine the influence of cycle conditions on oxygenated fuels' effectiveness as regards reduction in exhaust emissions.

Four different oxygenated additive packages were tested. Each package contained a combination of 2 synthetic oxygenates, which represented different chemical groups, namely: glycol ethers, maleates and carbonates. The oxygenates used as package components were selected on the basis of the most favorable influence on exhaust emissions when they were tested as sole oxygenated additives. The packages were evaluated at a concentration of 10 % v/v in diesel fuel. The base diesel fuel (DF) was a diesel fuel of the Euro 5 class. The same diesel fuel was used as a reference fuel for evaluation of the effectiveness of the

Table 2 Some properties of oxygenates used as package components

Chemical name	Triethylene glycol dimethyl ether	Tetraethylene glycol dimethyl ether	Diethyl maleate	Diethyl carbonate
Molecular weight, amu	178.23	222.28	172.18	118.13
Oxygen content, %(m/m)	36.0	36.0	37.3	40.7
Boiling point, °C	220	275	225	127
Density @ 20 °C, kg/m ³	987	1010	1064	975
Viscosity @ 20 °C, mm ² /s	2.5	4.1	n.a.	0.78
Flash point, °C	113	141	n.a.	25

Table 3 Base diesel fuel specifications

		Unit	Value
Cetane number		–	52.8
Cetane index		–	53.4
Density @ 20 °C		kg/m ³	827.7
Sulfur content		ppm	8.8
Oxygen content		%(m/m)	0.0
Viscosity	@ 20 °C	mm ² /s	4.096
	@ 40 °C	mm ² /s	2.607
Distillation	E250	%(v/v)	38.1
	E350	%(v/v)	–
	T95	°C	332.3
	FBP	°C	343.7
Aromatic	Total aromatics	%(m/m)	20.7
Hydrocarbons	Monoaromatics	%(m/m)	18.8
	Diaromatics	%(m/m)	1.7
	Tri+aromatics	%(m/m)	0.2
	Total PAH	%(m/m)	1.9

individual oxygenated additive package regarding emissions reduction. The properties of the oxygenates used as package components and base diesel fuel are presented in Tables 2 and 3, respectively. The oxygenated additive packages used in the research were marked with symbols: OP-1, OP-2, OP-3 and OP-4 and oxygenated fuels containing specific packages are marked as DF + OP-1, DF + OP-2, etc. Composition, oxygen content and cetane numbers of the research oxygenated fuels are given in Table 4. The remaining properties of research oxygenated fuels can be estimated on the basis of properties of base diesel fuel and oxygenated compounds (Tables 2 and 3).

The tests were carried out at the BOSMAL Automotive R&D Institute's Emissions Testing Laboratory (Fig. 1) using a Schenck 500/GS60 chassis dynamometer. An AVL CEC CVS system with an AVL CET-LD/20 type full-flow dilution tunnel and an AVL CEP-LD/100 PTS 60 l/min particulate sampling system, the CESAR control system and a Sartorius microbalance were used to measure exhaust emissions.

Table 4 Composition, oxygen content and cetane numbers of research oxygenated fuels

Oxygenated fuel	Composition	Oxygen content [% (m/m)]	Cetane number
DF + OP1	<ul style="list-style-type: none"> •Triethylene glycol dimethyl ether: 5 % v/v, •Diethyl maleate: 5 % v/v, •Diesel fuel: 90 % v/v. 	4.48	52.0
DF + OP2	<ul style="list-style-type: none"> •Triethylene glycol dimethyl ether: 5 % v/v, •Diethyl carbonate: 5 % v/v, •Diesel fuel: 90 % v/v. 	4.51	52.5
DF + OP3	<ul style="list-style-type: none"> •Tetraethylene glycol dimethyl ether: 5 % v/v, •Diethyl maleate: 5 % v/v, •Diesel fuel: 90 % v/v. 	4.42	53.6
DF + OP4	<ul style="list-style-type: none"> •Tetraethylene glycol dimethyl ether: 5 % v/v, •Diethyl carbonate: 5 % v/v, •Diesel fuel: 90 % v/v. 	4.55	53.4

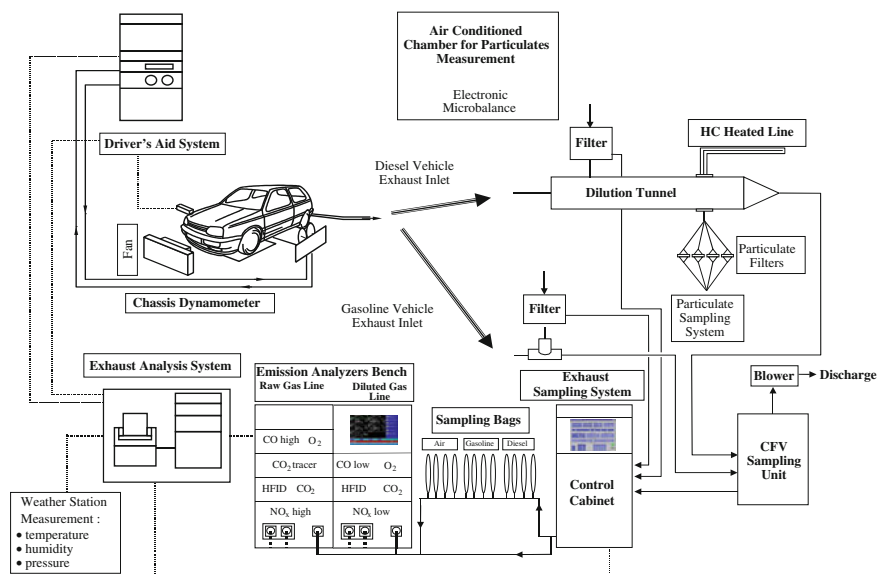


Fig. 1 Schematic of the exhaust emissions measurement system

For the each of fuels tested, at least two (depending on repeatability of the results) emissions tests during the NEDC cycle were carried out. Only one emissions test was performed each day. The mean values of each measurement series were taken for further analysis. The uncertainty of the emission measurement during the NEDC cycle was about 7 % for NO_x and 4 % for PM. A statistical analysis of the results was conducted and only those differences that were found to be statistically significant are reported.

Fig. 2 CO emissions over the NEDC for neat diesel fuel and oxygenated fuels

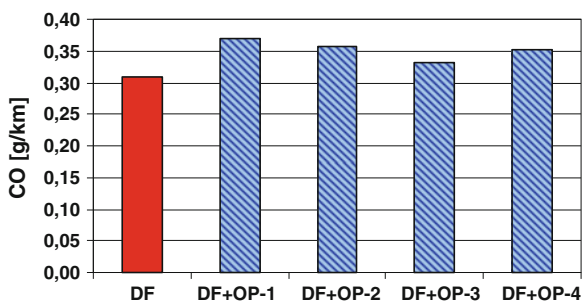
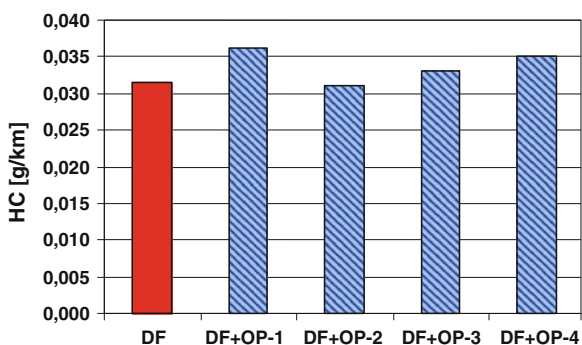


Fig. 3 HC emissions over the NEDC for neat diesel fuel and oxygenated fuels



3 Test Results and Discussion

3.1 Exhaust Emissions Over the NEDC

Carbon monoxide (CO) emissions over the NEDC were 8–20 % higher for all the oxygenated fuels than for neat diesel fuel (Fig. 2). All the oxygenated fuels contained components that when used as a sole oxygenated additives respectively decreased (glycol ethers) and increased CO emissions (maleates and carbonates), hence the resultant changes in CO emissions are consequences of both the positive and negative influences of specific oxygenates contained in the oxygenated additive packages.

The changes in hydrocarbon (HC) emissions over the NEDC caused by the application of oxygenated fuels ranged from –2 to +15 % (Fig. 3). The results are similar to these obtained when maleates and carbonates were used as sole components at a concentration of 5 %, and more favorable than results observed for maleates and carbonates at a concentration of 10 %. Finally, it should be noted, that from the point of view of HC, the most favorable changes in emissions were obtained when glycol ethers were used as sole components.

All the oxygenated fuels caused an increase in NO_x emissions over the NEDC. This increase ranged from 10 to 15 % (Fig. 4). Such a change in NO_x emissions

Fig. 4 NO_x emissions over NEDC for neat diesel fuel and oxygenated fuels

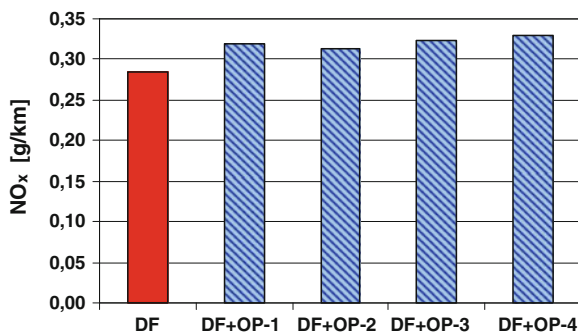
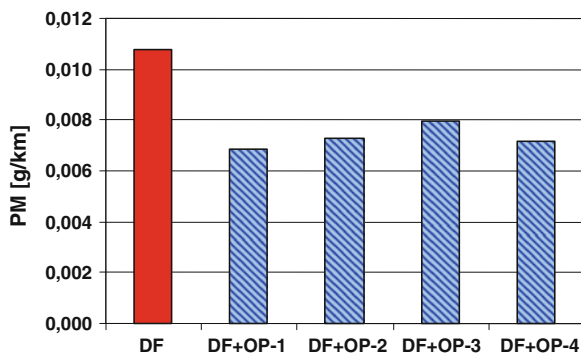


Fig. 5 PM emissions over the NEDC for neat diesel fuel and oxygenated fuels



should be assessed as less favorable than this caused by oxygenated fuels containing sole oxygenates at concentrations of 5 and 10 %.

The reduction in PM emissions observed for oxygenated fuels ranged from 26 to 36 % (Fig. 5). The highest reduction (36 %) was observed for the fuel containing triethylene glycol dimethyl ether and diethyl maleate (i.e. OP-1). Only a slightly lower reduction (33 %) was obtained for oxygenated fuel packages OP-2 and OP-4. It should be noted that similar, favorable results were also noted for some fuels containing individual oxygenated compounds, namely such components as some glycol ethers and diethyl carbonate.

The differences in CO₂ emissions (Fig. 6) between diesel fuel and oxygenated fuels were smaller than 2 % and thus they were within the uncertainty of measurement.

3.2 Exhaust Emissions Over the FTP-75

CO emissions over the FTP-75 cycle for the test vehicle fuelled with neat diesel fuel and oxygenated fuels are shown in Fig. 7. Similar to the NEDC, the application of fuels containing oxygenated additive packages also produced an increase in CO emissions over the FTP-75. The relative increases in CO emissions were

Fig. 6 CO₂ emissions over the NEDC for neat diesel fuel and oxygenated fuels

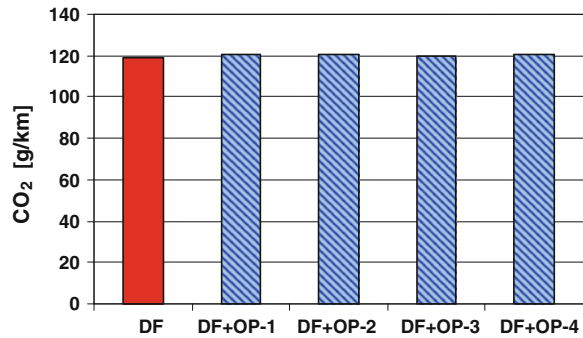
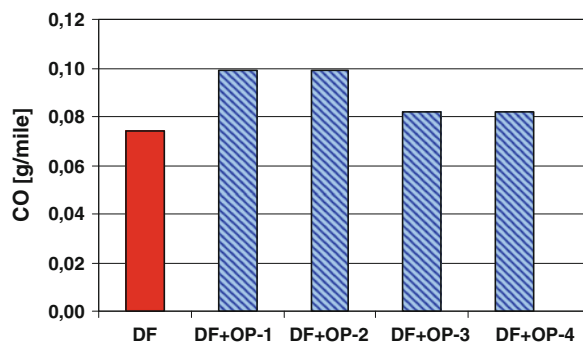


Fig. 7 CO emissions over the FTP-75 for neat diesel fuel and oxygenated fuels



higher over the FTP-75 and ranged from 11 to 34 %. It can be seen that the same oxygenated packages, namely OP-1 and OP-2, produced the highest CO emissions over both cycles.

HC emissions over the FTP-75 cycle for the test vehicle fuelled with neat diesel fuel and oxygenated fuels are shown in Fig. 8. Similarly to the NEDC, the application of fuels containing oxygenated additive packages also produced an increase in HC emissions over the FTP-75. Relative increases in HC emissions were higher over FTP-75 and amounted up to 28 %. It can be seen that different oxygenated fuels produced highest HC emissions for both analyzed cycles.

NO_x emissions over the FTP-75 cycle for test vehicle fuelled with neat diesel fuel and oxygenated fuels are shown in Fig. 9. In contrast to the NEDC, the application of fuels containing oxygenated additive packages produced some decreases in NO_x emissions over the FTP-75. These decreases, however, were rather slight—namely by up to 5 %.

PM emissions over the FTP-75 cycle for the test vehicle fuelled with neat diesel fuel and oxygenated fuels are shown in Fig. 10. Like over the NEDC, the application of fuels containing oxygenated additive packages also produced significant decreases in PM emissions over the FTP-75. The relative decreases of PM emissions were even higher than over the NEDC (by some percent) and amounted

Fig. 8 HC emissions over the FTP-75 for neat diesel fuel and oxygenated fuels

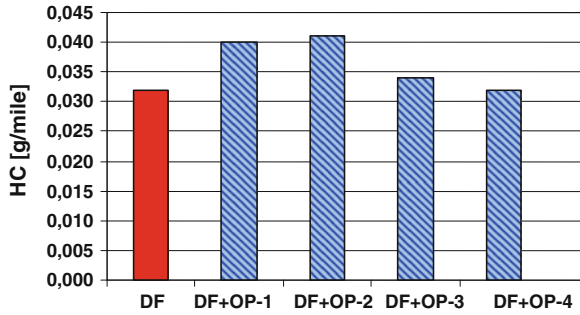


Fig. 9 NO_x emissions over the FTP-75 for neat diesel fuel and oxygenated fuels

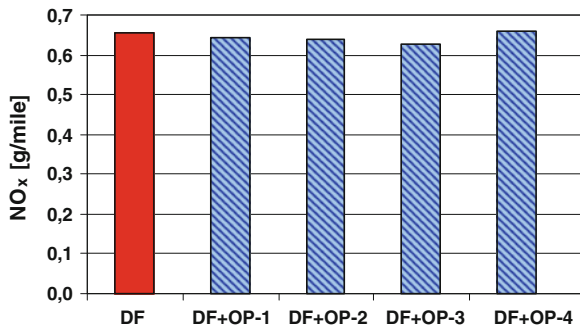
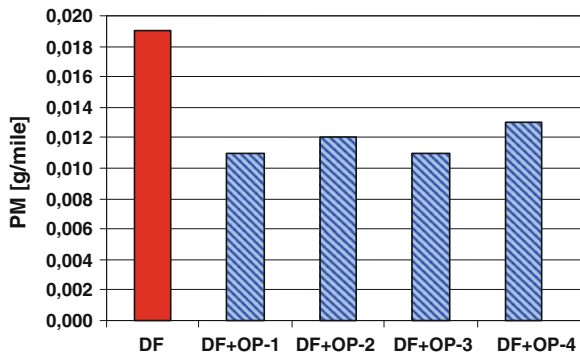


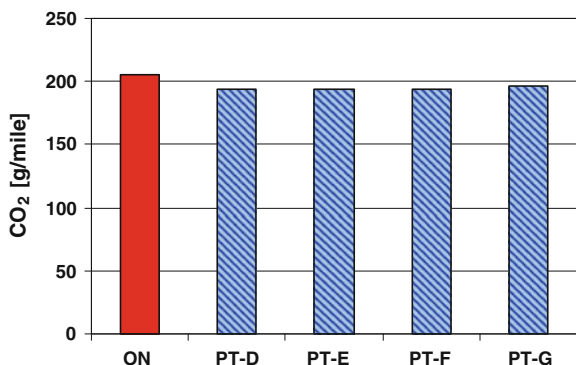
Fig. 10 PM emissions over the FTP-75 for neat diesel fuel and oxygenated fuels



from 32 to 42 %. It can be seen that the most effective PM emissions reduction over the FTP-75 cycle was with fuels containing diethyl maleate.

CO₂ emissions over the FTP-75 cycle for the test vehicle fuelled with neat diesel fuel and oxygenated fuels are shown in Fig. 11. It can be seen that for oxygenated fuels, CO₂ emissions are lower by some 5–6 %, the thus reduction in carbon dioxide emissions was more evident over the FTP-75 than over the NEDC.

Fig. 11 CO₂ emissions over the FTP-75 for neat diesel fuel and oxygenated fuels



4 Conclusions

The research carried out under the conditions of the NEDC and FTP-75 transient driving cycles showed that the influence of individual oxygenates on CO, NO_x and PM emissions was roughly additive when these oxygenates are applied together, that is as a package of additives. There was no such regularity for HC emissions. The research showed that the application of oxygenated additives generally produces a significant reduction in PM emissions and a slight change in NO_x emissions. An increase in CO and HC emissions was observed when maleates and carbonates were used as the sole oxygenates. This increase was significantly lower when the oxygenates mentioned above were applied in a package with glycol ethers.

The influence of the oxygenated additive packages was different over the NEDC and FTP-75 cycles. Generally, the packages produced more favorable changes in exhaust emissions over the FTP-75 cycle, which is more transient and dynamic (stronger accelerations). The reduction in PM emissions was higher during the FTP-75 cycle. In case of NO_x emission, it was higher (by a factor of a dozen or so) for oxygenated fuels than for neat diesel fuel over the NEDC, whereas over the FTP-75 it was slightly lower for oxygenated fuels than for diesel fuel. In the cases of CO and HC emissions, such a clear-cut relationship between type of cycle and emissions changes was not observed. Regardless of test conditions, no significant influence of oxygenated additive packages on CO₂ emissions was noted.

The application of oxygenated diesel fuels containing packages of oxygenated compounds caused a significant reduction in PM and a little change in NO_x emissions, so it produced favorable changes in the PM/NO_x emissions trade-off. These favorable changes in PM/NO_x emissions were, however, comparable to these achieved with use of the most effective individual oxygenates. The changes observed in CO and HC emissions are somewhat less important, as these exhaust components are effectively eliminated by catalytic converters. Nevertheless, changes in CO and HC emissions also showed that the oxygenated additive

packages that were tested within the research program described in this paper, are moderately competitive with the most effective individual oxygenates, that were previously tested by the authors.

Acknowledgments Support for this research was provided by the Polish Ministry of Science and Higher Education.

References

1. Stoner M, Litzinger T (1999) Effects of structure and boiling point of oxygenated blending compounds in reducing diesel emissions. SAE Paper 1999-01-1475
2. Natarajan M, Frame EA, Naegeli DW, Asmus T, Clark W, Garbak J, Gonzalez MA, Liney E, Piel W, Wallace JP (2001) Oxygenates for advanced petroleum-based diesel fuels: part 1 Screening and selection methodology for the oxygenates. SAE Paper 2001-01-3631
3. Gonzalez MA, Piel W, Asmus T, Clark W, Garbak J, Liney E, Natarajan M, Neageli D.W, Yost D, Frame EA, Wallace JP (2001) Oxygenates screening for advanced petroleum-based diesel fuels: Part 2 The effect of oxygenate blending compounds on exhaust emissions. SAE Paper 2001-01-3631
4. Gonzalez MA, Clark W, Wolf LR, Garbak JA, Wright KJ, Natarajan M, Yost DM, Frame EA, Kenney TE, Ball JC, Wallace JP, Hilden DL, King D (2002) Impact of engine operating conditions on low-NO_x emissions in a light-duty cid engine using advanced fuels. SAE Paper 2002-01-2884
5. Murayama T, Zheng M, Chikahisa T, Oh YT, Fujiwara Y, Shigeru T, Yamashita M, Yoshitake H Simultaneous reductions of smoke and NO_x from a DI diesel engine with EGR and Dimethyl carbonate. SAE Paper 952518
6. Akasaka Y, Sakurai Y Effects of oxygenated fuel nad cetane improver on exhaust emissions from heavy-duty di diesel engine. SAE Paper 942023
7. Delfort B, Durand I, Jaecker-Voirol A, Lacomme T, Paille F, Montagne X (2002) Oxygenated compounds and diesel engine pollutant emissions performances of new generation of products. SAE Paper 2002-01-2852
8. Kocis D, Song H, Lee H, Litzinger T (2000) Effects of dimethoxymethane and dimethylcarbonate on soot production in an optically-accessible DI diesel engine. SAE Paper 2000-01-2795
9. Hallgren BE, Heywood JB (2001) Effects of oxygenated fuels on DI diesel combustion and emissions. SAE Paper 2001-01-0648
10. Yeh LI, Rickeard DJ, Duff JLC, Bateman JR, Schlosberg RH, Caers RF (2001) Oxygenates: an evaluation of their effects on diesel emissions. SAE Paper 2001-01-2019
11. Porai P, Chandrasekaran S, Subramaniyam S, Jancirani J, Sahoo B (2004) Combustion and performance of a diesel engine with oxygenated diesel blend. SAE Paper 2004-01-0082
12. Nabi MN, Minami M, Ogawa H, Miyamoto N (2000) Ultra low emission and high performance diesel combustion with highly oxygenated fuel. SAE Paper 2000-01-0231
13. Bielaczyc P, Szczotka A, Kozak M, Merkisz J (2006) The influence of synthetic oxygenated fuel additives on diesel light duty vehicle exhaust emissions. FISITA 2006 World Automotive Congress, Paper F2006P048
14. Kozak M, Merkisz J, Bielaczyc P, Szczotka (2008) A Environmental performance of diesel-fuel synthetic oxygenates: maleates and carbonates. FISITA 2008 World Automotive Congress, Paper F2008-09-031
15. Kozak M, Merkisz J, Bielaczyc P, Szczotka A (2007) The influence of synthetic oxygenates on Euro IV diesel passenger car exhaust emissions. SAE Paper 2007-01-0069

16. Kozak M, Merkisz J, Bielaczyc P, Szczotka A (2008) The influence of synthetic oxygenates on Euro IV diesel passenger car exhaust emissions—Part 2. SAE Paper 2008-01-1813
17. Kozak M, Merkisz J, Bielaczyc P, Szczotka A (2008) The influence of synthetic oxygenates on Euro IV diesel passenger car exhaust emissions—Part 3. SAE Paper 2008-01-2387
18. Kozak M, Merkisz J, Bielaczyc P, Szczotka A (2009) Exhaust emissions from a diesel passenger car fuelled with oxygenated fuels. Combustion Engines 2009-SC1, Paper PTNSS-2009-SC-027
19. Kozak M, Merkisz J, Bielaczyc P, Szczotka A (2009) The influence of oxygenated diesel fuels on a diesel vehicle PM/NO_x emission trade-off. SAE Paper 2009-01-2696

A Study of Dual-Diluted Control Strategy for NG Engine

Yanchun Chen, Chao Wang, Dongxu Hua and Changbo Fu

Abstract NG engine which was popularized in the past two decades has better performance of emission and less operating cost comparing with engines consuming traditional fuel. To meet stricter emission regulations, some outer purifier methods (e.g. SCR) are applied but at the expense of increasing cost. Some research illustrated “dual-diluted” combustion mode, which is achieved by the fresh air dilution and recirculated exhaust gas (EGR) dilution, a better “inter purifier” method. In this paper, Propose and develop a model based EGR control strategy with an in-cylinder lambda model to realize “dual-diluted” combustion mode. The results show that the exhaust dilution rate and fresh intake air dilution rate can be calculated accurately. Meanwhile, through these two models, the “dual-diluted” combustion mode is realized.

Keywords Lean burn · NG engine · Dual-diluted · Control strategy

1 Introduction

Natural gas engine has similar power comparing with diesel engine which has the same displacement and the fuel economy of NG engine is much better than diesel engine because of the big gap between the prices of two kinds of fuels. Moreover, NG engine has greater potential to pass stricter emission standards and

F2012-B01-049

Y. Chen · C. Wang · D. Hua (✉) · C. Fu
China FAW R&D Center, Mainland, China
e-mail: huadongxu@rdc.faw.com.cn

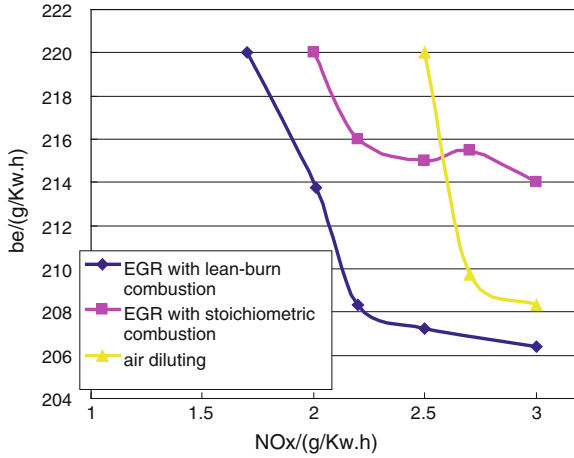


Fig. 1 The impacts of three ways of diluting on engine combustion and emission

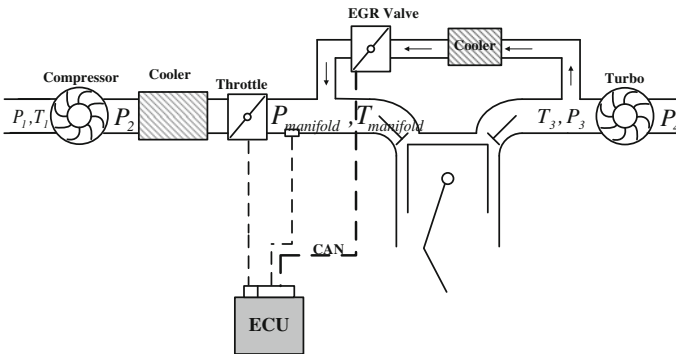
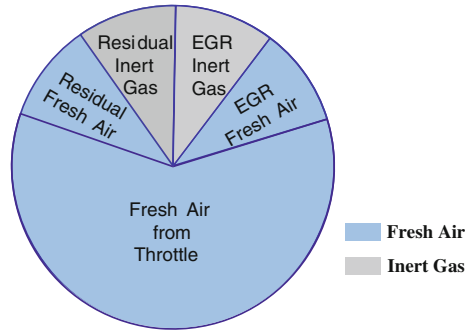


Fig. 2 Construction of EGR system

regulations [1]. In recent decades, much effort is put in research of combustion of NG engine to fulfill emission regulations. According to earlier research of NG engine performance, it is concluded that how three ways of diluting (a. air diluting; b. EGR with stoichiometric combustion; c. EGR with lean-burn combustion) impact engine combustion and emission. The results of research indicate that in the precondition of only inner-purification, all these types of diluting could satisfy limitation of NO_x of National 4 and 5 emission regulation [2]. And in aspect of fuel economy, dual-diluting is better than air-diluting which is better than EGR with stoichiometric combustion [3] (Fig. 1).

Therefore, the development and application of EGR system to NG engine has far-reaching meanings. The construction of EGR system of NG engine is shown in Fig. 2. To enlarge the application range of EGR, “High Pressure” EGR is essential

Fig. 3 Composition of in-cylinder gas



to ensure differential pressure between two sides of EGR valve, in other words, the inert gas should be used after inner cooler from the point before turbo where has high temperature and pressure.

The engine control system needs to resolve two issues:

- (1) Due to dual-diluted strategy, the effects of inert gas which is brought by external EGR to in-cylinder lambda should be considered and meanwhile relation between EGR ratio and EGR mass flow should not be ignored.
- (2) An algorithm is needed to calculate EGR mass flow during transient state according to different pressure and temperature.

2 Decouple of In-Cylinder Lambda Model and Dual-Diluted Model

2.1 Composition of In-Cylinder Gas

The fresh air passing through the throttle is the main composition of gas in cylinder. however, because of timing of intake valve and exhaust valve, there is some residual gas. Due to lean burn, internal residual gas is composed of inert gas and fresh air which is not burnt. The EGR gas also includes inert gas and fresh air. The Fig. 3 indicates the composition of gas in cylinder.

2.2 Definition of EGR Ratio and Conversion of EGR Ratio and EGR Mass Flow

Because of internal residual gas, EGR ratio is effective no matter with or without EGR system. EGR ratio is defined as following to unify the interfaces of control functions [4].

$$\text{EGR}_{\text{Ratio}} = \frac{\text{InertMassFlow}}{\text{InertMassFlow} + \text{AirMassFlow}} \quad (1)$$

Additionally, the relation between mass flow and cylinder charge [5] is linear as $\text{MassFlow} = \text{Fac} \times \text{CylinderCharge}$.

Fac is the factor only relevant to engine displacement and engine speed. Then, EGR ratio could be explained in a different way:

$$\text{EGR}_{\text{Ratio}} = \frac{\text{InertCharge}}{\text{InertCharge} + \text{AirCharge}} \quad (2)$$

In Eq. (2), AirCharge means total fresh substance in cylinder which could be burnt; InertCharge is total inert gas charge. In this way, the definition would always be effective whatever external EGR system or internal EGR system (e.g. exhaust VVT) will be applied.

After applying external EGR system:

$$\text{AirCharge} = \text{AirCharge}_{\text{Throttle}} + \text{AirCharge}_{\text{Int}} + \text{AirCharge}_{\text{Ext}} \quad (3)$$

$$\text{InertCharge} = \text{InertCharge}_{\text{Int}} + \text{InertCharge}_{\text{Ext}} \quad (4)$$

In Eqs. (3, 4), $\text{AirCharge}_{\text{Int}}$ is residual fresh gas charge; $\text{AirCharge}_{\text{Ext}}$ is external fresh gas charge contained in EGR mass; $\text{InertCharge}_{\text{Int}}$ is residual inert gas charge; $\text{InertCharge}_{\text{Ext}}$ is inert gas charge involved in EGR mass.

Lambda sensor is able to detect the proportion of fresh substance and inert gas in exhaust, so the Eq. (5) could be established:

$$\text{InertCharge}_{\text{Ext}} \times \lambda = \text{InertCharge}_{\text{Ext}} + \text{Aircharge}_{\text{Ext}} = \text{Charge}_{\text{Ext}} \quad (5)$$

Similarly, internal residual gas has the relation:

$$\text{InertCharge}_{\text{Int}} \times \lambda = \text{InertCharge}_{\text{Int}} + \text{Aircharge}_{\text{Int}} = \text{Charge}_{\text{Int}} \quad (6)$$

On the basis of Eq. (2–6), the relation between external EGR charge and EGR ratio could be concluded:

$$\text{Charge}_{\text{Ext}} = \text{AirCharge}_{\text{Throttle}} \times \frac{\lambda \times \text{EGR}_{\text{Ratio}}}{1 - \lambda \times \text{EGR}_{\text{Ratio}}} - \text{Charge}_{\text{Int}} \quad (7)$$

In conclusion, Eq. (7) makes the conversion from EGR ratio to EGR mass flow.

2.3 EGR Effects on Lambda

Generally, Lambda is used to describe the diluted extent of fresh air and can be calculated according to fuel mass and actual fresh air mass as following:

$$\lambda = \frac{\text{AirMassFlow}}{\text{FuelMassFlow} \times A / F_{\text{RatioStd}}} \tag{8}$$

After EGR system applied, lambda of inert gas is introduced and it could be expressed as the diluted extent of inert air:

$$\lambda_{\text{Inert}} = \frac{\text{InertMassFlow}}{\text{FuelMassFlow} \times A / F_{\text{RatioStd}}} \tag{9}$$

So after concept of dual-diluted EGR is introduced, total ratio of dilution could be explained by Eq. (10):

$$\lambda_{\text{AftEGR}} = \lambda + \lambda_{\text{Inert}} = \lambda \times \frac{(\text{AirCharge} + \text{InertCharge})}{\text{AirCharge}} \tag{10}$$

where,

$$\text{InertCharge}_{\text{Int}} = \frac{\text{Charge}_{\text{Int}}}{\lambda_{\text{LstCycle}} - 1} \tag{11}$$

$$\text{InertCharge}_{\text{Ext}} = \frac{\text{Charge}_{\text{Ext}}}{\lambda_{\text{DlyEGR}} - 1} \tag{12}$$

In Eq. (10–12), λ refers to lambda value before external EGR applied; $\lambda_{\text{LstCycle}}$ is lambda of residual gas after last stroke; λ_{DlyEGR} is lambda of external EGR gas and the delay is caused by the distance between cylinder and EGR valve.

3 Model Based EGR Flow Calculation

3.1 Model of EGR Mass Flow

A model of EGR valve is used to estimate the mass flow across the EGR valve which could satisfy the transient control:

$$\text{MassFlow}_{\text{EGR}} = A_{\text{EGR}} \frac{P_{\text{BefEGR}}}{\sqrt{R \times T_{\text{BefEGR}}}} \psi(P_{\text{AftEGR}}, P_{\text{BefEGR}}, k) \tag{13}$$

when $\frac{P_{\text{AftEGR}}}{P_{\text{BefEGR}}} \geq \left(\frac{2}{k+1}\right)^{k/(k-1)}$:

$$\psi(P_{\text{AftEGR}}, P_{\text{BefEGR}}, k) = \sqrt{\frac{2k}{k-1} \left[\left(\frac{P_{\text{AftEGR}}}{P_{\text{BefEGR}}}\right)^{2/k} - \left(\frac{P_{\text{AftEGR}}}{P_{\text{BefEGR}}}\right)^{(k+1)/k} \right]} \tag{14}$$

In other conditions:

$$\psi(P_{AftEGR}, P_{BefEGR}, k) = \sqrt{k \left(\frac{2}{k+1}\right)^{(k+1)/(k-1)}} \quad (15)$$

In Eqs. (13–15), k is isentropic exponent; P_{BefEGR} is pressure before EGR Valve; T_{BefEGR} is temperature before EGR; P_{AftEGR} is pressure of intake manifold; A_{EGR} is effective cross section area which is relevant to EGR opening degree.

3.2 The Definition of Standard Flow Mass

When all three conditions are fulfilled:

- (1) Pressure of upside EGR is standard ambient pressure(1013 hPa).
- (2) Temperature of upside EGR is 0 °C.
- (3) The pressure ratio of upside and downside EGR is less than 0.5283, i.e. the speed of gas flow must be sonic.

A standard mass flow is able to be defined at a certain opening, then Eq. (13) converts to:

$$MassFlowStd_{EGR} = A_{EGR} \frac{P_{Std}}{\sqrt{RT_{Std}}} \sqrt{k \left(\frac{2}{k+1}\right)^{(k+1)/(k-1)}} \quad (16)$$

where A_{EGR} is decided by throttle opening, due to its nonlinear, normally a quartic polynomial is used to indicate the relation between the section area and throttle opening degree.

$$A_{EGR} = a_4 \times \alpha^4 + a_3 \times \alpha^3 + a_2 \times \alpha^2 + a_1 \times \alpha + \alpha_0 \quad (17)$$

a_0, a_1, a_2, a_3 and a_4 in Eq. (17) are constants and the other four factors P_{Std}, R, k and T_{Std} in Eq. (16) are also constants. Therefore, flow mass $MassFlowStd_{EGR}$ is monotonic function of EGR Valve opening $\alpha \in [0, 100\%]$ and their relation can be represented as a map and calibrated.

3.3 Conversion Between Actual Mass Flow and Standard Mass Flow

When engine is running actual EGR mass flow is converted to standard mass flow as defined, and details of conversion is listed as follows:

Both sides of Eqs. (13, 16) divide both sides of Eq. (13, 16):

$$\frac{MassFlow_{EGR}}{MassFlowStd_{EGR}} = \frac{A_{EGR} \frac{P_{BefEGR}}{\sqrt{R \times T_{BefEGR}}} \psi(P_{AftEGR}, P_{BefEGR}, k)}{A_{EGR} \frac{P_{Std}}{\sqrt{RT_{Std}}} \sqrt{k \left(\frac{2}{k+1}\right)^{(k+1)/(k-1)}}} \quad (18)$$

Then at this opening degree the standard mass flow is:

$$MassFlowStd_{EGR} = \frac{MassFlow_{EGR}}{\frac{P_{BefEGR}}{P_{Std}} \times \sqrt{\frac{T_{Std}}{T_{BefEGR}}} \times \frac{\psi(P_{AftEGR}, P_{BefEGR}, k)}{\sqrt{k \left(\frac{2}{k+1}\right)^{(k+1)/(k-1)}}}} \quad (19)$$

where, $PartA = \frac{P_{BefEGR}}{P_{Std}}$ is pressure correction factor of EGR valve upside which could be obtained by EGR differential pressure sensor; $PartB = \sqrt{\frac{T_{Std}}{T_{BefEGR}}}$ is temperature correction factor and temperature could be measured by EGR valve temperature valve; $PartC = \frac{\psi(P_{AftEGR}, P_{BefEGR}, k)}{\sqrt{k \left(\frac{2}{k+1}\right)^{(k+1)/(k-1)}}$ is a stage function based on $\frac{P_{AftEGR}}{P_{BefEGR}}$. when $\frac{P_{AftEGR}}{P_{BefEGR}} \geq \left(\frac{2}{k+1}\right)^{k/(k-1)} \approx 0.5283$:

$$PartC = \frac{\sqrt{\frac{2k}{k-1} \left[\left(\frac{P_{AftEGR}}{P_{BefEGR}}\right)^{2/k} - \left(\frac{P_{AftEGR}}{P_{BefEGR}}\right)^{(k+1)/k} \right]}}{\sqrt{k \left(\frac{2}{k+1}\right)^{(k+1)/(k-1)}}} \quad (20)$$

In other conditions:

$$PartC = \frac{\sqrt{k \left(\frac{2}{k+1}\right)^{(k+1)/(k-1)}}}{\sqrt{k \left(\frac{2}{k+1}\right)^{(k+1)/(k-1)}}} = 1 \quad (21)$$

The equation is only related to pressure before/after EGR valve and isentropic exponent k, therefore, PartC could be represented by 1-D map based on pressure ratio.

3.4 Simplified Model of EGR Mass Flow

The following Figure shows a simplified prototype of EGR mass flow model based on Matlab/Simulink development platform. Table 1 means relation between standard mass flow and valve opening degree, Table 2 is Part C and Table 3 is Part B.

In Fig. 4, EgrMsFlw_Tgt is the target value of external EGR mass flow; Map is intake manifold pressure and can be used as the pressure after EGR; EgrVlv_BefP is upstream pressure of EGR; EgrT is the Temperature at EGR position and EgrPsn is the EGR opening.

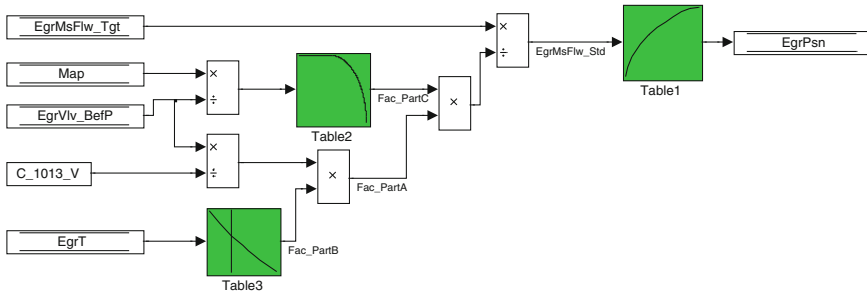


Fig. 4 Simplified prototype of EGR mass flow model

4 The Integration of EGR Control System

4.1 The Construction of EGR Control System

EGR control system utilizes model based open loop control method. The whole control method is simplified so that it could be easily realized and applied in embedded control systems. The Fig. 5 is the construction of control algorithm. Fun2 calculates desired EGR ratio including correction factors for desired EGR ratio because of different environment [6], however, it is not an important point in this paper; Fun3 converts desired EGR ratio to desired EGR mass flow based on Eq. (7); Fun4 gives the method of calculating target EGR valve opening degree which is described in detail in Chap. 3; Fun7 calculates the actual EGR flow mass according to EGR opening degree, also based on “inversed” theory mentioned in Chap. 3.

4.2 Integration

Although EGR control system is independent from other control systems, after EGR control system is introduced to original EMS, the impact to other control systems brought by EGR control should be considered.

(1) Lambda control subsystem

On basis of Eqs. (10–12), the required lambda value should be corrected due to the introduction of EGR control system.

(2) Air Charge control subsystem

The same intake manifold pressure does not mean the same intake air charge since EGR gas will affect engine intake efficiency. Therefore, EGR gas pressure should be excluded when using speed-density method to calculate air charge. Additionally, EGR gas also contains fresh substance which should be added to actual air flow mass.

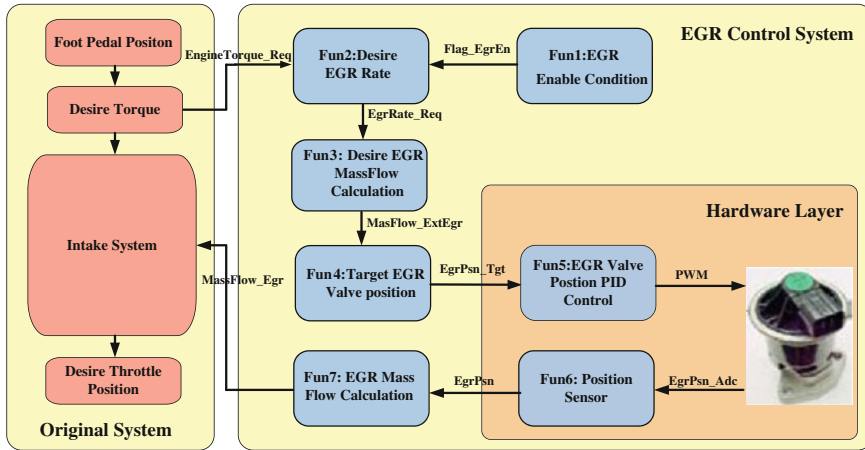


Fig. 5 Construction of EGR control sub-system

(3) Ignition control subsystem

EGR gas slows the speed of burning and MBT [5] will advance. When calculating the optimized ignition angle, the compensation brought by EGR should be considered.

5 Validation and Calibration of EGR Control System

5.1 Calibration Method

Calibration of required EGR ratio is not in the discussion of this paper since it relates to the EGR effects on engine combustion performance. Therefore, the calibrations of EGR control system focus on calibration of EGR mass flow of EGR valve.

The relation between external EGR mass flow, lambda and intake air mass could be deduced from Eq. (10). Where lambda is the air fuel ratio based on air diluting which could be calculated by EMS according to air mass and fuel mass; λ_{AirEGR} represents the total oxygen content after mixture including EGR gas burnt and it could be measured through lambda sensor mounted on engine exhaust system; Without EGR control system, after the calibration of original EMS is finished, AirCharge and ChargeInt are known. Let engine running at different working points, manually set the position of EGR valve then using Eq. (10) to calculate external EGR mass flow as feedback. Using EGR valve position, EGR mass flow and environment parameters around EGR valve, it is able to generate a fitting curve as the function of EGR mass flow and EGR valve opening degree. Figure 6 is the curve.

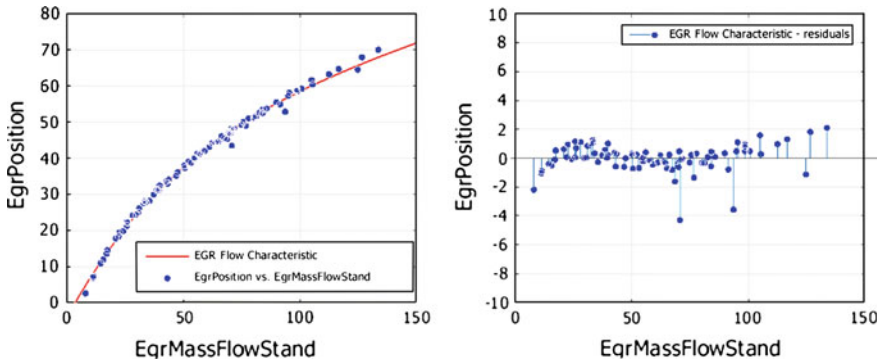
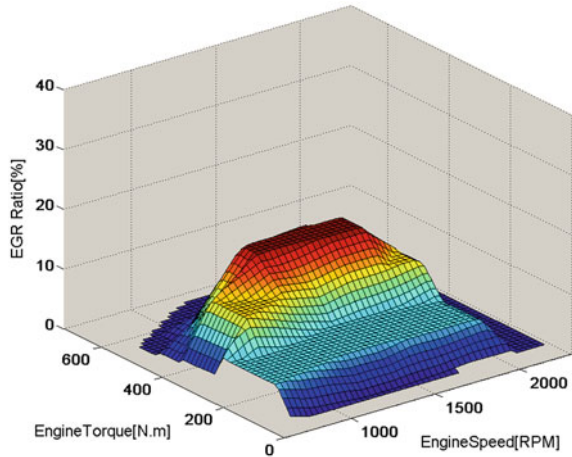


Fig. 6 The fitting curve of EGR mass flow and valve position

Fig. 7 Target EGR ratio



5.2 Validation of EGR Control System

CO₂ tracking method [7] could be used to measure actual EGR ratio, i.e. exhaust analyzer can be utilized to measure CO₂ in exhaust thus actual EGR ratio is measured.

EGR ratio of exhaust system can be calculated through CO₂ contents:

$$EGR_{Ratio} = \frac{CO_2In - CO_2Env}{CO_2Exh} \tag{22}$$

In equation, CO₂In is a volume fraction of intake mixture including EGR gas. CO₂Env is an environment CO₂ volume fraction (approx. 500 ppm) and it could be ignored when the EGR ratio greater than 3 %; CO₂Exh is CO₂ volume fraction in exhaust system.

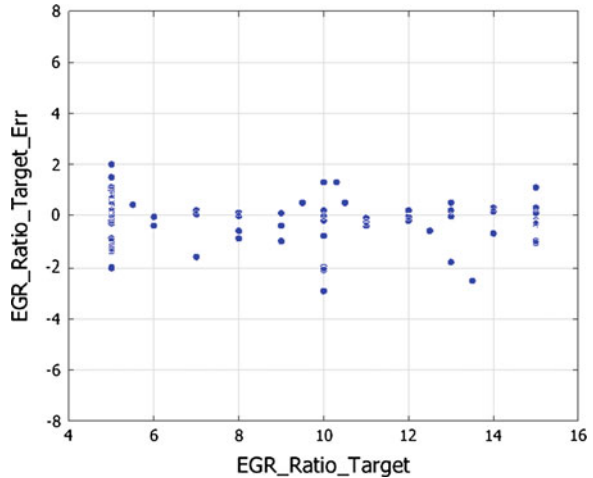
Fig. 8 EGR ratio deviations

Figure 7 is the target EGR ratio and Fig. 8 indicates the deviations between desired EGR ratio and actual EGR ratio measured through CO₂ tracking. The deviation is within 5 % and this control accuracy can satisfy EGR control requirement, therefore it validates the feasibility of EGR control strategy and calibration method.

6 Conclusion

This article analyzes the definition of EGR ratio and composition of in-cylinder mixture, thus it deduces the relation between EGR ratio and EGR mass flow. Moreover, it indicates how EGR control system impacts system lambda value. Then decouple of dual-diluted model could be realized. In addition, this paper develops EGR mass flow estimation method suitable for embedded system so that control of EGR valve and actual EGR mass flow estimation are realized thereby it makes the control system support the dual-diluted model. Lastly it illustrates the calibration method of EGR control system and validates the method using exhaust analyzer and the result of validation confirms the correctness and feasibility of EGR control system.

References

1. Dou H, Zhongchang L, Li J (2007) The Develop of electronic controlled lean burn NG engine. *Trans Csice* 25(2):137–143
2. GB 17691-2005 (2005) Limits and measurement methods for exhaust pollutants from compression ignition and gas fuelled positive ignition engines of vehicles. Standards press of china, Beijing

3. Wang Z (2010) The improvement on combustion and emissions of NG engine based on dual-diluted. Changchun
4. Longbao Z (2005) Internal combustion engine fundamentals, 2nd edn. China machine press, Beijing
5. (Germany) Robert Bosch GmbH (2009) Gasoline engine management (trans: Shen Wu). Beijing institute of technology press, Beijing
6. Gingrich JW, Callahan TJ, Dodge LG (2003) Humidity and temperature correction factors for NO_x emission from spark ignited engines. Southwest Research, San Antonio
7. Huang K, Han Y, Zhong M (2010) Development of dual flow EGR rate measurement system. Automobile Technol 9:51–57

Research and Development of Heavy-Duty NG Engine and its Key Technologies of Combustion

Huili Dou, Jun Li, Zhongshu Wang, Xiaocao Yu, Zhongchang Liu and Jingxue Li

Abstract In this paper, A heavy-duty NG engine and its electronic controlled system were developed. combustion stability, in-cylinder flow, burning rate and hazardous emissions were further investigated to develop optimized combustion control technologies for efficient and clean combustion on this engine. The electronic controlled system and NG supply system were designed in the condition of maintaining the universal parts of based diesel engine as many as possible. The combustion and emissions of NG engine were investigated by means of experiment and numerical simulation with the commercial 3D-CFD-tool STAR-CD. The in-cylinder flow and burning rate of NG engine were studied. Special-shaped combustion chamber was used to change the flow state. The results show that the engine thermal efficiency increases by 2 % compared with the original engine while using the cross-type rapid combustion chamber under 1450r/min,100 % load operating condition. Effect of three kinds of dilution methods on combustion and emissions performance from lean burn NG engine was investigated. These dilution methods include air dilution, stoichiometric combustion with EGR, and double dilution (extra air and EGR). The results show that double dilution method is superior to other methods no matter considering from fuel economy or NO_x emissions.

Keywords NG · Engine · Electronic-controlled · Combustion · Emission

F2012-B01-050

H. Dou (✉) · J. Li · J. Li
China FAW Co.,Ltd R&D Center, Changchun, China
e-mail: douhuili@rdc.faw.com.cn

Z. Wang · X. Yu · Z. Liu
State Key Laboratory of Automotive Simulation and Control,
Jilin University, Changchun, China

1 Introduction

Energy crisis and global environment deterioration have been the hot focus all over the world. The population of automobile is increasing year by year with technological progress and social improvements, which takes worse depletion of oil reserves, at the same time aggravates atmospheric pollution. Therefore great importance is attached to NG engines due to its advantages like rich gas resource, its low emissions, high cetane number and so on [1–4].

To improve the thermal efficiency and emissions performance of NG engines, NG lean burn combustion has been investigated widely by ICE researchers. It can be obtained that mixture adiabatic exponent increases at the end of combustion by rich air, and in favor of expansion work as well as thermal efficiency due to plenty fresh air. Peak of cylinder combustion temperature decreases by burning lean gas-air mixture; NO_x emissions have been controlled as well. HC emissions increase and burning rate becomes slow when the mixture is diluted to some extent, which is the bottleneck to high efficiency, ultra low emissions, limit the progress of lean burn technology [5–8].

The fuel economy can be improved by operating the engine with diluted mixtures (extra air or EGR). This will lower the combustion temperature and thus the heat losses. As a bonus, the raw NO_x emissions are reduced with high diluted mixtures. Pumping losses at part load are also reduced with these strategies.

Higher fuel economy can be achieved with lean burn operation. In this research, the combustion and emissions of NG engine were investigated by means of experiment and numerical simulation with the commercial 3D-CFD-tool STAR-CD.

2 Experimental Set Up and Procedure

The experiments were conducted on a multi-point injection, electronic controlled, lean burn NG engine. This engine is equipped with a multi-point port fuel injection system which was designed including development of injector, gas rail and NG filter and appropriate choice of key parts such as regulator and shut-off valve. The electronic controlled system of NG engine was developed which realized functions such as multi-point electronic injection, lean burn, λ close-looped feedback control, electronic throttle control, idle flashover, fault diagnosis and communication. Further engine specifications are presented in Table 1.

A CMF series flowmeter was used in order to measure mass flow rate of natural gas. CW440-1 eddy current dynamometer maximum rated power of 260 kW was used to measure engine brake torque. The dynamometer is controlled by an in-house developed control system that allows the dynamometer to be operated at constant speed mode.

Table 1 Specifications of the test engine

Bore	106 mm
Stroke	125 mm
Displacement	6.62 L
Cylinders	6, in line
Compression ration	12.0
Rated power(kW)	155@2300
Max torque (N-m)	700@1400

Emissions of HC, O₂, CO, CO₂ and NO were measured using an MEXA-7100DEGR series exhaust gas analyser made by Horiba. This device is a compact gas analyser which uses NDIR to detect CO, CO₂ and HC, and an electrochemical method for O₂ and NO. The O₂, CO, CO₂, and NO calibration were performed using a conventional span gas and gas divider.

A Kistler piezoelectric pressure transducer was installed in the roof of the combustion chamber of the 1th cylinder. The output signal from the sensor was passed through a charge amplifier, then sampled by a LabView card and a desktop PC. Signals are then analysed by an in-house developed combustion analysis tool. To synchronise the pressure measurements with the instantaneous volume of the combustion chamber, a high precision rotary incremental encoder was mounted on the engine crank shaft which gives a resolution of 0.1 °CA.

Figure 1 is schematic of engine control system.

Turbulence kinetic energy (TKE) could increase flame propagation speed and then improve engine thermal efficiency. A fast combustion chamber called Cross chamber has been developed, which is suitable for lean burn NG engine. As Fig. 2 shows, the left original chamber called Column chamber and the right novel combustion chamber called Cross chamber. Cross chamber can obtain higher TKE in cylinder using its corners. The higher TKE will promote exchange between burned and unburned mixture near the flame surface, and expand the flame surface area so that improve flame propagation rate.

In this study, effect of three kinds of dilution methods on combustion and emissions performance from lean burn NG engine was investigated. These dilution methods include air dilution, stoichiometric combustion with EGR, and double dilution (extra air and EGR). Air dilution is using extra air to dilute mixture, which can lower the combustion temperature, reduce NO_x emissions, and enhance fuel economy. Stoichiometric combustion with EGR can meet the need of using three-way catalytic converter, at the same time, reduce NO_x emissions.

The relative researches indicate that air dilution or stoichiometric combustion with EGR exists dilution limitations under different engine operating conditions, see Fig. 3. The ignition timing resulting in maximum efficiency is called MBT ignition (maximum brake torque ignition). The engine stability limits the dilution at low to medium loads due to high amount of residual gases from the previous combustion cycle. High loads and high amount of additional air or EGR results in too low exhaust energy for sufficient boost pressure. Knock limits the load when the amount of dilution decreases [2].

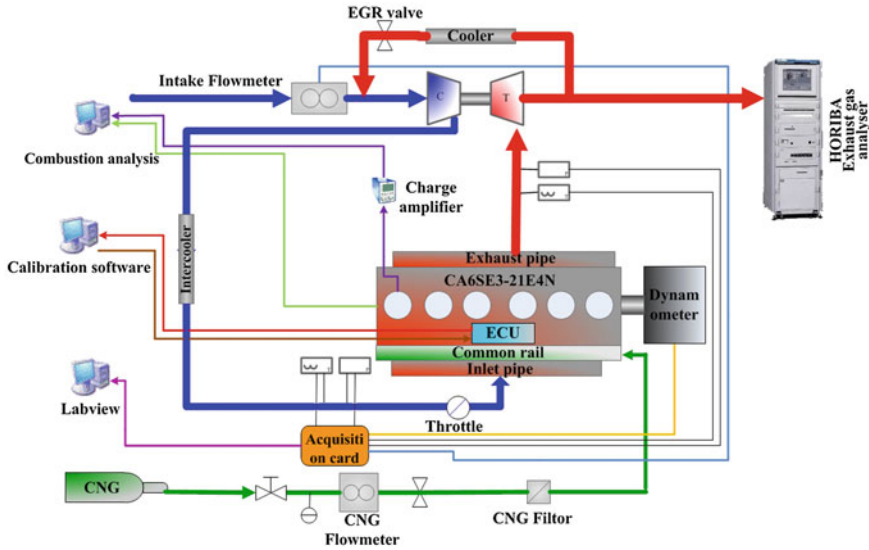


Fig. 1 Schematic of experimental setup

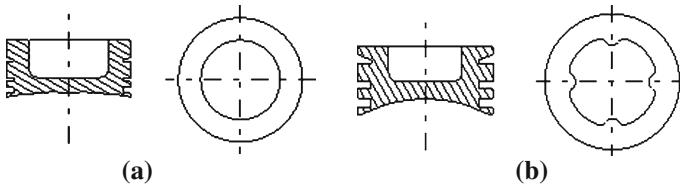


Fig. 2 The geometry of combustion chambers. a Column chamber. b Cross chamber

The method of double dilution that combined air dilution with EGR dilution is used to overcome the limitations of single air dilution or stoichiometric combustion with EGR method. Double dilution will reduce NO_x emissions while the engine fuel economy is maintained constant. Figure 3c shows the limitations on load and dilution using double dilution method.

In this study, engine combustion and emissions performance were tested with three kinds of dilution methods. The results of 1750 r/min, 75 %load operating condition will be discussed in this paper, and use HC emissions to show the limitation of dilution. During the testing, the engine power is constant, and as soon as HC emissions are more than 6 g/kW.h, excess air ratio or EGR rate will stop to increase further.

In this paper EGR rate is defined by CO₂ volume percentage in the intake manifolds after engine intake cooler, and that in exhaust gas, and environment air as well. Calculation formula as follows:

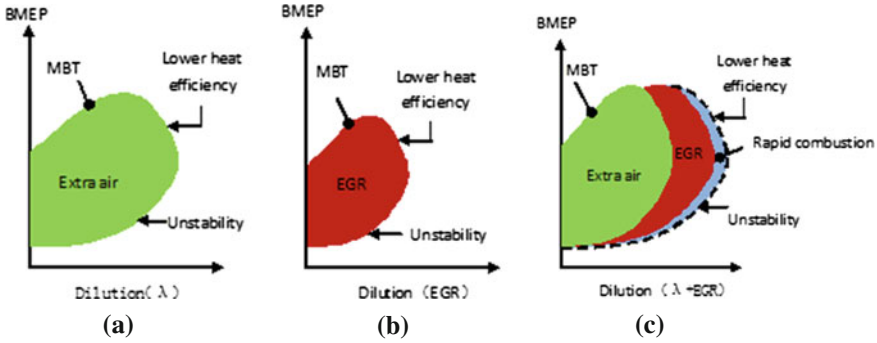


Fig. 3 Limitations in load and dilution (constant speed). a λ , b EGR, c $\lambda + \text{EGR}$

$$R_{EGR} = \frac{\varphi_{\text{CO}_2,\text{in}} - \varphi_{\text{CO}_2,\text{env}}}{\varphi_{\text{CO}_2,\text{out}} - \varphi_{\text{CO}_2,\text{env}}} \times 100 \%$$

Where, $\varphi_{\text{CO}_2,\text{in}}$ is CO₂ volume percentage in intake manifold after cooler, $\varphi_{\text{CO}_2,\text{out}}$ is CO₂ volume percentage in exhaust gas, $\varphi_{\text{CO}_2,\text{env}}$ is environment CO₂ volume percentage.

Excess air ratio λ is given by equations as follows:

$$\lambda = \frac{M_{\text{in}}}{M_{\text{CNG}} * (A/F)_{\text{sto}}}$$

where M_{in} is mass of intake fresh air, M_{CNG} is mass of consumed CNG, and $(A/F)_{\text{sto}}$ is stoichiometric air fuel ratio.

3 Results and Discussion

3.1 Effect of Combustion Chamber

The combustion process has been analyzed by using numerical simulation under 1450 r/min, 100 % load operating condition. Figure 4 shows radial distributions of TKE in combustion chamber, which are located in the middle of combustion chambers, and the crank angle is 12 °CA BTDC. It can be seen from Fig. 4, the high TKE field (TKE greater than 60 m²/s²) of Cross chamber are more than Column chamber.

Figure 5 shows average TKE in-cylinder versus crank angle of two combustion chambers under 1450 r/min, 100 % load operating condition. Average TKE of Cross chamber is higher than Column chamber, and the largest increase is near to 50 % when crank angle is near TDC.

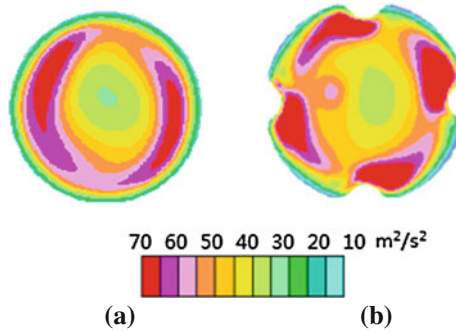
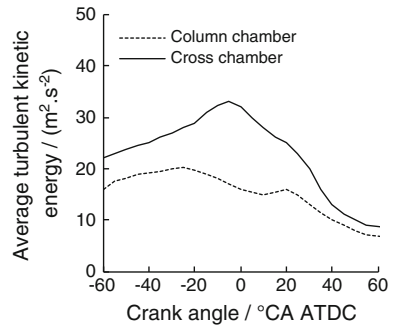


Fig. 4 TKE distribution sections of two combustion chambers. **a** Column chamber, **b** Cross chamber, (Crank angle 12 °CA BTDC)

Fig. 5 Average TKE versus crank angle (1450 r/min, 100 %load)



The combustion and emissions performances of NG engine with these two kinds of combustion chambers have been experimental investigated. Figure 6 shows combustion pressure and heat release rate in the above simulation operating condition. It can be seen that Cross chamber obtained higher peak of pressure and heat release rate than Column chamber, which due to higher TKE accelerates flame propagation speed and then increases burning rate. During the crank angle changing from 25 to 40 $^{\circ}\text{CA ATDC}$, Cross chamber obtained lower heat release rate than Column chamber that indicates the corresponding combustion duration of Cross chamber is shorter than Column chamber.

In order to study the effect of combustion chamber on engine operating process, full conditions have been investigated. Results of 1450 r/min, 25, 50, 75, 100 %load operating conditions are analyzed. Figure 7 shows test results of thermal efficiency, NO_x emissions, maximum combustion pressure, and maximum average combustion temperature, peak of heat release rate and centroid of heat release rate. It can be seen from Fig. 7a, Cross chamber has higher thermal efficiency than Column chamber and the increase rate tends to enlarge with the increasing of load. Taking 1450 r/min, 100 % load for example, the thermal efficiency of Cross chamber increases by 2 %. Figure 7b shows Cross chamber has

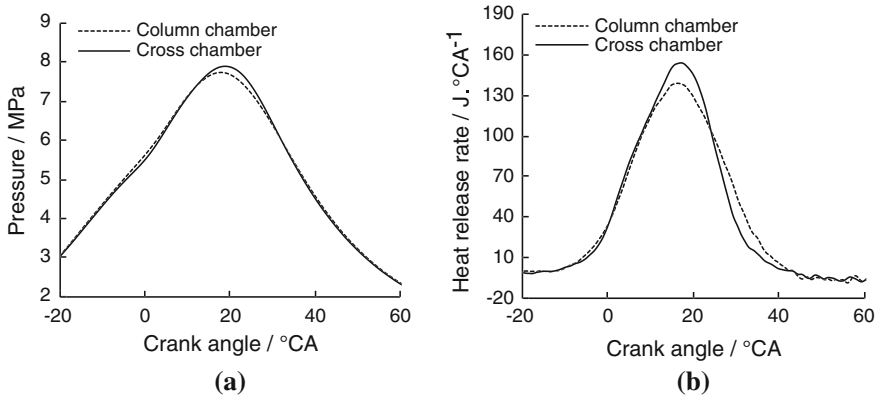


Fig. 6 Tested pressure and heat release rate histories (1450 r/min, 100 %load). **a** Pressure, **b** Heat release rate

more NO_x emissions than Column chamber, such as it increases by 1.2 g/kW.h under 1450 r/min, 100 % load. It is mainly because that fast burning rate leads to cylinder maximum combustion temperature increased, as shown in Fig. 7d. It can be seen from Fig. 7c, e, f the maximum combustion pressure and peak of heat release rate of Cross chamber are higher than Column chamber, at the same time, the centroid of heat release rate of Cross chamber is to move forward, which indicate Cross chamber can improve burning rate.

In conclusion, the Cross chamber enhanced in-cylinder TKE through structural design, which promotes flame propagation, accelerates burning rate and then increases thermal efficiency, but it will lead to NO_x emissions increase simultaneously.

3.2 Effect of EGR

The effects of air dilution method on engine combustion and emissions performance were studied. Figure 8 shows the effect of excess air ratio (λ) on brake specific fuel consumption (BSFC), NO_x emissions, HC emissions, CO emissions, and exhaust temperature before turbine. When λ increases from 1 to 1.2, BSFC decreases from 219 to 206 g/kW.h, and when λ increases from 1.2 to 1.5, BSFC increases from 206 to 208 g/kW.h. The variation of NO_x emissions is exactly opposite with the BSFC, and NO_x emissions reach the maximum when the λ is 1.2. The HC emissions are increasing with the rise of λ , and it is more than 6 g/kW.h when the λ runs over 1.5. The CO emissions are no more than 3.5 g/kW.h during the range of λ . With the increasing of λ , the exhaust temperature before turbine is linear downward trend, and the change is more than 80 °C.

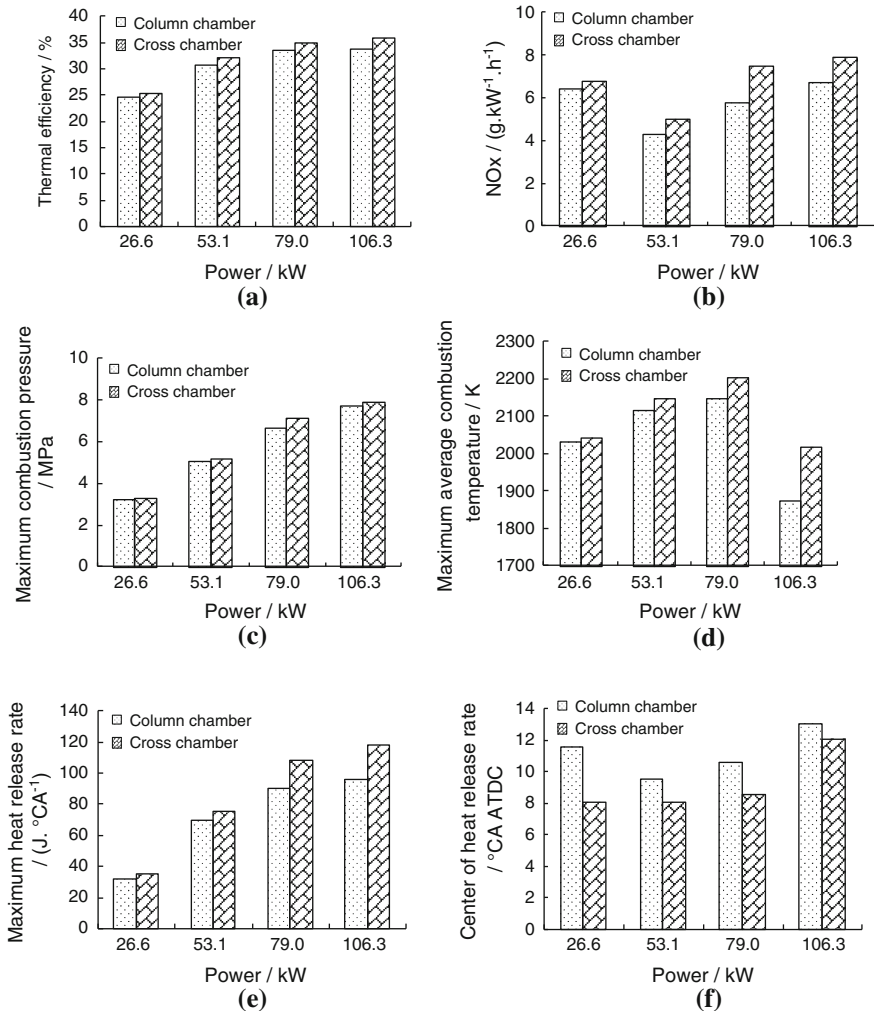


Fig. 7 The combustion parameters versus the engine power (1450 r/min). **a** Thermal efficiency, **b** NOx, **c** Maximum combustion pressure, **d** Maximum average combustion temperature, **e** Maximum heat release rate, **f** Center of heat release rate

The effects of stoichiometric combustion with EGR dilution method on engine combustion and emissions performance were studied. Figure 9 shows the effect of EGR rate on brake specific fuel consumption (BSFC), NOx emissions, HC emissions, CO emissions, and exhaust temperature before turbine. When EGR rate increases from 0 to 20 %, BSFC decreases from 219 to 216 g/kW.h, and when EGR rate increases from 20 to 26 %, BSFC increases from 216 to 220 g/kW.h. With the increasing of EGR rate, NOx emissions are linear downward trend, and the minimum is lower than 2 g/kW.h. The HC emissions are increasing with the

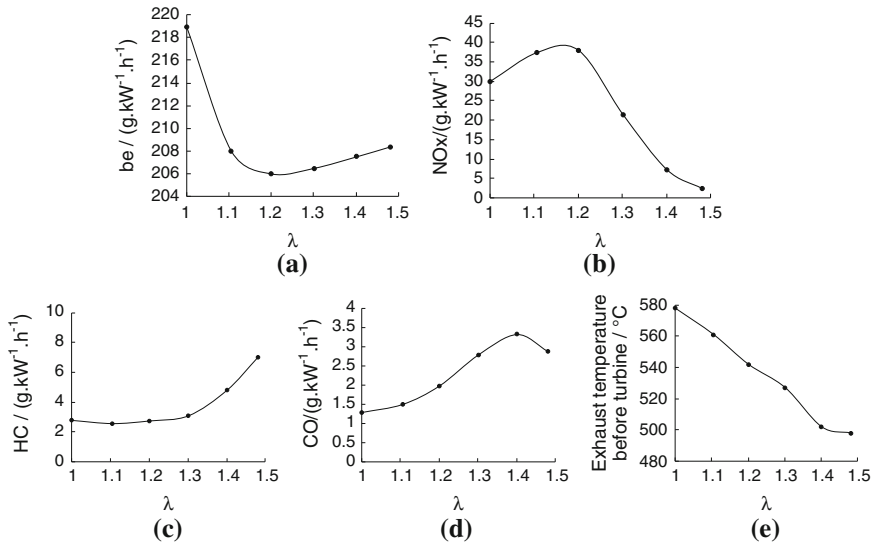


Fig. 8 λ versus emissions, fuel economy and exhaust temperature (1,750 r/min, 75 %load). **a** be, **b** NOx, **c** HC, **d** CO, **e** Exhaust temperature before turbine

rise of EGR rate, and it is more than 6 g/kW.h when the EGR rate runs over 25 %. The effect of EGR rate on CO emissions and exhaust temperature before turbine is not obvious, which can be ignored.

Figure 10 shows the effect of double dilution (λ is 1.45, increasing EGR rate) on brake specific fuel consumption (BSFC), NOx emissions, HC emissions, CO emissions, and exhaust temperature before turbine. When EGR rate increases from 0 to 2 %, BSFC decreases from 208.5 to 208 g/kW.h, and when EGR rate increases from 2 to 6.89 %, BSFC increases from 208 to 211 g/kW.h. With the increasing of EGR rate, NOx emissions are linear downward trend, and the minimum is lower than 2.2 g/kW.h. The HC emissions are slowly increasing with the rise of EGR rate, but it is more than 6 g/kW.h when the EGR rate runs over 6 %. The effect of EGR rate on CO emissions and exhaust temperature before turbine is not obvious, which can be ignored.

Here just show the effect when λ is 1.45, similar results were obtained when λ is 1.1, 1.2, 1.3, 1.4, 1.5 and so on.

In short, air dilution method can obtain superior fuel economy, stoichiometric combustion with EGR dilution method can acquire better control performance of NOx emissions and then double dilution method couples with advantages of the former dilutions, at the same time, it could further enhance fuel economy and lower NOx emissions. This is mainly because air dilution method supplies enough oxygen, which can improve combustion competition and fuel economy. Stoichiometric combustion with EGR dilution method can lower the combustion temperature, so NOx emissions can be controlled, but the fuel economy is

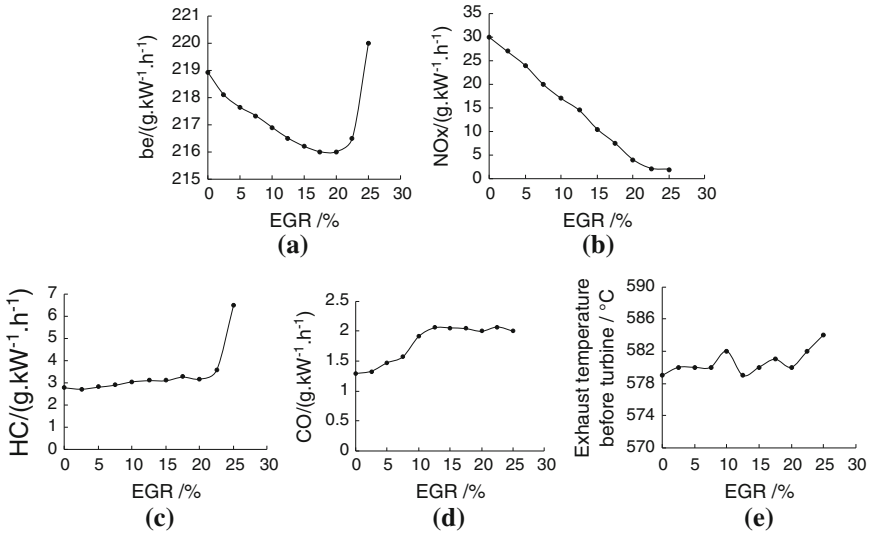


Fig. 9 EGR rate versus emissions, fuel economy and exhaust temperature (1,750 r/min, 75 %load). **a** be, **b** NOx, **c** HC, **d** CO, **e** Exhaust temperature before turbine

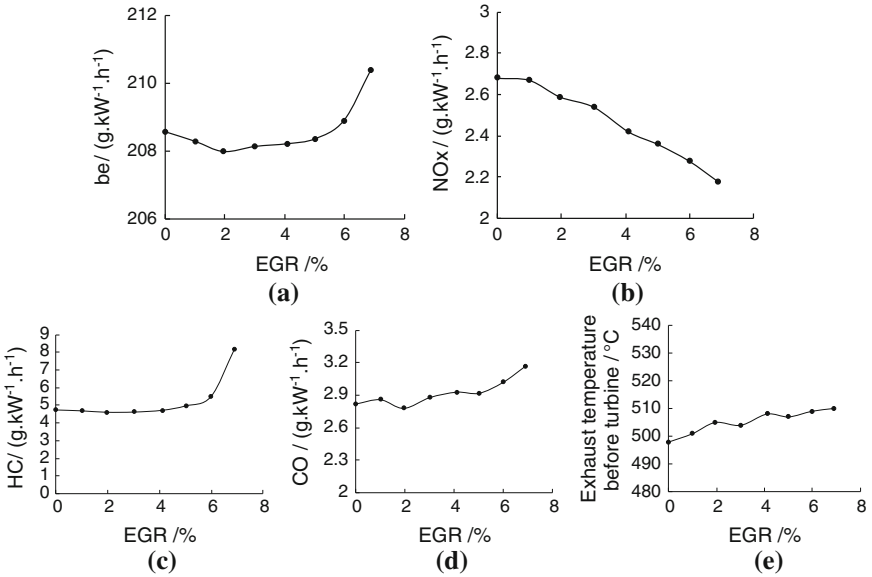


Fig. 10 EGR rate versus emissions, fuel economy and exhaust temperature with $\lambda = 1.45$ (1750 r/min, 75 %load). **a** be, **b** NOx, **c** HC, **d** CO, **e** Exhaust temperature before turbine

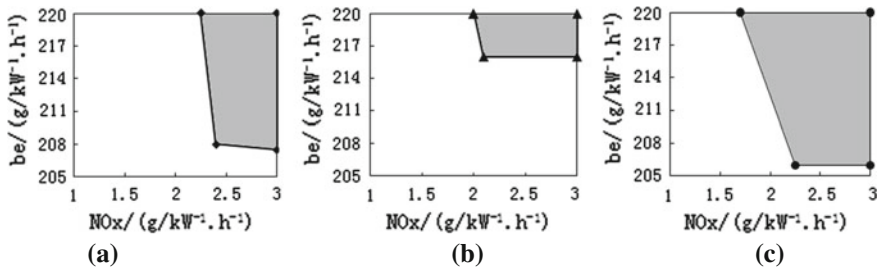


Fig. 11 NO_x emissions versus fuel economy under different dilute strategies (1750r/min, 75 %load). **a** Air dilution, **b** Stoichiometric combustion with EGR, **c** Twofold dilution

deteriorated. Double dilution method can supply extra air to meet the need of oxygen, at the same time, use EGR to lower the combustion temperature, and enhance thermal efficiency by decreasing the pumping loss. In summary, double dilution method is superior to other dilution methods no matter considering from fuel economy or NO_x emissions.

The effects of three kinds of dilution methods on engine fuel economy and NO_x emissions under 1750 r/min, 75 % load operating condition were studied by optimizing combustion parameters, such as spark timing, NG injection timing and so on. Figure 11 shows achievable control area, dark region as shown, when considering both fuel economy and NO_x emissions. It can be seen that air dilute manner could control NO_x emissions is 2.4 g/kW.h while BSFC is 208 g/kW.h, stoichiometric combustion with EGR could control NO_x emissions is 2.1 g/kW.h while BSFC is 216 g/kW.h, and double dilution could control NO_x emissions is 2.25 g/kW.h while BSFC is 205 g/kW.h.

4 Summary/Conclusions

The multi-point injection NG supply system was designed including development of injector, gas rail and NG filter and appropriate choice of key parts such as regulator and shut-off valve. The electronic controlled system of NG engine was developed which realized functions such as multi-point electronic injection, lean burn, λ close-looped feedback control, electronic throttle control, idle flashover, fault diagnosis and communication.

The in-cylinder flow and burning rate of NG engine were studied. Special-shaped surface of combustion chamber was used to change the flow state. The results show that the engine thermal efficiency increases by 2 % compared with the original engine while using the cross-type rapid combustion chamber under 1450 r/min, 100 %load operating condition.

Effect of three kinds of dilution methods on combustion and emissions performance from lean burn NG engine was investigated. These dilution methods

include air dilution, stoichiometric combustion with EGR, and double dilution (extra air and EGR). The results show that double dilution method is superior to other methods no matter considering from fuel economy or NO_x emissions.

Acknowledgments The research is supported by National Science Foundation of China under Project No.50906033.

References

1. Manivannan A, Tamilporai P (2003) Lean burn natural gas spark ignition engine-an overview. SAE paper, 2003-01-0638
2. Einewall P, Per Tunestal and Bengt Johansson (2005) Lean burn natural gas operation versus stoichiometric operation with EGR and a three way catalyst. SAE paper, 2005-01-0250
3. Dwyer HA, McCaffrey Z, Miller M (2004) Analysis and prediction of in-cylinder NO_x emissions for lean burn CNG/H₂ transit bus engines. SAE paper, 2004-01-1994
4. Shi Y (2005) Latest update on china's natural gas pipeline infrastructure and implications for NGV promotion in China. Clean Fuels-CNG/NGV- Hybrids-Fuel Cells China/Asia 9:6-7
5. Battoei Avarzaman M (2002) Investigation of completeness of combustion in CNG fueled spark ignition engines. Thesis for the degree of master of applied science at the university of Windsor
6. Atibeh PA, Dennis PA (2012) Lean burn performance of natural gas fuelled, port injected, spark ignition engine. SAE paper. 2012-01-0822.2012
7. Hirotomi T, Nagayama I, Kobayashi S, Yamamasu T (1981) Study of induction swirl in a spark ignition engine. SAE paper 810496
8. Arcoumanis C, Bicen AF, Vlachos NS, Whitelaw JH (1982) Effects of flow and geometry boundary conditions on fluid motion in a motored IC model engine. Proc Inst Mech Eng 196:1-10

Part II
Advanced Hybrid Electric Vehicle

Development of CHS Hybrid System for City Bus

Guangkui Shi, Renguang Wang, Hongtao Chen and Zhiguo Kong

Abstract A hybrid electric system with two sets of planetary gear and two electric motors has been developed for city bus, which can provide series/parallel driving mode for HEVs. The power train assembly of this system integrates functions of power coupling, automatic transmission and auto clutch. It's control system was also designed to provide good fuel economy and traction performance with fuel consumption improved by more than 30 %. The new system can meet requirements of HEVs and Plug-in HEVs, which provides a new choice for china automotive industry with satisfied cost and performance.

Keywords Hybrid power train · Two-motor drive · Power coupling · Locking mechanism

1 Introduction

Most of typical hybrid power trains are composed of engine, generator, motor and planetary gear sets with engine power distribution function is performed by planetary gear set. In these power trains, most of these systems can provide pure electric driving and series/parallel driving modes. But in these hybrid systems, the generator can only works as a generator with short time being an engine starter, and cannot provide driving torque for vehicle. How to make the generator works as

F2012-B02-006

G. Shi · R. Wang (✉) · H. Chen · Z. Kong
China Automotive Technology and Research Centre, People's Republic of China
e-mail: shiguangkui@catarc.ac.cn

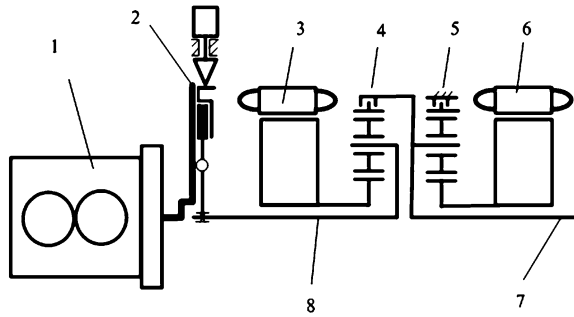


Fig. 1 Schematic of CHS power train for city bus 1 Engine, 2 shock absorbing and locking combination mechanism, 3 first motor, 4 first planetary gear set, 5 second planetary gear set, 6 second motor, 7 second shaft, 8 first shaft

a motor to provide driving torque for vehicle is one purpose of our research, and how to design planetary gear sets to reduce its complicity and cost are also our research focuses. Now a new power train system has been developed, CATARC Hybrid System(CHS), which can realize two motor driving function with addition of a locking mechanism to brake engine [1, 2].

CHS is a kind of hybrid system with two motors and two planetary gear sets as its features. And the product for city bus has been developed and in use for nearly two years with outstanding performances. The CHS for middle size bus and SUVs are also developed and being in testing. CHS system can provide driving torque with two motors working as driving motors in pure electric driving condition, which can improve dynamical performance for general HEVs and PLUG-in HEVs.

2 Composition of CHS Power Train

As shown in Fig. 1, the CHS system is mainly composed of engine, shock absorbing and locking combination mechanism, first motor, second motor, first planetary gear set, second planetary gear set, first shaft, second shaft and control system (HCU). And the shock absorbing and locking combination mechanism includes an electromagnet, lock pin, shock absorber, and pressing plate with around ring gear. It is used to lock engine in two motors driving mode.

The flywheel is connected with first shaft by means of shock absorbing and locking combination mechanism. Then first shaft is connected with carrier of first planetary gear set. The rotor shaft of first motor is connected with sun gear of first planetary gear set, and the rotor shaft of second motor is connected with sun gear of second planetary gear set. The ring gear of second planetary gear set is fixed with second motor shell. The power from second motor is transmitted from sun gear to carrier of second planetary gear set, then to second shaft for outputting to drive vehicle. With these main structure characteristics, the CHS system has four following features:

1. Shock absorbing and locking combination mechanism has two purposes. First is to reduce rotation vibration from engine. Second is to control rotation of carrier of first planetary gear set. When in pure electric driving condition, the carrier is locked and the engine cannot rotate, then two motor can work together to drive vehicle simultaneously.
 2. Each motor has its own case, and two end covers of motors form amounting case for two planetary gear sets which perform engine power distribution and power coupling of engine and motor. This configuration can benefit calibration and manufacture of electric motor, and cost was also reduced.
 3. The ring gears of two planetary gear sets are designed as all following structures. It means they are not fixed completely, and have small clearance between ring gear and its fixing position for alignment. This can reduce working and assembly precision requirements of planetary gear to save cost.
 4. The power from engine and motor are transisted to ring gear of first planetary gear set and carrier of second planetary gear set, and coupled here to second shaft for driving vehicle. These configurations provide no radial force on the structure and then simplify mechanical structure. The power from second motor is outputted from carrier of second planetary gear set, which can reduce the peak torque of second motor and size of motor to improve its power intensity of motor.
- With these characteristics, the CHS can meet the requirements of city bus which top speed is less 80 km/h.

3 Analysis of CHS Operation Modes in City Bus

CHS system can conduct 6 different operation modes, which include pure electric driving modes in low load and high load, hybrid mode, regenerative braking mode, pure generation mode, and grid charging mode. Basing on structure described in Fig. 1, these operation modes are described as following.

1. Pure electric driving mode in low load condition. With locking mechanism engaged, engine closed, and first motor rotation freely, the power battery provides electric power for second motor, then second motor drive vehicle according to vehicle moving direction requirement.
2. Pure electric driving mode in high load condition. For plug-in HEVs, the pure electric driving mode with high loads is adopted. With locking mechanism engaged and engine shutdown, the carrier of first planetary gear set cannot rotate. At this condition, the two planetary gear sets all works as speed reducers, the power battery provides electric power, and the driving power from two motor are coupled to drive HEV simultaneously.
3. Hybrid driving mode. The locking mechanism is disengaged, and engine starts. The power from engine is distributed into two transmitting paths. One part is to drive first motor to work as a generator, and the electric current is used to drive

second motor or charge power battery. Another part of engine power is transmitted to ring gear and coupled with the power from second motor to drive vehicle. The power transmitted between power battery and motor controller is mainly dependent on acceleration pedal input, vehicle speed and battery SOC.

4. Regenerative braking mode. During vehicle braking and decelerating conditions, the driving wheels of vehicle drive second motor work as a generator to produce electric power to charge power battery.
5. Pure generation mode. When the vehicle stopped, the ring gear of first planetary gear set cannot rotate. The locking mechanism disengaged, engine started. The engine drives the first motor work as a generator to charge power battery. The engine speed is controlled at 1,200 rpm with lowest fuel consumption.
6. Grid charging mode. When the HEV bus stops at charging station, the electric power from grid can be used to charge power battery to improve SOC for next day operation running, especially at night.

4 Electric Control System of CHS

4.1 Brief Introduction

At the conditions of vehicle starting and vehicle speed less than 24 km/h, the vehicle runs in pure electric driving mode. When vehicle speed is more than 24 km/h, the first motor works as a starter to start engine, the HEV is operated in hybrid mode. When vehicle decelerates and its speed is less than 12 km/h, the engine stops. In normal condition, if more driving torque is required or the SOC is less than target value, the engine runs at 1,500 rpm with load rate at 70–80 %. At the above condition, one third of engine power is used to drive first motor to generate, and two thirds used to drive vehicle directly. If the engine power is not needed, its rotating speed is reduced to idle speed. If the vehicle speed is more than 60 km/h, the engine is controlled operating from 1,500 to 2,000 rpm continuously with lower fuel consumption rate.

Figure 2 shows the schematic of the electric control system of the hybrid bus. The driver operation signals are input into the hybrid control unit (HCU) directly. And other components and subsystems in the vehicle are linked together through a system of networked communication. The command signals, the sensor feedback signals, and the system output variables interconnect the supervisory controller, and the subsystems and components through this automotive communication network. The type of networked communication used is high-speed controller area network (CAN). There are two CAN bus with 250 kbps transfer rate to achieve reasonable bus loading. The HCU is the core of system, and all the control strategy and supervisory function are embedded in it.

The main function of the strategy is energy management [3–5]. The energy management strategy is implemented by a power controller. It controls the energy

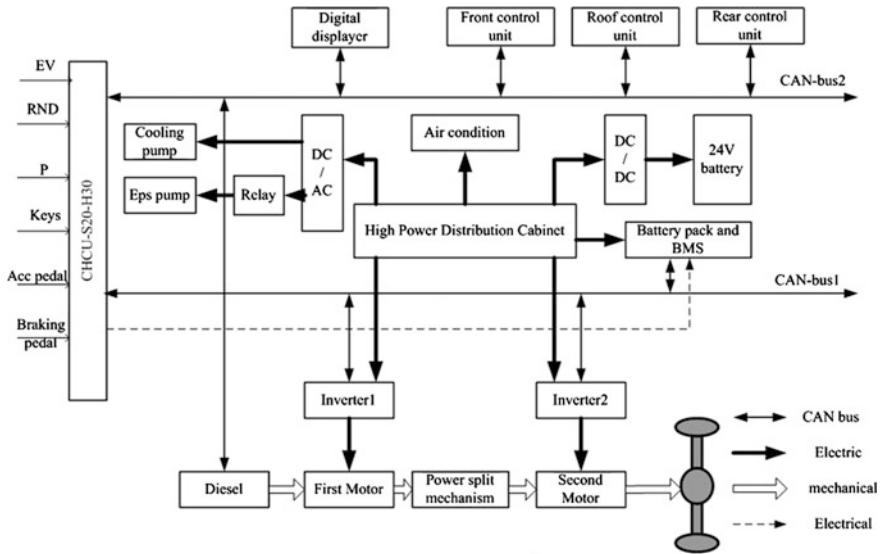


Fig. 2 Schematic of the electric control system

flow between all components, and optimizes electric power generation and conversion in the individual components.

4.2 Analysis on Control Strategy of CHS

Control strategy is the core of the control system, which can determine vehicle performance [4, 5]. It is the combination of the control method of engine, two motors, and locking mechanism in CHS system. The driver input requirements through brake and acceleration pedals, and the HCU ensures the vehicle smoothness and control reliability in order to get a good drivability. The signal of the pedals, especially the acceleration pedal, is used to control the output power in the second shaft, which is realized to regulate output of the motors and engine by HCU, as shown in Fig. 3. As shown in Figs. 4 and 5, the control strategy is described in detail in HEV mode and EV mode respectively. In this system, only the control of first motor torque adapts PI controller. The control method of engine speed and torque of second motor are conducted with looking up table and open-loop calculation respectively. Since the model of controlled objects is non-linear and not precise enough. The parameters of the PI controller are difficult to determine. Therefore two tables are introduced with expert experience to gain the parameters of the proportion and the integrity respectively.

To make the power battery provide instantaneous power and absorb regenerative braking energy at any time, the SOC of the battery pack need to be maintain a

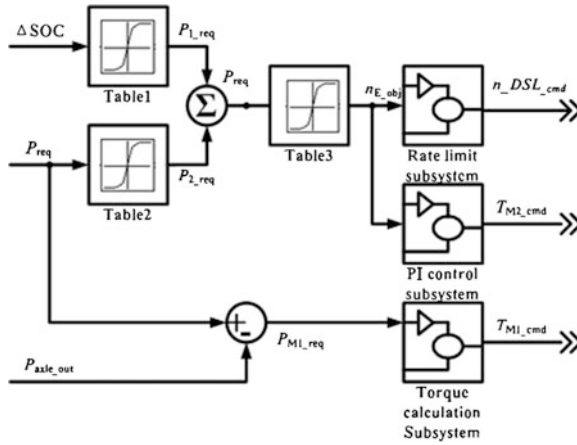


Fig. 3 Schematic of the control strategy

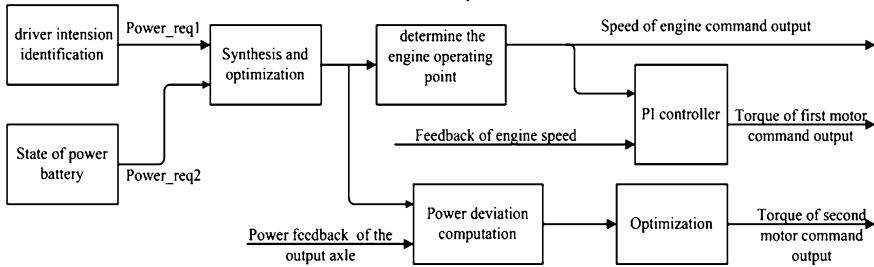


Fig. 4 Control realization process in HEV mode

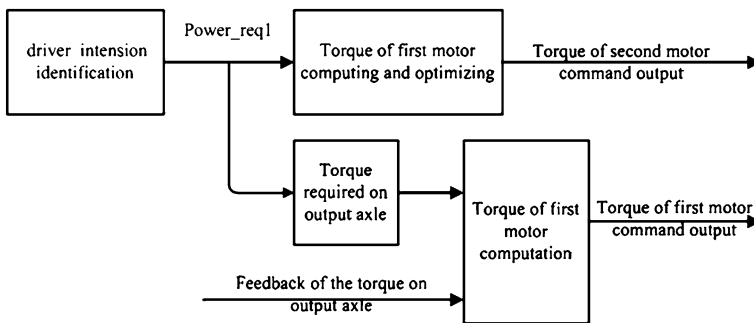


Fig. 5 Control realization process in EV mode

fixed range, which can improve vehicle life and lower the cost taking into account life of the battery. The delta between the aim and the object of the SOC is introduced to modify the required power of the system, as shown in Fig. 4.

Table 1 Dynamical performance of HEV city bus

Acceleration time from 0 to 50 km/h(s)	17
Maximum gradability (%)	>15
Maximum speed (km/h)	80

Table 2 General parameters of CHS power train for 12 m city bus

Basic parameter	Total mass (kg)	410	Continuous variable speed range(rpm)	0-2,250
	Max speed (rpm)	2,250	Max torque(Nm) (from 0 to 550 rpm)	3,000
First motor	Rate power (kW)	44.5	Peak power(kW)	71.2
	Rate speed (rpm)	1,700	Top speed(rpm)	5,000
	Rate torque (Nm)	250	Peak torque(Nm)	400
Second motor	Rate power (kW)	84	Peak power(kW)	147
	Rate speed (rpm)	2,000	Top speed(rpm)	7,500
	Rate torque (Nm)	400	Peak torque(Nm)	700



Fig. 6 12 m long city bus with CHS system under testing

To optimize fuel economy of HEV bus, operation points of engine are allowed to change slowly. As shown in Figs. 3 and 4, engine operation point is determined by driver’s input and SOC of power battery. Here, the increasing or decreasing rate of the algebraic power sum is limited step by step. The difference between the power command and the power output of the engine is compensated by the second motor instantaneously. During short time accelerating, the second motor can output power to meet most of power command, then the load of the engine is lighter and the fuel rate is lower. As a result, the engine operates in the region with higher efficiency and lower load rate in most conditions, which is benefit to the fuel economy of the HEV bus.

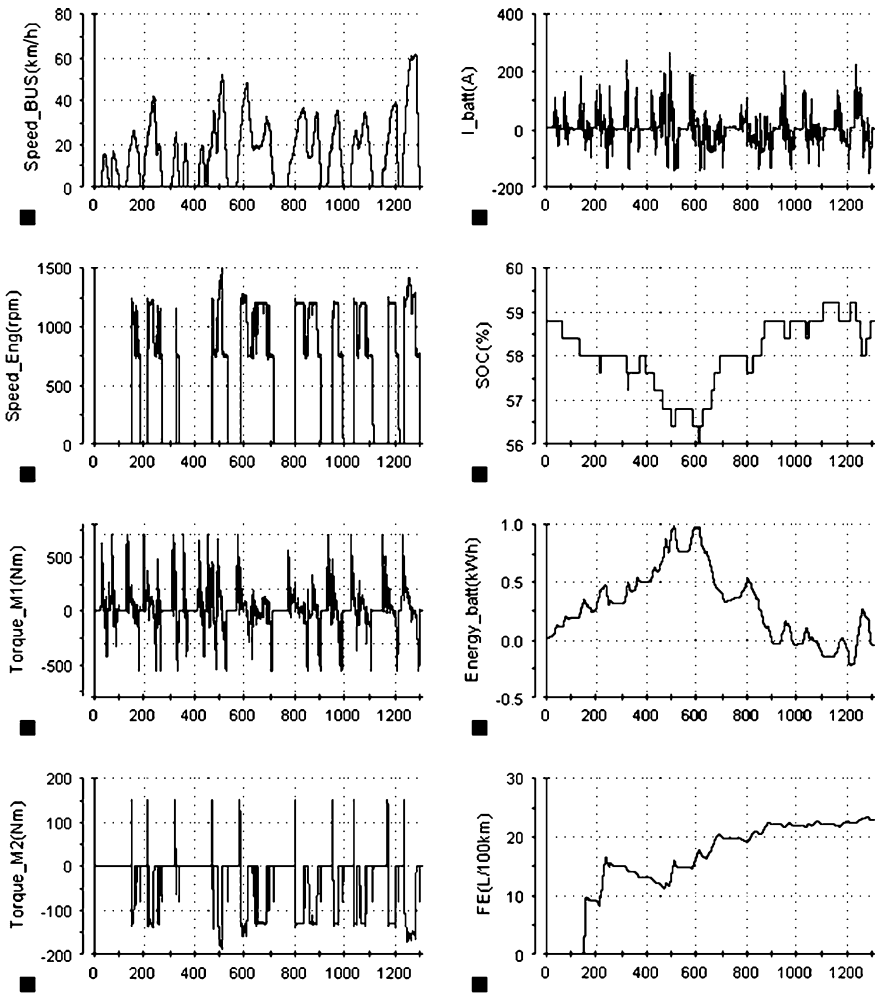


Fig. 7 Parts of experimental curves during the test cycle

5 CHS Application on City Bus and Test

5.1 Parameters of Power Train and HEV City Bus

CHS system was developed for 12 m long city bus. The dynamical performance parameters of this HEV city bus are listed in Table 1. For simplicity, the two planetary gear sets were designed in same sizes and parameters. The sun gear has 54 teeth, planetary gear has 30 teeth and ring gear has 114 teeth, so the gear ratio for planetary gear set is 2.111 and detail parameters of power train are listed in

Fig. 8 Operation point of engine during the test cycle

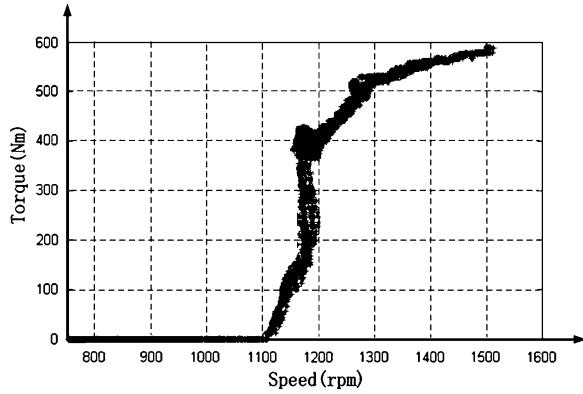


Table 2. Figure 6 is the picture of developed HEV city bus being tested in laboratory.

5.2 Test Results of HEV City Bus with CHS System

The HEV city bus had been tested in laboratory according to energy consumption test method of heavy hybrid electric vehicle of China National Standard (GB/T19754-2005). The test cycle is China typical city bus cycle. Figures 7 and 8 show curves of experimental results and engine operation points in the test cycle respectively. In Fig. 7, the profile of the bus speed is in accordance with the test cycle. During the cycle, the operation of the diesel engine is smooth and steady, which can benefit the fuel consumption of the bus. In this test, bus fuel consumption is 23.4L/100 km.

The torque of second motor varied rapidly within wide range to make the output power in the shaft to be the same with the driver power command. The curve of torque of first motor shows operations condition of engine. The current curve of power battery indicates the rapid response of second motor and regenerative braking of the bus. The variation of the SOC and energy output of power battery means that energy in balanced during the test cycle. And the computed instantaneous fuel consumption is effective, as shown in Fig. 7.

The fuel consumption has been tested in actual city bus operation conditions with full load in Dandong city in Liaoning province and Zhengzhou city in Henan province respectively. The fuel economy is less than 28L/100 km even in urban congestion conditions. And the HEV bus also has been tested in several conditions with constant velocity and simulated city operation conditions, all the test results shows the HEV city bus with CHS system has excellent fuel economy performance.

6 Conclusions

CHS hybrid system adopts two planetary gears sets and two motor to form hybrid power train system. And using locking device to lock engine to provide the function that two motor can drive the HEV simultaneously in pure electric driving mode. Corresponding controller with special strategies was developed for this power train system. In power train structure, the two motor are in two cases and the floating structure was used in planetary gear sets, which reduce manufacture difficulty and cost. CHS system was used in 12 m long HEV city bus successfully with good dynamical and economical performance. Comparison with current power train systems in China, CHS system can provide more traction torque with smaller size and lower cost. The parameters of CHS system are also needed to be optimized to improve vehicle performance, and its control strategy needed to be optimized too.

References

1. Zhao H, Shi G, Wu Z et al Hybrid power train system for motor vehicle. China patent:200810052817.8, 2010-12-08
2. Zhao H, Shi G, Wang R et al Hybrid control system for motor vehicle. China Patent: 201010159660.6, 2010-04-29
3. Chan CC (2002) The state of the art electric and hybrid vehicles. *Proc IEEE* 90(2):247–275
4. Ehsani M, Gao Y, Emadi A (2009) *Modern electric, hybrid electric, and fuel cell vehicles: fundamentals, theory, and design* (2nd edition). CRC Press, Boca Raton, 1-10
5. Nagasaka A (1998) Development of the hybrid/battery ECU for the Toyota hybrid system. SAE paper 981122

Optimization of an Extended-Range Electric Vehicle

Haitao Min, Dongjin Ye and Yuanbin Yu

Abstract Under the current technical circumstances, the high cost of the electrical vehicle is the biggest problem of the mass marketization. So how to reduce the cost on the promise that the dynamic performance requirements be met becomes more and more important. The purpose of this study is to develop a methodology to optimize an Extended-Range Electric Vehicle's parameters taking minimum drivetrain cost and the best fuel economy as objectives. Design parameters, including electric motor peak power, engine rated power, and battery capacity are reasonably set. The simulation result illustrates that a set of vehicle dynamic performance constraints are met, in the same time the production cost is reduced and the fuel economy is improved. Further study should optimize the control strategy variables, too. Thus, the fuel economy can be optimized in a further extent. What's new of this study in the field is taking production cost as one of the objectives to optimize the powertrain parameters. According to the ADVISOR simulation result, the fuel economy have been significantly improved and production cost has been reduced.

Keywords E-REV · Parameter-matching · GA · Optimization · Simulation

F2012-B02-009

H. Min (✉) · D. Ye · Y. Yu
State Key Laboratory of Automotive Simulation and Control,
Jilin University, Changchun, China
e-mail: minh_t_vsd@163.com

1 Introduction

The automotive emission has become one of the major sources of air pollution. So how to reduce the automotive exhaust is the most important task of the car industry. Developing electric vehicle types is a feasible way to solve this problem, but under current technical circumstances, mass popularization of electric vehicles encounters the issue of high production cost, and the main element of the production cost comes from the battery. It is too expensive to equip the full sized battery, but too short electric range it can run to install a small sized battery, besides, small sized battery would also cause the consumers' anxiety of the drive range. Adding the range extender on electric vehicle is a feasible way to solve the problem, thus, a new type of vehicle has been created—extended-range electric vehicle(E-REV). This solution could perfectly balance this contradiction, the consumers would no longer worry about the drive range, because the car can rely on gasoline, and the production cost could sharply been cut down, because full sized battery is no longer necessary, so that the new type of vehicle can adapt the competitive market. The remaining problem is just determine the all electric drive range and the powertrain components' parameters.

The parameters should be set on the purpose of reducing the powertrain productive cost on the promise that the dynamic demands been met, the first part of this paper preliminarily set these parameters but these parameters are not the best for the powertrain, because we didn't count the productive cost in when we set them. In the second section of this paper, we employed the NSGA_II(Non-dominated Sorting Genetic Algorithm) genetic algorithm optimized the above parameters, in the course of analysis, the function of `adv_no_gui` of ADVISOR has been circularly called, and the objectives of optimization are "improve the fuel economy and minimize the productive cost". The third section illustrates the fuel economy improvement and the cost reduction by comparing the ADVISOR simulation results.

2 Sizing of Components

Figure 1 shows the architecture of E-REV, the powertrain was constituted by driving motor, range extender, power battery and the main gear. The power flow was managed by a VCU(vehicle control unit).

The E-REV was derived from EV, so this type of vehicle inherit all the EV features, as we can see in Fig. 1, the drive power could only provided by the drive motor, because only the drive motor was mechanically connected to the wheels.

Table 1 shows the basic parameters of the prototype vehicle. The sizing and simulation task are all based on these parameters.

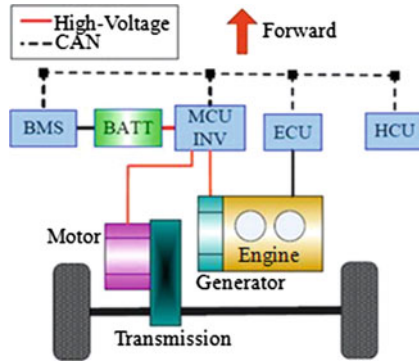


Fig. 1 Architecture of E-REV

Table 1 Prototype vehicle parameters

Parameter names	Values	Parameter names	Values
Kerb mass m_0 /kg	1,550	Gross weight m/kg	1,950
Rolling resistance coefficient f	0.012	Tire rolling radius r/m	0.317
Transmission efficiency η_t	0.93	Final ratio i_0	7.2
Frontal area A/m^2	2.0	Drag coefficient C_D	0.28

Table 2 Dynamic performance demands

		Test standard	Design criterion
Dynamic performance	Max Speed, km/h	GB/T 18385	Transitorily ≥ 140 Continuously ≥ 120
	0–50 km/h Accelerate time, s		≤ 5
	0–100 km/h accelerate time, s		≤ 15
	Gradeability, %		$\geq 30\%$

2.1 Motor Sizing

All the drive power is provided by the drive motor, to meet the design objectives, we must set the appropriate parameters of drive motor. Table 2 shows the dynamic demands of this vehicle.

The drive motor must simultaneously meet these demands, so we have to respectively set each parameters according to respective demand, and select the largest one.

The required power of a vehicle in a certain speed could be compute by using this formula [1]:

$$P_{max1} = \frac{mgv}{3600\eta_t} \left(f + \frac{C_D A v^2}{21.15mg} \right) \tag{1}$$

where m is the calculate mass, g is gravity acceleration, v is vehicle speed, η_t is transmission efficiency, C_D is drag coefficient, A is frontal area.

We set the power to 30.31 kW to meet the max speed demand. The relationship between gradient and the demanded power could be expressed as [2]:

$$P_{max2} = \frac{mgv_p}{3600\eta_t} \left(f \cos \alpha_{max} + \sin \alpha_{max} + \frac{C_D A v_p^2}{21.15mg} \right) \quad (2)$$

Here v_p is the set driving speed, α_{max} is the intersection angle between horizon and the slope.

According the formula and the curve, we set P_{max2} to 42.57 kW.

P_{max3} could be set according to formula (3) [2]:

$$P_{max3} = \frac{1}{1000} \left[\frac{\sigma m}{2t_a} (v_f^2 + v_b^2) + \frac{2}{3} mgf v_f + \frac{1}{5} \rho_a C_D A v_f^3 \right] \quad (3)$$

In this equation, σ is the mass conversion factor, v_f is the target speed, here it equals to 100 km/h or 59 km/h, v_b is the vehicle speed when the drive motor rotate in the rated speed, ρ_a is air density, t_a is the acceleration time. According to this equation we set P_{max3} to 64 k.

$$P_{Max} \geq \text{Max}[P_{max1}, P_{max2}, P_{max3}] \quad (4)$$

So P_{max} was set to 64 kW.

The rated power could be set according Eq. (5)

$$P_{rated} = \frac{P_{max}}{\lambda} \quad (5)$$

Set λ to 1.8, so

$$P_{rated} = 35\text{kW}$$

According to Eq. (6), the peak torque and the rated torque can be determined to 203.73 and 203.73 Nm.

$$P = \frac{T \times n}{9550} \quad (6)$$

2.2 Range-Extender Sizing

The design requirement of range-extender (R-E) is that the R-E is capable to provide the power to make the vehicle be drove at the speed of 120 km/h when the battery could not provide enough power to drive the vehicle. According to Eq. (2), the required power of the speed of 120 km/h is 21.04 kW, take the inverter efficiency in count, the R-E must be capable to output the power of 30 kW.

Table 3 Statistic table of various types of vehicles

Vehicle types	Voltage class (V)
Traditional vehicle electrical start assemble	12
Traditional vehicle ISG assemble	36
Hybrid vehicle which equips the ISG system voltage class	144
Series/parallel hybrid electric vehicle or all electric drive vehicle voltage class	288 ~ 350
Series/parallel hybrid electric bus or all electric drive bus voltage class	350 ~ 650

2.3 Battery Sizing

The selection of battery system plays an important role in the whole parameter matching, because the battery performance can determine the dynamic performance and the all-electric- drive-range. To set the parameters of battery, two demands must be met: a. The peak power of the battery must meet the dynamic performance demands; b. The battery capacity must be sufficient enough to meet the all-electric-drive-range demand [3–5].

We have to select the voltage class before we set the other parameters of the battery. Table 3 is a voltage class statistic table of some different types of vehicles.

According to the technological experience and current technology circumstances, the voltage class is set to 336 V.

Here we set all-electric-drive-range to 60 km, to meet this demand, the energy stored in the battery must meet non-equality (7):

$$E_B \geq \frac{mgf + C_D A v_a^2 / 21.15}{3600 \times DOD \eta_t \eta_{mc} \eta_b (1 - \eta_a) U_m} \times d_1 \tag{7}$$

and

$$E_B = U_m C_E / 1000 \tag{8}$$

According to (7), (8)

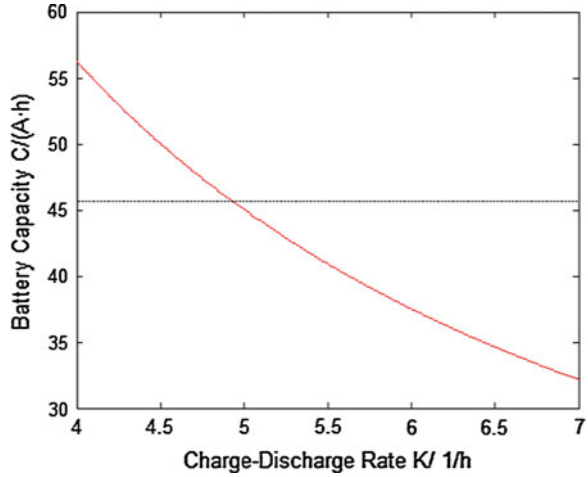
$$C_E \geq \frac{mgf + C_D A v_a^2 / 21.15}{3.6 \times DOD \eta_t \eta_{mc} \eta_b (1 - \eta_a) U_m} \tag{9}$$

DOD is the depth of discharge; $\eta_t = 0.93$, represents for the transmission efficiency; $\eta_{mc} = 0.9$, represents for the efficiency of drive motor; $\eta_b = 0.95$, represents for battery discharge efficiency; $\eta_a = 0.18$, represents for auto accessories energy consumption coefficient; $U_m = 336$ V, represents for voltage class; $V_a = 90$ km/h, it's the given speed for all-electric-drive; C_E represents the energy capacity determined by the all-electric-drive-range demand.

To meet the max power required by powertrain,

$$P_{batt_max_dis} = k C_p U_m / 1000 \tag{10}$$

Fig. 2 Battery capacity—charge–discharge rate



$$P_{batt_max_dis} = \frac{P_{max}}{\eta_{mc}} + P_A \tag{11}$$

so

$$C_p \geq \frac{1000}{kU_m} \left(\frac{P_{max}}{\eta_{mc}} + P_A \right) \tag{12}$$

$P_A = 4.5$ kW, represents for the vehicle accessory power.

According to (9) and (12) we can graph C_p and C_E in one coordinate system, as illustrated in Fig. 2.

The capacity of battery could finally be set by

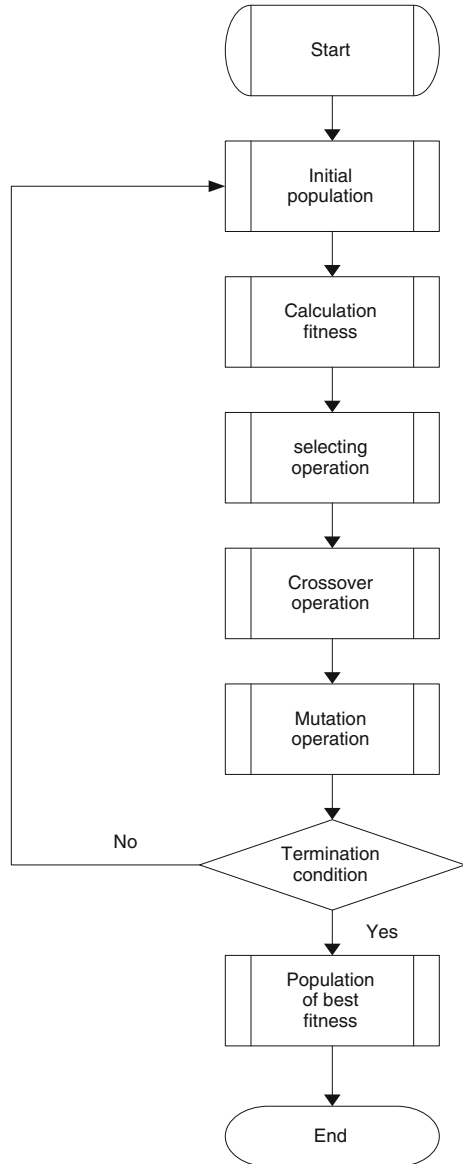
$$C = \min_{k^* = \text{Min}(k)} \{ \max[C_p(k), C_E(k)] \} \tag{13}$$

As illustrated in Fig. 2, the corresponding coordinates of the intersection of the red curve and the black line are $K = 4.93 \text{ h}^{-1}$ and $C = 45.67 \text{ A}\cdot\text{h}$.

3 Optimization of Powertrain Component Parameters

The powertrain of E-REV play a decisive role to the vehicle’s dynamic performance, total mass, and the fuel economy. We can optimize the powertrain parameters, on the promise that the dynamic demands be meet, to improve the fuel economy performance. By doing this we can cut down the production cost, reduce the total mass of the vehicle, and dramatically improve the fuel economy.

Fig. 3 The NSGA_II flow chart



In this paper, we employed the no gui function of advisor” adv_no_gui”, which was implanted into the optimization algorithm to be cyclically iterated, in the purpose of searching for the optimal result.

The method of calling the function of adv_no_gui is as following:

```
[error_code, resp] = adv_no_gui(action, input)
```

Error_code represents a binary number, if error_code = 0, means the function has been smoothly executed, and there is no any fault; if error_code = 1, means

Table 4 Optimization variables

Parameters	Introduction	Lower bound	Upper bound
motor_peak_power	Peak power of drive motor (kW)	30	80
Fc_max_available_power	Max available power of fuel converter (kW)	15	60
ess_cap_scale	The scale factor of battery (*)	0.5	5
C	Battery charging-discharging rate	0.75	5

Table 5 Optimization constrains

Parameters	Introductions	Demands
t ₁	0–50 km/h acceleration time, s	≤5
t ₂	0–100 km/h acceleration time, s	≤15
α	Gradeability, %	≥30 %
V _{max}	Max speed, km/h	Transitorily ≥ 140 Continuously ≥ 120
d ₁	All electric drive range, km	≥60
d	Total drive range, km	≥400

Table 6 Optimization results

Parameters	Results
motor_peak_power	60.0015
fc_max_available_power	27.1534
ess_cap_scale	1.2418
C	4.12
cost	12425.38
mpg	34.59

the execution has confronted some mistake; resp is a structure, the results of the program is stored in this structure; action is a character string, some specialized character strings are accordingly represent some corresponding operation, the character strings includes “initialize” “modify” “grad_test” “accel_test” “drive_cycle” “test_procedure” “other_info” “save_vehicle” and “autosize”, and every character string has its corresponding input parameters.

NSGA_II is an algorithm of optimization, this algorithm search the optimal chromosome by exerting the crossover and variation processing to the parents and offspring, the flow chart is illustrated as follow (Fig. 3).

The optimization problem could be mathematically described as (14)

$$\begin{cases} \min_{x \in \Omega} F(x) = [Cost(x), fuel_eco(x)] \\ stt_j(x) > 0, j = 1, 2, \dots, n \end{cases} \quad (14)$$

In (14), x generally represented all the main parameter of powertrain, Ω is the solution space, Cost(x) represents the production cost function, fuel_eco(x) represents for the fuel economy simulation result.

Fig. 4 Energy power before and after optimization

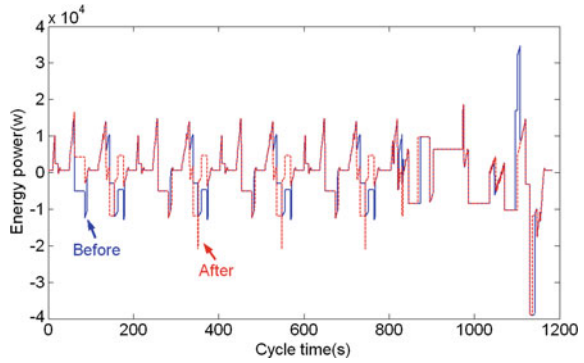
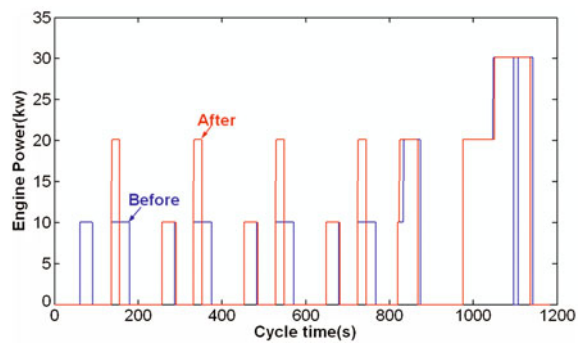


Fig. 5 Engine power before and after optimization



The chosen optimization variables are presented in Table 4

The optimization constrains are presented in Table 5

In the calculating processing of NSGA_II, the qualification of the production cost are in accordance with the following functions:

$$\text{Cost}_{\text{engine}} = \$12 \times P_E + \$424 \tag{15}$$

$$\text{Cost}_{\text{motor}} = \$ 13.7 \times P_M + \$190 \tag{16}$$

$$\text{Cost}_{\text{motor_ctr}} = \$ 8.075 \times P_M + \$235 \tag{17}$$

$$\text{Cost}_{\text{batt_Lilon}} = \$650 \times C/5 \times \text{Capacity}[\text{kWh}] \tag{18}$$

$$\text{Cost}_{\text{Batt_Acc}} = \$1.2 \times \text{Capacity}[\text{kWh}] + \$680 \tag{19}$$

In function (18), C represents for the Charge–Discharge Rate, this function was established according to our experience. The optimization result are presented in Table 6.

Advisor simulation comparison is presented as follows, the ADVISOR simulation model [6] was previously established (Figs. 4, 5, Tables 7, 8).

Table 7 Simulation results before optimization

Items		Results
Before optimization	Gradeability	32.3 % (at the speed of 30 km/h)
	Max speed	164.4 km/h
	0 ~ 50 km/h acceleration time	4.5 s
	0 ~ 100 km/h acceleration time	14.5 s
After optimization	Gradeability	31.6 % (at the speed of 30 km/h)
	Max speed	164.4 km/h
	0 ~ 50 km/h acceleration time	4.6 s
	0 ~ 100 km/h acceleration time	14.7 s

Table 8 Simulation result after optimization

Items	Results
Gradeability	31.6 % (at the speed of 30 km/h)
Max speed	164.4 km/h
0 ~ 50 km/h acceleration time	4.6 s
0 ~ 100 km/h acceleration time	14.7 s

Table 9 Comparison of the performance before and after optimization

	Gradeability	0–50 km/h acceleration time	0–100 km/h acceleration time	Production cost	Fuel economy
Before optimization	32.3 %	4.5 s	14.5 s	13158.6	8.4L/100 km
After optimization	31.6 %	4.6 s	14.7 s	12425.3	6.8L/100 km
Comparison	Dropped 2.21 %	Dropped 2.22 %	Dropped 1.38 %	Dropped 5.90 %	Increased 23.53 %

The simulation results comparison before and after powertrain parameter optimization is illustrated in Table 9.

4 Conclusion

A method of E-REV powertrain components parameter selection was mainly discussed in this paper. We preliminarily set the parameters to meet the dynamic demands, and then employed the NSGA_II genetic optimization algorithm to optimize the preliminarily selected powertrain parameters. Before and after optimization parameters were inputted into an previously established advisor model to compare the dynamic and fuel economy performance, which indicated that the fuel economy was significantly improved on the promise that the dynamic demands were met. In the same time the production cost was reduced, too.

In this paper, we just selected the powertrain parameters as optimization variables, and control strategy parameters were not selected. In the future study, we can select the control strategy parameters as optimization variables, and set the same optimization objective. Thus, we can get more optimal parameters.

References

1. Zhisheng Y (2000) Auto theory, the third edition. China Machine Press, Beijing
2. Ehsani M, Gao Y, Gay SE et al (2008) Modern electric vehicle, hybrid electric vehicle and fuel cell vehicle—fundamental principle, theory and design. China Machine Press, Beijing
3. Taylor W (1999) CFD prediction and experimental validation of high-temperature thermal behavior in catalytic converters. SAE paper 1999-01-0454
4. Wang B (2009) Study on the parametric design and control strategy of plug-in series hybrid electric bus. Jilin University Vehicle engineering academy, Changchun
5. Zhou S, Niu J, Chen F, Pei F (2011) A study on powertrain design and simulation for range-extended electric vehicle. *Automot Eng* 33(11):924–929
6. Haitao M, Dongjin Y, Yuanbin Y (2012) Analysis of control strategy for extended-range electric vehicle. *Switz, Appl Mech Mater* 135–136:261–267

Driving Intention Identification Method for Hybrid Vehicles Based on Fuzzy Logic Inference

Qingnian Wang, Xianzhi Tang and Lei Sun

Abstract The fuzzy logic inference system was developed to identify driving intention. The membership functions and rules of the fuzzy logic inference system were built by using mathematical statistics and neural network. The vehicle model was built based on a series–parallel hybrid vehicle using Cruise software. The driving intention inference system was designed in Simulink. The simulation is done based on Cruise and Simulink. The simulation results prove that the fuzzy inference system can identify driving intentions excellently and the control strategy based on driving intentions can help to reduce more fuel consumption.

Keywords Driving intention · Fuzzy inference · Hybrid vehicles · Neural network · Simulation

1 Introduction

Management of energy and distribution of torque are key issues in the development of hybrid electric vehicles, so an extensive set of studies have been conducted over the past two decades [1–12]. Many management strategies have been

F2012-B02-015

Q. Wang (✉) · X. Tang · L. Sun

State Key Laboratory of Automotive Simulation and Control, Jilin University, Jilin, China
e-mail: wqn@jlu.edu.cn

X. Tang

e-mail: 632988422@qq.com

used to solve these difficult problems. But few studies focus on drivers' intention identification. The drivers' intention cannot be identified precisely by simply using accelerator and brake pedal travel, so drivers' intention may be identified improperly. As a result, management of energy and distribution of torque are not proper correspondingly and performances of HEVs become unsatisfactory. In order to solve these problems, a driving intention identification method for hybrid vehicles is presented. The fuzzy logic inference system was developed to identify driving intention. The membership functions and rules of the fuzzy logic inference system were built by using mathematical statistics and neural network. The vehicle model was built based on a series-parallel hybrid vehicle using Cruise software. The driving intention inference system was designed in Simulink. The simulation is done based on Cruise and Simulink.

2 Different Driving Intentions and Selection of Identification Parameters

There are many different driving intentions during driving process. Driving intentions identification can make energy management unit know what driver needs indeed and can help design control strategy. Some driving intentions are chosen to be identified. They are five main intentions.

- Rapid acceleration
- Normal acceleration
- Slow acceleration
- High speed cruise
- Low speed cruise

There are also two operation modes to be identified.

- Economic mode
- dynamic mode

Some parameters should be chosen to identify driving intentions. There are five parameters have been chosen.

- acceleration mean value
- acceleration mean square deviation
- acceleration pedal travel
- acceleration pedal travel change rate
- vehicle velocity

Fig. 1 Membership functions of acceleration pedal travel

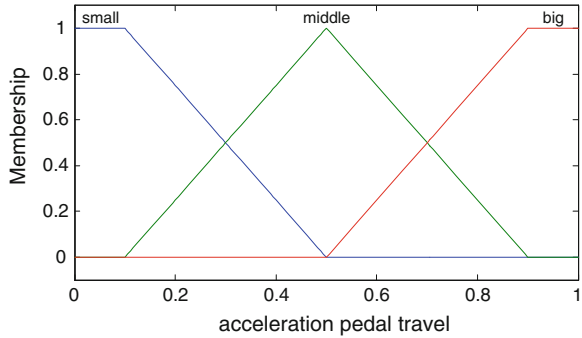
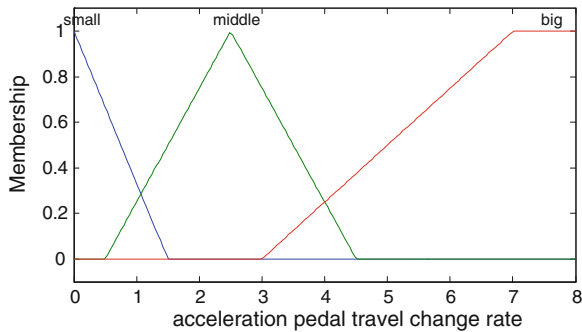


Fig. 2 Membership functions of acceleration pedal travel change rate



3 Design of Fuzzy Inference System

3.1 Design of Membership Functions

The linguistic terms are represented by fuzzy sets. Consider the variable “pedal travel” in Fig. 1. This variable is represented by the linguistic terms “small”, “middle” and “big”. These linguistic terms are represented by three fuzzy sets that are defined by the three membership functions in Fig. 1. The membership functions define the degree of membership of the variable in the three fuzzy sets. For example, if pedal travel is 0, the degree of membership in the fuzzy set “small” equals 1 and the degree of membership in the fuzzy set “big” equals 0. For pedal travel is 0.35, it is the other way around. One can imagine that there is a gradual transition from small to middle. This transition is represented by the overlapping interval in Fig. 1. The values in this interval belong to both fuzzy sets with various degrees of membership. Pedal travel 0.4 belongs to “small” with membership less than 0.5 and to “middle” with membership more than 0.5. So 0.4 belong to “middle” fuzzy set [13, 14]. The same as variable “pedal travel”, other four variables’ membership functions of the fuzzy logic inference system are depicted in Figs. 2, 3, 4, 5, 6.

Fig. 3 Membership functions of acceleration mean value

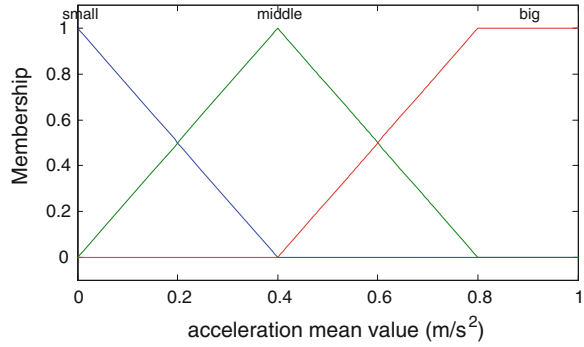


Fig. 4 Membership functions of acceleration mean square deviation

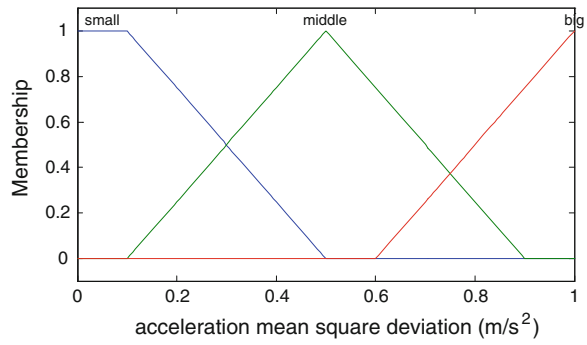
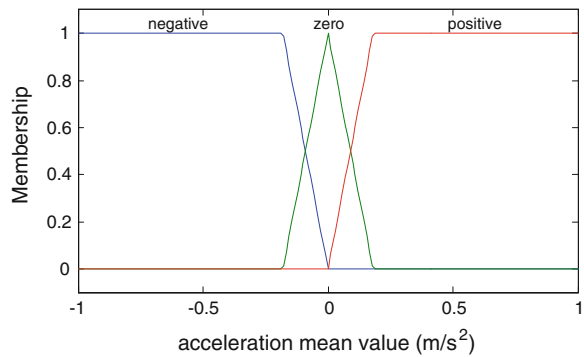


Fig. 5 Membership functions of acceleration mean value



3.2 Design of Fuzzy Rules

The basic idea of fuzzy logic inference system is to formulate human knowledge and reasoning, which can be represented as a collection of if—then rules, in a way tractable for computers. Most fuzzy inference rules can be concluded by expertise. The rules concluded by expertise are subjective and sometimes imprecise, when experts do not know what the rules exactly are. In this paper, fuzzy inference rules

Fig. 6 Membership functions of vehicle velocity

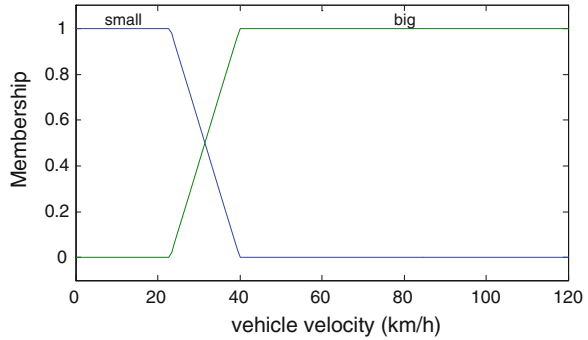


Table 1 Driving intentions frequency statistics

		Acceleration intentions		
		Slow	Normal	Rapid
Acceleration pedal	S/S	145	0	0
travel/change rate	S/M	127	0	0
	S/B	52	15	0
	M/S	130	48	0
	M/M	0	215	5
	M/B	0	183	12
	B/S	0	62	11
	B/M	0	0	100
	B/B	0	0	95

Table 2 Driving intentions probability statistics

		Acceleration intentions		
		Slow (%)	Normal (%)	Rapid (%)
Acceleration pedal	S/S	100	0	0
travel/change rate	S/M	100	0	0
	S/B	78	22	0
	M/S	73	27	0
	M/M	0	98	2
	M/B	0	94	6
	B/S	0	85	15
	B/M	0	0	100
	B/B	0	0	100

are gotten by mathematical statistics. Take the design of acceleration inference rules for example. Acceleration inference rules are designed according to Tables 1 and 2. Statistics and analysis of 1,200 groups experiment data are done in Tables 1 and 2.

The maximum probability intentions are chosen to be the rules. The rules abstracted from Table 2 are listed in Table 3.

Table 3 Acceleration intentions inference rules

		Acceleration pedal travel		
		Small	Middle	Big
Acceleration pedal travel change rate	Small	Slow	Slow	Normal
	Middle	Slow	Normal	Rapid
	Big	Slow	Normal	Rapid

Table 4 Cruise intentions inference rules

		Acceleration mean value		
		Small	Middle	Big
Vehicle velocity	Small	Normal	High speed cruise	Normal
	Big	Normal	Low speed cruise	Normal

Table 5 Operation mode intentions inference rules

		Acceleration mean square deviation		
		Small	Middle	Big
Acceleration mean value	Small	Economic	Economic	Economic
	Middle	Economic	Economic	Dynamic
	Big	Dynamic	Dynamic	Dynamic

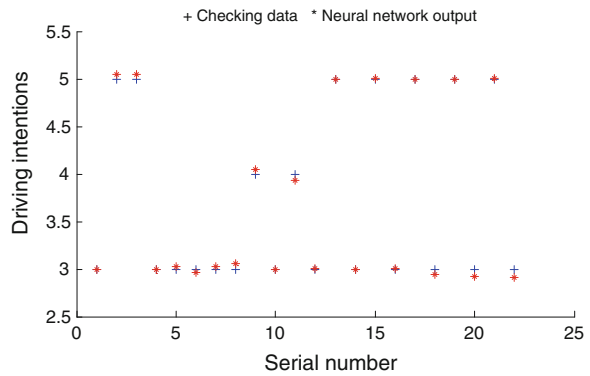
Table 6 Training data

Acceleration pedal travel	Acceleration pedal travel change rate	Driving intention
0.17	0.78	3
0.35	3.25	4
0.63	5.36	4
0.24	2.66	3
0.88	0.85	5
0.21	6.23	3
0.98	2.56	5
0.55	7.68	4
0.41	2.41	4
0.75	7.23	5
0.26	5.88	3
0.63	7.63	4
0.85	0.69	5
0.45	0.61	3
0.12	6.58	3
0.22	0.68	3
0.77	0.80	5
0.96	0.33	5
0.38	5.22	4
0.20	0.87	3
0.52	3.35	4
0.16	6.74	3

Table 7 Checking data

Acceleration pedal travel	Acceleration pedal travel change rate	Driving intention
0.13	2.36	3
0.75	2.85	5
0.88	0.64	5
0.22	0.82	3
0.17	4.18	3
0.23	5.23	3
0.42	0.88	3
0.36	0.69	3
0.38	3.42	4
0.23	2.61	3
0.55	5.88	4
0.16	7.68	3
0.85	0.77	5
0.41	0.62	3
0.86	6.58	5
0.25	0.72	3
0.96	0.80	5
0.23	0.55	3
0.78	5.88	5
0.26	0.83	3
0.95	3.32	5
0.18	7.65	3

Fig. 7 Checking result of neural network



The design method of Cruise and operation modes intentions inference rules are the same as acceleration intentions. Tables 4 and 5 are cruise and operation modes intentions inference rules.

Fig. 8 Optimized membership functions of acceleration pedal travel

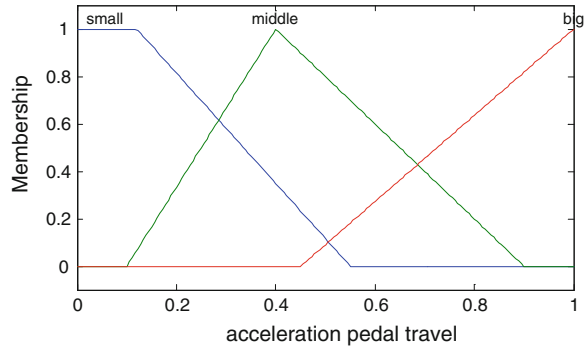


Fig. 9 Optimized membership functions of acceleration pedal travel change rate

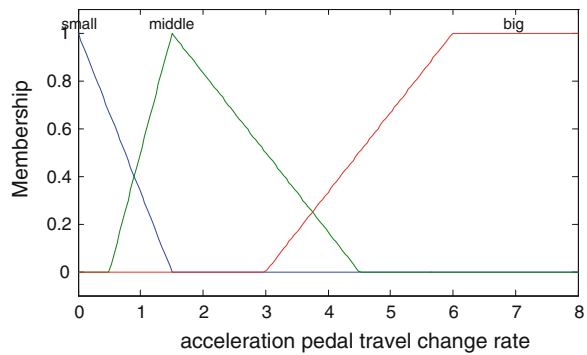
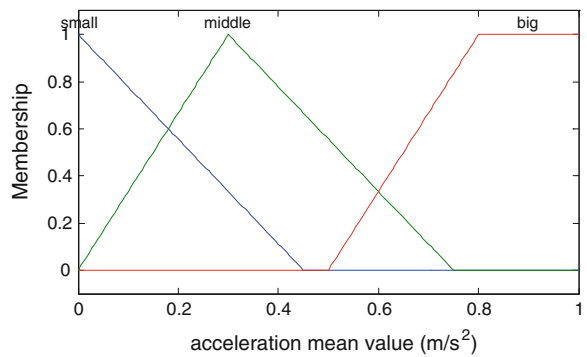


Fig. 10 Optimized membership functions of acceleration mean value



4 Fuzzy Inference System Optimization

Membership functions of fuzzy inference system have effect on inference result. Membership functions should be optimized to make inference result more precise. In this paper, membership functions are optimized by neural network. Take acceleration intentions inference system for example. Twenty two groups of

Fig. 11 Optimized membership functions of acceleration mean square deviation

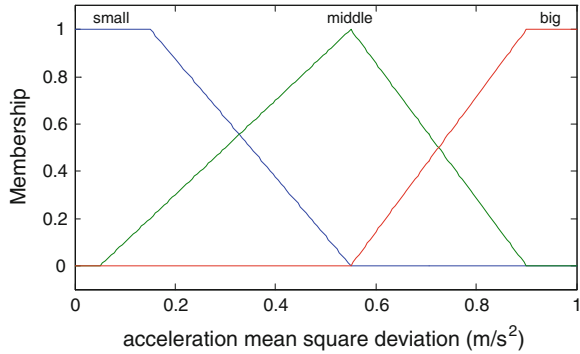


Fig. 12 Optimized membership functions of acceleration mean value

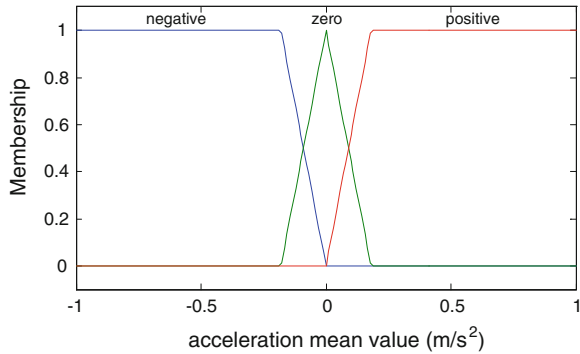
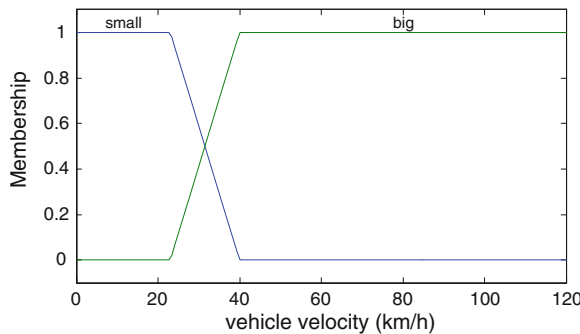


Fig. 13 Optimized membership functions of vehicle velocity



acceleration pedal travel and acceleration pedal travel change rate data are taken to train the neural network. Tables 6 and 7 are training data and checking data.

After training, the neural network output error is 0.08, which is small enough to satisfy design requirement. The neural network is checked by checking data. Figure 7 shows the checking result.

Figure 7 shows that output of neural network has very small error compared to real driving intention, which means the neural network has been well trained and the member functions of fuzzy inference system have been optimized during this

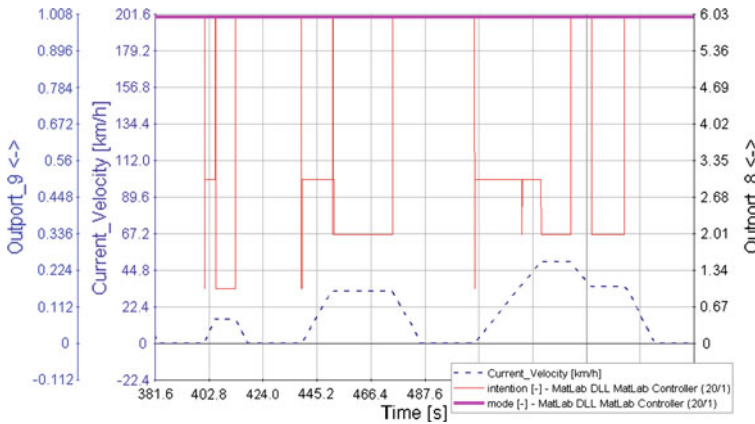


Fig. 14 Result of driving intention identification

Table 8 Contrast of simulation results

Cycle run	Fuel consumption with driving intention identification (L)	Fuel consumption without driving intention identification (L)	Save fuel (%)
NEDC	6.1	5.8	4.9
BEIJING	4.7	4.5	4.3
CHINAURBAN	4.53	4.5	1
EUDC	7	6.76	3.4
UDC	4.6	4.5	2.2
Average value	5.39	5.21	3.3

process. Figures 8 and 9 show the member functions of acceleration intention inference system optimized by neural network. Other member functions of other intention inference system are optimized also by neural network. They are shown in Fig. 10, 11, 12, 13.

5 Simulation of Control Strategy Based on Driving Intention Identification

To prove whether driving intention identification can help optimize control strategy, a comparison between driving intention identification control strategy and no driving intention identification control strategy have been done by using CRUISE software.

Figure 14 is the result of driving intention identification for NEDC cycle run. Dashed line is EDC cycle run. The red line is output of acceleration and cruise intentions identification result. No.1 is low speed cruise. No. 2 is high speed cruise.

Table 9 Contrast of simulation results

Prototype vehicle	Hybrid vehicle without driving intention identification	Save fuel
8.1L	5.39L	33 %

Table 10 Contrast of simulation results

Prototype vehicle	Hybrid vehicle without driving intention identification	Save fuel
8.1L	5.21L	35 %

No. 3 is slow acceleration. No. 4 is normal acceleration. No.5 is rapid acceleration. No.6 is brake. The pink line is output of economy and dynamic modes identification result. No.1 is economy mode. No. 2 is dynamic mode. Tables 8, 9, 10 are contrast of simulation results.

Contrast of simulation results show that control strategy based on driving intention identification can reduce fuel consumption and improve driving ability.

6 Conclusion

This paper presents a driving intention intelligent identification method for hybrid vehicles based on fuzzy inference. The membership functions and rules of the fuzzy logic inference system were built by using mathematical statistics and neural network. The control strategy has been designed based on driving intentions and the simulation has been done. The simulation results prove that the fuzzy inference system can identify driving intentions excellently and the control strategy based on driving intentions can help to reduce more fuel consumption.

References

1. Miller JM (2006) Hybrid electric vehicle propulsion system architectures of the e-CVT type. *IEEE Trans Power Electron* 21:756–767
2. Chan CC (2007) The state of the art of electric, hybrid, and fuel cell vehicles. *Proc IEEE* 95(4):704–718
3. Ehsani M, Gao Y, Miller JM (2007) Hybrid electric vehicles: architecture and motor drives. *Proc IEEE* 95(4)
4. Jalil N, Kheir NA, Salman M (1997) A rule-based energy management strategy for a series hybrid vehicle. In: *Proceedings of the American Control Conference*, vol 1. Albuquerque, NM, pp 689–693
5. Schouten NJ, Salman M, Kheir N (2002) Fuzzy logic control for parallel hybrid vehicles. *IEEE Trans Cont Syst Technol* 10(3):460–468
6. Won J-S, Langari R (2002) Fuzzy torque distribution control for a parallel hybrid vehicle. *Expert Syst* 19(1):4–10

7. Delprat S, Guerra TM, Rimaux J (2002) Control strategies for hybrid vehicles: optimal control. In: Proceedings, vehicular technology Conference (VTC 2002-Fall), vol 3. Vancouver, Canada, pp 1681–1685
8. Brahma A, Guezennec Y, Rizzoni G (2000) Optimal energy management in series hybrid electric vehicles. In: Proceedings of the American control conference, Chicago, IL, pp 60–64
9. Johnson VH, Wipke KB, Rausen DJ (2001) HEV control strategy for real-time optimization of fuel economy and emissions. SAE Paper No. 2001-01-1543
10. Jeon S-I, Jo S-T, Park Y-I, Lee J-M (2002) Multimode driving control of a parallel hybrid electric vehicle using driving pattern recognition. *J Dyn Syst Meas Contr* 124:141–149
11. Lin C-C, Filipi Z, Louca L, Peng H, Assanis D, Stein J (2004) Modelling and control of a medium-duty hybrid electric truck. *Int J Veh Des* 11(3/4):349–370
12. Zhu Y, Chen Y, Wu Z (2006) Optimization design of an energy management strategy for hybrid vehicles. *Int J Altern Propul* 1(12):47–62
13. Driankov D, Hellendoom H, Reinfrank M (1993) An introduction to fuzzy control. Springer, Berlin
14. Kono H (1998) Fuzzy control for hybrid electric vehicles. Master's Thesis, Department of Electrical Engineering, The Ohio State University

The Control Technologies of PMSM for FAW-TMH System

Cheng Chang, Huichao Zhao, Xiuhui Dong and Yandong Wen

Abstract In this paper, PMSM (permanent magnet synchronous motor) control technologies combined with HEV (Hybrid Electric Vehicle) application features are developed, which aim at FAW-TMH (Twin Motor Hybrid) system for B70HEV. The technologies are based on FOC (Field Oriented Control) theory and include multiple advanced control functions such as MTPA (Maximum Torque per Amperes) control with decoupling and anti-windup PI controller, PTB (Peak Torque Boost) control, high voltage utilization PWM modulation, deadtime compensation, DTC and map based deep field weakening control and so on. Those control technologies can meet the hybrid electric vehicle's performance requirement under different working conditions. What's more, the proposed deadtime compensation, DTC and map based field weakening control technologies are new in the e-motor controls field. Bench test and road test indicate that the developed PMSM control strategy meets the performance and reliability requirements of B70HEV.

Keywords PMSM · Control technologies · Control system · FOC · HEV

1 Introduction

The Besturn B70HEV, which was developed in 2006 by FAW (First Auto Work Corporation, China), realized excellent dynamic and economy performance (Fig. 1). The Besturn B70HEV is based on FAW-TMH powertrain platform

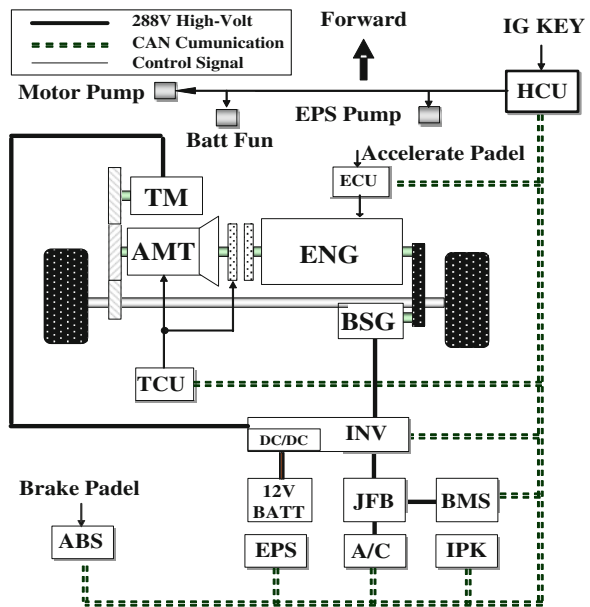
F2012-B02-016

C. Chang (✉) · H. Zhao · X. Dong · Y. Wen
FAW R&D Center, Changchun, China
e-mail: changcheng@rdc.faw.com.cn

Fig. 1 Besturn B70HEV



Fig. 2 TMH System Configuration

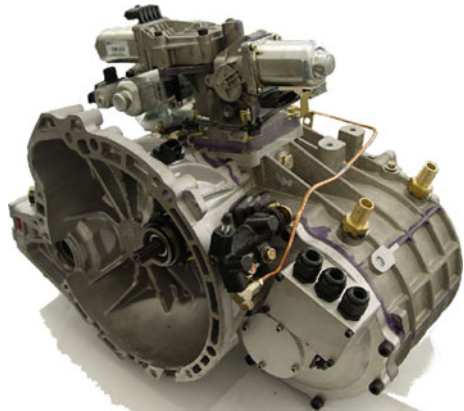


system, which contains a high-voltage Ni-H battery package, two PMSM drive motors. What's more, a PHEV is also under development based on FAW-TMH system. PMSM has been widely used in EV/HEV because of its high power, torque density and excellent efficiency. But PMSM control is the key issue, because HEV's application demands strict requirements of the PMSM control functionality and performance. So FAW has been working on advanced e-motor control strategy solution for FAW-TMH system to meet the requirements.

Table 1 Specifications of each unit

TM motor	Max. power	40 [kW]
	Max. torque	280 [Nm]
	Max. speed	7600 [rpm]
BSG motor	Max. power	10 [kW]
	Max. torque	50 [Nm]
	Max. speed	12000 [rpm]
Battery	Rated voltage	288 [V]
	Rated capacity	6 [Ah]

Fig. 3 TM-coupled AMT



2 Outline of FAW-TMH

Figure 2 shows the structure of FAW-TMH powertrain system, including 1.5L D-VVT engine, 5-speed AMT automatic transmission, two PM motors (BSG motors and TM motors), Ni-H battery pack. BSG (Belt Starter Generator) is coupled to the engine crankshaft through the belt. TM (main Traction Motor) is coupled to the AMT output crankshaft through the chain. FAW-TMH is full hybrid architecture which can achieve all the features of the hybrid system and achieve the saving rate of around 35.2 % under NEDC drive cycle. Table 1 shows the specifications of each unit [1].

Figure 3 shows the TM-coupled AMT. TM and AMT output shaft are connected by a chain. Motor housing, cooling system and AMT housing are integrated together. So it's compact and highly integrated. TMH is novel design and obtains the invention patents of China and the United States.

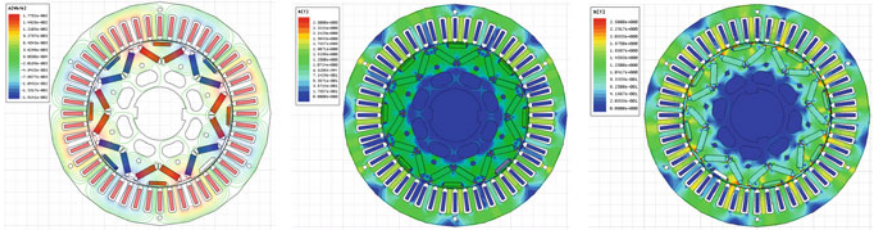


Fig. 4 Flux Line and Flux Density

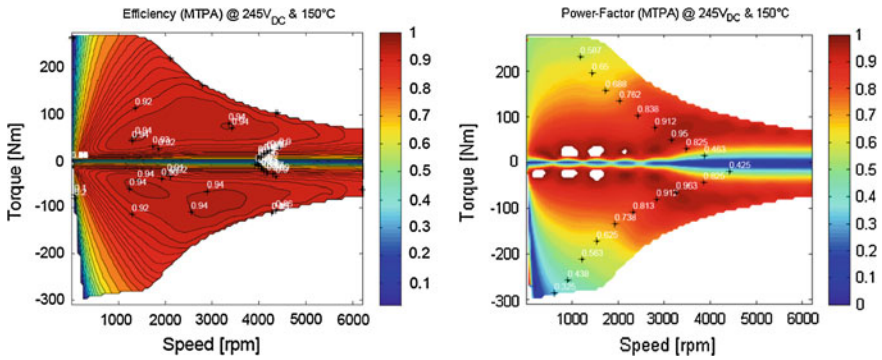


Fig. 5 Motor efficiency and power-factor at the lowest voltage and highest temperature

Table 2 Initial value of TM parameters

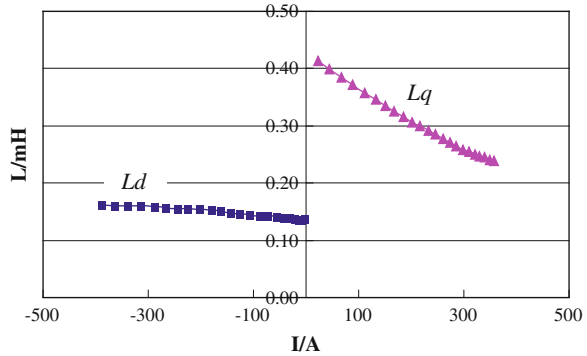
Flux	0.0788	WB
Rs	9.21	mΩ
Ld	0.15	mH
Lq	0.42	mH
Pole pairs	4	pairs

3 Motor Spec and Features

Taking ANSOFT software for simulation, results including the magnetic line, flux density, back EMF and load torque at nominal, as shown in Fig. 4. The torque of IPMSM is composed with magnetic torque and reluctance torque based on differences motor design. In order to utilize the reluctance torque, “V” shape magnet layout design for rotor is adopted. The motor efficiency and power-factor at the lowest voltage (245 V) and highest motor temperature (150 °C) is shown in Fig. 5 (Table 2).

Figure 4 shows that flux saturation will happen in heavy load, which leads to the changes of the motor body parameters, the inductance parameter changes as shown in Fig. 6 below.

Fig. 6 Curve for L_d and L_q in Saturation



From the above, we can get the conclusion that the power density and torque density are relatively high. Therefore, advanced e-motor control technology should be applied to enhance the output power of the drive motor system, simplify the difficulty of the motor design to optimize the system parameters.

4 PMSM Control Technologies

4.1 Static Mathematical Model of PMSM

The following parameters are defined to get the static mathematical model of PMSM:

- (1) Characteristic Current: $i_{ch} = \psi_m/L_d$,
- (2) Saliency: $\rho = L_q/L_d$.

The voltage formula and torque formula of PMSM are:

$$\begin{pmatrix} U_d \\ U_q \end{pmatrix} = \begin{pmatrix} R_s & -\omega L_q \\ \omega L_d & R_s \end{pmatrix} \begin{pmatrix} i_d \\ i_q \end{pmatrix} + \begin{pmatrix} L_d & 0 \\ 0 & L_q \end{pmatrix} \cdot \frac{d}{dt} \begin{pmatrix} i_d \\ i_q \end{pmatrix} + \begin{pmatrix} 0 \\ \omega \phi_f \end{pmatrix}$$

$$T_e = \frac{3}{2} P_n \cdot L_d \cdot [i_{ch} \cdot i_q + (1 - \rho) \cdot i_d \cdot i_q]$$

where, i_{ch} is the characteristic current, ψ_m is the rotor flux linkage, P_n is the pole pairs, L_d is d-axis inductance, L_q is q-axis inductance.

Figure 7 show the basic structure of motor control system that consists of two PMSM motors, an inverter and a battery package. The battery pack supplies DC voltage to the inverter. The inverter, which is a semiconductor switching device, performs switching at more than 1 kHz to convert the DC voltage into three phase AC voltage. The system also incorporates rotor position sensors, battery pack voltage sensor and motor AC current sensors.

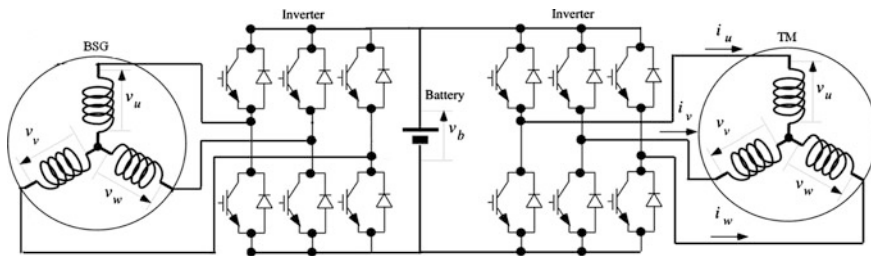
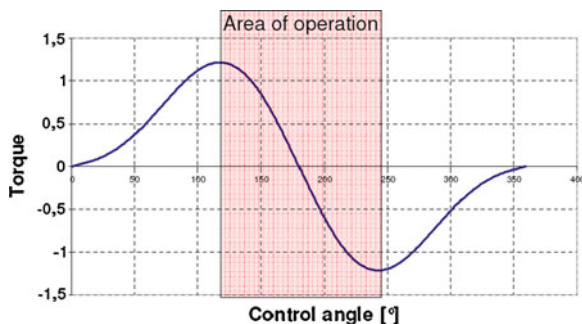


Fig. 7 Basic structure of motor control system

Fig. 8 Torque and current phase character



4.2 MTPA (Maximum Torque per Ampere) Control

B70HEV requires high torque output (280 Nm) during starting and low speed acceleration working conditions. So, in order to utilize the reluctance torque of the interior PMSM ($L_d \neq L_q$), in non-field weakening region, MTPA control is adopted. The torque-phase character can be described like Fig. 8 [2]. Every optimized current phase angle at which e-motor outputs the maximum torque should be found. From the following extremism formula and bench calibration data, we can get the current control trajectory for MTPA, as is shown in Fig. 9.

$$T_e = \frac{3}{2} Pn \cdot L_d \cdot [ich \cdot iq + (1 - \rho) \cdot id \cdot iq]$$

$$\frac{\partial(T^*/is)}{\partial id} = 0$$

$$\frac{\partial(T^*/is)}{\partial iq} = 0$$

Figure 10 shows the comparison between $id = 0$ and MTPA control in Non-field weakening control region based on the experiment data. We can get the conclusion that MTPA control can effectively increase the torque output under the

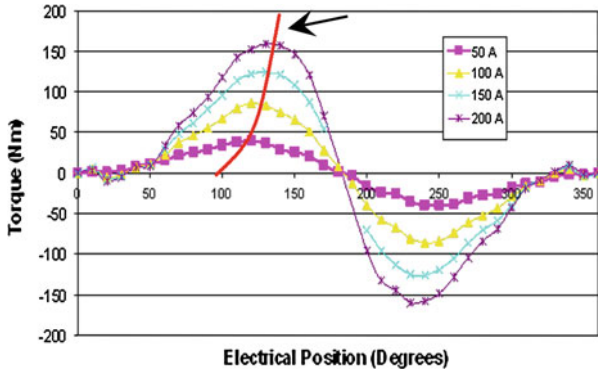


Fig. 9 Current trajectory under MTPA control

Fig. 10 Curve for Torque and Phase Current

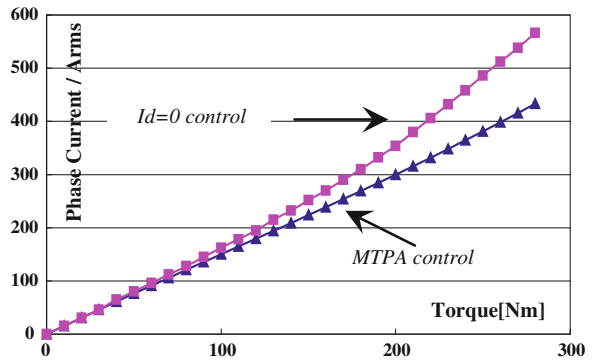
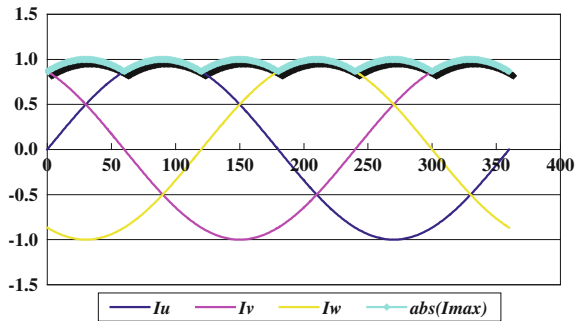
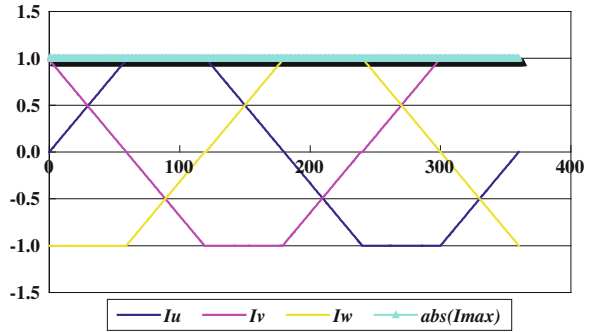


Fig. 11 Relationship between sine current and I_{max}



same system current capability limit. What's more, the experiment data shown in Fig. 10 indicates that the torque output character of $i_d = 0$ control is not linear actually because the flux linkage becomes saturated.

Fig. 12 Relationship between trapeziform current and I_{max}



4.3 PTB Control

Because of the IGBT module’s current capability limit, when the peak value of the sine phase current reaches the maximum value, the output torque can’t increase any more in the sine current wave drive mode.

Where, $I_{max} = \max [abs (I_a), abs (I_b), abs (I_c)]$

But we can know from Fig. 11 that there are only six points that the peak value reaches the limit (assume the maximum value equals 1) in one electric cycle. Otherwise, in the rest position, the current capability is not utilized fully. So, in order to increase the peak output torque at low speed region to meet the requirement of the HEV’s acceleration performance, this paper presents a PTB control method.

The PTB control method can be described in Fig. 12: At the peak value of the sine phase current, the controlled current wave transits from sine wave to trapeziform wave gradually, which can maintain the phase current peak value always equals the limit value. The maximum peak torque can increase about 4.9 % theoretically by adopting PTB control. Considering the balancing between the dynamic requirement and NHV requirement, PTB control is only used in dynamic driving mode because the trapeziform current can lead to torque ripple.

4.4 Deadtime Compensation Method

Voltage-fed pulse width modulation (PWM) inverters have gained increasing popularity in industrial and EV/HEV applications. A small lag called deadtime is inserted into PWM gate signal to avoid short circuit of the two switching devices of one inverter leg. But due to the presence of deadtime (usually $2 \sim 5 \mu s$) of the PWM square wave signal, the output voltage of the inverter will be distorted, which can cause the non-sinusoidal of the current control. As shown in Fig. 13. The real phase current deviates from the phase current command because of the deadtime’s influence. This can lead to torque vibration especially in the low speed range, when the vehicle is in EV driving mode.

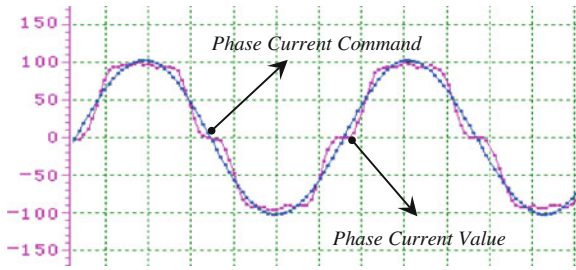


Fig. 13 Distortion of the Phase Current

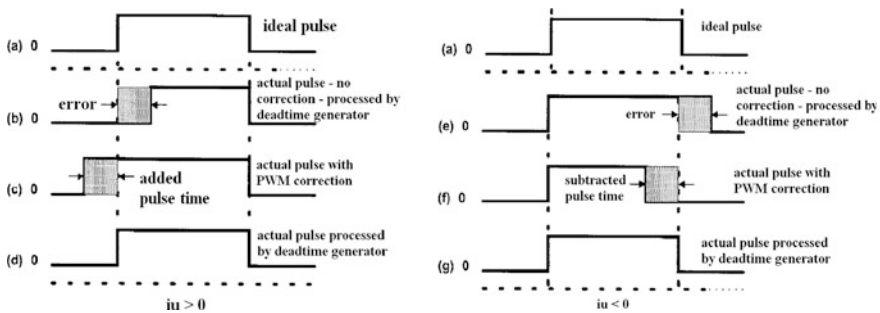


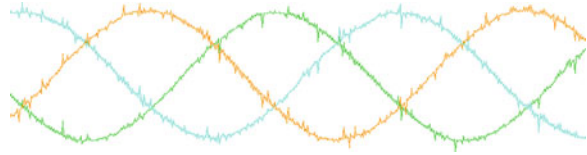
Fig. 14 Basic principle of the PWM square wave correction

For the deadtime compensation technology, the key issue is how to judge the polarity of the phase current. In general, current zero-across measurement method based on extra FPGA hardware circuit is widely used, but the current platform near the zero-across region and the unexpected noise can lead to the misjudgement of the polarity, especially when the current is very small. This may make the control performance even worse. What’s more, FPGA hardware needs extra cost.

This paper proposed a novel and simple method to judge the polarity of the phase current. As is shown in Fig. 13, the current command features highly sinusoidal, non-noised, and non-platform effect. So, the polarity of the phase current command can be recognized as the polarity of the phase current. Based on the above analysis, PWM square wave can be corrected referencing PBDCT (Pulse-Based Dead-Time Compensator) technology [3]. The basic principle is depicted in Fig. 14.

For $i_u > 0$, Fig. 14a shows the ideal PWM pulse wave. Fig. 14b shows the real PWM pulse wave affected by deadtime with no correction. To correct the error, a certain width pulse is added in advance before deadtime generation, as shown in Fig. 14c. Figure 14d shows the corrected PWM wave, which is identical to the ideal wave. For $i_u > 0$, the basic principle is the same, as shown in Fig. 14e–g.

Fig. 15 Current control wave after deadtime compensation



In this way, deadtime effect can be compensated easily without any extra hardware. The measured current control wave with deadtime compensation is shown in Fig 15.

4.5 Over-Modulation and Six-Step Switch Method

Due to the motor terminal voltage limitation, field weakening control must be applied to increase the IPMSM’s operation region. But the system stability and efficiency will decrease in field weakening control region. Increasing the battery voltage modulation ratio can help to increase the e-motor system output power and efficiency [4]. So increasing the battery voltage modulation ratio is a key issue.

Through traditional SVPWM modulation, 0.577 times battery voltage can be achieved at the maximum, which is the radius of the inscribed circle of the six basic voltage vectors. Over-modulation must be used in order to increase the modulation ratio from 0.577 to higher. But in over-modulation region, the integral function of the current PI loop must stop to avoid voltage saturation, so the current may become distorted. Ultimately as the modulation ratio increases to the maximum value of 0.707, the modulation method switches to six-step modulation, this is similar to the BLDC motor control. The maximum modulation ratio can be calculated by Fourier analysis.

$$U(t) = \frac{4U_{dc}}{\pi} \left(\sin \omega t + \frac{1}{3} \sin 3\omega t + \frac{1}{5} \sin 5\omega t + \frac{1}{7} \sin 7\omega t + \dots \right)$$

The base frequency voltage equals: $\frac{4U_{dc}}{\pi} \int_0^{\frac{\pi}{2}} \sin \omega t dt = U_{dc} / \sqrt{2} = 0.707U_{dc}$

In six-step modulation region, the voltage amplitude is constant, there is only one freedom for controlling, that is the voltage phase angle [5]. The traditional current vector control based on i_d and i_q is no longer applicable. So in this paper, voltage vector based FOC control is proposed and used, which can effectively enhance the stability and efficiency in the field weakening control region (Figs. 16, 17).

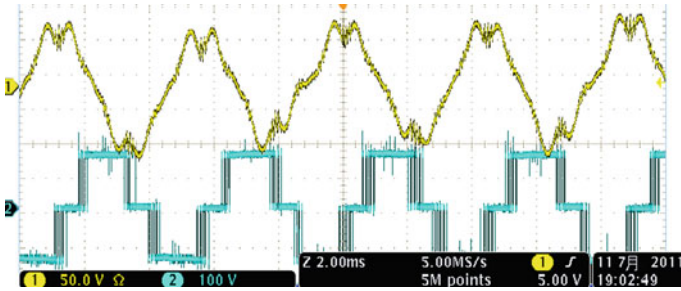


Fig. 16 Current and PWM wave in over-modulation

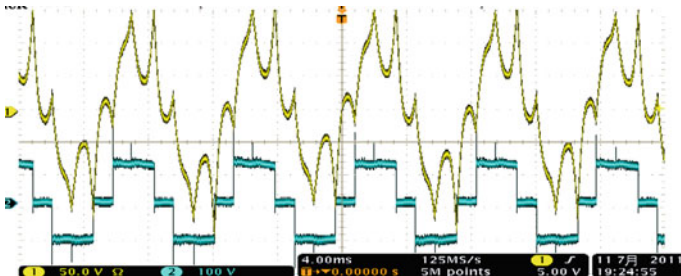


Fig. 17 Current and PWM wave in six-step modulation

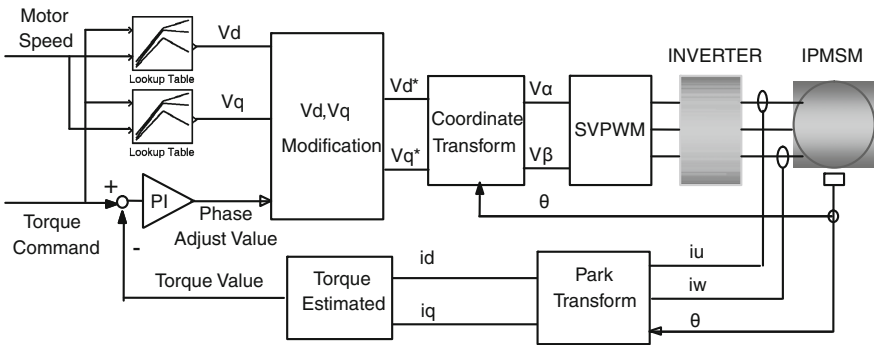


Fig. 18 Control block of the DTC and MAP based field weakening control

4.6 DTC and MAP Based Field Weakening Control

The traditional field weakening control method [6] is based on current vector control (d-axis current field weakening) which can achieve good efficiency combined with MTPA control under critical speed. But the stability gets worse when the speed becomes higher, also the battery voltage utilization factor is not the maximum. Current vector control based field weakening control can't resolve the

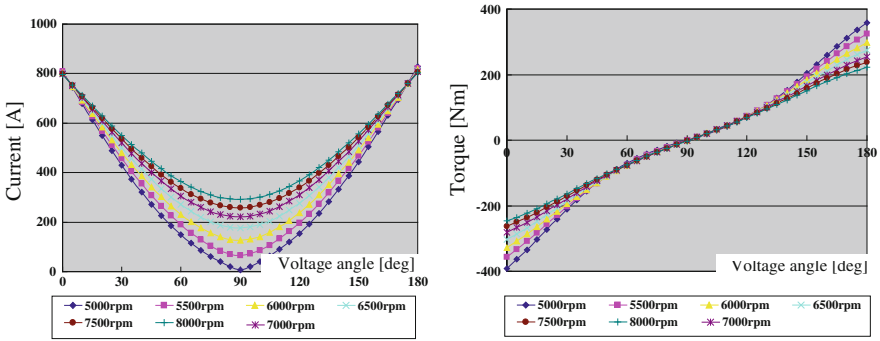


Fig. 19 Relationship between voltage angle and current and torque in field weakening control region

conflict between tuning i_d and i_q current independently (two freedom) and maintaining the terminal voltage unsaturated at the same time, which may lead to the risk of losing control. In order to decrease the risk, a certain voltage margin is reserved for current PI control, which will lead to even lower voltage utilization factor.

This paper proposed a novel DTC (Direct Torque Control) and map based field weakening control method, as shown in Fig. 18. The proposed method contains a feed forward control loop and a feedback compensation loop. The initial control setpoint (v_d and v_q) maps are achieved from the control map which was obtained from the bench calibration. The feedback PI loop is just used to adjust the tiny torque output error because of the change of the outer environment and motor parameters. The proposed control method has the following feature and advantages.

- 1) Terminal voltage amplitude is constant, which can avoid the voltage saturation;
- 2) voltage phase angle is the only control parameter for torque control;
- 3) six-step modulation can be used because the voltage amplitude maintains constant;
- 4) voltage margin reserved for PI is eliminated, which can improve the voltage utilization;
- 5) the conflict problem of the two freedom field weakening control methods is resolved.

From voltage equations:

$$i_d = \frac{R_s \cdot U_d + \omega L_q (U_q - \omega \phi_f)}{R_s^2 + \omega^2 L_d L_q}, \quad i_q = \frac{R_s \cdot (U_q - \omega \phi_f) - \omega L_d U_d}{R_s^2 + \omega^2 L_d L_q}$$

$$\begin{pmatrix} U_d \\ U_q \end{pmatrix} = U_s \cdot \begin{pmatrix} \sin \varphi \\ \cos \varphi \end{pmatrix}$$

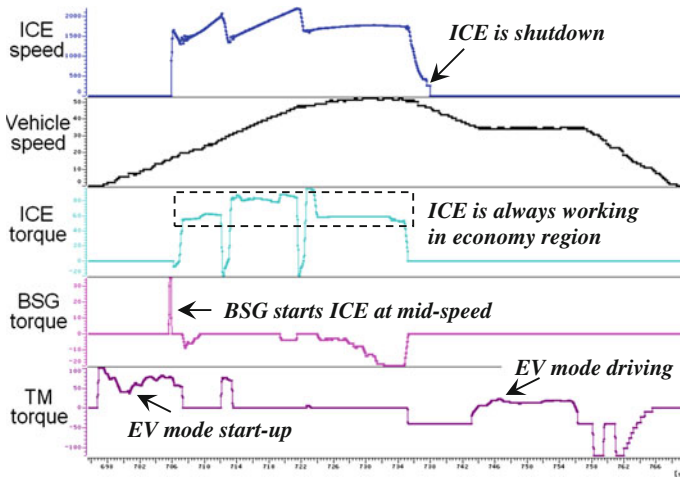


Fig. 20 Test results in the vehicle drive cycle

where, φ is the angle between d axial and voltage vector. Ignore the influence of phase resistance R_s :

$$i_d = \frac{1}{\omega} \frac{Us \cos \varphi - \varpi \phi_f}{L_d}, \quad i_q = \frac{1}{\omega} \frac{-Us \cdot \sin \varphi}{L_q}$$

From the above, we can get the following relationship between voltage angle and phase current and torque output. The curve is shown in Fig. 19.

$$i_s = f_1(Us, \varphi, \varpi) = \sqrt{\left(\frac{Us \cos \varphi - \varpi \phi_f}{\omega L_d}\right)^2 + \left(\frac{Us \cdot \sin \varphi}{\varpi L_q}\right)^2}$$

$$T_e = 1.5Pn \cdot [\phi_f i_d + (L_d - L_q) i_d \cdot i_q] = f_2(Us, \varphi, \varpi)$$

5 Test Results

Vehicle test indicates that the proposed and applied PMSM control technologies help to meet the performance and reliability requirements of B70HEV TMH System. As shown in Fig. 20, it can provide good control performance, respond the HCU control command quickly and effectively and help B70HEV to improve the vehicle drive performance and fuel consumption economy.

6 Conclusion

In this paper PMSM control technologies combined with HEV application features are proposed and developed. The proposed MTPA control with decoupling and anti-windup PI controller can increase the torque output and ensure the downsizing of e-motors. The PTB control can increase 4.9 % peak torque output theoretically. With the adopted PWM modulation method, voltage utilization can be increased from 0.577 to 0.707, which can reduce the iron loss so as to increase system efficiency. The proposed deadtime compensation method can reduce the torque ripple and increase the current control accuracy and stability. With the DTC and map based deep field weakening control method, higher operation speed is achieved and the control stability is increased, because the voltage saturated problem of two freedom control has been solved. Bench test and road test indicate that it meets the performance and reliability requirements of B70HEV.

References

1. Minghui Liu/s (2007) Development of FAW-TMHTM Full-Hybrid Platform, Automotive engineering, vol 10
2. Renyuan Tang/s (2008) Modern permanent magnet machines—theory and design. China machine press
3. Leggate D, Kerkman J (1997) Pulse-based dead-time compensator for PWM voltage inverters. *Ind Electron IEEE Trans* 44(2):191–197
4. Sasaki S, Sato E, Okamura M (2005) The motor control technologies for the hybrid electric vehicle. *Power electronics*, vol 02
5. Kazuaki Shingo, Kaoru Kubo, Toshiaki Katsu and Yuji Hata (2000) Development of electric motors for the TOYOTA hybrid vehicle PRIUS. 17th International Electric Vehicle Symposium, Dec
6. Gabriel Gallegos-Lopez, Fani S. Gunawan, James E. Walters (2005) Optimum torque control of permanent magnet AC machines in the field-weakened region. *IEEE Trans Ind Appl*, pp 1020–1028 (July–Aug)

Modeling and Simulation of Power Train System for Extended-Range Electric Vehicle Using Bond Graphs

Ke Song and Tong Zhang

Abstract Because the power train system of Extended-Range Electric Vehicle is a complicated multi-domain engineering system, a unified approach named Bond Graph has been used. The important drive components, especially battery, electric machine, wheel and Range Extender unit are modeled. The complex interactions among the components are taken into account in a complete multi-domain model. Once the power train system models have been developed, the dynamic behaviour of E-REVs is simulated under selected various driving cycles using rule-based energy management strategy. As important conclusion, the bond graph method has once again demonstrated its great potential for modeling technical systems with multi-domain physical fields. According to the simulation results, the significant benefits of E-REVs for the fuel reduction, emissions output and energy efficiency are proved.

Keywords Extended-range electric vehicle · Fuel cell range extender · Power train system · Bond graph · Modeling and simulation

F2012-B02-017

K. Song (✉) · T. Zhang
School of Automotive Engineering, Tongji University, Shanghai, China
e-mail: ke_song@hotmail.de

K. Song · T. Zhang
Clean Energy Automotive Engineering Centre, Tongji University, Shanghai, China

T. Zhang
Sino-German College, Tongji University, Shanghai, China

1 Introduction

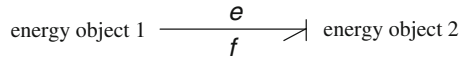
Extended-Range Electric Vehicles (E-REV) are principally battery electric vehicles with a relatively small auxiliary power unit (APU) to recharge the battery pack or directly to propel the vehicle during driving [1]. The small auxiliary power unit is normally called Range Extender (RE), which is with the propelling electric motor in series configuration. Compared to conventional hybrid vehicles, E-REVs could significantly reduce fuel consumption and emissions; compared with pure electric vehicles, E-REVs could increase the driving range, therefore it is seen as one of the most promising technological bridges between the vehicles of today and the sustainable concepts of tomorrow [2].

The E-REV power train system design process is aided by modelling and simulation technology. As a resurgent power train concept, issues as component modelling, power train system design, energy management strategies and vehicle simulation have been made by researchers using simulation tools such as Matlab/Simulink [3, 4]. Due to the complexity of E-REVs power train system, which is a multi-domain physical system consisting of mechanical, electrical, hydraulic, and thermodynamic systems, the modification of models in Matlab/Simulink environment is not convenient for engineers from different engineering fields. The basic of Matlab/Simulink modelling is mathematical equations of target technical system, e.g., the power train system of E-REV. Various variables are coupled with each other, and it is not easy to analysis the interactions between them. A small modification of one signal connection in Simulink submodel may disable the simulation of whole power train system model. Exactly the physical structure of one technical system could not be reflected/modelled by signal flow based simulation tools, such as Matlab/Simulink. In this chapter, the components and system models are developed by graphical modelling theory Bond Graph.

Bond Graph theory is developed by Prof. Paynter in 1959, and been used to describe and model interactions involving power exchange between technical subsystems from multidiscipline physical domains. This modelling method has been proven to be effective by modelling multi energy domain systems and investigating the dynamic performance by them [5–8].

The brief introduction to bond graph modelling is given in [Sect. 2](#). Some key components of a fuel cell E-REV power train system are modelled using bond graph in [Sect. 3](#), which are then integrated to be a complete system model. In order to using the traction battery as much as possible, thermostat energy management strategy is chose in this chapter. The simulation results of thermostat strategy by ECE driving cycle are presented in [Sect. 4](#). Finally, conclusions about E-REV and benefits of modelling of E-REV power train system using Bond Graph are given.

Fig. 1 Bond graph description of different physical fields



2 Introduction to Bond Graph Method

In bond graphs theory, the energy exchanges within a system are described using bonds which present the power exchanges. The effort variable and flow variable are associated with each bond, see Fig. 1. In general, the product of these two variables presents the transferred power. And these two variables have different interpretations in different fields of physics (Table 1).

As mentioned above, the main advantage of bond graph modelling could be summarized: (1) multi physical domains modelling is generalized using power exchange between component modelling unit; (2) model and submodel hierarchy a bond graph model of a system may be composed of lower level submodels which in turn may contain submodels as well. That means, physical system models are hierarchical in nature. (3) In contrast with other modelling methods based on mathematical equations, bond graph method don't need to know mathematical equations of target system prior. All mathematical/computational equations or governing relations are contained naturally in bond graph models. (4) bond graph models reflect the physical structure of target technical systems. Submodels are connected like corresponding components or devices in the real physical system.

3 Components and System Modeling of E-REV Power Train

3.1 System Layout

Figure 2 presents the power train system structure of investigated fuel cell E-REV in this chapter. The power train system consists mainly traction battery (Lithium iron phosphate), four in-wheel brushless direct current motors (BLDC motor), PEMFC (Proton Exchange Membrane Fuel Cell) range extender and DC/DC converter.

3.2 Bond Graph Model of Battery

There are numerous battery models developed for simulation of system performance of electric vehicles and hybrid electric vehicles, e.g., electrochemical, mathematical and equivalent circuit-based models. A Rint model is chosen in this chapter, the equivalent circuit of Rint battery model is shown in Fig. 3. The battery

Table 1 Examples of effort and flow in different physical fields [9]

Field	e : Effort (unit)	f : Flow (unit)
Mechanical	F : Force (N)	v : Velocity (m s^{-1})
Electrical	u : Voltage (V)	i : Current (A)
Chemical	μ : Chemical potential (J mol^{-1})	\dot{n} : Molar flow (mol s^{-1})
Hydraulic	P : Pressure (Pa)	\dot{V} : Volume flow ($\text{m}^3 \text{s}^{-1}$)
Thermal	T : Temperature (K)	\dot{S} : Entropy flow ($\text{J K}^{-1} \text{s}^{-1}$)

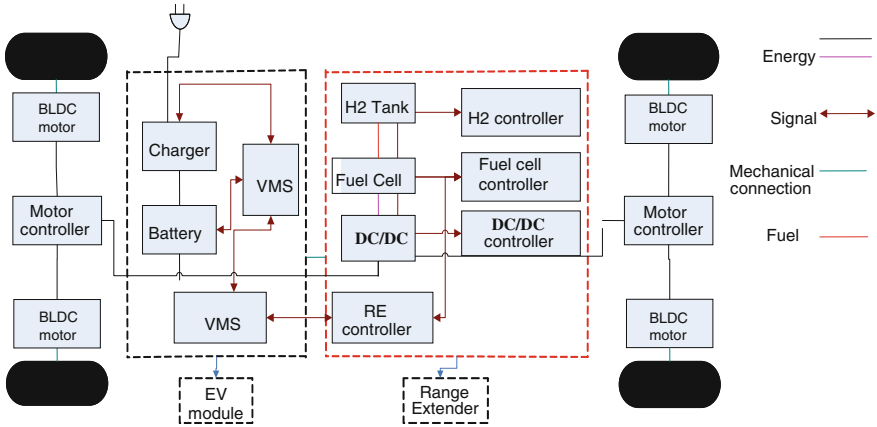
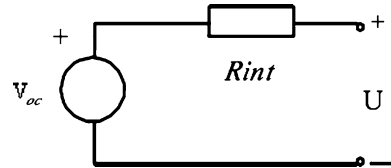


Fig. 2 Power train system of fuel cell E-REV

Fig. 3 Rint battery equivalent model



is abstracted as an ideal open-circuit voltage source V_{oc} connected with an internal resistance R_{int} series. So according to the model principle of bond graph in electrical system, the Rint battery could be modelled in Fig. 4.

3.3 Bond Graph Model of BLDC Motor

Figure 5 shows the equivalent electric circuit for a three-phase BLDC motor. The voltage comes from battery and DC/DC converter. The inductance (L) and equivalent resistance (R) of wound coil are taken into account.

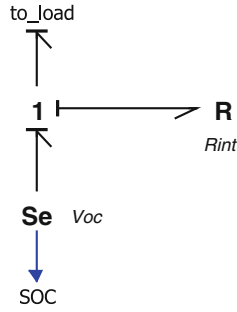


Fig. 4 Bond graph model of battery

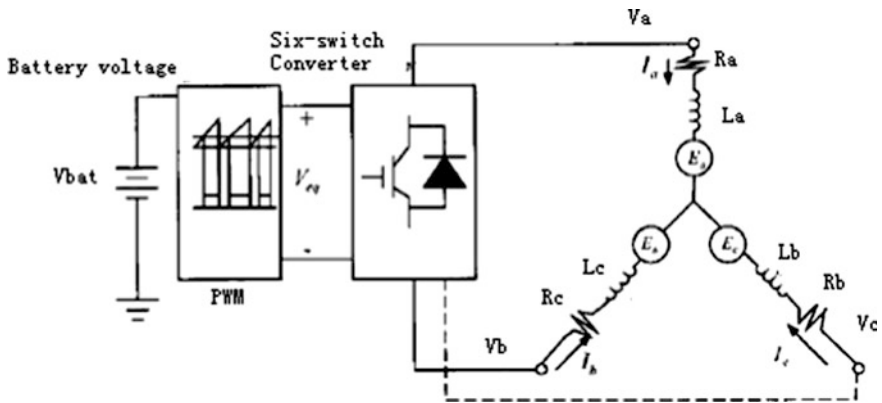


Fig. 5 Schematic diagram of three-phase BLDC motor

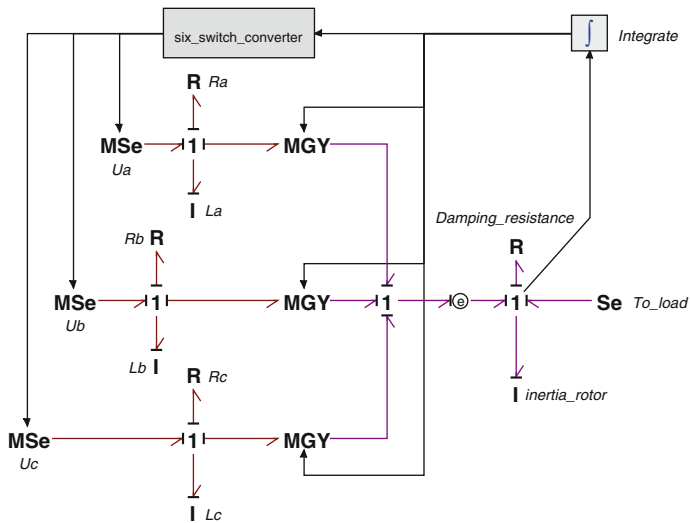


Fig. 6 Bond graph model of three-phase BLDC motor

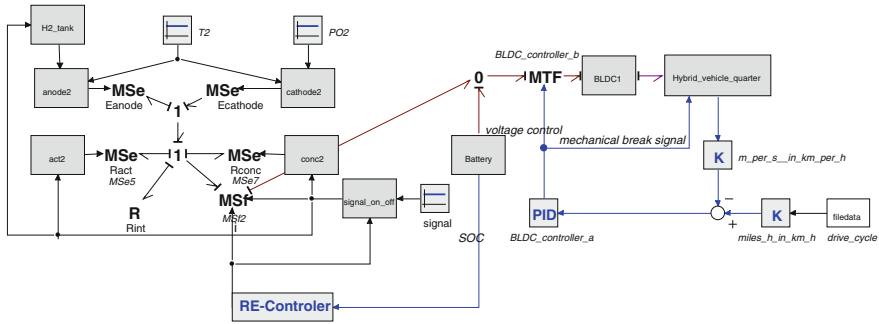


Fig. 9 Complete bond graph model for E-REV power train system

3.5 Bond Graph Model of Vehicle Body

In order to calculate the speed of E-REV, the rolling resistance and air dynamic resistance are taken into account, see Fig. 8.

3.6 Bond Graph Model of Complete Power Train System

The components bond graph models are integrated into one whole complete power train system model, see Fig. 9. The PID module is modelling the driver, the driving cycle data are filled in *drive_cycle* module.

4 Simulation and Results

The ECE driving cycle is chosen to make a simulation in this chapter. In order to investigate the feasibility of thermostat energy management strategy, the initial SOC of battery is set to 40 %, and the lower start-point of range extender is set to 50 %. So the range extender will start immediately at the beginning of the simulation. Figure 10 exhibits the simulation results of the fuel cell E-REV. Figure 10a shows that the actual speed can track the demanded speed well. Figure 10b exhibits the historical performance of battery SOC. And the thermostat energy management strategy is also validated. When the SOC of battery falls to 0.4, the Range Extender starts to work at a constant power point, it is about 5400 W in this chapter, see Fig. 10c. At the end of this simulation process, the vehicle went to standstill condition. The power generated from Range extender charged the battery so the SOC increased, see Fig. 10b. Summarily, these simulation results show that bond graph models are able to describe all physical

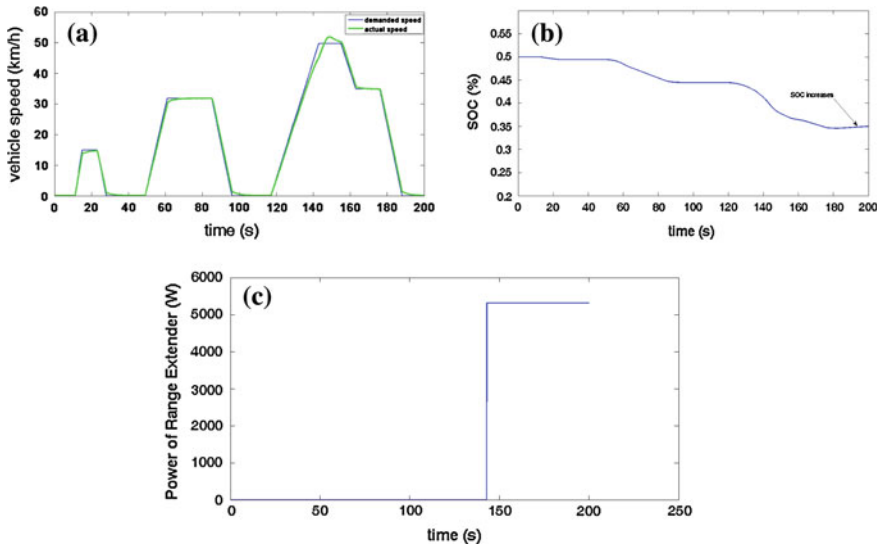


Fig. 10 a Vehicle speed tracking. b SOC of battery. c Power of range extender/thermostat energy management strategy

phenomena inside the E-REV and also fit for the energy management strategy design. Through the modelling and simulation process, no complex mathematical equations are needed. The complete power train system model of E-REV is modelled almost according to the physical structure of the target systems. That is a obvious advantage of bond graph modelling.

5 Conclusions

The academic community and automotive industry are paying much more and more attention to Range Extended electric vehicles. E-REVs are seen to be one of the most promising power train concepts for future vehicles. The fast growth of application and research about E-REV requires establishing accurate dynamic model to investigate the inside dynamic performance and design optimal control strategies. As a matter of fact the conventional modelling methods for power train system of electric vehicle and hybrid electric vehicle involve more computational/mathematical work. The bond graph method proposed in this chapter has been proved to be suitable and convenient in modelling of multi-domain system, such as power train system of E-REV. A graphical, accurate, easy to modify and capable for real time implementation E-REV power train system model is presented using bond graph in this chapter. The simulation results have shown accurately the dynamic performance of E-REV key components, and validated the chosen energy management strategy successfully.

References

1. Tate ED, Harpster MO, Savagian PJ (2008) The electrification of the automobile: from conventional hybrid, to plug-in hybrids, to extended-range electric vehicles. SAE paper 2008-01-0458
2. Song K, Zhang J, Zhang T (2011) Design and development of a pluggable PEMFC extended range electric vehicle. Second international conference on mechanic automation and control engineering (MACE)
3. Dong T, Zhao F, Li J, Jin Q, You Y (2011) Design method and control optimization of an extended range electric vehicle. IEEE vehicle power and propulsion conference (VPPC)
4. Varnhagen S, Same A, Remillard J, Park JW (2011) A numerical investigation on the efficiency of range extending systems using advanced vehicle simulator. journal of power sources. 196:3360–3370
5. Filippa M, Chunting M, Shen J, Stevenson RC (2005) Modeling of a hybrid electric vehicle powertrain test cell using bond graphs. Vehicular Technology. IEEE Transac 54:837–845
6. Gissingner GL, Chamaillard Y, Stemmelen T (1995) Modelling a motor vehicle and its braking system. J Math Comput Simul 39:541–548
7. Hrovat D, Tobler WE (1991) Bond graph modeling of automotive power trains. J Franklin Inst 328:623–662
8. Margolis D (2002) Bond graphs, modeling, and simulation in industry: some examples where costly mistakes could have been avoided. IEEE international conference on systems, man and cybernetics
9. Borutzky W (2010) Bond graph methodology development and analysis of multidisciplinary dynamics system models. Springer, London

Optimization of Hybrid Strategies with Heuristic Algorithms to Minimize Exhaust Emissions and Fuel Consumption

Michael Planer, Thorsten Krenek, Thomas Lauer, Zahradnik Felix, Bernhard Geringer and Michael Back

Abstract The hybrid powertrain is a promising concept to contribute to achieve future CO₂-targets. This paper describes a method to improve future automotive powertrains efficiently in real world driving conditions. Beside the optimization of the internal combustion engine and the electric components, the operating strategy of the hybrid powertrain is of particular importance to minimize the vehicles fuel consumption. A combination of start/stop operation, downspeeding, load-point shifting and pure electric driving can provide substantial fuel savings compared to conventional powertrains. However, in addition to the fuel consumption the more and more stringent future emission legislation must be taken into the account when optimizing the operating strategy. A fast light-off of the catalytic converters and a control of the converter temperatures during pure electric driving must be achieved. Therefore, numerous parameters have to be optimized simultaneously to realize the best solution for the hybrid powertrain. A numerical optimization approach was used to define the operating strategies efficiently for the mentioned goals. The results of this optimization were compared to the fuel consumption and the exhaust emissions of the conventional powertrain. The potential of a further strategy optimisation could be evaluated. Generally, it could be shown that long phases of electric driving combined with aggressive load point shifting to balance the battery's state of charge are most favorable in terms of efficiency. The phases of electric driving are additionally limited by the temperature drop of the catalysts

F2012-B02-023

M. Planer (✉) · T. Krenek · T. Lauer · Z. Felix · B. Geringer
Vienna University of Technology—Institute for Powertrains and Automotive Technology,
Vienna, Austria
e-mail: michael.planer@ifa.tuwien.ac.at

M. Back
DAIMLER AG, Stuttgart, Germany

and the lack of pollutant conversion after restart. This is a new and innovative approach to develop electrified powertrains efficiently. Finally it can be stated, that the numerical optimization method proved to be a powerful tool to support the development process of hybrid powertrains with numerous degrees of freedom.

Keywords Hybrid vehicles · Fuel consumption · Emissions · Numerical optimization · Operation strategies · Hardware in the loop

1 Introduction

The future availability of fossil fuels and growing environmental concerns have increased the pressure on automakers to develop fuel efficient vehicles with low emissions. The hybrid electric vehicle (HEV) is a possible approach to meet these demands.

Unlike conventional vehicles, a HEV has two power sources for propulsion [1]. Therefore, main challenges of hybrid powertrain development are the multiple degrees of freedom and a large diversity of powertrain architectures. Due to that fact, an optimal operating strategy is of specific importance in order to reduce the fuel consumption. However, an efficient determination of the vehicle's possible operating modes can only be achieved with a combination of numerical simulation and test bench measurements (Engine in the Loop—EiL). With this approach, accurate investigations on different electrified powertrain architectures and operating strategies in combination with an existing combustion engine are possible without the demand of hardware prototypes.

The described approach will be illustrated for a parallel hybrid powertrain. In order to find an operating strategy in the New European Driving Cycle (NEDC) with lowest fuel consumption, a self-developed algorithm was used that allows a numerical optimisation of the numerous degrees of freedom involved in the problem.

2 Investigated Powertrain Topologies

The basic conventional powertrain consists of a 6-cylinder SI engine that is coupled to an automatic transmission with a torque converter including a lock-up-clutch (Fig. 1, left picture). All upcoming investigation results are referenced to the conventional powertrain with start/stop capability.

For the hybrid powertrain the electric motor/generator (MG) is placed between the SI engine and the automatic transmission. A clutch between the SI engine and the MG provides the capability of pure electric driving. In contrast to the

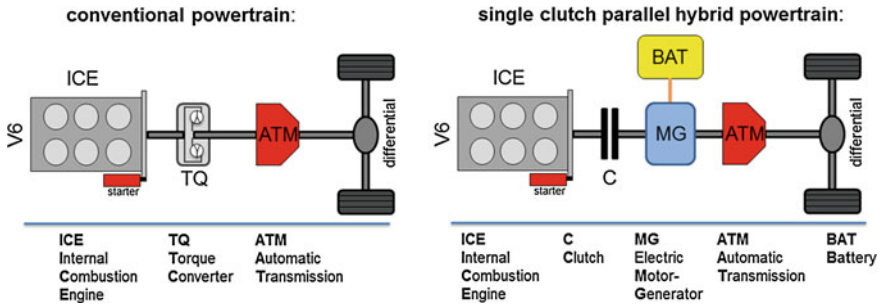


Fig. 1 Topology of the investigated powertrains

conventional powertrain, no torque converter is used because of a more efficient recuperation of brake energy and engine start-up [2].

3 Hybrid Functions: Operation Modes

Hybrid powertrains have the capability to realise start/stop, braking energy recuperation, load point shifting and electric driving strategies. A reduction of the fuel consumption and lowest exhaust emissions can only be achieved with an optimised strategy. Therefore a numerical optimisation method based on several heuristic approaches was used to attain the mentioned goals.

4 Simulation Model

The numerical simulation model is a closed loop longitudinal vehicle dynamics model including the exhaust system that was built up in the GT-Suite™-software from Gamma Technologies. The vehicle including a 6-cylinder SI engine, electric components and the mechanical components of the powertrain, was modelled in accordance to a close-to-series powertrain. To provide fast simulation times, the battery, the electric motor, the SI-engine and the automatic transmission were characterised with performance and efficiency maps. For all investigations real time capability was achieved.

The up- and downshift commands for the automatic transmission model were set in dependency of the engine speed. In order of following a given driving cycle, the driver of the vehicle is represented by a PI-controller.

In accordance to that, the purpose of providing a fast light-off of the catalytic converters and a control of the converter temperatures during pure electric driving can be achieved.

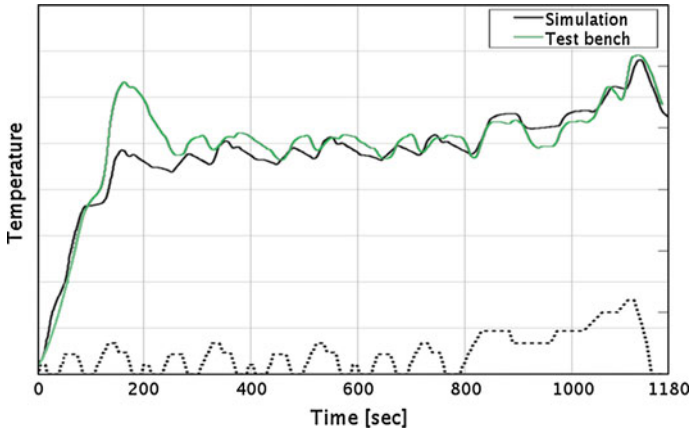


Fig. 2 Comparison of simulation and measurement

In addition to the dynamics simulation of the hybrid powertrain, a thermal model exhaust system was established and verified according to measurements from the test bed. The model consists of the thermal capacities and conductivities of the material. The enthalpy of the exhaust gas is transferred from the engine model. Due to that, Fig. 2 shows the comparison of the temperature between simulation and measurement inside the catalytic converter in NEDC. The differences in the first time steps are because of special exhaust system heat up strategies from the ECU and exothermic reactions in the three-way catalytic converter which could not be integrated in the model. This will be done in a further step.

As already mentioned, the minimisation of the fuel consumption and exhaust emissions requires a purposeful choice of the best hybrid operation strategy for the instantaneous vehicle speed and acceleration. Therefore, a distinction of the different vehicle states in the NEDC was made, i.e. phases of constant speed, constant acceleration and deceleration and stand-still were evaluated and optimised separately (Fig. 3).

For example, downsizing and down speeding are well known effective measures in order to reduce the fuel consumption [3]. However, an appropriate choice must be made for the given powertrain [4, 5]. Previous investigations have shown potentials in order to minimise the fuel consumption by using load point shifting [6].

Therefore, a speed dependent upshift command and a pure electric driving velocity is combined with a load point shifting factor for all individual segments of the NEDC (Fig. 3) with constant vehicle speeds and constant acceleration in order to balance the battery's state of charge (SOC). With the purpose to sense and control the temperature of the catalytic converters, a parameter which coordinates the engine state was implemented. If the catalytic converter temperature reaches a defined lower limit, the internal combustion engine was started to heat up to provide exhaust enthalpy.

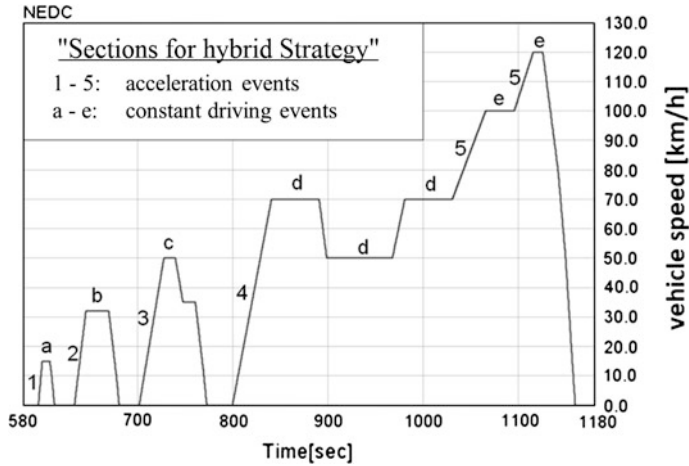


Fig. 3 NEDC-section separation

Table 1 Parameter definition

No.	Parameter
7	Variable speed dependant upshift-gear commands
10	Factor of load point shifting for all separated NEDC-segments
1	Maximum electric driving velocity

In order to find promising strategies to meet objectives a total of 18 parameters were taken to find their best combination (Table 1).

5 Optimisation Approach

The objective of the operation strategy is to minimise fuel consumption and exhaust emissions in the NEDC. To achieve the optimization of the hybrid powertrain with a large number of parameters in a reasonable time, a combination of meta-heuristic algorithms (see Fig. 4) was build up in order to handle the optimization. The advantage of this approach is that solutions will be continuously improved during the optimization process. Detailed information can be found in [7–10].

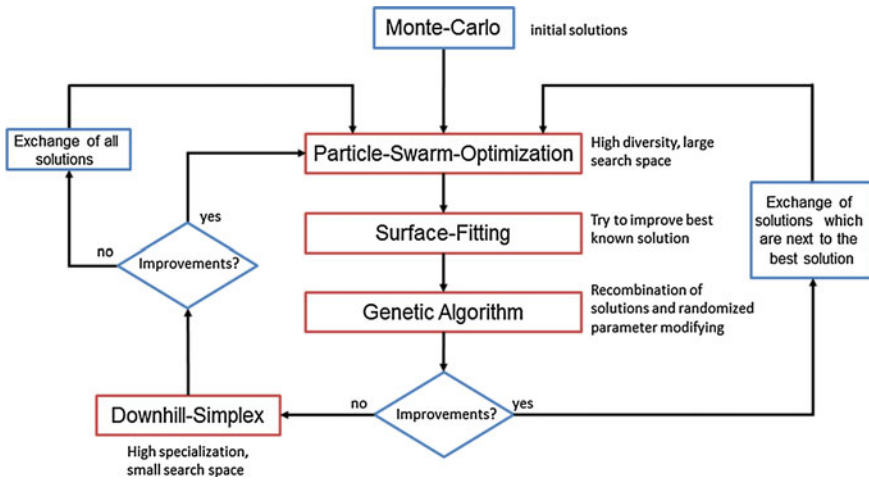
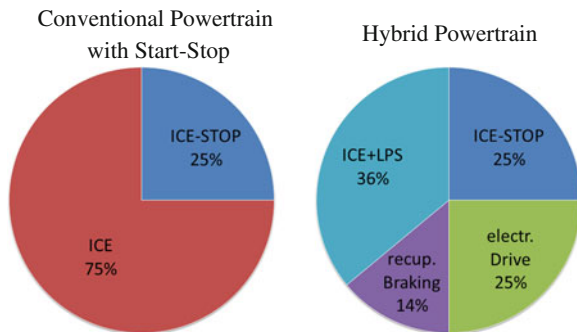


Fig. 4 Combination of meta-heuristic algorithms [13]

Fig. 5 Percentage of the operation modes in the NEDC



6 Results and Tendencies for the Operation Strategies

The best solution of parameter combination that could be found with the combined meta-heuristic algorithms was able to reduce fuel consumption by 25.8 % compared to the conventional powertrain with start/stop capability.

In order to get an impression of impact of operating strategies, Fig. 5 shows the percentage of the different operation modes (Table 2) within the NEDC.

The left pie chart shows that the conventional powertrain with start-stop capability is propelled by the internal combustion engine for 75 % of the cycle time. The internal combustion engine is shut off during the remaining time. The resulting strategy from the optimization approach, shown in the right pie chart, pursues the objective of a fast light-off of the catalytic converters including a minimisation of the fuel consumption and combines increased engine stand-still events with pure electric driving and load point shifting.

Table 2 Operation modes

ICE:	Conventional operation of the combustion engine
ICE-STOP:	Engine-stop events
ICE + LPS:	Operating the combustion engine with load point shifting/boosting
Electric drive:	Pure electric driving
Recup. Braking:	Recuperating energy while braking

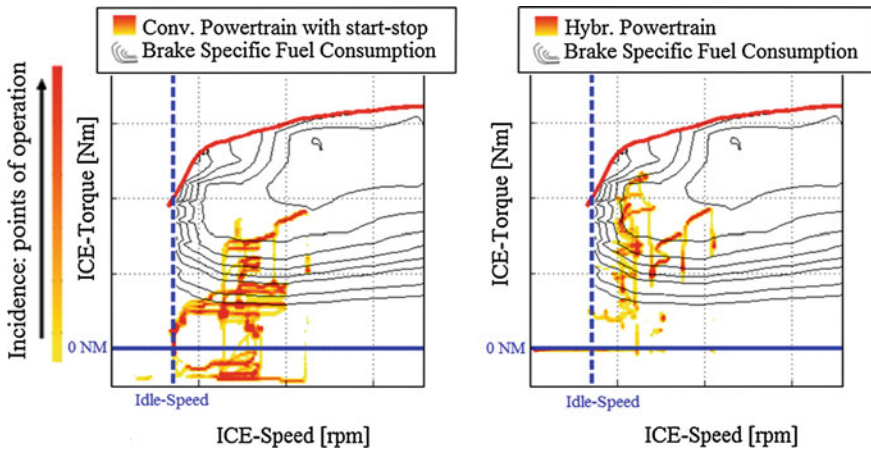


Fig. 6 Load spectrum

As shown in Fig. 5 the events of conventional engine operation are replaced by long electric driving and long engine stop events. The internal combustion engine is only used in combination with the capability of load point shifting to provide energy for pure electric driving and in order to balance the battery’s state of charge.

The tendency of long phases of electric driving combined with aggressive load point shifting in order to accomplish a higher efficiency can be clearly derived from the results. Figure 6 illustrates this trend.

Due to the fact of down speeding, the optimized hybrid strategy shifts operating points with a constant optimised factor in regions with higher efficiency. It becomes obvious from Fig. 6 that the operating points are shifted to a region of high fuel efficiency. The generated energy is stored in the battery and used for pure, highly efficient electric driving.

Due to this fact, the usage of a multiple-parameter optimisation approach has shown the enhanced optimization possibilities by means of an enhanced number of parameters. There are still reveals considerable further potentials for the fuel efficiency.

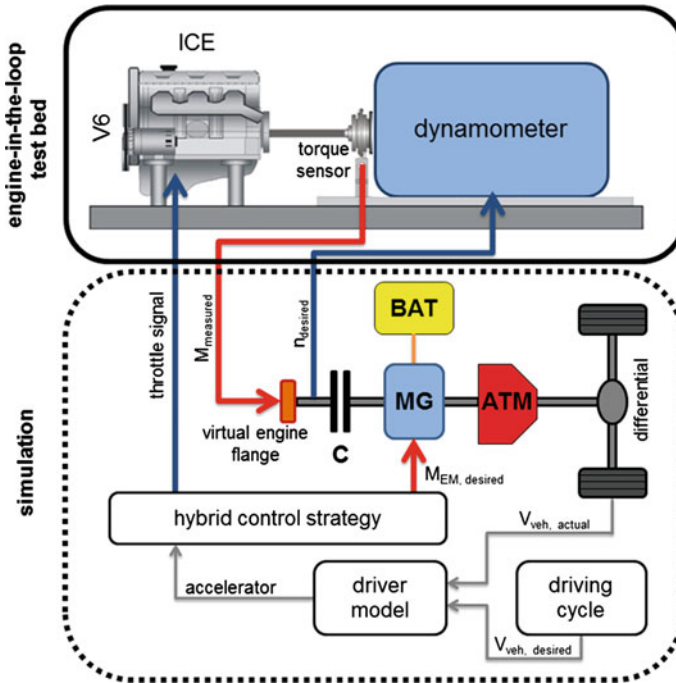


Fig. 7 Control of the engine in the loop test bed

7 Validation and Verification

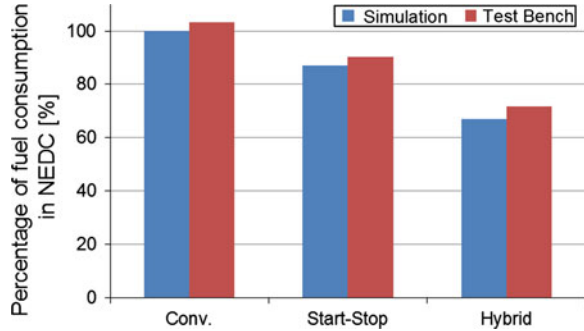
For the verification and validation process, the investigated engine was operated on an Engine-in-the-Loop test bench. For this purpose, the model of the combustion engine within the simulation was replaced by measured signals from the hardware [11].

The EiL-test bench was controlled using the LABCAR-software from ETAS. The closed loop control principle, which consists of hardware and software components, is shown in Fig. 7.

On the mechanical level, an interface is defined between the crankshaft of the real combustion engine and a virtual clutch. The connection between the test bed and the simulation is done by feeding the measured torque at the flange on the test bed into the virtual engine flange. Simultaneously, the calculated speed of the virtual engine flange is transmitted to the test bed dynamometer. In order to transfer the calculated throttle signal to the engine's control unit, the model's virtual bus system has to be connected to the real CAN bus system. [12]

The conventional powertrain with and without start/stop capability and the optimised single clutch parallel hybrid powertrain strategy were verified at the EiL-test bench. Figure 8 shows a good correlation between the simulation results and the measured fuel consumption at the test bench. Dynamic and cold-start

Fig. 8 Simulation vs. Test bench



effects are not considered within the stationary engine maps. Thus, slight differences between simulation and test bed results can be observed. However, the good agreement between simulation and experiment clearly shows that the numerical method is able to predict the potentials of the different strategies correctly.

8 Summary and Conclusion

The hybrid powertrain is a promising concept to contribute to the future CO₂-targets.

Besides the dimensioning of the internal combustion engine and the electric components, the operating strategy of the hybrid powertrain is of particular importance to optimise the vehicles fuel consumption. However, in addition to the fuel consumption the more and more stringent future emission legislation must be taken into the account when optimizing the operating strategy. A fast light-off of the catalytic converters and a control of the converter temperatures during pure electric driving must be achieved

A combination of start/stop operation, down speeding, load-point shifting and pure electric driving can provide substantial fuel savings compared to conventional powertrains including compliance with formalities. Due to the fact that numerous parameters have to be optimised, a numerical approach is useful to define the operating strategies efficiently.

Therefore a new and sophisticated approach with a numerical optimiser based on several heuristic methods was developed. The results of this optimization were compared to the fuel consumption of the conventional powertrain with start-stop capability. Generally, it became obvious that long phases of electric driving combined with aggressive load point shifting to balance the battery's state of charge are most favourable in terms of efficiency after reaching the light-off temperature of the catalytic converters. The strategies were verified on an Engine-in-the-Loop test bench.

In order to obtain a strategy for arbitrary driving cycles and real-life cycles, a more general formulation of the driving parameters and criteria has to be provided for optimisation what will be a future target.

References

1. Jefferson CM, Barnard RH (2002) Hybrid vehicle propulsion. WIT Press, Southampton, UK, pp 1–27
2. Planer M, Zahradnik F (2012) Hybrid power plant development: engine-in-the-loop—integration of combustion engine and HiL simulation. The ETAS Group Magazine—Real Times
3. van Basshuysen R (2007) Ottomotor mit direkteinspritzung. Vieweg Verlag, 1. Auflage, pp 205–211, ISBN 978-3-8348-0202-6
4. Salmasi FR (2007) Control strategies for hybrid electric vehicles: evolution, classification, comparison, and future trends. IEEE Trans Veh Technol 56(5)
5. Pisu P, Rizzoni G (2007) A comparative study of supervisory control strategies for hybrid electric vehicles. IEEE Trans Control Syst Technol 15(3)
6. Sundström O, Guzzella L, Soltic P (2008) Optimal hybridization in two parallel hybrid electric vehicles using dynamic programming. In: Proceedings of the 17th world congress, the international federation of automatic control, Seoul, Korea, July 6–11
7. Krenek T, Ruthmair M, Raidl G, Planer M (2012) Applying (hybrid) metaheuristics to fuel consumption optimization of hybrid electric vehicles. J Appl Evol Comput, pp 376–385
8. Nelder JAuMR (1965) A simplex method for function minimization. Oxford J: Comput J, Brit Comput Soc 7(4):308–313
9. Michalewicz Z (1996) Heuristic methods for evolutionary computation techniques. J Heuristics 1(2):177–206
10. Kennedy J, Eberhart R (1995) Particle swarm optimization. In: Proceedings of the IEEE international conference on neural networks 4:1942–1948
11. Helm S, Schneeweiss B, Winter S, Kozek M (2008) Hardware in the loop simulation of a hybrid powertrain. In: Proceedings of the international simulation multi-conference, Scotland, pp 16–19
12. Schneeweiss B, Teiner P (2010) Evaluation of NOx and fuel consumption reduction potential of parallel diesel-hybrid powertrains using engine-in-the-loop simulation. SAE Technical Paper 2010-32-0128. doi: [10.4271/2010-32-0128](https://doi.org/10.4271/2010-32-0128)
13. Planer M, Krenek T, Lauer T, Geringer B (2012) Optimisation of hybrid strategies with heuristic algorithm. In: 12th Stuttgart international symposium automotive and engine technology, FKSF—Research Institute of Automotive Engineering and Vehicle Engines, Stuttgart

Development for Control Strategy of ISG Hybrid Electric Vehicle Based on Model

Hongtao Peng, Zheng Li, Bin Chen, Jieyu Wu, Zhenglan Zhao, Yuehong Shu and Junjun Lei

Abstract The Control Strategy of ISG Hybrid Electric Vehicle is developed, which is based on model with reference of AUTOSAR standard, the system model is at the centre of the development process, from requirements definition and system design to implementation and testing. What the experiment proved is that the development of control strategy is of high efficiency and reliability, with the performance met the design requirements, and development time and cost reduced, meanwhile the portability and maintainability of system improved.

Keywords Control strategy · Simulation model · Automatic generation of code · AUTOSAR

1 Introduction

As the energy resources shortage and environment protection have become the major challenge for the world, it is imperative to alter the energy and power system for vehicle industry, the electric vehicle has become the essential choice for such alteration. More and more enterprises begin to develop electric vehicle, and the Chinese government is making every endeavour to support the development of electric vehicle.

F2012-B02-025

H. Peng (✉) · Z. Li · B. Chen · J. Wu · Z. Zhao · Y. Shu
Dongfeng Motor Corporation Technical Centre, Shiyan, China
e-mail: penght@dfmc.com.cn

J. Lei
Yangtze University, Wuxi, China

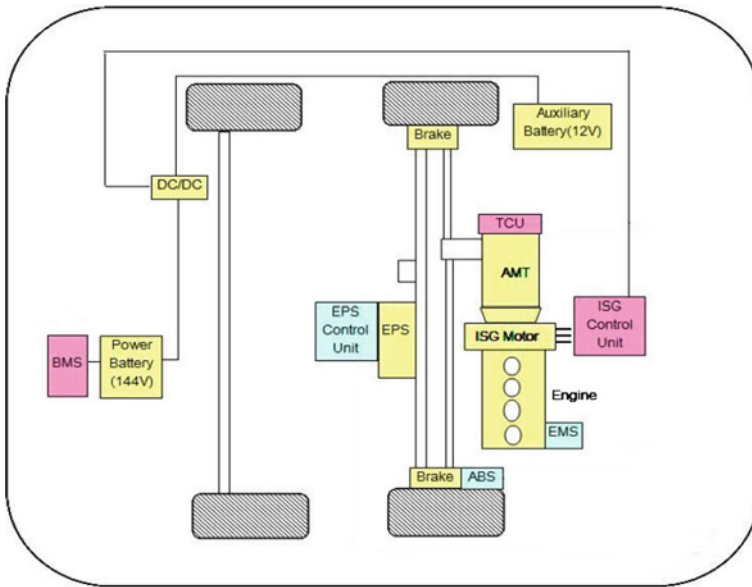


Fig. 1 The general arrangement of ISG hybrid electric vehicle

The complexity of automotive software and the needs for shorter development time and software portability require the development of new approaches and standards for software architectures, model-based design has become a widely used and accepted approach, and as a standard architecture for ECU networks, AUTOSAR (Automotive Open System Architecture) is already playing a significant role in the automotive industry, a model-based development process with AUTOSAR compliance enables the development of standardized software with high quality and efficiency.

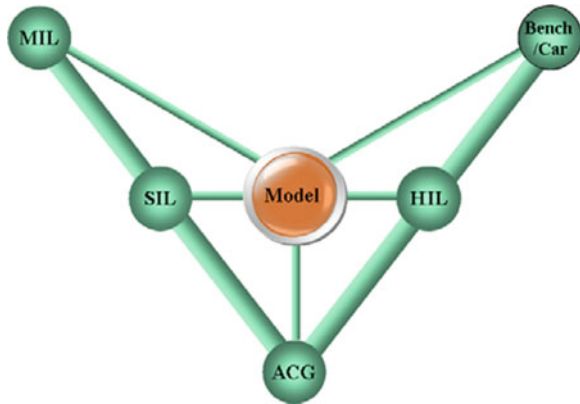
The project comes from the project of national 12th five-year-plan and national 863 plan. The ISG hybrid electric vehicle should show good power performance, good fuel economy and good emission performance.

According to conventional power train configuration and 3-D model, using ISG replacing the conventional starter and generator, the ISG can drive the vehicle and regenerate the brake power in the front wheels, the ISG Hybrid Electric Vehicle layout is shown in Fig. 1.

2 Model-Based Design

Model-Based Design for embedded control systems development involves a process centred on a model—from requirements capture to implementation and test. This model forms the “executable specification” that is used to communicate the

Fig. 2 Development process based on model



desired system performance. With Model-in-the-Loop (MIL) test, the control design is elaborated and continuously tested against requirements through simulation. Code is generated from models (abbreviation ACG). Software-in-the-loop (SIL), and hardware-in-the-loop (HIL) testing and verification and validation (V&V) of the algorithmic code may be done before deployment on the production vehicle, Calibration can be done on the test bench and car, Fig. 2 shows the development process. Model-based design activities keep the engineering process focused on error prevention and early error detection. Verification and validation early in a project can reduce the risks associated with late error detection [1].

2.1 MIL Testing

The simulation model of ISG Hybrid Electric Vehicle is established via matlab/simulink/state flow. Simulation model includes driver’s intention submodule, control strategy submodule which is the control algorithm parts that should be evaluated, plant model which consists of engine submodule, motor submodule, battery submodule and gear box submodule etc., result submodule and so on. Figure 3 shows the model.

We match the power train system, and research the control strategy of ISG Hybrid Electric Vehicle with the simulation model. First, we can calculate the power performance and the economy performance of the conventional vehicle, and then we can adjust and validate the model through the comparison between the simulation results and real experimental results. Afterward, we can use a validated vehicle model to simulate ISG Hybrid Electric Vehicle, such as matching motors and battery, researching the energy distribution strategy and regeneration strategy of braking energy, optimizing the work area of engine, motor, and battery, etc.

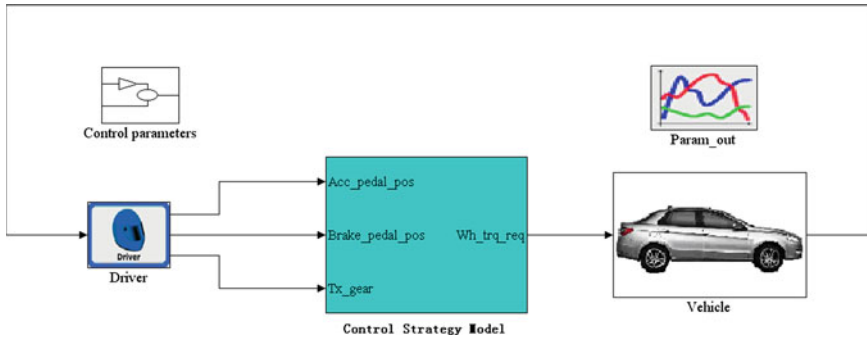


Fig. 3 MIL testing model

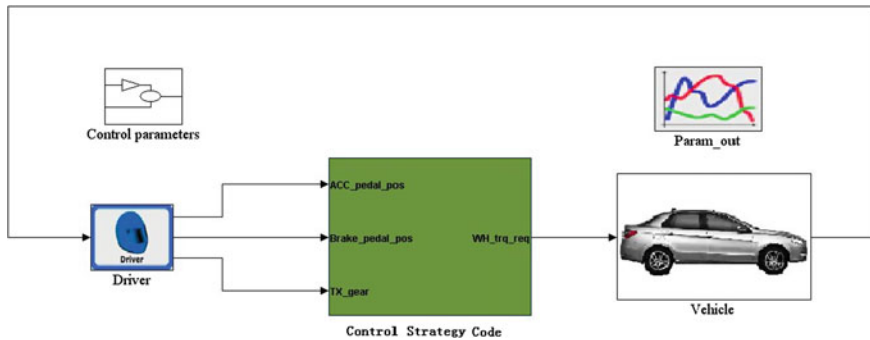


Fig. 4 SIL testing model

2.2 SIL Testing

After the functional verification is achieved, using the MIL testing, the complete software code can be generated. This generated software can be verified using SIL testing. For SIL testing, the generated software code can be wrapped into an s-function subsystem block. This wrapped s-function subsystem block can be used to test the functionality of the automatically generated code for the control strategy [1]. Figure 4 shows the model.

2.3 Automatic Generation of Code

A key step in Model-Based Design is the deployment of an algorithm as machine code onto a target processor in the production vehicle. The control strategy simulation model is generated C code under the Real-Time Workshop Embedded

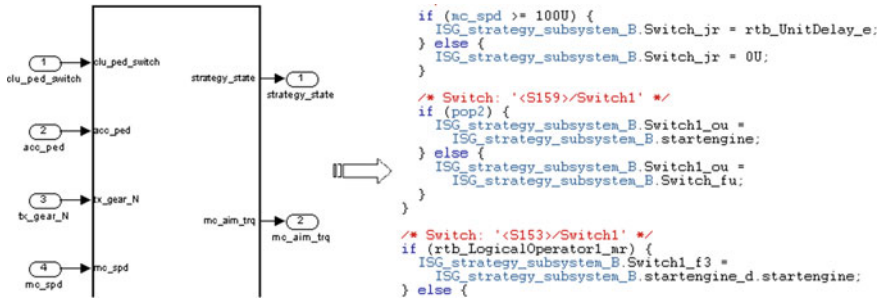


Fig. 5 The model of automatic code generation

Coder environment of MATLAB. The use of automatic code generation maintains the link between the model and the generated C source code. To change the algorithm later in the design process, it is easier to update the model and regenerate the C source code. This method allows the engineer to focus more on integrating algorithmic code and setting up the infrastructure for embedded system deployment. The generated code is integrated into the driver program, compiling the whole code, and downloaded to the HCU. The model of automatic code generation is shown in Fig. 5.

2.4 HIL Testing

HIL testing is different in comparison with MIL and SIL testing, MIL and SIL testing execute models and code on the PC, but HIL testing executes models and code on real ECU, so MIL and SIL testing are appropriate for initial control system development, HIL testing is appropriate for testing the total functions of the ECU running in real time, and the physical communication buses can be simulated and analyzed in a single or multiple ECU network. Figure 6 below shows a schematic connection between an ECU and a HIL system. The plant model and other I/O communication are executed in an HIL real-time system, and the ECU software is executed on a real ECU.

The HIL methodology enables ECU software validation before the hardware is available. HIL testing reduces the need for testing vehicles and can be used to conduct simulations of extreme situations without endangering people or equipment [2].

2.5 Bench Test

We use hybrid power train test facility to verify and calibrate the control strategy, and execute vehicle performance tests and special tests only use hybrid power train

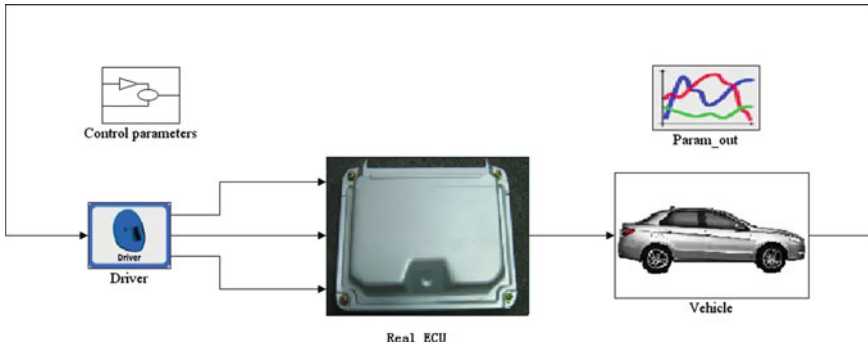


Fig. 6 HIL testing model

without the whole vehicle. With the test bench, we execute the following development tests of hybrid power train:

- Testing of power performance of the vehicle.
- Testing of brake performance of the vehicle.
- Testing of energy consumption using different driving cycles, such as NEDC cycle, and other designed driving cycles.
- Research, development and optimization of the control strategies of energy management and regeneration strategy of braking energy.
- Research and development of control strategies of gear shifting and actuators of AMT.

After the above processes have been finished, tests and calibrations will be carried out on the car. At first phase of the project, the MT ISG car was developed, and from the beginning of the project until now, we have finished bench test, city road test, winter test and summer test, etc., through these tests and calibrations, drivability was optimized and control strategy was further optimized and improved. Now the second phase of the project with AMT ISG car is being developed smoothly.

3 AUTOSAR

AUTOSAR represents the trend of automotive electronics industry development. A model-based development process with AUTOSAR compliance guarantees the development of standardized software with high quality and efficiency.

Figure 7 shows the defined architecture with the different software layers divided into three major areas [3].

AUTOSAR specifies a standard description format, i.e. “Software Component Description” to describe the component interface and the requirements on infrastructure and computing resources. For AUTOSAR software component (SWC),

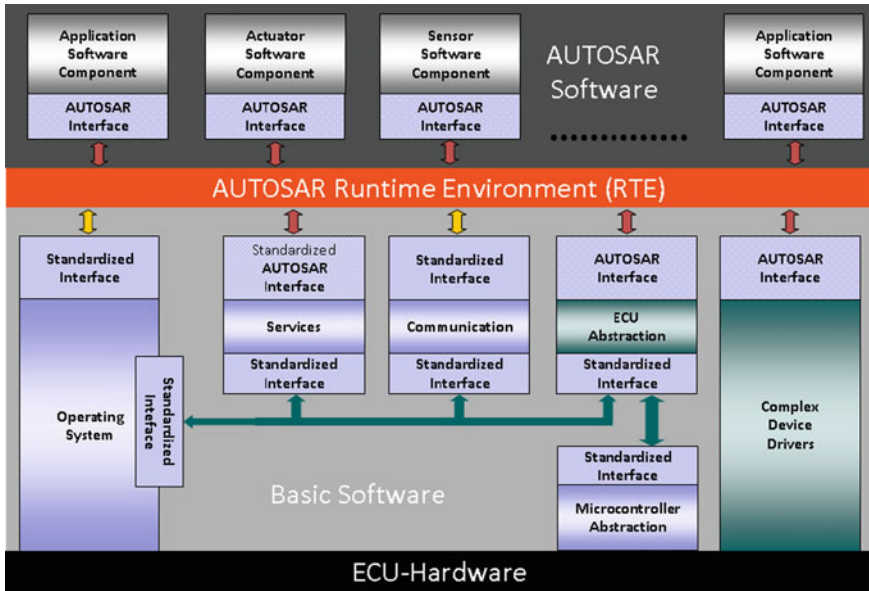


Fig. 7 The AUTOSAR software architecture

each control strategy component is a minimum function unit; it defines the interfaces to interact with other software components. For run-time environment (RTE), AUTOSAR specifies the communication between those software components which are residing on a technology independent abstraction layer. For AUTOSAR basic software (BSW), it includes I/O drivers, CAN drivers, complex device drivers, OS and services, etc. This infrastructure software is specific to the ECU, and provides a software platform for the application software.

With reference of AUTOSAR standard, we design software architecture in accordance with the hierarchical and modular architecture, which is very helpful for modularity, flexibility, transferability and re-usability of functions and helpful for the software updating and platform migration. The model is constructed in a way that the easier implementation of AUTOSAR-compliant software should be allowed by the component configuration, interface definition and interface abstraction so that the AUTOSAR requirements can be met. The component is mapped to an encapsulated subsystem in simulink, then separated and decoupled from the hardware, communication and operating system. The “runnables”, modelled as atomic sub-functions, is contained within the component. The entire component is reusable when logic for executing the sub-functions is encapsulated within the component. The component exposes well-defined interfaces in the form of ports, through which the component communicates to other software components.

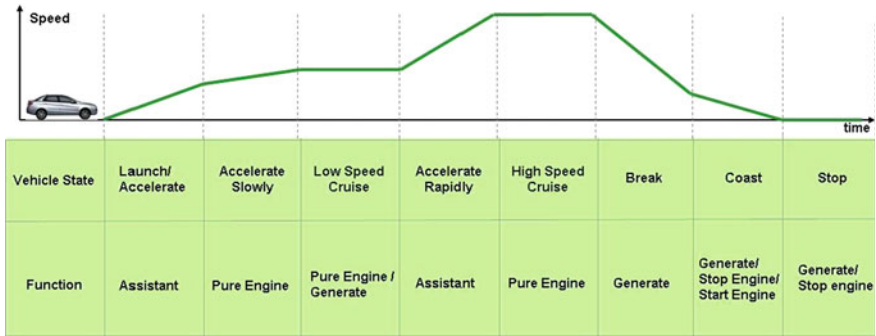


Fig. 8 The operation mode of the vehicle

4 Control Strategy

The hybrid vehicle, better than the conventional vehicle, depends greatly on its control strategy which has significant influences on vehicle fuel economy, performance and driveability. Therefore, designing an optimal control strategy which covers all requirements is of great interest. According to a typical driving cycle of ISG Hybrid Electric Vehicle, there are several working modes, as shown in Fig. 8.

1. Starting: Only the pure engine is used for start-up and low speeds.
2. Launching: The engine and motor both drive the wheels for rapid launching.
3. Normal Driving: While cruising, the engine and motor both drive the wheels, and power allocation is controlled to maximize efficiency of engine. As necessary, the motor also recharges the battery from surplus engine power or pure engine drive the wheels.
4. Acceleration: While accelerating or climbing, the engine and motor both drive the wheels.
5. Deceleration: While decelerating or braking, the “regenerative braking system” recovers kinetic energy as electrical energy, which is stored in the high-performance battery.
6. Stopping: When the vehicle speed is below a certain value, the engine shuts off automatically and the ISG stands ready to power up the vehicle.

The key technique for the HEV is to optimize the control strategy to reduce fuel consumption and emission. In the design of the control strategy, different structure hybrid vehicles need different control strategies with reasonable control and adjustment of energy flow distribution. Therefore, according to different optimization targets, different control strategies of energy management system should be selected to achieve optimal design goal under limited conditions. When designing the control strategy, the special features of each part and different operation modes ISG Hybrid Electric Vehicle are taken into consideration, and energy between engine and motor are reasonably distributed; we make the whole vehicle system

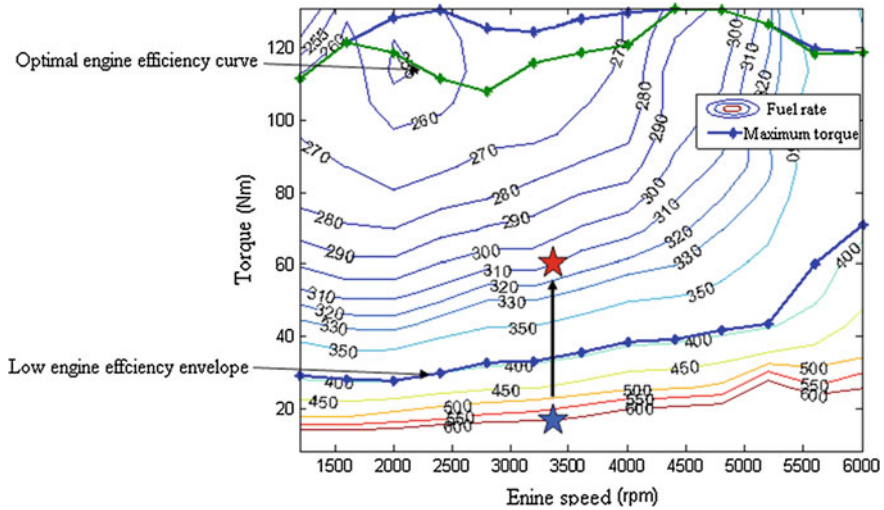


Fig. 9 The engine fuel rate

more efficient, fuel consumption lower and emission lower, and at the same time keep the driveability better.

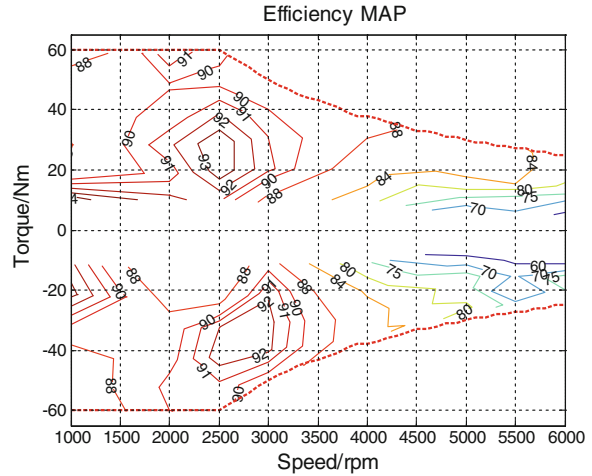
The instantaneous optimal control strategy is adopted, which is based on the optimal working curve of engine in the project. For the ISG Hybrid Electric Vehicle that is under a particular operating point, we optimize the entire power system for optimization goal to get the best instantaneous operating point, and then, based on instantaneous optimal system operating point, we redistribute various state variables dynamically. According to the economy and emission characteristics of the engine, an appropriate objective function is established through the optimal control theory. To minimize the objective function, we can achieve good power performance, fuel economy and emission performance.

$$\min(f) = \min \left\{ \omega_1 \left(\frac{a}{a_0} \right) + \omega_2 \left(\frac{b}{b_0} \right) + \omega_3 \left(\frac{c}{c_0} \right) \right\}$$

In the above equation, f is the objective function; a is the fuel consumption (L/100 km); b is actual emission (g/100 km); c is acceleration time (s); a_0 , b_0 and c_0 respectively are the aim values; ω_1 , ω_2 and ω_3 are the corresponding weight coefficients. Weight coefficient can be adjusted to change the degree of influence of each parameter.

When designing control strategy, the instantaneous efficiency of engine, motor and battery should be considered, the engine fuel rate is shown in Fig. 9 and the motor efficiency map is shown in Fig. 10. Combining with the actual running state, such as the temperature of engine, motor, battery and the braking energy recovery, etc., the best combination of energy between engine and motor is obtained. According to the control target, the optimal engine and motor operating points are determined. Our goal is to make the optimal system efficiency [4].

Fig. 10 The motor efficiency map



5 Conclusion

The Control Strategy of ISG Hybrid Electric Vehicle is researched and developed by building simulation model under Matlab/Simulink/State flow environment, and the system model is compliant with AUTOSAR standard which is at the center of the development process, from requirements definition and system design to implementation and testing. This approach provides a number of benefits such as reducing development time and cost, improving product quality, and generating a more reliable final product through the use of computer models for system verification and testing.

With this approach, proved by experiment, the development of ISG Hybrid Electric Vehicle control strategy is of high efficiency and reliability, with the performance met the design requirements and the portability and maintainability of system improved, meanwhile the development cost is greatly reduced, and the development cycle is shortened.

References

1. Vuli P, Badalament M, Jaikamal V (2010) Maximizing test asset re-use across MIL, SIL, and HIL development platforms. SAE Technical Paper 2010-01-0660
2. Syed F, Nallapa R, Grand KE, Ramaswamy D (2010) Embedded software tools enable hybrid vehicle architecture design and optimization. SAE Technical Paper 2010-01-2308
3. Rai D, Jestin TK, Vitkin L (2008) Model-based development of AUTOSAR-compliant applications exterior lights module case study. SAE Technical Paper 2008-01-0221
4. Hongtao P, Zheng L, Yu Z, Pingxing X, Yuehong S, Yong S, Yuan L (2010) Development for hybrid MPV control strategy. EVS25

Development of New Hybrid Transaxle for Front-Wheel Drive (FWD) 2.5-Liter Class Vehicles

Kunihiro Kobayashi, Takahisa Yashiro, Hiroshi Takekawa
and Kazuhiro Fujita

Abstract This paper explains the structure, characteristics, and performance of the newly developed P314 hybrid transaxle, which was developed for front-wheel drive (FWD) 2.5-liter vehicles. Lower mechanical and electrical losses and lighter weight than the conventional P311 were achieved by enhancing the motor cooling performance, improving the flow of the oil, and optimizing the shape of the casing. This transaxle is also applicable to a wider vehicle weight range and achieves better fuel economy while reducing cost.

Keywords Power transaxle · Hybrid system · Hybrid transaxle · Motor cooling · Electrical losses

1 Introduction

Automakers are facing growing demands to reduce vehicle CO₂ emissions and fuel consumption to help save resources and prevent global warming. Hybrid vehicles that combine an internal combustion engine with a motor/generator are regarded as an effective means of achieving these aims by improving fuel economy.

F2012-B02-026

K. Kobayashi (✉) · T. Yashiro · H. Takekawa
Toyota Motor Corporation, Toyota, Japan
e-mail: kunihiro@kobayashi.tec.toyota.co.jp

K. Fujita
Toyota Technical Development Corporation, Toyota, Japan

The world's first mass-produced hybrid system was installed in the Prius in 1997. Since then, a series of improvements culminated in the development of the P311 hybrid transaxle for passenger vehicles, which included a motor reduction device. Subsequently, the P314 hybrid transaxle was developed for 2.5-liter class front wheel drive (FWD) vehicles such as the new Camry, which was launched in 2011. Based on the P311 transaxle, the P314 retains the same basic motor configuration and uses the same gears.

However, the P314 transaxle was developed to accommodate the specifications of the new Camry, which include 10 % greater engine torque than the previous model and a wider range of sales destinations. This paper describes the structural and performance improvements incorporated into the new P314 transaxle.

2 Aims of Development

2.1 Motor Cooling Performance Improvement

The P314 transaxle for FWD 2.5-liter vehicles was developed to be compatible with a larger vehicle class than the previous transaxle to facilitate its adoption in future models. The motor cooling performance was improved to achieve this aim. More efficient motor cooling also reduces motor losses, thereby helping to improve fuel economy.

2.2 Fuel Economy Improvement

Class leading fuel economy was achieved by thoroughly reducing losses, such as motor and oil pump losses, as well as agitation loss in the transaxle.

2.3 Quiet Operation and Weight Reduction

The weight of the P314 transaxle was reduced while maintaining the required level of quiet operation by reducing the thickness and optimizing the shape of the motor cover.

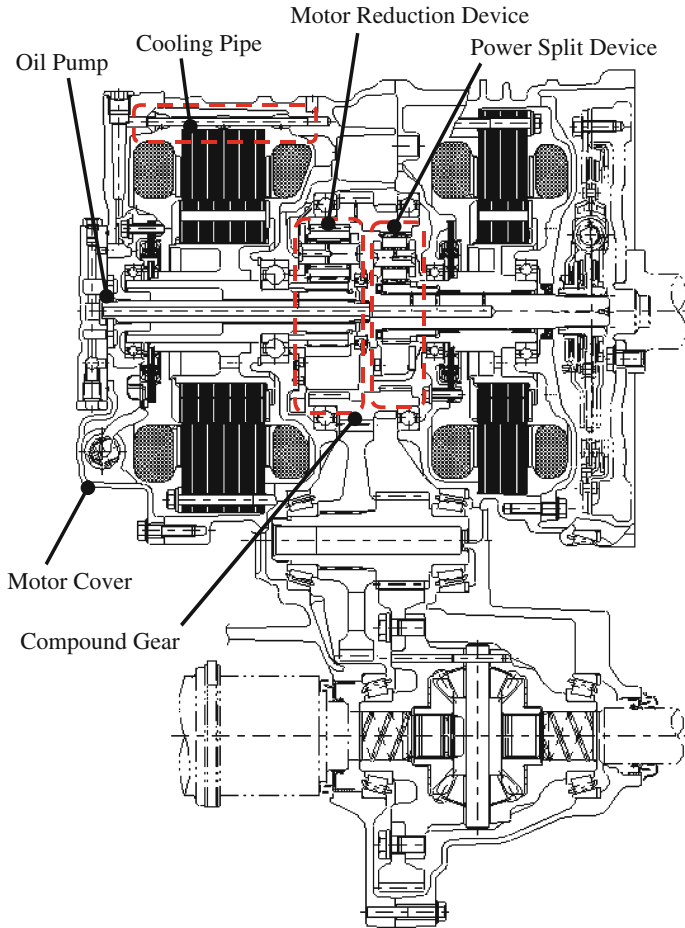


Fig. 1 P314 Cross section

Table 1 Specifications of new hybrid transaxle

	P314	P311
Max. engine torque	213 Nm	187 Nm
Max. engine output	118 KW	110 kW
<i>Motor</i>		
Max. output	105 kW	
Max. torque	270 Nm	
Motor reduction gear ratio	2.478	
Differential gear ratio	3.542	
Weight	106 kg	112 kg
Overall length	405 mm	

Fig. 2 Illustration of motor cooling in P311 transaxle

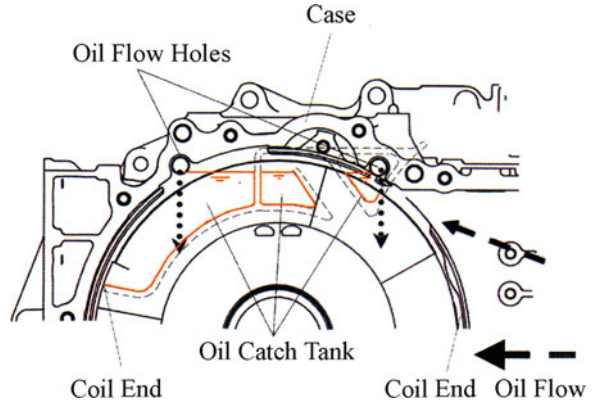
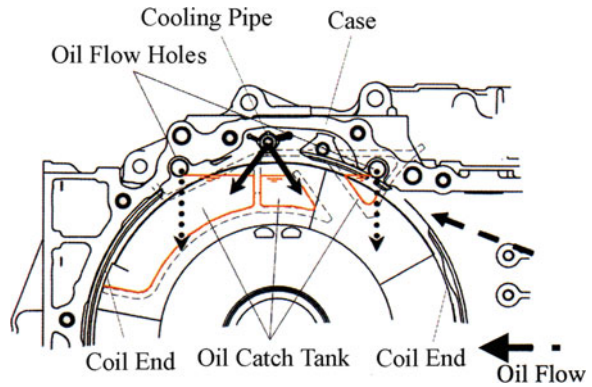


Fig. 3 Illustration of motor cooling in P314 transaxle



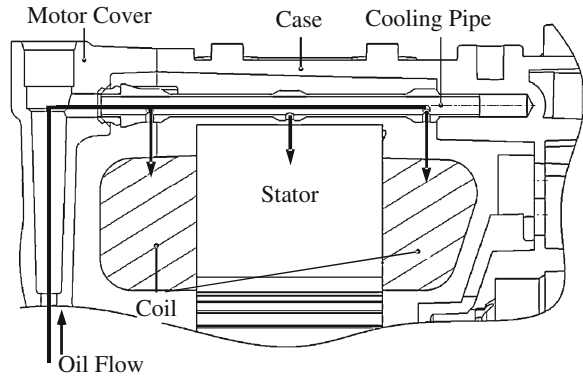
3 Main Specifications and Structure

Figure 1 shows the main cross section of the P314 transaxle and Table 1 lists the principle specifications. The P314 transaxle is provided with a new cooling pipe to improve the motor cooling performance. Accordingly, an oil path was added to the motor cover and the discharge capacity of the oil pump was increased. A compact layout was achieved by adopting the existing basic structure, which features a compound gear integrating two planetary gears, a counter drive gear, and a parking gear to the outside of the motor reduction device and power split device.

4 Motor Cooling Performance Improvement

The basic structures of the stator (3-phase alternating current, 8-pole, 48-slot distributed winding) and interior permanent magnet type rotor are unchanged from the P311 transaxle. However, the motor cooling performance was improved to

Fig. 4 Cross section of cooling pipe in P314 transaxle



facilitate adoption in future models. As shown in Fig. 2, the P311 transaxle has an oil catch tank at the top of the transaxle case that collects oil pumped up by the gears. The collected oil is then dripped onto the coil ends to cool the motor and generator.

In contrast, the cooling structure of the P314 transaxle features a cooling pipe in addition to the catch tank (Fig. 3). The oil pump in the P311 transaxle is used to lubricate the inside of the transaxle. In the P314, the discharge volume of this pump was increased and used to both lubricate the transaxle and cool the motor.

The position of the cooling pipe is shown in the sectional view in Fig. 1. Efficient cooling is achieved by discharging oil onto the stator through a cooling pipe located at the top of the stator. Figure 4 shows a sectional view of the cooling pipe. Adopting this pipe reduces the coil temperature by 11 % while retaining the same motor structure as the P311 transaxle. The temperature characteristics of the coil wires reduce copper loss, thereby helping to improve fuel economy. Furthermore, cooling the stator lowers the temperature of the rotor and the magnet due to heat transfer, which increases the efficiency of the motor.

5 Fuel Economy Improvement

5.1 Agitation Loss Reduction

The agitation loss was reduced to improve high speed fuel economy. Figure 5 shows the oil flow. As in the P311 transaxle, the P314 also includes an oil catch tank and cools the motor by pumping up oil using the gears. Another purpose of the oil catch tank in the P314 is to lower the oil surface inside the gear housing to reduce the agitation loss of the gears.

A straightening plate is also provided between the counter driven gear on the second axis and the ring gear on the third axis. This splits the oil flow between the counter drive gear and differential ring gear. The resulting improvement in oil flow

Fig. 5 Illustration of oil flow

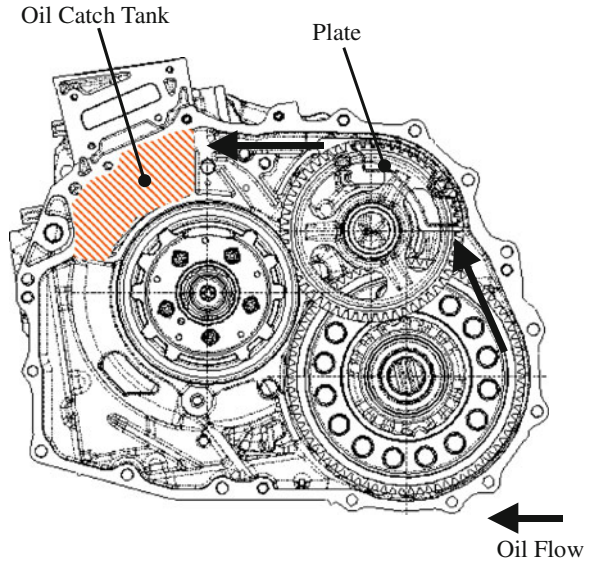


Fig. 6 Comparison of size with same oil discharge

New Tooth Profile	Trochoid
Diameter: 48.64mm t=5.5mm	Diameter: 54.57mm t=5.5mm

reduces the agitation loss. Agitation loss was also reduced by providing oil flow holes at the bottom of the counter drive gear to improve the discharge of oil from the inside of the compound gear. Ultimately, agitation loss was reduced by a total of approximately 15 %.

5.2 Adoption of Low-Loss Oil Pump

As described above, the discharge volume of the oil pump had to be increased compared to the P311 transaxle due to the addition of the cooling pipe. Since

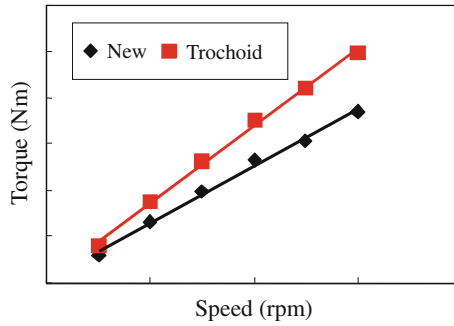


Fig. 7 Comparison of torque

		Cross Section
Reference	Original t=7.7mm	Flange, Bearing Leg
No.1	Original t=3.5mm	
No.2	Straight t=3.5mm	
No.3	Curve t=3.5mm	Oval
No.4	Doughnut t=3.5mm	Arc
No.5	Wave t=3.5mm	

Fig. 8 Motor cover basic shape examination

increasing the discharge volume with the same tooth profile would also increase the oil pump drive torque, an oil pump with a newly developed tooth profile was adopted to achieve the required discharge volume with low loss. Figure 6 compares the sizes of the new tooth and conventional trochoid profiles with the same theoretical displacement. Figure 7 compares the drive torque.

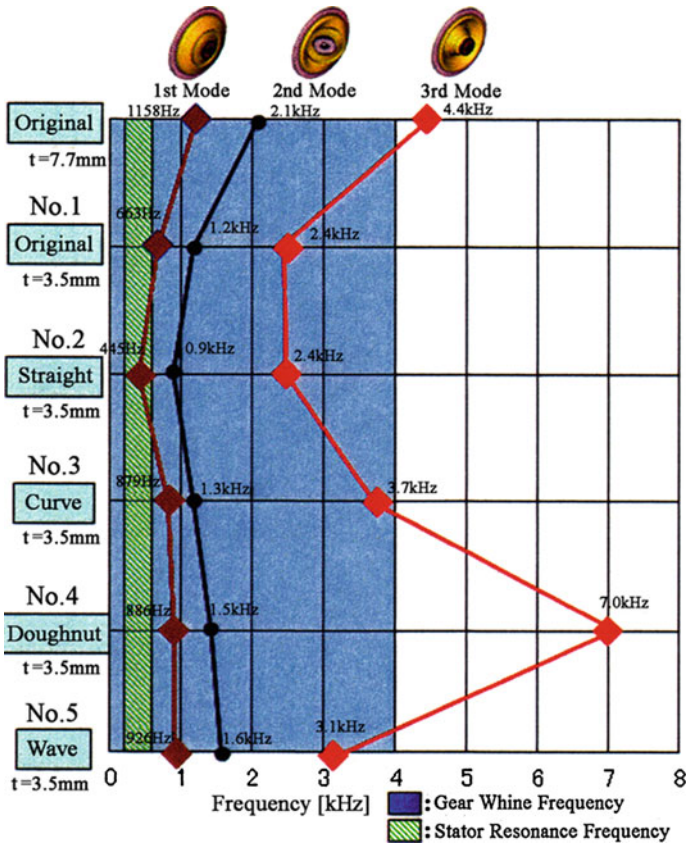


Fig. 9 Comparison of resonant frequency of motor cover

Unlike a trochoid curve, which determines the height of the teeth using the base diameter and the number of teeth, the new tooth profile can be varied freely in accordance with the curve creation parameters. As a result, the discharge volume can be increased without enlarging the rotor diameter. The new tooth profile reduced loss by approximately 25 % compared to the trochoid pump.

6 Weight Reduction and Quiet Operation

The shape of the motor cover was targeted to reduce the weight of the P314 transaxle. Optimizing the motor cover shape reduced weight while maintaining the required level of quiet operation. The level and frequency characteristics of gear whine (SPL) is determined by the mechanism shown in Eq. (1).

Fig. 10 Motor cover of P311 and P314 transaxles

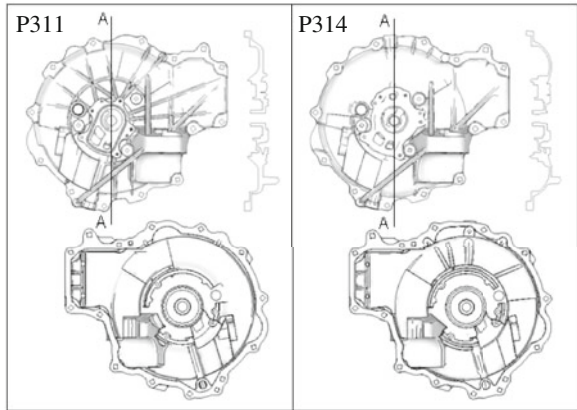
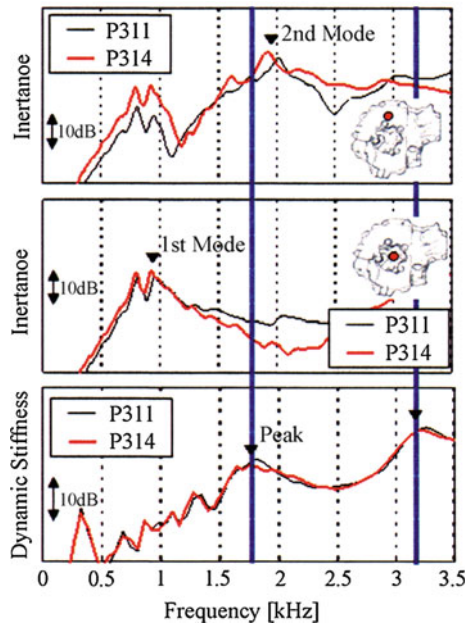


Fig. 11 Inertance of motor cover and dynamics stiffness of gear

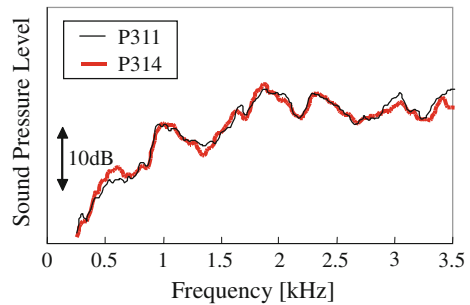


$$SPL = T.E \times D.S \times T.F \times S.S \tag{1}$$

where, T.E is the gear mesh transmission error, D.S is the gear mesh point dynamic stiffness, T.F is the transfer function, and S.S is the sound sensitivity.

In the P311 transaxle, the appropriate stiffness was achieved by making the general surfaces (i.e., those portions excluding the bearing leg and flange) thicker to dissipate resonance with the transaxle components in the normal gear whine frequency range. The development of the P314 transaxle examined how to make

Fig. 12 Actual gear whine values



the surfaces thinner to reduce weight while optimizing the surface shapes to compensate for the lower thickness. Figure 8 shows the examined shapes and Fig. 9 shows the resonance frequency of each vibration mode.

The following effects occur when the stiffness is lowered by reducing the surface thickness. With shapes 1 and 2, the resonance frequency of the out-of-plane 1st bending mode (1st mode, one joint in the circumferential direction) that forms the bulge close to the center of the cover approaches the out-of-plane resonance frequencies (200 and 600 Hz) of the stator, which is one of the most significant components. In comparison, this resonance frequency can be increased with shapes 3, 4, and 5 by creating a curved surface on the flange side.

Furthermore, by adopting the curved shape of No. 4 on the bearing leg side, the resonance frequency of the out-of-plane second mode (3rd mode, two joints in the circumferential direction) can be separated from the normal gear whine frequency range (4 kHz or less). Consequently, a doughnut shape was adopted.

Subsequently, as a countermeasure for the torsional 1st mode (2nd mode, one joint in the radial direction) that oscillates in separate upward and downward phases around a point close to the center, ribs were partially provided inside the cover in areas that do not effect the out-of-plane 1st and 2nd modes. This shape had the effect of suppressing torsional vibration.

Figure 10 shows the motor cover shapes of the P311 and P314 transaxles. Figure 11 shows the calculated results for driving point response and gear mesh point dynamic stiffness.

Despite reducing the surface thicknesses, the P314 transaxle achieved the same vibration characteristics and gear whine level as the P311 transaxle. Figure 12 shows the measured results (average values). Optimizing the motor cover shape reduced the weight of the portion around the motor cover by approximately 25 % without sacrificing quiet operation.

7 Conclusion

The new P314 hybrid transaxle was developed for installation in FWD 2.5-liter class passenger vehicles. Improving the motor cooling performance allowed the existing motor to be used and reduced motor loss. Thorough loss reduction helped to improve the fuel economy of the vehicle. Furthermore, a design that disperses resonance enabled further weight reduction to be achieved with the required levels of quiet operation.

Key Items for Future Hybrid Applications: Energy Storage and Power Electronics for Micro Hybrids up to Full Hybrids and EVs

Peter Willemsen, Feng Ji and Marc Nalbach

Abstract *Research/Engineering Question:* Micro-Hybrid applications like start/stop system and intelligent alternator control are well known and widely implemented to achieve first improvements regarding the reduction of CO₂ emission. Key items for their realization are the 12 V lead acid battery monitoring and power system stabilization approaches as well as optimizations of aerodynamics, enhanced warm cranking procedures and energy efficient electrification of power loads like electrical power steering systems. To achieve the upcoming CO₂ reduction targets in 2020 further optimization potentials have to be elaborated and have to be introduced. *Results/Conclusion:* Additional improvements can be achieved by extrapolated techniques like enhanced start/stop application, which means stop–start at vehicle speed of 30 km/h, and idle cruising/sailing. But these functionalities have a significant impact onto the stability and reliability of the power system based on the previous experiences with the common stop–start function. They can only be realized within a low voltage power system by the introduction of new enhanced energy storage solutions like additional batteries, double-layer capacitors or lithium-ion cells in combination with power electronics. By the prevention of high voltage implementations these solutions show a promising benefit to cost ratio in comparison to Full-Hybrid solutions. If further efficient functionalities like high power regenerative braking and electrical

F2012-B02-027

P. Willemsen (✉) · F. Ji
Hella Nanjing Technical Center, Nanjing, China
e-mail: peter.willemsen@hella.com

F. Ji
e-mail: feng.ji@hella.com

M. Nalbach
Hella KGaA Hueck and Co, Lippstadt, Germany

creeping are intended to implement, additional electrical measures have to be introduced. For instance a dual low voltage power system architecture with a system voltages lower than 60 V can be used to fulfill the requested energy and power capability of the power system for these corresponding vehicle functions. Double layer capacitors are suitable for high power regenerative braking due to their high charge acceptance and high current discharge capability. If functions with high energy demand like electrical creeping should be applied, then solutions using lithium ion cells are much more sufficient. Full-Hybrid and pure electric driven vehicles offer the maximum of CO₂ reduction potential. Here, nickel-metal-hydride or lithium ion batteries are used to reach the balance between power and high energy demand. *Methodology/Limitation:* Within this chapter the impact of these new vehicle applications onto the energy storage and their integration into the power system using power electronics is discussed from a supplier perspective based on actual pre- and series development projects.

Keywords Micro hybrid • Enhanced start/stop system • High-power recuperation • Energy storage • DC/DC converter

1 Introduction

In the recent years the Micro-Hybrid technology (start/stop system) has been successfully introduced into the market and widely accepted by vehicle manufacturers and drivers for its cost efficient realization and fuel reduction potential of 5–10 %. According to a new report from Pike Research, sales of micro-hybrid vehicles will experience strong growth in the coming decade, rising from 3 million units in 2011 to 37.3 million units p.a. by 2020 [1]. By that time, the market intelligence firm forecasts that start/stop vehicles will represent more than one-third of all light-duty vehicle sales.

With the demand for further fuel saving and CO₂ reduction, markets in Western Europe and Japan have been investigating technologies for further improvements. Enhanced start/stop systems that turn the engine off while the vehicle slows down and 48 V dual voltage system capable of high power regenerative braking and creeping are candidates for such advancements. To implement the technology into the vehicle, an additional energy storage system such as a double layer capacitor or a lithium-ion battery should be installed. Additionally, a DC/DC converter is needed to adapt the vehicle energy system to the voltage and current dynamics of the additional energy storage.

Enhanced start/stop and 48 V dual voltage systems are economic solutions compared to mild hybrid and full hybrid solutions and reduce the technological gap to these high-end, complex systems.

Table 1 Potential fuel saving due to extended stop time

NEDC	Speed threshold for stop engine (km/h)	Possible STOP part (%)	Possible STOP time (s)	Fuel saving per 100 km
Start/stop	0	22.5	266	0.54
Enhanced start/stop	5	24.8	293	0.60
Enhanced start/stop	30	32.5	383	0.78

2 Enhanced Start/Stop

One of the simplest ways to reduce fuel consumption is to turn off the engine when it is not being actively used. Start/stop system is based on this principle. Whenever the vehicle comes to a stop at a red traffic light or in traffic jam and the gear is put into neutral, the engine is switched off. When the driver presses down the clutch pedal, the engine automatically restarts. The logic for this process is typically handled inside a control unit such as the engine management system or the body controller. Start/stop systems will reduce fuel consumption from five to ten percent—depending on engine size and driving scenario.

In order to further reduce fuel consumption, and thus CO₂ emissions, enhanced start/stop systems are introduced to extend engine shut down time. The application of this can range from low speed applications such as shutting off the engine when the vehicle is coming to a standstill (e.g. in front of a traffic light) all the way to shutting off the engine at higher speeds when the vehicle is maintaining constant speed or decelerating (e.g. when driving downhill).

If the driver wants to accelerate (depressing the gas pedal) the engine restarts without delay. Depending on the behaviour of drivers, enhanced start/stop systems can save an additional eight percent compared to traditional start/stop systems.

Table 1 shows a basic simulation of fuel saving for enhanced start/stop systems based on New European Driving Cycle (refer to Table 1). If the engine is turned off when the vehicle speed is below 30 km/h, enhanced start/stop systems will have a potential engine off time of 383 s, while traditional start/stop systems only have a potential engine off time of 266 s. For an engine with an idle fuel consumption of 0.8 l/h, it means a fuel efficiency improvement of 0.24 l/100 km. Higher savings can be achieved if the system is also implemented for higher speeds (downhill coasting).

In enhanced start/stop systems, the engine off time is increased by turning off the combustion engine when vehicle speed is >0 km/h. During this period the alternator is not capable of supplying the power system of vehicle—this is critical because safety related electrical components must have reliable power supply at all times. The primary battery would be available to supply the power system, but this would lead to huge cycling of the battery which would result in a very short lifetime expectation. From a functional safety point of view also, if the primary battery fails and the combustion engine is already switched off, there is no electrical supply available even though the vehicle speed may be higher than 0 km/h.

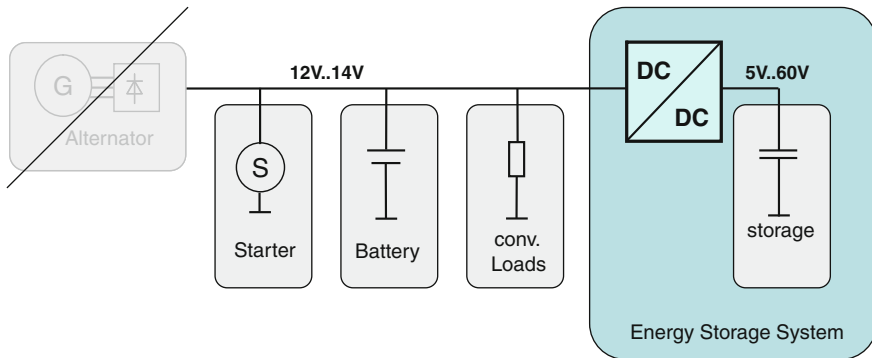


Fig. 1 Power system topology with an energy storage system for enhanced start/stop and coasting

At this point, electrically supported braking and steering would not be available, resulting in an unacceptable safety hazard.

Therefore an additional energy storage has to be implemented, that should provide power in coasting and engine off conditions. Its capacity requirements are not very high as it would only be a short term application—however a huge amount of charge/discharge cycles could be foreseen. Its energy density as well as the cycling capability has to match the application demand. A DC/DC converter is additionally needed to adapt the fluctuating voltage of the energy storage system to the 12 V power supply of the vehicle. The DC/DC converter normally also controls the charging and discharging of the energy storage system (Fig. 1) [2].

Double layer capacitors and lithium-ion batteries are both suitable choices for the additional energy storage. Lithium-ion batteries are superior in energy density, but double layer capacitors have a much higher cycling capability. Double layer capacitors could be then used with little degradation for the lifetime of a vehicle.

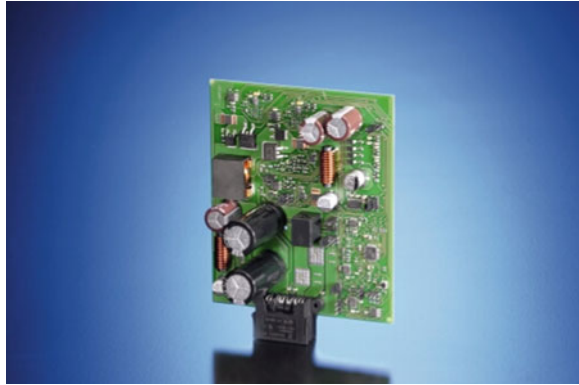
Double layer capacitors have some advantages as below:

- Long lifetime, high number of charge–discharge cycles (millions or more)
- High power density (the amount of available output power per unit of mass or volume)
- No danger of overcharging, so no full-charge detection is needed

Disadvantages are:

- Low energy density (the amount of available energy per unit of mass or volume) compared to battery technologies
- High self-discharge rate
- Low maximum voltage
- The voltage level is closely linked to the state of charge (SOC)—leading to a drop during discharge
- Cost.

Fig. 2 Energy storage module using double layer capacitors in combination with a DC/DC converter



To keep the output voltage constant despite of the discharge depth, the DC/DC converter implements a boost-buck switching regulator with energy loss. During charging phase, the DC/DC converter boosts the input voltage to a high level to charge the capacitor to a high SOC. Passive balancing is also implemented to balance the SOC difference between capacitors (Fig. 2) [2].

3 Recuperation and Creeping

The most popular measure to save fuel, based on available electrodynamic generators, is kinetic energy recuperation. High power peaks during braking are harvested and stored in the battery. So the braking energy is recovered and used to supply the power of the vehicle.

Low-power recuperation is already implemented in start/stop systems with limited efficiency due to the poor charge acceptance of lead-acid batteries and the low power rate of generators. To have an effective recuperation, high power rate generators or electrical motors (with power capability higher than 4 KW) should be used. Lithium-ion batteries or double layer capacitors are usually used instead of lead-acid battery to increase the battery charge acceptance.

The capability of the generator, energy storage, connectors and wiring harness towards current is usually limited to about 200–250 A for practical reasons (diameter) as well as for technical reasons (available battery technologies). The recoverable energy is thus limited by the current capability. A possible solution to increase the power capability without being limited by the current acceptance is to increase the voltage level. The capability for recuperation will thus increase in proportion with the increase of the voltage.

In order to avoid shifting the whole vehicle power system to an increased voltage, a secondary voltage level with an additional energy storage should be introduced. 48 V is preferred as it is well below the 60 V limit for electrical safety, where no expensive electrical protection measure is required. Another advantage

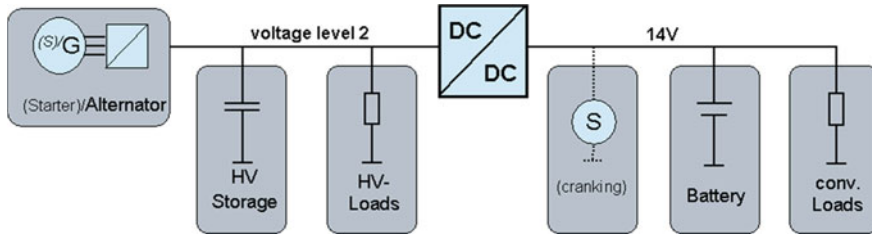


Fig. 3 48 V dual voltages for high power recuperation, high power load supply and electrical creeping

of bringing a secondary voltage level into the vehicle power system is to implement some high power loads (like electric cooling fan and electric power steering) which can easily be applied to the 48 V power net (Fig. 3) [2].

High power generators or electrical motors (4–10 KW) in recuperation systems can also be used for low speed vehicle creeping; the speed is related to the power rate of the electrical motor. In that case, it would bring additional fuel saving for it decreases the time when engine is working with low-efficiency (low speed of vehicle). Creeping will have the most benefit in city traffic situations where the vehicle is in a permanent stop-and-go condition.

Combined recuperation and creeping may have an additional potential fuel saving of 0.5 l/100–0.8 l/100 km based on different traffic conditions.

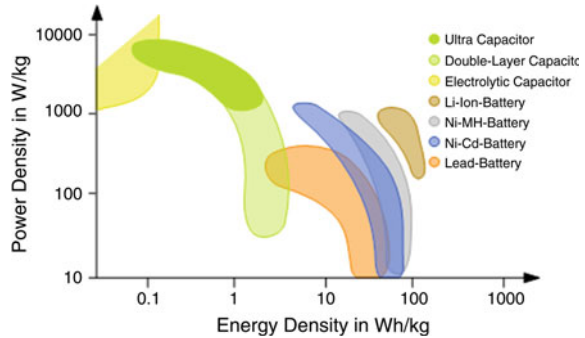
The energy storage systems in 48 V dual voltage architectures which are used to harvest high peak power during braking or coasting of the vehicle require the highest power density for highest recuperation efficiency. At the same time, a high energy density is also required for extending the range of creeping distance and reducing the weight of vehicle. The 48 V energy storage system is discharged during low speed creeping and is charged during braking, coasting and optionally at any time when the engine is running. This leads to huge charging/discharging cycles.

As recuperation applications require a high power density, batteries that are based on the movement of charge carriers in a liquid electrolyte and therefore have relatively slow charge and discharge times as well as a limited power density, are not the preferred option. Capacitors, on the other hand, can be charged or discharged faster, at a rate that is typically limited by the heating of the electrodes, and have a power density generally 10–100 times greater than lead-acid batteries. As a consequence, double-layer capacitors are a good choice for recuperation purpose.

However, the additional creeping function requires a high energy density. While double-layer capacitors have higher power density compared to batteries, their energy densities are perhaps 1/10 of that of a lead-acid battery. So batteries represent a more attractive option for creeping applications.

When it comes to implement both functions recuperation and creeping, batteries with high power density should be proper choice.

Fig. 4 Comparison of energy storage technologies



Lead-acid, Nickel-MetalHydride (Ni-MH) and Lithium-ion are popular battery technologies. Lithium-ion batteries are superior in terms of energy and power density. As a result, lithium-ion batteries are seen as the most promising solutions for the additional energy storage in 48 V dual voltage systems (Fig. 4).

Compared to other battery technologies, Lithium-ion batteries have the following important characteristics [3]:

- Their energy efficiency and charging/discharging efficiency are high.
- The voltage of a single-cell is high (three times that of Ni-MH batteries and twice that of lead-acid batteries), therefore leading to a comparatively low number of cells to achieve the desired voltage level. This is an advantage with regards to the number of needed parts and connections between terminals.
- Charging and discharging reactions produce relatively little heat.

Lithium-ion batteries have very strict working conditions regarding temperature and voltage. Damage, even explosions could happen if they are operated outside of the required range. A balancing between the battery cells is mandatory for an efficient usage and a long lifetime. So, together with the implementation of the lithium-ion battery, we have to introduce a battery management system that can properly monitor the operation of the lithium-ion battery.

The battery management system consists of the following functions [3]:

- Prevent the voltage of any cell from exceeding a limit- by stopping the charging current or requesting it to be stopped.
- Prevent the temperature of any cell from exceeding a limit—by directly stopping the battery current, requesting it to be stopped, or requesting cooling.
- Prevent the voltage of any cell from dropping below a limit—by stopping the discharging current.
- Prevent the discharging current from exceeding a limit.
- Calculate SOC,
- Monitor SOH (status of health)
- Balance battery cells to bring the SOC levels of the cells closer to each other, in order to maximize the battery capacity

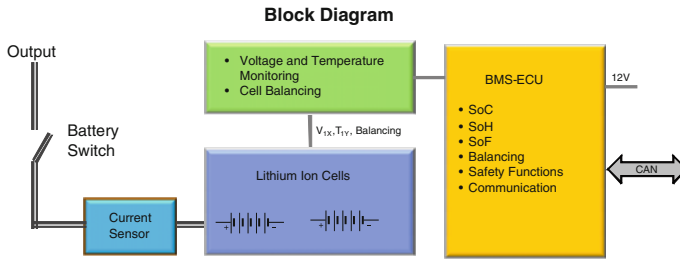


Fig. 5 System block diagram of battery management

- Calculate the internal resistance of cells to improve the accuracy of SOC and better control the balancing.
- Thermal Management to keep the temperature of the battery in a safe zone (Fig. 5).

Because the generator/electrical motor and the storage system are at a 48 V level, the energy must be converted to the regular 12 V power net. This can be done by a DC/DC converter. From the point of view of the 12 V system, this converter replaces the position and function of the conventional generator. This defines the minimum standards for the functional and safety requirements of the DC/DC converter. On the 48 V side, there may be also loads, especially high power loads. The power for these loads must not be transferred through the DC/DC converter, what would reduce its power rating. A typical power rating for such a DC/DC converter is in the range of 1.5–3 kW, depending on the size of the vehicle electrical equipment. The DC/DC converter must be able to transfer energy from 48 to 12 V with the maximum power rating at the highest possible efficiency, in order to maintain a high efficiency of the whole recuperation system. For backup reasons it should also be able to transfer energy in the opposite direction—from the 12 V lead-acid battery to the 48 V system.

Such a converter must fit the specific needs of each application, regarding

- Power and voltage rating,
- Cooling infrastructure such as liquid cooling or reliable forced convection.

Looking at the different requirements from different vehicle architectures, the hardware and software concepts require a modular application in order to satisfy the different system demands. At the same time the initial volumes of such systems are likely to be low, emphasizing the need for a modular platform approach in production and mechanical design.

Therefore an appropriate concept consists of

- proven standard components as well as design and standard connection technologies,

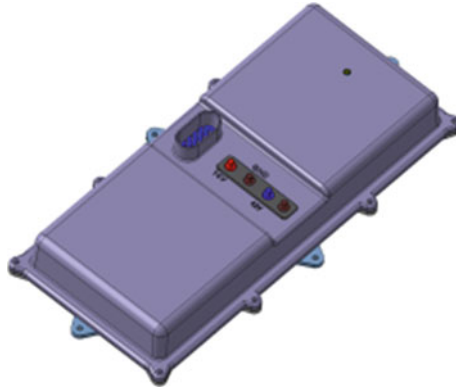


Fig. 6 3 kW DC/DC converter for dual voltage power system applications

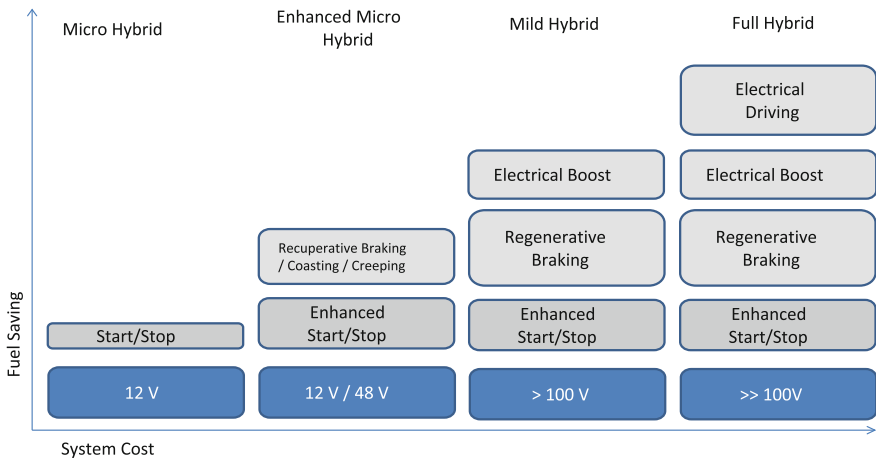


Fig. 7 Functions of micro hybrid up to full hybrid vehicles

- a modular power scaling and intrinsic redundancy by a multiphase approach and
- a high-speed power switching and flexible control (Fig. 6).

4 Conclusion

Enhanced start/stop systems further increase energy efficiency and further reduce CO₂ emissions compared to traditional start/stop systems thanks to their increased stop time of the engine. 48 V dual voltage systems with high power recuperation

and creeping are capable of even further fuel savings. Both technologies are economic to implement compared to mild hybrid and full hybrid vehicles. Compared to Mild-Hybrids these systems also have the advantage of reduced functional safety requirement (voltage below 60 V) and significantly lower cost (Fig. 7). As they are based on existing internal combustion engine vehicle architectures and available power electronics technologies, they could be implemented in a short time. For the Mega-Cities of today such solutions can be an important intermediate step before the availability of cost-efficient battery solutions for full electric vehicles.

References

1. Pike Research (2011) Stop-start vehicles. www.pikeresearch.com/research/stop-start-vehicles
2. Daisuke K, Carsten H, Marc N, André K (2011) DC/DC converters for fuel-efficient automotive applications. JSAE Annual Congress, 289-20115322
3. Andrea D (2010) Battery management systems for large lithium-ion battery packs. Artech House, Norwood. ISBN: 13 978-1-60807-104-3

Direct-Computation-Based Traction Motor Control for Dynamic Performance Improvement in Electric Vehicles

Xi Zhang and Chengliang Yin

Abstract This study is to propose a new control strategy to improve dynamic performance of the traction motor in the electric vehicle (EV) which is under command of considerable dynamic controls. Desired electromagnetic torque is derived from the torque feedforward loop. By introducing the indirect vector control, the q-axis current is acquired with the known motor torque and d-axis current. Voltage feedforward loop is to achieve d- and q-axis voltages for SVPWM generation. Considering control precision, PID adjustors in small ranges are also included for dynamic compensation of feedforward loops. With consideration of various EV operation conditions, the Matlab-based simulation and DSP-based experimental setup are deployed to verify the proposed strategy. Various curves illustrate the outstanding response ability of the proposed strategy, compared to the conventional three-loop method.

Keywords Direct computation · Traction motor · Feedforward compensation · Indirect vector · Electric vehicle

1 Introduction

Nowadays, development of electric vehicles (EVs) and hybrid electric vehicles has been the hottest topic in automobile industry. It is known that an EV is propelled

F2012-B02-033

X. Zhang (✉) · C. Yin
Institute of Automotive Engineering, Shanghai Jiao Tong University,
Shanghai, China
e-mail: braver1980@sjtu.edu.cn

by electricity which is stored in an energy storage system (ESS, e.g., batteries, ultracapacitors, or flywheels) [1, 2]. Usually, electric vehicles are referred to as pure EV or battery EV (BEV) in case that the main energy storage is a battery pack. The electric motor in a pure EV is mainly responsible for vehicle propulsion and sometimes for regenerative energy flow also.

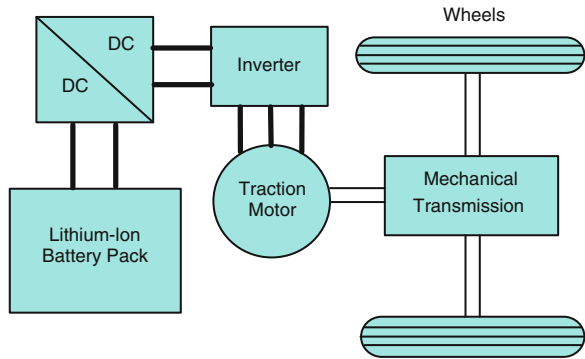
New design requirements are raised for electric motors and drive systems in EVs, such as high efficiency in wide speed and torque range, large torque output below base speed, automatic speed adjust functionality, and high controllability, steady-state precision and dynamic performance, due to poor on-road operation conditions [3–6, 8, 9]. While the material cost of a permanent magnet synchronous motor increases exponentially, this study turns the research sight to the induction motor.

Considerable advanced control schemes for traction motors in electric vehicles have appeared in literature to improve motor dynamic performance compared to conventional closed-loop control. A probabilistic fuzzy neural network (PFNN) control system was proposed for an in-wheel motor drive [7]. However, greater computational burden, proneness to overfitting, and the empirical nature of model development defect the control performance. Reference [6] presented a fuzzy-sliding mode speed control for two wheels electric vehicle drive to improve the system robustness. Unfortunately, the dynamic performance and steady-state precision is degraded due to the inherent chattering characteristic of sliding mode control.

Direct computation is deployed to improve the motor transient performance in poor operation situation filled with transients, and in the meantime guarantee the stability and precision. The proposed indirect vector control based hybrid control is suitable for this “direct” definition. Additionally, this proposed control could be simplified for its employment in a PMSM. Two control modes exist in this study, speed control and torque control, for different applications. In the speed control mode, the torque feedforward is embedded for calculation of motor electromagnetic torque. A torque observer is designed for estimating the load torque. Meanwhile the speed PID adjustor is responsible for small-range torque compensation. Sum of them forms the reference torque. While in the torque control mode, the reference torque is given directly. The indirect vector control is included for derivation of quadrature-axis currents. The desired voltages can be computed regarding the desired currents as inputs in the voltage feedforward link.

With consideration of real EV operation conditions, simulation results based on Matlab validate the correctness and superiority of the proposed strategy under dynamic response. The DSP implements the hybrid control strategy in real time, and experimental results verify the effectiveness not only under dynamic response but a standard drive cycle.

Fig. 1 Configuration of a pure electric vehicle



2 Modeling of Traction Motor

2.1 Electric Vehicle Structure

The configuration of a pure EV is shown in Fig. 1. The battery-powered electric vehicle is comprised of a battery for energy storage, an electric motor, and an inverter. The battery is charged through a charger which can be either carried onboard or fitted at the charging point. The inverter is responsible for the direction and amount of power flow to/from the electric motor such that the vehicle speed and moving direction can be controlled. It has to be noted that during the braking process, the battery is charged by regenerative energy. The DC–DC converter is used to match the battery pack voltage and that of the DC bus of the inverter and can be optional. The mechanical transmission shown here is a generic term for gears and speed reduction.

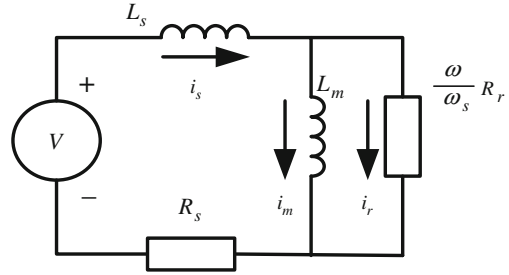
2.2 Traction Motor Mathematical Model

The dynamic state equation of the induction motor is expressed as:

$$\begin{pmatrix} L_m + L_s & -L_m \\ L_m & -L_m \end{pmatrix} \frac{d}{dt} \begin{pmatrix} i_s \\ i_r \end{pmatrix} + \begin{pmatrix} j\omega(L_m + L_s) + R_s & -j\omega L_m \\ j\omega_s L_m & -j\omega_s L_m - R_r \end{pmatrix} \begin{pmatrix} i_s \\ i_r \end{pmatrix} = \begin{pmatrix} V \\ 0 \end{pmatrix} \tag{1}$$

where the subscript “s” represents the Laplace operator; “r” is the rotor; and “m” denotes magnetizing. The currents and voltages here stand for the derivations through unitization from actual values.

Fig. 2 Equivalent circuit of induction motor through unitization



If the variables in Eq. (1) have to be transformed into RMS values, one should multiply these by $1/\sqrt{3}$; if the transformation into amplitudes is required, one should multiply the variables by $\sqrt{2}/\sqrt{3}$. Therefore, through unitization, the coefficients 3 or 2/3 for calculations of power or torque using actual values can be completely eliminated.

As a result, the equivalent circuit of the induction motor is depicted in Fig. 2.

3 Control Strategy Establishment

Figure 3 depicts the block diagram of the proposed hybrid control system for a traction induction motor in an EV. A switch could select the required control mode, speed control or torque control. Torque observation and feedforward is responsible for the derivation of torque command in the torque control mode, while this command could be from of the operator. The indirect vector control block is in charge of quadrature-axis currents commands through the electromagnetic torque, rotor flux and given direct-axis current. Voltage feedforward contributes for the desired voltage commands. All over the control flow, PID adjustors only deal with small range adjustment. Detailed explanations are provided next.

3.1 Indirect Vector Control

It can be indicated from Fig. 3 that the stator current is sum of magnetizing current and rotor current, expressed as

$$i_s = i_m + i_r \quad (2)$$

According to Kirchhoff's circuit law, the stator can be rewritten as

$$i_s = i_m + j \frac{\omega_s L_m}{R_r} i_m \quad (3)$$

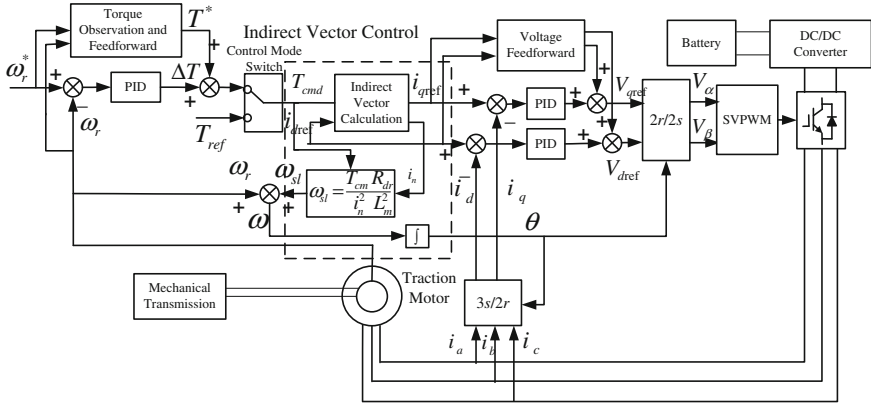


Fig. 3 Block diagram of the proposed hybrid control strategy

Electromagnetic power of the induction motor is usually calculated as

$$P = \frac{\omega}{\omega_{sl}} i_r^2 R_r \tag{4}$$

On basis of Eq. (1) and Fig. 2, two parts (i.e., the mechanical power and the copper loss) form the new electromagnetic power expression, given by

$$P = P_{\text{resistance}} + P_{\text{mech}} = i_r^2 R_r \frac{\omega}{\omega_{sl}} i_r^2 R_r + \frac{\omega - \omega_{sl}}{\omega_{sl}} i_r^2 R_r \tag{5}$$

The electromagnetic torque is related to the rotor current and the slip speed as

$$T = \frac{i_r^2 R_r}{\omega_{sl}} \tag{6}$$

Refer to the relation existing in Fig. 3, and the electromagnetic torque can be newly expressed below

$$T = \frac{\omega_{sl} L_m^2 i_m^2}{R_r} \tag{7}$$

Consequently, the slip speed can be depicted through the electromagnetic torque as

$$\omega_{sl} = \frac{TR_r}{L_m^2 i_m^2} \tag{8}$$

The direct- and quadrature-axis currents can be derived from the dq0 transformation. In the d-q coordinate system, i_d denotes the real part of the stator current while i_q stands for the imaginary part. In summary, $i_s = i_d + j i_q$. Based on theory of field oriental control (FOC), the magnetizing current is completely

supplied by the direct-axis current, namely, $i_m = i_d$. The quadrature-axis current equals the rotor current and is capable of expression by i_d as

$$i_q = \frac{\omega_{sl} L_m i_d}{R_r} \quad (9)$$

Consequently, the slip speed is delineated by

$$\omega_{sl} = \frac{TR_r}{L_m^2 i_d^2} \quad (10)$$

The above analysis assumes i_d to zero, however, when the set i_d suddenly changes, the accordingly magnetic field cannot change immediately and varies gradually. Therefore, one has to select proper i_q that is slightly different from Eq. (9) to explain the variation period of the air gap flux. i_n is defined as the net magnetizing current that is equivalent to i_d on the static state. $\frac{L_m}{R_r}$ is the time constant of i_n . We let

$$\frac{di_n}{dt} = \frac{R_r}{L_m} (i_d - i_n) \quad (11)$$

Thus the quadrature-axis current is rewritten as

$$i_q = \frac{\omega_{sl} L_m i_n}{R_r} \quad (12)$$

Then the slip speed can be newly expressed through i_n as

$$\omega_{sl} = \frac{TR_r}{L_m^2 i_n^2} \quad (13)$$

3.2 Feedforward Control

With intension to improve the transient performance of the induction motor, the torque feedforward is embedded such that the electromagnetic torque at some time instant is acquired by using the known moment of inertia, desired speed and observed load torque, expressed as

$$T^* = T_L + J\omega_r^* \cdot s \quad (14)$$

where s represents Laplace operator; J moment of inertia; ω_r^* desired speed. T_L denotes load torque estimated with assistance of the torque observer.

However, in this case, error exists between the calculated and actual values, so the it is required to design the desired torque T^* to be the sum of outputs of torque feedforward and speed PID adjustor, i.e.,

$$T_{cmd} = T^* + \Delta\omega \cdot \frac{K_d s^2 + K_p s + K_i}{s} \tag{15}$$

where K_d , K_p and K_i are the differential, proportional and integral gains, respectively.

The purpose of participation of the PID adjustor is to adjust the desired torque in a small range to ensure the speed tracking precision and the final zero static state error.

3.3 Torque Observation

Relationship between electrical and mechanical parameters could be described as

$$\frac{d}{dt} \begin{pmatrix} \omega_r \\ T_L \end{pmatrix} = \begin{pmatrix} 0 & \frac{1}{J} \\ 0 & 0 \end{pmatrix} \begin{pmatrix} \omega_r \\ T_L \end{pmatrix} + \begin{pmatrix} \frac{3}{2J}(i_q\psi_{sd} - i_d\psi_{sq}) \\ 0 \end{pmatrix} \tag{16}$$

Suppose that $X = \begin{pmatrix} \omega_r \\ T_L \end{pmatrix}$, $A = \begin{pmatrix} 0 & \frac{1}{J} \\ 0 & 0 \end{pmatrix} = \begin{pmatrix} 0 & a_k \\ 0 & 0 \end{pmatrix}$, $w = \frac{3}{2J}(i_q\psi_{sd} - i_d\psi_{sq})$, $Y = \omega_r$, $B = \begin{pmatrix} 1 \\ 0 \end{pmatrix}$, $C = (1 \ 0)$ and Eq. (16) can be rewritten as

$$\begin{cases} \frac{dX}{dt} = AX + Bw \\ Y = CX \end{cases} \tag{17}$$

The rank of the matrix $\begin{bmatrix} C^T : A^T C^T \end{bmatrix} = \begin{pmatrix} 1 & 0 \\ 0 & a_k \end{pmatrix}$ is 2, consequently the system is observable. The observer can be designed as

$$\frac{d\hat{X}}{dt} = A\hat{X} + Bw + L(CX - C\hat{X}) \tag{18}$$

where $L = \begin{pmatrix} l_1 \\ l_2 \end{pmatrix}$. The characteristic formula of the observer is delineated as

$$s^2 - l_1 s + a_k l_2 = 0 \tag{19}$$

The contents of L and should be properly selected to guarantee that poles of Eq. (19) lie in the left plane. Meanwhile the observer should be systematically stable and own fast-attenuation properties.

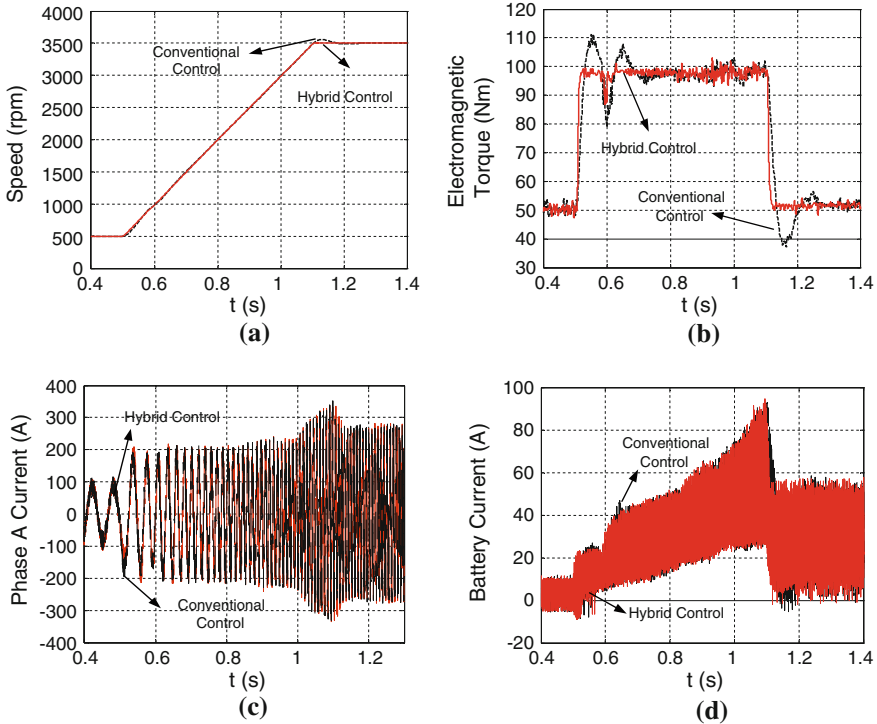


Fig. 4 Comparison between proposed hybrid control and conventional control. **a** Speed. **b** Electromagnetic torque. **c** Phase-A current. **d** Current of Lithium-ion battery

4 Simulation Results

MATLAB is employed as the simulation tool to model the proposed hybrid control system. A 4-pole induction motor rated with 152 kW acts as the controlled object. A load of 50.5 Nm is added to the motor output. A lithium-ion battery with high voltage of 288 V and capacity of 105 Ah is used as the energy storage system (ESS). A DC–DC converter is connected between the battery and the electric motor, boosting the input voltage 288–650 V that is suitable for inverter DC link. For better performance verification, the conventional closed-loop control is also simulated and compared with the proposed control for the induction motor.

Figure 4 depicts the simulated results under speed “step” response, including curves of speed, electromagnetic torque, phase current and battery current. The speed command is set to increase from 500 to 3500 rpm with the slope of 1500 rpm/s, which could be considered as a “step” variation. It can be seen from Fig.6 that there exists overshoot or undershoot in conventional control while the proposed hybrid control could resist the transients. Since turbulences defect the

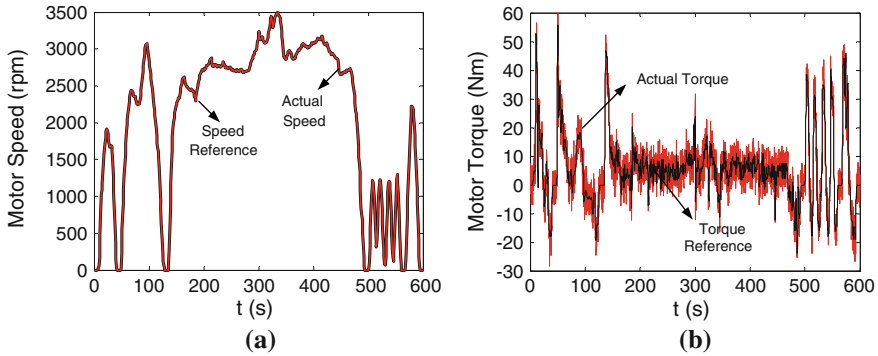


Fig. 5 Experimental results of two motor drive-load configuration under US06 cycle. **a** Motor speed. **b** Motor torque

transient performance and even the electric vehicle operation, the hybrid control for the traction motor is more capable of poor on-road operation filled with uncertain transients.

5 Experimental Results

In the experimental setup, two identical induction motors are linked sharing the same shaft. One acts as the drive motor, and the other is the load motor. The two induction motors are rated with 400 V voltage and 165 kW power. The number of motor pole pairs is 2, and the efficiency is 93 %. The maximum speed is 4000 rpm. A programmable DC system is utilized to emulate the set of a lithium-ion battery and a DC–DC converter.

To validate the real-time application feasibility of the proposed control strategy for electric vehicles, we use the software of Advanced Vehicle Simulator (ADVISOR) to acquire operation data of a standard drive cycle. The US06 cycle designed to test vehicle performance at high speeds and aggressive driving conditions is selected as the verification benchmark for the proposed hybrid control.

In ADVISOR, a pure EV configuration is pre-set. The electric motor is connected to a gearbox with speed ratio 5. According to the data from ADVISOR, the reference speed and torque curves (see Fig. 5) are configured in speed command and torque command for the load motor and drive motor, respectively. Consequently the US06 cycle could be simulated through cooperation of two identical motors sharing one shaft. The experimental results in Fig. 9 show satisfactory tracking and transient performance on both speed and torque, although there exist some unaffordable torque ripples.

6 Conclusion

This study completes the derivation process of an EV traction motor control strategy in order to enhance dynamic performance. The accordingly control system, integrated with indirect vector control, torque and voltage feedforward, is established. The Matlab-based simulation and DSP-based experimental results verify superiority of the proposed strategy, in case of various EV operation conditions.

References

1. Matthe R, Turner L, Mettlach H (2011) VOLTEC battery system for electric vehicle with extended range. *SAE Int J Engines* 4(1):1944–1962
2. Burke A (2010) Ultracapacitor technologies and application in hybrid and electric vehicles. *Int J Energy Res* 34(2):133–151
3. Cai C, Wang X, Bai Y et al (2011) Motor drive system design for electric vehicle. *Int Conf Electr Inf Control Eng (ICEICE 2011)* 1:1480–1483
4. Williamson S, Emadi A, Rajashekara K (2007) Comprehensive efficiency modeling of electric traction motor drives for hybrid electric vehicle propulsion applications. *IEEE Trans Veh Technol* 56(4):1561–1572
5. Kim D, Hwang S, Kim H (2008) Vehicle stability enhancement of four-wheel-drive hybrid electric vehicle using rear motor control. *IEEE Trans Veh Technol* 57(2):727–735
6. Nasri A, Hazzab A, Bousserhane IK et al (2009) Fuzzy-sliding mode speed control for two wheels electric vehicle drive. *J Electr Eng Technol* 4(4):499–509
7. Lin FJ, Hung YC, Hwang JC et al (2012) Digital signal processor-based probabilistic fuzzy neural network control of in-wheel motor drive for light electric vehicle. *IET Electr Power Appl* 6(2):47–61
8. Rahmam KM, Patel NR, Ward TG et al (2006) Application of direct-drive wheel motor for fuel cell electric and hybrid electric vehicle propulsion system [J]. *IEEE Trans Industry Appl* 42(5):1185–1192
9. Jeong YS, Lee JY (2011) Parameter identification of an induction motor drive with magnetic saturation for electric vehicle [J]. *J Power Electr* 11(4):418–423. URL: <http://www.engineering-village.com/controller/servlet/Controller?CID=quickSearchCitationFormat&searchWord1=%7bJeong%2C+Yu-Seok%7d§ion1=AU&database=1&yearselect=yearrange&sort=yr>

Energy Optimization for the Mild Hybrid Electric Vehicle with CVT Under Driving Conditions

Yongxia Zheng, Feng Zhao, Yugong Luo and Keqiang Li

Abstract For a hybrid electric vehicle (HEV) equipped with CVT (Continuously variable transmission), it's an important question in developing vehicle energy management that how to make engine, motor and CVT coordinate well to maximize the overall efficiency of the hybrid system. According to this problem, an energy optimization strategy for a CVT mild HEV is proposed which takes the maximum system efficiency as optimization objective and vehicle speed, accelerator pedal degree and battery SOC as state variables while the motor torque and CVT ratio as control variables. Based on a comprehensive consideration of the driver's actual operation, driving demand and efficiencies of key components, the strategy proposed in this paper realizes the overall efficiency's maximization and gets the optimal output torque of motor and the CVT target ratio under different driving conditions. The energy management strategy based on this optimization is tested by a self-established forward simulation model, showing that compared with the proto vehicle the equivalent 100 km fuel consumption is reduced by 26.4 % under NEDC driving cycle.

Keywords Hybrid electric vehicle · Continuously variable transmission · Energy optimization strategy · Accelerator pedal opening · Simulation verification

F2012-B02-036

Subsidized by electronic information industry development fund project of industry information ministry (research and industrialization of new energy automotive electronic control systems) and independent research project of state key laboratory of automotive safety and energy (zz2011-092).

Y. Zheng (✉) · F. Zhao · Y. Luo · K. Li

State Key Laboratory of Automotive Safety and Energy, Tsinghua University, Beijing 100084, China

e-mail: zyongxia@163.com

1 Forward

For hybrid electric vehicle equipped with CVT (Continuously variable transmission), its ratio can be adjusted continuously within a certain range, making the engine speed can be independent of the vehicle speed. It's an important question in developing vehicle energy management that how to maximize hybrid system's energy utilization efficiency and make engine, motor and CVT coordinate well by taking full advantage of the characters of motor and CVT [1].

Most previous researches only pursued to make engine work in high efficient area while ignored the influences of efficiencies of motor, battery and transmission system [1, 2]. Though a few researches were aimed at getting the highest system efficiency [3], the state variables were vehicle speed and acceleration which is hard to reflect the driver's intentions and feelings intuitively.

Taking an ISG-type CVT mild hybrid electric vehicle as research object and considering driver's actual operation, drive demand and the influences of key components' efficiency, this paper has proposed an energy optimization strategy for CVT mild HEV which takes the maximum system efficiency as optimization objective and vehicle speed, accelerator pedal degree and battery SOC as state variables while the motor torque and CVT ratio as control variables, and then optimize to get the target output torque of motor and the CVT target ratio under different driving conditions.

2 Energy Optimization System Under Driving Conditions

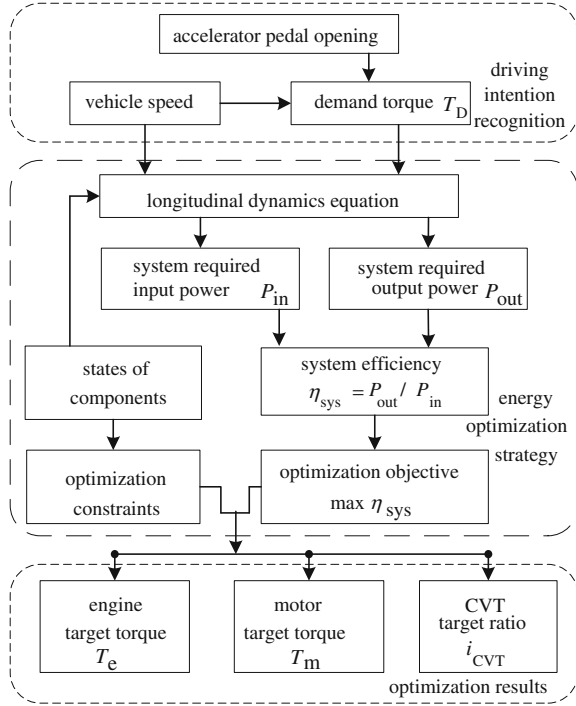
The energy optimization system shown in Fig. 1 is designed for CVT mild hybrid electric vehicle under driving conditions.

Firstly, get demand torque T_D meet the driving demand according to the vehicle speed and the accelerator pedal opening; Secondly, get the system required input and output power respectively for the three types of driving conditions(including pure engine mode, economic charge mode and boost mode) by combining the longitudinal dynamics equation with efficiencies of key components including engine, motor, battery and CVT, thus the hybrid system efficiency can be derived; Finally, takes the maximum system efficiency as optimization objective and states of components as constraints, then optimize to get the target output torque of motor and engine and the CVT target ratio under different driving conditions.

3 Driving Intention Recognition Under Driving Conditions

Firstly, recognize the driving intention before making the energy optimization strategy to obtain the demand torque T_D .

Fig. 1 Energy optimization system



The vehicle speed and accelerator pedal opening determine the torque required jointly. The “nine-defined method” [4] has been used in this paper, based on measured data of original vehicle, the vehicle demand torque surface is fitted integrated with the power and smooth adjustment factor formulated after defining demand torque of nine key points which represent vehicle worm, large accelerate and the highest speed and other working conditions [5].

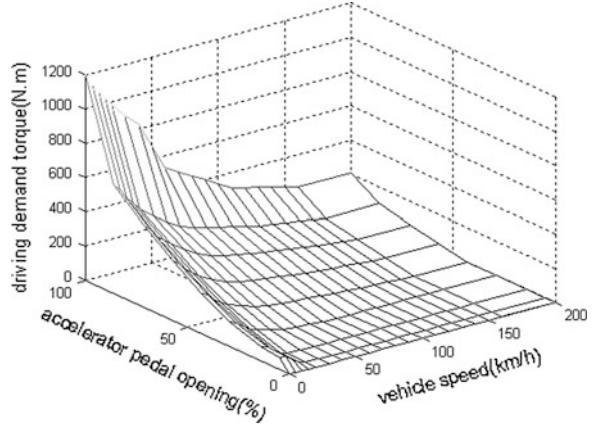
The driving demand torque defined surface acting on the rear of transmission shown in Fig. 2 is developed based on the method above.

4 Energy Optimization Strategy Under Driving Condition

It is necessary to analyze the transmission relation among various components of the hybrid system when making energy optimization strategy. The following dynamics equation of drive system under driving conditions is built according to vehicle theory [6].

$$\begin{aligned}
 & \left(mgf \cos \alpha + mg \sin \alpha + \frac{C_D A u^2}{21.15} + m \frac{du}{dt} \right) r \\
 & = T_D i_0 - I_r \dot{\omega}_r - (I_e \dot{\omega}_e + I_m \dot{\omega}_m) i_{CVT} \eta_{CVT} i_0
 \end{aligned} \tag{1}$$

Fig. 2 Driving demand torque surface



where: m is vehicle quality; f is rolling resistance coefficient; α is road slope angle; C_D is air resistance coefficient; A is vehicle frontal area; r is wheel radius; T_D is driver demand torque; i_0 is final drive ratio; I_r is wheel inertia; ω_r is wheel speed; I_e is engine inertia; ω_m is motor speed; i_{CVT} is CVT ratio; η_{CVT} is CVT efficiency.

The engine and motor are coaxial connected, so the following relationship exists between the two speeds:

$$\dot{\omega}_e = \dot{\omega}_m = \dot{\omega}_r i_0 i_{CVT} + \omega_r i_0 di_{CVT}/dt \quad (2)$$

$$\begin{cases} \omega_r = u/r \\ \dot{\omega}_r = (du/dt)/r \end{cases} \quad (3)$$

4.1 Energy Optimization Strategy of Pure Engine Mode

In this mode, the engine output torque is fully used to meet the demand torque T_D . Take engine power as the system required input power, such as formula (4) below:

$$P_{in} = T_e \omega_e / \eta_e \quad (4)$$

where: T_e is engine torque; η_e is engine efficiency.

The system required output power refers to the power used to overcome the vehicle resistance including the rolling resistance, gradient resistance, air resistance and acceleration resistance, specifically showed as the following equation:

$$P_{out_engonly} = (mgf \cos \alpha + mg \sin \alpha + \frac{C_D A u^2}{21.15} + \delta m \frac{du}{dt} + (I_e + I_m) \frac{i_0^2 i_{CVT} \eta_{CVT} u di_{CVT}}{r^2 dt}) u \quad (5)$$

where: δ is auto rotating mass conversion factor, expressed as following:

$$\delta = 1 + [I_r + (I_e + I_m)i_{CVT}^2i_0^2\eta_{CVT}]/mr^2$$

The system required output power in pure engine mode can be converted to the following form by solving Eqs. (1, 2, 3) and (5) simultaneously:

$$P_{out_engonly} = T_D i_0 u / r \tag{6}$$

Define the ratio of the system required output and input power as the system efficiency, and get the system efficiency of pure engine mode, expressed as formula (7) below.

$$\eta_{sE} = \frac{P_{out_engonly}}{P_{in}} \tag{7}$$

Then take the formula (4) and (6) into Eq. (7):

$$\eta_{sE} = \frac{T_D i_0 u \eta_e}{T_e \omega_e r} \tag{8}$$

The fundamental objective of this study is to maximize the hybrid system efficiency, so set the energy optimization objective function of pure engine mode as formula (9).

$$\begin{array}{l}
 \text{Max}(\eta_{sE}) \\
 \left. \begin{array}{l}
 \omega_r = u/r \\
 \omega_e = \omega_r i_0 i_{CVT} \\
 T_e i_{CVT} \eta_{CVT} = T_D \\
 T_e \in [T_{emin}, T_{emax}] \\
 \omega_e \in [\omega_{emin}, \omega_{emax}] \\
 i_{CVT} \in [i_{CVTmin}, i_{CVTmax}]
 \end{array} \right\} \text{s.t.} \tag{9}
 \end{array}$$

Analyze the formula (8) and (9) comprehensively and the following conclusion can be get: the system efficiency η_{sE} of this mode depends on the vehicle speed u , demand torque T_D , engine torque T_e and CVT ratio i_{CVT} . At the same time T_D depends on vehicle speed and accelerator pedal opening APS. Therefore, the energy optimization essence of pure engine mode is: look for the optimal CVT ratio i_{CVT} and engine torque T_e making the system efficiency maximize under the premise of certain vehicle speed and accelerator pedal opening.

Get the optimization results of this mode shown in Figs. 3 and 4 by using sequential quadratic programming algorithm.

It can be seen from the results that the hybrid system overall efficiency is higher under medium speed, medium accelerator pedal opening condition, the maximum value reaches about 0.28. But, it is lower under other conditions.

Fig. 3 System efficiency of pure engine mode

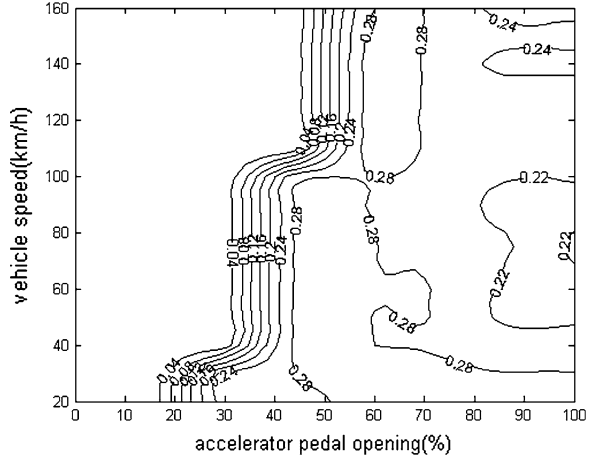
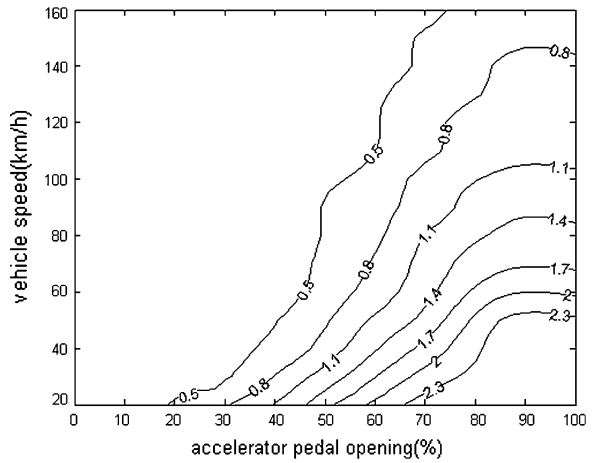


Fig. 4 CVT target ratio of pure engine mode



4.2 Energy Optimization Strategy of Economic Charge Mode

During economic charge mode, the motor operates in power generation state, part of the engine output torque is used to meet the driver’s demand, the other part for power generation. All power comes from the engine. Still take the engine power as the system required input power, expressed as formula (4).

The following relationship exists between battery charging power and the motor torque in this mode:

$$P_{\text{batchr}} = T_m \omega_m \eta_{\text{mchr}} \eta_{\text{batchr}} \tag{10}$$

where: T_m is motor torque; η_{mchr} is motor generation efficiency; η_{batchr} is battery charging efficiency.

Regard the sum of power used to overcome the vehicle resistance and battery charging power as the system demand output power. Combine Eqs. (1, 2, 3, 5) with (10) and get the system required output power:

$$P_{\text{out_generate}} = T_D i_0 u / r + T_m \omega_m \eta_{\text{mchr}} \eta_{\text{batchr}} \quad (11)$$

Still define the ratio of the system required output and input power as system efficiency, and get the system efficiency of economic charge mode, expressed as following:

$$\eta_{\text{sG}} = (T_D i_0 u / r + T_m \omega_m \eta_{\text{mchr}} \eta_{\text{batchr}}) \eta_e / (T_e \omega_e) \quad (12)$$

Take the maximum overall efficiency of hybrid system as the optimization objective, and get the energy optimization objective function as formula (13).

$$\begin{aligned} & \text{Max}(\eta_{\text{sG}}) \\ & \left\{ \begin{array}{l} T_D = (T_e - T_m) i_{\text{CVT}} \eta_{\text{CVT}} \\ P_{\text{batchr}} = T_m \omega_m \eta_{\text{mchr}} \eta_{\text{batchr}} \\ \omega_r = u / r \\ T_e \in [T_{\text{emin}}, T_{\text{emax}}] \\ \omega_e \in [\omega_{\text{emin}}, \omega_{\text{emax}}] \\ T_m \in [0, T_{\text{mmax}}] \\ |P_{\text{batchr}}| \in [0, P_{\text{batmax}}] \\ i_{\text{CVT}} \in [i_{\text{CVTmin}}, i_{\text{CVTmax}}] \\ \text{soc} \in [\text{soc}_{\text{Min}}, \text{soc}_{\text{Max}}] \end{array} \right. \quad (13) \end{aligned}$$

Analyze the formulas above comprehensively, it can be seen that the system efficiency η_{sG} of this mode depends on the vehicle speed u , accelerator pedal opening APS, battery SOC, engine torque T_e , motor torque T_m and CVT ratio i_{CVT} . So the energy optimization essence of this mode is: search the optimal CVT ratio i_{CVT} , engine torque T_e and motor torque T_m making the system efficiency maximize under the premise of certain vehicle speed, accelerator pedal opening and battery SOC.

Apply the sequential quadratic programming algorithm to get the optimization results of this mode, they are shown in Figs. 5, 6 and 7 when SOC is 0.4.

Compare Fig. 5 with Fig. 3, it can be seen that for small accelerator pedal opening condition, the hybrid system works more efficient in economic charge mode than working in pure engine mode, such as a speed of 25 km/h when accelerator pedal opening is 25 %, the system efficiency can reach 0.24 in economic charge mode, yet it is 0.16 in pure engine mode. Therefore, the overall system efficiency under small accelerator pedal opening condition can be improved if the hybrid system works in economic charge mode, improving the vehicle economy.

Fig. 5 System efficiency of economic charge mode

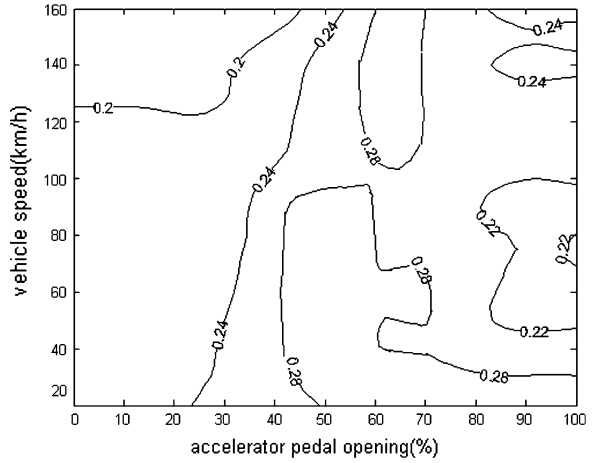
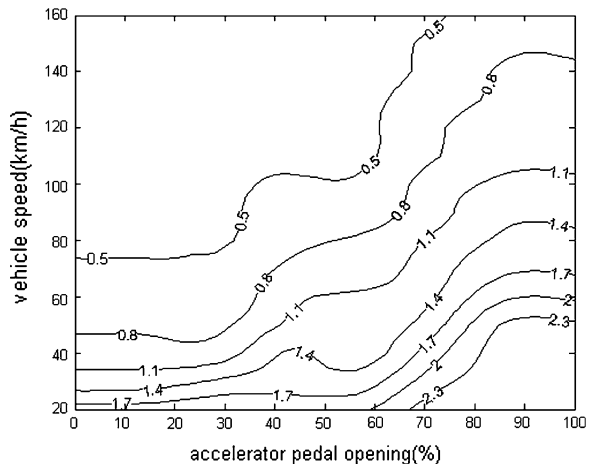


Fig. 6 CVT target ratio of economic charge mode



4.3 Energy Optimization Strategy of Boost Mode

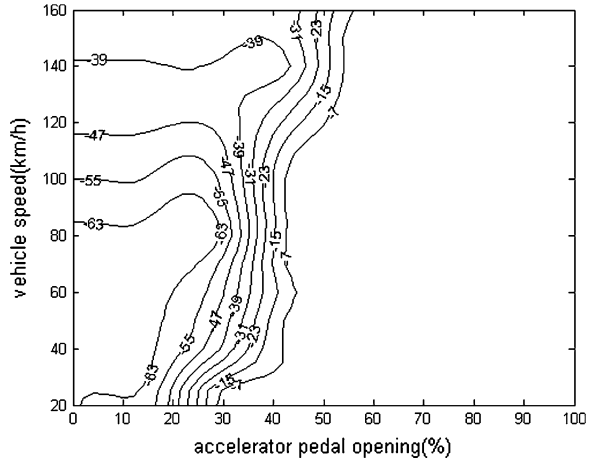
The motor works in electric state under this mode, engine and motor would meet the vehicle driven demand jointly. The object of this paper cannot be charged externally, so all the vehicle driven energy come from the engine fundamentally. Take the engine power as system required input power as before, expressed as formula (4).

The following relationship exists between battery discharge power and the motor torque under this mode:

$$P_{batdis} = (T_m \omega_m / \eta_{m ds}) / \eta_{batds} \tag{14}$$

where: $\eta_{m ds}$ is motor electric efficiency; η_{batds} is battery discharge efficiency.

Fig. 7 Motor target torque of economic charge mode



Make the system required output power defined as the sum of power used to overcome the vehicle resistance and battery discharge power. Combine Eqs. (1), (2), (3), (5) with (14) to get the system required output power in boost mode:

$$P_{out_motor} = T_D i_0 u / r - (T_m \omega_m / \eta_{m ds}) / \eta_{bat ds} \tag{15}$$

In this mode, system efficiency is defined the same way as the two modes before, and then get the system efficiency:

$$\eta_{sM} = (T_D i_0 u / r - T_m \omega_m / \eta_{m ds} \eta_{bat ds}) \eta_e / (T_e \omega_e) \tag{16}$$

Take the maximum overall efficiency of hybrid system as the optimization objective, and get the energy optimization objective function of boost mode as formula (17).

$$\begin{aligned} & \text{Max}(\eta_{sM}) \\ & \left\{ \begin{aligned} & T_D = (T_e + T_m) i_{CVT} \eta_{CVT} \\ & \omega_r = u / r \\ & P_{bat ds} = (T_m \omega_m / \eta_{m ds}) / \eta_{bat ds} \\ & T_e \in [T_{emin}, T_{emax}] \\ & \omega_e \in [\omega_{emin}, \omega_{emax}] \\ & T_m \in [0, T_{mmax}] \\ & P_{bat ds} \in [0, P_{batmax}] \\ & i_{CVT} \in [i_{CVTmin}, i_{CVTmax}] \\ & soc \in [soc_{Min}, soc_{Max}] \end{aligned} \right. \tag{17} \end{aligned}$$

Fig. 8 System efficiency of boost mode

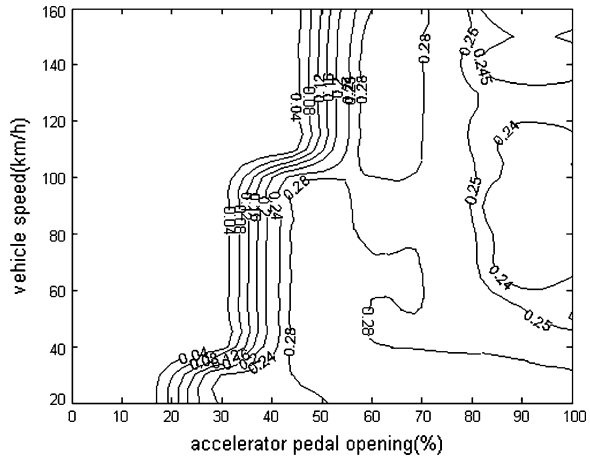
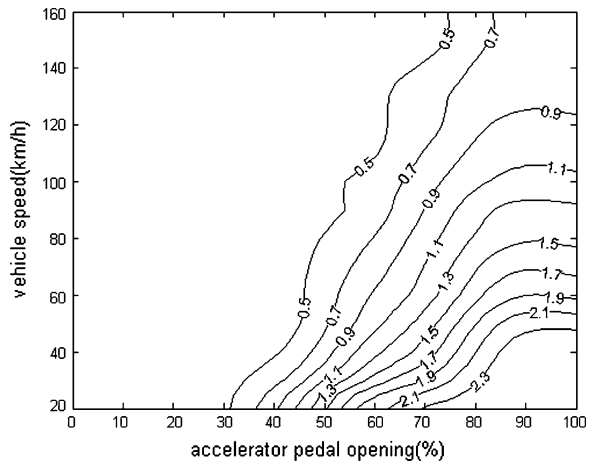


Fig. 9 CVT target ratio of boost mode



Analyze the formulas above comprehensively, it can be seen that the system efficiency η_{SM} of this mode depends on the vehicle speed u , accelerator pedal opening APS , battery SOC, engine torque T_e , motor torque T_m and CVT ratio i_{CVT} . So the energy optimization essence of this mode is: find the optimal CVT ratio i_{CVT} , engine torque T_e and motor torque T_m making the system efficiency maximize under the premise of certain vehicle speed, accelerator pedal opening and battery SOC.

Use sequential quadratic programming algorithm to get the optimization results of this mode, they are shown in Figs. 8, 9 and 10 when SOC is 0.4.

Compare Fig. 8 with Fig. 3, the conclusion can be drawn that for large accelerator pedal opening condition, the hybrid system works more efficient in boost mode than working in pure engine mode, for example a speed of 60 km/h when accelerator pedal opening is 85 %, the system efficiency can reach 0.25 in boost mode, yet it is about 0.22 in pure engine mode. Therefore, the overall system efficiency under large

Fig. 10 Motor target torque of boost mode

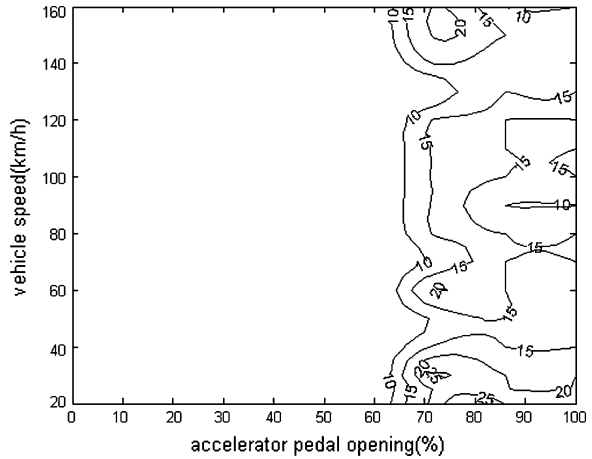
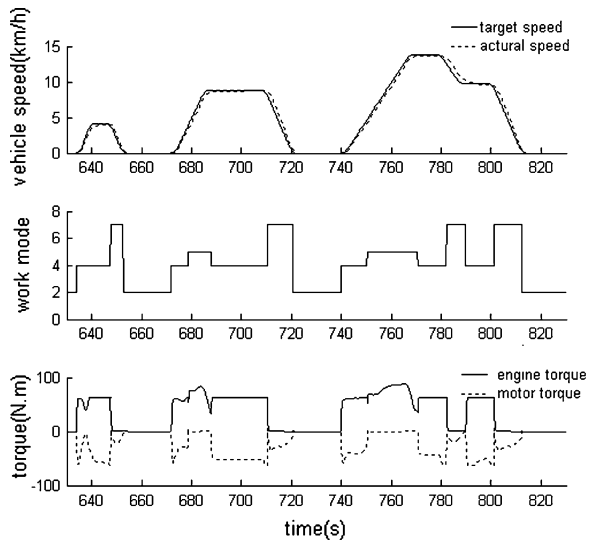


Fig. 11 630 ~ 830 s piece of data



accelerator pedal opening condition can be improved if the hybrid system works in boost mode, which is conducive to get a better vehicle economy.

5 Simulation Verification

A forward simulation model of CVT hybrid vehicle is built to verify the energy management strategy based on this optimization and the results as following has been analyzed: the speed following condition, vehicle work mode, working points of engine and motor and so on. The interception 630 ~ 830 s piece of data is shown in Fig. 11.

Table 1 Simulation result of fuel consumption

Simulation consumption (L/100 km)	Proto consumption (L/100 km)	Saving rate (%)
6.74	9.16	26.4

Analyze the simulation result of 100 km fuel consumption under NEDC driving cycle, and Table 1 gives the final results. From the results we can see that compared with the proto vehicle the equivalent 100 km fuel consumption is reduced by 26.4 % under NEDC driving cycle, verifying the effectiveness of energy optimization strategy proposed.

6 Conclusions

The CVT hybrid car energy optimization strategy has been developed for pure engine mode, economic charge mode and boost mode, and optimization results have improved the overall efficiency of hybrid system, the energy management strategy based on this optimization can reduce vehicle fuel consumption by 26.4 %, indicating that the optimization strategy can play the fuel saving advantage of CVT hybrid vehicle effectively.

The strategy proposed in this paper have taken driver's actual operation and drive demand into account as well as efficiencies of key components, and accelerator pedal opening has been treated as one of state variables, reflecting the driver's intention and feelings more intuitively.

References

1. Zou N (2009) Study on power coupler and ratio control for HEV with continuously variable transmission. Jilin University, Jilin
2. Lee H, Kim H (2002) Improvement in fuel economy for a parallel hybrid electric vehicle by continuously variable transmission ratio control. *Automobile Eng* 219(3):45–68
3. Hu M (2007) Study on energy management strategy for mild hybrid electrical vehicle with CVT. Chongqing University, Chongqing
4. Lei Z, Yugong L, Diange Y et al (2007) Development of hybrid powertrain control system for parallel-series hybrid electric vehicle. *Chin J Mech Eng* 43(4):125–131
5. Dai Y, Luo Y, Bian M et al (2009) Dynamic coordinated control for a full hybrid electric vehicle with single motor. *Automot Eng* 31(10):919–923
6. Zhisheng Y (2006) Vehicle theory. China Machine Press, Beijing

Development of Plug-in Hybrid System for Midsize Car

Matsumoto Shinichi, Takeuchi Hiroaki and Itagaki Kenji

Abstract In recent years, various energy sources have been investigated as replacements for traditional automotive fossil fuels to reduce CO₂ emissions, respond to instabilities of the supply of fossil fuels, and to reduce emissions of air pollutants in urban areas. Toyota Motor Corporation considers the PHEV, which can use electricity efficiently, to be the most practical solution to these issues. Toyota already began sales of the Prius Plug-in Hybrid in 2012 in the U.S., Europe and Japan, and also will introduce to the Chinese market. This is the first PHEV to be mass-produced by Toyota Motor Corporation. Prior to this, in December 2009, Toyota introduced 650 PHEVs through lease programs for verification testing in China, the U.S., Europe and Japan. The system of mass-production vehicle specifications has major improvements in response to the results of this verification testing. As a result, EV range was increased with a smaller battery, and the system weight has been drastically reduced. Additionally, the vehicle clears the most stringent emissions regulations in different regions, and was granted Enhanced AT-PZEV credit in California. This paper discusses the development of the plug-in hybrid system for this mass-produced vehicle.

Keywords Plug-in hybrid vehicle (PHEV) · Verification test · Fuel efficiency · EV range · PHEV system

F2012-B02-037

M. Shinichi (✉) · I. Kenji
Toyota Motor Engineering & Manufacturing (China) Co., Ltd,
Changshu, China
e-mail: shin@matsu.tec.toyota.co.jp

T. Hiroaki
Toyota Motor Corporation, Toyota, Japan

1 Introduction

Various issues related to automobiles, such as reducing CO₂ emissions, resolving energy security problems, and reducing emissions of air pollutants in urban areas, must be solved in order for people to continue to enjoy the enjoyment of driving, and the pleasure of having the comfortable moveable space that automobiles currently provide. For the past several years, hybrid vehicles (HEVs) have been one countermeasure to these issues. The fuel consumption reduction effects of HEVs have achieved major improvements in fuel efficiency and reductions in exhaust emissions compared to a conventional gasoline vehicle. Furthermore, in addition to these merits, utility and reliability are now the same as a conventional vehicle, and recently the number of HEVs sold has increased drastically as prices have fallen (Fig. 1).

Furthermore, the introduction of electric vehicles (EVs) is a possible means of reducing CO₂ and other exhaust emissions. By using electric power from the power grid, it is possible to reduce emissions of CO₂ and air pollutants to zero during driving. However, even when using the latest Lithium-ion battery technology, energy density is limited to about 1/50 of that of fossil fuels, and the cruising range on a single charge is rather short. While the cruising range can be increased in proportion to the size of the battery, sacrifices must be made in the cabin and luggage space. Also, larger batteries lead to drastic increases in the weight and cost of the vehicle, and therefore are not practical. Additionally, charging a large capacity battery from an external source in a short period of time would require a DC external charger with capacity for high electric output, which requires the installation of dedicated infrastructure.

Accordingly, when considering these limitations, it appears that EVs probably will not totally replace the conventional gasoline vehicle, now or in the near future. It is assumed that, in the short term, the EV will function as a commuter vehicle that covers short distances.

A PHEV combines the merits of an EV, since it has zero emissions during driving with electric power, with the merits of an HEV, since it does not sacrifice any of the practicality of a standard vehicle. For example, cruising range is equal to or better than that of a conventional gasoline vehicle. This paper discusses the PHEV system used in the Prius plug-in hybrid, the first PHEV mass-produced by Toyota Motor Corporation.

2 Characteristics and Merits of PHEVS

The unique characteristics of PHEVs are further described below. As discussed earlier, the PHEV combines the merits of both EVs and HEVs. One approach to the PHEV system design is to increase the capacity of the battery from that of the existing HEV and install an on-board charger to the vehicle. Initially, after a full

Fig. 1 Sales volume of hybrid vehicles

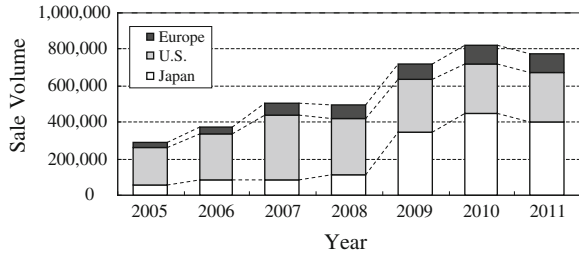


Fig. 2 The concept of PHEV

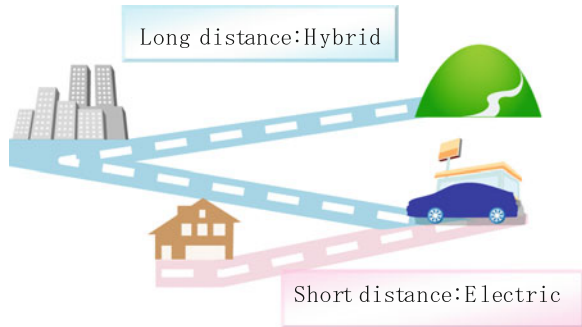
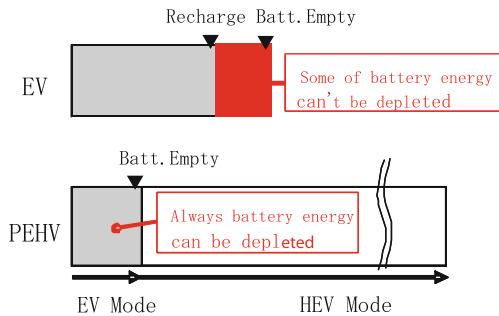


Fig. 3 The advantage of PHEV



charge of the battery, a PHEV configured in this way will run primarily on electric energy. After the battery is depleted, the engine is operated intermittently, as an HEV normally runs. By configuring the system in this way, the vehicle is primarily an EV for short distances, and it can run as an HEV with the engine for long distances after the battery is depleted (Fig. 2). This gives the vehicle cruising range equivalent to a conventional gasoline vehicle or an HEV and ensures utility and convenience. Furthermore, since an EV cannot run when the battery is depleted, it is necessary to arrive at a charging point before this happens. For this reason, it is difficult to use up all of the energy in the installed battery when driving with an EV. However, a PHEV differs from an EV in that the driver can use up all of the battery energy without hesitation because the vehicle can be driven with the engine even if the battery is depleted (Fig. 3). This is another advantage of the PHEV.

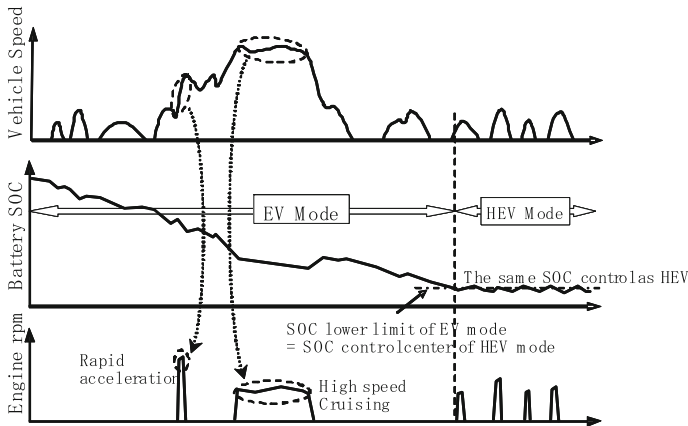


Fig. 4 PHEV system operation

A PHEV has two driving modes. After the battery has been fully charged, the vehicle normally operates in EV mode [sometimes called charge depletion (CD) mode], in which electricity is the primary source of drive energy. In EV mode and normal driving conditions, PHEV performance is similar to that of an EV. Depending on the PHEV system configuration, even during EV mode, the engine might operate to supply driving power when a large amount of power is necessary for rapid acceleration or high speed cruising. The other driving mode is HEV mode [sometimes called charge sustain (CS) mode], which starts after the battery is depleted. In this mode, the engine is used as the primary source of drive energy, and the system is operated so that the battery state of charge (SOC) is maintained around the middle of controlled value that is programmed in advance, in the same way as an HEV. These are shown in Fig. 4.

3 Results of Verification Tests

Prior to this development, verification testing of PHEVs has been performed since December 2009 in China, the U.S., Europe and Japan, and the findings were useful in the development of this system. The EV range was set at 21.7 km and this vehicle achieved 59 g/km in fuel efficiency under new European driving cycle (NEDC).

The results of the verification tests are described below. More than 600 vehicles were tested in various locations around the world and data related to driving and charging was recovered from each vehicle for analysis. The analyzed data from vehicles tested in China, the U.S., France, and Japan was then compared. In China, the results were obtained from the verification test performed in Tianjin. The results for France were obtained from the test performed in Strasbourg, which involved 70 vehicles and was the largest test performed around the world. Table 1 outlines the scope of the data obtained in each region.

Table 1 Outlines of the data collected

Parameter	China	USA	France	Japan
No. of vehicle	13	65	67	145
Starting date	2011/4/1-	2010/6/1-	2010/4/15-	2009/12/8-
Mileage	123,562 km	595,510 km	1,302,885 km	1,262,363 km
Average mileage per year	12,600 km	13,400 km	19,000 km	9,500 km
Trips (times)	14,889	53,397	108,025	167,884
Charging event (times)	2,502	10,672	20,821	37,448

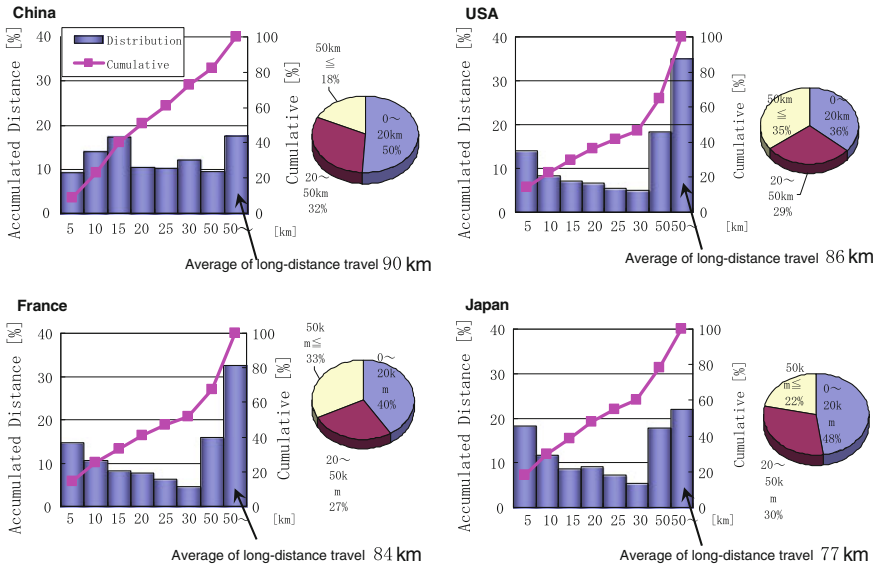


Fig. 5 Distance per trip (distribution expressed in % of total km)

Figure 5 shows the frequency distribution for driving distance per trip and the per trip integrated driving distance in each region. In China and Japan, this proportion was one-fifth of trips exceeded 90 km. In contrast, in Strasbourg and the U.S., approximately one-third.

Furthermore, the test confirmed that more than half of trips in Japan were short enough to be covered by a PHEV with an EV range of 20 km or less.

Figure 6 shows the frequency for driving distance per charge and the per charge integrated driving distance. Here, the driving distance per charge is defined as the distance between one charge and the next charge. In each region, a high proportion of the distance per charge exceeded 50 km (70–80 %). When the distance per charge exceeded 50 km, the average per charge distance in France and the U.S. was 204 and 180 km, respectively. In contrast, the average per charge distance over 50 km in Japan was slightly shorter at 132 km. This shows that drivers were charging the PHEV after the number of trips had built up to a certain amount.

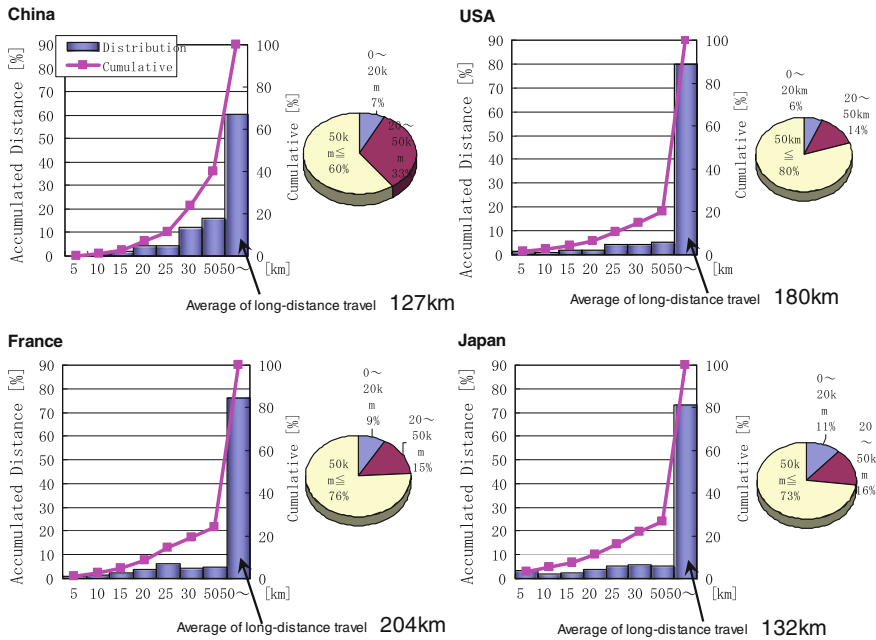


Fig. 6 Distribution of distance travelled between charging events

When the charging frequency decreases, the number of trips per charge increases by the same amount. This has the effect of increasing the frequency of long-distance trips per charge.

Figure 7 shows the daily average number of charges and fuel consumption for each vehicle. The data is organized in sequence starting from the vehicle with the highest number of charges. The graphs indicate that, in each region, the vehicles that were charged most frequently tended to have the best fuel consumption. However, large differences were observed in the number of charges per user in each country. More than half of the users charged the vehicle less than once per day. This generated the large gap in the fuel consumption reduction effect.

Figure 8 shows the fuel consumption reduction effect for each driving distance per charge, compared to a conventional internal combustion engine (ICE) vehicle. The fuel consumption of the ICE vehicle was calculated from the driving distance and the fuel efficiency of the ICE vehicle, assuming that the ICE vehicle was driven the same distance as the PHEV. The fuel efficiency value used was the average value for the same class of automatic transmission (AT) ICE vehicle calculated by actual driving in each country. The results confirmed a large fuel consumption reduction effect in each region. This effect was relatively large in China, which had a high distribution of short-distance trips per charge due to the high frequency of short trips and frequent charges observed in that country.

It has been confirmed by actual verification tests that PHEV with approximately 20 km EV range has the potential of lower fuel consumption in each country such

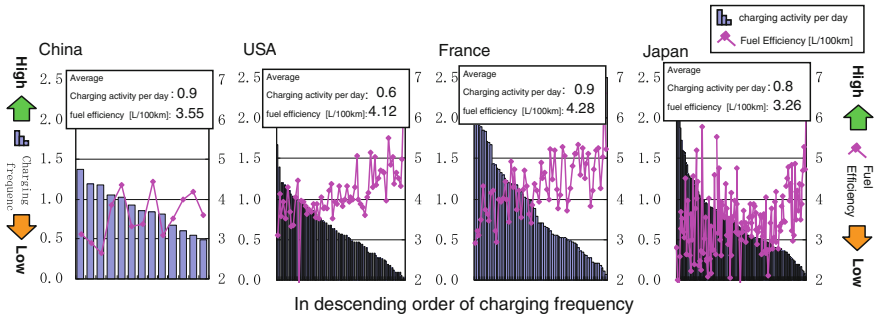


Fig. 7 Daily average number of charges and fuel consumption

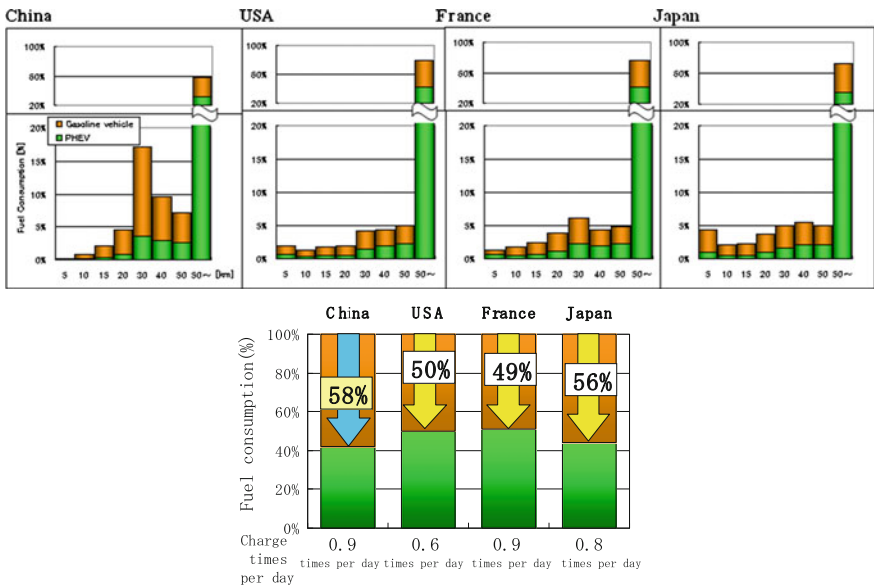


Fig. 8 Fuel consumption reduction effect

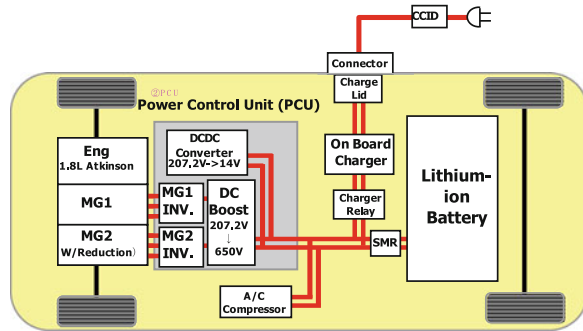
as China, the U.S., Europe and Japan. More significant fuel reduction effect can be achieved if charging activity can be increased.

4 Development Objectives for this PHEV System

This PHEV system was developed for the Prius plug-in hybrid, which is Toyota’s first mass-produced PHEV, as stated above.

The objectives of the PHEV system development explained in this chapter were as described below.

Fig. 9 System configuration of newly developed PHEV system



- Reduce PHEV system weight and cost.
- Make improvements based on the results of the verification testing from the lease vehicles released in 2009.
- Improve electricity consumption efficiency.

5 PHEV System Configuration

5.1 PHEV System Type

The series parallel type PHEV system, which has a mechanical power path from the engine to the tire, was chosen for this Prius plug-in hybrid because a plug-in hybrid system could be configured at a relatively low cost by effectively using components of the base vehicle (i.e., the Prius HEV). In addition, once the battery energy is depleted and the system shifts to HEV mode, higher system efficiency and better HEV mode fuel economy could be achieved.

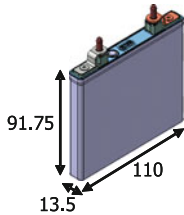
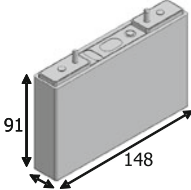
5.2 System Configuration

The newly developed PHEV system configuration is shown in Fig. 9. The major changes from the base HEV are as shown below.

- (1) The battery pack uses a high energy type Lithium-ion battery cell.
- (2) An external charge system that is compatible with AC 120 V/240 V is installed.
- (3) The EV drive functions are expanded (EV maximum power is expanded, EV maximum vehicle speed is higher, and EV range is longer).

The details of each component are discussed in order below.

Table 2 Lithium-ion battery cell

	'09 Model	'12 Model
Type	Li-ion	Li-ion
Exterior		
Nominal voltage	3.6 V	3.7 V
Nominal capacity	5 A h	21.5 A h
Weight	245 g	726 g

5.3 Battery Cells

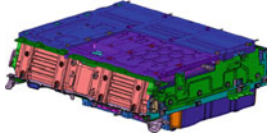
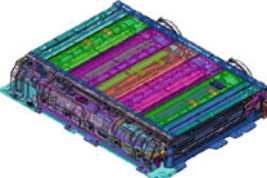
High energy density Lithium-ion battery cells with characteristics suited for a PHEV were newly developed for this vehicle (Table 2). This battery cell also achieved input and output power that is high enough for PHEV requirements (i.e. EV driving power, engine cranking power during cold situations, regeneration input power for regenerative brake and so on). By using these battery cells, system weight and cost were both drastically decreased when compared to the 2009 model which adopted a different type of Lithium-ion battery cell.

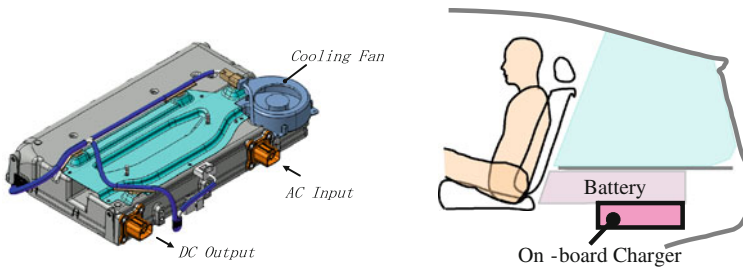
5.4 Battery Pack

A frame construction was adopted for the battery pack to ensure high strength and rigidity (Table 3). Additionally, an aluminum extruded material was used for the frame construction to reduce its weight as well. The combined effects of using of this frame construction and the battery cell mentioned above reduced the weight of the battery pack to about half that of the 2009 model which resulted in much improvement in specific energy and specific power of the battery pack (Table 3), and drastically reduced the volume of the battery pack as well. As a result, despite increasing the total battery energy to more than three times the base vehicle (Prius), the cabin and luggage space have been kept the same as the base vehicle.

Additionally, two air cooling fans were installed to ensure sufficient battery cooling performance. The voltage of each battery cell is monitored by a battery monitoring unit, which prevents each battery cell from being overcharged or over discharged. A battery pack has four stacks each comprising 14 cells (total of 56 cells), and the battery total voltage is 207.2 V. By matching the battery total voltage with the base vehicle (Prius), the input voltage of the high voltage components connected in parallel to the battery (DC/DC converter, air conditioning

Table 3 Battery pack

	'09 Model	'12 Model
Type	Li-ion	Li-ion
Exterior		
Gross energy	5.2 W h	4.4 kW h (−14 %)
Total voltage	346 V	207 V
Weight	160 g	82 kg (−49 %)

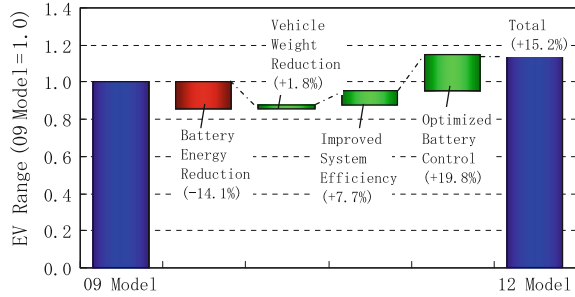
**Fig. 10** On-board charger

inverter) was made the same as in the base vehicle, enabling the use of common parts, which contributed to reducing the PHEV system cost. Furthermore, the specifications of some high voltage parts were revised due to concern about increased heat load caused by the higher electrical current created by the expanded EV driving functions, as described above.

5.5 On-Board Charger

The on-board charger (Fig. 10) was designed with an input voltage range from AC 100–AC 240 V, in order to ensure compatibility with the Chinese, American, European and Japanese power grid. The maximum output of the charger is 2 kW, and a full battery charge is possible in about 2.5 h at AC 120 V, and in about 1.5 h at AC 240 V. This charger adopts an air-cooled system, so as to keep the flexibility of its location. As a result, it could be installed below the battery pack and was located without affecting the layout of the cabin and engine compartment. This charger achieved high efficiency through adoption of low-loss parts for power devices and the optimization of the power conversion control system. This charger

Fig. 11 EV range improvement in NEDC



and its control system are compliant with the SAE J1772 Level 1 and Level 2 charge standards, as well as the IEC61851-1 Mode 2 and Mode 3 charge standards.

6 Performance

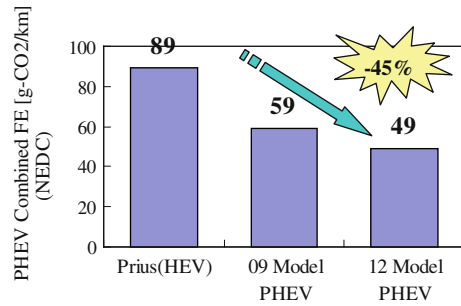
6.1 EV Range

EV range was set at 25.0 km under NEDC. Compared to the 2009 model, the total battery energy was reduced by 14 %, but optimization of the battery control (which includes improved battery SOC detection) and improvements in electricity consumption efficiency (which includes optimal control of the DC boost converter) have ensured around 15 % better EV range (Fig. 11). EV maximum speed is around 100 km/h, and EV maximum power is increased by about 1.8 times of the original Prius HEV.

6.2 Fuel Efficiency

In the case of a PHEV, it is thought that the frequency of HEV mode driving will be high, although this depends on how the driver uses the vehicle (e.g., driving distance, charge frequency). Therefore, HEV fuel efficiency is very important as it is in a conventional HEV. The newly developed PHEV system has increased battery volume and has an added on-board charger, which increase the weight of the vehicle around 40 kg in comparison to the base vehicle. However, HEV fuel efficiency is almost the same as the base vehicle owing to reduced battery internal resistance due to the adoption of Lithium-ion cells and the optimized control tuning. Additionally, maximum regenerative power is increased by 20 %, compared to the original Prius HEV, by using this Lithium-ion battery. Thus on-road fuel efficiency can be improved.

Fig. 12 PHEV combined fuel economy (NEDC)



As shown by the certification result (NEDC Combined FE of Plug-in EV mode and HEV mode) In Europe, the plug-in combined CO₂ value improvement can lead to around 45 % reduction compared to the already base HEV (Fig. 12).

6.3 Emissions

Even in EV mode, if the drive power exceeds the maximum battery power, the engine will start to supplement it. To meet the world's most stringent emission standard even when this situation occur, the PHEV system control is optimized so that the distribution of battery and engine power were optimized during first engine start situation. Throttle control and ignition timing tuning were optimized for cold engine start emission reduction, and injector specifications were revised for emission performance stabilization. With these efforts, this vehicle meets the most stringent emissions regulations in each region. Additionally, with the addition of plug-in EV driving functions, this vehicle was granted Enhanced AT-PZEV credit in California (Table 4).

7 Future Outlook

It will not be possible to avoid the need to effectively use electricity as a source of drive power for automobiles, to help respond to the various issues facing them, such as energy security problems, CO₂ emissions, and reducing emissions of air pollutants.

PHEV uses electricity as an energy source in the same way as an EV, yet ensures the same level of utility and convenience as the conventional HEV. Additionally, a system configuration with a relatively low increase in cost in comparison to the conventional HEV was made possible by using many components in common with the conventional HEV. In this case, considering the balance between the total performance of the vehicle and the price, it is important to select suitable amount of the battery.

Table 4 Emission results

	Prius (HEV)	12 Model PHEV
U.S. (CA)	AT-PZEV	Enhanced AT-PZEV
Europe	Euro5	Euro5
Japan	J-SULEV	J-SULEV

When considering these facts, Toyota believes that the PHEV is currently the most practical solution for utilizing grid power. In the future, by using more electricity from renewable energy sources, it will be possible to drive with a lower impact to the environment, and it is hoped that further advances in battery technology (such as reduced cost, increased energy density) will allow the more effective use of electric energy for automobiles.

8 Conclusions

- The potential of lower fuel consumption was verified by actual verification tests of the PHEV with approximately 20 km EV range in each country such as China, the U.S., Europe and Japan.
- Toyota Motor Corporation began sales of the Prius plug-in hybrid, its first mass-produced new PHEV from Toyota, in January 2012.
- A Lithium-ion battery cell optimized for the PHEV was developed, and the mass of the system, such as the battery pack, was reduced in comparison to the model released in 2009.
- The system was configured with the minimum possible amount of changes from the base vehicle (Prius) to achieve cost reductions.
- EV range in NEDC is 25.0 km.

References

1. Yamamoto M, Takaoka T, Komatsu M, Gotoda Y: Development of a Toyota plug-in hybrid vehicle, SAE 2010-01-0839
2. Takaoka T, Komatsu M, Biebuyck B: Newly developed Toyota plug-in hybrid system and its vehicle performance under real life operation, SAE 2011-37-0033
3. Kamichi K, Yamamoto M, Fushiki S, Yoda T, Koijma K, Kurachi S: Development of plug-in hybrid system for midsize car, SAE 2012-01-1014

Study on System Efficiency and Power Flow Optimization for Dual-Mode Hybrid Electric Vehicle

Li-jin Han, Chang-le Xiang, Wei-jing Yan, Yun-long Qi and Ran Liu

Abstract *Research and/or Engineering Questions/Objective:* Most research of the power-split hybrid vehicle haven't taken the efficiency of the planetary-gear system which changes according to the gear ratio into account and merely consider the power lose based on the mechanical-electric energy conversion and determined the control strategy. The objective of the study is to achieve optimized management and cooperative control of the power flow by building an exact model of hybrid power system and analyzing the efficiency. *Methodology:* The mechanical loss of the Dual-mode coupling mechanism planetary system is caused by gear mesh, clutch friction, oil seal and bearings. The loss has intimated connection with the parameters of the system status. This chapter has studied the relationship between system parameters and transmission efficiency of planetary transmission in coupling system. It also has built the efficiency model of the planetary transmission in coupling system and amend the model by test. Build a comprehensive efficiency model of the hybrid vehicle, by considering the power loss of engine, battery, motor and other components and mechanical loss of planetary transmission in coupling system, and this model reflects the distribution of the system power flow. So we could achieve the optimized control of system power flow under the requirement of the driver. *Results:* The planetary transmission efficiency and hybrid vehicle comprehensive efficiency has been described by the functions of system power flow distribution status. By considering of the equivalence relations between battery pack charge/discharge and engine fuel consumption, this

F2012-B02-038

L. Han (✉) · C. Xiang · W. Yan · Y. Qi
School of Mechanical Engineering, Beijing Institute of Technology, Beijing, China
e-mail: lj.han@163.com

R. Liu
Patent Examination Cooperation Center of the Patent Office SIPO, Beijing, China

chapter has built the optimized model of system power flow control. *Limitations of this study*: An important limitation of the current study is the calculating of the drag losses of the clutch/brake at very high rotating speed, and the designing of the test bench which should has the ability to measured more than one motor power accurately. So specialize tests of component and corresponding testing equipments are needed. *What does the chapter offer that is new in the field including in comparison to other work by the authors*: The modelling of planetary transmission efficiency of power coupling system in the dual-mode hybrid system is new. *Conclusions*: By studying the system efficiency not only revealing how the system works of the system but also guiding the optimize management of the system power flow.

Keywords Dual-mode · HEV · System efficiency · Power flow optimization · Control strategy

1 Overview

The dual-mode power split hybrid system is a strong mixed series–parallel hybrid system based on the planetary gear mechanism. The continuously variable transmission can be achieved by manipulated through the clutch, brake and other components. A dual-mode hybrid system and its speed relationship showed in Fig. 1. The single-mode hybrid vehicle introduced by Toyota obtained great success [1]. Compared to single-mode hybrid system because the dual-mode hybrid system increases the planetary gear and manipulated components, so it can obtain a wider speed range and reduce the power demand of the generator/motor to meet the high-power and off-road vehicle driving requirements. The dual-mode hybrid system introduced by GM in the SUV and bus has been successfully applied [2].

One of the advantages of dual-mode hybrid system is able to obtain better fuel economy; an important reason is that the comprehensive efficiency of the powertrain has been improved. Figure 1 shows the coupling mechanism consists of three planetary rows, two manipulated components and two motors which can be seen as a new type of transmission, the transmission can achieve a continuously variable transmission through power conditioning. Motor A and motor B in the system both can be used as a generator or a motor. The sum of the power of the two motor can absorb the power of the discharge of the battery pack and can also charge the battery pack. The coupling system is a multi-input multi-output system, and according to the difference between charge and discharge of the battery pack, it can also be seen as a varying input or varying output system. Therefore the study of the efficiency of the system is much complicated. Papers [3, 4] study the efficiency of dual-mode coupling mechanism under the premise of a variety

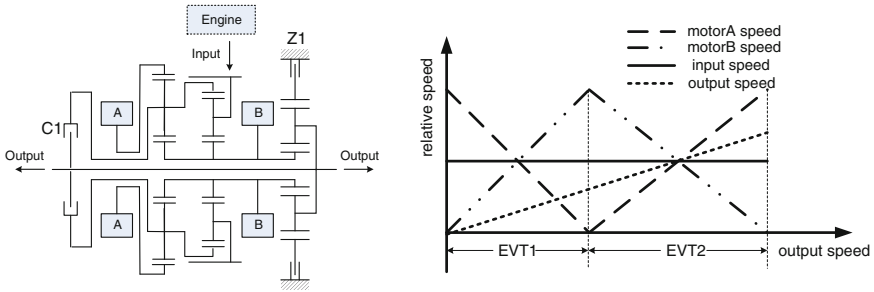


Fig. 1 Structure diagram and speed diagram of a dual-mode hybrid system

assumptions, without considering the mechanical loss of the planetary-gear system. Paper [5] taking the mechanical loss into account, but the calculation is relatively simply, and did not consider the impact on the efficiency of the system of charging and discharging of the battery pack. This chapter studied and explored the comprehensive efficiency of the system based on a comprehensive analysis of the efficiency of the dual-mode hybrid system coupling system, and proposed a optimal control strategy based on the system efficiency [6, 7].

2 Efficiency Analysis of Coupling System

Figure 1 is a dual-mode hybrid system transmission diagram. It has two operating modes the input-split (EVT1) and compound-split (EVT2), consists of three planetary gears, a clutch C1, a brake Z1 and motor A, B. The input-split mode is realized by engaging the brake Z1, and the compound-split mode, by engaging the clutch C1. The relationship between speed torque of the motor A, B and the speed torque of input, output can be achieved by deduced from the basic speed torque relationship of the planetary gear, see (1–4).

EVT1:

$$\begin{bmatrix} n_a \\ n_b \end{bmatrix} = \begin{bmatrix} \frac{(1+k_1)(1+k_2)}{k_1 k_2} & -\frac{(1+k_3)(1+k_1+k_2)}{k_1 k_2} \\ 0 & 1+k_3 \end{bmatrix} \begin{bmatrix} n_i \\ n_o \end{bmatrix} \tag{1}$$

$$\begin{bmatrix} T_a \\ T_b \end{bmatrix} = \begin{bmatrix} -\frac{k_1 k_2}{(1+k_1)(1+k_2)} & 0 \\ -\frac{1+k_1+k_2}{(1+k_1)(1+k_2)} & \frac{1}{1+k_3} \end{bmatrix} \begin{bmatrix} T_i \\ T_o \end{bmatrix} \tag{2}$$

EVT2:

$$\begin{bmatrix} n_a \\ n_b \end{bmatrix} = \begin{bmatrix} -\frac{1+k_2}{k_1} & \frac{1+k_1+k_2}{k_1} \\ 1+k_2 & -k_2 \end{bmatrix} \begin{bmatrix} n_i \\ n_o \end{bmatrix} \tag{3}$$

$$\begin{bmatrix} T_a \\ T_b \end{bmatrix} = \begin{bmatrix} -\frac{k_1 k_2}{(1+k_1)(1+k_2)} & \frac{k_1}{1+k_1} \\ -\frac{1+k_1+k_2}{(1+k_1)(1+k_2)} & \frac{1}{1+k_1} \end{bmatrix} \begin{bmatrix} T_i \\ T_o \end{bmatrix} \quad (4)$$

where n_a and n_b is the speed of MG A and B, T_a and T_b is the torque of MG A and B, n_i and n_o is the input and output speed of the coupling system, T_i and T_o is the input and output torque of the coupling system, k_1 , k_2 , k_3 is the planetary gear ratio of each planetary gear, and k is the ratio of the tooth number of ring gear to the tooth number of sun gear.

From the most primitive definition of efficiency, aiming at multi-input multi-output system, define its efficiency for all output and input power ratio, which is the input power minus the power loss of all aspects of the coupling system, and then divided by input power. The power loss in the coupling mechanism includes: the planetary-gear mesh power loss, energy conversion power loss in motor A and B, drag power loss in clutch and break, power loss of the sealing components, bearing power loss and so on. However, due to the clutch and break in the dual-mode hybrid system has a relatively high drag speed, the power loss is affected by the relative speed between driving and passive friction plate, lubricating oil pressure, friction plate clearance, and the shape of the friction surface grooves, and a number of factors remains to be further research, so this is temporarily not considered. The power loss in the sealing elements and the bearing compared to the power loss in the meshing and motor energy conversion, the small proportion of their effects are ignored. Therefore, the coupling mechanism efficiency can be described as:

$$\eta_{\text{coup}} = 1 - \varphi_{p1} - \varphi_{p2} - \varphi_{p3} - \varphi_a - \varphi_b \quad (5)$$

where φ_{p1} , φ_{p2} , φ_{p3} is the ratio of the gear mesh power loss and the total input power for each planetary gear. φ_a , φ_b is the ratio of the power loss in motor A, B and the total input power.

To facilitate the analysis, we first study the conditions when the battery pack has neither charging nor discharging, which equal to maintain the balance of electric power between the motor A and motor B. The relative power method is used in calculate the planetary gear meshing loss power to get the system power loss in mode EVT1 and mode EVT2. If the efficiency of motor A, B use theirs mean value, and assume the same efficiency of generation and electric conditions, then the coupling efficiency is only related to the transmission ratio. When inner meshing efficiency of the planetary gear take 0.98, external meshing efficiency take 0.97, the average efficiency of motor take 0.90, the efficiency of the coupling mechanism with the transmission ratio variation shown in Fig. 2.

It can be seen from Fig. 2, that coupling system has a relative high efficiency when the power of motor A or B is zero. These points are called mechanical points. At mechanical point the electric energy conversion power loss is zero. EVT1 has one mechanical point and EVT2 has two mechanical points, the efficiency of the mechanical point is 100 % when other power loss is not considered.

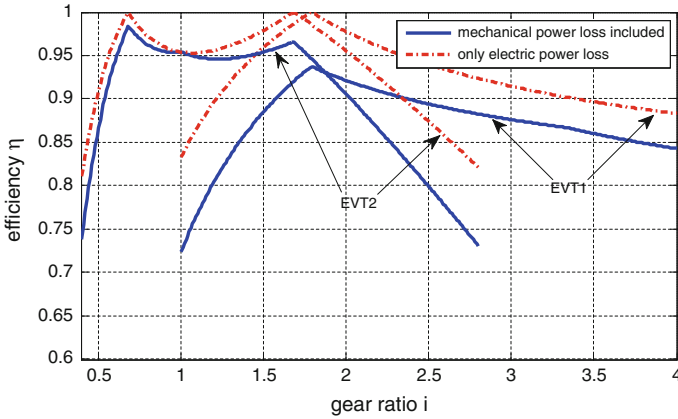


Fig. 2 Efficiency of the coupling mechanism with the transmission ratio variation

With the transmission ratio extending on both sides of the mechanical point, the efficiency in mode EVT1 monotonically decreasing. Mode EVT2 has a high efficiency between the two mechanical points, but outside the two mechanical points it monotonically decreasing. At the cross section between EVT1 and EVT2, the more efficient mode should be choosing. When designing the parameter in the system, the commonly used vehicle speed should correspond to the mechanical point, and to avoid the vehicle driving in a small or large transmission ratio. The scheme shown in Fig. 1, it's optimum transmission ratio range from 0.5 to 3.5, meeting the requirements of the most drive demand. The solid line in Fig. 2 is the power loss considering the planetary gear mesh efficiency. Figure 3 compares the power loss between electrical power and gear mesh power. It can be seen from the figure that system power loss is mainly the loss of electrical power, but mechanical power loss cannot be ignored. Loss of electric power in some regions is relatively large, so the vehicle should not work in this area. Mechanical power loss during normal use conditions are basically controlled within 5 %.

The preceding analysis does not consider the charge and discharge of the battery pack. If define P_{ele} as the charging and discharging power of the battery pack, and its value is positive when discharge and negative when charging. Motor A, B and the battery pack constitutes the balance of electric power. Define the output torque coefficient as follows:

$$\rho_T = \left(1 + \frac{9,549P_{ele}}{n_i T_i} \right) i_c \tag{6}$$

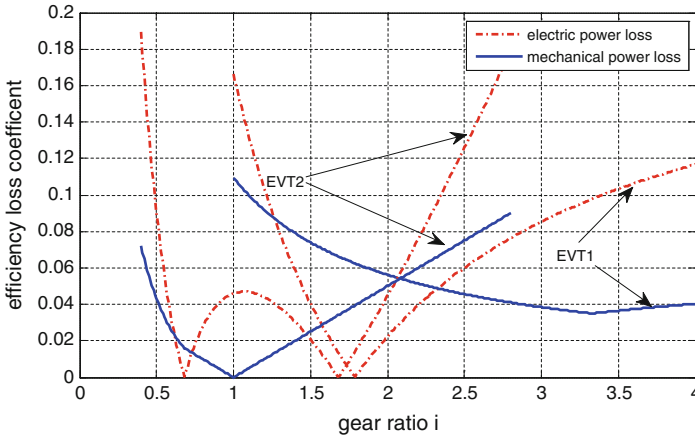


Fig. 3 Electric power and mechanical power losses comparison

The coupling mechanism efficiency expression considering charging and discharging of the battery pack can be achieved by analyzing the efficiency of the coupling mechanism.

EVT1:

$$\varphi_{p1} = \frac{1}{(k_1+1)} \left| \frac{1+k_3}{i_c} - 1 \right| |1 - \eta_p| \tag{7}$$

$$\varphi_{p2} = \frac{1}{1+k_2} \left| \frac{1+k_3}{i_c} - 1 \right| |1 - \eta_p| \tag{8}$$

$$\varphi_{p3} = \frac{k_3}{1+k_3} \left| \frac{\rho_T}{i_c} \right| |1 - \eta_p| \tag{9}$$

$$\varphi_a = \left| 1 - \frac{(1+k_3)(1+k_1+k_2)}{(1+k_1)(1+k_2)i_c} \right| |1 - \eta_{elea}| \tag{10}$$

$$\varphi_b = \left| \frac{\rho_T}{i_c} - \frac{(1+k_1+k_2)(1+k_3)}{i_c(1+k_1)(1+k_2)} \right| |1 - \eta_{eleb}| \tag{11}$$

EVT2:

$$\varphi_{p1} = \frac{1+k_2}{1+k_1} \left| \rho_T - \frac{k_2}{1+k_2} \right| \left| \frac{1}{i_c} - 1 \right| |1 - \eta_p| \tag{12}$$

$$\varphi_{p2} = \frac{k_2}{1+k_2} \left| \frac{1}{i_c} - 1 \right| |1 - \eta_p| \tag{13}$$

$$\varphi_{p3} = 0 \tag{14}$$

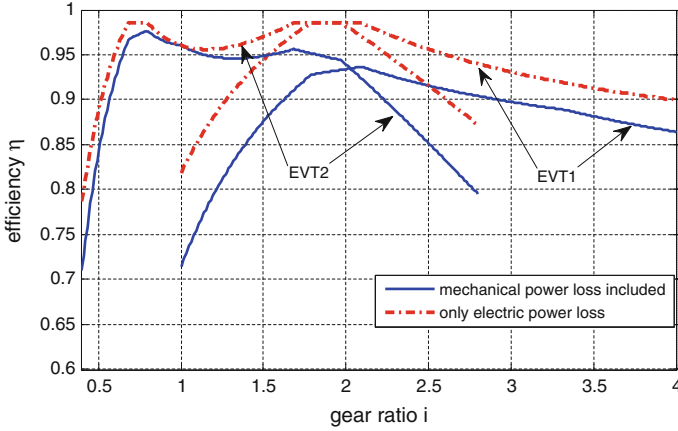


Fig. 4 Efficiency of coupling system with the change of transmission ratio

$$\varphi_a = \frac{1 + k_1 + k_2}{1 + k_1} \left| \rho_T - \frac{k_2}{1 + k_2} \right| \left| \frac{1}{i_c} - \frac{1 + k_2}{1 + k_1 + k_2} \right| |1 - \eta_{\text{elea}}| \quad (15)$$

$$\varphi_b = \frac{k_2}{1 + k_1} \left| \frac{1}{i_c} - \frac{1 + k_2}{k_2} \right| \left| \rho_T - \frac{1 + k_1 + k_2}{1 + k_2} \right| |1 - \eta_{\text{eleb}}| \quad (16)$$

where, $i_c = \frac{n_i}{n_o}$, transmission ratio of the coupling mechanism; η_p is meshing efficiency of the planetary gear; $\eta_{\text{elea}} = \eta_a^{-\text{sign}(n_a \cdot T_a)}$, $\eta_{\text{eleb}} = \eta_b^{-\text{sign}(n_b \cdot T_b)}$, respectively for the efficiency of motor A and motor B. Motor A and B can work in four quadrants.

Figure 4 shows the efficiency of coupling system with the change of transmission ratio, when battery pack charging at certain power. Figure 5 is the comparison between mechanical and electrical power at the same battery pack charging power. According to the figure, the efficiency of the coupling mechanism at mechanical points is less than 100 % even ignore the power loss of meshing in the planetary gear. This is due to the battery pack is charging, the power of the two motors cannot simultaneously be zero. Therefore there must be electrical power loss. The electric power loss coefficient remain unchanged within a certain region near the mechanical points, mainly due to the motor A and motor B work as generators in this region, charging the battery pack together. Other conditions, two motor as a generator and a motor, the difference of two motor power charging the battery pack. Whether the battery pack charge or discharge has litter effect on the mechanical power loss. As part of the engine power convert into electrical power to change the battery pack by the motor, in EVT1 mode the total power through the third planetary line is smaller, which make a smaller mechanical power loss. Thus, it can be inferred that when the battery pack discharge, EVT1 mode mechanical power loss is larger.

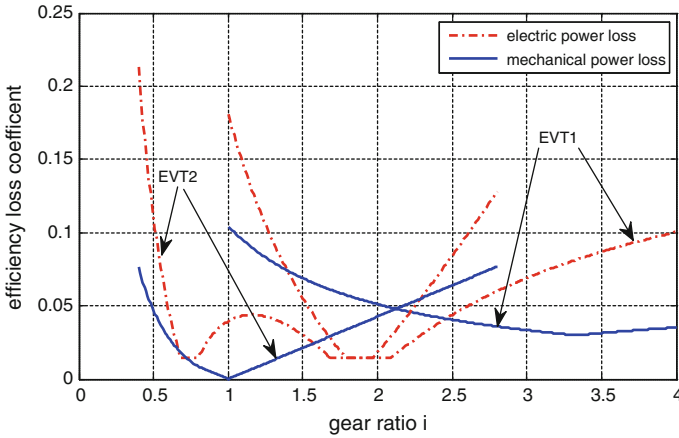


Fig. 5 Comparison between mechanical and electrical power when battery pack charging

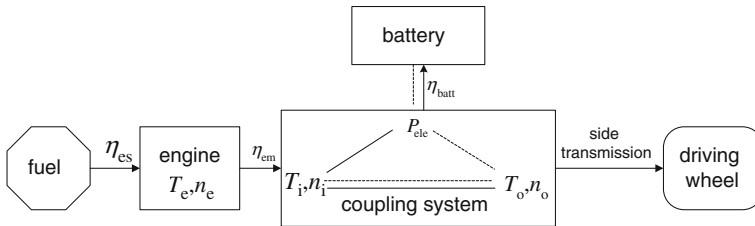


Fig. 6 Dual-mode hybrid system power flow transmission route

3 Overall Efficiency of Hybrid System

In the hybrid system, the coupling system efficiency is part of the efficiency of overall system. To measure the overall efficiency of the system also need to consider the loss of the power of the engine and battery pack. Engine fuel conversion power loss accounts for the main part. So we can change the operating point of the engine by change the status of the motor in the coupling mechanism. Thereby the engine fuel conversion efficiency can be improved. So the overall efficiency of the hybrid system can achieve optimal through appropriate matching control. The dual-mode hybrid system power transfer relationship shown in Fig. 6.

Among them, η_{es} is the conversion efficiency of fuel to the engine power, related to the engine operating points, which can be obtained from the engine universal characteristics. η_{em} is the ratio of effective power of the engine used to drive the vehicle and the engine mechanical power. Part of the consumption of the engine mechanical power losses in the intake and exhaust system, air filter, etc.

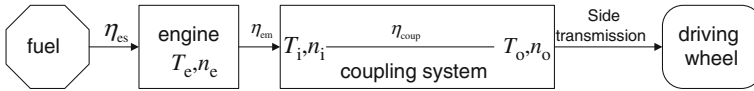


Fig. 7 Transmission route power flow of the hybrid system when the battery pack does not work

Another part is used to drive auxiliary equipment, such as pumps, water pumps, etc. in addition, if there is front drive between engine and coupling system, the power loss is contained in it.

There are two conditions to be discussed. One is that the battery pack does not work, where $P_{ele} = 0$; the other is when the battery pack participate in the work, where $P_{ele} \neq 0$.

1. $P_{ele} = 0$

The dual-mode hybrid system power flow in transmission line can be simplified as shown in Fig. 7.

The overall efficiency of the system:

$$\eta_z = \eta_{es}\eta_{em}\eta_{coup} \tag{17}$$

η_{coup} is the efficiency of the coupling mechanism, refer to the formula (5) to calculate. η_{em} can be considered as a fixed value which has litter relationship with the engine operating state. η_{es} is related to the engine operating point, so the speed and torque of the engine should be firstly determined. Use the engine speed as the known conditions, to determine the engine power by (18), then, the engine torque can be obtained. By checking the engine universal characteristic table can get the current operating point of the engine fuel conversion efficiency.

$$P_e = \frac{P_o}{\eta_{em}\eta_{coup}} \tag{18}$$

Take the scheme showed in Fig. 1 as an example, at a certain output power, with different output speed and engine speed, the system efficiency variation shown in Fig. 8. Engine fuel conversion efficiency and the efficiency of the coupling mechanism variation are showed in Fig. 9. It can be seen from the figure that engine fuel conversion efficiency has large impact on the overall efficiency of the system. Therefore in some study on the hybrid vehicle control strategy, they use engine operating point for the optimal object. The speed torque relationship of the coupling mechanism planetary gear constraints the operating point of the engine. Too small or too large transmission ratio will has a significant effect on the overall efficiency of the system. The efficiency distribution law of the coupling system is different from that of the engine fuel conversion; therefore both the efficiency of the coupling mechanism and the engine fuel conversion efficiency need to be considered.

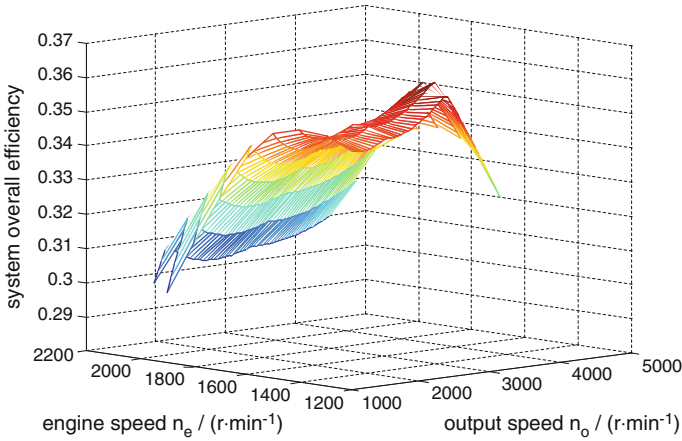


Fig. 8 System overall efficiency variation

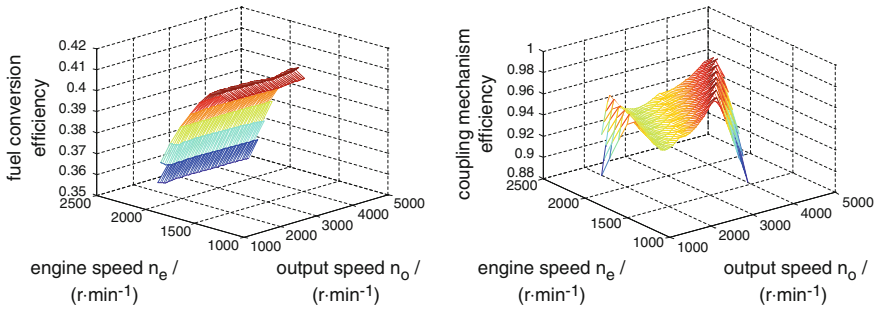


Fig. 9 Engine fuel conversion efficiency and coupling mechanism efficiency variation

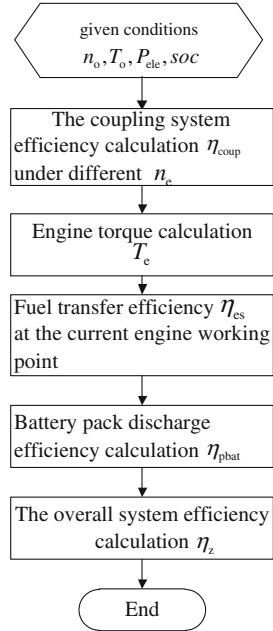
2. $P_{ele} \neq 0$

When $P_{ele} > 0$, the battery pack discharges, and works as a driving force. There are two power sources, the engine and battery pack. The dotted line in Fig. 6 shows its power flow direction;

When $P_{ele} < 0$, the battery pack charges and works as the load. At this time the system has only one power source—the engine, and the solid line in Fig 6 shows its power flow direction. The overall efficiency of the Electrical–Mechanical compound transmission system can be expressed as follows:

$$\eta_z = \begin{cases} \frac{P_e \eta_{em} + P_{ele}}{P_e + P_{ele}} \eta_{coup} & \text{when } P_{ele} > 0 \\ \frac{P_o - P_{ele} \eta_{pbat}}{P_e} \eta_{es} & \text{when } P_{ele} \leq 0 \end{cases} \quad (19)$$

Fig. 10 The calculation process of the efficiency of the hybrid system



As can be seen from the above definition, when $P_{ele} \leq 0$, the definition of the overall system efficiency is consistent with the case of $P_{ele} = 0$. Figure 10 shows the system efficiency calculation process.

The coupling efficiency η_{coup} can be calculated by the formula (5), and the engine power is determine by the formula (20).

$$P_e = \begin{cases} \frac{P_o - P_{ele}}{\eta_{coup}\eta_{em}} & \text{when } P_{ele} > 0 \\ \frac{P_o}{\eta_{coup}\eta_{em}} - \frac{P_{ele}}{\eta_{em}} & \text{when } P_{ele} \leq 0 \end{cases} \quad (20)$$

The engine output torque can be derived from the engine power and engine speed. As soon as the working point of the engine is determined, the fuel conversion efficiency can be obtained by look-up table in this operating point, and the battery pack discharge efficiency is determined by its SOC and charge–discharge power. Thus, the overall efficiency of the system can be calculated.

Take the program of Fig. 1 for example, at a certain output power and SOC, set the battery pack charge- discharge power to 50, 100, −50, and −100 kW, respectively. The overall system efficiency variation under different output speed and engine speed is shown in Fig. 11.

Figure 11 shows the battery pack charge–discharge power has some effect on system efficiency, but the general trend doesn't change much. In order to further observe how the battery pack charge–discharge power affects the efficiency of the overall system efficiency, the two-dimensional curves at the engine speed 1,300, 1,500, 1,700, 1,900 and 2,100 r/min are extracted from the above

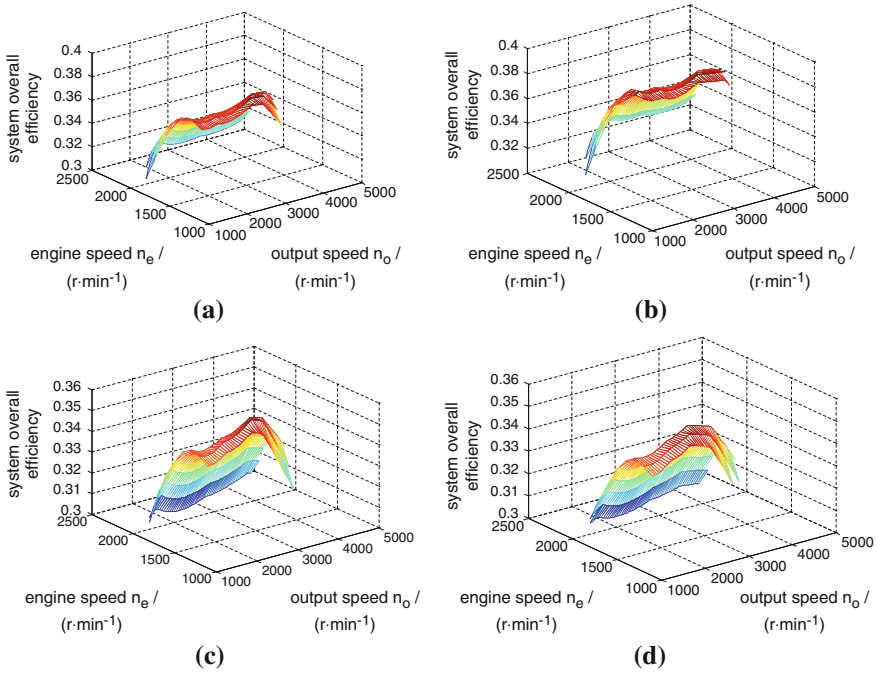


Fig. 11 The overall system efficiency variation under different charge–discharge battery power, **a** $P_{ele} = 50$, **b** $P_{ele} = 100$, **c** $P_{ele} = -50$, **d** $P_{ele} = -100$ kW

three-dimensional curve, as shown in Fig. 12. It can be seen that, as the battery pack changes from charge to discharge, and with the increase of the discharge power, the system efficiency showed an increase tendency.

When the output power is determined, the more electric power absorbed, the less the engine power required. Thus, the engine can run at a lower speed range. From the engine fuel conversion efficiency figure, it can easily be seen that the engine fuel conversion efficiency is higher at a relatively low speed. Meanwhile, the above calculation result is achieved when the battery pack SOC is 0.6. At that time, the internal charge–discharge resistance of the battery pack is relatively small, the power loss is thus little, and the electric power loss has little effect on the system efficiency. With the changing of SOC, the effect of electric power loss on system efficiency will gradually become larger.

4 The Optimal Control Strategy Based on Optimal Efficiency of the Power Flow

The overall efficiency of the electrical–mechanical compound transmission system is not only related to vehicle speed, but also concerns engine speed, SOC,

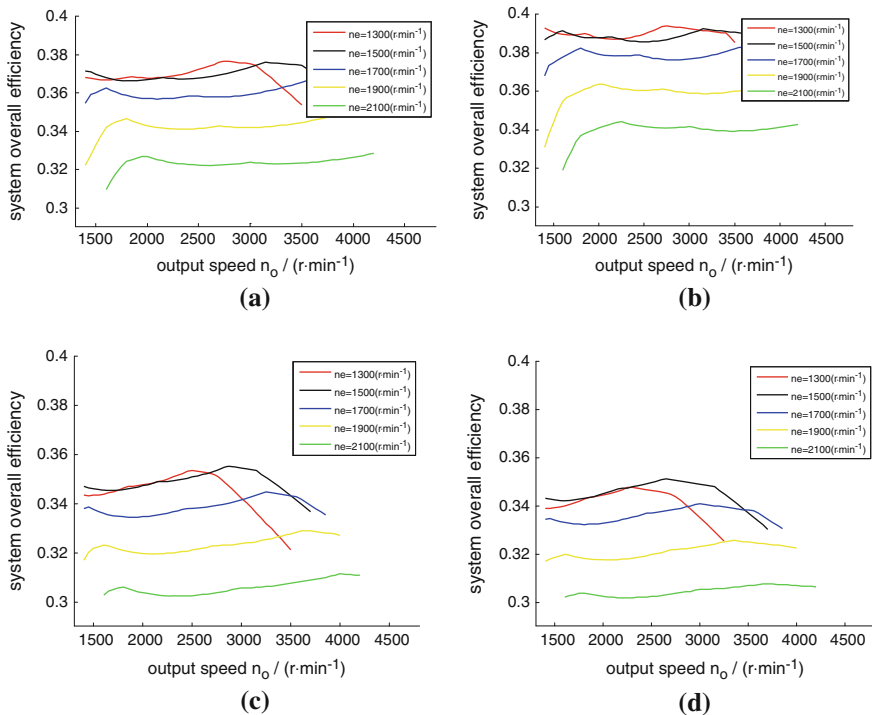


Fig. 12 The effect of the battery pack charge–discharge power and engine speed on the system efficiency, **a** $P_{ele} = 50$, **b** $P_{ele} = 100$, **c** $P_{ele} = -50$, **d** $P_{ele} = -100$ kW

demanded vehicle power, the battery pack charge–discharge power, and so on. The optimal control strategy based on the optimal efficiency of the power flow is aimed at the optimal system efficiency under different driving conditions. Among them, the speed is the feedback of the real-time vehicle state of motion; the SOC represents the estimation of the state of charge of the battery pack; the vehicle power demand shows the driver’s motivation, relating to the throttle angle and vehicle speed. When the driver’s operation and vehicle conditions are identified, these three figures are known, with only the engine speed and battery pack remaining that can be used for control and regulation, which affects the system efficiency to a relatively large extent. Based on the optimal system efficiency model, the engine speed and the battery pack charge–discharge power can be determined under the current conditions, and then the engine and the motor target operating point can be achieved, thus the control strategy targeting at the optimal system efficiency can be established. The optimal system efficiency shows as follows (Fig. 13).

Build the simulation model of the electrical–mechanical compound transmission system, and simulate under the above control strategy. The results show

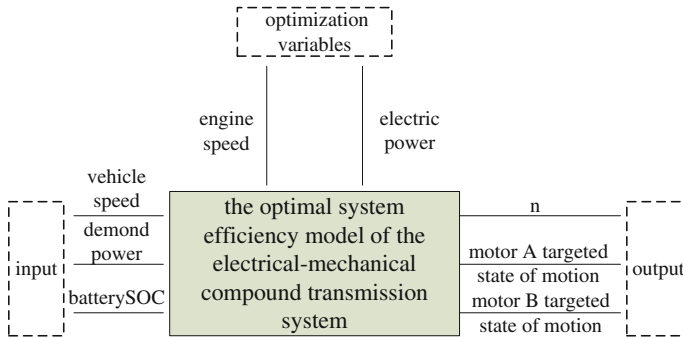


Fig. 13 The optimal control strategy based on the optimal efficiency of the power flow

that, compared with the rule-based control strategy, the vehicle fuel economy increased.

5 Conclusion

Unlike the traditional mechanical transmission system, the efficiency of the Electrical–Mechanical compound transmission system is more complex, since it is a typical multi-input multi-output system, and the input and output variables are also changeable. First of all, the definition of the coupling mechanism efficiency is put forward from the perspective of power loss between the input and the output, and the expressions of the efficiency of the coupling system, considering energy conversion power loss of the motor and the planetary gear meshing loss, are derived. Then the system efficiency is further explored considering the energy conversion loss between engine and battery pack, and the main factors affecting the overall efficiency of the system are studied. Fuel conversion efficiency of the engine plays a big role in that, whereas the coupling efficiency only affects the overall efficiency when the gear ratio is too large or too small. Thus, to achieve the optimal efficiency of the dual-mode hybrid system, we can change the distribution ratio of the power flow. On this basis, the optimal control strategy based on the optimal efficiency of the power flow was put forward, and the simulation results show that it not only improves the system efficiency, but also the vehicle fuel economy.

References

1. Miller JM, Everett M (2005) An assessment of ultra-capacitors as the power cache in Toyota THS-II, GM-Allision AHS-2 and Ford FHS hybrid propulsion systems[J]. IEEE 05: 481–490

2. Grewe TM, Conlon BM, Holmes AG (2007) Defining the general motors 2-mode hybrid transmission [C]. SAE Paper 2007-01-0273
3. Ahn K, Cho S, Lim W, et al. (2006) Performance analysis and parametric design of the dual-mode planetary gear hybrid powertrain [J]. *Automob Eng* 220(D): 1601–1614
4. Kim J, Kang J, Kim Y, et al. (2010) Design of power split transmission: design of dual mode power split transmission [J]. *Int J Automot Technol* 11(4): 565–571
5. Kang J, Choi W, Hong S, et al. (2011) Control strategy for dual-mode power split HEV considering transmission efficiency [J]. *IEEE*. doi: 978-1-61284-247-9
6. Mashadi B, Emadi SAM (2010) Dual-mode power-split transmission for hybrid electric vehicles [J]. *IEEE Trans Veh Technol* 59(7): 3223–3232
7. Liu J (2007) Modeling, configuration and control optimization of power-split hybrid vehicles [D]. University of Michigan, Ann Arbor, MI

Development of Commercial Hybrid Vehicle Automatic Transmission System

Chiaki Umemura, Kazumi Ogawa, Toshinori Murahashi
and Yasutoshi Yamada

Abstract As demands for a reduction in CO₂ emissions and higher vehicle fuel efficiency are escalating on a global scale, needs not only for passenger hybrid vehicles but also for commercial hybrid vehicles are arising accordingly. In 2008, we developed Automatic Transmission (AT) system with Hino Motors which was compatible with hybrid vehicle [1], therefore, this time, we developed a new hybrid front module containing a front clutch mechanism, which is intended to further optimize the hybrid AT system and capable of disconnecting the hybrid vehicle motor and the engine, to achieve better compatibility with the AT system.

Keywords Hybrid system · Commercial vehicle · Automatic transmission · Motor · Clutch

1 Overview of the System

The objective of this development is to realize a hybrid vehicle by adding a hybrid front module on a conventional AT of a diesel engine vehicle.

Followings are main development requirements.

- The hybrid front module should be as short as possible in a power line length to install the front module in-between an engine and AT.
- The front clutch should have sufficient reliability and durability to be used for a commercial vehicle application.

F2012-B02-040

C. Umemura (✉) · K. Ogawa · T. Murahashi · Y. Yamada
Aisin Seiki Co., Ltd, Kariya, Japan
e-mail: c-ummr@rd.aisin.co.jp

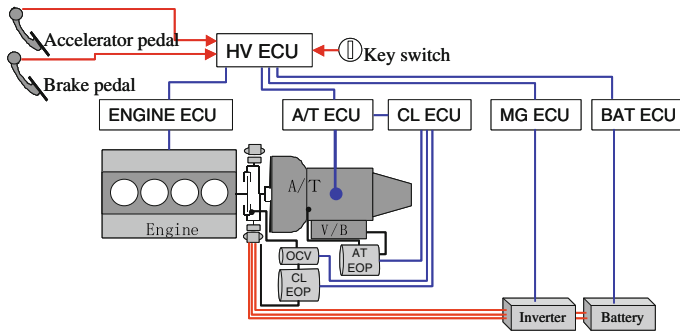


Fig. 1 System configuration diagram

- Engine idle stop function should be realized in Drive range without any specific operations.

The system configuration diagram is shown in Fig. 1, and a cross section of the unit is shown in Fig. 2.

1.1 Hybrid Front Module

We achieved a compact hybrid front module by reducing its overall length so that it is easy to mount on a vehicle. The key technology to the success of the compact module was the adoption of a multipole, concentrated-winding, thin type motor and a multiplate wet clutch system with high torque capacity.

1.1.1 Features of Motor

The characteristics required of the motor were (1) being capable of generating high torque in the low engine speed range with the characteristics of commercial diesel engines taken into account and (2) being a thin and compact structure due to the restriction on the overall length and made smaller in diameter while being capable of housing a clutch inside the motor. To fulfil these requirements, the relationship “Torque $\propto D^2 * L$ (D : inside diameter of stator, L : laminated thickness of the core)” must be considered, and it is desirable that the diameter of the motor be increased within the permissible mounting range. In addition, using a multipole motor is effective in achieving a motor with a small inside diameter because such a motor helps reduce the width of the stator and of the rotor back yoke. However, the maximum number of motor poles is restricted by issues relating to manufacture and the control frequency.

We consequently decided to adopt the configuration described below as a solution to these requirements. As the first step, we selected a permanent magnet

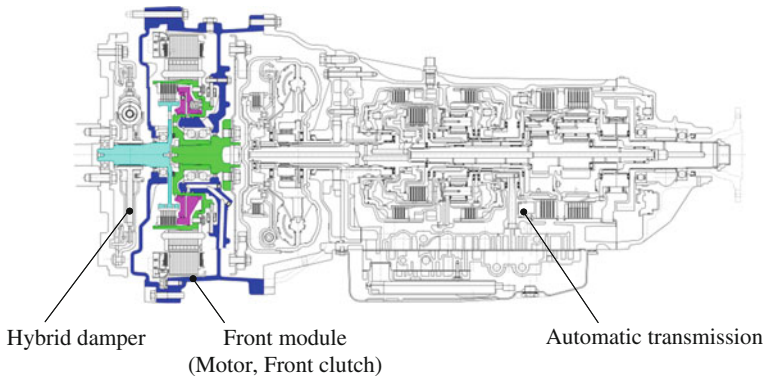
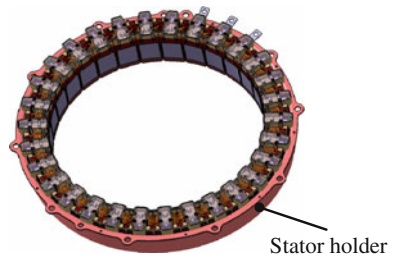


Fig. 2 Cross section of the unit

Fig. 3 Stator



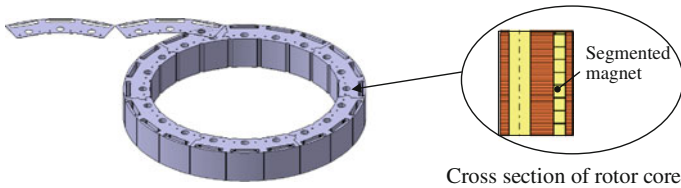
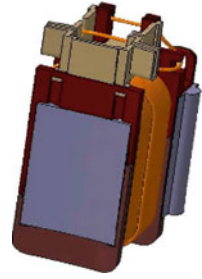
type motor, which was more compact than other types of motors in size, and a concentrated-winding type stator, which was effective for a thin shaft type motor with distinguished productivity. We applied a 20-pole 30-coil configuration to the motor with the motor control frequency taken into account. Concentrated-winding had superiority in the length of the coil ends but needed to be connected with a power feeding member. We, therefore, adopted a bus ring structure and succeeded in reducing thickness in the overall length direction by downsizing the coil ends.

Furthermore, cooling the motor by using oil inside the front module, the motor size became much compact than air-cooled type motor.

The stator is improved in manufacturability as a result of the adoption of a segmented core structure. The segmented type stator makes a greater contribution than integral type stator to a reduction both in material yield and in press equipment costs. In the winding process, stator teeth are regularly wound one by one, resulting in increase in the space factor. Individual stator teeth subassemblies are held and fixed by ring-shape stator holder. Inside diameter, accuracy, which is difficult to achieve in holding segmented cores, is kept at a high degree of accuracy by optimizing the process.

The stator is shown in Fig. 3. The stator teeth sub-assy is shown in Fig. 4.

The features of the motor rotor are described in the following sentences. The rotor adopted is an interior permanent magnet (IPM) type and characterized by a

Fig. 4 Stator teeth sub-assy**Fig. 5** Rotor core

flux barrier pattern magnet layout, which ensures superiority in the achievement of the rotor inside diameter. (Figure 5: Rotor core). And by segmenting the magnet into thin pieces along the rotor stacking direction, eddy current loss inside the magnet is largely reduced (Fig. 5: Cross section of the rotor core).

The rotor core we adopted is also of a segmented structure. This contributes to reduced material yield and reduced press equipment costs similarly to the stator core. In addition, this segmented core is punched from a steel strip with an arch-shape unit coupled, wound up in spiral form, and makes up the rotor core assembly.

The motor specifications are shown in Table 1.

1.1.2 Features of Front Clutch

To transmit high torque from a diesel engine, increase durability as commercial vehicle, and achieve compact mounting, a multiplate wet hydraulic clutch system is housed inside the aforementioned high torque, thin type motor. Normally closed type clutch is adopted to minimize the effect of a possible clutch system failure on the vehicle, and the multiplate wet clutch is kept ready to transmit torque at all times.

The clutch is disengaged mainly when the driver releases the accelerator pedal and the vehicle is decelerating, so that engine friction is disconnected and the amount of energy regenerated by the hybrid motor is increased compared to a

Table 1 Motor specifications

Item	Specification
Motor type	Permanent magnet type synchronous motor
Voltage	288 V
Maximum torque	350 Nm
Maximum output	36 kW

situation with the clutch engaged. This clutch system feeds pressure by means of an electric oil pump (EOP), and the clutch ECU keeps the clutch system in an optimum control state in concert with the AT ECU.

The front clutch disengaging time affects how much electric energy the motor can regenerate during motor regenerating braking, and the front clutch engaging time affects how quick vehicle can reaccelerate after a driver pushes the acceleration pedal from the motor regenerating braking during the front clutch disengaged.

Therefore, we targeted the front clutch disengaging time approximately 1.0 s, and engaging time approximately 0.5 s. To achieve the time requirements, following items are optimized: an oil passage from the EOP to a clutch oil chamber, a clutch piston shape, a check valve shape, an oil drain passage, and so on.

Figure 6 shows the front clutch cross section. When the EOP is turned off, the front clutch is engaged. To disengage the front clutch, the EOP is turned on and pumps the oil out of the front module. Next, the oil control valve is switched to clutch disengage side so that the oil is charged into the clutch chamber. Finally, the clutch piston is pressed to the right side, and the clutch is disengaged. To engage the clutch, EOP is turned off. Next, switch the oil control valve to clutch engage side so that the oil is drained from the clutch chamber through the check valve and oil drain passage. Finally, the clutch piston is back to the original position, and the clutch is engaged.

1.2 Automatic Transmission

Figure 7 shows the AT incorporated in the D range idle stop function.

A hydraulic pressure supply system assisted by an EOP is added to a six-speed AT for commercial vehicles, which covers a torque capacity up to 600 Nm, for the purpose of achieving the D range idle stop function, supplying oil to the clutch inside the AT when the vehicle is stopped (the engine is not running), and preventing a shock resulting from a delay in AT control hydraulic pressure rise when the vehicle restarts to run.

To minimize electric power consumption of the EOP, the oil is only supplied to the 1st gear clutch unit.

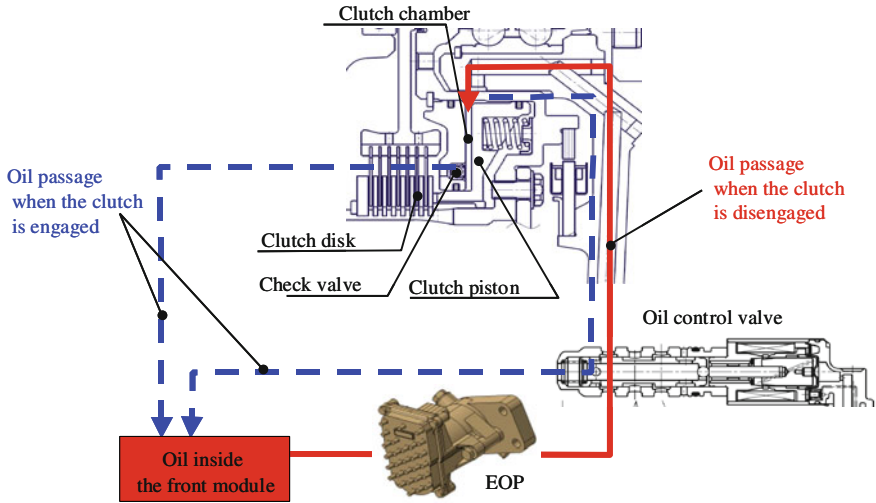
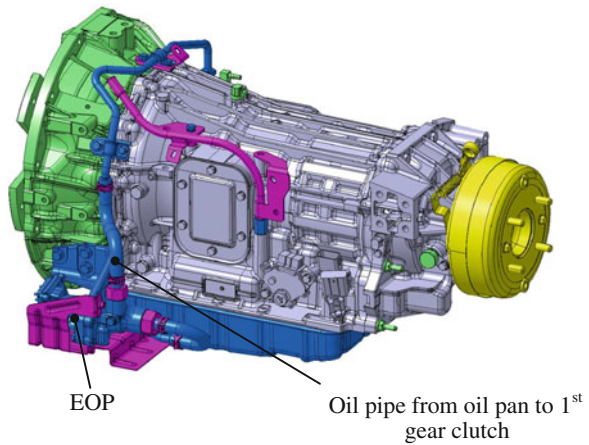


Fig. 6 Front clutch cross section

Fig. 7 Automatic transmission



1.3 Hybrid Damper

To improve the noise & vibration (NV) performance of drive train system as the main purpose, we newly developed a high-capacity hybrid damper capable of high torque of diesel engines for commercial vehicles at low engine speed by taking advantage of hybrid damper technology that is widely used for passenger vehicles on the market (shown in Fig. 8).

Fig. 8 Cross section of hybrid damper

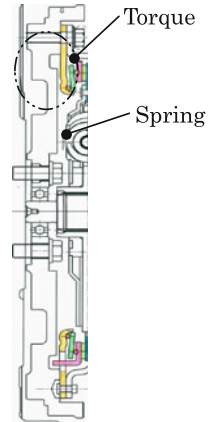
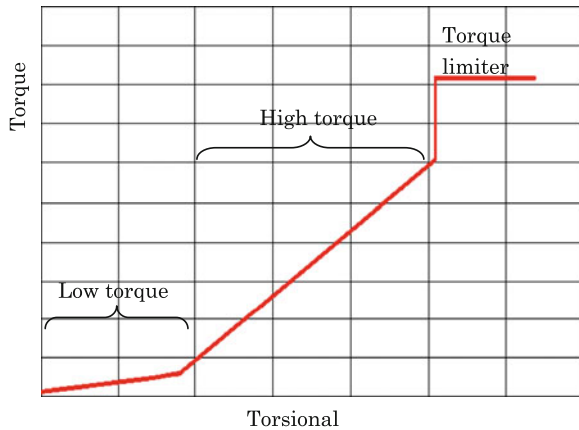


Fig. 9 Characteristics of hybrid damper



The main features of this damper are a large-capacity and long-life torque limiter which can cut excessively high input torque, and two-stage spring characteristics for vibration absorption in the low engine speed range and torque transmission in the high torque range (shown in Fig. 9).

2 System Control

To reaccelerate a vehicle quickly after a driver pushes the acceleration pedal from the motor regenerating braking during the front clutch disengaged, the front clutch, the engine, and the AT are cooperatively controlled.

The front clutch is controlled without using any sensors such as stroke sensor. Clutch disengagement control begins in response to an accelerator OFF signal, and the completion of clutch disengagement is determined based on the difference

Fig. 10 Front clutch time chart

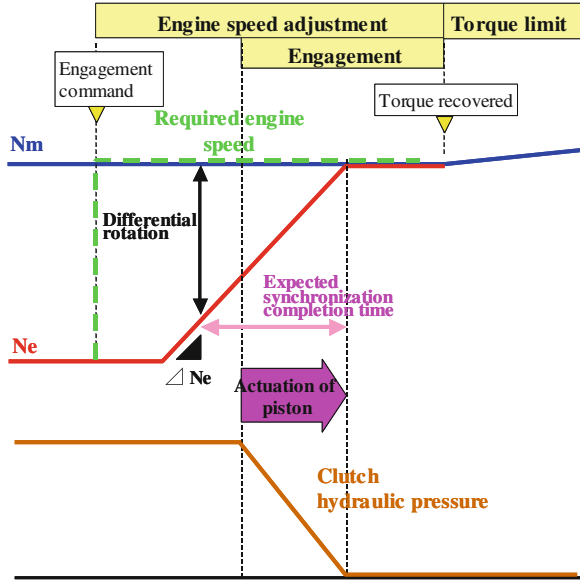
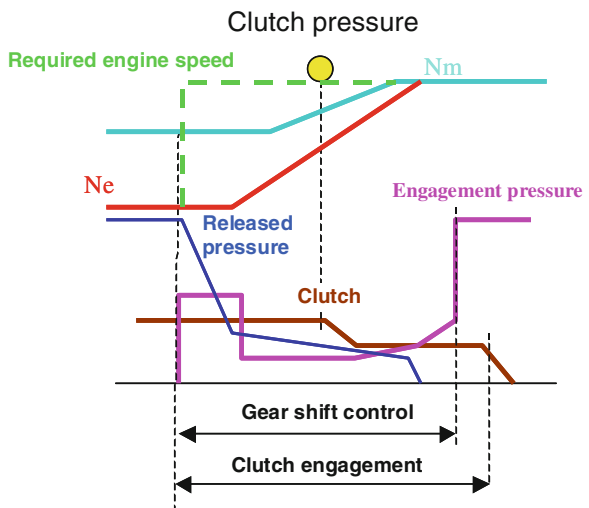


Fig. 11 Clutch control time chart accompanied by kick-down



between the engine speed and the motor speed. In clutch engagement, a command to increase the engine speed is output to the vehicle ECU to synchronize the engine speed with the motor speed, and, at the same time, a clutch engagement command is output through prediction of the time of the synchronization completion between the engine speed and the motor speed. Whether the clutch engagement is completed is determined based on the difference between the engine speed and the motor speed and by the timer (Fig. 10).

In rapid acceleration, front clutch engagement and an AT kick-down occur at the same time. In this case, these events are completed in a shorter time by outputting the aforementioned command to increase the engine speed based on the predicted engine speed after an AT gear shift (Fig. 11).

3 Conclusion

We developed successfully hybrid AT system with a front module that can easily make a conventional AT vehicle into a hybrid vehicle. By using this system, we will contribute to effective use of fossil fuel and reduction of green house gas emissions.

Reference

1. Simei M (2010) "Development of 6 speed automatic trans system for commercial hybrid vehicle," AISIN engineering report Vol. 14

A Dynamic Coordinated Control Strategy for Mode-Switch of Hybrid Electric Vehicle Based on the Effect Control

Na Zhang, Feng Zhao and Yugong Luo

Abstract Due to the shock caused by unstable transmission of power in the mode-switch process and the difficulty of obtaining engine torque in real time, a dynamic coordinated control strategy for mode-switch of hybrid electric vehicle based on the effect control is put forward. The control strategy of engine torque is designed, which is used to reduce the abrupt changes of engine torque by limiting its changing slope. Motor torque control strategy based on motor speed closed-loop is proposed, motor speed taken as feedback control variable is easy to be measured accurately in real time. It avoids the problem of inaccuracy engine torque estimation. A simulation model is built on the platform of Matlab/Simulink and AEMSim. The results show that the dynamic coordinated control strategy can make the fluctuation of motor speed and vehicle speed decreased and effectively improve the vehicle's ride comfort.

Keywords Hybrid electric vehicle · Mode-switch · Dynamic coordinated control · Effect control · United simulation

F2012-B02-043

National “863” High-tech Projects (2011AA11A208); Beijing Excellent Talent cultivation (2011D009004000001)

N. Zhang (✉) · F. Zhao · Y. Luo

State Key Laboratory of Automotive Safety and Energy, Tsinghua University,
Beijing 100084, China

e-mail: flygirlzn@163.com

1 Introduction

The engine and motor's dynamic characteristic is different, the clutch has its own feature, which will cause the torque fluctuation. It causes the shock of transmission components and the unstable power. So the ride comfort of vehicle becomes poor [1].

Aiming at this problem, Tong Yi [2] of Tsinghua university put forward a dynamic coordinated control method, that is, 'the open control of engine torque' + 'the estimate of engine dynamic torque estimate' + 'the compensation of motor torque'. But in practice, the method of online estimate engine torque can't meet the requirement of real-time, Ji Ercong [1] of Ji Lin university proposed a method, which is limiting the engine torque changing's slope and using the motor torque as compensation, but engine torque is difficult to obtain accurately in the method. Based on it, Yang Yang [3] of Chong Qing university control engine torque by PID algorithm and clutch by using the fuzzy control algorithm, but the method also need for engine torque in real-time, Toyota THS parallel-series system has peculiar planetary gear structure, with the compensation of motor ensures the smooth of mode-switch [4], but this approach is not commonly used.

This paper takes a hybrid electric vehicle as the research object. Aimed at the problems of mode-switch, the paper puts forward a dynamic coordinated control strategy based on the effect control. The control strategy sets the motor speed measured easily in real time as feedback, avoiding the accurate difficulty in accurate estimation in real time of engine torque. As a result, it reduces the shock of mode switch. At last, a united simulation platform is built by Matlab/Simulink and AMESim. The results show that the dynamic coordination control strategy effectively improves the ride comfort in mode-switch process.

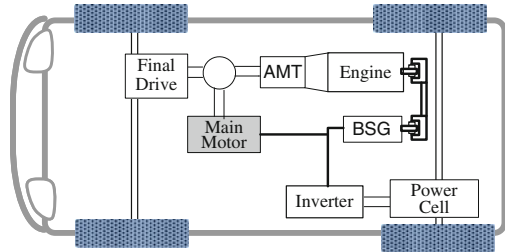
2 Object of Study

In this paper, a hybrid vehicle is the study object as shown in Fig. 1 [5]. The hybrid electric vehicle consists of the engine, the permanent magnet (PM), belt driven starter generator (BSG), automatic mechanical transmission (AMT) and the battery. Among them, PM is set in the back of AMT, and connected to final drive and vehicle wheel directly. BSG is connected to the front end of the engine.

3 Dynamic Coordinated Control Strategy for Mode-Switch

As shown in Fig. 1, the driving modes can be divided into pure electric mode and engine drive mode two categories in the hybrid system. Before formulating dynamic strategy coordinated control, we analysis the process of switching between the two modes.

Fig. 1 The structure of hybrid electric vehicle



3.1 The Problem Analysis of Mode-Switch

For the research object of the hybrid system, the process from pure electric mode change to engine driven mode includes two processes, the engine start process and clutch engaging process. Engine start process is finished by BSG. During the process, the clutch is completely cut off, which will not affect vehicle ride performance. But in the clutch engaging process, because the difference of dynamic response between engine and motor and the influence of clutch own characteristic, it will cause the fluctuation of the synthetic torque which leads the transmission of power unsmooth to influence the vehicle ride comfort. From engine driven mode to pure electric mode, due to disconnection of the clutch, it will cause the impact to influence the vehicle ride comfort.

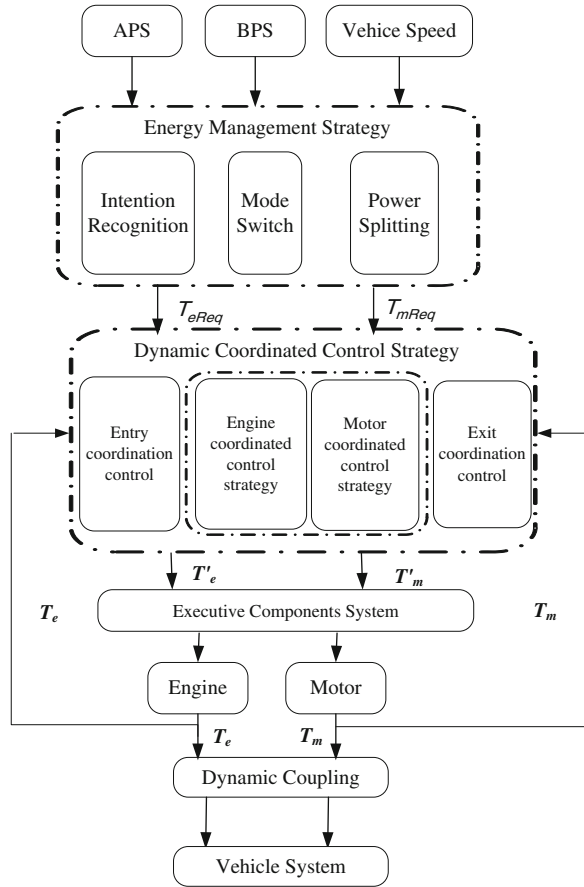
3.2 The General Structure Of Dynamic Coordination Control Strategy for Mode-Switch

In order to solve these problems, this paper designs the general structure of dynamic coordination control strategy for mode-switch as shown in Fig. 2. It includes driver operation input, energy management strategy, dynamic coordination control strategy, executive components system and vehicle system. This paper has made concrete analysis for dynamic coordination control strategy.

As is shown in Fig. 2, T_{eReq} and T_{mReq} are demand torque of engine and motor formulated by energy management strategy. T'_e and T'_m are command torque of engine and motor formulated by dynamic coordinated control strategy. T_e and T_m are actual torque of engine and motor. ω_i is the actual speed of motor.

The dynamic coordinated control strategy includes entry coordinated control, engine torque control strategy based on slope limit, motor torque control strategy based on speed loop and exit coordinated control four parts. Among them, entry and exit coordinated control are used to judge if the coordinated control strategy will be conducted. Engine torque and motor torque are controlled by engine torque control strategy based on slope limit and motor torque control strategy based on speed loop.

Fig. 2 The general structure of dynamic coordination control strategy for mode-switch



3.3 The Dynamic Coordination Control Strategy for Mode-Switch Based on the Effect Control

From engine driven mode to pure electric mode and from pure electric mode to engine driven mode are discussed in this paper. The control principles and methods of the two processes are similar, only the entry and exit coordination strategies are different.

3.3.1 Entry Coordination Control Strategy

The entry coordination strategy includes the entry logic of two processes as described above.

(1) From pure electric mode to engine driven mode

When the hybrid electric vehicle is in engine driven mode in the present moment, and in pure electric mode in a previous control cycle, the hybrid system will entry into the coordination of mode-switch.

(2) From engine driven mode to pure electric mode

When the hybrid electric vehicle is in pure electric mode in the present moment, and in engine driven mode in a previous control cycle, the hybrid system will entry into the coordination of mode-switch.

When the vehicle don't meet for above conditions, the engine and motor will perform the demand torque of engine and motor formulated by energy management strategy.

3.3.2 Exit Coordination Control Strategy

The exit coordination strategy includes the exit logic of two processes as described above.

(1) From pure electric mode to engine driven mode

When the hybrid system is in engine driven mode, the clutch is engaged and the difference between actual torque of engine and the demand torque formulated by energy management strategy is in a certain range, it will exit the coordination control strategy.

(2) From engine driven mode to pure electric mode

When the actual torque of engine is less than idling torque, the clutch will be disengaged, and sometimes later it will exit the coordination control strategy.

3.3.3 Engine Torque Control Strategy Based on Slope Limit

The basic principle of engine torque control strategy about the two processes described previously is similar. It reduce the impact of engine torque mutations by limiting change rate of engine torque.

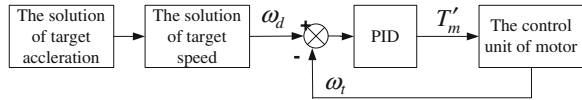
(1) From pure electric mode to engine driven mode

In the process, engine command torque is designed as shown in formula (1).

$$T_e' = \text{Min}(K_1 t, T_{er}) \quad (1)$$

In formula (1), K_1 is scaling factor, t is the cumulative occurrence time from pure electric mode to engine drive mode.

Fig. 3 The motor torque control strategy based on the closed-loop of motor speed



(2) From engine driven mode to pure electric mode

In the process, engine command torque is designed as shown in formula (2).

$$T'_e = \text{Min}(T_0 - K_2t, T_{er}) \tag{2}$$

In formula (1), K_2 is scaling factor, t is the cumulative occurrence time from engine drive mode to pure electric mode and T_0 is engine torque when mode-switch happens.

3.3.4 Motor Torque Control Strategy Based on the Closed-Loop of Motor Speed

The control principles and methods of the two processes are similar about motor torque control strategy.

This paper supposes road adhesive condition is good, the relationship of motor speed and vehicle speed is:

$$n_{pm} = \frac{60 \cdot i_{fd} \cdot v}{2 \cdot \pi \cdot r} \tag{3}$$

In formula (3), n_{pm} is the motor speed, v is the vehicle speed, r is the wheel radius, and i_{fd} is the ratio of reduction final drive.

The fundamental purpose of the coordination control is to avoid the shock of mode-switch by reduce vehicle speed. According to formula (3), the change of motor speed can reflect the change of vehicle speed in this hybrid electric system. So, the vehicle comfort can be improved by the control of motor speed measured easily to reduce the fluctuation of vehicle speed.

The process of mode-switch in hybrid system is short. Driver's driving intention is the same. In other words, the vehicle acceleration is not changed during the process.

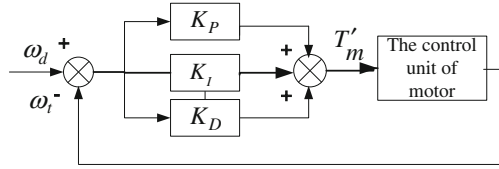
According to the above opinions, this paper proposed the motor torque control strategy based on the closed-loop of motor speed as shown in Fig. 3.

In Fig. 3, ω_d is the target motor speed.

Firstly, the target angle acceleration α_d is the average angular acceleration of motor before n control cycle when mode-switch happens. The formula is shown as follows in detail.

$$\alpha_d = \frac{1}{n} \left(\frac{(\omega_t - \omega_{t-1})}{\Delta t} + \frac{(\omega_{t-1} - \omega_{t-2})}{\Delta t} + \dots + \frac{(\omega_{t-(n-1)} - \omega_{t-n})}{\Delta t} \right) \tag{4}$$

Fig. 4 The PID control algorithm of motor torque



In formula (4), ω_t is the real speed of motor when mode-switch happens, ω_{t-1} is the real speed of motor before a control cycle when mode-switch happens, ω_{t-n} is the real speed of motor before n control cycle when mode-switch happens, and Δt is control cycle.

Secondly, the motor acceleration remains unchanged in mode-switch process. According to formula (4), the target speed of motor is solved.

$$\omega_d = \omega_t + \alpha t \tag{5}$$

Finally, as shown in Fig. 4, taking the difference of target speed and real speed of motor as input and the motor torque output, the PID control algorithm can make the motor speed and vehicle speed stable so that the shock of mode-switch process is reduced.

In Fig. 5, K_P , K_I and K_D are respectively proportion link parameters, integrator parameters and differential link parameters.

The transfer function about the PID control algorithm of motor torque is shown as follows:

$$G(s) = K_p + \frac{K_I}{s} + K_D \cdot s \tag{6}$$

4 Simulation Results and Analysis

Aimed to the strategy proposed in this paper, a simulation model is built on the united platform of Matlab/Simulink and AEMSim to do simulation validation.

4.1 The Frame of United Simulation Platform

The united simulation model based on Matlab/Simulink and AEMSim is shown as follows.

In Matlab/Simulink, there are driver model [6], energy management strategy model, dynamic coordinated control strategy model and s-function model. In AMESim, there are engine model, motor model, BSG model, limited torque clutch model, reduction final drive model, vehicle model and Interface model.

AMESim has rich model base, the user can built custom module or simulation model with actual physical system. It adopted complex interface to make model

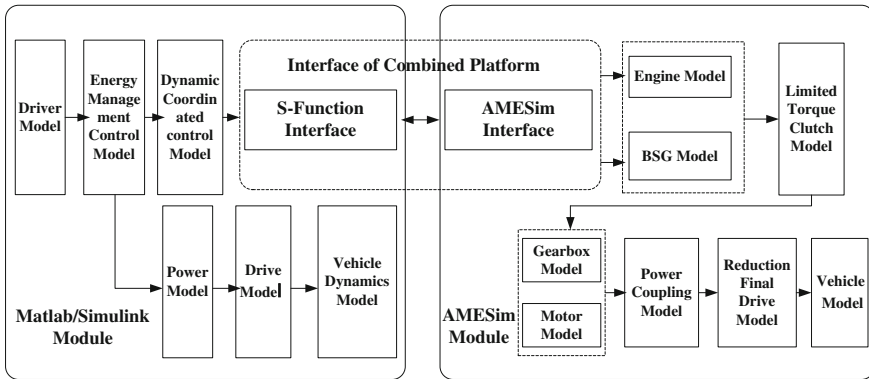
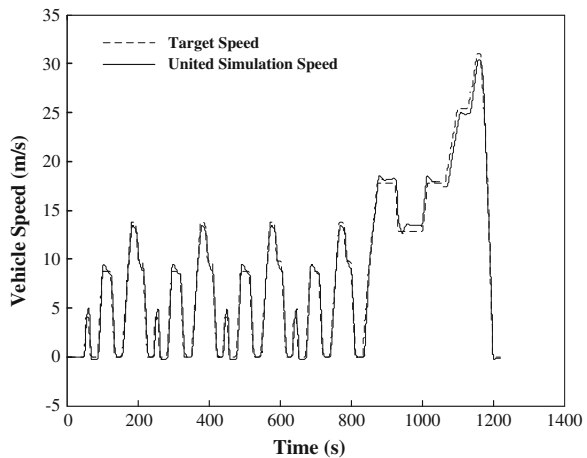


Fig. 5 The Frame diagram of united platform

Fig. 6 The simulation result of united simulation platform



simple. It uses the intelligent model scale to choose the most effective calculation method for the high precision and stability of the simulation results. Simulink can take the advantage of MATLAB’s numerical computation ability and building model on control system. A simulation model is built on the united platform of Matlab/Simulink and AEMSim [7, 8] with the advantage of two sets software in the numerical computation and building control system.

The NEDC driving cycles is used to verify the united platform. The Fig. 6 is the simulation result.

Form the Fig. 6, the trend of united simulation speed is consistent of target speed in the whole cycle. The maximum error is within 8 %. The result shows that the platform can be used to verify the control strategy.

Fig. 7 The contrast of united simulation vehicle speed

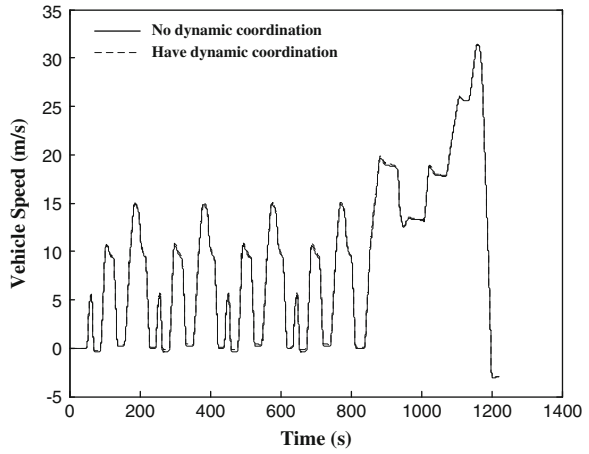
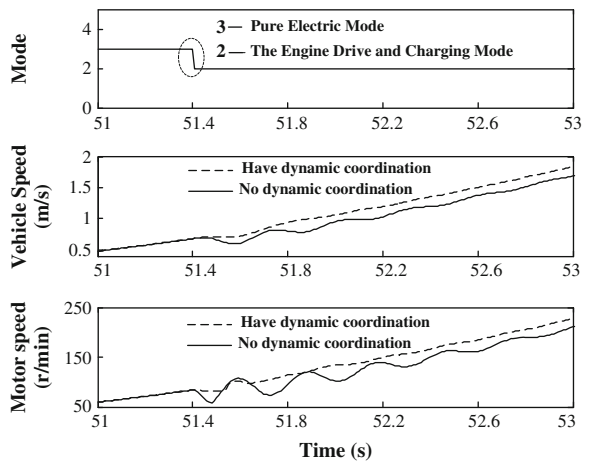


Fig. 8 Partial enlargement of mode-switch in 51.41 s



4.2 The Simulation Verify of Control Strategy

Using the NEDC driving cycles, this paper tests the correction of coordinated control strategy on the platform. The result is shown in Fig. 7.

There are 3 figures (Figs. 8, 9, 10) which are partial enlargements. So the control effect is seen clearly in these figures.

Fig. 9 Partial enlargement of mode-switch in 90.05 s

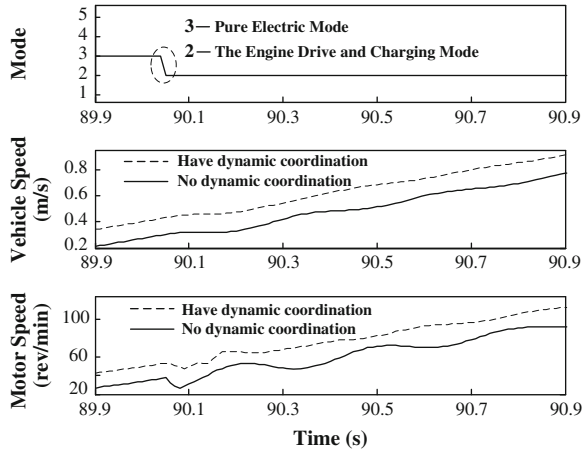
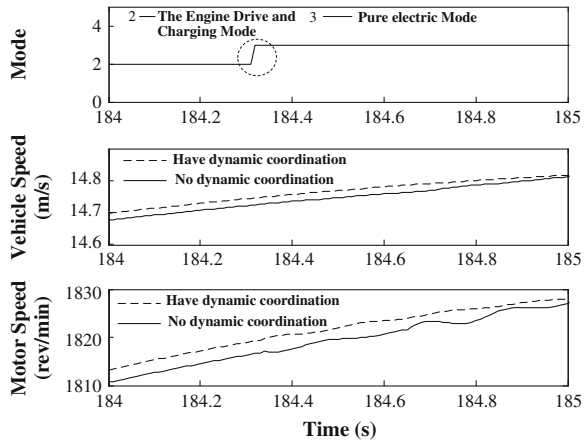


Fig. 10 Partial enlargement of mode-switch in 184.32 s



4.2.1 The result analysis of Mode-Switch from Pure Electric Mode to Engine Driven Mode

From Fig. 8, at 51.41 s, hybrid system changes from pure electric mode to engine driven mode. The fluctuation of motor speed reaches 51 rpm without the dynamic coordinated control, while the fluctuation of motor speed is only 22 rpm reduced by 42 % with the dynamic coordinated control in mode-switch process. From the results, we can see that the proposed strategy can reduce the fluctuation of motor speed and vehicle speed in mode-switch process and improve the vehicle’s ride comfort.

In Fig. 9, hybrid system changes from pure electric mode to engine driven mode at 90.05 s. In the process, the fluctuation of motor speed reaches 26 rpm without the dynamic coordinated control, while the fluctuation of motor speed is

only 12 rpm reduced by 42 % with the dynamic coordinated control. We can see that the control strategy can reduce the shock of mode-switch process.

4.2.2 The Result Analysis of Mode-Switch from Engine Driven Mode to Pure Electric Mode

From Fig. 10, at 184.32 s, hybrid system changes from engine driven mode to pure electric mode. From the results, because of the rapid response of motor, the affection of vehicle's ride comfort is little without dynamic coordinated control. It is only 3 rpm. With the dynamic coordinated control, the motor speed is almost no fluctuations and the vehicle's ride comfort is further improved.

5 Last Word

This paper proposes a dynamic coordinated control strategy for mode-switch of hybrid electric vehicle based on the effect control. According to the research of this paper, we get the following conclusions:

- (1) The dynamic coordinated control strategy can reduce the shock of mode-switch by coordination control between engine and motor system, the smooth of vehicle is proved.
- (2) The dynamic coordinated control strategy takes the motor speed measured easily as feedback control variable. It avoids the difficulty of inaccuracy engine torque estimation.

References

1. Ji E (2006) Study on the coordinated control for mode-switch of parallel hybrid electric system. Ji Lin University
2. Tong Y, Ouyang M, Zhang J (2003) Real-time simulation and research on control algorithm of parallel hybrid electric vehicle. *Chiese J Mech Eng* 39(10):156–161
3. Yang Y, Wenhui Y, Datong Q, Zhihui D (2011) Coordinated torque control strategy for driving-mode-switch of strong hybrid electric vehicle. *J Chongqing Univ* 34(2):74–81
4. Douba M, Ng H, Larsen R (2001) Characterization and comparison of two hybrid electric vehicles(HEVs)-honda insight and toyota prius. In: SAE 2001-01-1335
5. Li K, Chen T, Luo Y (2009) A new concept of intelligent environmental friendly vehicle . China, CN200810223099, 2009.2.4(In Chinese)
6. Yifan D (2009) The control strategy for a new full hybrid powertrain structure. *Automot Eng* 31(10):919–923
7. Hu A (2006) The research of regenerative braking system based on AMESim-Simulink co-simulation. Ji Lin University
8. Jin L (2004) United simulation technique with AMESim and Matlab/Simulink [J]. *Inf command control syat simul technol* 26(5):62–64

‘Commercial Vehicle Electrification’ Challenges in Dimensioning and Integration in the Entire Vehicle

Winter Martin

Abstract Main topics are the development and build-up of an 18 ton hybrid truck with a parallel hybrid drive train. With this truck it is possible to drive up to 3 km in the pure electric driving mode. In this R&D Project, a hybrid truck has been developed with an integrated motor generator (IMG) including a clutch system for pure electric driving, a Li-Ion power battery, electrified traction voltage auxiliaries (steering pump, air compressor and climate compressor) and the cooling system for the new power components. The first part of the chapter shows a detailed system layout of the hybrid truck that has been developed. [Chapter 2](#) shows the developed simulation model which is used for the dimensioning and for detailed simulations of hybrid drive trains. A special focus has been laid upon the operation strategy of hybrid commercial vehicles. To gain high market shares for hybrid trucks, the total cost of ownership will be the main driver, so the development of affordable hybrid components (battery, traction system, auxiliaries) with high efficiency and the development of optimized overall hybrid vehicles systems has to be the short term objective.

Keywords Commercial vehicle · Hybrid · Total cost of ownership · Operation strategy · Electric auxiliaries

F2012-B02-054

W. Martin (✉)
Engineering Center Steyr, Magna Powertrain, Steyrerstrasse 32,
4300St. Valentin, Austria
e-mail: martin.winter@ecs.steyr.com

1 Introduction

One thing it commonly agreed upon is the fact that hybrid and electric vehicles will be an important part of future transportation. How long it will take that these technologies will gain a noticeable market share and how big this share will be, is heavily discussed by market analysts.

After the current hype of clean/green/blue technologies, what will be the real driver for these technologies? The only thing that can drive the hybrid and electric commercial vehicle market for a long time is a decrease of the total cost of ownership (TCO). Additional features like pure electric driving or electric power supply for trailer auxiliaries have further influence to decrease the TCO.

ECS has entered this market with the vision to provide full service hybrid and electrical commercial vehicle development and low volume production. One of these steps is the build-up of a hybrid commercial vehicle carried out with a holistic development process, starting from vehicle benchmarking, vehicle and component specification, design, and integration up to application and component production.

MAGNA Powertrain—ECS offers long term experience in truck development augmented with new technologies and the capability to bring the component and system prices down to more affordable values.

In the following chapters most of the example material is taken from ECS's R&D projects to provide a deep insight on the components and systems.

2 System Layout

For the R&D project “Hybrid Commercial Vehicle Demonstrator” a P2 parallel heavy duty hybrid truck solution was chosen targeted for local distribution and partly intercity transportation (Fig. 1).

As an additional feature, the possibility for pure electrical driving has been added. To achieve this target, an additional clutch between the ICE and the electric motor and electric auxiliaries are necessary. The electrification of the steering pump, the brake air compressor and the AC-compressor are implemented as prototype components.

For the cooling of the power electronics and the electric motor an additional cooling circuit is needed. For future high volume industrial implementation, the target has to be to include this cooling circuit into the low temperature cooling circuit of the ICE. All the inverters and the power distribution unit (HVDU) are concentrated into a so-called HV-box; which provides additional protection against water, dust and EMC (Fig. 2).

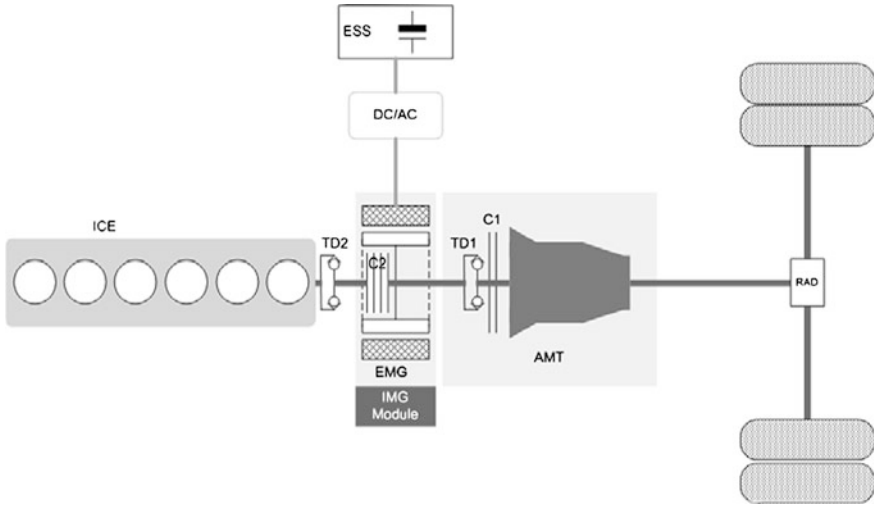


Fig. 1 P2 parallel hybrid architecture

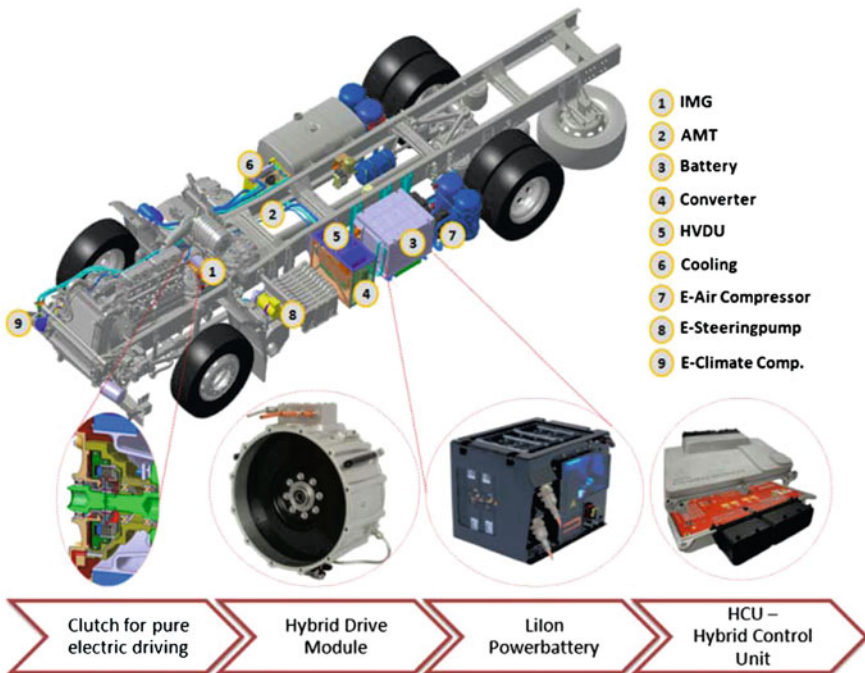


Fig. 2 Parallel hybrid system layout

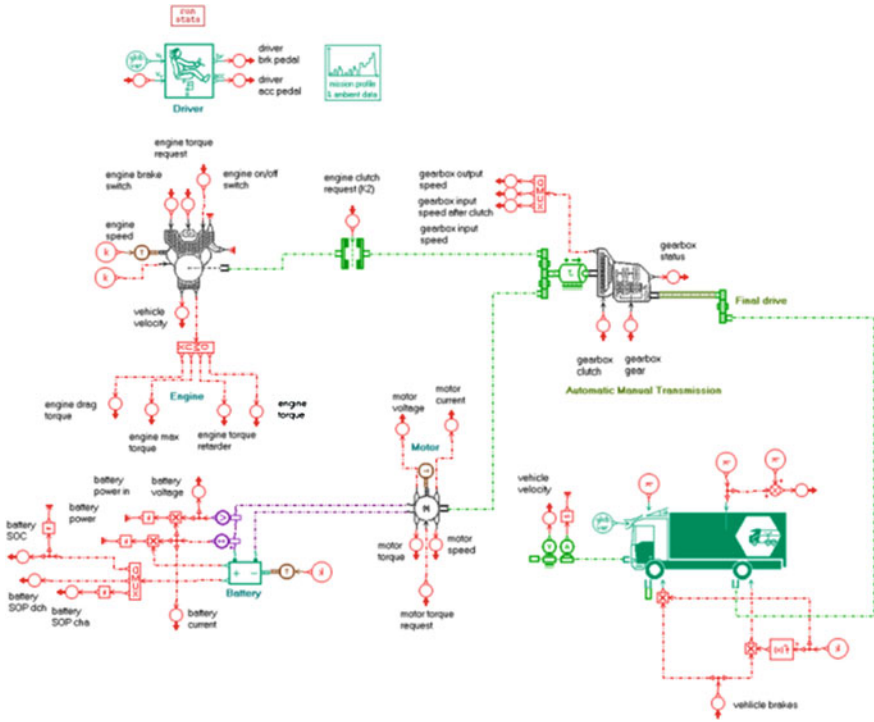


Fig. 3 Longitudinal simulation model

3 System Simulation

3.1 Longitudinal Dynamics Simulation

The vehicle dynamics’ simulation model is implemented in a multi physics simulation tool, see Fig. 3.

This model was used for simulation of energy management, fuel consumption analysis and also for detailed power train investigations. The engine model is implemented as a consumption map and the electric motor model consists mainly of an efficiency map.

In the beginning the implemented vehicle’s dynamic model and the fuel consumption results have been validated with measured data of the conventional vehicle. For the simulations, different driving cycles were applied, such as the HUDDS, the JE05 and a company specific city driving cycle.

3.2 Thermal Simulation

For the thermal management of the hybrid components an additional cooling package has been installed. The configuration of the engine cooling package is the same as for the conventional vehicle. The temperature level of the coolant at the exit of the traction motor of about 65 °C is mainly determined by the IMG's inverter. Besides the motor and power electronics the electrically driven auxiliaries (AC-compressor, power steering pump and brake air compressor) have been included in the coolant circuit. There are three parallel flow paths for the heat transport. The e-machine cooler has been arranged behind the battery cooler because the required temperature level for power electronics and e-machines is higher than that for the battery. One optimization target is an optimal distribution of the coolant flow through the individual paths according to the cooling demands. Therefore, maximum allowable temperature levels and temperature differences have been specified for all components. As the software KULI is capable of handling optimization runs with multiple optimization targets, these tasks have been done automatically.

To control the fluid inlet temperature level of the power battery in the range of 25–30 °C under all operating conditions, a rather complex thermal management system was implemented. The cooling system for the battery contains a coolant circuit and a refrigerant circuit. The refrigerant circuit was included in the battery cooling system to be able to maintain the required battery temperatures at high ambient temperatures. To avoid the installation of an additional refrigerant circuit, a dual-loop refrigerant circuit has been chosen by modifying the existing refrigerant circuit of the air conditioning of the driver's cabin. For the heat transfer from the coolant circuit to the refrigerant circuit a chiller has been integrated. Dual-loop refrigerant circuits are well known from passenger cars, e.g., for individual air conditioning of front and rear air zones. Using two expansion valves, the chiller and evaporator can be controlled individually. To reach the optimum temperature under cold conditions as soon as possible, a PTC heater has been installed. The heater warms up the coolant upstream of the battery, as long as the fluid temperature has not reached the desired level. That is why the fluid is pumped through the cooler bypass.

3.3 Co-Simulation Environment

To combine the longitudinal driving simulation and the thermal simulation, a co-simulation environment was applied. The master simulation program is Matlab/Simulink. Figure 4 shows that the thermal simulation model receives gets the values for the power loss results of the electric components (e.g., electric motor and battery) from the driving simulation.

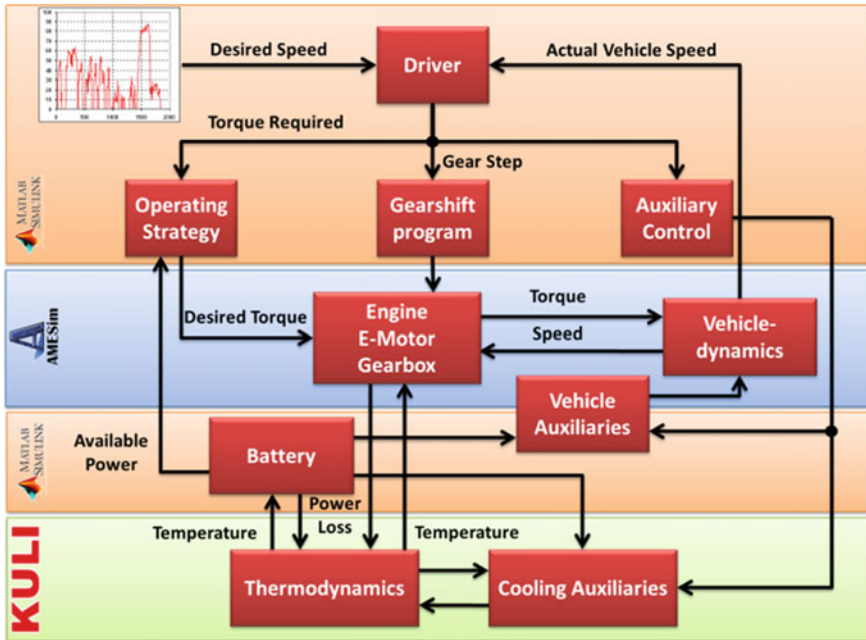


Fig. 4 Co-simulation environment

The output of the thermal simulations is the temperatures of the components and the power consumption of the cooling auxiliaries. The temperatures are monitored by the energy management in the hybrid control unit to keep the temperature limits of the parts. The power for the auxiliaries is provided by the battery which affects the fuel consumption to by the on demand control. To accelerate the simulation runs, different time steps for driving simulation and thermal simulation have been used. Due to the thermal inertia of the cooling system, the simulation time step size of the thermal simulation is much larger than that of the driving simulation.

4 Hybrid Components

Besides the energy storage system, the most evident hybrid components belonging to the drivetrain are the integrated motor generator (IMG) and the traction inverter.

The IMG contains the stator and rotor of the electric machine, the multidisc wet clutch and a CFD optimized water cooling circuit. The IMG is designed to work as a retrofit solution for the drivetrain, so there is no necessity to change the ICE or gearbox interface.

To get a rather short 3 phase connection of the IMG to the traction inverter, the HV-box is mounted as near as possible to the IMG, so that the cable losses and EMC are low.

Fig. 5 IMG module

The energy storage system consists of the battery pack, the supervision and control electronics, the safety battery disconnect unit and a fuse, which is implemented as a service disconnect as second functionality. The integrated water cooling circuit conditions the battery to the needed temperature range (Fig. 5).

Battery chemistry of the current Li-ion batteries is very sensitive to temperatures outside a range from 25 to 35 °C and lifetime will be reduced if it is massively used outside this range.

With the external conditioning circuit the battery is heated up with a heater at low ambient temperatures. At medium temperatures the cooling is done by a radiator and in hot conditions the battery is cooled with an additional chiller which is installed in the AC circuit of the driver's cab (Fig. 6).

For pure electric driving the three main auxiliaries were electrified. All three components (inverters for all three aggregates and also the 650–24 V DCDC-converter) are realized as prototypes. Simulation results have shown that the intelligent, on demand control of the components has the ability for further improvements of the vehicle's efficiency. Especially the ICE speed independent control of the steering pump has a high fuel consumption reduction potential. The influence of the break air compressor is rather low, but it could be used to recuperate breaking energy into the pneumatic circuit for later use. The analyses for the influence of the AC-compressor are ongoing.

For the control of the whole hybrid vehicle ECS has developed a new ECU called hybrid control unit (HCU). The function of the HCU is to integrate the hybrid system into the vehicle. Therefore, it is necessary to split the signalling of the original vehicle and incorporate the hybrid functionality into the messages of the original vehicle. Currently there are no special gearboxes, or brake management systems available, that are aware of the different hybrid possibilities. So the signal busses are split-up at the HCU and all relevant messages are modified and forwarded to their recipients. Especially the split-up of the communication

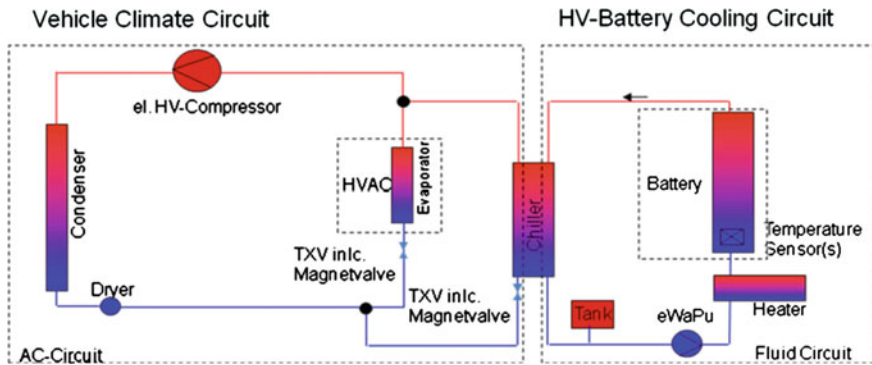


Fig. 6 Battery thermal conditioning system

between ICE and gearbox is necessary because the torque and speed information from the ICE would be incorrect in the most driving situations. The additional torque from the e-machine has to be added to the message reporting to the gearbox. For shifting operations the electric machine has to provide the requested speed or torque. In pure electric driving mode the messages from the ICE are missing completely, so the HCU has to generate the messages for the gearbox itself. The higher level functionality of the HCU mainly consists of the hybrid operating strategy and the dynamic management. Furthermore the HCU is also used for controlling the electric auxiliaries and the thermal management of the hybrid system (Fig. 7).

5 Operating Strategy for HCU

For the development of the operating strategy a plant model of the commercial vehicle was built up and calibrated with parameters and measurements of the original mule vehicle. The newly developed models for the battery, the IMG (e-machine, clutch), automated manual transmission and the auxiliaries were incorporated into the vehicle model. They can be used as a plant model for the operating strategy, dynamic management and all component control strategies for the vehicle. With this vehicle simulation model it is possible to develop control strategies which are optimized for the entire system, not only for a single component. Since the hybrid vehicle has much more parameters which can be influenced and a very complex energy storage system (dependent on: temperature, age, charge level ...), it is much more important to have a closed simulation loop.

The software on the HCU consists of two main parts. The basic software, which contains all hardware features of the HCU and the application software. Between these two parts an intermediate layer was introduced for easy AUTOSAR interfacing.

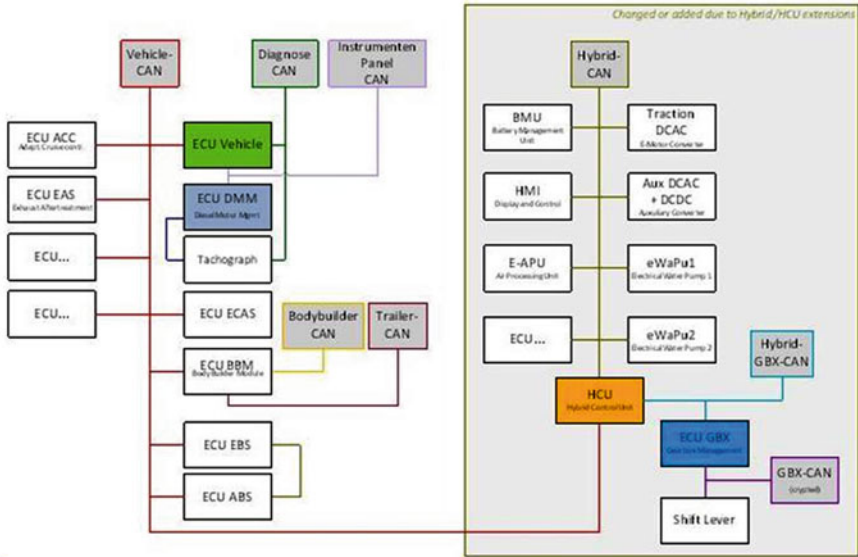


Fig. 7 Hybrid CAN-bus architecture

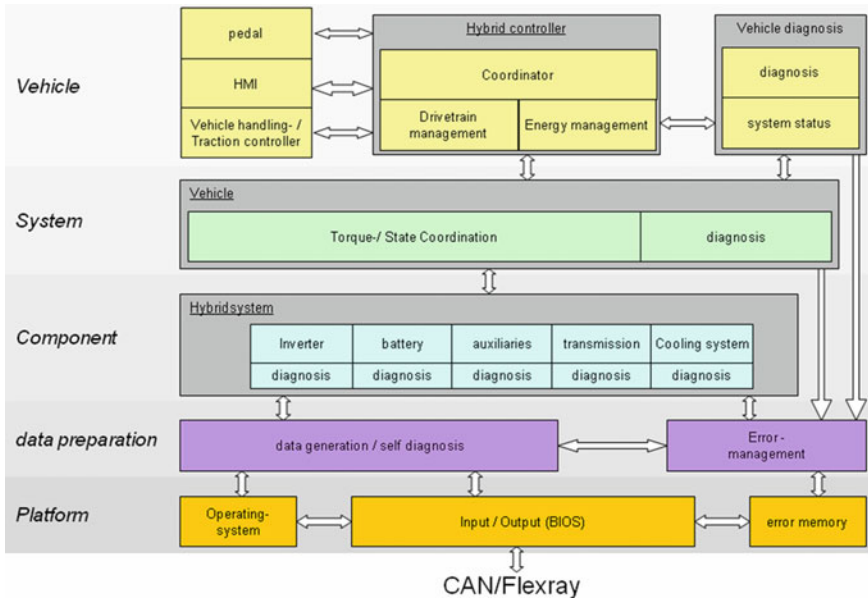


Fig. 8 Block diagram of HCU software

In the block diagram of the HCU software (Fig. 8) the 5 layers of the SW are shown. Layer 1 (platform) and 2 (data preparation) are mostly application independent. Layer 3 includes the component controllers of the system and the diagnosis of the components, where the actual component state is guarded (nominal state and actual state). On the system level, the torque coordination of the traction system is done.

On the vehicle level the operating strategy has been implemented, including upper level input handling, HMI and diagnosis.

Plug-In Hybrid Vehicle with a Lithium Iron Phosphate Battery Traction Type

Danut Gabriel Marinescu, Ion Tabacu, Florin Serban, Viorel Nicolae, Stefan Tabacu and Ionel Vieru

Abstract To promote in the academic environment the ways for reducing global warming produced by the Sport Utility Vehicles, the grand hamster—electric way 4WD concept has developed within the University of Pitesti. It is a Plug-in Hybrid Vehicle powered in electric/hybrid modes by a Lithium Iron Phosphate (LiFePO_4) traction battery technology, 205 V, 12 kWh. The concept is developed on the Dacia DUSTER crossover vehicle, 4 × 2 series version by implementing an electric propulsion system in the rear axle. The objective of this project is to realize a 4WD environmentally-friendly vehicle maintaining the leisure of driving the vehicle in the city using the continuously variable transmission (CVT) in the electric mode and the diesel motorization outside of the town in the thermal mode. The architecture is parallel type and E-4WD with a standard diesel engine 1,5 dCi FAP, 79 kW(107 bhp) and 6 speed manual gearbox in the front, and an asynchronous electric motor 31 kW (41 bhp) coupled with the reduction and differential gearbox unit at the rear. The traction battery is monitored by a battery monitor and charged by an embarked charger. The charging and discharging of the battery is authorized by the Battery Management System. The paper presents the firsts performances of the vehicle on the road tests.

Keywords Passenger car · Plug-in hybrid vehicle · Parallel HEV · Electricway-4WD · LiFePO_4 battery

F2012-B02-062

D. G. Marinescu (✉) · I. Tabacu · F. Serban · V. Nicolae · S. Tabacu · I. Vieru
Automotive Engineering Research Centre, University of Pitesti, Pitesti, Romania
e-mail: dan.marinescu@upit.ro

1 Introduction

The concept car GRAND HAMSTER—ELECTRIC WAY 4WD (Fig. 1) is developed within in the *Automotive Engineering* Research Centre from University of Pitesti in order to achieve an ecologic vehicle on the mechanical platform of the DACIA DUSTER crossover car. This car is produced by the Automobile Dacia—Group Renault, at their plant near the city of Pitesti.

The study is an academic attempt and has no connection with the projects or future car models of Dacia-Group Renault.

The following development objectives were established for this project in order to obtain a low cost ecologic crossover car:

- Reduction of pollutant emission under 115 g CO₂/km using a Plug-in Hybrid Electric Propulsion system *EcoMatic Hybrid System*, Diesel-Electric type, with the *ThermoSTAT*, preheating engine system;
- Automatic transmission comportment (Electric Continuously Variable Transmission type) behavior at low and mild speed when the vehicle runs in the electric mode, with speed under 80 km/h;
- Running 4 wheel drives part time using the PHEV architecture organised in motorized solution E-4WD;
- Cockpit ventilation and auxiliary battery (12 V) recharging by the Photovoltaic Panel placed on the roof.

2 Architecture of the Hybrid Vehicle

The architecture of the hybrid powertrain *EcoMatic Hybrid System (Energy conversion with auto Matic Hybrid System)* is a parallel system type, with torque addition and with two shafts. The organization of this hybrid propulsion equipment *Plug-in* type is done by dividing it in two parts, (motorized solution E- 4WD, Fig. 2): the diesel powertrain in the front side and the electric powertrain in the rear side.

The advantages of this design layout are:

- Simplification of the mechanical transmission by eliminating the additional device specific to the 4WD, that transfer the engine power to the rear axle;
- Capitalizing the all wheels drive (E-4WD, part time) in hybrid mode;
- Improved vehicle stability obtained by adequate control of the electric motor drive torque and regenerative braking torque;
- Shock reduction when changing the functioning mode (from the electric mode to the thermic mode and vice versa), due to the “elastic” link between the front and the rear wheels;
- Minimum changes upon the base vehicle DACIA DUSTER 4W2, which give us both the cost reduction of the functional model and the possibility of using it in the traffic, in order to perform the road tests.



Fig. 1 The GRAND HAMSTER ELECTRIC WAY 4WD concept car developed by University of Pitesti and based on the Dacia Duster car [1, 2]

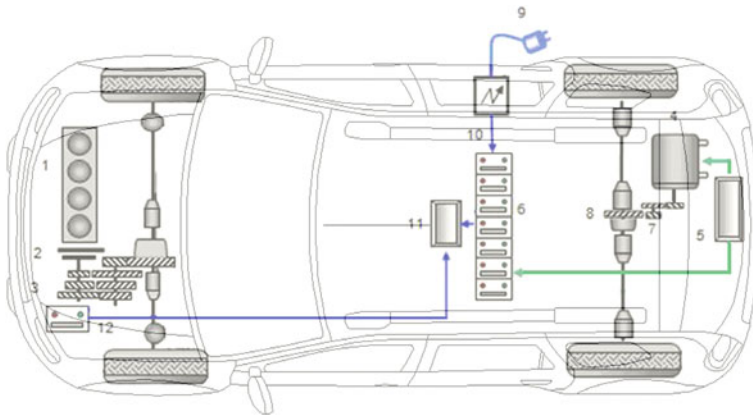


Fig. 2 Architecture of the GRAND HAMSTER—ELECTRICWAY 4WD : 1—Diesel Engine; 2—Automatic clutch; 3—Manual gearbox; 4—Electric Motor/Generator; 5—Control Motor; 6—HV Traction Battery; 7—Rear reductor; 8—Rear diferential; 9—220 V AC NET; 10—AC/DC Traction Battery Charger; 11—DC/DC Auxiliary Battery Charger; 12—12 V Auxiliary battery

3 Diesel Powertrain System

The diesel powertrain system of the GRAND HAMSTER E- 4WD include the standard diesel engine Renault 1,5 dCi FAP—K9 K THP 896, 1461 cmc, direct common rail with turbo compressor and intercooler. The performances are: 79 kW (107 bhp)@4000 rpm, 240 Nm @ 1750 rpm.

Fig. 3 The clutch decoupling device for improving regenerative braking



The driveline includes a friction clutch and the 6 manual gearbox. Similar to *GRAND SANDERO* concept [3] to increase the process of recuperating the energy in decelerating periods, after driving in thermal mode, a hydraulic system (in construction) decouples automatically the clutch (Fig. 3).

In the engine compartment (Fig. 4) was mounted an additional facility used for brake vacuum in the electric mode. It includes an electric pump fuelled at 12 V, 650 mm Hg and very low noise level assisted by a vacuum tank 2,5 liter and a switch sensor.

The throttle signal for the electric motor when the vehicle running in electric mod is provided by the throttle box resistive type (0–5 K ohm) potentiometer; it is placed also in the engine compartment and actuated by the throttle pedal by cable.

In order to enhance the reduction of the pollutants under 115 g/km CO₂ by avoiding as much as possible the cold starting of the diesel engine, it was designed the *ThermoSTAT* preheating system similar to the *HAMSTER* concept system [4]. This system has a thermal isolated chamber of 5 L volume, which contains the engine cooling liquid, resulted from the previous operation of the engine. It features a recirculation pump and an electromagnetic valves system, controlling the liquid flow to the engine and to the passenger compartment (if it is necessary). Moreover, one electrical heating resistance, fuelled with 240 V AC electricity from the network, runs during parking periods (when the vehicle is plugged-into charge the traction battery) or fuelled when necessary by the traction battery. A dedicated computer (in construction) controls the preheating of the liquid and the liquid flow to the engine or to the HVAC system of the passenger compartment, depending on the situation (Fig. 5).

Fig. 4 The engine compartment with the auxiliary new components: the electric vacuum pump and the electric motor throttle box



Fig. 5 The tank of the *ThermoSTAT*, the preheating engine system



4 Electric Powertrain System

Figure 6 shows the general scheme and the main component of the electric powertrain system of the GRAND HAMSTER ELECTRIC WAY 4WD: the electric drive system, the traction battery system, the recharging batteries system, the high voltage wiring circuit and the low voltage wiring circuit.

4.1 Electric Drive System

The electric drive system developed on the rear side of the vehicle (Fig. 7, left) is coupled on the new rear axle developed for this E 4WD concept.

The electric drive system includes an AC induction motor (asynchronous motor type), a mechanical transmission and a Traction Inverter Module.

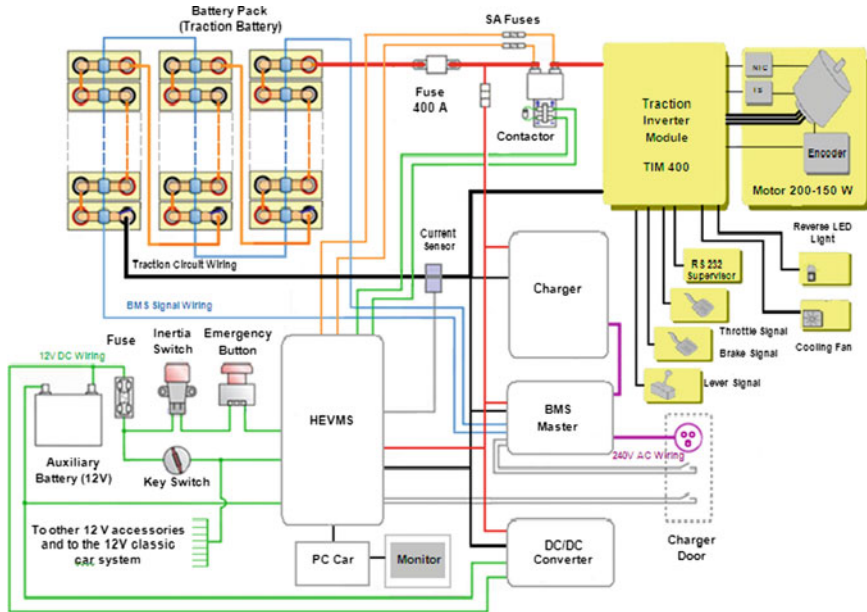


Fig. 6 The electric powertrain system of the GRAND HAMSTER E 4WD



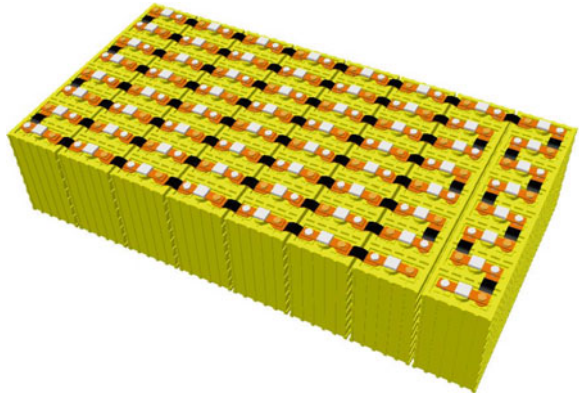
Fig. 7 The rear axle and the electric drive mounted on the frame in the rear side of the GRAND HAMSTER E 4WD

The electric motor, 200–150 W liquid cooled, made by MES SA—Swiss, provides a constant 18 kW (24.5 bhp), and has a peak output of 31 kW (42 bhp). It generates a constant torque of 90 Nm @ 2850 rpm, or a peak of 160 Nm @ 1400 rpm.

The mechanical transmission includes the reduction and differential gearbox unit and two new shafts with homokinetic joints.

The electric motor control is TIM (Traction Inverter Module) 400 type, an AC motor drive control designed by MES-SA—Swiss for electric and hybrid vehicles. The electric system was calibrated using the MES SA software, first on the experimental electric motor test bench and then on the vehicle roller test bench (Fig. 13).

Fig. 8 The 64 cells LYP 60 AHA arrangements in the compact traction battery pack. (CATIA modelling)



4.2 Traction Battery System

The Traction Battery System includes the battery pack, the Battery Management System and the Battery Monitor System.

The battery pack is Lithium Iron Phosphate (LiFePO_4) technology 205 V, 12 kWh. It has 64 modules LYP 60 AHA from *Winston*, PR China, coupled in series (Fig. 8). These cells are mechanical coupled with a special frame placed on the floor of the rear side of vehicle (Fig. 9).

The Battery Management System includes 64 BMC (Battery Management Cells) and a Management Control Unit MCU-EV2, provided by *EV Power Australia*.

The Battery Management Cell is an analogue cell module suitable for *Winston LFP60 AHA*. Connecting the signal output from the serial cell module and the master unit, we realized the protection to overcharge and over-discharge. The battery pack Master Unit monitors the signal of the cell modules and acts to prevent charging or discharging if the heartbeat signal is broken.

The Battery Monitor System includes the battery monitor, a gauge, a 500 A shunt resistor and a 10:1 pre-scaler. The battery monitor is an “e-xpert pro-hv” from *TBS Electronics Holland*. (Fig. 12). This e-xpert pro selectively displays the battery voltage, the charge and discharge current, the consumption, the remaining battery capacity and the time remaining.

This instrument monitors also the 12 V auxiliary battery of the car.

4.3 Recharging Batteries System

The recharging batteries system includes the charging traction battery circuit 240 VAC/205 VDC and the recharging auxiliary battery circuit 205 VDC/12 VDC.

The recharging traction battery circuit includes the on-board battery charger, the energy cost meter device, the inlet charge and the charging cable.



Fig. 9 The electric equipment components placed in the rear side of the vehicle: Traction battery (*in front*), the AC/DC battery charger (*vertical left*), DC/DC auxiliary battery charger (*left*); Traction Inverter Module, electric general contactor, manual connector (Anderson type) and the input energy cost meter (*right*)

Fig. 10 The on-board traction battery charger and the solar controller (*up*)



The on-board battery charger adopted (Fig. 10) is ZIVAN NG3 type, single phase, from Italy.

This charger is an isolated, high frequency switch mode charger suitable for lithium battery pack. It is fully automatic and microprocessor controlled, with internal protection against overload, short circuit, incorrect connection and voltage transients. The characteristics are: input ~ 240 V 15A single phase AC, nominal pack voltage ~ 205 V, charge rate ~ 8 A, efficiency $\sim 85\text{--}90\%$, operating temperature range: $\sim 20\text{--}50$ °C.

To recharge the 12 V auxiliary battery we use a DC/DC converter 205 V/12 V in the electric mode, to supply the low voltage electric network that fuelled among others the “gourmand” auxiliary vacuum electro-pump and the electro-hydraulic steering group.



Fig. 11 The photovoltaic modules on the roof of the hybrid concept GRAND HAMSTER ELECTRICWAY 4WD

The 12 V battery charger adopted is SWS 1000 L12 from *TDK-Lambda* France. The characteristics are: input voltage 85–265VAC or 120–350VDC, output voltage 9,6–14,4VDC efficiency –84 %, operating temperature range: –20–50 °C.

The recharging system of 12 V auxiliary battery is completed by an assembly of photovoltaic cells placed on the car’s roof (Fig. 11).

This photovoltaic panel includes 4 photovoltaic modules special designed for the dimensions and the curvature of the car’s roof. They are coupled in series in pairs (front and rear), and then the two subsets in parallel. The main parameters of the photovoltaic panel are: Total no. of cells 72 (18/module) by PR China; technology of the cells *Si-mono*; total panel area 1.33 m² nominal power at STC 185 W, maximum power point current 9.84 A; Maximum power point voltage 17.79 V.

The recharging is controlled by a solar controller *LS1024R* by PR China, a light type protecting the battery from being over charged by the solar photovoltaic panel.

5 Mode of Operation

The control panel of the traction electrical equipment, situated in the central console (Fig. 12), includes the *EV/HEV* switch, the *Emergency* red button in the centre and the *Reverse—Neutral-Drive* selector for the electric mode on right. A red LED confirms the “Traction Enable” state of the system.

The GRAND HAMSTER vehicle will have the following operational main modes (Fig. 3):

Parking (1) and **traction battery recharging** (plug-in) by coupling the Vehicle to Grid by special charging cable. The maximum charging time is 6–8 h.

Starting (2, 10) and **running** (3, 11), with low to mild-range speed in the *electric mode*, when the electric motor takes its energy from the traction battery.



Fig. 12 The central console with the control panel of the electrical equipment: the selector button *EV-HEV*, the batteries monitor (traction battery and auxiliary battery) and the selector button *Reverse-Neutral-Drive*. Up, the PC car monitor and the *VBox Raceologic* display monitor

This operation mode is a non-pollutant and occurs on short distances in urban driving conditions. The autonomy (for the energy of the battery 12 kWh) in the electric mode is 50–80 km. The maximum speed in this electric mode is 80 km/h. The pure electric mode is command by pushing the *EV/HEV* button (Fig. 12).

In this mode only the rear wheels will be actuated, the motor control (TIM) being realised through the electrical acceleration pedal featuring a potentiometer sensor; the master-vacuum is assisted by an auxiliary vacuum electropump and the electrohydraulic steering is also active.

Driving on normal conditions (4), in the *thermal mode*, which ensures performances (acceleration, autonomy, etc.) close to those of the standard diesel car. Moreover, when driving at low loads (5) by recharging the battery, the engine specific load is increased, thus improving the engine efficiency. This is made by the electric motor operating as a generator.

Sudden acceleration (6), in the hybrid mode providing increased dynamic performances by simultaneous operation of the diesel engine and the motor. The speed range in the hybrid mode depends upon the motor power, the operational rotation speed range and the rear transmission ratio. In this stage, this specific hybrid mode is not operational.

All wheels drive (7), in the *hybrid mode E 4WD*, obtaining increased driveability on the slippery roads. This mode is operational only for the low speed (<25 km/h).

Regenerative braking (8), when decelerating by replacing the classical engine brake with a process of transforming the vehicle's kinetic energy in electric energy, reusable afterwards in the acceleration process. This is made by the electric motor operating as a generator. In order to do this, the brake pedal was modified.

Stop and the engine stops automatically (9), cutting the fuel consumption and pollutant emissions.

Tools connecting at traction battery and the eng&gen (12), an operation mode allowing supplementary functions absent to other hybrid vehicles.

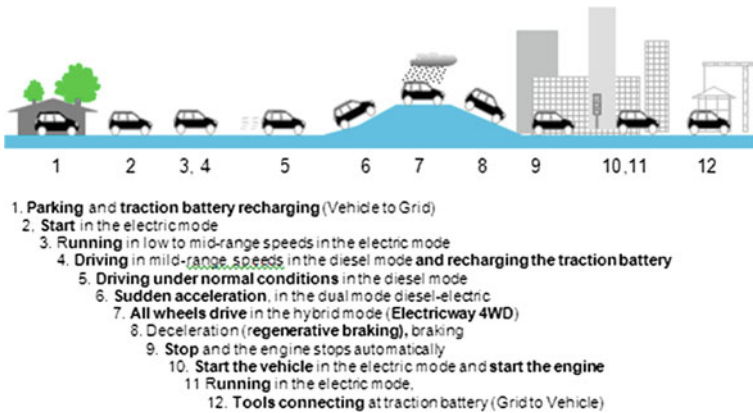


Fig. 13 The Electric Drive System calibration with MES Software in electric mode on the vehicle roller test bench (*left*) and the firsts tests on the

6 Tests and Performances

The Electric Drive System calibration is was done in the *Alternative Propulsion System and Renewable Energies* laboratory using the specific MES SA Software (Fig. 13, left) and the vehicle roller test bench.

To monitor the parameters registered during the road tests in the first step we have used an equipment *VBox Raceologic* (Fig. 12, up).

The *VBox Mini* is a low cost, self-contained GPS data logging and display system suitable for a large range of vehicle testing applications.

The main performances obtained in the electric mode on the firsts partial road tests are:

- Maximum speed : 80,5 km/h;
- Maximum acceleration: 0,2 g;
- Accelerations times: 0-50 km/h—8,5 s; 0-80 km/h—27,5 s
- Autonomy: 50-80 km.

7 Conclusions

The GRAND HAMSTER E-4WD project, deployed within the *Automotive Engineering Research Centre, Alternative Propulsion System and Renewable Energies* laboratory, offered an experimental vehicle to study the ways of reducing the pollutant emissions of DACIA DUSTER car.

Considering its specific operating modes, this ecologic vehicle could be used as utility vehicle for special services in areas with environmental restrictions. In addition, its battery with high voltage (205 V) and high capacity (12 kWh) may allow supplying the specific equipment in remote areas requiring a motor-



Fig. 14 circuitModes of operation of the GRAND HAMSTER ELECTRIC WAY 4WD

generator group. This function could facilitate the client's acceptance of additional costs.

The *EcoMatic Hybrid System (Energy conversion with autoMatic Hybrid System)*, diesel-electric version, a parallel two shafts, plug-in type, organized in a motorized solution E- 4WD (Electricway- 4WD) mounted on this demonstrator in diesel-electric version is designed to be applied to all types of Dacia cars.

For reaching the target of emissions under 115 g/km CO₂, a diesel engine Renault K9 K, EURO 5 has been used. Starting is assisted by the *ThermoSTAT* system, an auxiliary system for preheating. This system uses both the thermal energy from the engine and the electricity from the network (through the plug-in system).

Our academic research on this subject will continue with the following stages:

- Performing the road tests in order to determine all the performances in real conditions, yet unrealized. To achieve this we shall use a *Datron Correvit* performance measuring device available in our laboratory;
- Simulation of the driving, consumption and performances of the car with the CRUISE software from AVL Austria. Although by the AVL courtesy we have this software, this action has been delayed because of the lack of experimental data on the vehicle.
- The engine has Stop@Start system implemented;
- Adaptation of an improved HEVMS (Hybrid Electric Vehicle Management System) able to extend to all operating modes presented in Fig. 14.

The research laboratory has a dynamometric roller test bench and road testing equipments, allowing the development of future projects regarding the ecological propulsion of vehicles and the extension of the co-operation with other interested teams, with similar research objectives.

Acknowledgments This work was financially supported by the Romanian Ministry of Education, Research and Innovation and the University of Pitesti. We benefited of the help from AUTOMOBILE DACIA GROUP RENAULT, RENAULT TECHNOLOGIE ROUMANIE, LEAR ROMANIA, MES S.A—Swiss, AVL Austria and CONTINENTAL AUTOMOTIVE ROMANIA, and we express our gratitude to them.

References

1. www.auto-bild.ro, “Premiera mondiala- Duster la Priza”, no-21/17—30 2011
2. Marinescu DG, Tabacu I, Tabacu S, Serban FI, Nicolae V, Vieru I (2012) A plug-in hybrid diesel-electric vehicle EVS26 -worldwide international battery, hybrid and fuel cell electric vehicle symposium and exhibition, Los Angeles
3. Marinescu DG, Tabacu I, Serban F, Clenci A, Tabacu S (2008) Plug-in hybrid electric vehicle E- 4WD type, 4th european conference on alternative energies for the automotive industry. Futuroscope- Poitiers, France
4. Marinescu DG, Tabacu I, Tabacu S (2010) Research regarding the development of a plug-in hybrid electric vehicle, F2010-A-089, FISITA Congress 2010, Budapest

Design and Simulation of Air Cooled Battery Thermal Management System Using Thermoelectric for a Hybrid Electric Bus

Vahid Esfahanian, Saber Ahmadi Renani, Hassan Nehzati,
Nima Mirkhani, Mohsen Esfahanian, Omid Yaghoobi and Ali Safaei

Abstract Dynamic and electric parameters of HEVs and EVs such as acceleration, regenerative braking and battery charging/discharging depend on the battery system performance. Excessive or uneven temperature rise in a module or pack of battery reduces the life cycle significantly. Therefore, improving the battery thermal management system (BTMS) is very important for reliability and cost of vehicle. The objective of this paper is to design an air cooled battery thermal management system using thermoelectric to maintains the temperature of battery in appropriate range at stressful and abuse conditions. An air flow with fans, heat sinks, fins and thermoelectrics is used for battery thermal management of hybrid electric bus to improve temperature uniformity and reduce maximum cell temperature. A battery pack consists of 12 smaller packs containing 14 porch cells with series design is selected for this study. This Li-ion battery pack specifically designed for the hybrid electric bus produced by Vehicle, Fuel and Environments Research Institute (VFERI). A detailed three-dimensional thermal model of designed battery pack has been developed using the fundamental heat transfer principles and CFD (computational fluid dynamics) analysis tools to predict the temperature distributions in cells and packs. The air flow for the battery thermal management of porch Li-ion cells is numerically analyzed using a three-dimensional CFD model. The numerical results indicate that the temperature of battery maintain below 35 °C while keeping the cell temperature difference below 5 °C during high charge/discharge rates and ambient temperature more than 40 °C. In

F2012-B02-065

V. Esfahanian · S. A. Renani (✉) · H. Nehzati · N. Mirkhani · M. Esfahanian
· O. Yaghoobi · A. Safaei
Vehicle, Fuel and Environment Research Institute (VFERI),
University of Tehran, Tehran, Iran
e-mail: saberahmadi1991@gmail.com

other studies though using the air as the heat transfer medium for BTMS may be simpler, cheaper and smaller than heat transfer by liquid, but it is not recommended because it is not as effective as heat transfer by liquid. In this paper, a new method is presented that improves air cooling thermal management with help of thermoelectric. It is more effective than usual air cooling thermal management. Thermal modeling of a Li-ion battery air cooling pack suitable for hybrid electric bus using thermoelectric shows that such an approach can keep the cell temperature in the pack below the upper safety limit (35 °C) in high-rate discharge rates and under ambient temperatures higher than 40 °C.

Keywords Hybrid electric bus · Battery thermal management system · Air cooled · Thermoelectric

1 Introduction

Concerning huge demand of energy and increasing air pollution particularly at big cities, manufacturers and governments are trying to find new substitutes for conventional vehicles and buses. One of the affordable and practical options is electric vehicles (EVs) and hybrid electric vehicles (HEVs). Electric drive systems are appealing to become practical because they offer the affordable technology that reduces vehicle emissions and fuel use, increases efficiency and enhances performance. This has led manufacturers and governments to invest in development of commercially hybrid electric transit buses. Transit buses are considered as the best candidates for hybrid technology application because they normally operate on predictable routes with frequent starts and stops and available space for batteries and the other extra components. Currently there are many manufacturers all around the world produce hybrid transit buses.

The performance and life-cycle costs of electric vehicles (EV), hybrid electric vehicles (HEV) and hybrid electric buses depend inherently on batteries. Battery pack performance directly affects the all-electric (zero-emission) range, power for acceleration, fuel economy, and charge acceptance during energy recovery from regenerative braking. Because the battery packs cost and performance also affect the cost and reliability of the vehicle, any parameter that affects the battery pack must be optimized [1]. Hybrid electric buses and (hybrid) electric vehicles need large-scale batteries. These batteries generate much heat during rapid charge and discharge cycles at high current levels, such as during quick acceleration, with various chemical and electrochemical reactions [2].

Thermal management affects the battery performance including: electrochemical system; round trip efficiency; charge acceptance; power and energy capability; reliability; cycle life and cost. The appropriate operating range of Li-ion batteries must be between 25 and 40 °C, and temperature difference from module to module below 5 °C [3]. Thermal management is more important during rapid charge and discharge and when ambient temperature is more than 40 °C.

Using air or liquid are two common ways for cooling batteries in hybrid electric buses and vehicles. Considering simplicity, weight, cost, space limitation and maintenance, use of air for battery thermal management is better approach than use of liquid. In the case of air cooling thermal management system, if the battery temperature rises higher than 66 °C, it would be difficult to cool it to below 52 °C [4]. Furthermore, at stressful and abuse conditions, especially at high discharge rates and at high operating or ambient temperatures (>40 °C), air-cooling will not be proper, and the non-uniform distribution of temperature on the surface of the battery becomes inevitable [2].

In this paper, a new method that improves air cooling thermal management with the help of thermoelectric is presented. It is more effective than usual air cooling thermal management. With the use of thermoelectric, air cooled battery thermal management system can keep batteries temperature below 35 °C during rapid charge/discharge and ambient temperature upper than 40 °C.

2 Battery Thermal Management System Design

2.1 Battery Pack Configuration

An air flow with fans, heat sinks, fins and thermoelectrics is used for battery thermal management system of hybrid electric bus to improve temperature uniformity and reduce maximum cell temperature. The battery pack consists of 12 smaller packs made up of 14 porch cells with series design is selected for this study. This pack specifically designed for the hybrid electric bus produced by VFERI.

Heat transfer with air is achieved by directing air across the battery pack. The forced air system consists of four centrifugal fans flow air between cells. Cells are cooled with air flow through fin between them. As illustrated in Fig. 1, there is one fin between each two batteries. These fins increase heat exchange between cells and reduce their temperatures.

For enhancing the heat transfer, two heat sinks used in the direction of air flow at the inlet of centrifugal fans. As illustrated in Fig. 2, the cold side of thermoelectrics at the top of heat sink absorbs heat generated by battery cells and combination of two heat sink and two fans (at upper part of battery pack) remove the heat produced by thermoelectric.

3 Selection of Thermoelectric

Heat is generated in a battery cell by entropy change from electrochemical reactions and Joule's effect (ohmic heating). At practical EV and HEV rates, the heat generated or consumed due to the reversible entropy change resulting from cell electrochemical

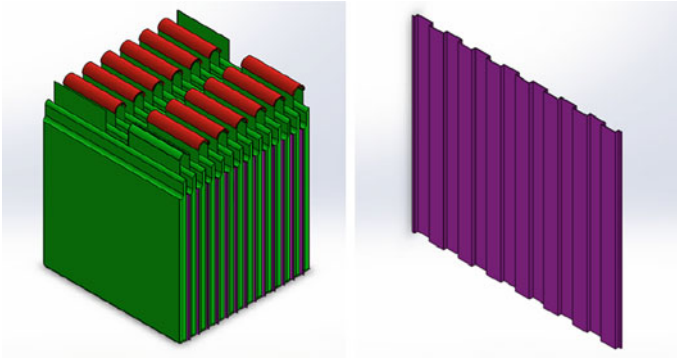


Fig. 1 Fins between battery cells

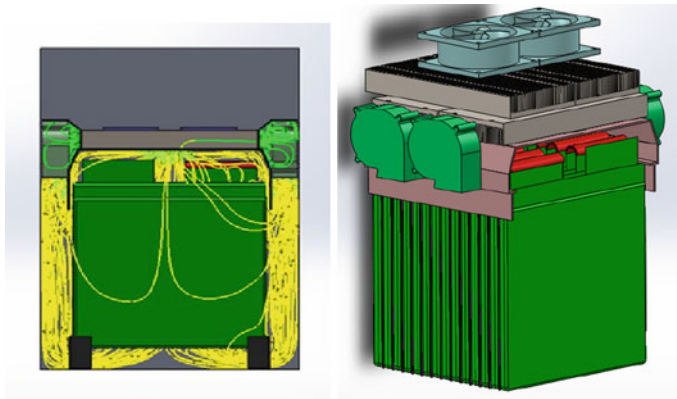


Fig. 2 Location of battery thermal management system components

reactions is usually small compared to the heat generation resulting from ohmic and other irreversible effects present in the cell. If the heat generated in the cell is not removed, it is stored, raising the temperature of the cell [1].

The current of battery cell depends on control strategy and drive cycle. The average current during drive cycle is calculated by using simulated model of vehicle and the heat generated from the battery cell can be calculated using electrical power equation. Practically, the maximum generated heat can be estimated by battery cells during continuous work for 20 min at 5 % slope in hot weather with 40 °C temperature.

Since the calculated heat generated by battery cells must be removed by thermoelectrics, the cooling capacity of selected thermoelectrics must be higher than the heat generated by all of battery cells in the pack. In this study, the maximum generated heat is about 200 W and will be removed by four

Table 1 Specifications of used thermoelectric

Name	N	V_{max} (v)	I_{max} (A)	DT_{max} (°C)	$Q_{c,max}$ (W)	COP_P	Q_{cP} (W)	COP_{SP}	Q_{cSP} (W)
TEC1-19915T125	199	25	15	68	265	1.139	145.161	1.805	48.944

thermoelectrics. The design for thermoelectrics is rectangular design in which it can work in two operating cases; parallel topology and series–parallel topology. The operating system can change between these two topologies.

For optimal operation, the thermoelectrics must work in their optimal voltage for the most of their operating driving cycle and at the maximum reachable cooling capacity during abuse conditions.

In series–parallel topology, the thermoelectrics voltages equal to optimal voltage, so this topology is suitable for most of the operating time. In parallel topology, the thermoelectrics work at maximum achievable cooling capacity, so this case is used for abuse and stressful conditions such as rapid charge and discharge rate, hot weathers, and when the voltage of auxiliary battery is low.

Specifications of the used thermoelectric (TE) are summarized in Table 1. The selected thermoelectric satisfy demanded heat during normal and abuse conditions.

4 Methodology of Simulation

There are many approaches as a numerical method in the field of applied Computational Fluid Dynamics (CFD). In this study, in order to perform the battery thermal management, Finite Element Method (FEM) has been utilized to design an appropriate system for cooling the batteries by making use of thermoelectric and fans.

5 Selection of Fins

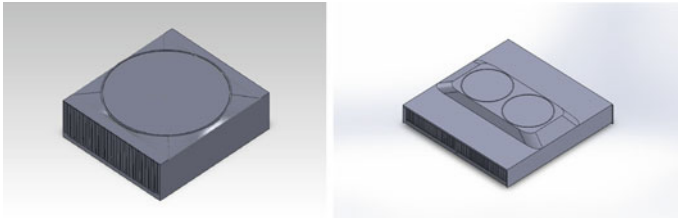
Process of designing and optimization of an air cooled battery thermal management system contains some stages. First of all, each battery cell and adjacent fin has been simulated with an estimated mass flow rate of the coolant air to obtain an appropriate fin width. The flow rate assumed 5 cfm for the space between two battery cells.

The results for three situations based on the fin width are summarized in Table 2. The optimized fin width can be selected based on the pressure drop through the cell and temperature of the cell surface.

It is important to note that another influential parameter for Li-ion batteries is temperature variation at a cell surface that affects the internal interaction in the batteries, so this amount should not exceed 5 °C.

Table 2 Results of simulation for three different fin widths

Fin width	Air pressure drop (Pa)	Max. temperature of the cell surface (°C)	Temperature variation in a cell surface (°C)
5 mm	11	35	5
4 mm	20	33.5	4
3 mm	37	33	4

**Fig. 3** Single fan and single heat sink

As it can be seen from Table 2, the desired heat transfer and an appropriate pressure drop occurred simultaneously with the 4 mm fin width.

6 Selection of Upper Fans and Heat Sinks

The next step before the main battery pack design is choosing a combination of heat sink and fan (upper part of the total pack) in order to remove the heat produced by thermoelectrics. Several fans and heat sinks have been simulated and results have been evaluated to achieve the permissible temperature at the hot surface of the thermoelectric.

Two kinds of heat sinks and different fans have been utilized to make several configurations as candidates for the upper section. Two main sets among those analyzed are shown for instance in Fig. 3.

This part of the thermal management system is optimized subject to the air pressure drop through the heat sink and then the maximum temperature at the hot surface of TE is obtained. Two types of design shown in Fig. 3 contain the totally different components. The left one shows bigger fan and heat sink and the right one includes shorter components with two fans and to heat sinks.

These two sets yield the most acceptable results and also similar ones among the others. But some intangible aspects affect the ultimate selection. Bigger hub diameter results in a less effective heat transfer in the middle core of the heat sink, so using two-fan configuration avoids this problem and also results in less pressure drop through heat sink. Furthermore this type has economical feature with respect to mass production of the hybrid bus.

Table 3 Thermo physical properties of a battery cell

Thermal conductivity (W/m ³ k)	Specific heat (J/kg.k)	Density (kg/m ³)
10	1000	2173.44

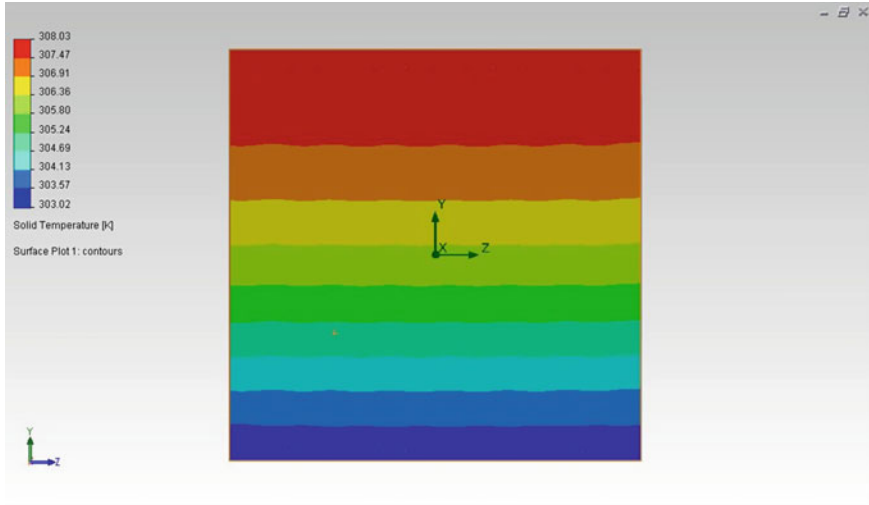


Fig. 4 Contours of temperature in the hot surface

7 Simulation Result

One of the noticeable points in the simulation of battery thermal management is to assign the thermal properties of battery cells. Density can be calculated from cell specification data of the battery published by Kokum Co. and the Ref. [5] and [6] introduce values for thermo physical properties of lithium batteries. The used values for thermo physical properties for battery are given in Table 3.

For the 4 mm width fin, the temperature contours of mid surface of a battery cell are given in Fig. 4.

Figure 5 illustrates the flow trajectories which represent the uniform flow through each channels made by the fin configuration and for given pressure drop. The simulation results validate the design procedure which is performed based on maximum temperature and pressure drop.

Table 4 summarizes operating parameters of fan inlet. Hot surface of the TEs is modeled with a surface source which generates 100 kW heats.

Fan operation in the Flow Simulation can be modeled by its operation parameters and characteristic curve which shows the pressure difference versus the flow rate. Table 4 shows the operating parameters for one of the fans inlet.

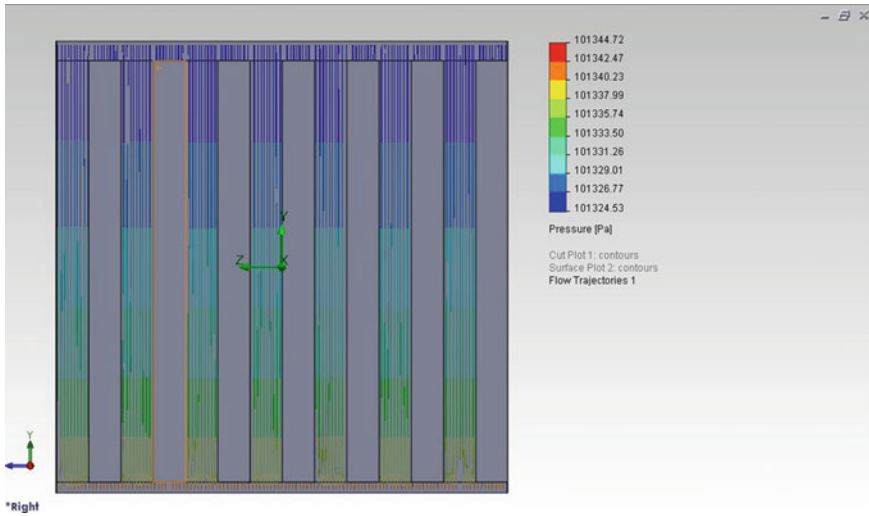


Fig. 5 Flow trajectories with pressure contours

Table 4 Operating parameters of fan inlet

Local parameters					Integral parameters	
Parameter	Minimum	Maximum	Average	Bulk average	Parameter	Value
Pressure (Pa)	101344	101688	101556	101556	Mass flow rate (kg/s)	0.04079
Velocity (m/s)	9.180	20.681	18.705	18.705	Volume flow rate (m ³ /s)	0.03608
Temperature (Fluid) (K)	312.83	313.38	312.87	312.87	Surface area (m ²)	0.00395

Contours of temperature given in Fig. 6 illustrate that in the critical condition with the ambient temperature of 40 °C, hot surfaces of TEs reach the maximum temperature of about 53 °C which is applicable with respect to transient condition of 100 kW heats generation of TEs.

Results of four centrifugal fans and battery cells are given in Table 5. The lower and main part of the battery pack is cooled by the circulating air flow that absorbs heat from battery cells. In this state each TE is simulated by a surface source which produces—50 kW heats.

These results must be consistent with the previous results using the single cell and fin analysis. Total volume flow rate can be calculated as follows:

$$4 \times 0.00835 = 0.0334 \text{ m}^3/\text{s} = 71.12 \text{ cfm}$$

Fig. 6 Temperature distribution of hot side of TEs

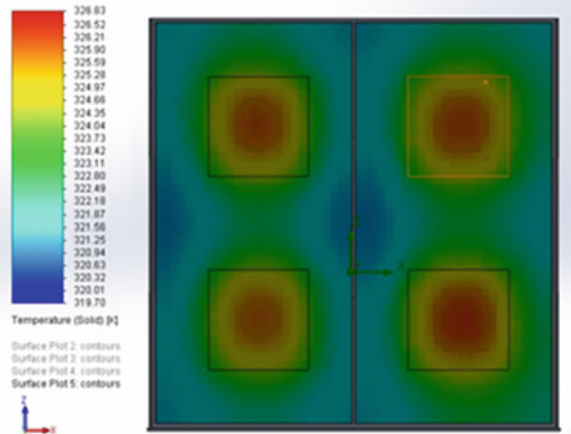


Table 5 Operating parameters of centrifugal fan inlet

Local parameters					Integral parameters	
Parameter	Minimum	Maximum	Average	Bulk average	Parameter	Value
Pressure (Pa)	101526	101879	101713	101713	Mass flow rate (kg/s)	0.01009
Velocity (m/s)	14.663	56.085	25.773	25.773	Volume flow rate (m ³ /s)	0.00834
Temperature (fluid) (K)	291.95	295.60	292.07	292.07	Surface area (m ²)	0.00083

Fig. 7 Temperature contours of the cell at the worst conditions

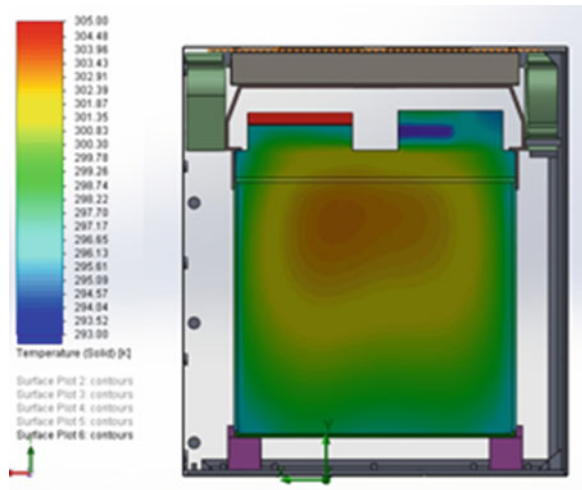
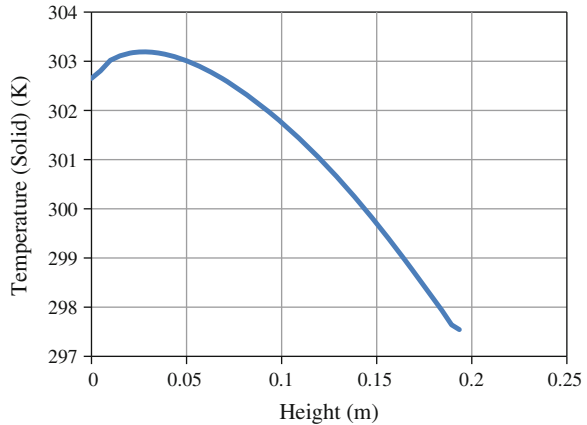


Fig. 8 Temperature Distribution through the cell at the worst condition



So for the space between each two cells, approximately we have the volume flow rate of $\frac{71.12}{14} = 5.08$ cfm which verifies the assumed flow rate for simulation of single cell and fin.

Figure 7 shows the contours of temperature for the cell at the worst condition which represents the acceptable 6 °C temperature gradient across the cell and maximum temperature of about 30 °C.

Figure 8 also gives the temperature variations in height through this special cell.

8 Conclusion

In this study, the design of an air cooling battery thermal management system is discussed. Hybrid electric buses and (hybrid) electric vehicles need large scale batteries which generate much heat during rapid charge and discharge cycles at high current levels. Therefore, Thermal management system is very important and affects reliability, life-cycle and cost of EVs and HEVs. The designed BTMS, uses thermoelectric to obtain an appropriate temperature distribution through the battery cells in the critical conditions. This system is simulated using a three-dimensional CFD model for the hybrid electric bus produced by Vehicle, Fuel and Environments Research Institute (VFERI). The results indicate that air cooling thermal management with help of thermoelectric can meet the demand of upper safety limit (35 °C) and reduce the temperature difference of the cell at the worst condition to about 6 °C. Furthermore by making use of a designed set with double set of fans and two heat sinks, heat generated by cells can be removed and the maximum temperature of hot surface of thermoelectric become less than 53 °C.

Acknowledgments The authors would like to acknowledge the support of Vehicle, Fuel and Environment Research Institute (VFERI).

References

1. Pesaran AA, Vlahinos A, Burch SD (1997) Thermal performance of EV and HEV battery modules and packs, 14th international electric vehicle symposium, Orlando, 15–17 Dec
2. Rao Z, Wang S, (2011) A review of power battery thermal energy management. *Renew Sustain Energy Rev*, Sep 2011
3. Pesaran AA (2002) Battery thermal models for hybrid vehicle simulations. *J Power Sources* 110(2):377–382
4. Nelson P, Dees D, Amine K, Henriksen G (2002) Modeling thermal management of lithium-ion PNGV batteries. *J Power Sources* 110(2):349–356
5. Pesaran AA (2001) Battery thermal management in EVs and HEVs: issues and solutions, Advanced automotive battery conference
6. Gao L, Liu S, Dougal RA, Member S (2002) Dynamic lithium-ion battery model for system simulation. *IEEE Trans Compon Packag Technol* 25(3):495–505

Analysis of Rotor's Magnetic Bridge and Yoke Design to EM's Performance Influence

Ming Han, Wenxiang Huang and Pingliang Luo

Abstract With the development of new energy vehicle technology, smart and high efficiency driving motors are needed, now permanent magnet machine is the most suitable type. Mostly the IPM rotor structure is used for it can take full advantage of reluctance torque so as to fulfil weakened flux control, however, the magnet bridge's shape in rotor lamination will cause remarkable influence to motor's performance. In this chapter, one Integrated Motor and Generator (IMG) type machine is taken as an example to investigate rotor magnet bridge and its yoke thickness to motor's performance impact, with the FEM (Finite Element Method) electromagnetic simulation, the reasonable rotor structure was explored, and the final designed EM's electromechanical performance can satisfy system's requirement.

Keywords Electric vehicles · Permanent magnet machine · Integrated motor and generator · Inserted permanent magnet · Magnet bridge

1 Introduction

1.1 Interior Permanent Magnet Machine with V-Shape Magnet Structure

With the development of new energy vehicle technology, smart and high efficiency driving motors will be the optimized option for the passenger vehicles for its big

F2012-B02-069

M. Han · W. Huang (✉) · P. Luo
United Automotive Electronic Systems, Co., Ltd, Shanghai, China
e-mail: Wenxiang.Huang@uaes.com

high efficiency area, especially for the Interior Permanent Magnet (IPM) machine, higher overload performance and power density can be achieved benefit for the reluctance torque caused by asymmetric magnet circuit structure, as well as good field weaken performance to enlarge its operation speed [1].

As a joint venture with BOSCH, UAES (United Automotive Electronic Systems Co. Ltd.) has found the electric machine section to develop IPM machines for local new energy vehicle's driving system, now the products contain SMG (Separate Motor & Generator), IMG series for different passenger vehicles [2] now the team has own the core competence to design, manufacturing and finish the function test and endurance test.

The electromagnetic torque can be expressed as:

$$\begin{aligned} T_{em} &= \frac{mpE_0U}{\omega X_d} \sin \theta + \frac{mpU^2}{2\omega} \left(\frac{1}{X_q} - \frac{1}{X_d} \right) \sin 2\theta \\ &= mp[\Psi_f I_q + (L_d - L_q) I_d I_q] \end{aligned} \quad (1)$$

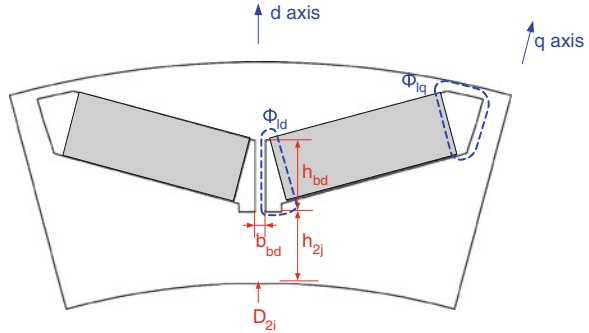
From this equation we can find that PMSM's electromagnetic torque was a combination of permanent magnet torque caused by armature reaction with PM field and magnetic reluctance torque caused by asymmetric magnetic circuit between d and q axis [3] therefore, more and more OEM's adopted a V-shape IPM structure rotor to improve its salient ratio so as to enhance the reluctance torque. Another advantage for IMP structure is that with the teeth shoe's protection the permanent magnet's anti-demagnetization performance will be enhanced too, such as the lamination shape used in Toyota Camry, Lexus and Prius hybrid systems, all of them are with V-shape IPM structure [4]. However, there is one rib connecting the iron cores between each magnet poles so as to protect the lamination from deforming cause by centrifugal force when the motor is in high speed operating condition, we can call this rib as d-axis magnet bridge or magnet bridge for short.

1.2 The Influence from Magnet Bridge and Yoke Thickness

There are two pieces of magnets per pole in the V-shape IPM machine, so in most case one air pocket is left in each side of the magnets to minimize the field leakage, however, one magnet bridge is needed in the middle of the magnet pole for safe considering the centrifugal force, and the thickness of the rotor yoke should be guaranteed, these two parts will influence motor's performance. In this chapter, one IMG motor is used for example to investigate the performance penalty cause by changing the two parts, the rotor structure and related parameters were illustrated as in Fig. 1.

Assume the total magnetic field generated by each piece of magnet is Φ_f , and the flux leakage caused by d and q axis bridge is Φ_{ld} and Φ_{lq} , so the active flux per pole can be expressed as:

Fig. 1 The schematic diagram of one rotor pole and related parameters



$$\Phi_a = 2(\Phi_f - \Phi_{ld} - \Phi_{lq}) \tag{2}$$

In this design, d axis flux leakage hold the most leakage for a big air pocket is opened under q axis bridge, so here only Φ_{ld} is concerned, in the next part of the paper the magnet bridge usually stand for d axis bridge except for special comments. In Fig. 1 b_{bd} and h_{bd} is used to stand for the bridge width and height, and h_{2j} is the height of rotor yoke. This chapter will study these parameters' changing to the performance influence based one FEM simulation, and the appropriate design proposal will determined based on both electromagnetic and mechanical considering.

2 The Analysis Based on FEM Simulation

2.1 Investigation of Magnet Bridge Width to Em's Performance Influence

Based on the original prototype, keep the same magnet bridge height $h_{bd} = 8.0$ mm and the same air gap 1.5 mm for magnetic barrier as before, only change the width b_{bd} from 1.5 to 1.0 mm so as to minimize the d axis bridge flux leakage Φ_{ld} , thus the peak torque and peak power will achieved, the machine's performance will enhanced. Two FEM models were built and the same current was given, Fig. 2 shown the simulation result of field distribution of each model, and the main result were listed in Table 1.

From Fig. 2a and b we can see that the flux leakage mainly happened through d axis bridge, with a thinner magnet bridge will make the leakage decreased obviously, the simulated peak torque at 500 rpm increased from 220.76 to 227.68 N m, and the its peak power at 3000 rpm increased from 29.66 to 30.82 kW (3–4 % improvement for EM performance). The improvement will enhanced if the magnet width became thinner, however, due to the mechanical point studied before, lower than 1 mm will cause disadvantage to the strength, so now we will keep the same

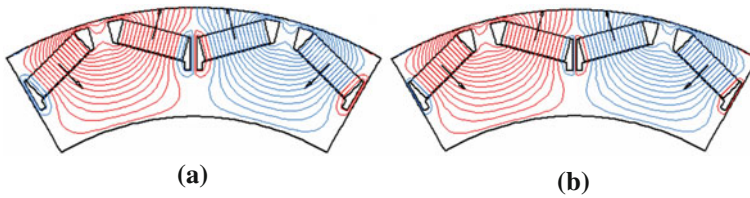


Fig. 2 The magnetic field distribution in each rotor with different bridge width. **a** $b_{bd} = 1.5$ mm
b $b_{bd} = 1.0$ mm

Table 1 The simulated peak torque and peak power with different magnet bridge width

b_{bd} (mm)	h_{bd} (mm)	$T_{max, 500}$ (Nm)	$P_{max, 3,000}$ (kW)
1.5	8.0	220.76	29.66
1.0	8.0	227.68	30.82

Table 2 The simulated peak torque and peak power with different magnet bridge width

b_{bd} (mm)	h_{bd} (mm)	$T_{max, 500}$ (Nm)	$P_{max, 3,000}$ (kW)
1.0	8.0	227.68	30.82
1.0	7.5	227.62	30.78
1.0	7.0	227.72	30.80
1.0	6.5	227.60	30.79
1.0	6.3	227.39	30.75

width $b_{bd} = 1.0$ mm and investigate the bridge height to the peak performance's influence.

2.2 Investigation of Magnet Bridge Height to Em's Performance Influence

If the magnet width is fixed, shorter magnet bridge height will be good to release the stress inside the magnet bridge, and will also leave enough space for rotor yoke. However, the shorter h_{bd} , the more flux leakage will happened, an investigation was done based on FEM simulation with shorted magnet bridge step by step below, and Fig. 4 show the compared models with h_{bd} of 7.5 and 6.3 mm, the simulation result was listed in Table 2:

From the simulation result we can see that the magnet width has little influence to motor's peak performance, and the shorter h_{bd} , the bigger rotor yoke height can be achieved, or from a change of perspective, if the motor's performance is guaranteed, we can increase the rotor inner diameter D_{2i} so as to increase the

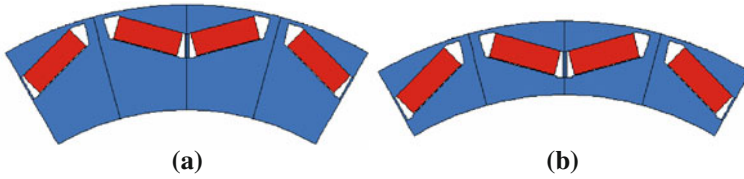


Fig. 3 Different rotor model with different inner diameters **a** $D_{2i} = 132$ mm **b** $D_{2i} = 150$ mm

specific power, the rotor inertia will decreased too. Next step we will investigate the influence caused by yoke height to motor's performance.

2.3 Investigation of Yoke Height to Em's Performance Influence

Keep the same magnet bridge size $h_{bd} \times b_{bd} = 6.3 \times 1.0$ mm, different models with different rotor inner diameter increased from 132 to 150 mm is built, the compared rotor model and simulated result was shown in Fig. 3 and Table 3:

From the statistics in Table 3 we can see that when the inner diameter increased from 132 to 150 mm (the rotor yoke height decreased from 13.3 to 4.3 mm), the penalty to its peak torque is only 1 N m, however, if 4.3 mm height rotor yoke is adopted, the limitation will came from mechanical side, next step we will check the rotor's mechanical strength at its maximum speed through FEM simulation.

3 Mechanical Strength Simulation Based on Fem Calculation

As for mechanical design, there will be a contradiction with electromagnetic performance, for slim magnet bridge will cause stress concentration, such as for the V-shape IPM in Figs. 3, 4 dangerous point can be find in both d axis bridge and q axis bridge while rotor operate with high speed. Thanks to the effort of mechanical team's support, UAES has developed the co-simulation competence with electromagnetic simulation, now we can do the mechanical simulation simultaneous and automatically with each planned models, the investigation result shows that the smaller width of the bridge, the bigger chamfering can be cut in the air pocket of each side of magnets, so the stress in DP 1 and DP 2 released a lot, but the stress in DP 3 will be increased.

For higher power density and lower moment of inertia is needed for driving motors, the inner diameter can be increased to 150 mm, but too thinner yoke will also cause higher stress in point DP 1, so the balanced dimensions should be find by a scenario of simulations with different values of the 3 variables h_{bd} , b_{bd} and D_{2i} , as well as the related chamfering in the air pocket.

Table 3 The simulated peak torque and peak power with different rotor inner diameters

$h_{bd} \times b_{bd}$ (mm)	D_{2i} (mm)	$T_{max, 500}$ (Nm)	$P_{max, 3,000}$ (kW)
6.3×1.0	132	227.39	30.75
6.3×1.0	148	226.86	30.75
6.3×1.0	149	226.75	30.73
6.3×1.0	150	226.39	30.71

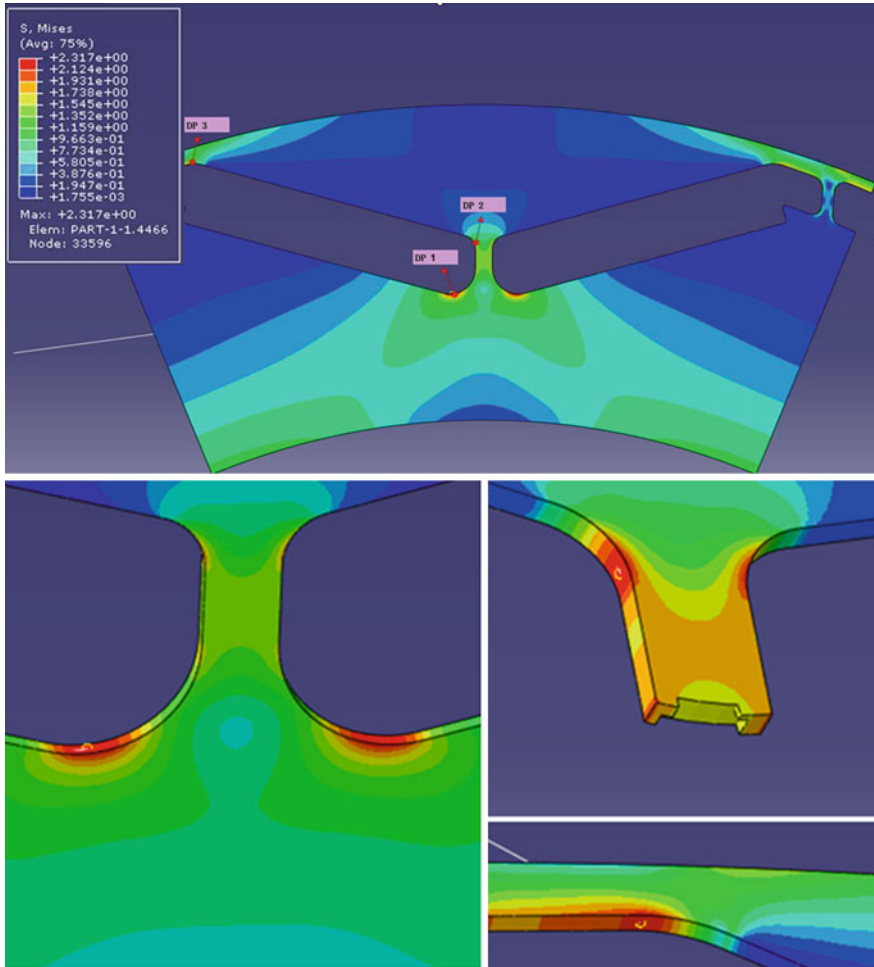


Fig. 4 Dangerous point investigation

In the real machining of this project, the chamfering is used in all air pocket to disperse the stress, the research result show that when the motor is operate in high speed, the maximum stress happened in the inside of the air pocket near the yoke,

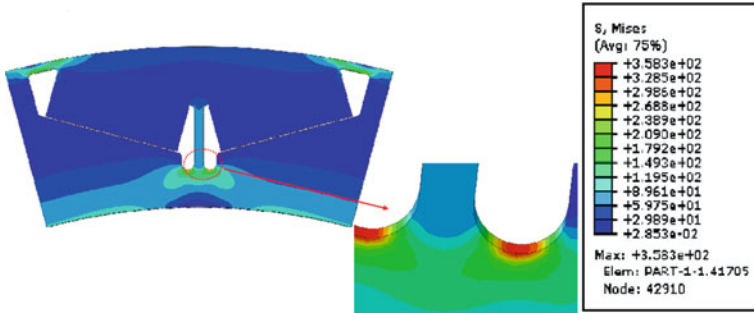


Fig. 5 The final model and simulation result of MISES stress considering the chamfering

the chamfering with 1.5 mm is used here, and the magnet bridge dimension is 6.8×1.0 mm in the final proposal, the rotor yoke height is 6.8 mm, the new model and simulated stress distribution under 7,200 rpm is illustrated in Fig. 5:

The simulation result show that the maximum MISES stress is 358.3 Mpa under maximum speed 7,200 rpm, which is no more than the yield strength (376 Mpa), no plastic deformation happened.

4 Conclusion

The dimension of magnet bridge in V-shape IPM rotor will cause remarkable influence to PMSM's peak performance, especially for the width of magnet bridge, and the height of magnet bridge and rotor yoke's influence is limited. This chapter studied the three parameters' influence to one IMG motor's performance based one the FEM simulation, finally an optimized design proposal is obtained, the peak performance improved 3–4 % with less material cost, and no deform will happened at its highest operation speed.

References

1. Denki Jidousha Kudou System Chosa Senmon Linkai (1999) The latest technology of electric vehicles. OhmshaLtd., Japan
2. UAES Product Manuals. 2011
3. Renyuan T (2008) Modern permanent magnet machines, theory and design. China Machine Press, Beijing
4. Burrell TA, Campbell SL, Coomer CL (2011) Evaluation of the 2010 Toyota prius hybrid synergy drive system. Oak Ridge National Laboratory, Tennessee

HyBoost: An Intelligently Electrified Optimised Downsized Gasoline Engine Concept

Jason King, Matthew Heaney, James Saward, Andrew Fraser, Mark Criddle, Thierry Cheng, Guy Morris Morris and Paul Bloore

Abstract The UK Technology Strategy Board (TSB) sponsored HyBoost project was a collaborative research programme to develop an ultra efficient optimised gasoline engine concept with “Intelligent Electrification”. The basis of the concept was use of a highly downsized 1.0 L boosted engine in conjunction with relatively low cost synergistic ‘12+X’ Volt electrical management system and electrical supercharger technologies to deliver better value CO₂ reduction than a full hybrid vehicle. Project targets of 99 g/km CO₂ as measured over the European Drive Cycle (EDC) in a standard 2011 Ford Focus whilst maintaining the same performance and driveability attributes as a 2009 production 2.0 L version of the car were achieved, and a potential route through to <85 g/km CO₂ identified. Ricardo was supported by a consortium consisting of Ford, Controlled Power Technologies, Valeo, the European Advanced Lead Acid Battery Consortium, Imperial College London and the UK TSB.

Keywords Gasoline · Engine · Downsizing · Boosting · Electrification

F2012-B02-070

J. King (✉) · M. Heaney
Ricardo UK Ltd Shoreham Technical Centre, BN3 5FG Shoreham-by-Sea, UK
e-mail: jun.zhang3@uaes.com

J. Saward · A. Fraser
Ford Motor Company, UK

M. Criddle · T. Cheng
Valeo, France

G. Morris · P. Bloore
Controlled Power Technologies, UK

1 Introduction

Mandating of road vehicle fuel economy is becoming a global phenomenon, with legislation or binding agreements for substantial improvements coming into force in Europe, the US, Canada, Australia, Japan and China. Passenger cars are a primary focus of this legislation, with future targets calling typically for continuing improvement of 3 % per year as shown in Fig. 1.

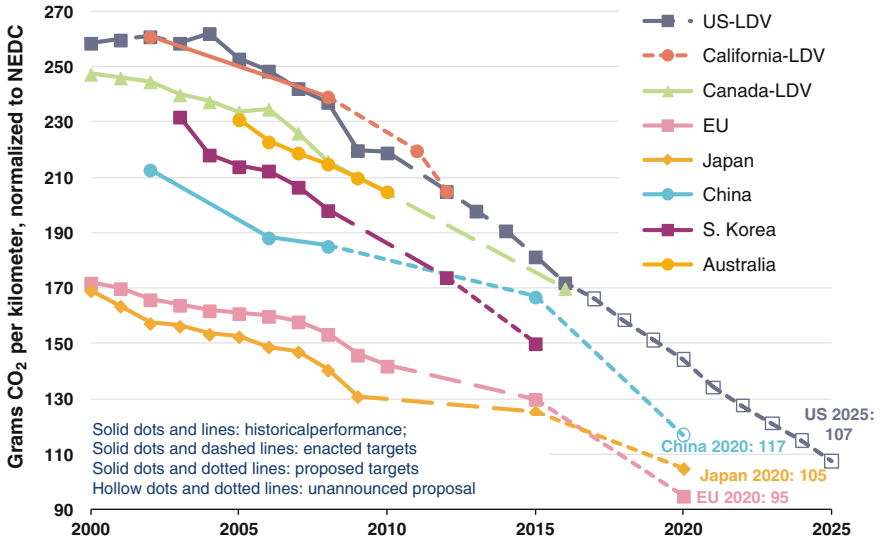
To put this change into context: in Europe, an average of 1.6 % per year improvement has been achieved over the last decade, driven by the now superseded Voluntary Agreement. This is a world-leading pace of change, despite missing the VA targets. Future legislation in the major markets now requires that this pace of change must be doubled, for example in Europe a new car fleet average tailpipe CO₂ emission of 130 g/km must be achieved, with phase-in from 2012 to 15, with even tougher targets currently set for 2020.

The mass-market advancement of Hybrid vehicles still requires significant reduction in product cost. Recent analysis by Ricardo (updating the 2003 DfT/DTI “Low Carbon Roadmap”) indicates that current Hybrid cars only offer marginal Total Cost of Ownership savings unless these cost reductions are realised. This analysis also continues to indicate that deploying low cost technologies across a large number of vehicles remains more cost-effective than deploying costly technology to a few.

In the UK and Europe, the Diesel engine is currently established as the fuel-efficient solution for the majority of passenger cars sold. However, its significant incremental cost over a gasoline engine arising from the cost of precision fuel injection and exhaust after-treatment devices forms a higher proportion of the purchase price. Furthermore, rising demand for Diesel fuel rather than gasoline impairs the efficiency of the refinery (meaning that CO₂ savings on a “well to wheel” basis are becoming less attractive) and pushes up the price of Diesel fuel. The aim of the HyBoost concept was to combine cost-effective hybridisation with synergistic gasoline engine downsizing technologies to offer a CO₂/performance trade-off better than today’s more costly full hybrids and high efficiency Diesels.

2 HyBoost Concept

HyBoost targets were to deliver a C-segment model year 2011 (MY2011) Ford Focus demonstrating a 30–40 % reduction in CO₂ emissions as measured over the EDC (to below 100 g/km) versus a baseline MY2009 2.0 L Naturally Aspirated (NA) gasoline engine version of the passenger car whilst maintaining the comparable vehicle performance and driveability attributes. Figure 2 shows a simple scheme of the concept with the 2.0 L NA engine replaced with a downsized DI gasoline engine equipped with a conventional fixed geometry turbocharger (FGT) delivering superior steady state power and torque levels. A Front End Accessory



[1] China's target reflects gasoline fleet scenario. If including other fuel types, the target will be lower.
 [2] US and Canada light-duty vehicles include light-commercial vehicles.

Fig. 1 Future passenger car fuel economy targets and legislation *Source* Passenger vehicle greenhouse gas and fuel economy standards: a global update—ICCT

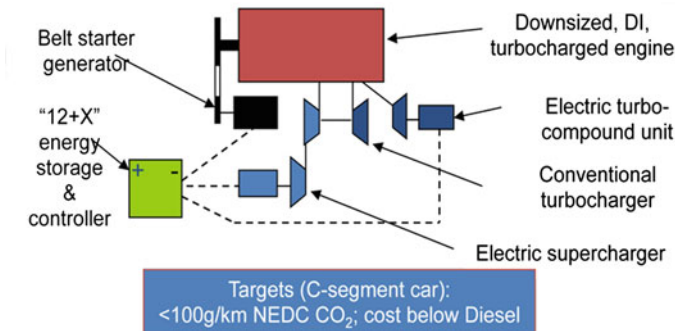


Fig. 2 HyBoost concept scheme

Drive (FEAD) mounted Belt Starter Generator (BSG) gave micro hybrid functionality of stop/start and more efficient motoring and generation enabled through the higher voltage “12+X” (typically between 18 and 27 V) energy storage of an ultra capacitor system. Energy recovered during deceleration events could be deployed in a sophisticated boosting system combining a 12+X electric supercharger “blowing through” the conventional turbocharger and/or the BSG torque assist system, using the electrical energy optimally to achieve good transient response or improved fuel consumption. The component systems have previously

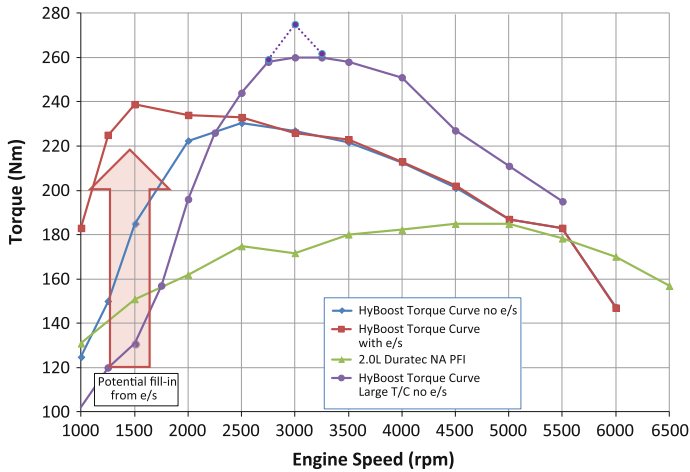


Fig. 3 Ford 2.0 L Duratec versus HyBoost torque curves comparison

been demonstrated individually at 12 V, but not brought together in this synergistic combination as a “12 + X” system.

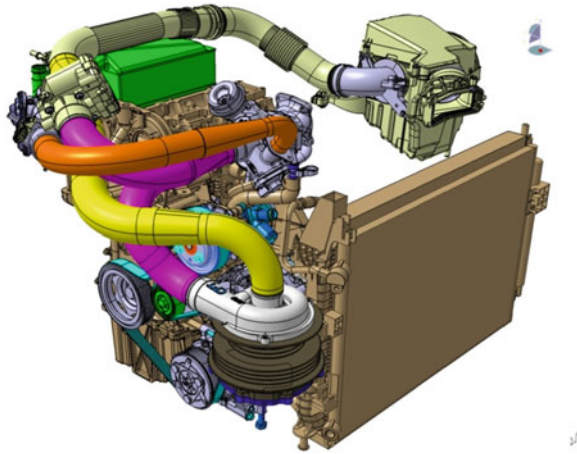
The project also included exploration of electric turbo compounding (shown in the scheme but not fitted to the HyBoost car) and a novel energy storage technology for further enhancements to efficiency and cost respectively, but these items are not covered in this paper.

3 Results and Discussion

3.1 HyBoost Engine and Boost System

HyBoost uses a modified near production Ford 1.0 L 3 cylinder turbo GDI Eco-Boost base engine. This gives 50 % downsizing over the baseline engine. Figure 3 shows the steady state torque curves of the two engines, and the superior performance of the HyBoost engine can be clearly seen. The Ford 2.0L Duratec engine produces peak power and torque levels of 107 kW at 6000 rpm and 185 Nm at 4000 rpm respectively. This compares to the HyBoost (with no electric supercharger assist) peak power and torque levels of 105 kW at 5500 rpm and 234 Nm at 2500 rpm respectively, which were achieved through re-optimisation of the boosting system, use of a new intake air path required to include the electric supercharger, and fitment of a new high efficiency Valeo Water Charge Air Cooler (WCAC) system. The WCAC system was specified with a very high (relative to engine size and performance) heat rejection capability of between 16 and 18 kW, and this was key to enabling excellent charge cooling to mitigate knocking and

Fig. 4 CAD model of the HyBoost powertrain showing the Valeo 12+X electric supercharger and associated intake pipework



maintain lambda 1 operation through to full load, resulting in excellent Brake Specific Fuel Consumption (BSFC) across the entire operating map.

As the engine becomes more aggressively downsized several potential issues arise with regards to perceived performance. Firstly, the main issue is turbocharger lag, where the device itself takes time to build up boost pressure and the subsequent transient torque curve does not meet the steady state torque curve. Secondly, often there can be a big difference between the low engine speed “NA” torque (typically 8–11 bar BMEP), where the FGT is not able to deliver any significant boost pressure even during steady state conditions, and peak torque, which can be as high at 34.5 bar BMEP in the case of HyBoost with a larger turbocharger fitted. This also can give a perceived turbocharger lag feel during vehicle launch even if the boosting system response is more than adequate. To counter these effects, HyBoost uses a Valeo 12+X 3.3 kW electric supercharger to mitigate turbocharger lag in addition to enabling some degree of torque augmentation to the base engine, and a CAD model of the device is shown on the engine in Fig. 4.

Figure 3 also shows the full load¹ torque curve of HyBoost with the electric supercharger running from 1000 to 2000 rpm engine speed. The following key benefits of the electric supercharger can be determined from the detailed analysis performed on the HyBoost project:

- The electric supercharger provides additional boosting capability beyond the FGT and thus enables significant steady state and transient torque augmentation in the lower engine speed range. The FGT also behaves as a pressure ratio multiplier of the electric supercharger boost so is effectively an in-series, 2-stage compressor system. This gives the potential to address the large step up seen between low and mid speed torque

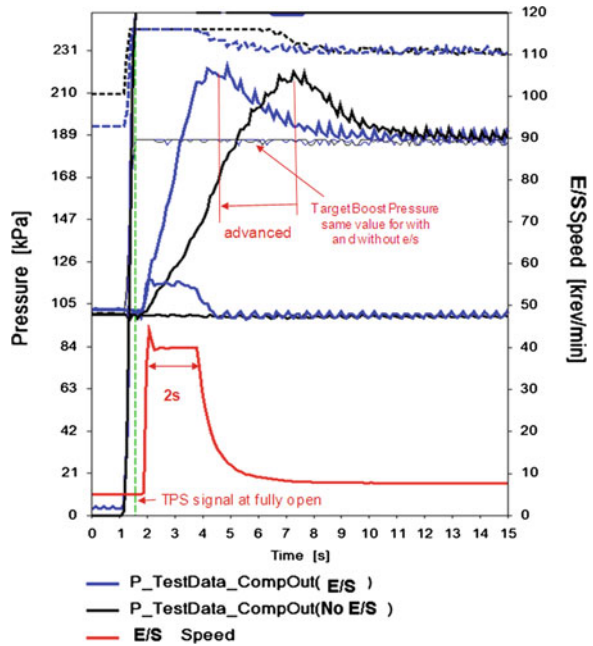
¹ Note that full load performance availability is dependent on available stored energy.

- Figure 3 shows there is a thermodynamic multiplication of the electric supercharger power through the engine. At 1000 rpm the torque rises from 125 to 183 Nm with the electric supercharger assistance, which is equivalent to a 6.1 kW increase in power at this speed (13.1–19.2 kW respectively). At 1500 rpm the rise is from 185 to 239 Nm, which is an 8.48 kW increase, and both of these improvements were achieved with an input of only 1.8 kW to the electric supercharger. This equates to a 47 and 29 % increase in engine torque at those speeds respectively, and transiently the proportional increase in engine torque could be even higher dependant on the boost response without the electric supercharger assistance
- As a function of the higher engine power achieved with the electric supercharger assistance more energy is naturally released to the FGT turbine, enhancing its run-up
- The air mass flow and pressure ratio provided by the electric supercharger is essentially free if provided from stored recovered energy (although the system can run in self-sustaining mode as long as the generator can provide the required energy and the electric supercharger remains within temperature limits). This results in a lower Indicated Mean Effective Pressure (IMEP) required to generate boost than it would be for a conventional turbo or supercharged engine for the same Brake Mean Effective Pressure (BMEP). With downsized gasoline engines IMEP levels can be very high and it can be extremely challenging to operate the engine at these levels without significantly compromised combustion (retarded spark timing and high levels of fuel cooling to control Exhaust Gas Temperature), that can then translates into a degradation in “real world” fuel economy

Application of the electric supercharger to mitigate turbocharger lag required only relatively short bursts of usage, typically in the order of 1–3 s, with the engine returning to conventional thermodynamic only (without electrical assist) operation as soon as possible. Figure 5 shows some early test bed data taken on prototype phase engine with a 12 V electric supercharger fitted. Here a load step is used at constant engine speed to evaluate the boost response with and without the electric supercharger running. Following a pedal stamp to Wide Open Throttle (WOT) from a minimum load condition the boost pressure rise is measured, and the graph shows that the time to peak boost is halved with the electric supercharger running for 2 s than without the electric supercharger running. This testing was far from optimum but shows the benefit of the electric supercharger, and the 12+X electric supercharger proved to be capable of achieving maximum speed of greater than 60,000 rpm in less than 200 ms and a maximum pressure ratio of 1.6 bar with high motor efficiency. Subsequent vehicle performance and driveability attributes were maintained with the 50 % engine downsizing as shown in Table 1 later in the paper.

Finally from Fig. 3 the torque curve from a revised larger turbocharger fitted to the HyBoost engine is shown with application of a Valeo-supplied Low Pressure cooled WOT Exhaust Gas Recirculation (LP WOT EGR) system. A peak power

Fig. 5 HyBoost load step boost response using 12 V the electric supercharger on test bench



and torque of 112 kW at 5500 rpm and 260 Nm at 3000 rpm respectively was achieved despite the engine not being optimised for these high levels of specific output. The detriment of the larger turbo can be seen below 2250 rpm where the engine torque drops off considerably, however, in this case aggressive use of the electric supercharger can be utilised to “fill in” the curve if necessary, as shown by the large arrow. In HyBoost’s case, with a primary project focus on low CO₂, the main benefit of the larger turbocharger was considerably reduced pumping across the device at part load, resulting in a measured average 2 % improvement in BSFC at the key drive cycle engine speeds and loads.

From the powertrain downsizing alone a 27 % reduction in fuel consumption was measured over the EDC versus the baseline primarily through reduced engine pumping losses and better BSFC for the same vehicle tractive load. Advanced Design of Experiments calibration techniques were used to gain a further 2 % improvement. Also, due to the high engine torque output achieved a six speed manual transmission with significantly higher gear ratios was sourced from a Diesel engine application in the same base vehicle, realising a further 4 % reduction in drive cycle CO₂ whilst still achieving the performance targets.

Table 1 Powertrain and vehicle attributes comparisons

Vehicle	2009 ford focus 2.0 L duratec	2011 ford focus 1.6 L EcoBoost	2011 ford focus 1.0 L HyBoost P/T	2010 Toyota prius
Maximum power PS (kW)	145 (107) @ 6000 rpm	150 (110) @ 5700 rpm	143 (105.5) @ 5500 rpm	99 (73) @ 5200 rpm Hybrid system net power = 136 (100) @ 5200 rpm
Peak Torque (Nm)	185 @ 4000 rpm	240 @ 1600 rpm (o/b)	234 @ 2500 rpm	142 Nm
0–62 mph ^a (secs)	9.2	8.6	9.2	10.4 s
31–62 mph ^b (secs)	11.9	8.6	11.2	–
Max. speed (mph)	128 mph	130 mph	128 mph	112 mph
Cycle CO2	Reduction	Baseline (0 %)	18 %	42–52 %
	47 %			

3.2 HyBoost Micro Hybrid System

The HyBoost Valeo StARS™ 12+X BSG is capable of 4 kW in motoring and 6 kW in regeneration mode, with the energy being stored in a 200 F ultra capacitor pack (UCaps). A 2.2 kW DC/DC converter allowed energy to be moved between the standard vehicle 12 V lead-acid battery and the UCaps. The benefits of the micro hybrid system can be split up into three key areas:

3.2.1 Smart Charging

Smart charging over the EDC is enabled though the capability of the BSG to regenerate aggressively during “zero fuel” tip out and braking events. More than sufficient energy is recovered to meet the vehicle’s base electrical loads. Currently the legislative drive cycle requires that the battery and UCap state of charge must be the same at the beginning and end of the cycle, but all the regenerated energy is fed back into the UCaps, however, there is a bleed back of some stored energy from the UCaps through the DC/DC converter to maintain the 12 V battery State of Charge (SOC). The neutral charging strategy resulted in a typical 4 % improvement in drive cycle CO₂.

3.2.2 Stop-Start

The majority of current stop-start systems operate in neutral gear only, which is to say that the engine does not stop until neutral has been selected and the clutch

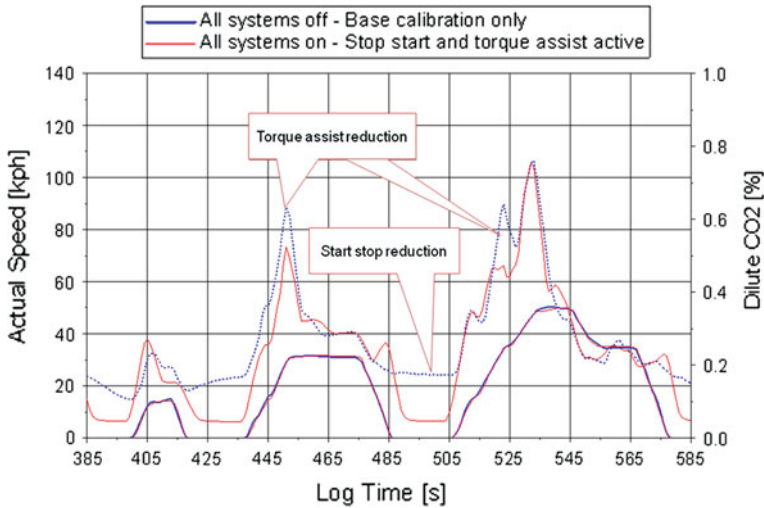


Fig. 6 Stop-start and torque assist benefits over ECE15

released. The engine then starts when the clutch is pressed again ready for the next pull away. Stop-start in neutral gives approximately a 4 % benefit over the drive cycle. However, on the EDC the gear selection point before the pull away is approx 2 s before the car needs to drive, and so essentially it means the engine can be idling for between 2 and 4 s when the vehicle speed is 0 km/h. Due to the capability of the BSG to start the engine quickly and, if required, assist the “drive” of the engine during pull away, a more aggressive in-gear strategy can be used so before driving away on the cycle the gear can be selected but the engine does not actually start until the driver starts lifting his or her foot off the clutch. Similarly, coming off the hills on the ECE15 section of the cycle the engine is stopped when the clutch is depressed and the vehicle speed is 0 km/h, but still in gear. Figure 6 shows the instantaneous CO₂ benefits (solid line) of stop-start and torque assist over the ECE15. Stop-start in-gear gives an extra 1 % improvement in CO₂ over stop-start in neutral only.

3.2.3 Torque Assist

Figure 7 shows the initial simulation of BSG behaviour (StARS Torque, +ve torque is motoring mode, -ve torque is regeneration mode), electric supercharger operation (e/s flag) and UCap SOC over the whole EDC. From this graph it can be seen that there is sufficient recovered energy in the UCaps from regeneration events to employ BSG torque assist, and this is primarily used during the ECE15 pull away transients. The effect of the BSG torque assist is reduced engine fuelling requirements and results lower cycle CO₂. Optimisation on the vehicle actually realised benefits over the Extra Urban Drive Cycle (EUDC), as shown in Fig. 8, as

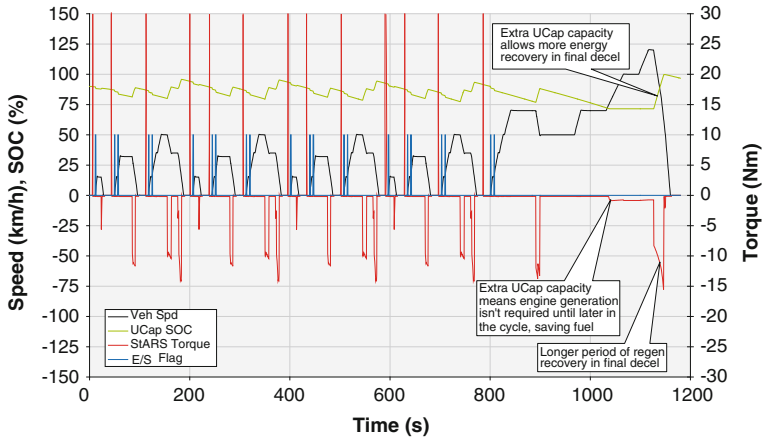


Fig. 7 StARS 12+X and electric supercharger operational simulation over the EDC

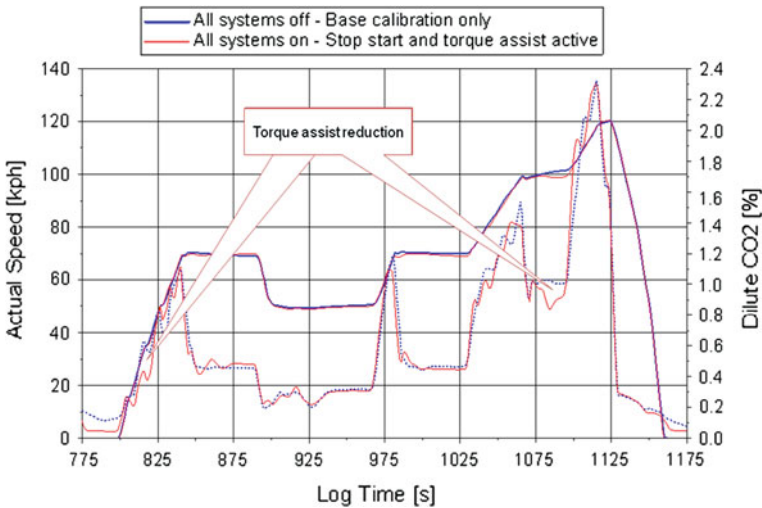


Fig. 8 Torque assists benefits over EUDC

well as the ECE15, as shown above in Fig. 6. Additionally, it was possible to drive the entire cycle with no electric supercharger operation, and the CO₂ improvement from torque assist was 3.5 %, giving a total combined micro hybrid benefit of 12.5 %.

When operating the vehicle with a more aggressive driver demand than seen over the whole EDC, the stored energy was then distributed to the BSG (for direct launch assist) and/or the electric supercharger (for lag mitigation) dependant on the engine speed, load and rate of change of pedal demand. A complex control strategy was developed to supervise the operation of HyBoost’s key systems.

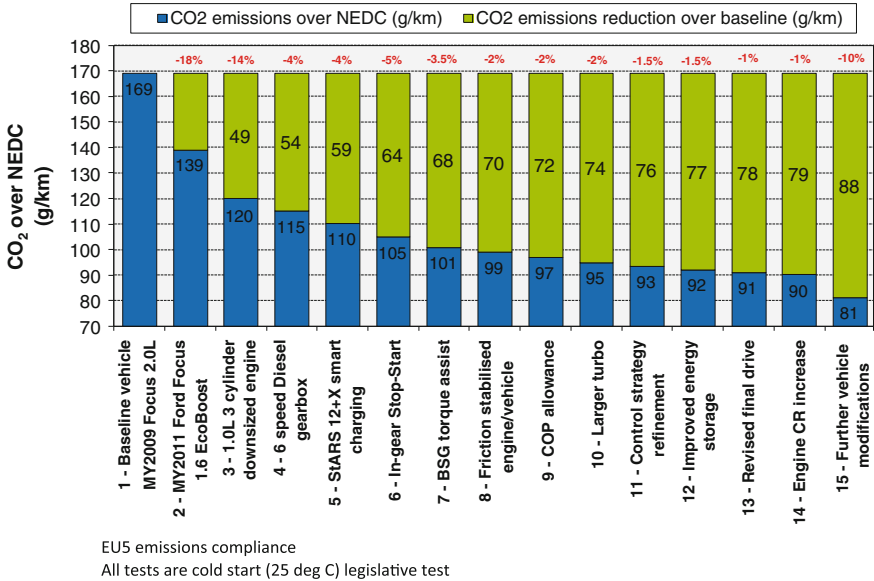


Fig. 9 HyBoost vehicle CO₂ glide path

3.3 HyBoost Co₂ Glide Path and Performance Status

Figure 9 shows a slightly simplified CO₂ glide path for the project from the baseline vehicle to HyBoost demonstrator vehicle. The results in the chart are based on cold start (25 °C) tests undertaken following the legislative procedure, and meet EU5 emissions standards.

Starting from left to right the breakdown of the chart is as follows:

- (1) Baseline vehicle MY2009 Ford Focus 2.0L NA PFI gasoline vehicle with 5 speed gearbox 169 g/km CO₂
- (2) MY2011 Ford Focus 1.6L EcoBoost production vehicle, an 18 % improvement to 139 g/km CO₂
- (3) Installation of the Ford Fox 1.0L engine replacing the 1.6L engine, BSG fitted and utilising a standard charging strategy, slightly higher friction of a FEAD capable of working with the full BSG functionality, a 14 % improvement to 120 g/km CO₂
- (4) Installation of the six speed Diesel gearbox with higher ratios, a 4 % improvement to 115 g/km CO₂
- (5) StARS™ 12+X smart charging employed, a 4 % improvement to 110 g/km CO₂
- (6) In-gear stop-start, a 5 % improvement to 104.7 g/km CO₂
- (7) BSG torque assist, a 3.5 % improvement to 100.8 g/km CO₂

- (8) Mileage stabilisation of car, a 2 % improvement to 98.8 g/km CO₂
- (9) 2 % Conformity of Production (COP) allowance to 96.8 g/km CO₂
- (10) Large turbo tested with 2 % improvement to 94.9 g/km CO₂

The engine supplied and used in the vehicle was brand new, as was the HyBoost car itself. Typically the vehicle may be aged anywhere between 4,000 and 20,000 km to ensure that it has been “stabilised”. This was not undertaken on HyBoost due to project time constraints and it is Fords experience that up to a 2 % improvement in cycle fuel consumption could be gained, and this is shown in line 8 above. A manufacturer specified Conformity of Production (COP) allowance of 2 % has been included in line 9–2 % is generally the minimum figure used by most OEM’s, and this could be increased to 4 or even 6 %.

From detailed engine and vehicle simulation and testing undertaken on the project a series of five additional small improvements were identified that could result in a further significant reduction in fuel consumption beyond the 99 g/km CO₂ target, bring the concept down to an equivalent level achieved by a similarly sized full hybrid vehicle. These are also shown on Fig. 9, and can be summarised as follows:

- (11) Control strategy refinement from further development work to fully optimise the system would be expected to give at least a further 1.5 % improvement in EDC CO₂
- (12) Similar to 11, better utilisation of the current UCaps, or even a minimal increased storage on the vehicle has been shown through simulation to be beneficial as the re-generation opportunities over the EDC have not been fully optimised at the current stage of concept development
- (13) The six speed Diesel gearbox was an off-the-shelf un-modified production box. Vehicle drive cycle simulation showed that the final drive could be slightly lengthened to give an additional 1 % improvement in EDC CO₂. The performance attributes, primarily the 0–62 mph time, could be maintained as the vehicle could achieve 62 mph in 2nd gear with the longer final drive whereas it currently requires a shift to 3rd gear, which takes up approx 0.4–0.5 s of the current 0–62 mph time
- (14) From a combination of the large turbocharger and LP WOT EGR tested on the engine test bed it was determined that the engine compression ratio (CR) could be increased by an estimated 0.5–0.7 ratios, which could result in an approximate 1 % improvement in EDC CO₂
- (15) Minimal use of Eco-car specific parts such as Eco-tyres, aero tweaks, etc. would be expect to give a further 10 % improvement

Table 1 compares the key powertrain and vehicle attributes of the baseline vehicle versus the 2011 Ford Focus 1.6L EcoBoost, the 2011 Ford Focus with the HyBoost powertrain, and the 2010 Toyota Prius. It can be seen that HyBoost concept proved to be capable of achieving the CO₂ levels of a full hybrid (dependant on the hardware utilised, as shown in Fig. 9) but with superior performance attributes. However, it should also be noted that the cost of the HyBoost concept powertrain system was estimated at one third of the full hybrid, and total



Fig. 10 HyBoost system implementation in ford focus vehicle

weight increase of system was also less than 20 kg versus the base 2.0 NA engine, and several hundred kilograms less than for the full Hybrid when including the battery pack and supporting electrical architecture in the measurement. Off cycle fuel consumption, as assessed on the Artemis drive cycle, remained excellent due to the engines ability to maintain high efficiency even at full load through excellent combustion characteristics and lambda 1 operation everywhere. Figure 10 shows the completed HyBoost vehicle.

4 Summary and Conclusions

The HyBoost concept demonstrated that use of a highly downsized, boosted engine in conjunction with relatively low cost synergistic ‘12+X’ Volt management system and electrical supercharger technologies can deliver better value CO₂ reduction than a full hybrid vehicle. System incremental cost has been estimated below that of Diesellisation, giving strong potential for market advancement. In summary:

- The project enabled improvements in the state-of-the-art in stop/start systems and boosting, both of which will become ubiquitous in advanced passenger cars.
- Full system functionality was achieved and a CO₂ glide path identified that was better than first predicted to levels below a current benchmark full hybrid
- The HyBoost vehicle is technically a “Hybrid” (a micro/mild hybrid, with up to 6 kW of electrical power) and can be marketed as such, offering similar CO₂ performance but without the purchase or lifetime cost concerns of larger battery systems
- It was shown that HyBoost technologies can be applied to existing base engines with a relatively low level of re-engineering, thus reducing the cost of implementation in a product range and extending the applicability of the base engine (which may be offered in three or four power trims, from naturally aspirated through boosted to HyBoost configurations)
- HyBoost technologies are modular, meaning that economies of scale can be realised at component level by suppliers
- As demonstrated on the project, HyBoost technologies offer the scope for good real world fuel economy because downsizing, full load stoichiometric operation and exhaust energy recovery are effective at higher loads
- Vehicles equipped with HyBoost technologies have potential to fall below some of the incentivised CO₂ thresholds shown in Fig. 1, therefore adding to their market appeal
- The HyBoost system has reduced dependence on “commodity” materials such as Copper or Lithium (compared to a Full Hybrid) and precious metals (Compared to a Diesel with advanced after-treatment, or even a Fuel Cell); hence its success (and linked environmental benefit) is less vulnerable to fluctuating commodity prices, and its life-cycle environmental impact is potentially superior

References

- Owen N, King J (2009) HyBoost TSB submission documents
- Bower ET (2010) How do we maintain transient response whilst continuing to downsize, MSc Thesis, Cranfield University, UK
- Owen N, Jackson N (2009) A new look at the Low Carbon Roadmap, IMechE seminar on low carbon vehicles, Ricardo UK Ltd, UK

Development of B70HEV and B50PHEV Based on Faw-TMH Powertrain

Jun Li, Minghui Liu, Dongqin Liu, Ziliang Zhao and Xingwang Yang

Abstract With the targets of low carbon emissions and optimization of energy consumption, FAW developed the Twin Motor Hybrid system (FAW-TMHTM), which has obtained patents in both China and the United States. The system includes the hybrid dedicated engine, a traction motor (TM), a clutch, an automatic manual transmission (AMT), a BSG, a new battery system and other key assemblies. This hybrid powertrain can be extended to plug-in system easily. This configuration has all the full hybrid functions such as Start-Stop, pure electric driving and regenerative brake. As the application of this system, FAW has developed B70HEV and B50PHEV. In NEDC, B70HEV can achieve a reduction of 35.2 % in fuel consumption, which can meet the European “130 g CO₂/km” emissions regulations in 2012. B50PHEV can achieve a reduction of more than 60 % in fuel consumption in NEDC.

Keywords FAW-TMH · HEV · PHEV · Configuration evaluation · AMT

1 Introduction

The shortage of petroleum, environment problems like air pollution and the greenhouse effect are becoming more and more serious. It requires more energy efficient and cleaner products to deal with these problems. It has been widely accepted that vehicle electrification is a good choice. To make the electric vehicles

F2012-B02-073

J. Li (✉) · M. Liu · D. Liu · Z. Zhao · X. Yang
FAW R&D Centre, Changchun, China
e-mail: lj_qy@faw.com.cn

as perfect as traditional vehicles, there are many technical problems need to be solved. The main problem lies in the accumulation of electric energy. Nowadays, the power density, rapid charging, safety and cost are the bottlenecks which restrict the popularization of electric vehicle. Under this background, with the advantages of electric vehicles and traditional vehicles, full hybrid and plug-in hybrid technology are the compromise. Full hybrid technology can remarkably improve fuel economy and emissions with small cost increase.

FAW R&D centre has been developing the hybrid technology since 1998. In 2000, a new hybrid configuration named Twin Motor Hybrid system (FAW-TMHTM) was brought forward. As the application of this system, BESTURN B70 HEV was developed in 2008. Benefited from the good plug-in expansibility of this system, BESTURN B50 PHEV was developed in 2010.

This paper will introduce the development of FAW-TMHTM, and describe two hybrid products based on this powertrain configuration.

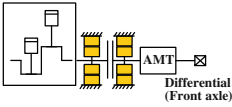
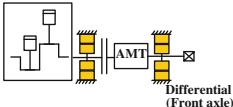
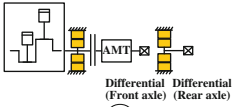
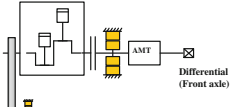
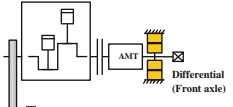
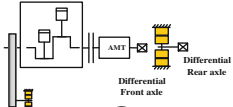
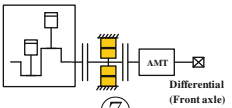
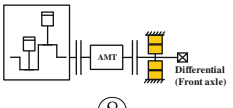
2 Besturn Twin Motor Full Hybrid System

The main full hybrid configurations widely used in the world are as follows: Toyota Hybrid System (THS or HSD, Toyota), Two-Mode (GM, BMW, Chrysler), Parallel hybrid (P2, VW) and Hybrid4 (Peugeot). In the analysis of advantages and disadvantages of various full hybrid configurations, engineers from FAW put forward an evaluation method of full hybrid configurations. It mainly concerns the realization difficulty, cost, and the potential performance. This method was founded on the capital and technology conditions of the company. Firstly, it set each performance index a weighting coefficient, and then scored every performance index, finally gave a comprehensive index to each of these configurations. By evaluation, FAW adopted the twin motors full hybrid system as shown in Table 1 and Fig. 1, which hereinafter was referred as FAW-TMH configurations (Table 2).

In this configuration, the internal combustion engine and the traction motor could drive the vehicle individually. The required torque of driving the vehicle could be distributed into any ratio between the two power sources. On this premise, the engine and the motor both could work in the efficient operating points. The switches of the operation modes were easy. This configuration had all of the operating modes of hybrid such as engine start/stop, pure electric driving, series driving, associated driving, and regenerative braking.

Figure 2 shows the evaluation of TMH and THS based on the evaluation method mentioned above. The results are as follows: TMH has the function of speed and torque decoupling. The fuel economy of TMH is equivalent to that of THS. TMH can solve the problem of power interruption in the process of automatic manual transmission shifting. It makes the adoption of AMT possible. What's more, the motor power of TMH is also smaller than that of THS, so the cost is less than THS. TMH has advantage in development period and initial

Table 1 Typical full hybrid structure configurations

TM location	Front of AMT	Rear of AMT	Axle drive
ISG	 ①	 ②	 ③
BSG	 ④	 ⑤	 ⑥
-	 ⑦	 ⑧	-

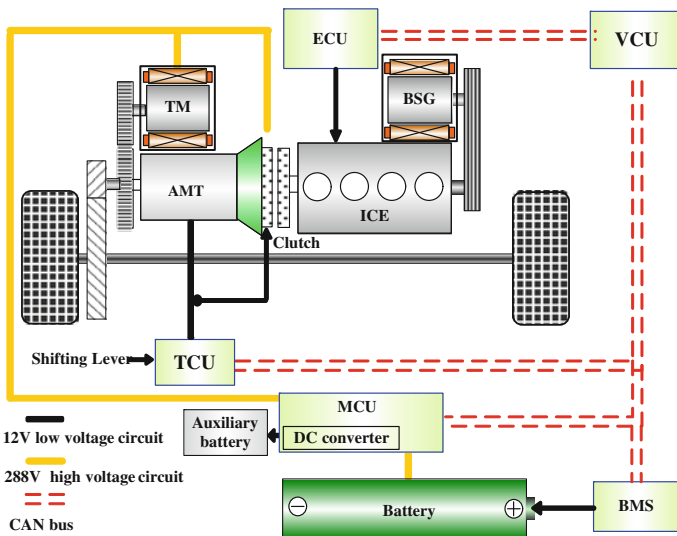
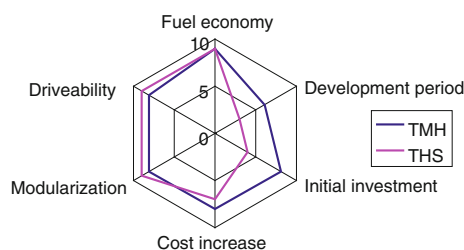


Fig. 1 TMH Configuration

investment because of the use of existing engine and transmission technology. The planetary gearbox technology in THS has the function of electric continuous variable transmission and can hold two motors in one case which have good

Table 2 Configuration evaluation

Performance index	Weighting coefficient (%)	①	②	③	④	⑤	⑥	⑦	⑧
Fuel economy	20	7	9	7	7	9	5	7	3
Cost increase	20	3	3	3	5	7	5	7	5
Fun to drive	10	9	7	7	9	7	7	9	7
Driveability	15	7	9	9	7	9	9	5	3
Development period	10	5	5	5	7	7	5	5	7
Modularization	15	3	3	3	5	7	5	7	7
Initial investment	10	3	3	3	5	7	5	5	9
Total	100	5.2	5.7	5.3	6.3	7.7	5.8	6.5	5.4

Fig. 2 Comparative analyses of TMH and THS

modularization. In conclusion, the overall properties of TMH and THS are equivalent.

3 Development of Besturn B70HEV

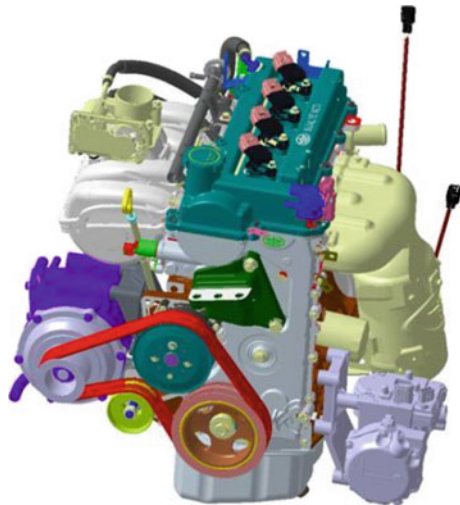
By applying the TMH full hybrid configuration to B70 model, FAW developed the BESTURN B70HEV (Table 3).

3.1 Dedicated Engine for Hybrid Vehicle

To increase the load ratio of engine, engine with small displacement was adopted. Different from B70 model mounted with a 2.0 L engine, the hybrid model was equipped with a 1.5 L engine. The dedicated engine was an update of the CA4GA5 engine. There were many advanced technologies used in this engine such as DOHC, electronic throttle control and variable valve timing. The generator and power steering pump were cancelled. Air conditioning compressor was driven by an electric motor. To meet the requirement of driving and electric power generation, a dedicated poly V-belt was developed. Frequent start-stop made the emissions worse, so the proportion of three-way catalyst was modified (Fig. 3).

Table 3 Basic specification of B70HEV

Curb weight (kg)	1524	
Length/Width/Height (mm)	4705/1782/1465	
Wheel base (mm)	2675 mm	
Track (mm)	Front: 1540, Rear: 1540	
Seating capacity	5 passengers	
Drive line	FF	
Engine	Displacement (L)	1.497
	Peak power (kW/rpm)	74/6000
	Peak torque (Nm/rpm)	135/4400
Traction motor	PMSM (40 kW/300Nm)	
BSG	PMSM (10 kW/50Nm)	
Battery	Lithium-ion battery (5.3Ah/300 V/36KW)	
Maximum speed (km/h)	>170	
Maximum gradeability (%)	>30	

Fig. 3 The dedicated Engine for HEV

3.2 Integration of Motor and AMT

In the TMH configuration, the traction motor and the AMT are integrated. The output shaft of the motor and the output shaft of the transmission were coupled by high-speed metal silent chain. This design made the motor and the AMT in one shell. The scheme made full use of the limited space of the engine bin, which overcame the difficulty of layout in engine bay, seal of motor water cooling, seal of motor shaft oil and other difficulties in integrated design. This program could also easily realize the AMT shifting without power interruption and the pure electric driving. What's more, this configuration had the advantages of compact structure, high transmission efficiency, lightweight and low cost (Fig. 4, Table 4).

Fig. 4 Traction motor coupled AMT

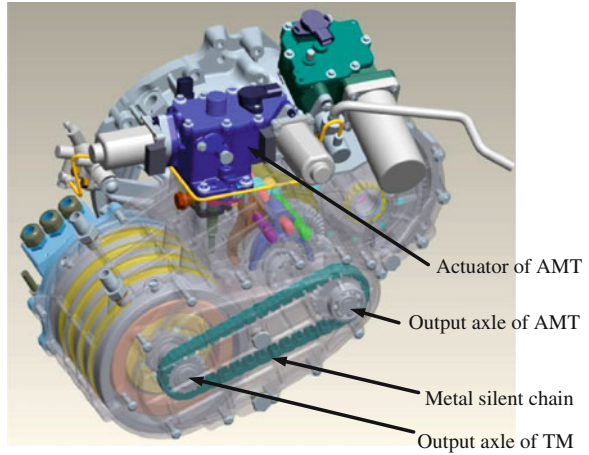


Table 4 Specification of AMT

Technical Data	Transmission type	Automatic manual transmission
	Model number	5T150AMT
	Maximum input torque (Nm)	150
	Gear ratio (1/2/3/4/5/R)	3.091/1.895/1.241/0.919/0.756/3.214
	Main reduction gear ratio	4.313

Table 5 Specification of the battery

Nominal capacity (Ah)	5.3
Nominal voltage (V)	300
Power (KW)	44
SOC precision	≤5 %
Internal resistance (Ω)	<0.3

3.3 Lithium-Ion Power Battery

Lithium-ion power battery was adopted as power supply in this full hybrid system. Lithium ion battery has good thermal diffusivity. This characteristic made it convenient to adopt air cooling system. PWM hierarchical control was used in battery pack air cooling system of the battery pack. The cooling fan speed control system increased the system efficiency and improves the NVH performance. The battery system of B70HEV had a power density of 850 W/kg; (Table 5).

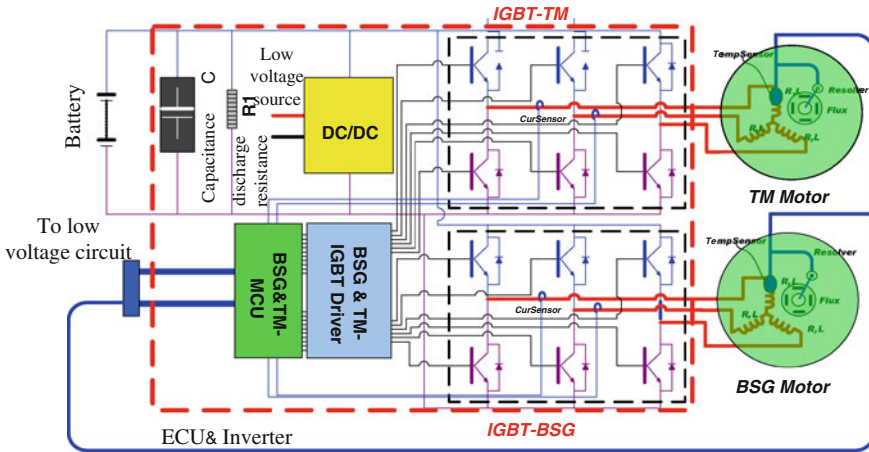
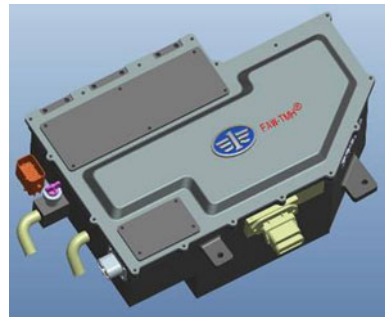


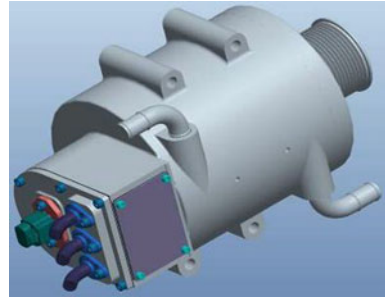
Fig. 5 Block diagram of motor system

Fig. 6 Motor controller



3.4 Motor System

The block diagram of motor system is shown in Fig. 5, including the control circuit, a BSG and a traction motor. The motor controller had three layer frames. The electric circuit was in upper and lower layer and in middle layer was water-cooling system. This structure integrated the BSG control unit, the traction motor control unit, inverter, DC/DC converter and electric air conditioning high voltage interface. The whole system was in one shell. The power density was 5.9 kw/L. With the characteristics of quick torque dynamic response and high operating accuracy, the motor could compensate for the shortcomings of the engine torque response lag, and then improved the dynamic response characteristics of the vehicle, finally improved the vehicle driveability. (Figs. 6, 7 and Table 6).

Fig. 7 BSG motor**Table 6** Specification of motor system

Item	BSG	Traction motor
Type	PMSM	PMSM
Peak power (kW)	10	40
Nominal power (kW)	5	20
Peak torque (Nm)	50	300
Nominal torque (Nm)	25	130
Speed range (rpm)	0 ~ 1,2000	-2,000 ~ 8,500
Valid diameter (mm)	130	200
Valid length (mm)	120	190

3.5 Control Technologies

In order to meet the challenges of drivability, fuel economy and strict emissions regulations, based on the TMH system, a series of control technologies were applied to BESTURN B70HEV.

3.5.1 Compensation for Power Interruption

As mentioned above, the output shafts of the traction motor and AMT were connected by a chain. This configuration made it possible to drive the vehicle in the shifting intervals of AMT. This technology compensated for the power interruption, and then improved the power performance of the vehicle equipped with AMT.

There are five stages in the process of AMT shifting.

1. Fuel Cut-Off
2. In this stage, the engine torque was reduced gradually, and then the BSG generating torque was also decreased. At the same time, the traction motor torque increased for vehicle driving.
3. Disengagement of clutch

4. Firstly, BSG generating torque was reduced to 0, then the engine torque was reduced gradually to 0, finally the clutch was disengaged completely. In this section, the driving force came from the traction motor only.
5. Gear selection and shifting
6. In this stage, AMT finished the operation of gear selection and shifting in 300 ms.
7. Engagement of clutch
8. The engine torque and the BSG generating torque is 0.
9. Fuel feeding
10. In this stage, the engine torque increases gradually, the traction motor torque decreases gradually. When the engine torque increases to a certain level, the generating torque is restored gradually.

3.5.2 Rapid Start of Engine

To reduce fuel consumption in the city cycle, engine in hybrid vehicle is turned off if the vehicle idling is over a certain time. It needs rich mixture to start the cold engine successfully. In the start process, the incomplete combustion of gas mixture will create much detrimental emissions and need extra fuel. Due to the problem mentioned above, it is difficult to set a time threshold when to stop the engine in the idling process. With a BSG motor, this problem was overcome because the BSG motor can drive the crankshaft into a high speed without fuel feeding. The use of BSG in the process of engine starting reduces fuel consumption and emissions, and improves starting comfort as well.

3.5.3 Regenerative Braking

Regenerative braking is one of the core technologies of hybrid. It concerns vehicle dynamic characteristics, generating characteristics of motor, battery safety assurance and charging characteristics and other problems. According to the strength of braking, the automobile braking mode can generally be divided into hard braking, moderate braking and light braking. Regenerative braking system should guarantee safe driving firstly. So it must meet some requirements.

1. Satisfy the braking safety requirements, conform to the driver's braking habits;
2. Consider the generating characteristic and output capacity of traction motor;
3. Ensure the battery safety during the charging process and prevent overcharge.

The requirements of regenerative braking are also factors need to be considered in motor selection. After verification, we found that 30 kW motor can meet the requirements of regenerating braking. What's more, because the braking regulations were also concerned, so the available energy in braking was limited.

Nevertheless, this technology has great potentialities in fuel economy. After using the regenerative braking system, 9 % fuel was saved in BESTURN B70HEV.

3.6 Performance Index

3.6.1 Economy Index

With the help of hybrid technology, fuel economy of B70HEV was improved greatly. In NEDC, the fuel consumption of the hybrid model is 5.9 L/100 km. Compared to the conventional model; it saved more than 35.2 % fuel, and met 130 g/km CO₂ emissions regulation in Europe in 2012.

3.6.2 Emission Index

The worldwide emissions regulation is increasingly strict. The emissions quality during the process of engine start is the worst. The BSG in FAW full hybrid system could propel the crankshaft to a high speed, which improved low-temperature starting performance of the engine. These initiatives were very useful to reduce engine emissions. The emissions level of B70HEV is as follows: THC: 0.048 g/km; CO: 0.519 g/km; NO_x: 0.045 g/km.

4 Development OF B50PHEV

The plug-in hybrid vehicle based on the TMH configuration had the Blended type plug-in hybrid function under ECE R101 regulation. In CD (Charge Depleting) Mode, the power was mainly from the battery, the engine worked only when more power was needed. In CS (Charge Sustaining) mode, the engine worked as in hybrid mode. Compared to the AER (ALL Electric Range) plug-in hybrid vehicle, this type of plug-in hybrid vehicle had advantage in cost, and what's more, the performance of the vehicle in the whole driving range changed little. It shared the technology platform with full hybrid system and most assembly products. Under this technical background, based on the BESTURN B70HEV, a plug-in model was developed by adding the charging system and using a new larger capacity battery pack (Table 7).

Table 7 Specification of B50PHEV

Item	Sub item	B70HEV	B50PHEV
Vehicle size	Curb weight (kg)	1,524	1,650
	Length/width/height (mm)	4705/1785/1465	4600/1785/1435
	Wheel base (mm)	2675	2675
Engine	Model	CA4GA5H	
	Displacement (L)	1.497	
	Peak power (KW/rpm)	74/6000	
	Peak torque (Nm/rpm)	135/4400	
Traction motor	Model	PMSM	
	Power/torque (KW/Nm)	40/300	
	Top speed (rpm)	7600	
BSG motor	Model	PMSM	
	Power/torque (KW/Nm)	10/50	
	Top speed (rpm)	12000	
Battery	Model	Lithium-ion battery	
	Capacity (Ah)	5.3	35
	Voltage (V)	300	320
	Peak power (KW)	44	50
Transmission	Type	5 speed AMT	

4.1 Charging System

FAW B50 plug-in hybrid model was equipped with a slow charging interface. The user could charge the battery at night in the household. In order to ensure the safety of the charging process, the on-board charger provided 12 V auxiliary power for some control unit.

4.2 Performance index

PHEV can operate with the battery power only. Once the SOC of battery decreases to a certain level, PHEV works in the same way as HEV. Today, customers hope that pure electric range of PHEV is as long as possible, but the energy density of battery is not as high as fossil fuel at present. In ECE drive cycle, FAW BESTURN B50PHEV's pure electric driving range reached 40 km. In NEDC, the model could run more than 70 km in CD mode.

Referring to the calculation methods of fuel consumption and electricity consumption on electric vehicles according to ECER101, the results were obtained as follows (Tables 8 and 9).

BESTURN B50PHEV not only had all the advantages of full hybrid vehicle, but extended the pure electric range which met the requirements of urban short-distance travel. When in the high-speed and long-distance traveling, it operated in

Table 8 Fuel consumption according to ECER101

Item	Time 0 ~ 100 km/ h	Max. speed	CD mode electricity consumption	CD mode fuel consumption	CS mode fuel consumption	Total fuel consumption
Value	12.5 s	110 km/ h	6.8kWh/100 km	2.2 L/100 km	6 L/100 km	3.2 L/ 100 km

Table 9 Result of B50 model

Item	Time 0 ~ 100 km/h	Fuel consumption
Value	13.6 s	8.5L/100 km

hybrid mode with good dynamic performance and fuel economy. The fuel consumption of B50PHEV was 3.2 L/100 km, which was 60 % less than that of B50 model.

5 Conclusion

FAW established an evaluation method of hybrid configuration. After analysis of the mainstream hybrid configurations around the world, the twin motors hybrid was chosen because of the advantage in cost and driving performance. This hybrid powertrain could be extended to plug-in system easily, and had good application prospects. Through the development of B70HEV and B50PHEV, FAW has mastered the hybrid technology and accumulated experience in hybrid system development. Based on the work above, FAW will supply inexpensive and clean vehicle soon.

The Research of Electromagnetic Fields During Testing of a Hybrid Powerplant and a Hybrid Car Prototype

Elena Teriaeva

Keywords Electromagnetic field · Hybrid vehicle · Bench test

As a result of an intensive use of the electric power in the last third of the 20th century the new significant factor of negative impact on the person and environment was created—electromagnetic pollution. With development of scientific and technical progress there are new sources of electromagnetic radiation that lead to increase of the scale of their influence, growth of intensity and the time of exposure of electromagnetic fields to the person. Considering the risks connected with electromagnetic pollution of urbanized territories, it is necessary to carry out an appraisal of the electromagnetic field and a contribution to an electromagnetic background of all widespread sources, including car.

The modern automobile, as one of the achievements of scientific and technical progress, not only made people more mobile and provided easy movement but also became a major source of negative impacts on populated areas, with significant influence on the quality of the environment and human health. Nowadays ecological safety of the car is generally based on estimation of accepted levels of noise, the content of harmful substances in the fulfilled gases and impact of these blowouts on the atmosphere. However according to some literary data the share of electromagnetic pollution by motor transport of the urbanized territories makes 18–32 % [1]. We consider that the increasing of cars (especially hybrid) on city highways will lead to change the level of an electromagnetic field. That is why the problem of research and decrease of internal and external electromagnetic fields parameters of the hybrid car becomes very actual [2].

Solving problems of ecological safety at a development stage of new samples of equipment is most effective way [3]. Therefore we carried out researches of

F2012-B02-074

E. Teriaeva (✉)

Moscow State University of Mechanical Engineering (MAMI), Moscow, Russia
e-mail: teryaeva.elena@gmail.com

Table 1 Frequency ranges of electrical equipment cars

N ^o	Source of electromagnetic radiation	Frequency ranges (MHz)
1	Ignition system	0.1–500
2	Sound signal	0.1–500
3	Turn indicator	0.3–30
4	Electric motors (screen wiper, fan)	0.3–250
5	Electrical equipment system (chains with powerful loadings, generating installations)	0–100
6	Tension of an onboard network	1–1000

internal and external electromagnetic fields of the hybrid car at a stage of the car power plant testing.

During the process of researching this problem an analysis of the frequency range of electrical equipment and electronics of modern cars was done. Frequency characteristics of electrical equipment of the car are presented in Table 1. Apparently from the provided data the electrical equipment of motor transport is source of electromagnetic fields, both in low-frequency, and in radio-frequency ranges that, undoubtedly, makes the contribution to formation of an electromagnetic background of the urbanized territories.

Today practically all researches of electromagnetic fields of the car are directed on researching of electromagnetic compatibility with other means in a radio-frequency range. As to data on impact of electromagnetic fields of motor transport on environment, the analysis of existing sources showed their insufficiency and discrepancy. Also now practically there are no methods and results of research of the mechanism of emergence and spatial distribution of amplitude and power parameters of external and internal electromagnetic fields of the car, and also normative documents and the recommendations limiting their negative impact on the person and environment [4].

The modern hybrid car represents a vehicle actuated by system «an internal combustion engine—the electric motor». Distinguish hybrid cars with the consecutive, parallel and series-parallel (mixed) interaction of electric motors and an internal combustion engine (ICE) [5]. For identification of levels of an electromagnetic field and development of the subsequent recommendations about decrease in its negative influence on environment and the person, researches at a stage of testing of the series-parallel scheme of the combined power plant of the hybrid car (Fig. 1) were carried out. This installation can work in several modes:

- “electric motor mode”
- “electric motor–ICE mode”
- “ICE-generator mode”

The main sources of electromagnetic field in the considered scheme are asynchronous electric motors with alternate current on industrial frequency of 50 Hz and the tension converter which is necessary for their work (inverter). It is

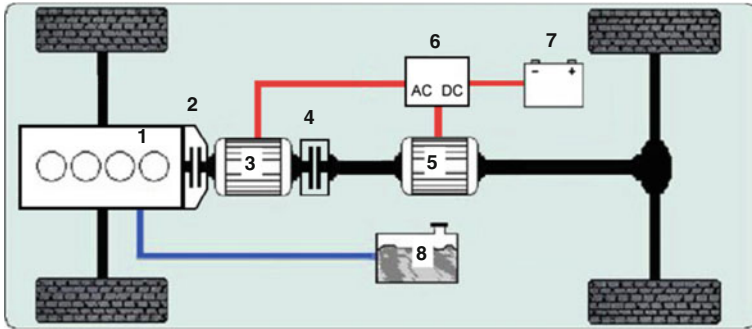


Fig. 1 Series-parallel circuit of hybrid vehicle powertrain: 1—ICE7; 2—connecting clutch; 3—reversible electric machine; 4—connecting clutch; 5—reversible electric machine, 6—converter of electric energy; 7—storage of electrical energy, 8—fuel tank

possible to assume that internal and external fields of the hybrid car are generated at frequency of 50 Hz, and also at frequencies caused by operation of the tension converter.

Now there is no method for detection of electromagnetic fields of a source at testing of the hybrid car power plant.

We offer the following method of definition of electromagnetic characteristics of a source of an electromagnetic field: round a source of an electromagnetic field the measuring surface conditionally gets out. As a measuring surface we accept a semi-sphere or a measuring surface which is located at the same measuring distance of d from a parallelepiped bending around a tested source of electromagnetic field (Fig. 2). The sizes of a parallelepiped should correspond to outline dimensions of a source. The measuring distance should be no more than 0.5 m, but also not less than 0.25 m. Points of measurements are necessary to have on a measuring surface. The quantity of measurement points should be not less than five. They should be located as it is specified in Fig. 2.

Researches have been made in the bench tests of sequentially-parallel scheme of combined power plant of hybrid car in “electric motor mode” in two frequency ranges of 5 Hz–2 kHz and 2–400 kHz. Results are presented in the Table 2.

On histograms (Fig. 3) the ratio of the received results with some established maximum permissible levels (MPL) of electromagnetic fields influence on the person is presented.

These results should be considered as preliminary. Further researches is needed to study the electromagnetic fields arising in various hybrid powertrain configurations: series, parallel and series-parallel (mixed), as well as arising electromagnetic fields during different modes of operation of electric motors and loads.

For research of internal electromagnetic fields of the hybrid car we offer the following technique.

During developing of the methodology there was took into account the results of the negative effects of electromagnetic fields on humans, which are given in various literature. On the basis of the data analysis the following levels of

Fig. 2 The scheme of measurement of electromagnetic fields at carrying out bench tests of power plant of the hybrid car

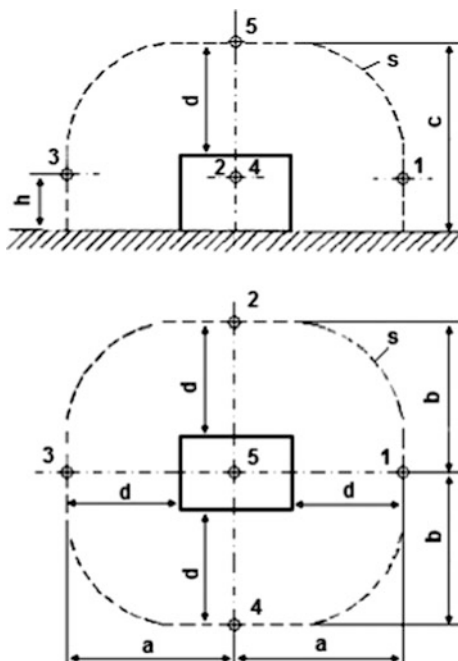


Table 2 Results of bench tests

Characteristics of an electromagnetic field	Point 1	Point 2	Point 3	Point 4	Point 5
Frequency ranges 5 Hz–2 kHz	$E = 2 \text{ V/m}$ $B = 1 \text{ mT}$	$E = 3 \text{ V/m}$ $B = 0,81 \text{ mT}$	$E = 6 \text{ V/m}$ $B = 1,34 \text{ mT}$	$E = 22 \text{ V/m}$ $B = 1,13 \text{ mT}$	$E = 6 \text{ V/m}$ $B = 1,73 \text{ mT}$
Frequency ranges 2–400 kHz.	$E = 3,38 \text{ V/m}$ $B = 54 \text{ nT}$	$E = 6,21 \text{ V/m}$ $B = 42 \text{ nT}$	$E = 0,79 \text{ V/m}$ $B = 76 \text{ nT}$	$E = 11,82 \text{ V/m}$ $B = 39 \text{ nT}$	$E = 3,18 \text{ V/m}$ $B = 26 \text{ nT}$

measurement points arrangement relative to a car floor were chosen: Level 1 (genitourinary system)—0.3 m, level 2 (cardiovascular system)—0.7 m; level 3 (brain)—1 m.

Researches of an internal electromagnetic field of the hybrid car were carried out in five point of salon (on a workplace of the driver and passenger seats) at all three levels (Fig. 4). Researches are carried out at the test-bench for testing of a car prototype equipped with parallel hybrid scheme combining an internal combustion engine and an asynchronous electric motor of alternating current of 35 kW output at motion of a car in “electric motor mode”.

As a result of researches of an electromagnetic field and comparison of the received data with a regulation of electromagnetic fields existing in the Russian Federation, the following ratios are received:

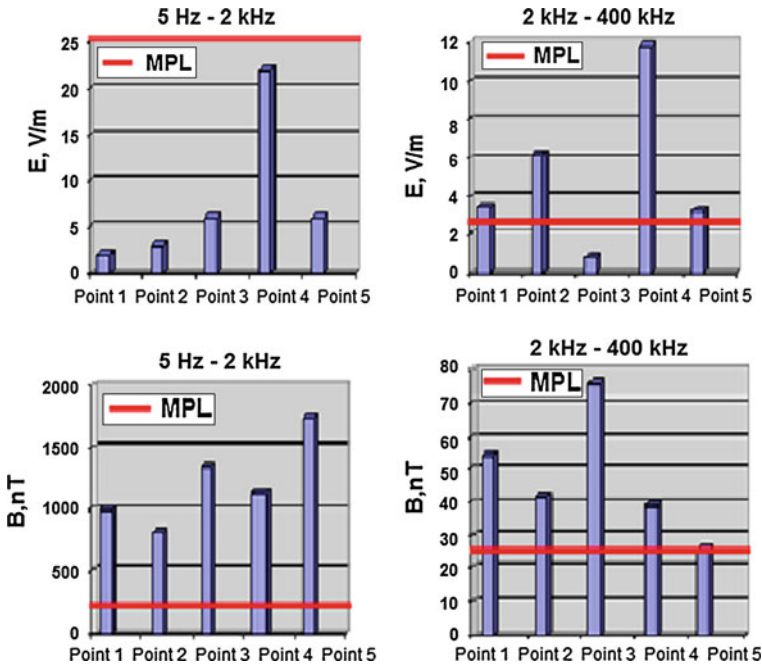


Fig. 3 The research results during bench testing power plant of hybrid car (on the top showed the values of electric intensity of the electromagnetic field—E, V / m at the bottom showed values of magnetic induction electromagnetic field B, nT)

- (1) In the frequency range 5 Hz–2 kHz the value of the electric field should not exceed 25 V/m. The maximum value received at carrying out measurements makes 202 V / m that exceeds admissible norms in 8 times. Limiting value of a magnetic induction in this range makes 250 nT, we fixed excess of this value in 5 times—1290 nT (Fig. 5).
- (2) In a range of frequencies of 2–400 kHz a value of magnetic induction should not exceed 25 nT. During researches 48 nT were received—that exceeds admissible norm in 1.9 times.(Fig. 6). Value of intensity of electric field in this range of frequencies equaled 0,001 V / m and didn't change in various points of measurement therefore on histograms aren't presented.
- (3) At frequency of 50 Hz of value of intensity of electric field E (V/m) and intensity of a magnetic field of H (A/m) on a workplace of the driver and passenger seats don't exceed the established limits. Values of intensity of an electric and magnetic field are presented on Fig. 7

In our opinion, results of testing and a comparative assessment of the received results with an existing regulation of electromagnetic fields showed a need of regulatory base creation, which establish admissible values of electromagnetic fields parameters at their impact on the driver (taking into account features of his work) and passengers. It is necessary to give special attention to influence the

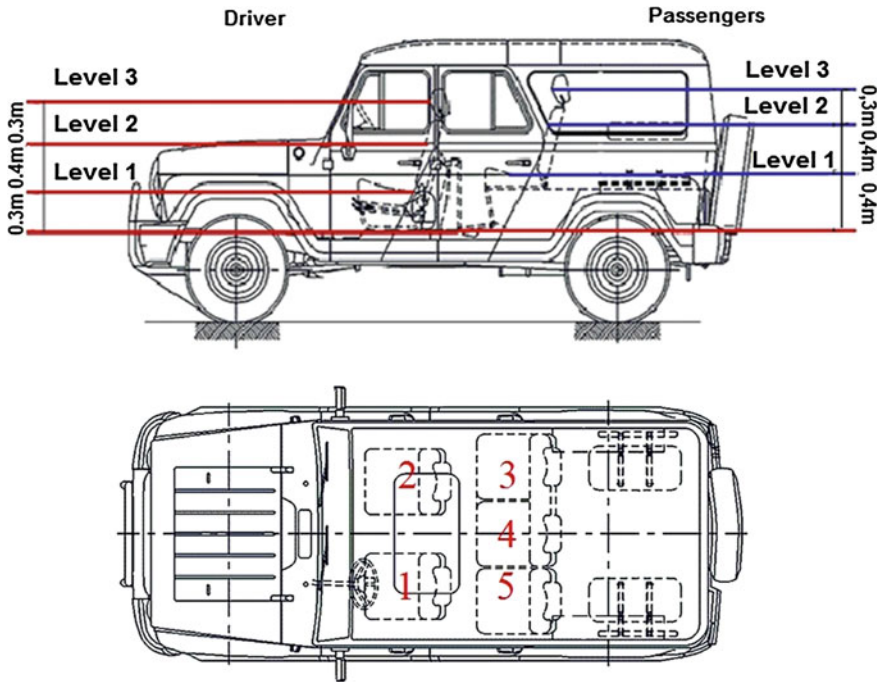


Fig. 4 The location of points and levels of measurement in the car: *red* levels of measurement for the driver and passenger in the front seat, *blue* for passengers in the backseat

electromagnetic fields arising in hybrid cars, on the driver seat, whose work differs complex influence of negative factors (noise, vibration, quality of air in the salon, the increased intensity and monotony of work).

We assume that dependence of the characteristic of electromagnetic fields on loading, hybrid powertrain types and body structure will be various. Therefore, further researches on definition of spatial distribution of amplitude and power parameters of an electromagnetic field are necessary.

The purpose of monitoring of an electromagnetic background along city highways and identification of a contribution of motor transport is its formation the following technique which has a number of features was developed:

1. Research of electromagnetic field (E, N) parameters an electromagnetic field (E, N) depending on a mode of behavior of vehicles:
 - idle running;
 - dispersal;
 - the established mode;
 - braking.
2. Research of electromagnetic field parameters depending on the intensity of traffic.

Fig. 5 Results of researches on the stand for testing of the prototype car in the frequency range 5 Hz–2 kHz (on the *top*—values of electric intensity of the electromagnetic field—E, V/m, at the *bottom*—values in the histograms of the magnetic induction in the electromagnetic field, nT)

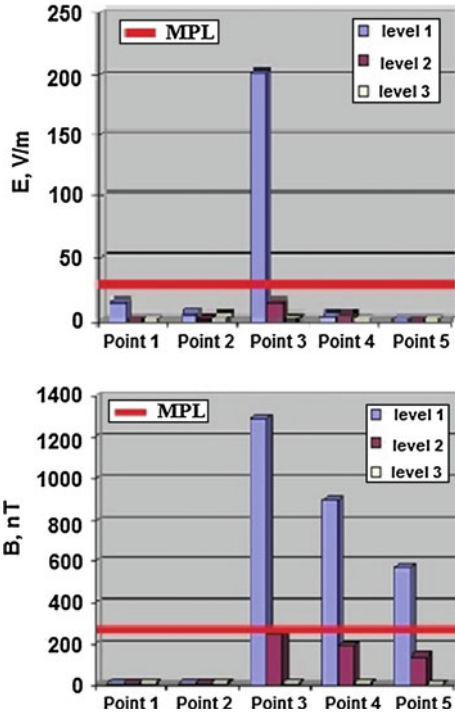
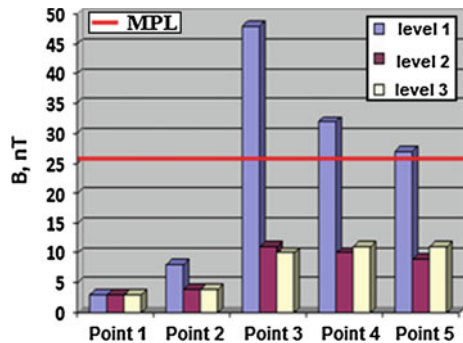


Fig. 6 Results of researches on the stand during testing of the prototype vehicle (frequency range 2–400 kHz)



3. Researches at different distances from the highway.

Measurements of parameters of an electromagnetic field were carried out in frequency ranges of 5 Gts-2 of kHz, 2–400 of kHz and on frequency of 50 Hz. In the analysis and processing of the received results indications of devices which arose when passing trolleybuses, when giving sound signals which increased average values repeatedly weren't considered Table 4.

Results of researches of electromagnetic fields along highways are given in Tables 3, 4, 5.

Fig. 7 Results of researches on the stand during testing of the prototype car at a frequency of 50 Hz (on the *top* shows the values of electric intensity of the electromagnetic field—E, V/m, at the *bottom* histogram values of the magnetic field—H, A/m)

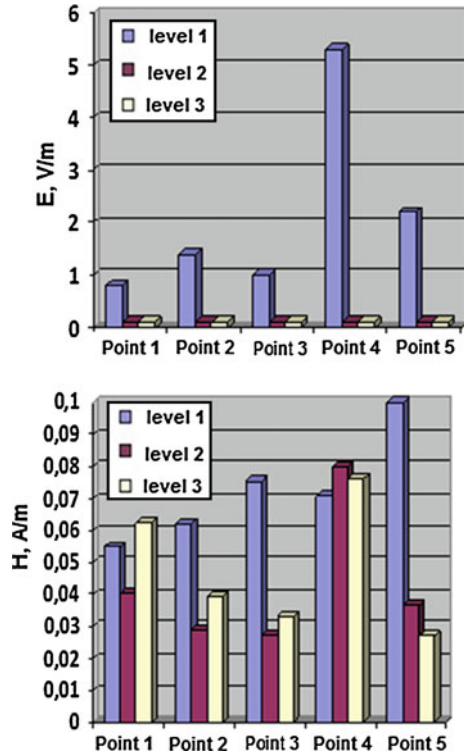


Table 3 The parameters of the electromagnetic field, depending on the mode of transport

№	Transport mode of behavior	Characteristics of an electromagnetic field in a frequency range 5 Hz–2 kHz		Characteristics of an electromagnetic field in a frequency range 2–400 kHz		H, A/m
		E, V/m	B, mT	E, V/m	B, nT	
1	Idle running;	0	0,00	0,16	0	0,03
2	Dispersal;	1	0,00	0,24	0	0,041
3	The established mode;	3	0,01	0,65	1	0,068
4	Braking.	0	0,00	0,10	0	0,04

The analysis of results of measurements allowed to draw the following conclusions:

- the greatest values are received at the established mode of movement of motor transport. Therefore, further researches should be carried out in this mode of movement.
- evident dependence of intensity of electric field in a range of 5 Hz–400 kHz and intensity of a magnetic field on frequency of 50 Hz from intensity of traffic is received. Values of a magnetic induction in a frequency range of 5 Hz–400 kHz

Table 4 Values of parameters of an electromagnetic field depending on intensity of traffic

№	Transport mode of behavior	Indicators of an electromagnetic field in a frequency range 5 Hz–2 kHz		Characteristics of an electromagnetic field in a frequency range 2–400 kHz		Characteristics of an electromagnetic field at frequency 50 Hz
		E, V/m	B, mcT	E, V/m	B, nT	
1	Idle running;	0	0,00	0,16	0	0,03
2	Dispersal;	1	0,00	0,24	0	0,041
3	The established mode;	3	0,01	0,65	1	0,068
4	Braking.	0	0,00	0,10	0	0,04

Table 5 Values of parameters of an electromagnetic field depending on removal of an edge are expensive

№	Distance from an edge of a carriageway, m	Indicators of an electromagnetic field in a frequency range 5 Hz–2 kHz		Characteristics of an electromagnetic field in a frequency range 2–400 kHz		Characteristics of an electromagnetic field at frequency 50 Hz
		E, V/m	B, mcT	E, V/m	E, V/m	
1	0	112	0,01	0,32	1	0,232
2	1	86	0,01	0,22	1	0,186
3	2	62	0,01	0,17	1	0,172
4	3	40	0,01	0,03	1	0,113
5	4	17	0,01	0,01	1	0,09
6	5	10	0,01	0,01	1	0,072

do not change and do not depend on intensity of traffic. Values of intensity of electric field on frequency of 50 Hz change slightly.

- at increase in distance from an edge of the road there is a reduction of parameters of an electromagnetic field.

Thus, the received results show dependence of electromagnetic field parameters on a mode of movement, intensity of movement of motor transport and distance from a road edge that confirms the made assumption of influence of transportation streams on an electromagnetic background of the urbanized territories.

Analyzing the received preliminary results, we consider that channelized researches are actual and it is necessary to continue work on the following directions:

- electromagnetic monitoring along city highways;
- research of spatial distribution of amplitude and power parameters of an external and internal electromagnetic field of the hybrid car that will allow to solve essentially new problems of decrease in negative impact of this field on the person and environment at a car design stage.

This research were carried out under the direction of the professor, Doctor of Engineering Grafkina and the professor, Doctor of Engineering Nyunin.

References

1. Volodina NA, Starostin AK (1997) Problems of electromagnetic compatibility of electronic equipment and electrical equipment of vehicles—M: NIIAE, 260
2. Grafkina MV, Teryaev EP An urgency of probe of electromagnetic fields of the car// Information systems and models in scientific probes, the industries and ecology—Tula: innovative technologists, 201: pp 107–109
3. Grafkina MV (2006). Ecological design of production—M: MGTU “MAMI” p 224
4. Grafkina MV, Nyunin BN (2012) Probe of thin structure of infrasonic and electromagnetic fields of the car//Izvestia MGTU MAMI, No. 3 p 180–184
5. URL: <http://www.avtonov.svoi.info/hybrid.html>

Research on the Efficiency of the Dual-Mode Hybrid Vehicle

Weiying Yan, Changle Xiang, Lijin Han and Donghao Zhang

Abstract The dual-mode power-split-type hybrid transmission system is a typical multi-input and -output system, hence the efficiency analysis is complicated compared with conventional vehicles. In this chapter, a comprehensive efficiency model of the dual-mode hybrid vehicle is built on the basis of power loss analysis, including the engine fuel conversion power loss, the charge/discharge power loss of the battery pack and the coupling mechanism power losses. The exact model of the coupling system is investigated considering the motor loss, gear spin loss, clutch/brake loss, bearing loss and sealing loss. Besides, a control strategy is further developed to achieve the optimal system efficiency by selecting the engine operation point and the power of the battery pack. The simulation results show that the new strategy can greatly improve the fuel economy of the vehicles.

Keywords Hybrid · Dual-mode · Efficiency · Optimization · Control strategy

F2012-B02-075

W. Yan (✉) · C. Xiang · L. Han · D. Zhang
Beijing Institute of Technology, Beijing, China
e-mail: 496606522@qq.com

C. Xiang
National Key Lab of Vehicular Transmission,
Beijing Institute of Technology, Beijing, China

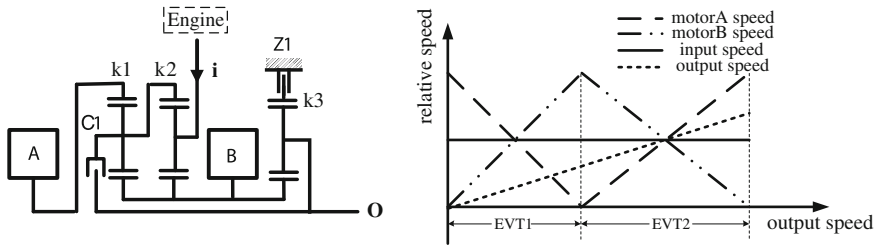


Fig. 1 Dual mode PST and its speed characteristic diagram

1 Introduction

The multi-mode electro-mechanical composite transmission has been drawing much attention since the Toyota Prius successfully launched into market in 1997, it is a single-mode hybrid vehicle. General Motors has been committed to the development of multi-mode hybrid system since the 1990s, and has applied for dozens of related patents [1–3]. In early 2005, GM combined with Daimler Chrysler and BMW to develop a dual-mode power-split-type hybrid transmission system (PST), which now has achieved a successful application. Compared with conventional vehicles, the fuel economy is improved by 20–54 % [4].

Figure 1 shows the structure of the dual-mode PST. Motor A and B can work either as generator to provide energy to the battery pack, or as a motor to drive the vehicle. Therefore, this coupling mechanism is a multi-input and multi-output system. Besides, the charging and discharging power of the battery pack are changeable. Hence, the input and output components of the system are variable, which all contributes to the complexity of the efficiency analysis of the dual-mode PST.

The control strategy of dual-mode PST. In paper [5] is built upon the basis of efficiency analysis without considering the mechanical power loss. Although chapter [6] makes it up, the calculation is still relatively simple, and does not take the impact of electrical power loss into account. In this chapter, a system efficiency model of the dual-mode hybrid vehicle is proposed based on the energy loss analyses, which includes engine loss, electrical loss and mechanical loss. And the results are used to propose an operation control strategy.

2 The System Model of the Dual-Mode Hybrid Vehicle

Figure 2 illustrates the energy flow of the dual-mode hybrid vehicle. It is obvious that the system is mainly composed of three parts: the battery pack, the engine and the power coupling system. The power coupling system consists of three planets row, clutch C1, brake Z1, MGA and MGB.

Fig. 2 Energy flow analysis of dual-mode hybrid system

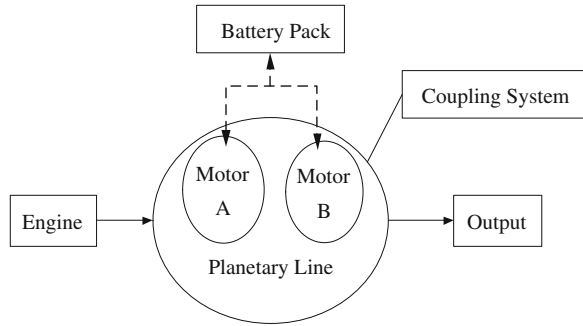


Table 1 Two operational status of control parts

	Z_1	C_1
EVT1	●	○
EVT2	○	●

Note ○ shows separation
● shows engagement

In this paper, the system efficiency model is built from the perspective of power loss. Define the system efficiency as the ratio of output power to the input power. That is, the input power minus all of the power losses of the system, and then divided by the input power (Table 1).

It can be seen from Fig. 2, the system power loss mainly consists of the following aspects: the thermal power loss of the engine, the energy conversion loss of the MG, the battery pack’s charge/discharge power loss, as well as mechanical power losses in the planetary coupling mechanism.

2.1 The Efficiency of the Coupling System

The power loss of the Coupling system mainly includes gear spin loss, clutch and brake loss, sealing loss, the bearing loss and churning loss. Since no churning gear is included in the structure, the churning loss is not studied in this paper.

2.1.1 Planetary Line Efficiency

Professor M.A.Крејес’s study [7] shows superiority when the planetary mechanism is complex, thus it is chosen to calculate the planetary line efficiency.

Take EVT2 mode for example, clutch C_1 is engaged and brake Z_1 is opened. Based on the speed relationship of the internal and external meshing single-star planetary gear set, the rotational speed satisfies the following relationship:

$$\begin{bmatrix} n_a \\ n_b \end{bmatrix} = \begin{bmatrix} -\frac{1+k_2}{k_1} & \frac{1+k_1+k_2}{k_1} \\ 1+k_2 & -k_2 \end{bmatrix} \begin{bmatrix} n_i \\ n_o \end{bmatrix} \quad (1)$$

Where n_a is the rotational speed of MGA, n_b is the speed of MGB, n_i is the input speed of coupling system, k is the characteristics parameters, it is the ratio of the ring gear number of teeth to the sun gear number of teeth.

1. Define the overall speed ratio of the coupling system as:

$$i_c = \frac{n_i}{n_o} \quad (2)$$

Then, it can be calculated that:

$$i_c = \frac{n_i}{n_o} = 1 - \frac{k_1}{(1+k_2)} \frac{(n_a - n_b)}{(n_b + k_1 n_a)} \quad (3)$$

2. Based on Professor M. A. Крејћес's study,

$$k'_i = k_i (\eta_i)^{\alpha_i} \quad (4)$$

where η_i is the efficiency of the converted mechanism. Set the internal and external meshing efficiency of a single-star planetary gear to 0.99 and 0.98 respectively. Thus, the efficiency of the converted mechanism is $\eta_i = 0.98 \times 0.99 = 0.97$.

The index α_i in Eq. (4) can be obtained by the following formula:

$$\alpha_i = \operatorname{sgn} \left(\frac{k_i}{i_c} \cdot \frac{\partial i_c}{\partial k_i} \right) \quad (5)$$

Where sgn represents the symbolic function.

3. Finally, by replace k_1, k_2 with k'_1, k'_2 , the corrected overall transmission ratio i'_c can be obtained. In conclusion, the efficiency of the coupling system considering the gear spin loss can be achieved by the following formula:

$$\eta_{mesh} = \frac{i'_c}{i_c} \quad (6)$$

Accordingly, dynamic analysis of the single-star planetary gear set considering gear spin is rewritten as follows:

$$T_{ii} : T_{qi} : T_{ji} = 1 : k'_i : -(1 + k'_i) \quad (7)$$

2.1.2 MG Loss

It is assumed that the auxiliary systems of the vehicle do not need electric power, and then the electric power of the two motors and the charge/discharge power of the battery pack are balanced.

$$T_A n_A \eta_A^{-\text{sgn}(n_A \cdot T_A)} + T_B n_B \eta_B^{-\text{sgn}(n_B \cdot T_B)} + P_{bat} = 0 \tag{8}$$

Where η_A, η_B represents the efficiency of MGA and MGB, that can be obtained through performance test. To simplify the calculation, it is assumed that the efficiency of the motor/generator is 90 %.

Based on the speed-torque relationships that were previously derived for the dual-mode PST, the MG loss is as follows:

$$P_{loss_gm} = T_A n_A (\eta_A^{-\text{sgn}(n_A \cdot T_A)} - 1) + T_B n_B (\eta_B^{-\text{sgn}(n_B \cdot T_B)} - 1) \tag{9}$$

2.1.3 Clutch and Brake Loss

The towing loss is achieved when the clutch and brake are not engaged. That is, at EVT1 mode, towing loss only exists in clutch C1, whereas at EVT2 mode, it only exists in brake Z1.

Newton’s law of viscosity is applied to calculate the towing loss, the dynamic equation is as follows [8]:

$$P_L = \frac{\pi^2}{573 \times 10^3 h} z \mu \Delta n^2 (R_2^4 - R_1^4) \tag{10}$$

In the equation, μ is the dynamic viscosity of the oil, and it is assumed to be a constant; h is the clutch gap; z is the number of friction faces; Δn is slip speed; R_1, R_2 , represents the inner and outer radius of the oil film between the clutch plates.

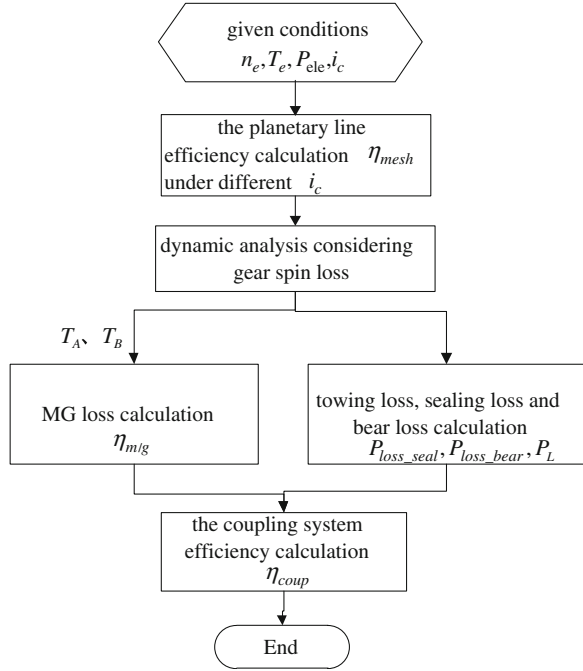
2.1.4 Bearing Loss

The bearing friction loss can be approximately calculated as follows:

$$\begin{cases} P_{loss_bear} = \frac{\pi M}{30} \\ M = F \mu d / 2 \\ F = \sqrt{F_a^2 + F_r^2} \end{cases} \tag{11}$$

Where M is the friction torque of the bearing; μ represents friction coefficient; F is the load of the bearing; d is its inner diameter; F_a, F_r are the axial and radial load of the bearing.

Fig. 3 The calculation process of the efficiency of the coupling system



2.1.5 Sealing Loss

$$P_{loss_seal} = 7.9 \times 10^{-9} \left(\sum_{j=1}^k d_j n_j \right) \tag{12}$$

where d_j is the journal of the j th seal, and n_j is speed.

In summary, the coupling efficiency calculation process of the dual-mode PST considering various power losses is as follows Fig. 3:

Set the power of the battery pack $P_{bat} = 0$, the changing regularity of the coupling system efficiency for each dual-mode PST operation mode over speed ratio is shown in Fig. 4.

It can be seen in Fig. 4 that the coupling efficiency is relatively higher at the point where the power of motor A or B is zero, which are named mechanical points (MP), since there is no power flows through the electrical path, all the power generated from the engine flows through the mechanical path. Thus, the power loss in the electrical path is zero, and the transmission efficiency is 100 %. The structure in Fig. 1 has one MP in EVT1 mode and two MPS in mode EVT2. Figure 4 illustrates that in EVT2 mode, the efficiency between the two MPs is relatively higher, and decreases as the operation points deviated from the MP. In EVT1 mode, as it has only one MP, the farther the speed ratio is from the mechanical point, the lesser the efficiency will be due to the power circulation. The

Fig. 4 The changing regularity of the coupling system over speed ratio

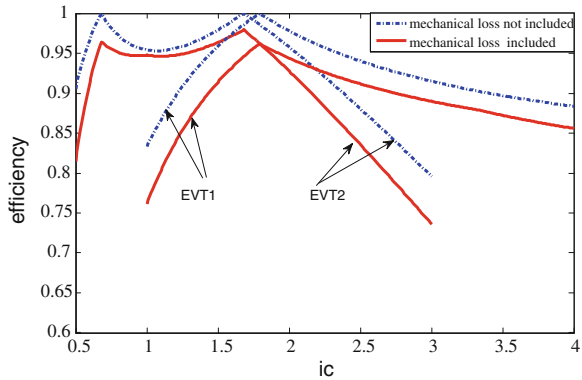
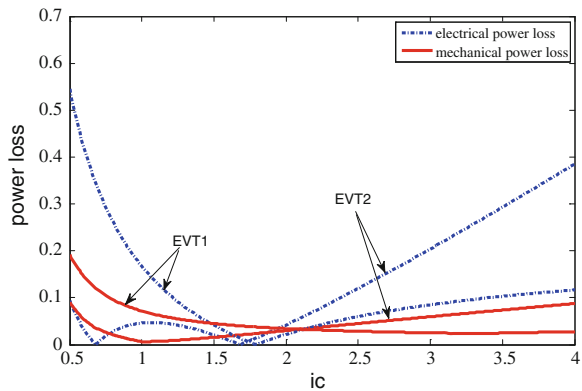


Fig. 5 The comparison between the electric power losses and mechanical losses

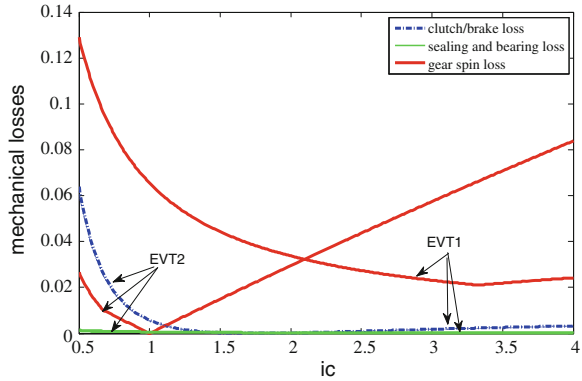


dual-mode PST has different efficiency under the same speed ratio, the higher one means the better fuel economy, and should be a priority choice. The solid line in Fig. 4 considers both the MG power loss and mechanical power losses of the coupling system, whereas the dotted line only takes the MG power loss into account.

To further study the power loss of the Hybrid system, Fig. 5 depicts the comparison between the electric power losses and mechanical losses. Since the power of battery pack is set to zero, the electric power losses of the system only includes the MG power loss. It can be seen that the system power losses are mainly caused during the MG's energy converting process, but this doesn't mean that the mechanical power loss is ignorable. In some regions, the change rate of electric power loss is relatively higher, these are the areas where the vehicle should not work in. Comparatively, the mechanical power losses change gently in most cases.

Figure 6 clearly illustrates the composition of mechanical losses. We can see from the figure that the gear spin loss contributes for the major part, followed with the towing losses of clutch and brake, which shows a very small difference between the two modes, and is bigger only when the overall speed ratio is

Fig. 6 The composition of mechanical losses



relatively small. As a contrast, the green part of the curve in Fig. 6 represents the sealing loss and bearing loss, which shows minimal effect on the overall efficiency of the coupling mechanism, and thus can be ignored in the following research.

2.2 The Efficiency of the Coupling System

In the hybrid system, the coupling efficiency is only a part of the overall system efficiency. To measure the overall efficiency of the system, we also need to consider the loss of the engine and the battery pack. When the operation point of the engine is determined, its fuel convention efficiency can be obtained by look-up table. The charge/discharge efficiency of the battery pack is determined by both SOC and the charge/discharge power. Thus, the overall efficiency of the system can be calculated.

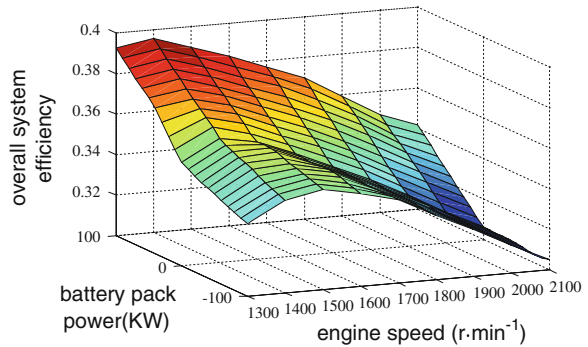
When the power of battery pack is above zero ($P_{bat} > 0$), it works as a power source, as a result, the system has two sources of power—the engine and the battery. When the power of battery pack is below zero ($P_{bat} < 0$), it works as a load, and at this time the system only has one power source—the engine.

Define the overall efficiency of the dual-mode hybrid system as:

$$n_{sys} = \begin{cases} \frac{P_o}{\frac{P_e + P_{bat}}{\eta_e \eta_{dis}}} & \text{when } P_{bat} > 0 \\ \frac{P_o - P_{bat} \eta_{chr}}{P_e / \eta_e} & \text{when } P_{bat} \leq 0 \end{cases} \quad (13)$$

In the equation, P_o is the demand power of the vehicle; η_{chr}, η_{dis} represents the charge and discharge efficiency battery pack respectively; η_e is engine thermal efficiency.

Fig. 7 The changing regularity of the overall system efficiency



3 Control Strategy Based on the Optimal Overall System Efficiency

To improve the fuel economy of the vehicle, it is important to analyse the overall efficiency of the dual-mode hybrid system. Through appropriate control, when the MG status in the coupling mechanism changes, the operating point of the engine changes as well, thus improves the fuel conversion efficiency, so that the overall efficiency of the dual-mode hybrid system can reach the optimal point.

Based on this theory, the control strategy of the structure in Fig. 1 is studied. When the vehicle is running, the speed, which represents its state of motion, is certain; The throttle opening and the speed of the vehicle together characterize the driver’s intent, it directly relates to the demand power; The SOC is the estimator of the battery pack’s state of charge. When the vehicle’s operation state is given, the above three parameters are determined at a certain value. At this time, the variables that can be used to control and regulate the engine state only remains the engine speed and the charge/discharge power of the battery pack.

Suppose the current vehicle state is as follows: vehicle speed $v = 60$ km/h, the power demanded $P_o = 500$ KW, and the SOC is 0.6. Let the battery pack charge/discharge power changes from -100 to 100 KW, the engine speed changes from $1,200$ to $2,200$ r/min, the calculated overall efficiency of the system is shown in Fig. 7.

From the above figure, it is clear that the charge/discharge power of the battery pack has certain effect on the overall system efficiency. As the discharge power increases, the system’s overall efficiency tends to increase. The mainly reason is that when demand power is fixed, the more electric power absorbs, the smaller the required engine power will be, thus the engine can operate at a relatively lower speed range. It can be seen from the engine fuel conversion efficiency map (Fig. 8b) that the engine fuel conversion efficiency is higher at a lower speed. Figure 8a depicts the comparison of engine power loss, the electric power loss (battery power loss and the MG power loss included), and the mechanical power losses in the coupling system. Obviously, the proportion of engine power loss is the largest, the electric power loss followed, and the mechanical power loss is the

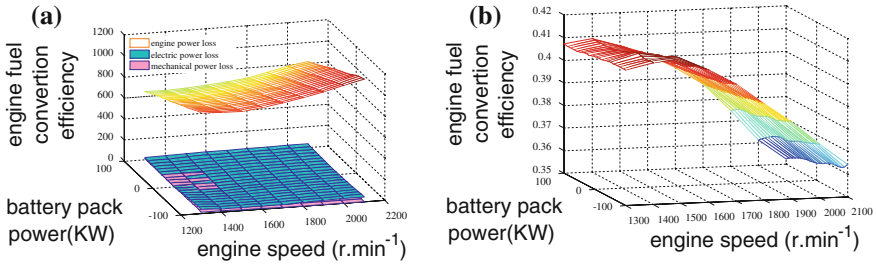


Fig. 8 The power losses of the system and engine fuel conversion efficiency

tiniest. Hence, the control strategies widely studied are mostly based on the controlling of the engine operation point to its optimal operation line. Meanwhile, the above calculation results assume the SOC is 0.6, at this point, the internal charge/discharge resistance of the battery pack is relatively small, therefore, the power loss is not big. As a result, the electric power loss has little effect on the system efficiency. As the SOC changes, the effect of battery pack power loss on the system efficiency will gradually increase.

It can be concluded from the calculation results of Fig. 7 that, when $P_{bat} = 100$ KW, $n_e = 1,500$ r/Min, the overall efficiency of the system is the highest $\eta_{sys} = 0.391$. However, when $P_{ele} = -80$ KW, $n_e = 2,100$ r/Min, the overall efficiency reaches the lowest level $\eta_{sys} = 0.304$, with a difference of 28 %. Thus, the optimal control strategy based on efficiency study can greatly improve vehicle fuel economy.

4 Conclusions

Unlike the traditional mechanical transmission system, the efficiency of the dual-mode Electrical-Mechanical compound transmission system is more complex, since it is a typical multi-input and multi-output system. Above all, the definition of the coupling mechanism efficiency is put forward from the perspective of power loss between the input and the output, considering energy conversion power loss of MG, the gear spin loss, clutch and brake loss, sealing loss and the bearing loss. It is concluded that the MG power loss plays a big role in the power losses of the coupling system, following with the gear spin loss. However, the bearing loss and the sealing loss are so tiny that they can be ignored. Then the system efficiency is further explored by taking the energy conversion loss of the engine and battery pack into account. Besides, the main factors influencing the overall efficiency of the system are studied. The results show that fuel conversion efficiency of the engine plays a big role, whereas the coupling efficiency only affects the overall efficiency when the gear ratio is too large or too small. On this basis, the control strategy based on the optimal efficiency of the system is put forward. The simulation results show that it greatly improves the vehicle fuel economy.

References

1. Alan GH, Donald K, Michael RS (2003) Electrically variable transmission with selective input split, compound split, neutral and reverse modes: USA, 6527658 B2 [P], 4 Mar 2003
2. Michael RS, Donald K (2000) Two-mode, compound-split, vehicular transmission having both enhanced speed and enhanced tractive power: USA, 6090005 [P]. 18 Jul 2000
3. Alan GH (2005) Two range electrically variable power transmission: USA, 6945894 B2 [P]. 20 Sep 2005
4. Grewe TM, Conlon BM, Holmes AG (2007) Defining the general motors 2-mode hybrid transmission [C]. SAE Paper 2007-01-0273
5. Kukhyun A, Sungtae C, Wonsik L et al (2006) Performance analysis and parametric design of the dual-mode planetary gear hybrid powertrain[J]. *Automob Eng* 220(D): 1601-1614
6. Jaeyoung K, Woulsun C, Sunghwa H et al (2011) Control strategy for dual-mode power split HEV considering transmission efficiency[J]. *IEEE*, 978-1-61284-247-9
7. Mouliu C, Yinguo F, Yu L (2004) Application of speed-ratio approach in the efficiency calculation of planetary transmission[J]. *Manufacturing Information Engineering of China*, 33(6)
8. Zhenguang K, Biao M (2003) Modeling and Calculation of Vehicle Transmission Watt Loss[J]. *Vehicle power technology* 2:25-28

Power Transmission Properties of Dry Hybrid V-Belt with Protuberant Tension Member on Contact Surfaces of Blocks: It's Effect with Respect to Speed Ratio

Hirotoishi Kawakami, Kazuya Okubo, Toru Fujii,
Hiroyuki Sakanaka and Ryuichi Kido

Abstract The purpose of this study is to investigate the effect of protuberance on the power transmission properties of the Continuously Variable Transmissions (CVT) with dry hybrid V-belt under several conditions of speed ratio. The power transmission properties were examined in three conditions of speed ratio ($i = 0.5, 1.0$ and 2.0) by using three type belts in which the height of the protuberance was $0, 0.06$ and 0.09 mm, respectively. Both pulley thrusts on driving and driven pulley and contraction force were measured by using load cells. Rotating speeds of the both pulley shafts and the torque to the both pulleys were measured by speed pickups and torque meters, respectively. To evaluate of the power transmitting properties of the CVT, thrust ratio, conversion ratio, transmitting efficiency and slip ratio were investigated. It was found that the highest maximum thrust ratio, conversion ratio, transmitting efficiency and allowable driving input torque were obtained when protuberant tension member was used with 0.09 mm of height, respectively. In any condition of speed ratio, applying the protuberance on the side sliding surfaces was effective to improve the power transmission properties.

Keywords CVT · Dry hybrid V-belts · Power transmitting properties · Speed ratio

F2012-B02-076

H. Kawakami (✉)

Graduate student of Doshisha University, Kyoto, Japan

e-mail: dtl0336@mail4.doshisha.ac.jp

K. Okubo · T. Fujii

Department of Mechanical Engineering, Doshisha University,

1-3 Tatara-miyakodani, Kyotanabe, Kyoto 610-0321, Japan

H. Sakanaka · R. Kido

Bando Chemical Industries, Ltd, 1242-5 Mogami, Momoyama-cho, Kinokawa,

Wakayama 649-611, Japan

1 Introduction

Public attentions are widely focused on Continuously Variable Transmissions (CVT) to improve the fuel consumption of automobiles [1–3]. For many automobiles, metal type V-belt are generally used in recent years, however, it has a problem of remarkable energy loss at oil pump [4, 5]. To improve the efficiency of driving train having metal type V-belt, power loss of the oil pump should be reduced, because high oil pressure is kept to maintain the contraction force on the pulleys. In contrast, dry hybrid V-belt type CVT has been expected again to reduce the energy consumption, because oil pump is not necessary to apply contraction force in the system. Past study showed that some transmitting properties of dry hybrid V-belt were improved by applying the protuberances on the side sliding surfaces [6]. In that study, however, the effect was shown only under a condition of low speed ratio, while they should be discussed under any conditions of speed ratio.

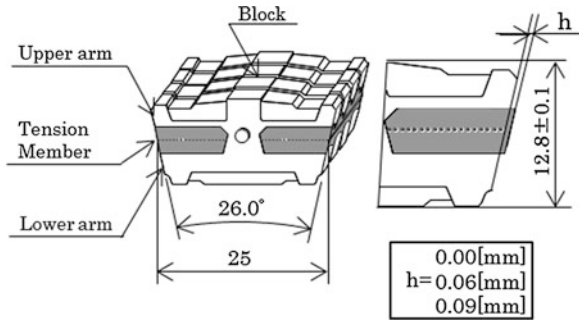
The purpose of this study is to investigate the effect of protuberance on the power transmission properties of the dry hybrid V-belt under several conditions of speed ratio. The power transmission properties were examined in three conditions of speed ratio ($i = 0.5, 1.0$ and 2.0) by using three type belts that the height of the protuberance was $0, 0.06$ and 0.09 mm, respectively. Both pulley thrusts on driving and driven pulley and contraction force were measured by using load cells. Rotating speeds of the both pulley shafts and load torque to the both pulleys were measured by speed pickups and torque meters, respectively. To evaluate of the power transmitting properties of the CVT, thrust ratio, conversion ratio, power efficiency and slip ratio were investigated.

2 Experimental Procedure

2.1 Structure of Dry Hybrid V-Belt

Figure 1 shows assembled dry hybrid V-belt assembly used in this study. Dry hybrid V-belt consisted of 204 lateral H-shaped blocks individually connected by a pair of tension members. In order to obtain a high transmitting performance and durability, blocks consist of a core made of aluminum alloy covered with heat resistance resin. The tension members had aramid fibers and rubber to satisfy high tensile strength, stiffness and flexibility. The tension members were inserted into the grooves between upper and lower block remaining the protuberances from the side sliding surfaces. To compare the test results, the height of the protuberance was $0, 0.06$ and 0.09 mm, respectively.

Fig. 1 Assembly of dry hybrid CVT belt



2.2 Test System

Figure 2 shows the schematic view of testing system of dry type CVT. The power was supplied by an AC motor and transmitted from the driving pulley to the driven pulley through the dry hybrid V-belt. To apply the transmitting torque, the electric powder brake was connected to driven pulley. The rotational speed of the driving pulley was controlled by using an electric inverter. The groove width of driving pulley was constrained by a conventional DC motor. The driven pulley was subjected to a constant thrust by an oil-pressured actuator. Both pulley thrusts on driving and driven pulley (Q_{DR} , Q_{DN}), and contraction force (F_s) were measured by using load cells. Rotating speeds of the both pulley shafts (N_{in} , N_{out}) and the torque to the both pulley (Tr_{in} , Tr_{out}) were measured by speed pickups and torque meters, respectively.

3 Experimental Method

The conditions in this study are presented in Table 1. The rotational speed of driving pulley N_{DR} and the driven pulley thrust Q_{DN} were set to 1,000 rpm and 2 kN, respectively. The applied torque to the driving pulley Tr_{in} was gradually increased up to the sliding slip state of the belt keeping 0.5, 1.0, and 2.0 of speed ratio.

4 Experimental Results and Discussion

4.1 Effect of Protuberance on Pulley Thrust

Figure 3 shows variations of thrust ratio $\Lambda = Q_{DR}/Q_{DN}$ with respect to the torque ratio at 1.0 of speed ratio. Torque ratio r is calculated by following equation.

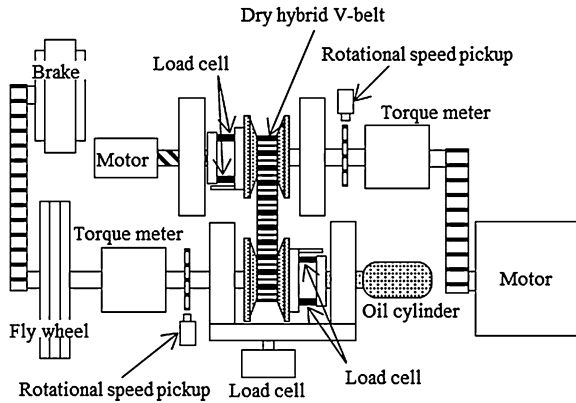


Fig. 2 Test system

Table 1 Experimental method

Speed ratio $i[-]$	0.5	1.0	2.0
Input revolution speed N_{in} (rpm)	1,000		
Applied torque T_{in} (NM)	0–100		
Pulley thrust on driven pulley Q_{DN} (N)	2,000		

$$r = \frac{T_{in}}{T_c} \quad (1)$$

The thrust ratio was increased as torque ratio increased and the highest thrust ratio was obtained when $h = 0.09$ mm. Figure 4 shows variations of maximum thrust ratio $\Lambda = Q_{DR}/Q_{DN}$ with respect to the speed ratio.

Maximum thrust ratio was decreased as speed ratio increased and the highest maximum thrust ratio was also obtained when the height of protuberance of tension member was 0.09 mm.

4.2 Effect of Protuberance on Conversion Ratio

Figure 5 shows variations of the conversion ratio F_s/Q_{DN} with respect to the torque ratio at 1.0 of speed ratio.

The conversion ratio was almost increased as torque ratio increased. Figure 6 shows variations of the maximum conversion ratio $(F_s/Q_{DN})_{max}$ with respect to the speed ratio. The maximum conversion ratio increased with the decreasing of speed ratio. The highest maximum conversion ratio was obtained when protuberant tension member was used with 0.09 mm of height.

Fig. 3 Variation of thrust ratio with respect to torque

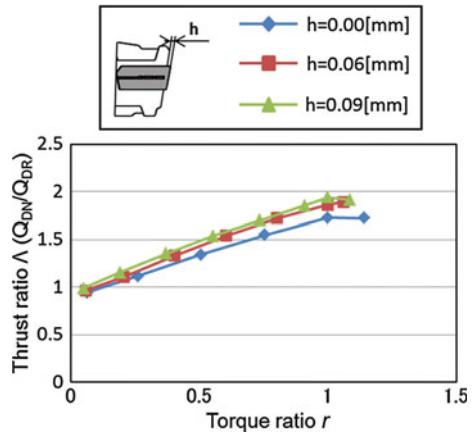


Fig. 4 Variation of thrust ratio with respect to speed ratio (torque ratio $r = 1.0$)

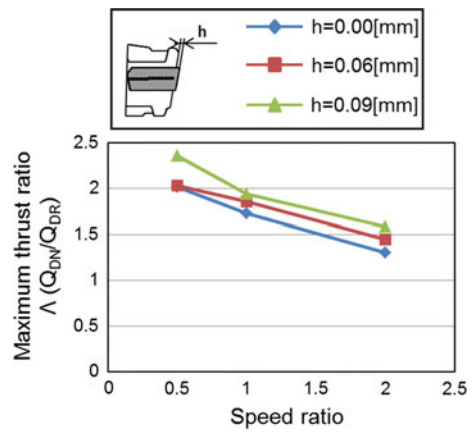


Fig. 5 Variation of conversion ratio with respect to torque ratio ($i = 1.0$)

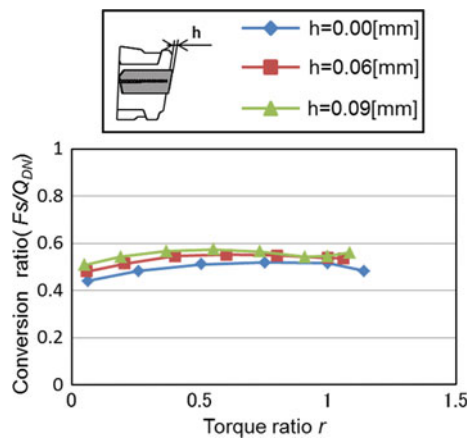


Fig. 6 Variation of conversion ratio with respect to speed ratio

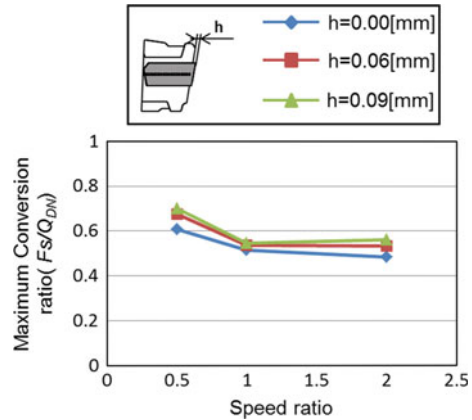
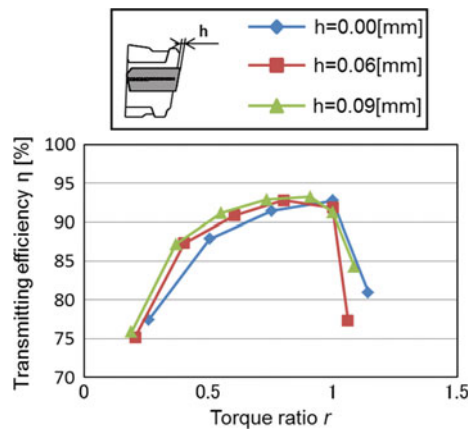


Fig. 7 Variation of transmitting efficiency with respect to torque ratio ($i = 1.0$)



4.3 Effect of Protuberance on Transmitting Efficiency

Figure 7 shows variations of transmitting efficiency η with respect to the torque ratio at 1.0 of speed ratio. Transmitting efficiency η is calculated by following equation.

$$\eta = \frac{Tr_{out}N_{out}}{Tr_{in}N_{in}} \times 100 \tag{2}$$

The maximum transmitting efficiency was obtained in case of 1.0 of torque ratio. The highest transmitting efficiency was obtained when protuberant tension member was used with 0.09 mm of height. Figure 8 shows the variations of maximum transmitting efficiency with respect to the speed ratio. The highest maximum transmitting efficiency was obtained when protuberant tension member was used with 0.09 mm of height. The highest maximum transmitting efficiency was also obtained when 1.0 of speed ratio.

Fig. 8 Variation of transmitting efficiency with respect to speed ratio

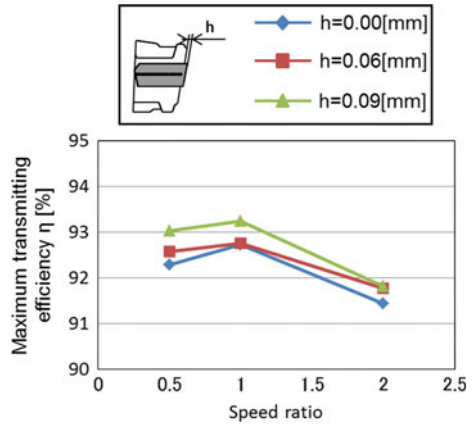
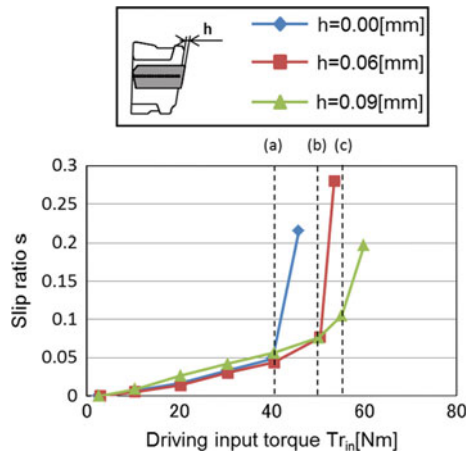


Fig. 9 Variation of slip ratio with respect to driving input torque (i = 1.0)



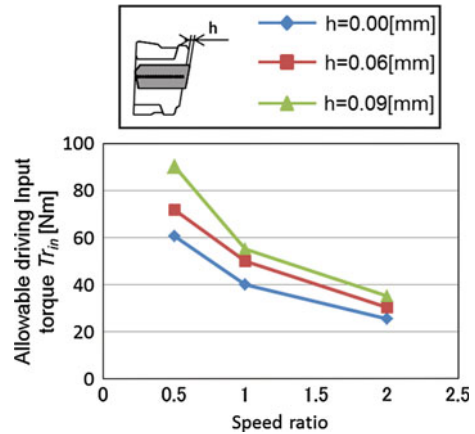
4.4 Effect of Protuberance on Allowable Transmitting Torque

Figure 9 shows variations of slip ratio with respect to the driving input torque at 1.0 of speed ratio. Slip ratio s is calculated by the following equation.

$$s = 1 - \frac{N_{in}}{N_{in0}} \tag{3}$$

The slip ratio was increased as driving input torque increased, respectively. As shown Fig. 9, the point (a), (b) and (c) at which the slip ratio changed dramatically are defined as allowable driving input torque. The highest allowable driving input torque was obtained when protuberant tension member was used with 0.09 mm of height. Figure 10 shows variations of allowable driving input torque with respect to the speed ratio. Allowable driving input torque was

Fig. 10 Variation of maximum driving input torque with respect to speed ratio



decreased as speed ratio increased and the highest allowable driving input torque was obtained when protuberant tension member was used with 0.09 mm of height, respectively.

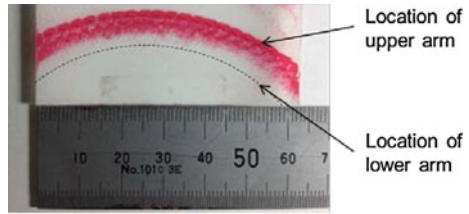
4.5 Difference of Contact Pressure Distribution Due to Applying Protuberance

The change of distribution of contacting pressure between belt and pulley was evaluated by conventional pressure measurement film (Fujifilm Prescale Ultra Super Low Pressure, FUJI PHOTO FILM CO., LTD.) at 1.0 of speed ratio. In the test, intensive dark color was observed, if the area had been locally subjected to high contacting pressure over 0.2 MPa.

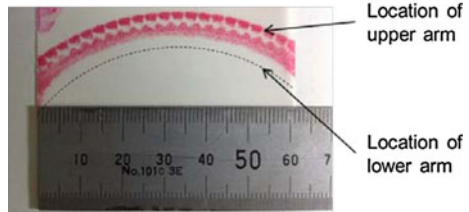
Figure 11 shows the observed images of pressure distributions obtained by the pressure measurement films on (a) original ($h = 0$ mm) and (b) modified belt ($h = 0.09$ mm). Comparatively low contact pressure under driving state was suggested around the upper arm of the belt by the result of observed light mark when power was transmitted by modified belt. In opposite, the result of remarkably intensive dark color suggested that locally high contact pressure was applied to the upper arm of original belt. This result suggests that contact force of the tension member was relatively increased when protuberant tension member was used with 0.09 mm of height. It was explained that transmitting properties should be improved by the increase of the load of the tension member where high coefficient of friction was shown under driving state.

It is found that applying the protuberance on the side sliding surfaces of the dry hybrid V-belt type CVT was effective to increase the power transmission properties in any condition of speed ratio.

Fig. 11 Observed images of pressure distribution obtained by the pressure measurement films



(a) $h=0.00$ mm



(b) $h=0.09$ mm

5 Conclusions

1. The highest maximum thrust ratio, conversion ratio, transmitting efficiency and allowable driving input torque were obtained when protuberant tension member was used with 0.09 mm of height, respectively.
2. Transmitting properties should be improved by the increase of the load of the tension member where high coefficient of friction was shown under driving state.
3. In any condition of speed ratio, applying the protuberance on the side sliding surfaces was effective to improve the power transmission properties.

References

1. Amijima S et al (1989) Study on axial forces and its distribution for a newly developed block-type CVT belt. *JSAE Rev* 10(3):23–29
2. Shimizu H et al (2000) Development of 3-D simulation for analyzing the dynamic behavior of a metal pushing V-belt for CVTs. In: *SAE 2000 world congress*, pp 31–36
3. Fujita M et al (2004) Development of 3-D simulation for power transmitting analysis of CVT driven by dry hybrid V-belt. In: *2004 International continuously variable and hybrid transmission congress*
4. Ide T et al (2000) Effect of belt loss and oil pump loss on the fuel economy of a vehicle with a metal V-belt CVT. In: *Seoul 2000 FISITA world automotive congress*, vol 2, pp 883–888
5. van der Sluis F et al (2007) Efficiency optimization of the pushbelt CVT, *SAE technical paper* 2007, pp 313–321
6. Kido R et al (2004) A study of factors affecting conversion ratio from thrust to tension in dry hybrid belt for CVT. In: *The JSME international conference on motion and power transmissions 2004*, pp 286–289

A Comparative Analysis of Optimization Strategies for a Power-Split Powertrain Hybrid Electric Vehicle

Jackeline Rios and Pierluigi Pisu

Abstract In this paper, two strategies based on the use of roadway traffic prediction data to optimize the energy consumption of Hybrid Electric Vehicles are compared. For both strategies, predictive traffic data is sent to the supervisory controller in order to adjust the Equivalent Consumption Minimization Strategy (ECMS). In the first approach, the predicted driving profile is divided into time horizons of equal length and the optimal control input is calculated for each of them. In the second approach, the control input is periodically recalculated, thus, adapting to changes in the predicted driving profile. While both strategies reduced energy consumption, the second approach showed its superiority with a maximum improvement of 6.85 %.

1 Introduction

According to the Research and Innovative Technology Administration RITA [1] the energy consumption in the transportation sector accounted for 28.6 % of the total energy consumption in the U.S. in 2009. The U.S. Energy Information Administration [2] estimates that fuel consumption worldwide related to the transportation sector will increase to 60 million barrels of oil per day by 2035,

F2012-B02-077

Research supported by the National Science Foundation under Grant No. 0928744. Any opinions, findings, and conclusions or recommendations expressed in this material are those of the author(s) and do not necessarily reflect the views of the National Science Foundation.

J. Rios (✉) · P. Pisu
Clemson University, Greenville, SC 29607, USA
e-mail: jackelr@clemson.edu

which corresponds to around 61 % of the world's total oil supply. Thus, improving the vehicles' fuel efficiency is a key factor to reduce the pressure on the environment, satisfy governmental regulations and reduce dependence on foreign oil.

Hybrid electric vehicles (HEV) are viable alternatives to gasoline powered vehicles. HEVs powertrain architecture contains an internal combustion engine, electric motors, and two or more energy storage systems (ESS). This vehicle architecture requires an Energy Management Strategy which controls the energy distribution among the devices in the powertrain in such a way that the power requested by the driver, the performance and the safety conditions are satisfied.

The presence of more devices in hybrid powertrain systems i.e. the ESS, and electric motors, allows for more degrees of freedom. This implies that the power required to move the vehicle can be split into one or both of the on-board energy sources which makes fuel consumption optimization more challenging. Moreover, factors such as the availability of charging stations, electricity and gas prices, and emissions are also important to solve an energy optimization problem. Hence, new advanced energy management strategies that do not compromise the overall safety and performance of the vehicle are required.

Dynamic programming (DP) is commonly used to solve the energy control problem for HEVs. It is a numerical algorithm based on Bellman's principle of optimality that allows finding an optimal control sequence to minimize the required objective function [3–5]. However, the main drawback of this method is the high computational load which prevents its real time implementation. On the other hand, the equivalent consumption minimization strategy (ECMS) allows finding a sub optimal solution, by converting the global optimization problem into a local one [6], showing potential for real time implementation [7]. The ECMS algorithm requires a tuning process in order to estimate the value of the average powertrain efficiency in the future [6]. Furthermore, the use of additional information about future driving conditions, i.e. predictive traffic data, can also be used in the solution of the energy control problem, thus increasing the benefits in energy efficiency [8–10].

In this paper, two different objective functions are proposed to solve the energy control problem by using model predictive control techniques. In the first approach, the driving profile is divided into sections or time horizons of equal length and the optimal control input is calculated for each of them. In the second approach, the algorithm is tuned for the complete driving profile at first. Then, the optimal control input is recalculated and updated periodically using the remaining part of the predicted driving profile. Simulations were carried out to evaluate and compare the performance of the two approaches under different values for the time horizon and updating time. The results demonstrate that the proposed strategies can be feasible solutions to the energy control problem of HEVs. This paper is organized as follows: the modeling of the power-split HEV is presented in [Sect. 2](#) and [Sect. 3](#) deal with the energy management problem. The proposed approaches are explained in [Sect. 4](#) and the results are presented and discussed in [Sect. 5](#). Finally, some conclusions are given in [Sect. 6](#).

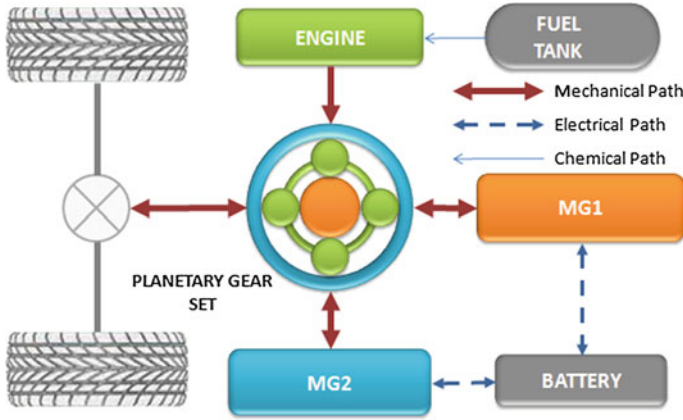


Fig. 1 Block diagram of a power-split powertrain

2 Vehicle Modeling

The simulator used in this study was based on the forward-looking model of a HEV with power-split configuration as illustrated in Fig. 1. The parameters used as a reference to implement the model in MATLAB/Simulink are summarized in Table 1 and correspond to the parameters of the Toyota Prius Second Generation.

The performance of the two electric machines (MG1, MG2) is simulated through static efficiency maps while for the engine, a first order dynamics is considered. Both electric machines can work as a motor or as generator; however, MG2 acts primarily as an electric motor and MG1 mainly as an electric generator.

Into the model, the information flows forward from the driver to the wheels. The driver block outputs the throttle and brake commands according to the difference between the desired speed defined by the driving cycle and the simulated current speed.

The vehicle dynamics is derived from the Newton’s Second Law of motion, as defined in (1).

$$m_v \frac{dv}{dt} = F_{traction} - F_a - F_g - F_r \tag{1}$$

where $F_a = \frac{\rho_{air} C_d A_f v^2}{2}$, $F_g = m_v g \sin(\alpha)$, $F_r = m_v g C_r \cos(\alpha)$, v is the longitudinal speed, m_v is the mass of the vehicle, $F_{traction}$ is the traction force of the vehicle [N], C_d is the drag coefficient, C_r is the rolling resistance coefficient A_f is the vehicle frontal area ρ_{air} is the density of air [kg/m³], α is, the road grade g is the acceleration due to gravity [m/s²] Table 1.

The power request P_{req} , in (2), is a function of the throttle α and the brake β commands as defined in (2).

$$P_{req}(t) = \alpha(t)(P_{fc,Max} + P_{el,Max}) - \beta(t)(P_{brake,Max}) \tag{2}$$

Table 1 Main parameters of the vehicle

Vehicle parameter	Symbol	Value
Vehicle mass [kg]	m	1,330
Aerodynamic drag coefficient	C_d	0.26
Vehicle frontal area [m ²]	A_f	2.16
Rolling resistance coefficient	C_r	0.007
Tire radius [m]		0.3175
Engine		
Rated Power @ 5,000 rpm [kW]	P_{ice}	57
Torque @ 4,200 rpm [N.m]	T_{ice}	111
Generator		
Continuous power output [kW]	$P_{GE,out}$	15
Max torque output [N.m]	$T_{GE,Max}$	153.5
Max speed [rpm]	$\omega_{GE,Max}$	10,000
Electric motor		
Continuous power output [kW]	$P_{EM,out}$	25
Max torque output [N.m]	$T_{EM,Max}$	400
Max speed [rpm]	$\omega_{EM,Max}$	6,700
Battery		
Rated voltage [V]	V	201.6
Capacity [A.h]	Q_{batt}	6.5

$$0 < \alpha(t) < 1$$

$$0 < \beta(t) < 1$$

where $P_{brake,Max}$ is the maximum braking power $P_{fc,Max}$ is the maximum power of the fuel converter i.e. internal combustion engine for this study, and $P_{el,Max}$ is the maximum power of the electric machines $P_{MG2} - P_{MG1}$ in [W].

The Internal Combustion Engine (ICE), MG1 and MG2 are coupled together through the planetary gear set (PGS) which splits the power among them. The PGS comprises one set of planet gears mounted on an arm known as the carrier. The carrier containing the planet gears rotate around a central gear known as the sun. The planet gears also meshes with an outer gear known as the ring. In the implemented model, the generator (MG1) is connected to the sun, the electric motor (MG2) is connected to the ring and the ICE is connected to the carrier.

Thus, by the interaction among the components of the PGS, the speed of the generator ω_{MG1} is a function of the motor speed ω_{MG2} and the engine speed ω_{ice} as shown in (3).

$$\omega_{MG1} = \frac{(R+S)}{S} \omega_{ice} - \frac{R}{S} \omega_{MG2} = 3.6 \omega_{ice} - 2.6 \omega_{MG2} \quad (3)$$

Where R is the number of teeth of the ring gear and S is the number of teeth of the sun gear.

The torque relation among the components, determined for the PGS, is defined by (4) and (5)

$$T_{ice} = J_{ice}\dot{\omega}_{ice} + 3.6T_{MG1} \quad (4)$$

$$T_{MG2} = T_f - 2.6T_{MG1} \quad (5)$$

In which J_{ice} is the ICE inertia, T corresponds to torque and the subscript f represents the final drive.

The speed of the engine is calculated from the dynamic Eq. (6).

$$J_{ice}\dot{\omega}_{ice} = -\alpha_{ice}\cdot\omega_{ice} + T_{ice} + (T_{MG2} - T_{MG1}) - T_f \quad (6)$$

3 Energy Management Problem

The primary function of the energy management is to determine the optimal power distribution between the fuel converter and the electric storage system at any time [11, 12]. For this work, the fuel converter refers to the internal combustion engine (ICE) and the electric storage system (ESS) to the battery. Thus, the cost function for this energy control problem can be defined as:

$$\text{Min}_{\{P_{ICE}(t), P_{MG1}(t), P_{MG2}(t)\}} \int_0^{T_f} \dot{m}_f(\tau) d\tau \quad (7)$$

Subject to the constraints:

$$P_{req}(t) = P_{ICE}(t) + P_{MG2}(t) - P_{MG1}(t) \nabla t$$

$$0 < SOC_{min} \leq SOC \leq SOC_{max} < 1$$

$$0 \leq P_{ICE}(t) \leq P_{ICE,max}(t)$$

$$0 \leq \omega_{ICE}(t) \leq \omega_{ICE,max}(t)$$

$$0 \leq T_{ICE}(t) \leq T_{ICE,max}(t)$$

$$P_{MGi_{min}}(t) \leq P_{MG,i}(t) \leq P_{MGi_{max}}(t) \quad i = 1, 2$$

$$\omega_{MGi_{min}}(t) \leq \omega_{MG,i}(t) \leq \omega_{MGi_{max}}(t) \quad i = 1, 2$$

$$T_{MGi_{min}}(t) \leq T_{MG,i}(t) \leq T_{MGi_{max}}(t) \quad i = 1, 2$$

where T_f is the duration of the trip, \dot{m}_f is the fuel flow rate p is power T is torque ω is speed, MGi refers to the i electric motor/generator ICE refers to the engine, P_{req} is the power request and SOC is the state of charge of the battery.

DP is a method commonly used to solve the global optimization problem. However, it requires the continuous problem to be discretized, thus requiring a very fine grid so that the approximation error can be negligible. Also, it requires exact a priori knowledge of the driving profile which constitutes a major drawback of this approach making impossible its real time implementation. Thus, the results obtained with DP are commonly utilized as a benchmark to evaluate the benefits of alternative real-time implementable strategies.

To overcome the problem of high computational load, the global optimization can be replaced by a local optimization in which the problem becomes a minimization of the equivalent fuel flow rate $\dot{m}_{f,eq}$ each instant of time, under the same constraints as in the global approach.

$$\text{Min}_{\{P_{ICE}(t), P_{MG1}(t), P_{MG2}(t)\}} \dot{m}_{f,eq}(t) \forall t \quad (8)$$

And:

$$\dot{m}_{f,eq}(t) = \dot{m}_{f,ICE}(t) + \dot{m}_{f,eq,batt}(t)$$

where $\dot{m}_{f,ICE}$ is the fuel flow rate consumed by the ICE and $\dot{m}_{f,eq,batt}$ represent an equivalent fuel flow rate related to the use of the battery power.

This local optimization is known as the equivalent consumption minimization strategy (ECMS) and constitutes the base of the energy management strategy used in this work.

For the case of the power-split HEV, the equivalent fuel consumption is defined as

$$\begin{aligned} \dot{m}_{f,eq,batt}(t) = \frac{s}{Q_{LHV}} & \left[\left(\frac{P_{MG2} - P_{MG1}}{\eta_{PE}\eta_{b,dis}} \right) \gamma_1 + (P_{MG2} - P_{MG1})\eta_{b,chg}(1 - \gamma_1)\gamma_2 \right. \\ & \left. + \frac{(1 + sig(\gamma_3))}{2} \gamma_3 + \frac{(1 - sig(\gamma_3))}{2} \gamma_3\gamma_4 \right] \end{aligned} \quad (9)$$

Where

$$\gamma_1 = \frac{1 + sign(P_{MG2})}{2}$$

$$\gamma_2 = \frac{1 - sign(P_{MG2}P_{MG1})}{2}$$

$$\gamma_3 = \frac{P_{MG2}}{\eta_{PE}\eta_{b,dis}} - \eta_{PE}\eta_{b,chg}P_{MG1}$$

$$\gamma_4 = \frac{1 + sign(P_{MG2}P_{MG1})}{2}$$

With Q_{LHV} the fuel low heating value, S an equivalence factor, η_{PE} is the power electronics efficiency, and $\eta_{b,chg}, \eta_{b,dis}$ are the battery efficiencies for charging/ discharging condition.

In addition, the implemented energy control strategy includes an engine on–off routine to obtain further reduction in fuel uses. Thus, when the engine speed is equal to idle and the power request is less than the maximum power of MG2 for more than a predefined time, the engine is turned off. If the former two conditions are satisfied but not the condition of time, the supervisory controller splits the power between the engine and the MG2 according to the minimization of the equivalent fuel cost function. Once the engine is off and if the power request is less than the maximum MG2 power, the controller compares the cost of starting the engine and the cost of using the MG2 alone to decide an optimal power distribution strategy.

4 ECMS Tuning

In Eq. (9) the equivalence factor S is an optimization parameter to be tuned and is related to the average powertrain efficiency in the future. The optimal value of S will be different for diverse driving profiles. That is, an S value that assures a close to optimal use of the battery energy for a particular driving cycle, can lead to poor use of the battery in others. This can be explained by the fact that the energy available for regeneration is a critical parameter that determines the amount of fuel required to recharge the battery and guarantee a sustaining operation.

When addressing the issue of tuning the S coefficient, the energy control problem should be formulated as a global optimization problem and the cost function is defined as in (10).

$$\text{Min}_{\{s\}} \int_0^{t_f} \text{Min}_{\{P_{ICE}(t), P_{MG1}(t), P_{MG2}(t)\}} \dot{m}_{f,eq}(\tau) d\tau \quad \forall \tau \tag{10}$$

In this work, two approaches are proposed to adjust the parameter S in the ECMS. The first approach avoids the requirement of complete knowledge of the future conditions while the second approach allows adaptation to changes in the initially predicted velocity profile.

Approach 1

This approach is intended to get the maximum benefit by utilizing real-time roadway traffic data. The optimization is done for time horizons of equal lengths. Thus, the driving cycle is divided in sections according to the desired length. The optimization is done for each section to find the optimal control input $S(k)$, avoiding the requirement of knowledge about the entire driving profile. The cost function for the optimal control problem at each time horizon becomes

Table 2 Fuel economy for single S value

Driving cycle	S_{opt}	MPG
UDDS	4.4	55.45
FHDS	3.3	67.94

$$\text{Min}_{\{s(k)\}} \int_{t_0+kT}^{t_0+T+kT} \text{Min}_{\{P_{ICE}(t), P_{MG1}(t), P_{MG2}(t)\}} \dot{m}_{f,eq}(\tau) d\tau \forall \tau, k = 0, 1, \dots, N-1 \quad (11)$$

Where t_0 is the time at the beginning of the current optimization horizon, T is the optimization horizon length, k is the optimization horizon number and N is the total number of optimization horizon windows.

Approach 2

In this approach the complete driving profile is used at first, but the optimal control input is recalculated and updated every T seconds for the remaining part of the predicted driving profile. Thus, allowing adaptation to changes in the driving profile along the route.

The optimization problem is stated as

$$\text{Min}_{\{s(k)\}} \int_{t_0+kT}^{t_f} \text{Min}_{\{P_{ICE}(t), P_{MG1}(t), P_{MG2}(t)\}} \dot{m}_{f,eq}(\tau) d\tau \forall \tau, k = 0, 1, \dots, N-1 \quad (12)$$

With t_f the final time for the driving profile.

5 Results and Discussion

For comparison purposes, each approach was tested under the Urban Dynamometer Driving Schedule (UDDS) and the Federal Highway Driving Schedule (FHDS) each one repeated for 3,600s and assuming a 100 % accurate speed profile prediction. Initially, a single optimal value for the S coefficient that minimizes the fuel consumption for each driving cycle was found. The results are summarized in Table 2.

A. Approach 1

According to the results in Table 3, initially the fuel economy improves for bigger time windows. This suggests that bigger time windows would yield better results. However, for time horizons 600, 900 and 1,200s the MPG value was smaller than the value obtained for 300s. For time windows less than 300s, there is not enough opportunity to take full advantage of the battery energy. While for time windows greater than 300s, there is a large variation in the driving profile, thus, a constant value of S is not enough to optimize the fuel economy. Consequently, 300s corresponds to the optimal value for the time horizon length. That means that

Table 3 Fuel economy using approach 1 to tune the S coefficient

Driving cycle	Time horizon [s]	MPG	Improvement (%)
UDDS	60	53.52	-4.89
	120	56.34	0.11
	300	58.68	4.28
	600	56.67	0.70
	900	56.76	0.86
	1200	56.37	0.17
FHDS	60	66.78	-1.69
	120	67.99	0.076
	300	68.71	1.13
	600	68.43	0.72
	900	68.04	0.14
	1200	67.86	-0.11

Table 4 Fuel economy using approach 2 to tune the S coefficient

Driving cycle	Updating time window[s]	MPG	Improvement (%)
UDDS	60	60.41	6.85
	120	60.35	6.76
	300	59.20	4.95
FHDS	60	69.58	2.35
	120	69.32	1.98
	300	69.05	1.60

it is required to have a prediction of the speed profile for the upcoming 300s at each instant of time.

It is also important to highlight that the improvement percentage is bigger for the UDDS cycle, which is consistent with the fact that there is more variation in the driving conditions for this driving cycle than for the FHDS cycle.

B. Approach 2

According to the results summarized in Table 4, this approach yields better fuel economy than approach 1, due to the use of the remaining part of the driving cycle and the continuous updating of the coefficient S .

It is also important to point out the lower MPG values obtained for bigger updating time for the S coefficient which suggest in this approach a small window size is better to get maximum benefits.

6 Conclusions

It has been demonstrated that model predictive control techniques are useful to reduce energy consumption in HEVs using the ECMS algorithm as the base of its energy control strategy, while keeping its potential for real time implementation.

In the first approach, roadway traffic prediction data is sent to the supervisory controller to tune the ECMS algorithm for a particular horizon time length. The results showed that 300s is the optimal time horizon size, resulting in fuel economy improvements of 1.13–4.28 % when compared to the case of a constant S value for the complete predicted driving cycle. In the second approach, the control input is periodically recalculated, allowing adaptation to changes in the predicted driving profile along the entire trip. The simulations revealed that 60s becomes an optimal updating time for this case, with fuel economy improvements of 2.35–6.85 %.

According to the results it has been demonstrated that the proposed control strategies represent practical solutions to the energy control problem of Hybrid Electric Vehicles.

References

1. Research and innovative technology administration—RITA, bureau of transportation statistics (2010) National transportation statistics 2010, Washington (available at: http://www.bts.gov/publications/national_transportation_statistics/html/table_04_04.html)
2. US Energy Information Administration (2010) International energy outlook. DOE/EIA-0484 (2010), Washington
3. Sharer A, Rousseau D, Karbowski, Pagerit S (2008) Plug-in hybrid electric vehicle control strategy comparison between EV and chargedepleting options. In: Proceedings of SAE world congress. Detroit, April 2008
4. Marano V, Tulpule P, Stockar S, Onori S, Rizzoni G (2009) Comparative study of different control strategies for plug-in hybrid electric vehicles. In: Proceedings of 9th international conference of engines and vehicles, Capri. SAE Technical Paper 2009-24-0071, Sep 2009
5. Bertsekas D (2000) Dynamic programming and optimal control. Vol 1 2nd edn, Athena Scientific, Belmont
6. Pisu P, Koprubasi K, Rizzoni G (2005) Energy management and drivability control problems for hybrid electric vehicles. In: Proceedings of 44th IEEE conference on decision and control and European control conference. CDC-ECC
7. Serrao L, Onori S, Rizzoni G (2011) A comparative analysis of energy management strategies for hybrid electric vehicles. *J Dyn Syst Meas Contr* Vol 133/031012-1
8. He Y, Rios J, Chowdhury M, Pisu P, Bhavsar P (2012) Forward power-train energy management modeling for assessing benefits of integrating predictive traffic data into plug-in-hybrid electric vehicles. *Transp Res Part D Transp Environ* 17(3):201–207
9. He Y, Chowdhury M, Ma Y, Pisu P (2011) Merging mobility and energy vision with hybrid electric vehicles and vehicle infrastructure integration. *Energy Policy* 41:599–609
10. He Y, Chowdhury M, Pisu P, Ma Y (2012) An energy optimization strategy for power-split drivetrain plug-in hybrid electric vehicles. *Transp Res Part C Emerg Technol* 22:29–41, ISSN 0968-090X [10.1016/j.trc.2011.11.008](https://doi.org/10.1016/j.trc.2011.11.008)
11. Tulpule P, Marano V, Rizzoni G (2009) Effects of different PHEV control strategies on vehicle performance. In: proceedings of American control conference pp. 3950–3955, 10–12 June 2009
12. Bingzhan Zhang, Mi CC, Mengyang Zhang (2011) Charge-depleting control strategies and fuel optimization of blended-mode plug-in hybrid electric vehicles. *IEEE Trans Veh Technol* 60(4):1516–1525, May 2011

Part III
Plug-in Electric Vehicle

Development of a Compact-Class Range Extended Electric Vehicle Demonstrator

Michael Bassett, Jonathan Hall, John Powell, Simon Reader,
Marco Warth and Bernd Mahr

Abstract MAHLE has developed a dedicated Range Extender engine which has been focussed on meeting the requirements for a compact-class range-extended electric vehicle. In order to enable further development and refinement of the Range Extender system (e.g. NVH attributes of the engine), the module has now been installed into a demonstration vehicle. A current production gasoline fuelled compact-class car was used as a donor vehicle and converted into a range-extended electric vehicle (REEV). The all-electric driveline specification has been developed to meet the performance criteria set for the demonstrator, matching the acceleration and maximum speed capabilities of the conventional donor vehicle. Also, a target electric only range has enabled the battery pack capacity to be specified. The resulting vehicle is intended to reflect likely, near to market, steps to further the wider adoption of electric vehicles in the compact-class passenger car segment. This study gives details of the REEV vehicle developed and the Range Extender system integration. Additionally, the proposed operating strategy for the engine is described and simulation results show the fuel efficiency anticipated over the current legislative drive-cycle.

Keywords Range extender · Electric vehicle · NVH · Engine · Vehicle demonstrator

F2012-B03-004

M. Bassett (✉) · J. Hall · J. Powell · S. Reader · M. Warth · B. Mahr
MAHLE Powertrain Ltd, Northampton, Great Britain
e-mail: mike.bassett@gb.mahle.com

M. Warth
e-mail: marco.warth@mahle.com

1 Introduction

The transport sector alone is responsible for 23 % of energy-related CO₂ emissions [1]. Contrary to the trends in most other sectors, total greenhouse gas emissions of the transport sector are still increasing and are predicted to grow further in the coming years [2]. This is driven by the rapidly expanding global vehicle fleet which is anticipated to increase by over 63 % during the next 20 years [3]. Thus, present automobile development efforts are keenly focused on measures to reduce the CO₂ output of vehicles.

Because electric vehicles (EVs) do not generate pollutants during usage, and they can potentially rely on energy provided by a selection of renewable sources, they are the focus of much current interest. However, due to the present capabilities of battery technology, the overall range of such a vehicle is limited. Furthermore, once the battery is depleted relatively long recharging times are currently required before the vehicle is available for use again. Battery cost, range capability, and also possibly ‘range anxiety of the driver’, are still viewed as barriers to the widespread adoption of pure EVs [4, 5].

Range extended electric vehicles (REEVs) overcome many of the short-comings of EVs by having a ‘Range Extender’ (REx) unit, which consists of an onboard fuel converter that converts a liquid fuel, such as gasoline, into electrical energy whilst the vehicle is driving. This enables the traction battery storage capacity to be reduced, though still maintaining an acceptable vehicle driving range.

2 MAHLE Range Extender

MAHLE has developed a dedicated REx engine, shown in Fig. 1, to identify the requirements and challenges faced in the development of the components for such engines. The REx engine design has been focussed on meeting the requirements for a compact-class REEV. During the concept phase of the project key attributes for the engine were identified and a full evaluation of the different possible layouts for the REx engine was undertaken to assess the most suitable for the intended application. The specifications of the resulting Range Extender Unit are summarised in Table 1.

The fuel consumption of the REx unit has been measured, and the total system efficiency map is shown in Fig. 2. A maximum total system efficiency (combined efficiencies of the engine, generator and inverter) of 31 % has been achieved.

The REx unit has been designed to be as light, efficient and cost effective as possible. Normally for in-line 2-cylinder engines, one or two balancer shafts would be used to compensate for the residual primary forces. Instead, a 180–540 °CA firing interval was specifically chosen for this range extender application as this solution has no primary out of balance forces. This firing order gives no firing

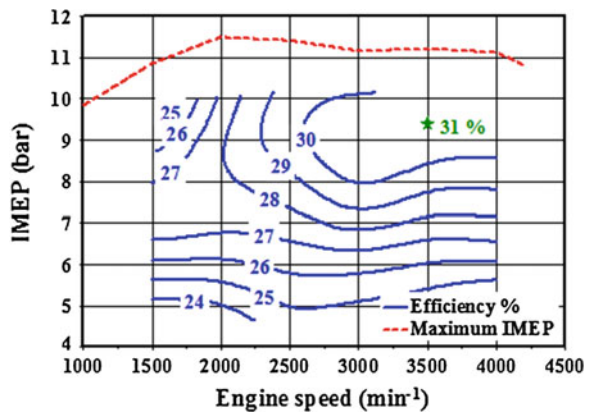


Fig. 1 MAHLE’s range extender engine

Table 1 MAHLE REx engine key technical specification summary

Technical specifications	
Layout	In-line 2-cylinder, 4-stroke, gasoline
Engine displacement	0.9 L
Bore/Stroke	83.0 / 83.0 mm
Compression ratio	10:1
Valvetrain	SOHC, 2 valve head, roller rocker arms
Fuel injection	Port fuel injection
Engine control	MAHLE flexible ECU
Generator	38 kW water-cooled permanent magnet axial flux generator
Maximum power	30 kW at 4,000 min ⁻¹
Peak torque	72 Nm between 2,000 and 4,000 min ⁻¹
Emissions target	Euro 6
Dimensions	327 × 416 × 481 mm
Installation angle	Vertical or horizontal
Engine dry weight	50 kg (70 kg with generator)

Fig. 2 MAHLE range extender unit total system efficiency map



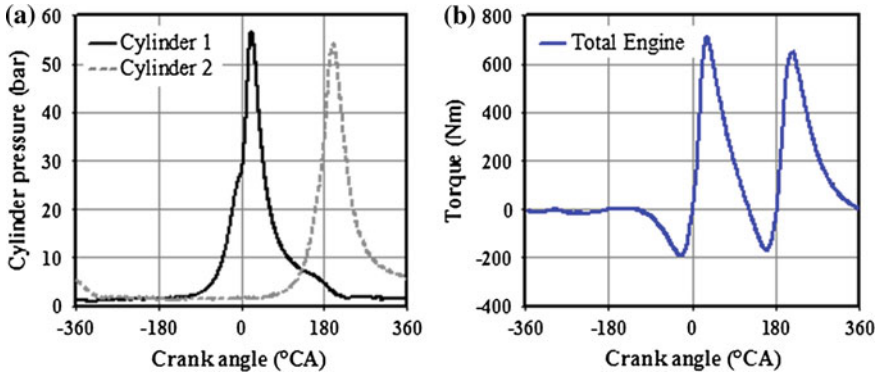


Fig. 3 a Cylinder pressure traces. b Total engine cyclic crank-shaft torque profile (2,000 min^{-1} , 80 % load)

events in the 1st revolution of the engine cycle and two firing events in the 2nd revolution of the cycle. Figure 3a shows the in-cylinder pressure traces for both cylinders, plotted relative to the TDC angle of cylinder 1. It can be seen that the firing events occur only 180 °CA apart. The resulting total engine cyclic torque is shown in Fig. 3b.

Comparison of Fig. 3a with Fig. 3b, which shows resulting combined effect of the cyclic torque contributions of the two cylinders, reveals the relationship between cylinder pressure and crank torque, where it can be seen that the cyclic torque profile is dominated by the torque peaks occurring during the expansions strokes of the two cylinders. Considering the cyclic torque contribution for cylinder 1, at the start of the cycle (-360 °CA in Fig. 3a) the 1st 180 °CA of the cycle correspond to the induction event and the torque of the cylinder is roughly zero (friction is neglected in these plots). The next 180 °CA (-180 – 0 °CA) is the compression stroke, and it can be seen that the torque contribution of this portion of the cycle is negative, with a peak negative torque of 200 Nm. The expansion stroke takes place between 0 °CA and 180 °CA, this is where all the positive crank work is generated during the cycle, and it can be seen that over 600 Nm of positive crank torque is generated during this stroke. The exhaust stroke takes place from 180° to 360 °CA, and it can be seen that this stroke has a small negative contribution on the engine torque profile shown in Fig. 3b.

The very low rotational inertia and uneven torque distribution over the engine cycle gives rise to large speed fluctuations during the cycle. Figure 4a shows measured cyclic speed fluctuations when operating at a cycle average speed of 2,000 min^{-1} and 80 % load. It can be seen that the engine slows during the 1st 360 °CA of the cycle where no firing torque occurs and then speeds up over the next revolution in two jumps, corresponding with the two firing pulses. When a constant torque load is applied to the engine via the generator the engine speed can be seen to have a peak to peak speed variation of up to 740 min^{-1} .

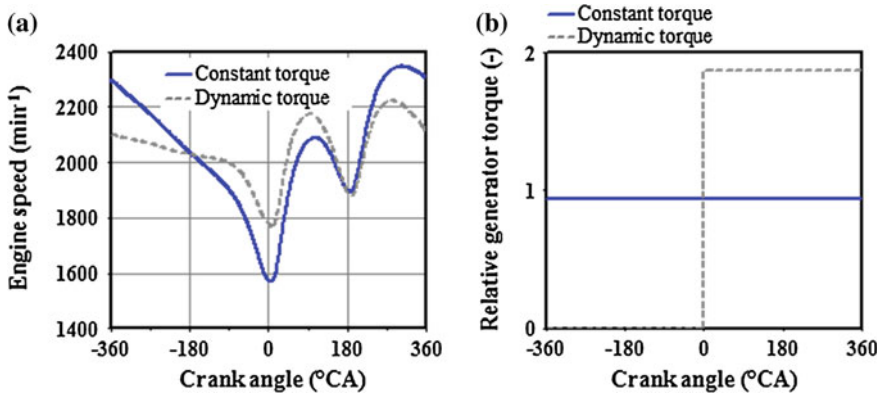


Fig. 4 a Cyclic speed fluctuation ($2,000 \text{ min}^{-1}$, 80 % load). b Dynamic torque control of generator

A dynamic control strategy for the generator has been devised, where it is switched off during the 1st revolution of the engine cycle and then activated at twice the mean cyclic torque during the 2nd revolution, as depicted in Fig. 4b. Figure 4a shows the effect of this dynamic torque control strategy on the engine speed, where it can be seen that the cyclic speed variation is almost half of that observed using constant torque generator control. Further testing has demonstrated that the dynamic torque control of the generator yields similar benefits across the entire operating range of the engine.

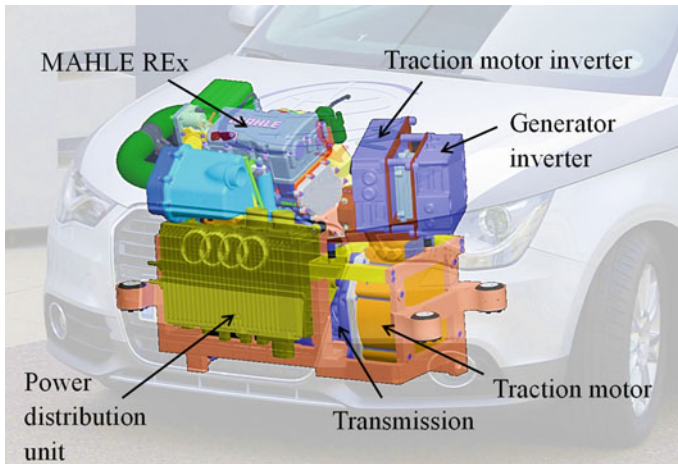
3 REEV Demonstrator Vehicle

In order to enable further development and refinement of the NVH attributes of the REX unit it has been installed into a demonstrator vehicle. A current production, compact class, vehicle has been fitted with an electric drive-line and the MAHLE range extender engine and the resulting vehicle is intended to reflect likely near to market steps for REEVs. It is believed that the market for REEV, of purely series-hybrid configuration, is for vehicles of compact class and smaller. This is primarily due to the lack of a direct coupling between the range extender engine and the wheels, which could enable higher high-speed cruising efficiencies in charge-sustaining mode, but adds considerably to the driveline complexity. MAHLE also wanted to demonstrate the compact nature of its 30 kW engine by installing it in a sub-compact class vehicle. The vehicle selected for the basis of the conversion was an Audi A1 1.2 TFSI. The REEV specification has been developed with the target of meeting the performance of the conventional baseline vehicle (Table 2).

The compactness of the traction motor and transmission used in the demonstrator vehicle has enabled the MAHLE REX unit to be installed alongside them within the original engine bay of the baseline vehicle, as shown in Fig. 5. By virtue

Table 2 REEV demonstrator performance targets

Parameter	Units	Base vehicle	REEV
0–100 km/h acceleration time	s	11.7	12.0
Maximum speed	km/h	180	145
Grade ability	%	–	20
Maximum speed on 6 % grade	km/h	–	90
Pure EV range	km	–	>60

**Fig. 5** REEV demonstrator layout

of its 2-cylinder configuration and fully integrated axial flux EVO Electric generator, the MAHLE REx unit is appreciably shorter than the 1.2 L, turbo-charged, 4-cylinder baseline engine it is replacing. Likewise, the EVO Electric AF-130 traction motor [6] has a very narrow package envelope because of the axial flux configuration used. The inverters for the traction motor and the REx unit generator have been packaged above the traction motor and transmission, in this location they are close to the respective motor/generator units that they control, as it is desirable to minimise the cable length between the inverter unit and motor to help minimise the radio noise generated, given the high frequency current switching between the inverter and motor.

All components are controlled by a master vehicle control unit (VCU), which has been developed in-house by MAHLE Powertrain using the MAHLE Flexible ECU (MFE) as a basis. This is the same base unit used to control the engine but with a different control structure developed from a clean sheet to control the electric vehicle and interface with the required vehicle sub-systems. The system architecture for the demonstrator vehicle is shown schematically in Fig. 6. The REx engine and generator are both controlled by the engine control unit (ECU), whereas the remainder of the REEV systems are controlled by the master vehicle control unit.

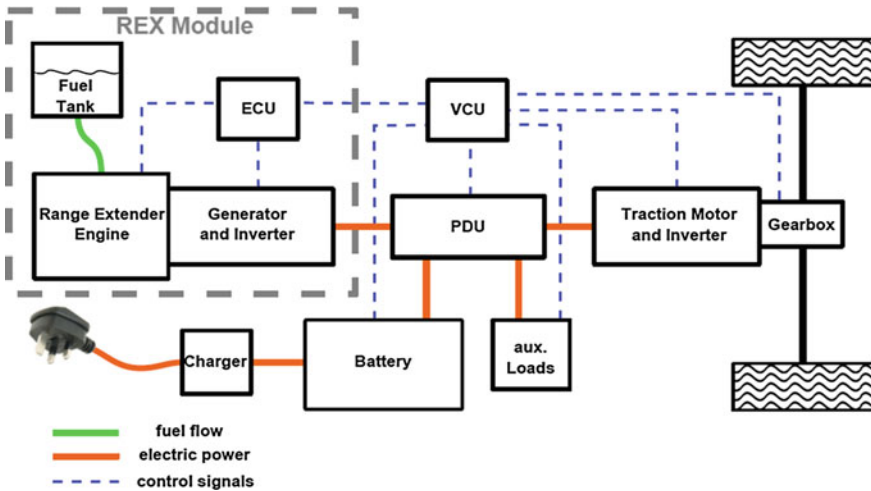


Fig. 6 Schematic of REEV demonstrator system architecture

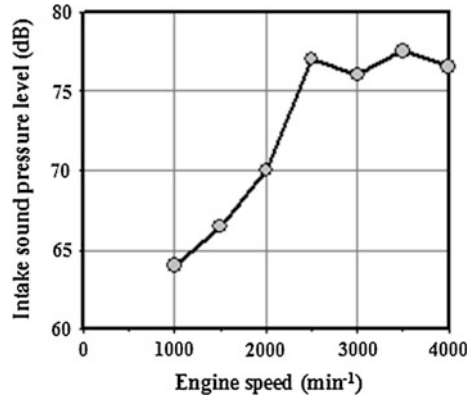
4 Intake System Acoustic Optimisation

Engine noise is a critical area for range extender engines, as the sudden starting of a combustion engine in an otherwise silent EV presents specific challenges with regards to NVH. It is desirable to keep the engine as unobtrusive to the occupants as possible. Comprehensive 1-D gas flow calculations, using a correlated GT-Power model of the engine have been undertaken, to minimise the sound pressure level emitted from the intake orifice without compromising the performance or efficiency level of the engine already achieved.

The intake system of the range extender engine tunes from the volume upstream of the throttle, rather than at the plenum at the end of the primary inlet runners, thus utilising the secondary pipe length and improving packaging and avoiding the need for excessively long primary runners [7]. This feature was retained, but the original airbox was replaced with a resonator box to enable the increase in volume needed from the airbox to attenuate the inlet pulsations, but retain the tuning needed. The air-filter volume was moved further upstream and increased in size to have a volume of approximately 4 L. The location and volume were optimised using GT-Power within the available package space under the vehicle bonnet. Additionally, a quarter-wave resonator pipe in the dirty air pipe, upstream of the air-filter volume entry also yielded significant orifice noise reductions. The revised inlet system for the demonstrator vehicle is shown, packaged within the demonstrator vehicle, in Fig. 5.

At $4,000 \text{ min}^{-1}$, full load, the inlet orifice sound pressure level was reduced by over 10 dB. This large reduction in orifice noise from the inlet system was achieved without any significant reduction in engine performance or fuel efficiency. The resulting calculated inlet orifice noise for the engine at full load across the operating speed range, is shown in Fig. 7.

Fig. 7 Calculated inlet orifice sound pressure level with optimised intake system



5 Range Extender Operating Strategy

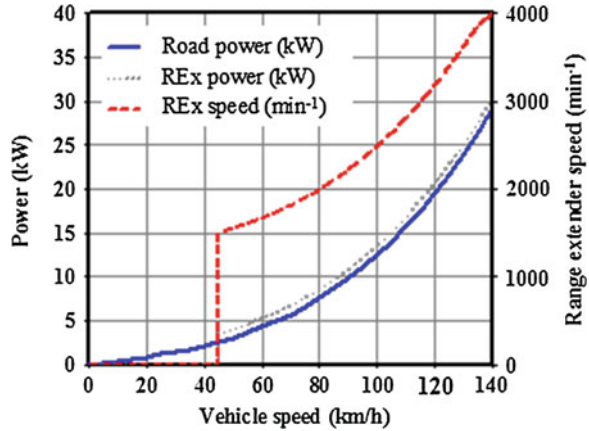
The operating strategy of the range extender engine has been devised to maximise the fuel economy of the vehicle, whilst maintaining an acceptable NVH characteristic. Additionally, intra-cyclic speed fluctuations have been minimised to ease the burden on the engine management system and enable repeatable control characteristics.

Previous studies indicated that low load and low speed operating points were best for achieving catalyst light-off, whilst minimising the cumulative tail-pipe emissions levels prior to light-off being achieved [7]. Testbed simulations of NEDC test cycle operation indicated that the emissions levels of the engine could be kept to around 30 % of the Euro 6 limits.

To minimise the declared vehicle CO₂ emissions based on the European test procedure it is desirable to achieve as high an electric operating range as possible and to minimise the CO₂ emissions measured in the minimum battery state of charge test. This drives a strategy that does not start the range extender unit until the battery has reached the minimum allowable State of Charge (SOC), to maximise the EV range, and also does not recharge the battery, but simply sustains it at the minimum SOC. This is because any energy that is added to the battery during the minimum state of charge test is not credited by the test procedure, but creates additional CO₂ emissions whilst being generated.

Therefore the proposed operating strategy for a REEV would be, for example, to activate the REX unit once the battery SOC falls to 0.25 and to only slightly above the instantaneous road load power requirement, of the order of 1 kW (although this will have to be modulated slightly based on instantaneous battery SOC). Figure 8 shows the road load power requirement of the demonstrator vehicle, along with the proposed REX unit power output and resulting REX operating speed. When battery SOC allows, it is planned to avoid range extender operation at power demands below 5 kW (or 45 km/h), however, at low SOC levels the REX unit will have to be activated and operated at 5 kW in order to avoid further battery depletion due to continued low speed driving.

Fig. 8 Vehicle road power requirement and proposed REX unit operation



6 REEV Demonstrator Fuel Consumption

Following the testing of the REX unit, it is possible to use the system efficiency to simulate the fuel consumption of the MAHLE compact-class REEV demonstrator. A model of the baseline vehicle has also been created to enable a comparison of the REEV with a conventional vehicle. The fuel consumption has been analysed over the NEDC and the results presented have been weighted according to the European ECE 101 test procedure [8].

Starting with a fully charged battery, the hypothetical REEV model was analysed over repeated NEDC tests until the REX engine started. The resulting electric range was found to be over 70 km. Based on the European ECE 101 test procedure, the weighting factor applicable to the CO₂ value resulting from NEDC test performed at the minimum state charge is 0.25.

The baseline vehicle model achieves a NEDC CO₂ figure of 120 g/km. The REEV model includes the measured fuel consumption for the MAHLE range extender engine and weighted tail-pipe CO₂ figure achieved for the REEV is less than 40 g/km, which represents a reduction of 67 % compared to the baseline vehicle.

7 Conclusions

MAHLE has created a range extended electric vehicle using its own purpose-designed engine and in the process converted an Audi A1 into a full REEV. The aim of this work was to assess and demonstrate the characteristics and capabilities of the MAHLE range extender engine in a real vehicle application. The design and realisation of the vehicle has been completed and simulation has provided an indication of the final performance and efficiency ratings of the vehicle.

References

1. Energy Technology Perspectives (2010) Scenarios & strategies to 2050. International Energy Agency, ISBN 978-92-64-08597-8, Paris, July 2010
2. Kampman B, Leguijt C, Bennink D, Wielders L, Rijke X, de Buck A, Braat W (2010) Green power for electric cars—development of policy recommendations to harvest the potential of electric vehicles, Delft, Jan 2010
3. World Oil Outlook 2010 (2011) Organization of petroleum exporting countries, Jan 2011
4. Investigation into the scope for the transport sector to switch to electric vehicles and plug-in hybrid vehicles, Report published by Department for Business Enterprise and Regulatory Reform (BERR) and the Department for Transport, Oct 2008
5. Brooker A, Thornton M, Rugh J (2010) Technology improvement pathways to cost-effective vehicle electrification. SAE paper No. 2010-01-0824
6. EVO Electric AF-130 datasheet: http://www.evo-electric.com/file_download/27
7. Warth M, Bassett M, Hall J, Korte V, Mahr B (2011) Design and development of the MAHLE range extender engine. 20th Aachen colloquium automobile and engine technology
8. E/ECE/324-E/ECE/TRANS/505 Regulation No 101 Rev 2, Annex 8. 29th April 2005

Modeling of the Lithium Battery Cell for Plug-In Hybrid Electric Vehicle Using Electrochemical Impedance Spectroscopy

Hyun-sik Song, Tae-Hoon Kim, Jin-Beom Jeong, Dong-Hyun Shin, Baek-Haeng Lee, Byoung-Hoon Kim and Hoon Heo

Abstract Online simulations are utilized to reduce time and cost in developing and optimizing the performance of plug-in hybrid electric vehicle (PHEV) and electric vehicles (EV) systems. One of the most important factors in an online simulation is the accuracy of the model. In particular, a model of a battery should accurately reflect the properties of the actual battery. However, precise dynamic modelling of a high-capacity battery system, which significantly affects the performance of a PHEV, is difficult because of its nonlinear electrochemical characteristics. In this study, a dynamic model of a high-capacity battery cell for a PHEV is developed by the extraction of the equivalent impedance parameters using electrochemical impedance spectroscopy (EIS). Based on the extracted parameters, a battery cell model is implemented using MATLAB/Simulink, and charging/discharging profiles are executed for comparative verification.

Keywords Lithium battery · Plug-in hybrid electric vehicle · Electrochemical impedance spectroscopy · Dynamic simulation · Battery equivalent circuit

F2012-B03-005

H. Song (✉) · B.-H. Kim · H. Heo
Korea University, Suoel, Korea
e-mail: hssong@katech.re.kr

T.-H. Kim · J.-B. Jeong · D.-H. Shin · B.-H. Lee
Korea Automotive Technology Institute, Cheonan, Korea

1 Introduction

On account of rising oil prices and the need to reduce the amount of greenhouse gas according to the UN Framework Convention on Climate Change, there has been active research on environmentally friendly, high-efficiency vehicles, including hybrid electric vehicles (HEVs), plug-in hybrid electric vehicles (PHEVs), and electric vehicles (EVs). As the specifications required for the parts used in these environmentally friendly vehicles are highly variable in the development phase, model based simulation is performed to reduce the time and cost required for developing and optimizing the system and its parts.

The performance of an environmentally friendly vehicle is significantly affected by its high-capacity battery system. However, it is difficult to implement a simulation model of a battery system that accurately reflects the battery's dynamic characteristics during charging and discharging because of its nonlinear electrochemical properties. Accordingly, simulations are generally performed using a simplified battery model or a hardware-in-the-loop simulation (HILS) associated with the actual battery [1, 2]. Although research has been performed on this type of battery modelling [3–5], most studies have dealt with low-capacity batteries in the range of several ampere-hours, and there have been very few attempts to validate these models with studies or experiments on high-capacity battery cells of dozens of ampere-hours required for PHEVs or EVs.

This study examined various equivalent impedance models of 20 Ah lithium battery cells for PHEVs and elicited parameters for each of their state-of-charge (SOC) using electrochemical impedance spectroscopy (EIS) to enable implementation of high-capacity battery cell models with MATLAB/Simulink. Furthermore, we selected charging/discharging profiles to compare dynamic characteristics between the elicited models and actual battery cells. The simulation results were also compared against actual experimental results according to the selected profiles to calculate the error rate of each model.

2 Lithium Battery Characteristics and Electrochemical Impedance Spectroscopy

A battery is an electrochemical device that converts chemical energy into electric energy during discharging and does the opposite during charging. Therefore, the electrochemical properties of a battery determine its dynamic and static characteristics, and accurately analyzing and representing those properties enables the implementation of a model that closely represents the characteristics of the actual battery.

Major internal electrochemical reactions of a lithium battery include Ohmic loss, charge transfer loss related to the properties of the interface between the electrode and electrolyte, and diffusion loss [6]. Figure 1 shows a Nyquist plot of the electrochemical reaction of a lithium battery.

Fig. 1 Nyquist plot of electrochemical reaction

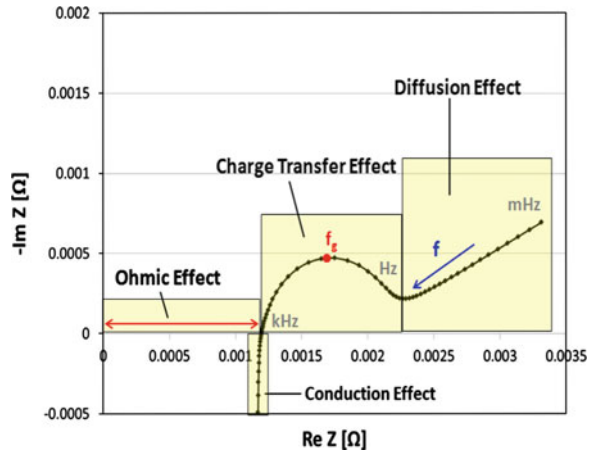



Table 1 Specifications of PHEV battery cell

	Type	Lithium polymer
	Rated capacity	20 Ah
	Rated voltage	3.70 V
	Maximum voltage	4.20 V
	Minimum voltage	2.50 V

EIS refers to a technique which involves applying a small perturbation to each frequency range of the impedance to be measured, analyzing the voltage in the response to the applied small perturbation, and eliciting the parameters of the impedance model. The impedance model that can be constructed with EIS varies depending on how the elements that represent each electrochemical property are configured [7].

In this study, we used a WEIS500 electrochemical workstation to acquire the battery impedance spectrum and measured the impedance in the 10 mHz to 1 kHz frequency range. In order to guarantee linearity in the experiment, perturbation current was restricted to 5 % or less of the charge, and we ensured that there was no variation in the amount of electric charge before and after the experiment. Impedance was measured in 20 % intervals from 20 to 100 % of SOC at room temperature (25 °C). Table 1 outlines the specifications of the PHEV high-capacity lithium battery cell used in this study, and Fig. 2 shows the impedance spectrum of the cell measured for each SOC.

We constructed four equivalent impedance models to model the corresponding cell, as shown in Fig. 3, and elicited parameters for each model based on the measured impedance spectrum. Figure 3a depicts an equivalent model (Model 1) consisting of a simple resistor, defined as internal resistance R_i , which is the sum of series resistance R_s and charge transfer resistance R_{ct} . Figure 3b is a model that

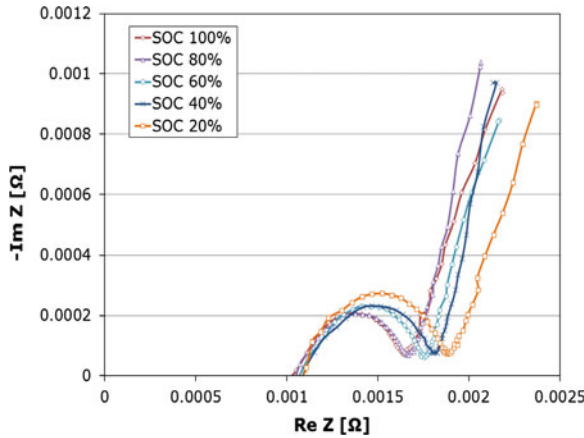


Fig. 2 Impedance spectrums of a PHEV battery

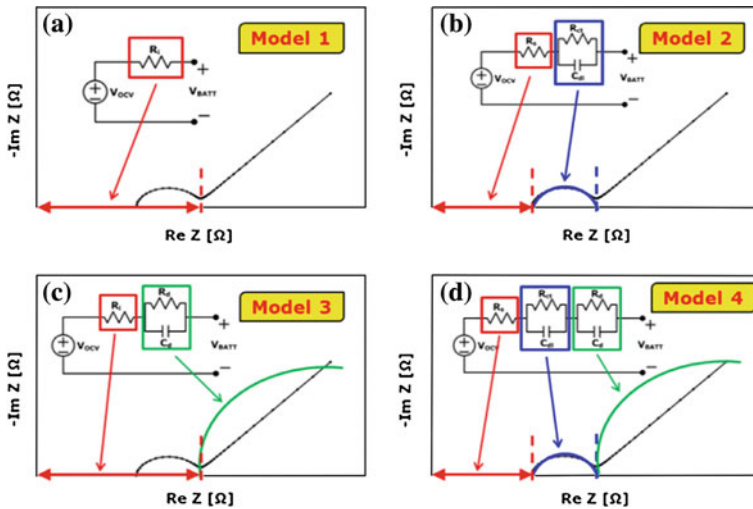


Fig. 3 Estimation method of the equivalent impedance for each model

reflects the resistance region and the charge transfer region (Model 2). It is an equivalent parallel RC circuit of the high-frequency charge transfer region and series resistance R_s . Figure 3c is a model that reflects the resistance region and the diffusion region (Model 3). It is an equivalent parallel RC circuit of the low-frequency diffusion region and internal resistance R_i . Finally, Fig. 3d is a model that incorporates all the regions (Model 4) consisting of series resistance R_s and two parallel RC circuits.

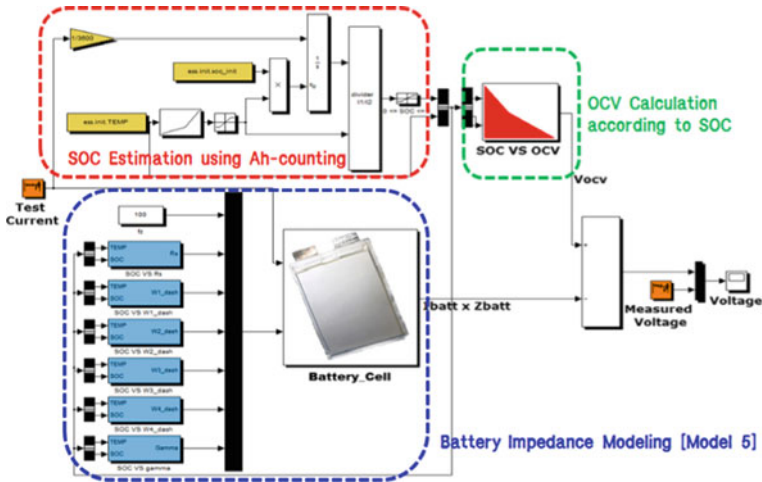
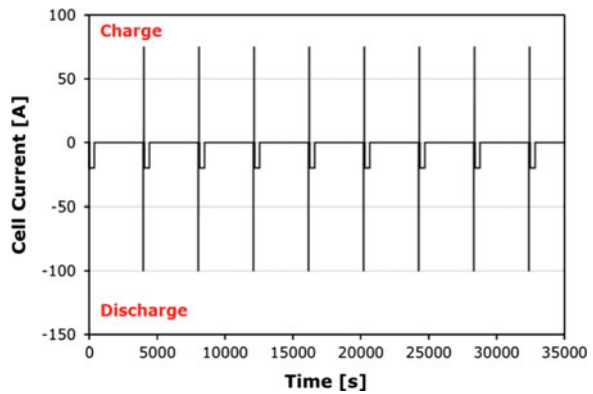


Fig. 4 MATLAB/Simulink block diagram

Fig. 5 Current waveform of the HPPC profile



3 Simulation and Validation Results

3.1 Simulation Using MATLAB/Simulink

For the simulation of the elicited lithium battery cell model, we created a dynamic characteristics model based on equivalent impedance and implemented a battery model using MATLAB/Simulink, as shown in Fig. 4. Applying the conventional ampere-hour counting method and a compensation method that utilizes the open-circuit voltage (OCV) to estimate the SOC, the implemented battery cell model calculates the terminal voltage of the battery cell by reflecting the OCV according

Fig. 6 Current waveform of the CDCL profile

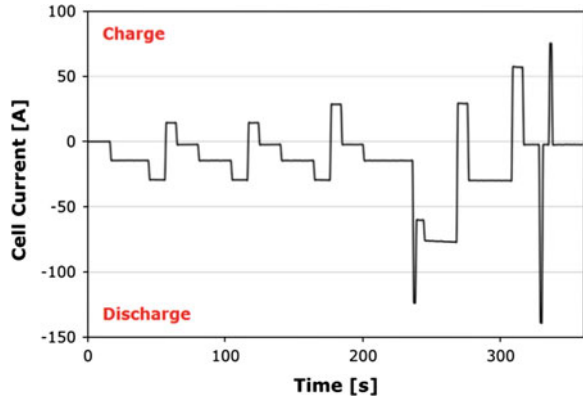


Fig. 7 Simulation results of the HPPC pattern

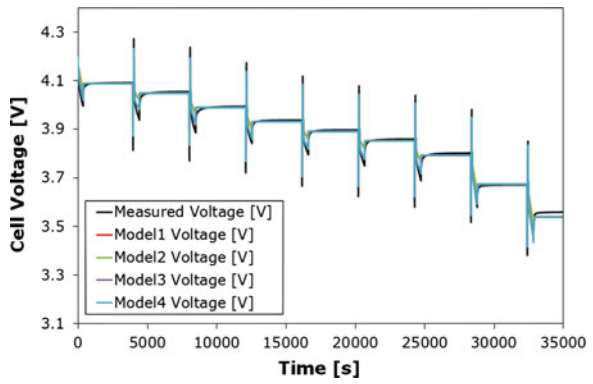
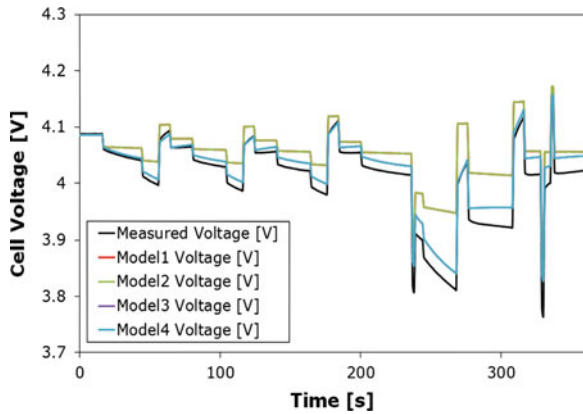


Fig. 8 Simulation results of the CDCL pattern



to the estimated SOC and the voltage variation in the dynamic characteristics model. The impedance parameters of the dynamic characteristics model are modified and applied to the model in real time through a look-up table (LUT).

3.2 Validation and Consideration of Each Model

In order to compare the properties of the simulation model obtained in this study and those of the actual battery cell, we conducted charging and discharging experiments according to the profiles shown in Fig. 5, which are explained in the PHEV Battery Test Manual issued by the Idaho National Laboratory (INL) of the U.S. Department of Energy [8]. The hybrid pulse power characterization (HPPC) test profile shown in Fig. 5 is effective for comparing the steady-state characteristics of each SOC of the model and the actual battery because charging and discharging pulses are applied while the SOC is discharged to 10 %. The charging-depleting cycle life (CDCL) shown in Fig. 6 is adequate for comparing the dynamic characteristics of the simulation model and the actual battery because charging and discharging are repeated frequently.

In order to compare the accuracies of the equivalent models by analyzing the results of the simulations and experiments, the difference between the measured voltage and simulation voltage was divided by the operating voltage range from 0 to 100 % of the battery cell's SOC to calculate the error rate (ε). The error rate quantitatively indicates how accurately the model used in the simulation reflects the properties of the actual battery; the smaller the error rate, the better the model represents the actual battery. In addition, we calculated the average value of the absolute error ($|\bar{\varepsilon}|$), the maximum error rate (ε_{\max}), and the sum of the squared errors (SSE) to compare the accuracies of the models. Figures 7 and 8 display the simulation results of each model according to HPPC and CDCL test patterns, and Figs. 9 and 10 show the error rates calculated for each model.

Based on the validation results of each elicited model, we were able to confirm that there was no difference in terms of the simulation voltage waveform and error distribution rate between Models 2 and 4, which included the impedance of the high-frequency charge transfer region, and Models 1 and 3, which did not include a high-frequency region. This suggests that in HPPC and CDCL testing of the high-capacity battery cell used in this study, influence from the equivalent impedance of the charge transfer region was minimal, resulting in almost no difference in the waveform and error rate calculation. Furthermore, we were able to confirm that Models 3 and 4 provide a closer representation of the actual voltage and have smaller average values of absolute error and maximum error rates than Models 1 and 2. Accordingly, it can be concluded that including equivalent impedance that indicates the diffusion region (rather than the charge transfer region) provides a more accurate model of the PHEV high-capacity battery cell used in this study.

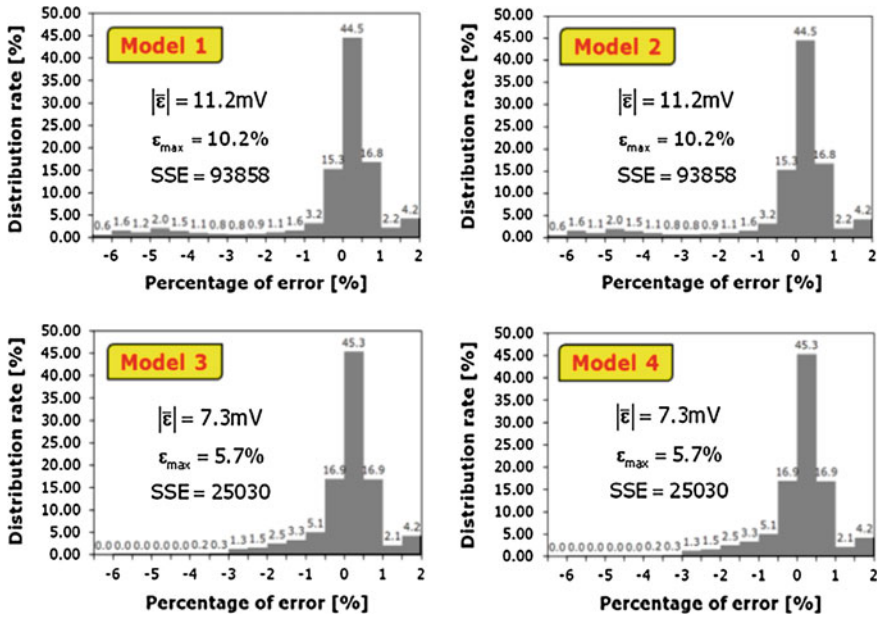


Fig. 9 Error rate comparison of the HPPC pattern for each model

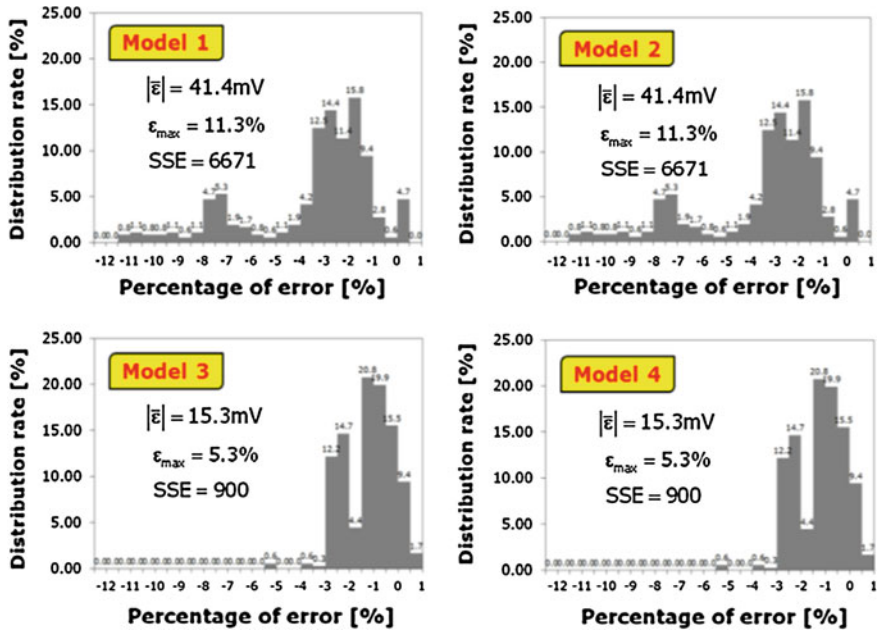


Fig. 10 Error rate comparison of the CDCL pattern for each model

4 Conclusions

In this study, we performed high-capacity lithium battery cell modelling for a real time simulation in order to reduce the time and cost required to optimize and develop environmentally friendly vehicle systems. We examined various equivalent impedance models for high-capacity 20 Ah lithium battery cells for PHEVs, extracted parameters for each SOC of the cells using EIS, and enabled the implementation of a high-capacity battery cell model with MATLAB/Simulink. Furthermore, we selected charging and discharging profiles for the comparison of dynamic properties between the estimated models and the actual battery cell and compared the experimental results according to the selected profiles and simulation results of each model to calculate the error rate.

References

1. Nabi S, Balike M, Allen J, Rzemien K (2004) An overview of hardware-in-the-loop testing systems at Visteon. SAE paper (2004-01-1240)
2. Dhaliwal A, Nagaraj SC, Ali S (2009) Hardware-in-the-loop simulation for hybrid electric vehicles-an overview, lessons learnt and solutions implemented. SAE paper (2009-01-0735)
3. Dong TK, Kirchev A, Mattera F, Kowal J, Bultel Y (2011) Dynamic modelling of Li-ion batteries using an equivalent electrical circuit. *J Electrochem Soc* 158(3):A326–A336
4. Zhang H, Chow MY (2010) Comprehensive dynamic battery modelling for PHEV applications. In: *Proceedings IEEE Power and Energy Society General Meeting*
5. Guezennec Y, Choi W, Choi T (2012) Optimized dynamic battery model suited for power based vehicle energy simulation. *Int J Automot Technol* 13(1):133–141
6. Jossen A (2006) Fundamentals of battery dynamics. *J Power Sources* 154:530–538
7. Lee JH, Choi W (2011) Novel state-of-charge estimation method for lithium polymer batteries using electrochemical impedance spectroscopy. *J Power Electron* 11(2):237–243
8. Idaho National Lab (2008) Battery test manual for plug-in hybrid electric vehicles. Rev. 0

On-Board Powerplant Numerical Optimization of Internal Combustion Engines in Series Hybrid-Powertrains

Thorsten Krenek, Thomas Lauer, Bernhard Geringer
and Bacher Christopher

Abstract Serial-hybrid-powertrains in extended-range electric vehicles (E-REV) pose different requirements to internal combustion engines (ICE) than conventional vehicles. In E-REVs ICEs are not used for propulsion but for battery charging and cabin heating. This work deals with the design of ICEs in serial-hybrid-powertrains. It considers different operating strategies as well as the dimensioning of the electric components of the powertrain and the thermal management. Therefore, a longitudinal dynamic model was developed using GT-SUITE including the ICE and the thermal management. The engine was operated on a test bench in parallel to create the necessary maps for the numerical investigations. Due to the high amount of parameters that can be optimized when determining the operating strategies and dimensioning the components, by a numerical optimization method that was developed and customized for this problem. The numerical investigations showed that for higher vehicle speeds the direct propulsion of the ICE is more efficient while for lower speeds the operation of the ICE as a generator is the more efficient strategy. Additionally, the influence of the ambient temperature on the efficiency was taken into account. At low ambient temperatures it is necessary to heat up the driver's cabin electrically. Using a thermal numerical model it was possible to show the dependency on the energy consumption, the component dimensioning and the configuration of the operation strategies. The most favourable powertrain setup and the most efficient

F2012-B03-007

T. Krenek (✉) · T. Lauer · B. Geringer
Institute for Powertrains and Automotive Technology,
Vienna University of Technology, Vienna, Austria
e-mail: thorsten.krenek@ifa.tuwien.ac.at

B. Christopher
Institute of Computer Graphics and Algorithms,
Vienna University of Technology, Vienna, Austria

operating strategies were achieved by using the described numerical optimization method. The new and comprehensive approach was to consider the entire vehicle including mechanical components, thermal components and operating strategies in the numerical model setup and the holistic optimization of them using self-developed numerical optimization software.

Keywords Power-split hybrid-powertrain · Numerical optimization · Range-extended electric vehicle · Thermal management · Internal combustion engine

1 Introduction

In serial-hybrid-powertrains internal combustion engines (ICEs) are not used for propulsion but for battery charging and cabin heating. So there are different requirements to ICEs compared to the usage in conventional vehicles [1]. Some strategies of ICEs which are generally implemented to achieve lower fuel consumption and emissions, like the de-throttling of the intake system at part load operation, are abundant and can be omitted, because the ICE is mostly operated at high load [2]. On the other hand, the electrification of the powertrain offers numerous parameters to optimize the efficiency. As a consequence a lot of influencing variables can be varied and therefore optimization software is necessary to achieve the best possible solution in terms of efficiency and driving range. In this work an extended-range electric vehicle (E-REV) based on the Chevrolet Volt topology is considered [3]. It is primarily used for electric drive and uses a power-split hybrid powertrain with two electrical machines for propulsion and electrical energy generation (see Fig. 1).

The power-split is realised using a planetary-gear-set (PGS) (see Fig. 1) where the ICE and the electric machine 1 (generator) are connected to the ring gear and the traction motor 2 is connected to the sun gear.

In case of a low battery state of charge (SOC), an ICE is used for charging the battery and partially for propulsion. This work deals with the dimensioning of the main powertrain components as well as with the optimization of the operation strategies in dependency of different ambient temperatures, driving cycles and ICEs. Furthermore, the thermal management for the ICE, the battery and the driver's cabin are considered.

2 Component Dimensioning

The main components for dimensioning of the considered vehicle which were investigated in this paper are the battery, the electric machines and the ICE. These components have a high influence on the overall efficiency and the electric range.

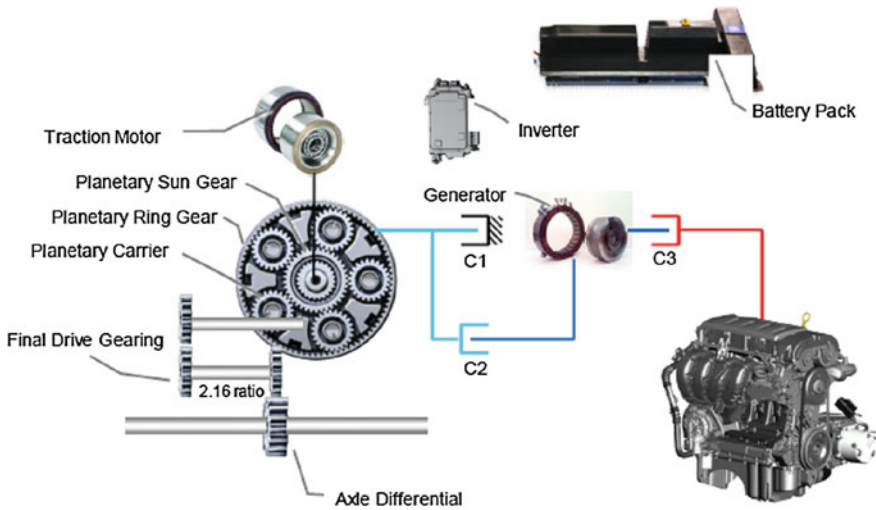


Fig. 1 Kinematic architecture of the investigated powertrain [3]

2.1 Battery

The capacity of the battery mainly influences the electric range of the vehicle. But a higher capacity also means higher costs, weight and a higher available space in the vehicle. Another relevant property is the maximum amount of electrical power which can be used for discharging and charging the battery. In this case, following [3], a 16 kWh battery has been chosen for the optimization process. With this assumption a reasonable compromise of driving range and weight is achieved.

2.2 Electric Machines

For the considered vehicle the electric machines are used for propulsion and electric power generation. As a consequence, an operation at highest efficiency is necessary to achieve an acceptable driving range. In this work two types of electric machines are considered: A permanent magnet synchronous (PMSM) and asynchronous (ASM) e-machine (see Fig. 2) because these types of electric machines are used for the considered powertrain [4]. The efficiency map of [5] is used for the PMSM. The efficiency map of the ASM has been reconstructed from a “single speed one-motor electric drive” efficiency map [6] where the efficiency is defined as traction power delivered to the axle divided by the electric power input.

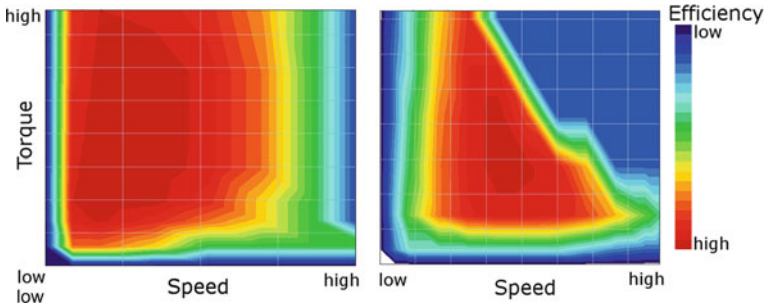


Fig. 2 Efficiency maps of the PMSM [5] (left) and ASM (right)

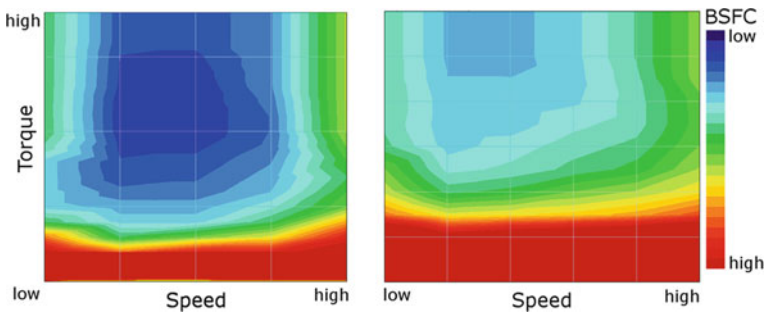


Fig. 3 Brake specific fuel consumption (BSFC) maps of the turbo charged diesel [10] (left) and natural aspired gasoline (right) engine

2.3 ICE

In E-REVs the ICE is mainly used for operating the electrical generator. In the considered vehicle it is also possible to directly use the mechanical energy of the ICE for propulsion [6]. Another important aspect of the ICE is the waste heat recovery of the cooling water to heat up the driver’s cabin and battery. To see the fuel consumption of different ICEs two different types of ICEs, a natural aspired gasoline engine with 60 kW and a more efficient turbo charged diesel engine with 40 kW (see Fig. 3) have been used for investigations. The fuel consumption measurements for the natural aspired gasoline engine have been done by the Institute for Powertrains and Automotive Technology.

3 Operation Strategies

In E-REVs many different operation strategies are possible, but generally they can be divided into the two main categories: electric only and range-extended drive when a minimum battery state of charge is reached [2]. At the serial-hybrid mode the ICE operates the electrical generator and the electrical energy is used as power supply of the propulsion e-machine, the auxiliary systems and for charging the battery. Additionally, the vehicle has the ability to operate as power-split hybrid with a direct power flow from the ICE to the wheels (“combined mode”) to avoid power losses by repeated power conversion.

To evaluate the operation strategies the US6 and NEDC driving cycles were used. The US6 is a high dynamic cycle with a high average vehicle speed and the NEDC has a significantly lower average speed and dynamic. Because this work is focused on the requirements on the ICE, only range-extended modes are considered. To optimize the numerous parameters that are involved in the operating strategies, an optimization software was developed.

4 Optimization Software

Figure 4 shows the process chart of the optimization algorithm that was developed by the Group of Algorithms and Data Structures from the Vienna University of Technology [7].

First, initial solutions for the optimization process will be generated using a Monte-Carlo Algorithm because generally there is no information about the search space and it is necessary that the initial solutions are well distributed. The main optimization consists of a particle-swarm optimization (PSO) and a genetic algorithm (GA). The PSO is used when the solutions are well distributed in the search space. During the PSO optimization process the parameter values of the considered solutions are changed in the direction of the best known solution. Additionally, this best known solution is further improved with a surface-fitting method after the PSO. After this procedure the parameter values of different solutions are recombined and randomly changed using the GA. If an improved solution is not achieved, a downhill-simplex approach is applied on the specialized similar solutions. Detail information about the algorithm is given in [8]. In comparison to the included Design of Experiments method of GT-SUITE this approach has the advantage that solutions will be further improved during the optimization process by using information from existing solutions.

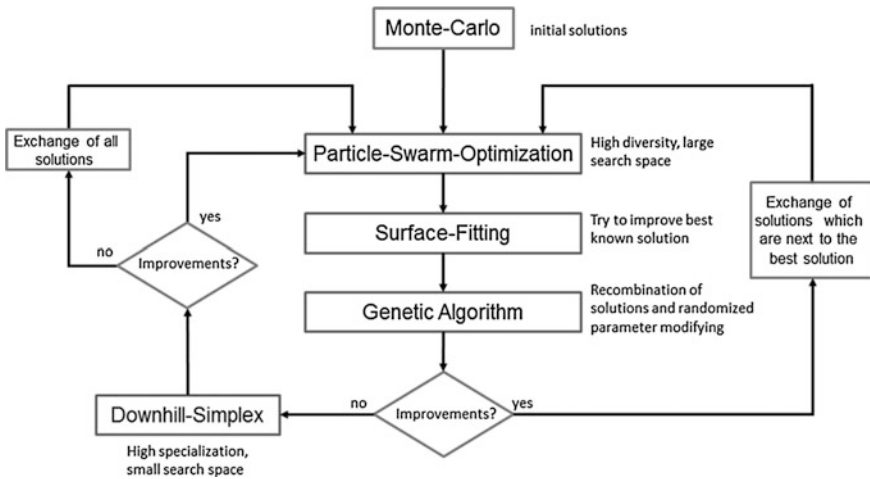


Fig. 4 Optimization software process chart [7]

5 Thermal Management

Modern lithium-ion batteries must be operated at a specific temperature range [9]. Therefore, the battery must be electrically heated at low ambient temperatures. In comparison to electric vehicles, HEVs and E-REVs have the ability to partially use the heat of the ICE to heat up the driver's cabin and battery at low ambient temperatures. However, in contrary to conventional vehicles the ICE is shut-off during considerable time ranges. Therefore, it is necessary to consider the temperature of the cooling water and the necessary heat for the battery and the driver's cabin when optimizing the operating strategy.

6 Simulation Model

For the planned investigations a longitudinal model of the vehicle including the engine and its thermal management was created with the commercial software GT-SUITE from Gamma Technologies.

6.1 Longitudinal Model

This model is used for simulating the complete vehicle for a given driving cycle. Especially for optimization purposes the ICE is simulated by using specific fuel consumption maps. It is also possible to include the thermal management of the

ICE, battery and the driver's cabin. This model, including the thermal management, is used for the further explained investigations. It offers the opportunity to vary a lot of parameters which influences the operation strategy. So it is necessary finding a good parameter set with acceptable time effort.

6.2 Thermal Management Model

To get information about the heat up and cool down behaviours of the ICE, the battery and the driver's cabin, a thermal management model has also been developed. It is possible to use the waste heat of the ICE and battery for heating up the driver's cabin. If there is not enough waste heat available, it is necessary to use an electric heater.

7 Results of the Numerical Investigations

First, the influence of the battery capacity on the fuel consumption and the electric range has been investigated. The weight change of the car has been considered with 10 kg/kWh [9]. Because of the lower vehicle weight a smaller battery capacity always results in lower energy consumption caused by the reduced required energy operating the vehicle. As a consequence, the recommended battery capacity only depends on the required minimum electric range. The influence of the battery capacity variation with a fixed operation strategy in the NEDC at normal conditions (20 °C ambient temperature) is shown in Fig. 5.

The speed threshold, at which the range-extended mode switches from "Serial-Hybrid" to the "Combined" mode, is another important parameter which has a high influence on the fuel consumption. Generally for higher vehicle speeds it is more efficient to use the mechanical power of the ICE directly for propulsion because the conversion of the energy is avoided. The speed threshold depends on the chosen electric machines, the ICE, the gear-ratios of the planetary-gear-set (PGS) and the traction demand. A typical behaviour for different constant vehicle speeds is shown in Fig. 6.

As a final step, the most important parameters of the vehicles were optimized simultaneously with the goal to find the best specification in terms of driving efficiency. For the operation strategy nine parameters were optimized. The most important parameters of the operation strategy were the minimum operation speed of the ICE, the gear configuration of the PGS, the vehicle velocity threshold between the different operating modes and the target speed for the traction electric machine. Based on the results of the previously described investigations, the lower bound of the vehicle velocity threshold switching from serial-hybrid to the "combined" mode was set to 30 km/hr. For dimensioning of the electric machines

Fig. 5 Electric range and energy consumption in dependency of the battery weight

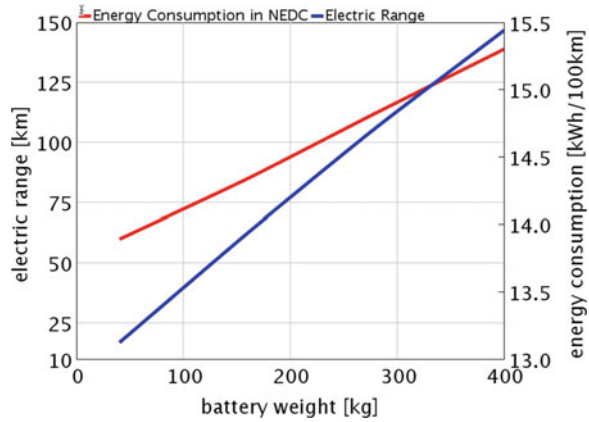
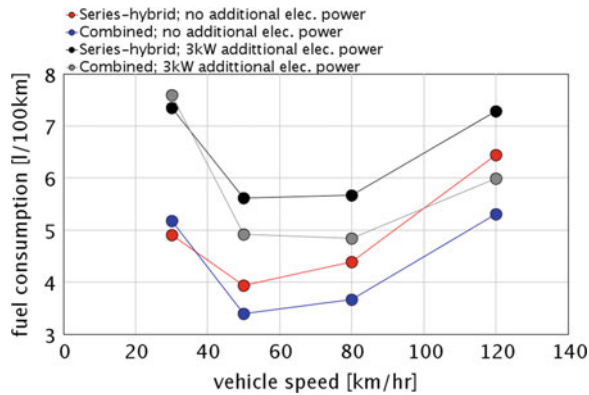


Fig. 6 Fuel consumption at constant vehicle speed in serial-hybrid and combined range-extended mode



it was taken into account with four parameters, which are multipliers for the torque and speed values of the electric machine’s efficiency maps.

Additionally there are constraints for the optimization process:

- Balanced SOC at the end and the beginning of the driving cycle. For an unbalanced SOC a penalty value, which depends on the difference to the initial SOC and the mean efficiency of the ICE-generator unit, will be added to the fuel consumption.
- The heat up time to reach the target cabin temperature of 22 °C is limited to seven minutes.
- The lowest allowed SOC level of 0.2 must not be undershot.
- The elasticity has to sufficient to realise the vehicle’s acceleration during the given driving cycles.

For this approach the two explained ICEs at two different ambient temperatures (−20, 20 °C) in two different driving cycles (US6 and NEDC) were investigated. The SOC at the beginning of the driving cycle was 0.3. Because the results of the

Fig. 7 Fuel consumption at normal and cold conditions in the US6 and NEDC driving cycle

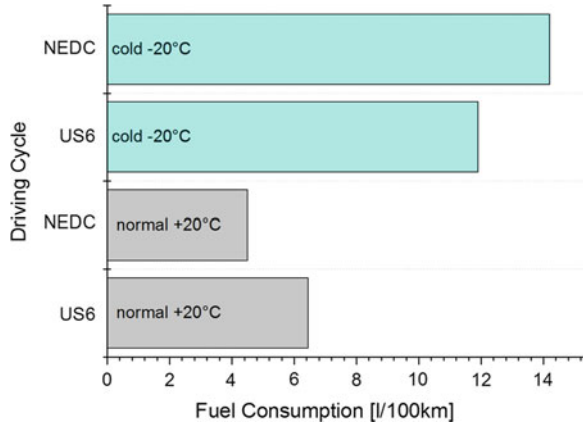
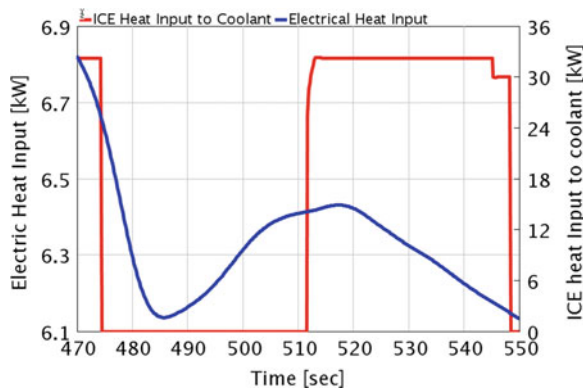


Fig. 8 Effect to the electric heat requirement in the NEDC driving cycle if the ICE is turned off and on



diesel engine are similar to these of the petrol engine, except of the lower fuel consumption, the results of the diesel engine are no longer being considered. At the ambient temperature of 20 °C the thermal management of the driver’s cabin has not been considered. At –20 °C ambient temperature the driver’s cabin needs to be heated, either with the electric heater or by using the waste heat of the cooling water. The results of the fuel consumption show a big difference between the –20 and 20 °C ambient temperature solutions (see Fig. 7).

This is caused by a high additional amount of electrical energy required at the beginning of the driving cycle. At this time the ICE coolant is too cold, so no waste heat recovery is possible and the driver’s cabin has to be heated electrically only. Figure 8 shows the effect of the electric heat demand and Fig. 9 shows the effect to the ICE coolant temperature if the ICE is turned off and on.

Another big difference can be seen at the “ice speed for low charging demand” parameter. This parameter influences the speed of the ICE at low battery charging demand at the “serial-hybrid” mode. Because of the requirement of a balanced SOC at the end and at the beginning of a driving cycle this speed is used when the

Fig. 9 Effect to the ICE coolant temperature in the NEDC driving cycle if the ICE is turned off and on

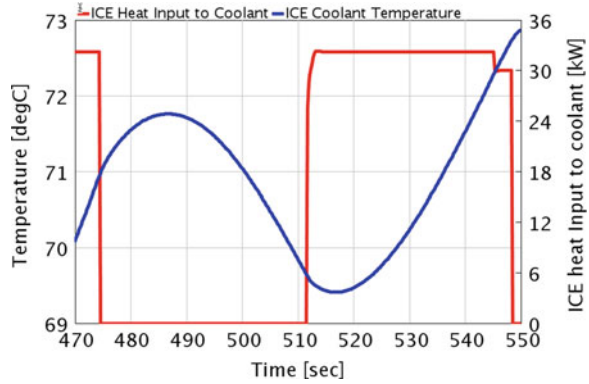
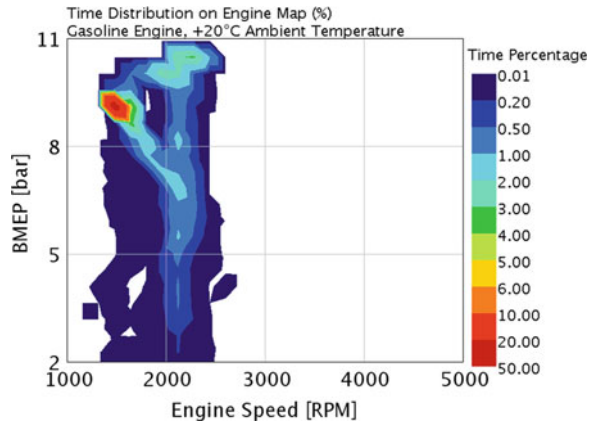


Fig. 10 Time distribution of engine at normal conditions (20 °C ambient temperature) in the US6 driving cycle



SOC is near the level of the SOC at the beginning of the driving cycle. This parameter value is also used for the target speed at the “combined” mode. As it can be seen in Figs. 10 and 11 most of time the ICE is running at this speed. Under normal conditions (20 °C ambient temperature) it is more efficiency to run the generator at lower speeds (see Fig. 10) and at lower power output, because the battery will be charged slower and on average more electrical energy can be used directly from the generator and not from battery.

At very cold conditions (−20 °C ambient temperature) it is necessary to run the ICE at higher speeds (see Fig. 11) and power output, because of the additional power demand of the electric heater. Using the waste heat of the ICE reduces the amount of electrical power (see Fig. 8).

The configuration of the PGS is mainly influenced by the ICE and the EM2 electric machine. At the “combined” range-extended mode the ICE has the highest influence and at the “serial-hybrid” mode the EM2 machine has the highest influence, because it is the only device applied to the PGS.

Fig. 11 Time distribution of engine at cold conditions (– 20 °C ambient temperature) in the US6 driving cycle

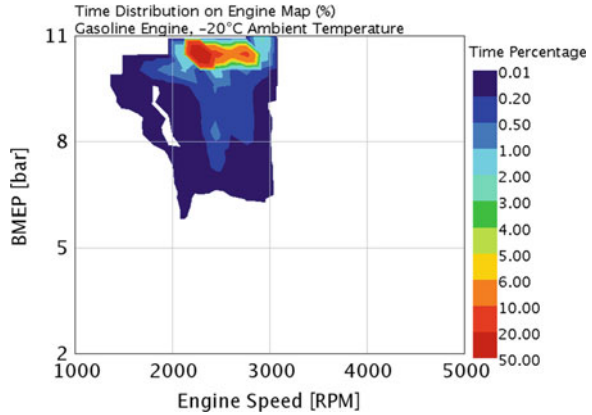
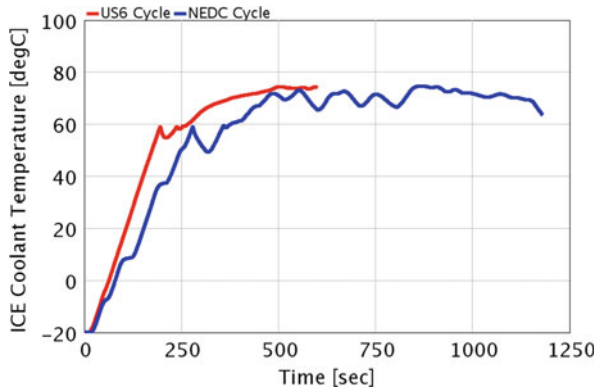


Fig. 12 Coolant temperature in the US6 and NEDC driving cycle



The comparison of the two different driving cycles at normal conditions (see Fig. 7) shows higher fuel consumption for the US6 because the average vehicle velocity is more than two times higher as in the NEDC and the US6 cycle and has a significantly more alternating velocity profile. At very cold conditions these circumstances are completely different because the average energy which is needed for the US6 is much higher than in the NEDC and so the waste heat can be used earlier for heating the cabin (see Fig. 12).

In conclusion, to find good hybrid-powertrain configurations it is necessary considering different environmental conditions and driving cycles. But in all considered scenarios it makes sense to use ICEs which have a low minimum brake specific fuel consumption at high engine loads because at serial-hybrid powertrains it is possible to run the ICE at high load independent of the power demand. The additional electrical energy can be stored in the battery. So it is not really necessary to optimize them for partial load points.

8 Summary and Outlook

In this work a comprehensive numerical simulation model of an E-REV has been used for component dimensioning and operation strategy optimization, considering different driving cycles, ambient temperatures and ICEs. The results show, that at cold ambient temperatures it is more efficient to run the ICE at higher speeds and higher power output, because the amount of electric energy for cabin heating can be reduced by using the waste heat of the ICE coolant. Generally it's necessary considering all parameters together for optimization. The results of the investigations show that it's more time efficient to optimize the parameters in groups, if there is enough information about the parameter dependencies. To handle such problems the optimization software will be further improved and enhanced by the Institute of Computer Graphics and Algorithms adding e.g. neural nets, user input during the optimization process and parameter clustering.

References

1. Brooke L (2010) Optimizing ICEs for hybridization. SAE Automotive Engineering International, 2010-01-05:9–11
2. Grebe U, Nitz L (2011) Voltec—das antriebssystemsystem für chevrolet Volt[J], MTZ—Motortechnische Zeitschrift, Wiesbaden: Springer Vieweg: 343–351
3. Grebe U, Nitz L (2011) Electrification of general motors vehicles—A portfolio of solutions. 32. Internationales wiener motorensymposium, VDI-Fortschritt Berichte, Reihe 12, Nr. 735 [M] Düsseldorf: VDI-Verlag, , ISBN 978-3-18-373512-9
4. Rahman K, Anwar M, Schulz S, Kaiser E, Turnbull P, Gleason S, Given B, Grimmer M (2011) The Voltec 4ET50 Electric Drive System. SAE Int. J. Engines. doi:[10.4271/2011-01-0355](https://doi.org/10.4271/2011-01-0355)
5. Bucherl D, Nuscheler R, Meyer W, Herzog HG (2008) Comparison of electrical machine types in hybrid drive trains: induction machine vs. permanent magnet synchronous machine[J], Proceedings of the 2008 international conference on electrical machines: 4
6. Miller M, Holmes A, Conlon B, Savagian P (2011) The GM “Voltec” 4ET50 Multi-Mode Electric Transaxle. SAE Int. J. Engines. doi:[10.4271/2011-01-0887:1102-1114](https://doi.org/10.4271/2011-01-0887:1102-1114)
7. Planer M, Krenek T, Lauer T, Geringer B (2012) “Optimisation of hybrid strategies with heuristic algorithm” [J] 12th stuttgart international symposium “Automotive and engine technology”, FKSF—research institute of automotive engineering and vehicle engines stuttgart
8. Krenek T, Ruthmair M, Raidl G, Planer M (2012) Applying (hybrid) metaheuristics to fuel consumption optimization of hybrid electric vehicles, Applications of evolutionary computation [J], Springer. pp: 376–385
9. Matthe R, Turner L, Mettlach H (2011) VOLTEC Battery System for Electric Vehicle with Extended Range [J]. SAE Int. J. Engines. doi:[10.4271/2011-01-1373](https://doi.org/10.4271/2011-01-1373)
10. Schreiner K (2011) Basiswissen verbrennungsmotor [M]. Wiesbaden: Springer Vieweg, ISBN 978-3-8348-1279-7

Torque-Vectoring Driveline for Electric Vehicles

**Bernd-Robert Hoehn, Karsten Stahl, Philipp Gwinner
and Ferdinand Wiesbeck**

Abstract The range of electric vehicles is limited due to the battery capacity. As a result of high prices for batteries as well as a rising weight using additional battery modules, both the feasible level of electric recuperation and the efficiency of the system have to be as high as possible. Therefore, the Technische Universität München has developed and designed a new torque-vectoring system for electrical powertrains. Besides the main driving machine a second smaller superimposing electric motor combined with a superimposing gear makes it possible to recuperate brake energy for all driving situations. Especially in curves with high lateral forces the new system reaches higher recuperation values than comparable systems. The system size of the superimposing machine is only about 5 % of the vehicle's driving power. Due to the continuously variable power delivery there are no slipping losses, i. e. such as those of wet clutches. The overall losses in the presented powertrain are only 10 % of the losses compared to existing systems. Gearbox efficiency results, which were calculated with a simulative model, are presented for straight-ahead driving and cornering. Varying deceleration values for these driving conditions, efficiency values are illustrated for different recuperation levels with or without the superimposing machine being activated.

Keywords Torque-vectoring · Electric city vehicle · Planetary gear train · Gearbox efficiency · Recuperation

F2012-B03-009

B.-R. Hoehn (✉) · K. Stahl · P. Gwinner
Gear Research Center (FZG), Technische Universität München, Munich, Germany
e-mail: hoehn@fzg.mw.tum.de

F. Wiesbeck
Institute of Automotive Technology, Technische Universität München, Munich, Germany

Fig. 1 MUTE at the international motor show 2011 (IAA)



1 Electric Vehicle “Mute”

The electric vehicle “MUTE” has been developed at the Technical University of Munich and was presented at the IAA in September 2011 (Fig. 1). Together with several industrial partners MUTE was designed for two passengers and urban/suburban use in particular. Related to the vehicle class L7e the net weight of the vehicle is limited to 400 kg, the continuous driving power is restricted to 15 kW. Thanks to the low weight as well as the attached importance to an aerodynamic design allows a maximum speed up to 75 mph. The primary energy storage consists of a rechargeable lithium-ion-battery with a capacity of approximately 10 kWh ensuring a range of at least 100 km referred to customer-oriented driving cycles.

Both the restricted package space as well as the realized safety concept leads to a rear axle drive. Further requirements such as high driving dynamics in combination with narrow tires to reduce roll resistance can cause extreme driving conditions. Especially driving conditions where brake energy is recuperated pose a major challenge for the powertrain design.

As the powertrain features an “Active Differential” using a torque-vectoring (TV) unit, which was first presented in [1], all requirements mentioned before can be achieved to the fullest satisfaction.

2 Powertrain Layout and Function

The MUTE powertrain [2] can be divided into three gear assembly groups combined with two electric motors as shown in Fig. 2. The drive machine in combination with the axle gear is used for drive and recuperation driving conditions. In order to keep the dimensions and weight of the permanent magnet synchronous drive machine low, a high axle gear ratio of 9.1 is used, achieved by two helical spur wheel sections. The high axle ratio results in a maximum speed of 10,000 rpm of the drive machine at a vehicle speed of 75 mph. With a torque up to 60 Nm to

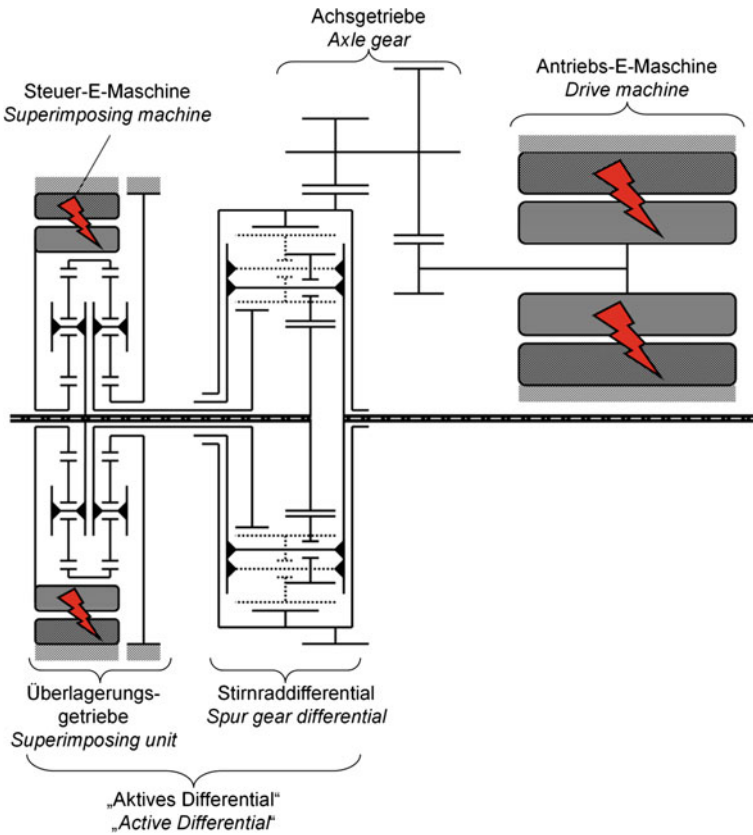


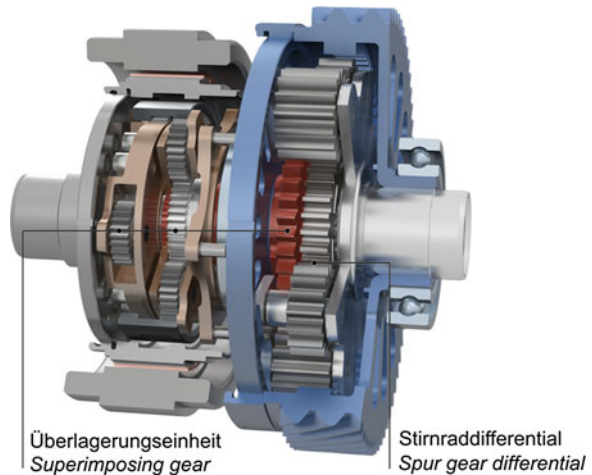
Fig. 2 Schematic structure of the MUTE powertrain

be available, given demands in terms of acceleration and the vehicles climbing ability are met. A spur gear differential, more compact and lighter in comparison to conventional differentials, features a 50:50 torque distribution at the wheels for any straight-ahead operating condition. Moreover, the torque-vectoring unit is deactivated and runs without any load for straight driving so that there is no power consumption during this driving conditions.

In conventional powertrains with a differential, wheel torques are equal due to the differential’s inner transmission ratio. In contrast, a torque-vectoring system can distribute the torque to each wheel independently and can be used for several purposes, such as to improve the vehicle’s efficiency and range, passengers comfort, driving dynamics and the traction [2]. The TV system for MUTE is established by a superimposing unit and a small electric machine connected to the differential via the red highlighted sun gear (Fig. 3), both units referred to as “Active Differential”.

If the torque-vectoring is to be activated, the superimposing machine can be considered as a motor or a generator, depending on the actual driving condition.

Fig. 3 Spur gear differential and superimposing unit



If torque is transferred to the faster turning wheel, the superimposing machine works as a driving machine and as a generator in the opposite case.

The superimposing unit consists of two identical planetary gears of which one sun gear is fixed to the housing and the other one connected to the torque machine. If torque is provided by the superimposing machine, torque is increased by the superimposing gear with the gear ratio of 12.5 whereby a redistribution of torque is caused within the differential. This effect results in an increase of torque at one wheel and a decrease of the same amount at the other wheel. Due to the high superimposing gear ratio a difference in torque at the wheels up to 500 Nm can be achieved with a low acting torque of 40 Nm at the superimposing machine. A further advantage of the layout of this TV system has to be pointed out as the speed of the superimposing machine is a function of the difference in speed of the wheels. This is why the machine speeds can be kept low. Furthermore, the superimposing machine is standing still if both wheels rotate with the same speed (straight-ahead driving). Thanks to the low speeds and torques the machine gets along with less than 2 kW. Designed as a torque motor the superimposing gear is integrated into the superimposing unit so that a compact construction is achieved. In sum, the gearbox including the TV system and an aluminium casing reaches a weight of approx. 20.5 kg (without drive machine and drive shafts).

3 Benefits of the Torque-Vectoring System

The wheel individual torque distribution of torque-vectoring systems results in several benefits compared to conventional systems. In addition to an increase of driving dynamics stabilizing measures can be conducted in critical driving conditions as well. That is why the full-fledged MUTE torque-vectoring system can not only assign the optimum torque to each wheel depending on the grip potential,

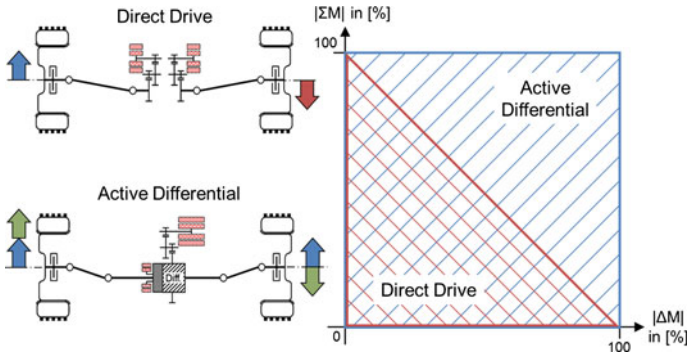


Fig. 4 Benefits of the active differential compared to a direct drive

but also take influence on the lateral driving dynamics. Furthermore, there is a higher torque range to be available thanks to the special layout of MUTE’s powertrain with an Active Differential as shown in Fig. 4.

On the horizontal axis one can see the difference in torque at the wheels whereas on the vertical axis the overall axle torque is plotted. Compared to a direct Drive, the active differential can use the full range of torque. As the torques of the direct drive are operatively coupled to each other (red triangle), it is not possible to use the torque range of an Active Differential (blue square). Thus, the direct drive can’t use the full drive torque in combination with a difference in torque at the wheels and vice versa. Using the active differential torque redistribution can be achieved even while applying the maximum drive torque. Consequently, the superimposing unit causes only a difference in torque at the wheels and doesn’t increase or decrease the axle torque.

In conclusion, the powertrain can be considered as an assembly of two sub-systems. The axle gear provides the drive torque and the superimposing unit the appropriate torque distribution to the wheels. This separation of functions regarding longitudinal and lateral dynamics involves key benefits in comparison to alternative systems in terms of the operating performance. Using an electrically actuated superimposing unit, wheel torques can be adjusted independently and continuously with high dynamics.

4 Modelling of Expected Transmission States

For modelling the transmission efficiency of the Active Differential it is necessary to specify the relevant transmission states. In a quasi-stationary state torque and speed of the two driven wheels define the transmission state, which is directly connected to the driving state of the vehicle. Therefore, they need to be derived from the expected vehicle driving states.

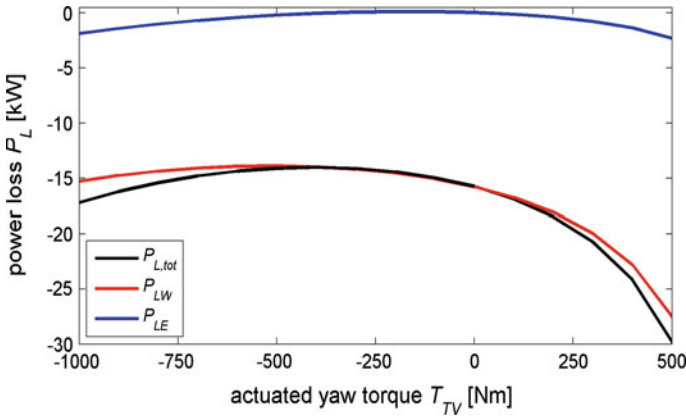


Fig. 5 Power loss over actuated yaw torque for cornering at $v = 25$ m/s, $a_x = -3$ m/s², $r = 100$ m

The quasi-stationary state of a conventional, passive vehicle accelerating or decelerating in a turn is adequately specified by the speed v , the longitudinal acceleration a_x , and the radius of the trajectory r . For a vehicle with torque-vectoring capabilities these three parameters may be achieved with different steering angles depending on the actuated yaw torque. So additionally, the actuated yaw torque T_{TV} is necessary to fully define its driving state. A control strategy needs to be implemented, which gives a value T_{TV} as a function of v , a_x and r .

A numeric model of the MUTE specifically designed for the fast evaluation of quasi-stationary turns has been developed and validated through the existing MBS model. With this model parameter variations are possible in a very efficient way, which makes it suitable for the numeric mapping of control strategies that can be described as optimisation problems.

For the definition of relevant transmission states the minimisation of the power losses at the wheels has been chosen. In Fig. 5 the power losses at the wheels $P_{L,W}$, the electric power $P_{L,E}$ necessary for the active differential and the total power losses $P_{L,tot}$ are plotted dependent on T_{TV} for an exemplary parameter set. The example shows a minimum of $P_{L,tot}$ at $T_{TV} = 400$ Nm with about 2 kW less power losses than the passive vehicle.

For the following evaluation of the transmission efficiency, the transmission states of a vehicle at the energetic optimum are used.

5 Gearbox Efficiency

Powertrain efficiency plays a major role for the design of electric vehicles in order to increase range as well as to achieve higher recuperation potentials. For driving conditions where brake energy is recuperated, gearbox efficiency in particular has

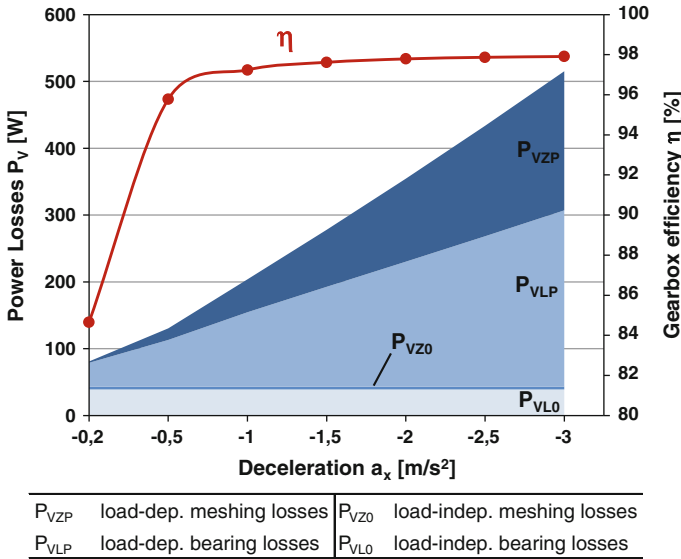


Fig. 6 Break down of power losses and gearbox efficiency

to be as high as possible. That is why MUTE’s Active Differential is designed with planetary gears which are characterized by a variety of gear ratios as well as high efficiencies and small axial dimensions.

The efficiency of MUTE’s gearbox is calculated with the FVA-software WTplus [3] for different operation conditions of the vehicle. The numerical analysis of the program considers losses such as load-dependent and load-independent meshing losses as well as load-dependent and load-independent bearing losses.

Figure 6 shows the break down of these losses for straight-ahead driving at 14 m/s with different deceleration values and no slip. Higher deceleration results in higher braking torques and recuperation power. As straight-ahead driving is considered, the superimposing unit is without any load for this driving condition. The gearbox features high efficiencies over 95 % for decelerations higher than -1 m/s^2 . For low torques gearbox efficiency is falling due to a low power input (low torque in particular) so that the input power has to compensate load-independent losses, which are a function of speed.

Gearbox efficiency is rising for higher torques (recuperation levels) as the load-independent losses lose their influence compared to increasing load-dependent losses.

Figure 7 shows the gearbox efficiency for recuperation in a cornering with a fixed curve radius for different vehicle velocities and decelerations. For the numeric gearbox model calculation results achieved by the active vehicle model described in the chapter before are used. Wheel torques and speeds for the different vehicle states are the input parameters for the gearbox model. The numeric model

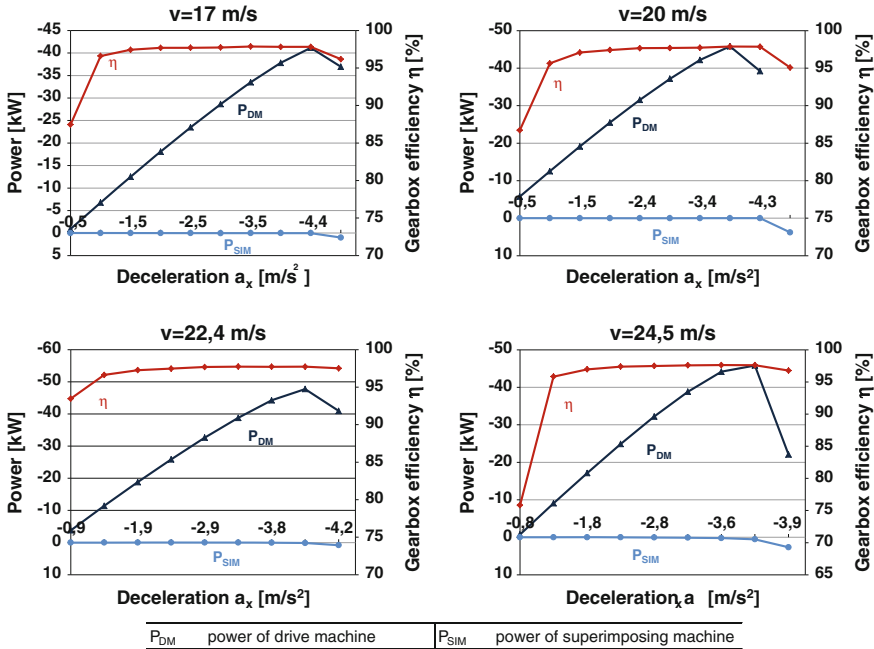


Fig. 7 Gearbox efficiency for cornering and different vehicle velocities

then calculates the statics and kinematics of the whole gearbox such as the resulting power of the drive and superimposing machine as well as the gearbox efficiency. The gearbox features high efficiencies greater than 95 % for all driving conditions to be considered. Furthermore, a high difference in torque at the wheels can be achieved with low torques and acting power (<1 kW) at the superimposing machine due to a high superimposing gear ratio.

6 Conclusion

A new innovative powertrain for electric vehicles with a torque-vectoring function was presented. Using an Active differential it was shown that high powertrain efficiencies can be reached for different driving conditions. Especially for high loads and recuperation levels the gearbox features its efficiency optimum. Even in cornering driving conditions high recuperation values can be achieved with the gearbox efficiency to be over 95 %.

Due to the special layout of MUTE’s powertrain in comparison to existing torque-vectoring systems losses due the use of wet clutches can be avoided. Future efficiency analyses of the gearbox will concentrate on critical driving conditions where the superimposing machine is acting with a higher load reaching its limits.

References

1. Hoehn BR, Wirth C, Kurth F (2009) Aktives differential mit torque-vectoring-funktion Automobiltechnisches kolloquium. Technische Universität München, Munich
2. Hoehn BR, Stahl K, Lienkamp M, Wirth C, Kurth F, Wiesbeck F (2011) Electromechanical powertrain with torque vectoring for the electric vehicle mute of the TU München. VDI: Transmissions in Vehicles 2011, Friedrichshafen
3. Hoehn BR, Michaelis K et al (2008) WTplus 2.0, Lehrstuhl für maschinenelemente der Technischen Universität München, Forschungsstelle für Zahnräder und Getriebebau (FZG)

Plug-In Hybrid Vehicle Powertrain Design Optimization: Energy Consumption and Cost

João P. Ribau, João M. C. Sousa and Carla M. Silva

Abstract The scope of this study is to optimize the component sizing of a fuel cell powered PHEV (PHEV-FC), using a genetic algorithm (GA) to optimize component cost for a typical urban taxi fleet usage. A simplified heuristic methodology is the first approach for the PHEV design. Cost functions for the components are estimated as well as specific power functions to perform the vehicle component sizing and cost evaluation. The used GA aims to optimize the cost of the designed vehicle and evaluate performance constrains (maximum speed and acceleration, electric range, overall performance) using an external tool, a vehicle simulator software ADVISOR, automated with the algorithm (*in loop*). A real measured driving cycle and official New European Driving Cycle (NEDC) are used for the vehicle simulations. Different fuel cells, motor and battery and a range of battery module number are the input data for the GA optimization regarding component selection. The initialization of the heuristic method relays on the vehicle specific power (VSP) methodology, namely on maximum power requirements of the specified driving cycle. It assumes efficiencies and main characteristics) of the components to perform an iterative calculation, followed by a trial and error evaluation. The GA is capable to tune the component sizing to the respective performance requirements. It can be seen that the cost may not have a direct relation with the consumption, since that different components lead to different vehicle weight and performance. An important limitation of the current

F2012-B03-012

J. P. Ribau (✉) · C. M. Silva

Technical University of Lisbon, Instituto Superior Técnico,
Department of Mechanical Engineering, IDMEC/DTEA, Lisbon, Portugal
e-mail: joao.ribau@ist.utl.pt

J. M. C. Sousa
CSI/IDMEC—LAETA, Lisbon, Portugal

methodology is that the vehicle optimization is fully dependent on the assigned driving cycle and performance constraints. Input data and GA parameter tuning deserves exhaustive work to achieve more precise results. The heuristic method although very fast to achieve results lacks sensitiveness regarding the proposed constraints to the design, since the evaluation process is made after the design. The GA allows adjusting better solutions to the requirements of the driving cycle and constraints, and independently selecting the fuel cell, motor and battery. Both heuristic and GA method results are compared with a conventional diesel taxi vehicle (ICEV). The designed PHEV-FC with the lowest cost and compliant with the requirements resulted from the GA method and was powered by a 24 kW fuel cell, a 130 kW motor, and a 251, 17 kWh Li-ion battery pack. Using the real Lisbon downtown driving cycle, the optimized PHEV-FC achieved a 2.1 MJ/km daily taxi service, which represents less 18 % of energy consumption than the ICEV taxi. The best results produced for the PHEV design regarding the real driving cycle have 67 % higher energy consumption and are 80 % more costly than NEDC, since NEDC it is a less demanding cycle.

Keywords Plug-in hybrid vehicle · Optimization · Fuel cell · Energy consumption · Retail cost

Nomenclature

BAT	Battery
CD	Charge depleting
CS	Charge sustaining
EV	Electric vehicle
FC	Fuel cell
GA	Genetic algorithm
HEV	Hybrid electric vehicle
ICE	Internal combustion engine
ICEV	ICE vehicle
MC	Electric motor
PHEV	Plug-in HEV
PHEV-FC	Plug-in HEV powered by fuel cell
SOC	State of charge
VSP	Vehicle specific power

1 Introduction

Forecasts indicate increases for world primary energy demand by 36 % between 2008 and 2035, or 1.2 % per year on average, from which oil remains the dominant fuel in the energy mix. In EU-27 the total energy consumption reached 1113

MTOe in 2009, where transport sector represented approximately 33 % [1]. The road transport accounts nearly 80 % of the transport sector energy demands.

Some of the alternative road vehicle technologies are already being addressed by several car manufactures such as hybrid electric vehicles (HEV), plug-in hybrid electric vehicles (PHEV) and full electric vehicles (EV) [2, 3]. HEVs at their most basic forms simply mean a vehicle that uses two or more distinct power sources, usually a fuel converter like an internal combustion engine (ICE) or a fuel cell (FC) with a battery to propel the vehicle [3, 4]. Improving batteries and cost profiles will bring the next big step in the electrification of automobiles, either in the form of plug-in capabilities (PHEVs) or pure EVs. PHEVs promise to provide batteries capable of pure electricity operation for at least 32 km [5], more than the average daily commuting distance for Europe of 22 km [6]. EVs since they only have a battery as energy storage/producer, have their distance range a lot limited relatively to HEVs and conventional vehicles. Then, PHEVs eliminate what has been the major objection to EVs, their limited range, since PHEVs have a second energy source, the FC or ICE. PHEVs are designed to use a charge depleting strategy for the battery (CD mode, which uses only battery/electricity power), alike to the EVs. The battery is discharged till it reaches a minimum state-of-charge (SOC), and then a charge sustaining strategy (CS mode, which uses the fuel converter as second source of energy) is engaged, in similarity to the HEV [3, 4, 7]. PHEVs are still being announced and its market place is still poor, and at the current time, the major disincentive to buy such vehicles is the purchase price of the vehicles. Costs and a more specific HEV component analysis is being addressed [8–11]. Alternative technologies and fuels can lead to great improvements; however the design of the vehicle in terms of component selection and energy management strategy has an important role in energy consumption [3, 4]. Electric and hybrid vehicles present different energy management strategies [4, 7, 12], and its optimization, using several different techniques, can lead to great improvements [4, 13, 14].

Vehicle component design optimization is also in development [4]. Particle Swarm Optimization method was already studied to optimize the fuel cell hybrid vehicle powertrain component sizing, namely to minimize the cost, mass and volume of the fuel cell and supercapacitor, using MatLab/Simulink [15]. Global optimization to perform component sizing regarding different vehicle powertrains, using simulation software *in-the-loop* with the algorithm was also studied [16]. Methodology for the optimization of PHEVs component sizing using parallel chaos optimization algorithm, regarding cost minimization, using ADVISOR [17] to perform vehicle simulation, was used other studies [18]. The component design optimization ensures that the vehicle components are designed to achieve efficiently the most probable purpose of the vehicle (and also in compliment with the energy management strategy).

This study aims to compare a heuristic methodology to design a fuel cell powered PHEV (PHEV-FC) with a genetic optimization algorithm whose objective function respects primarily to retail cost regarding vehicle's main components: electric motor, fuel cell, and battery. The vehicle is applied for taxi service in Lisbon city.

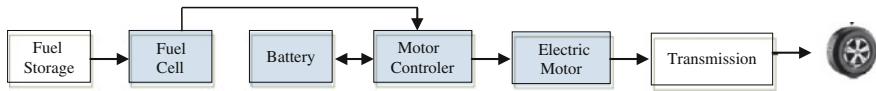


Fig. 1 Shows a basic configuration of a series PHEV-FC, and the main components highlighted

Table 1 Conventional, reference, ICEV taxis [20]

	Lisbon taxi (ICEV)
Weight (kg)	1405
<i>ICE</i>	
Nominal Power (kW)	100
N.m @ rpm/maximum Speed (rpm)	270@2000/4200
Accessory power (W)	1000
Tire rolling radius (m)	0.320
Aerodynamic drag coefficient	0.28
Frontal area (m ²)	2.50
Time(s) 0–100 km/h	11
Max. speed (km/h)	210

The PHEV design will be based on the performance and the body of an existing taxi: a conventional internal combustion vehicle (ICEV) diesel fuelled. The genetic algorithm is used to select the more appropriate components of the PHEV in terms of power, power/energy density for the electric motor, fuel cell and Lithium battery. The constraints are maximum acceleration time from 0 to 100 km/h, top speed, maximum electric range and driving cycle accomplishment. The optimized PHEV configuration is simulated in official New European Driving Cycle (NEDC) [19], and a real measured driving cycle, using vehicle simulation software ADVISOR [17].

2 Methodology

The development of a methodology to design a fuel cell powered PHEV (see Fig. 1) starting from the performance and body of a conventional diesel ICEV is the main scope of this study (see Table 1). The targeted application of the vehicle is to perform taxi service in Lisbon city. A conventional ICEV representative of a real taxi (see Table 1) and a real measured driving cycle (see Table 2, Fig. 2) are simulated for comparison purposes [20]. The ADVISOR [17] is used as vehicle simulation software. An optimization process will be used to ensure that the designed PHEV-FC besides achieving specific constrains as maximum acceleration, maximum speed and a minimum electric operation (battery use only) range (Table 3), is also the option with lower cost within the range of available components for the design. Maintaining the base frame of the conventional ICEV the objective is to optimize the vehicle design selecting the electric motor, fuel cell and battery (as well as battery module number).

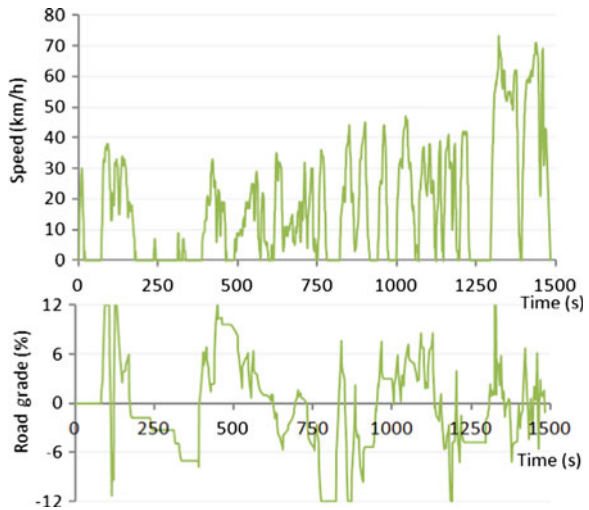
Table 2 Driving cycle’s characteristics: duration time, distance, average speed, positive average acceleration, maximum VSP, positive average VSP, number of stops and idle time

Driving cycle	Time (s)	Distance (km)	Avg. speed (km/h)	Pos. avg. accel. (m/s ²)	Maximum VSP (kW/kg)	Pos. average VSP (kW/kg)	# stops	Idle time (s)
<i>LisbonDt</i> [20]	1485	7.3	17.74	0.84	7.40E-2	6.65E-3	27	464
NEDC [19]	1184	10.9	33.21	0.54	2.57E-2	5.16E-3	13	298

Table 3 Performance constraints

Time 0–100 km/h (s)	< 12
Top speed (km/h)	> 120
Electric range (km)	> 20

Fig. 2 *LisbonDt* measured driving cycle. Speed (km/h) and road grade (%)



2.1 Case Study

Lisbon taxi service comprises near 3490 vehicles performing an average daily distance of 207 km (average service of 7.3 km) with an occupancy rate averaging 1.2 passengers per service [21]. This taxi fleet to be analysed is mainly composed by the conventional ICEVs shown in Table 1. Real driving data measured within Lisbon Metropolitan area, by using a speed sensor, a GPS system equipped with a barometric altimeter and data recovery from the OBD (On-Board Diagnostic) interface, was used to represent a driving schedule, Lisbon downtown (*LisbonDt*) for this study (Fig. 2). Table 2 shows *LisbonDt* driving cycle characteristics as well the official NEDC (no road grade). The PHEV to be studied in order to

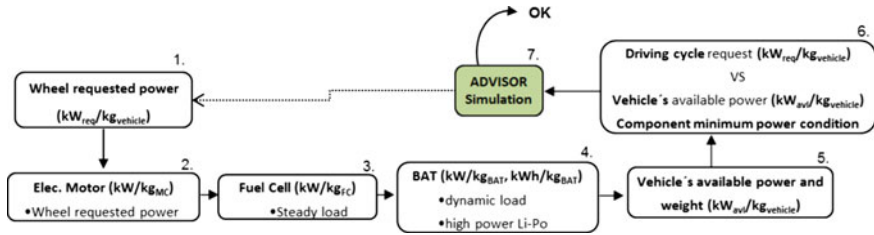


Fig. 3 PHEV component selection method

substitute the ICEV fleet are powered in a series configuration, and the fuel converter will be hydrogen fuelled fuel cell (FC) rather than the original diesel ICE. The PHEV to be designed must fulfil minimum requirements, presented in Table 3.

2.2 First Approach: PHEV Design

A first approach to the design will be based on heuristic method. To achieve the PHEV-FC configuration, the fuel converter power was downsized, and the vital components (electric motor, fuel cell and battery) selection was made according to the following steps (see Fig. 3) [20]: (1) Using a VSP based methodology [22, 23] the wheel power requested to the vehicle per unit of mass (kW/kg) was determined for *LisbonDt* (Table 2). (2) Average driveline efficiencies were taken into account and the electric traction motor, MC, was sized to fulfil the wheel requested power, torque and speed [3, 4]. Using a specific power density assigned to the component the weight was determined (the same was done for all the following components (see Table 4). (3) The FC is designed to supply the steady (average) load as possible [4, 24], and its nominal power is in commitment with the average requested power outlined from the *LisbonDt*. (4) The battery was designed to respond mostly to the dynamic loads [4, 24], but when the CD mode is engaged (all electric mode) the battery must be able to supply the full power requested from the MC. (5) The powertrain architecture in terms of components and auxiliaries will determine not only the vehicle's available power but also its weight. (6) An iterative process is performed between the driving cycle requested power per unit of mass, $kW_{\text{requested}}/kg$, with the vehicle's available power, $kW_{\text{available}}/kg$, to achieve a minimum/optimum value of kW/kg for the vehicle and its components. (7) The vehicle with the corresponding components is simulated in the respective driving cycle, *LisbonDt* (see Table 2) using ADVISOR vehicle simulation software [17]. The designed PHEV-FC must be capable to fulfil the requested performance.

For each component, a specific power function was used to estimate the component mass (see Table 4). For the lithium battery a specific energy capacity

Table 4 Estimated specific power densities (and energy for battery) assigned to the respective components

	MC (kg) [25–28]	FC (kg) [29–32]	BAT (kg), (kWh/kg) [33–38]	
A	0.205 kW + 48.995	$7E-05 \text{ kW}^3 - 0.018 \text{ kW}^2 + 3.336 \text{ kW} - 3.414$ + (auxiliary sys ~53 % total mass)	$-1E-15 \text{ kW}^2$ + 3.389 kW– 5E–12	Medium (Wh/kg) $3E-06(W/kg)^2 - 0.032(W/kg) + 159.3$ Low energy (Wh/kg) $1E-06(W/kg)^2 - 0.004(W/kg) + 45.4$
B	48.5	$1E-06 \text{ kW}^4 - 0.0003 \text{ kW}^3 + 0.031 \text{ kW}^2 + 0.167 \text{ kW} - 0.105 \text{ kW} + 5.754$ + (auxiliary sys ~53 % total mass)		High energy (Wh/kg) $-1E-06(W/kg)^2 - 0.012(W/kg) + 196.8$

Table 5 Estimated retail costs (\$) for electric motor, fuel cell and battery

Average cost estimations	MC (\$)	FC (\$)	BAT (\$)
	16.5 kW	79.5 kW	kWh. $(365.32 \ln(W/Wh) + 187.65)$
References	[8, 39]	[8, 40–43]	[8]

was also estimated. The functions used were based on several real components commercially available. Their data and main characteristics were gathered and an overall power density estimation function was adjusted to the data points. The same was made for the battery specific energy capacity. The results are truly dependent on these input data, and different data will naturally lead to different estimations, as well to different results. The more exhaustive work is done on this area, more precise are the results.

Table 4 have two sets of estimations, A shows an average estimation from the data collected, and B shows high specific power data estimations. The heuristic method concerned only to the estimations A, while GA method used a range of values for the component characteristics based on both estimations. A retail cost for each component was estimated and used to attribute a “virtual” cost to the designed vehicle. The costs estimated in Table 5 were based in several cost analysis studies.

Following the iterative method (see Fig. 3) the achieved possible results of PHEV-FC design are presented in Table 6. These results take only into account the maximum power required to perform the *LisbonDt* driving cycle based on VSP methodology [22, 23]. The type of battery and the energy capacity greatly influence the cost results. The components characteristics in Table 6 result from using a medium estimation, or a low or high energy option for the battery (see Table 4).

Table 6 Estimated results for the PHEV-FC design: *LisbonDr* máx power, vehicle available power and its weight, virtual retail cost, and components characteristics

<i>LisbonDr</i>	Vehicle (A)	Vehicle weight [kg]	Virtual cost \$		FC		BAT		Energy capacity [kWh]											
			min	max	Power [kW]	Weight [kg]	Power [kW]	Weight [kg]	Medium	Low	High									
P_{req} [kW]	P_{av1} [kW]	+ 70 kg _{driver}	29157.5																	
143.9	144.0	1943.5	max	45723.9	160.0	81.8	17.2	118.8	191.5	649.0	97.4	28.7	125.5							

Table 7 Available components and genes. The values range includes nominal power of the components, energy density options for the battery (Table 4) and the module number

Component (Gene)	Values range	Genes encoding range
FC	[10, 13, 15, 18, 20, 23, 27, 30] kW (x2, estimations A and B)	[1–16]
MC	[100, 115, 130, 145, 160, 175, 190] kW (x2, estimations A and B)	[1–14]
BAT	[medium power, high power] x [medium, low and high energy]	[1–6]
BAT mod. number	[50, 150] modules	[50, 150]

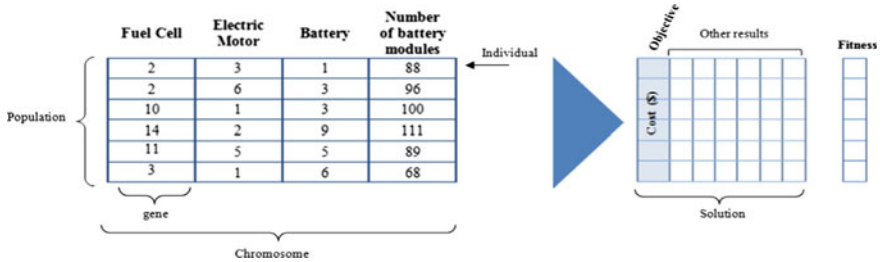


Fig. 4 Chromosome structure, population, genes, individuals, and associated objective and fitness

Virtual cost represents the sum of the estimated retail cost of FC, MC and BAT, and its min and max range represents the different battery options.

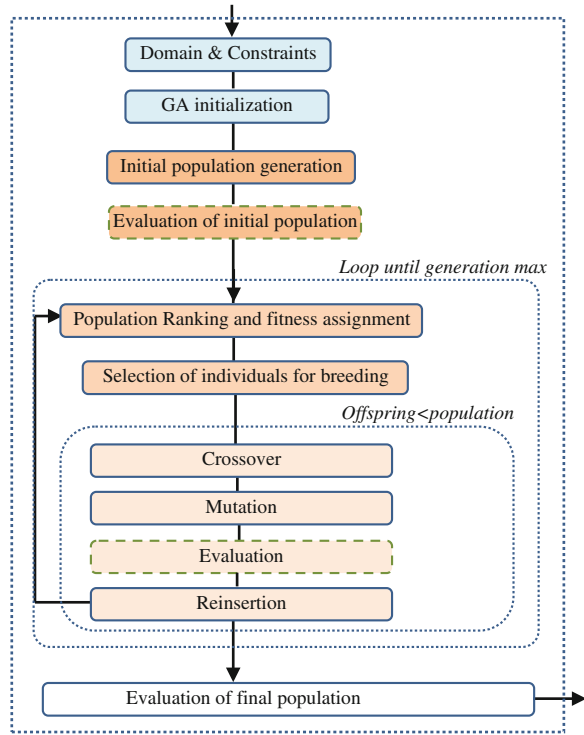
2.3 Vehicle Optimization

The optimization problem can be resumed in “What is the best combination of electric motor, fuel cell, and battery for a PHEV?” The objective is to design a PHEV-FC (Fig. 1) with the lower cost, but capable to perform a certain driving cycle and to comply specific constrains as maximum acceleration, maximum speed and a minimum electric operation (battery use only) range.

2.4 Objective, Domain and Constraints

The new PHEV-FC design will be based on the base frame of a real conventional taxi diesel vehicle (Table 1). The base frame adapted to PHEV modifications (plus 4 % the original weight), wheels (light weight wheels around 40 kg) and new

Fig. 5 Design algorithm scheme



transmission (around 50 kg) were assumed to weight 1093 kg. ([8, 44], Table 1). Adding to the base of the vehicle, the PHEV main components are added, namely the electric motor, the fuel cell, and the battery.

The designed PHEV-FC in *First Approach* section (see Tables 4, 5 and 6) can be used as initial vehicle, as a reference, for the optimization algorithm initialization. Taking into account the achieved components of this initial vehicle a range of components were chosen to be available to perform the design: several different electric motors, fuel cells and batteries, with different power characteristics (Table 7). Using the specific power functions given by estimations A and B in the Table 4 the available components are shown in (Table 7).

When evaluating a vehicle the performance constraints to be achieved in this study must satisfy the ones presented in Table 3, regarding acceleration time, a maximum speed, and electric range (using only battery power). Assuming that the vehicle frame, transmission, and auxiliary systems maintain similar for the different PHEV-FC designs, the objective function focuses on direct comparison between the different component choices. The objective function can be expressed as the sum of the estimated retail costs of the MC, FC, and battery, BAT (see Table 5), (see Eq. 1):

$$f(x) = \$_{FC} + \$_{MC} + \$_{BAT} \tag{1}$$

Optimize the component selection can be seen as a constrained optimization problem, defined as in Eq. 2. Where the objective function has to be minimized, and has a solution, x , belonging to the solution space, Ω , which defines the lower and upper bounds of the variables of the cost function (Tables 5 and 7). The inequality $g_i(x)$ represents the n constraints (Table 3). In resume, between the components choices available, it can be 1,344 different combinations, each of one composing a vehicle to be evaluated and to calculate the cost.

$$\underset{x \in \Omega}{\text{Minimize}} f(x) \text{ s.t. } g_i(x) \leq 0, \quad i = 1, 2, \dots, n \quad (2)$$

2.5 Optimization Algorithm: Genetic Algorithm

A GA is a stochastic global search and optimization method, and its creation was inspired in natural biological evolution [45]. A GA functions on a population of potential solutions and it applies the principle of survival of the fittest preliminary solution to produce successively better approximations to a solution. A modularized Genetic and Evolutionary Algorithm Toolbox for MatLab software [45, 46] was used for the optimization in this study, which the objective is to optimize the vehicle design in order to minimize a virtual cost attributed to such design. A genetic algorithm works by building a population of chromosomes which is a set of possible solutions to the optimization problem. The GA chromosome structure is composed by individuals that contain information, genes, representing the respective components (Fig. 4). Each individual can be seen as a candidate solution regarding to a designed PHEV-FC. The set of individuals is intended as a population.

The MC, FC, BAT and battery module number define the 4 genes composing the chromosome (see Fig. 1 and 4). Each element composing a chromosome string is encoded in integer values (Table 7) representing a specific file of a component or the battery module number within range of possible values to be chosen as input of the algorithm accordingly to the available components inputted (see Table 7 as in *Objective, Domain and Constraints* section).

The GA initialization (Fig. 5) refers to important parameters needed to initialize the GA. The generation gap defines the number of offspring relative to the “old” population, or the rate of individuals to be selected for breeding and crossover. The crossover rate defines the probability of two individuals combine their genes to perform crossover [45]. The generation gap was chosen to be 0.8, the crossover rate 0.6, the population size, N , and the number of generations were varied. The mutation rate in this study is equal to $1/(\text{variables per individual})$ [45], defining the rate of mutation between genes of individuals after crossover.

The GA starts with random generation of the initial population (Fig. 5), building the chromosome structure with the possible genes available (see Table 7): N individuals are created, composed by 4 elements (generated randomly) that represent each a specific component file and the number of battery modules.

Table 8 Heuristic method results for PHEV-FC design, and ICEV

Conventional ICEV taxi		Energy consumption		Daily(MJ)	Maximum speed (Km/h)	Max. acceleration (time 0–100 km/h)	Electric range (km)
Driving cycles	Over cost (\$)	Fuel (MJ/km)	Elec. (MJ/km) ^a				
<i>NEDC</i>	0	2.55	–	2.55	210	11	–
<i>LisbonDt</i>		4.78	–	4.78			–
Designed PHEV-FC taxi (heuristic method)							
Driving cycles	Over cost (\$)	Energy consumption		Daily(MJ)	Maximum speed (Km/h)	Max. acceleration (time 0–100 km/h)	Electric range (km) ^c
		Fuel (MJ/km) ^b	Elec. (MJ/km) ^a				
<i>NEDC</i>	40494	1.76	1.24	1.60	156.5	7.4	60.2 (170,218)
<i>LisbonDt</i>		2.66	1.81	2.49			42.02 (116,149)

^a CD operation (battery only)^b Fuel used in CS operation^c Electric range in CD using low energy option BAT (med, high energy options in brackets)

Table 9 a and b: GA results for the PHEV design in NEDC

GA parameters ^a	Over cost (\$)	Energy consumption		Daily (MJ/km)	Maximum speed (km/h)	Max. Acceleration (time 0–100 km/h)	Electric range (km)	
		Fuel (MJ/km) ^b	Elec. (MJ/km) ^c					
$N = 4, Gen = 10$	16029	1.29	1.14	1.27	156.3	7.6	22.7	
$N = 10, Gen = 20$	15259	1.29	1.14	1.27	156.6	7.9	21.3	
$N = 20, Gen = 50$	13875	1.28	1.13	1.27	156.5	7.9	20.5	
GA Parameters ¹	FC nom. power (kW)	MC nom. power (kW)	BAT nom. power (kW)	BAT nom. power (kW/h)	BAT energy cap. (kWh)	BAT volt. (V)	BAT module number	Vehicle mass (kg)
$N = 4, Gen = 10$	15.68	112.43	435.31	11.95	246.33	67	1293	
$N = 10, Gen = 20$	15.68	130.59	409.32	11.23	231.63	63	1300	
$N = 20, Gen = 50$	12.14	112.43	389.83	10.70	220.60	60	1226	

^a GA parameters: population size, N, and maximum generations, *Gen*

^b Fuel used in CS operation

^c CD operation (battery power only)

Table 10 a and b: GA results for the PHEV design in *LisbonDt*

GA parameters ^a	Over cost (\$)	Energy consumption		Maximum speed (km/h)	Max. acceleration (time 0–100 km/h)	Electric range (km)	
		Fuel (MJ/km) ^b	Elec. (MJ/km) ^c				
$N = 4, Gen = 10$	33048	2.26	1.61	154.5	5.9	29.3	
$N = 10, Gen = 20$	25220	2.36	1.58	155.3	6.1	23.1	
$N = 20, Gen = 50$	24960	2.14	1.60	155.2	6.3	23.3	
GA Parameters ¹	FC nom. power (kW)	MC nom. power (kW)	BAT nom. power (kW)	BAT energy cap. (kWh)	BAT volt. (V)	BAT module number	Vehicle mass (kg)
$N = 4, Gen = 10$	34.20	147.02	300.15	21.93	452.23	123	1382
$N = 10, Gen = 20$	26.87	161.73	243.00	16.94	349.28	95	1251
$N = 20, Gen = 50$	23.51	129.73	251.00	17.30	356.63	97	1362

^a GA parameters: population size, N , and maximum generations, Gen

^b Fuel used in CS operation

^c CD operation (battery power only)

Table 11 Resume of results design in LisbonDt

Solution	Over cost (\$)	Energy consumption Daily, 207 km (MJ/km)	FC nom. power (kW) ^a	MC nom. power (kW)	BAT nom. power (kW)	BAT energy cap. (kWh)	Vehicle mass (kg)
Conventional ICEV	0	4.78	100	–	–	–	1405
Heuristic	40494	2.49	17.2	160	192	29	1873
GA: N = 20, Gen = 50	24960	2.08	23.51	129.73	251	17.3	1362

^a Fuel converter: Fuel cell for PHEV’s and ICE for conventional

When a population is generated is posteriorly evaluated (Fig. 5), where each assembled vehicle (or each individual) is simulated in certain conditions in vehicle simulation software, ADVISOR [17] attributing each individual a set of results: cost, energy consumption, maximum speed, maximum acceleration, and electric range.

ADVISOR, NREL’s ADvanced VehIcle SimulatOR [17], is a set of model, data, and script text files for use with Matlab/Simulink. Each component that composes a vehicle is represented by a different file. In order to use the ADVISOR within the GA, a special function was used, *adv_no_gui*. This function is provided in a file (MatLab M-File: *adv_no_gui.m*) of ADVISOR, that when called from the Matlab Command window gives the ability to run ADVISOR without its graphical user interface (GUI) allowing its use being automatized with the GA algorithm.

After simulation the performance constraints (Table 3) are evaluated, and if not achieved a penalty factor is added to the genes, increasing the cost objective value. At least one individual must not be penalized, or a new population (initial) must be generated. Both simulation and performance analysis form the *Evaluation* process of the algorithm (see Fig. 5). A fitness profile is assigned to each individual of the population, and since the objective is to minimize the cost, better fitness is assigned to individuals with lower cost.

The selection function uses the scaled fitness values to select the parents of the next generation. The selection function assigns a higher probability of selection to individuals with higher scaled values. Accordingly to the individual’s fitness and the generation gap rate, the selection of the individuals for crossover is performed using stochastic universal sampling [45, 46].

Afterwards, a Crossover routine is applied, where vector entries, or genes are selected, from a pair of individuals in the current generation and are combined to form a child individual. Single point crossover routine (where part of the first parent is copied and the rest is taken in the same order as in the second parent) is used. Next a mutation process occur, using a real-value operator, mutating children by applying random changes to individual’s genes (higher probability mutation grater is the mutation) in the current generation. A mutation process adds to the diversity of a population. At this point the offspring population is completed, then

after being evaluated (similarly to the evaluation process explained behind) the offspring individuals are reinserted into original population maintaining the best fitted individuals, by replacing the least fitted.

3 Results

The PHEV-FCs design with the associated cost resulting from the *First approach* heuristic method can be seen in Table 6 for Vehicle, and also on Table 8. The different driving cycles produce different results, since the *LisbonDt* is more demanding. The overcost associated presented in the results (Tables 8, 9, 10) is the additional cost relative to the FC, MC and BAT implementation replacing the ICE, catalyst and particle filter, and transmission of the conventional ICEV. The associated cost of the ICEV represents only these components cost [47] as near 4990\$.

Different results from the GA are presented in Tables 9 and 10, regarding the NEDC and real driving cycle respectively. The daily energy consumption regards to the sum of electric consumption during electric range, and the fuel consumption during the rest of the day (207 km). The different GA parameters can greatly influence the results. The population size increasing not always means more precise results or greater result. A small population size provides an insufficient sample size over the space of solutions for a problem, but a large population requires larger amounts of evaluations and has a more computational cost. It can be seen that GA parameter tuning is extremely important. Table 11 resumes the results from both methods and compares with the convention ICEV regarding simulations on the *LisbonDt* driving cycle.

4 Conclusion

The heuristic method although very fast to achieve results lacks sensitiveness regarding the proposed constraints to the design, since the evaluation process is made after the design. The initialization of this method relays on the VSP methodology, namely on maximum requirements of the driving cycle. It assumes efficiencies and main characteristics (mostly nominal power) of the components to perform an iterative calculation, and finally a trial and error evaluation using a vehicle simulator. The components in this method have a fixed mathematical relation. The GA method performs the evaluation process (using ADVISOR) *in loop* with the algorithm, and permits to adjust better solutions to the requirements of the driving cycle and constraints, and independently select the fuel cell, motor and battery. It can be seen that the cost may not have a direct relation with the consumption, since that different components lead to different vehicle weight and performance. According to the importance of the input data and the GA

parameters, future work should focus on GA parameter tuning and more exhaustive data collection, to achieve more precise results. The lowest cost designed vehicle, compliant with the requirements, was powered by a 24 kW fuel cell, a 130 kW motor, and a 251 kW, 17 kWh battery. Using the real Lisbon downtown driving cycle, the optimized PHEV-FC achieved a 2.1 MJ/km daily taxi service, which represents less 18 % energy consumption than ICEV. The best results produced for the PHEV design regarding the real driving cycle have 67 % higher energy consumption and are 80 % more costly than NEDC, since NEDC it is a less demanding cycle. Acknowledgments

Thanks are due to FCT for the PhD financial support SFRH/BD/68569/2010. The authors would like to acknowledge MIT Portugal project “Assessment and Development of Integrated Systems for Electric Vehicles” (MIT-Pt/EDAM-SMS/0030/2008).

References

1. World Energy Outlook 2009, and 2010. International Energy Agency (IEA), Web: <http://www.worldenergyoutlook.org/> accessed on 2012-06-07
2. Baptista P, Tomás M, Silva C (2010) Hybrid plug-in fuel cell vehicles market penetration scenarios. *Int J Hydrogen Energy* 35(18):10024–10030
3. Fuhs E (2009) Hybrid vehicles and the future of personal transportation. CRC, Boca Raton
4. Ehsani M, Gao Y, Emadi A (2010) Modern electric, hybrid electric and fuel cell vehicles—fundamentals, theory, and design. CRC Press, Boca Raton
5. Barkenbus J (2009) Our electric automotive future: CO2 savings through a disruptive technology. *Policy soc* 27:399–410
6. TANDBERG. Environmental benefits of video telework for individuals, companies, and communities. TANDBERG 2006, http://internetinnovation.org/files/special-reports/TAN_WhtPpr_Green_FINAL.pdf accessed on 2012-02-05
7. Baptista P, Ribau J, Bravo J, Silva CM, Adcock P, Kells A (2011) Fuel cell hybrid taxi life cycle analysis. *Energy Policy* 39:4683–4691
8. Kromer MA, Heywood JB (2007) Electric powertrains: opportunities and challenges in the U.S. light-duty vehicle fleet. Sloan Automotive Laboratory, Massachusetts Institute of Technology, Cambridge
9. Van Vliet OPR, Kruithof T, Turkenburg WC, Faaij APC (2010) Techno-economic comparison of series hybrid, plug-in hybrid, fuel cell and regular car. *J Power Sources* 195:6570–6585
10. Shiau C-SN, Samaras C, Hauffe R, Michalek JJ (2009) Impact of battery weight and charging patterns on the economic and environmental benefits of plug-in hybrid vehicles. *Energy Policy* 37:2653–2663
11. Silva C, Ross M, Farias T (2009) Evaluation of energy consumption, emissions and cost of plug-in hybrid vehicles. *Energy Convers Manage* 50:1635–1643
12. Silva C, Ross M, Farias T (2009) Analysis and simulation of “low-cost” strategies to reduce fuel consumption and emissions in conventional gasoline light-duty vehicles. *Energy Convers Manage* 50(2):215–222
13. Sciarretta A, Guzzella L (2007) Control of hybrid electric vehicles—a survey of optimal energy-management strategies. *IEEE Control Syst Mag* 27(2):60–70
14. Dextreit C, Hannis G, Burnham K, Haas O, Assadian F, Yue W (2005) Power management techniques for hybrid vehicles. Jaguar and land rover technical research, jaguar cars, engineering centre, whitley, Coventry, control theory and applications centre, Coventry University, UK

15. Hegazy O, Van Mierlo J (2010) Particle swarm optimization for optimal powertrain component sizing and design of fuel cell hybrid electric vehicle. 12th International conference on optimization of electrical and electronic equipment, Basov, pp 601–609
16. Karbowski D, Freiherr von Pechmann K, Pagerit S, Kwon J, Rousseau A (2009) Fair comparison of powertrain configurations for plug-in hybrid operation using global optimization. SAE World Congress, Detroit SAE paper 2009-01-1334
17. Wipke K, Cuddy M, Burch S (1999) ADVISOR 2.1: A user friendly advanced powertrain simulation using a combined backward/forward approach. IEEE Trans Veh Technol 48:1751–1761
18. Xiaolan Wu, Cao Binggang, Li Xueyan, Jun Xu, Ren Xiaolong (2011) Component sizing optimization of plug-in hybrid electric vehicles. Appl Energy 88(3):799–804
19. DieselNet, Web: <http://www.dieselnet.com/> accessed on 2011-06-11
20. Ribau J, Silva C (2011) Conventional to hybrid and plug-in drivetrain taxi fleet conversion. European Electric Vehicle Congress, Brussels
21. IMTT—Instituto da Mobilidade e dos Transportes Terrestres Web: <http://www.imtt.pt/sites/IMTT/English/> accessed on 2011-07-05
22. Frey H, Zhang K (2007) Implications of measured in-use light duty gasoline vehicle emissions for emission inventory development at high spatial and temporal resolution. 16th annual international emission inventory conference, Raleigh
23. Frey HC, Choi HW, Pritchard E, Lawrence J (2009) In-use measurement of the activity, energy use, and emissions of a plug-in hybrid electric vehicle. Proceedings, 102nd annual conference and exhibition, air and waste management association, Detroit, Michigan Paper 2009-A-242-AWMA
24. Larminie J, Lowry J (2003) Electric vehicle technology explained. Wiley, London
25. UQM technologies Web: <http://www.uqm.com/> accessed on 2012-01-15
26. Remy International Inc. Web: www.remyinc.com/ accessed on 2012-01-15
27. Magtec Hybrid and Electric Drives Web: www.magtec.co.uk/ accessed on 2012-01-15
28. VectoPower Electric Motors Web: www.vectopower.com accessed on 2012-01-15
29. Department of Energy Web: energy.gov
30. Ballard Power Systems Web: www.ballard.com/ accessed on 2012-01-15
31. Hydrogenics—Advanced Hydrogen Solutions Web: www.Hydrogenics.com accessed on 2012-01-15
32. Horizon Fuel Cell Tech Web: www.horizonfuelcell.com/ accessed on 2012-01-15
33. Stark Power Batteries Web: www.starkpower.com/ accessed on 2012-01-15
34. KOKAM Web: <http://www.kokam.com/new/> accessed on 2011-09-15
35. A123 Systems Lithium Ion Battery Manufacturer Web: www.a123systems.com/ accessed on 2012-01-15
36. Panasonic Battery Web: www.batteryupgrade.com.pt/ accessed on 2012-01-15
37. SAFT Web: www.saftbatteries.com/ accessed on 2012-01-15
38. EIG Web: www.eigbattery.com/ accessed on 2012-01-15
39. Delorme A, Pagerit S, Sharer P, Rousseau A (2009) Cost benefit analysis of advanced powertrains from 2010 to 2045. EVS 24, Norway
40. Satyapal S (2011) Fuel cells and hydrogen joint undertaking general stakeholders assembly
41. Ahluwalia RK, Wang X, Kwon J, Rousseau A (2011) Drive-cycle performance and life-cycle costs of automotive fuel cell systems. Fuel Cell Seminar and Exposition, Orlando
42. DOE Hydrogen and Fuel Cells Program Record. Web: http://www.hydrogen.energy.gov/program_records.html accessed on 2012-03-15
43. International Partnership for Hydrogen and Fuel Cells in the Economy. Fuel cell cost analysis summary. Prepared by IPHE representatives from China, Korea, and the United States, 2007, 2008
44. GREET Model—The Greenhouse Gases, Regulated Emissions, and Energy Use in Transportation Mode. Web: <http://greet.es.anl.gov/> accessed on 2012-08-15

45. Chipperfield A, Fleming J, Pohlheim H, Fonseca C (1994) Genetic algorithm toolbox for use with Matlab. Technical report No. 512, Department of automatic control and systems engineering, University of Sheffield
46. Genetic Algorithm Toolbox for MATLAB[®]. Department of Automatic Control and Systems Engineering of the University of Sheffield, UK. Web: <http://www.shef.ac.uk/acse/research/ecrg/gat> accessed on 2012-02-11
47. Edwards R, Larive J, Mahieu V, Rouveiolles P (2011) Well-to-wheels analysis of future automotive fuels and powertrains in the European context. Concawe, JRC, EUCAR

Simulation-Based Energy Flow Study of Purely Electric-Drive Vehicles

Bin Wang, Mian Li, Min Xu and Jianhua Zhou

Abstract In order to analyse and improve the energy efficiency of electric vehicles (EVs), an efficient, effective and accurate simulation model of vehicular systems is established from the energy flow point of view. The proposed model includes sub-systems of energy storage, energy consumption, energy transmission, vehicle dynamics, driver model, and vehicle controller. A case study, based on Nissan Leaf, is implemented for validation of the proposed model. Finally, the energy flow and consumption distributions are demonstrated. Due to its openness and expansibility, the model can be used for design optimization of EVs and the results obtained would provide a guidance to design an EV in a more systematic and optimal way.

Keywords Energy flow · Electric vehicles · Simulation model · Optimization

1 Introduction

Due to environmental and energy concerns, electric vehicles (EVs) have drawn more and more attentions all over the world, both in industry and academic institutes. There are numerous publications discussing all kinds of EVs, including Hybrid EV (HEV), Plug-in Hybrid EV (PHEV), pure battery powered EV, battery

F2012-B03-014

B. Wang · M. Li · M. Xu (✉) · J. Zhou
National Engineering Laboratory for the Automotive Electronic Control Technology,
Shanghai Jiao Tong University, 800 Dongchuan Road 200240 Shanghai, China
e-mail: mxu@sjtu.edu.cn

and super-capacitor (SC) EV, and etc. [1, 2]. When designing an EV, many design variables and parameters, such as the number and capacity of batteries as well as the type and arrangement of motors, must be carefully determined to achieve the essential goals—better energy economy and vehicle performances [3, 4]. Simulation modelling provides us an indispensable and effective way for the evaluation and analysis of EVs.

Although there are significant amount of literature discussing simulation modelling of EVs, most of them focused on detailed techniques and new developments of key components of EVs, such as modelling of batteries, fuel cells, motors, supervisory powertrain controller and so on. There are also several kinds of commercialized software such as AVL Cruise that can be used to conduct a complete simulation model for the study of EVs. However, they are usually packaged and can't be modified to achieve design optimization based on energy flow analysis. Furthermore, they focus on various perspectives such as powertrain configurations and vehicle dynamics, but not specified for the study of energy flow of EVs [5]. In this regard, it is quite important to develop a simulation model of EVs that can focus on energy flow, so that the study of energy storage, transformation, dissipation can be analysed thoroughly. An energy-flow simulation model of EVs can be very helpful for the reconfigurations of power components, design optimization of EVs at the system level, and optimization of operational strategies in the future study.

An efficient, effective and accurate simulation model of vehicular systems from the energy point of view, which can also be called as the energy flow simulation model, is proposed in this chapter. Through simulation, the energy economics and energy flow distributions among major components of EVs can be analysed quantitatively under various scenarios and conditions. In addition, impacts from the variations of key components (e.g., batteries, electric motors, different powertrain topologies) on vehicle performance can be assessed. One objective of this study is to build up a simple but accurate platform for case studies using existing EVs parameters and conditions. Through the analysis of different impacts from different energy related configurations on the vehicle performance, the energy flow, distribution and consumption can be demonstrated clearly for EVs. Moreover, this is a manageable “analysis” model implemented with optimization methods that can design an EV to achieve the essential goals of improving energy economy and vehicle performance. Case studies of typical EVs using the developed simulation model will be demonstrated in this work. The results focus on the energy distributions among major components of the energy transformation and consumption sub-systems when operating under various scenarios and conditions; thus the energy economics can be analysed. The results from this study would be a guidance to design an EV with its key components in a more systematic and optimal way.

In Sect. 2, the model is described in details. Section 3 shows the case study using the proposed model. The conclusion is given in Sect. 4.

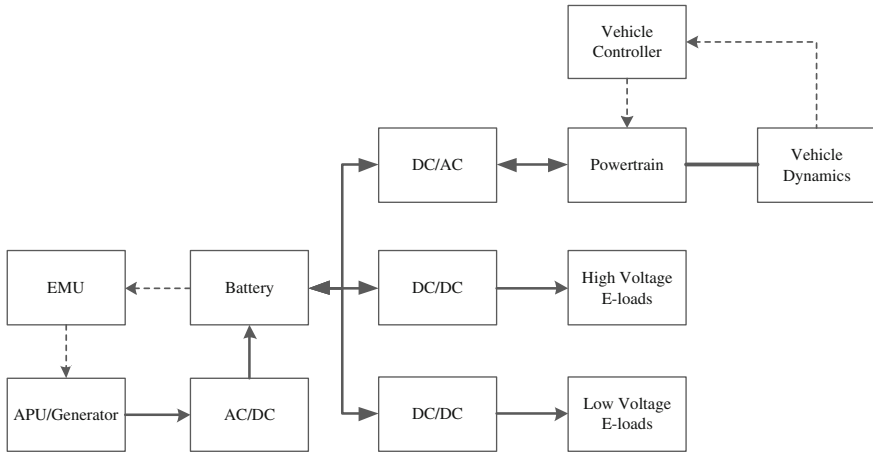


Fig. 1 Structure of the general EVs based on the energy point of view

2 Model Development

Generally speaking, from the energy point of view, the key components of an EV include batteries, auxiliary power units (APU), converter/inverter, motors, and the transmission. The basic structure of the simulation model is shown in Fig. 1.

Those components can be categorized into the following subsystems: energy storage, energy transmission, energy consumption, vehicle dynamics, the driver model, and vehicle controller. Furthermore, each subsystem is composed of some key components. In this chapter, MATLAB/Simulink is used to develop the simulation model due to its openness and expansibility, and the final model is shown in Fig. 2. In the following paragraphs, each subsystem will be briefly introduced.

2.1 Energy Storage Subsystem

Energy storage subsystem stores and provides energy to the entire vehicular system and absorbs the energy regenerated from braking. This part of the simulation model includes the battery, APU, and energy management unit (EMU).

2.1.1 Battery Model

Batteries, as the key energy supply element, play an important role in EVs nowadays. The internal resistance model is used to describe the characteristic of batteries [6]. The output current of the battery model I_{bat} is determined by the power P_{bat} required by all energy consumption components:

2.2 Energy Transmission Subsystem

Energy transmission subsystem, including the DC/DC converter, inverter, clutch, and transmission, delivers electrical or mechanical energy for the downstream component. It is significant that the type of the energy delivered by the energy transmission component will not be changed. Hence, those can be categorized into two scenarios, for electrical energy transmission and for mechanical energy transmission.

From the energy point of view, their efficiencies are the primary factors to be considered.

$$P_{\text{output}} = P_{\text{input}} \cdot \eta_{\text{trans}} \quad (3)$$

where P_{input} is the input power of the component, P_{output} is the output power, and η_{trans} is the efficiency of the energy transmission sub-system.

As for the electrical energy transmission model, the rectifier (AC/DC), inverter (DC/AC), and converter (DC/DC) are required to transmit the electrical energy between different electric equipment. Taking the converter (DC/DC) as an example, the conversion efficiency is related to the input voltage and power [7], so a look-up table established from test or empirical data is utilized.

The clutch and the transmission belong to the mechanical energy transmission model. When engaged, the mechanical power, in forms of torque (limited by the clutch) and rotary speed, is transmitted from the motor to the gearbox (i.e., the transmission) via the clutch. The transmission efficiency of gearbox varies with different gear ratios.

2.3 Energy Consumption Subsystem

Energy consumption subsystem is the most complicated part in this simulation model, which includes the electric motor, high voltage e-loads (electric loads) and low voltage e-loads. These components consume most of the power supplied by batteries and the APU.

2.3.1 Electric Motor Model

The electric motor, as the major energy consumption component, transforms electric power to mechanical power. For an EV, various types of motors are available, such as BLDC (brushless DC) motors, PMSMs (permanent magnet synchronous motors), and induction motors. The output rotational speed and torque of motors are the most concerned issues. In the proposed model, the former is determined by the present speed of the vehicle and the latter is determined by a load signal which will be provided by the vehicle controller. Energy regeneration

during braking is also taken into consideration and the motor acts as a generator transforming the mechanical braking energy to electric power. Due to different mechanisms of driving and braking models, the power balance equations are as shown in Eqs. (4a, 4b):

$$T_{dr}\omega_m = P_{ele} \cdot \eta_{dr}(T_{dr}, \omega_m) \quad (4a)$$

$$T_{br}\omega_m = P_{ele}/\eta_{br}(T_{dr}, \omega_m) \quad (4b)$$

where the subscripts dr and br represent the driving model and braking model respectively, T is the mechanical torque of the motor, ω_m is the rotational speed of the motor, η is the efficiency of the motor, and the P_{ele} is the electric power of the electric motor.

2.3.2 Reconfigurable Chassis

A significant feature of EVs different from conventional vehicles is that the powertrain topology can be very flexible, i.e., different powertrain topologies can be implemented in EVs, such as central front drive, central rear drive, in-wheel front drive, in-wheel rear drive, and any combination of them. The key property of the developed model is the ability to study the energy flow of different reconfigurable powertrain topologies.

2.3.3 High Voltage E-loads

High voltage e-loads usually include the air conditioner (AC) and battery thermal management system. High voltage e-loads consume quite a lot of power generally. Power consumed by the AC mainly is used for three parts: heat exchanged with the environment, heat dispatched by people, and power to bring in fresh air [8]. Each part can be calculated as follows:

The heat exchange with the environment P_1 :

$$P_1 = \alpha A(T_1 - T_2) \quad (5)$$

where α is the conductive coefficient of the whole vehicle, which is usually $1 \sim 3 \text{ W}/(\text{m}^2\text{K})$; A is the area of the car; T_1 is the temperature of the environment, and T_2 is the target temperature.

The heat dissipated by people P_2 :

$$P_2 = n \cdot 0.89 \cdot 116 + 170 \quad (6)$$

where n is the number of passengers. Usually the heat dispatch by the driver is 170 W.

Finally the power to let in fresh air P_3 :

$$P_3 = (n + 1)v\rho(H_1 - H_2) \quad (7)$$

where v is the new air volume required by one person per hour, ρ is the air density, H_1 and H_2 are the enthalpy of the air of the environment and air in the vehicle, respectively.

As for the battery thermal management system, its function is to maintain the temperature of the battery pack to ensure its good performance. The heat power generated by the battery package is calculated as follows [9]:

$$P_{\text{bat_heat}} = I_{\text{bat}}^2 R_{\text{bat}} \quad (8)$$

where $P_{\text{bat_heat}}$ is the heat flow generated by the battery pack.

Due to the temperature difference between the battery pack and the environment, the heat generated by the battery would be dissipated. The calculation of the heat dissipation P_{diss} is:

$$P_{\text{diss}} = N_{\text{bat}}K(T_{\text{bat}} - T_{\text{env}}) \quad (9)$$

where T_{bat} and T_{env} are the temperatures of battery pack and the environment respectively, K is the thermal heat transfer coefficient of the battery pack, and N_{bat} is the number of battery cells.

The net heat, i.e., the difference between the heat generated by the battery and the heat dissipated by the battery pack, is absorbed by the battery itself. As for the calculation of the temperature of battery pack T_{bat} , the equation is shown as follows:

$$P_{\text{bat_heat}} - P_{\text{diss}} = N_{\text{bat}}m_{\text{bat}}c_{\text{bat}}(T_{\text{bat}} - T_{\text{initial_bat}}) \quad (10)$$

where $T_{\text{initial_bat}}$ is the initial temperature of battery pack, m_{bat} is the mass of battery cells, c_{bat} is the specific heat capacity of battery cells.

2.3.4 Low Voltage E-loads

In EVs, electrical equipment using power supplied at 12 or 24 V voltages are called low voltage e-loads, including the lights, electric power steering (EPS), and etc. Low voltage e-loads as necessary accessories also need to be considered from the energy point of view.

2.4 Vehicle Dynamics

Through the clutch and transmission, the torque from motor(s) is delivered to the wheels. The function of this block is to calculate the driving/braking force, the

acceleration/deceleration, and finally the speed of the vehicle. Because of the driving mode and braking mode, differential scenarios are considered in this proposed model [3]. As for the driving force during acceleration, the equation used to set up the model is as follows:

$$\begin{cases} F_{dr} = T_{dr} \frac{G_{trans}}{R_{wheel}} \eta_{trans} \\ M v_{veh} \dot{} = F_{dr} - F_r \end{cases} \quad (11)$$

where F_{dr} is the driving force on the wheels through the powertrain from the motor(s), G_{trans} is the gear ratio of the driveline, R_{wheel} is the radius of the wheel, M is the nominal weight of the vehicle, v_{veh} is the vehicle speed, and F_r is the resistance force that acts on the vehicle including the aerodynamic drag force, rolling resistance and road slope force.

During deceleration, the equations are changed as follows:

$$\begin{cases} F_{e_brk} = T_{br} \frac{G_{trans}}{R_{wheel}} \eta_{trans} \\ M v_{veh} \dot{} = F_{e_brk} - F_r - F_{h_brk} \end{cases} \quad (12)$$

where F_{e_brk} is the electric braking force generated by the electric motor(s) and F_{h_brk} is the mechanical braking force generated by the hydraulic braking system.

2.5 Driver Model

In order to close the loop in the proposed model, the behaviour of the driver needs to be simulated using the driver model [10]. Since the lateral force of the vehicle are not considered, the classical PID controller, adopted for the driver model, is enough for this proposed model compared to some elaborated driver models (e.g., fuzzy model, hybrid model, etc.).

Given the reference speed and the actual speed of the vehicle, the controller will determine the pedal position so as to determine the load signal of the motor. To avoid the saturation of the PID controller, an anti-windup approach is applied.

2.6 Vehicle Controller

The function of the vehicle controller is to calculate the load signal of the traction devices (e.g., electric motors) and determine the load distribution between the front and rear axles during both acceleration and deceleration.

2.6.1 Load Signal Calculation

When the vehicle is in the driving mode, the load signal of the traction devices corresponds to the acceleration pedal position, and in the braking mode, the total required braking torque $T_{\text{total_brk}}$ is determined by the deceleration pedal position. Then given the deceleration and vehicle speed, the mechanical braking torque is determined. The load signal of the electric motor $l_{\text{e_brk}}$ during deceleration is calculation from:

$$l_{\text{e_brk}} = \frac{T_{\text{total_brk}} - T_{\text{h_brk}}}{T_{\text{Max_motor}}} \quad (13)$$

where $T_{\text{max_motor}}$ is the maximum braking torque determined by the performance curve of the motor during the deceleration given the current speed.

2.6.2 Load Distribution on the Front and Rear Axles

The gravity center of the vehicle moves forward during deceleration and backwards when acceleration. Hence, the load distribution is different as shown in Eqs. (14a, 14b), respectively:

$$\frac{W_f}{W_r} = \frac{L_b + h_g j/g}{L_a - h_g j/g} \quad (14a)$$

$$\frac{W_f}{W_r} = \frac{L_b - h_g j/g}{L_a + h_g j/g} \quad (14b)$$

where W_f and W_r are the loads on the front and rear axles respectively, L_a and L_b are the distance from the gravity centre to the front and rear axles respectively, h_g is the height of gravity centre, j is the acceleration or deceleration of the vehicle, and g is the gravity acceleration.

3 Case Study

A typical EV, Nissan Leaf, is selected to validate the developed model as the case study. Nissan Leaf is a five-door hatchback electric vehicle manufactured by Nissan since 2010. Its power system was named as one of Ward's "10 Best Engines". It is 100 % electric and no fuel is required with the top speed of 90 miles/h [11]. Parameters of this vehicle used in the case study are obtained from the public domain [12], as shown in Table 1.

Some complementary data required in the simulation model are predicted or estimated based on those public parameters or default settings in the model.

Table 1 Nissan leaf specifications

Dimensions	<i>Length</i>	4,445 mm	<i>Width</i>	1,770 mm
	<i>Height</i>	1,550 mm	<i>Wheelbase</i>	2,700 mm
Motor	<i>Max power</i>	80 kW	<i>Max torque</i>	280 N m
		@2,730 ~ 9,800 rpm		@0 ~ 2,730 rpm
Battery	<i>Type</i>	Laminated lithium-ion battery	<i>Total capacity</i>	24 kW h
	<i>Number of module</i>	48	<i>Power output</i>	over 90 kW

3.1 Range Estimation

The range of battery electric vehicles (BEVs) driving at constant speeds is an important measure of vehicle performance. The comparison of the drive ranges between the official performances of Nissan Leaf [13] and results generated by the proposed model is shown in Table 2. Those results agree to each other in a general way and the ranges from the simulation are generally somehow lower than those from the official data. One possible reason for those differences is that not all of vehicle parameters of Nissan Leaf are available to us.

For EVs, the range estimation based on driving cycles is more realistic for real drive conditions than those at constant speeds. From the Ref. [11], the range of Nissan Leaf using US EPA LA4 City Cycle is about 160 km/charge, while the result from the proposed model is 155.30 km. The simulation result is very promising and the difference is only 2.94 % for this case.

3.2 Energy Flow Study

One of the objectives of this work is to investigate and analyse the energy flow and energy efficiency of EVs at the vehicular system level. Through the analysis of different impacts from different energy related configurations on the vehicle performance, the energy flow, distribution, and consumption are demonstrated by this model. The results from this study provide a guidance to design an EV in a more systematic and optimal way. In this study, the New European Driving Cycle (NEDC), which is one of the most “robust” driving conditions for city traffic scenarios, is selected [14, 15]. The driving mode and braking mode are explained respectively, as follows.

3.2.1 Driving Mode

The energy distribution of electric vehicles and the energy flow chain from the battery to vehicle dynamics, including the high voltage e-loads, the electric motor, and driveline, are studied with the low voltage e-loads being disabled.

Table 2 Comparison of range @ constant speeds

No.	Speed (km/h)	Range (km)	
		Official	Simulation
1.	72	192	178
2.	88	160	140
3.	96	144	123
4.	104	128	115
5.	112	120	100
6.	120	110.4	88
7.	128	100.8	81

In Fig. 3, energy distributions among the components at different speeds are shown. From the output energy of the battery to the input energy of high voltage e-loads, the energy is mainly dissipated by DC-DC converters. For the traction motor, there are power losses on the inverter as well as on the motor due to copper losses, iron losses, friction, windage of the motor [3]. Energy dispatched on the driveline, from the output shaft of the traction motor to the wheels, consisting of the clutch, gear box, prop shaft, and differential, is due to the transmission friction. Besides, the driving resistance including rolling resistance, aerodynamic drag, and acceleration force, needs to be considered too.

In Fig. 4, the output power of the battery is normalized as one for each speed. Due to the energy loss and dissipation from the transmission friction, heating, and driving resistance, etc., the normalized energy of the each component from the battery to wheels is less than one.

Energy consumptions of the components mentioned above with respect to the time (in seconds) are illustrated in Fig. 5. It is shown that apart from the power transformed to vehicle dynamics, there are much power consumptions on high voltage e-loads, the motor (motor loss), and the driving resistance.

3.2.2 Braking Mode

E-braking, also known as regenerative braking, is an energy recovery approach that can slow down a vehicle by converting its kinetic energy back to electric energy. During this process, the motor works as a generator. The total braking torque required consists of two parts: the mechanical braking torque and e-braking torque. The percentage of e-braking torque needs to be determined appropriately. This percentage is related to the deceleration of the vehicle represented as a relative value with respect to the gravity acceleration, as well as the vehicle speed.

With respect to the effect of the e-braking, it's very important for us to improve the driving range of the electric vehicle. The current load and the low voltage e-load including EPS and lights are disabled too.

Figures 6 and 7 illustrate 3D plot of energy flow efficiency chain against vehicle speed during e-braking. The vehicle kinetic energy is normalized as one

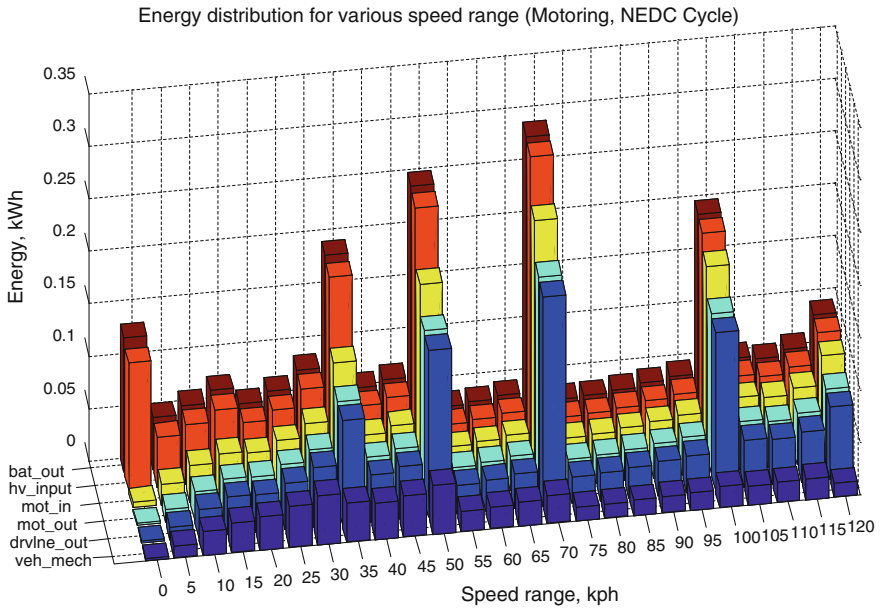


Fig. 3 Energy distributions ranges among components at different speeds

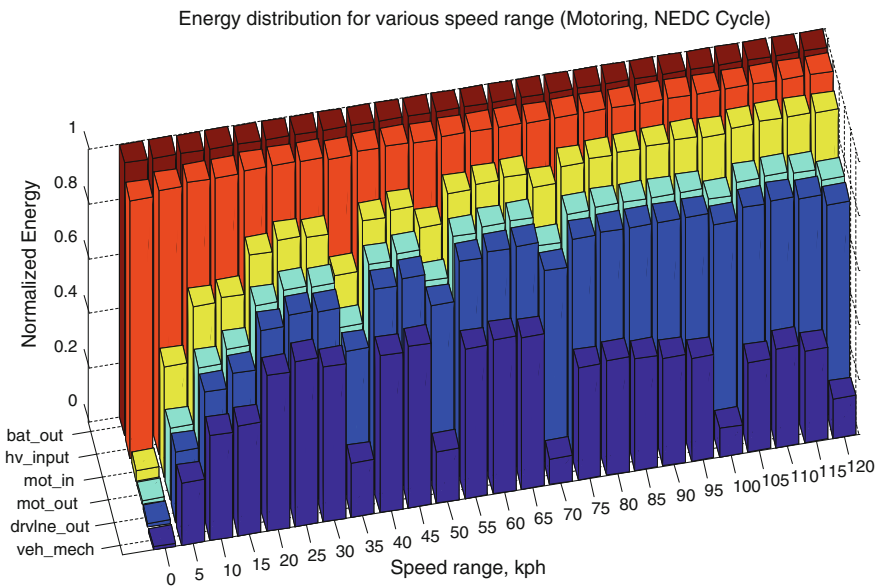


Fig. 4 Normalized energy distributions among components at different speeds

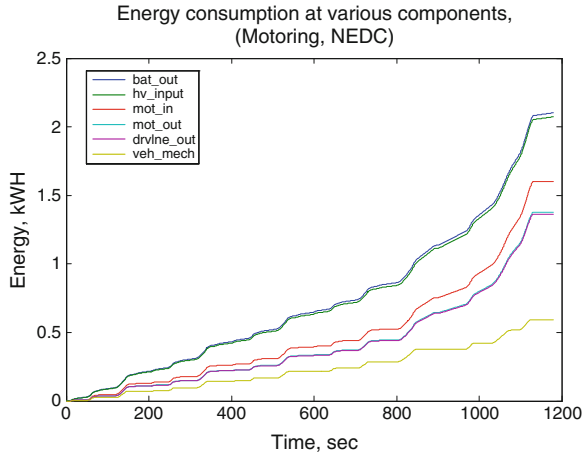


Fig. 5 Energy consumptions of various components without e-braking

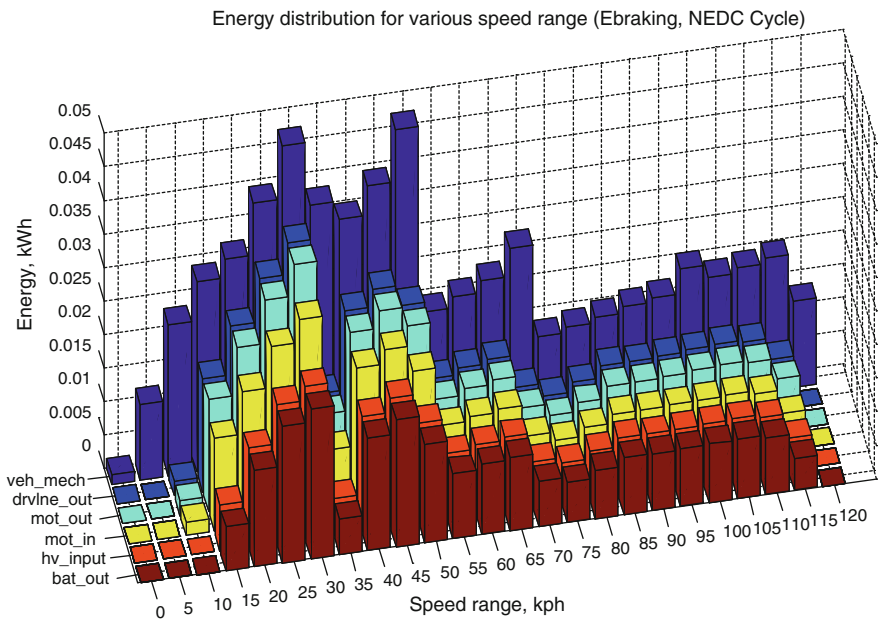


Fig. 6 Energy distributions among different components w.r.t. speed with e-braking

unit, and the regenerative braking energy transformed to various components are also normalized with respect to the kinetic energy. About 30– 50 % of the kinetic energy can be recovered in the speed range of 15–115 km/h.

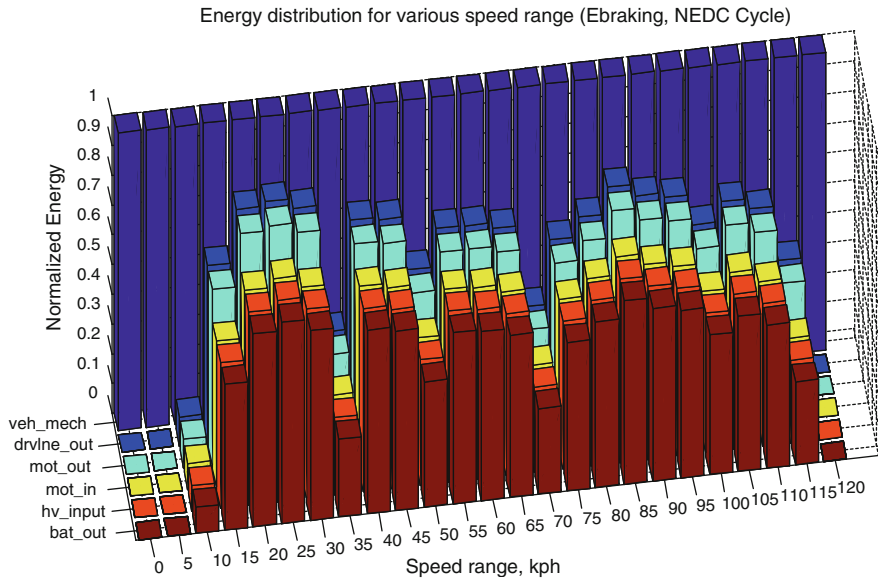


Fig. 7 Normalized energy distributions among different components w.r.t. speed with e-braking

Fig. 8 Energy consumptions of different components with e-braking

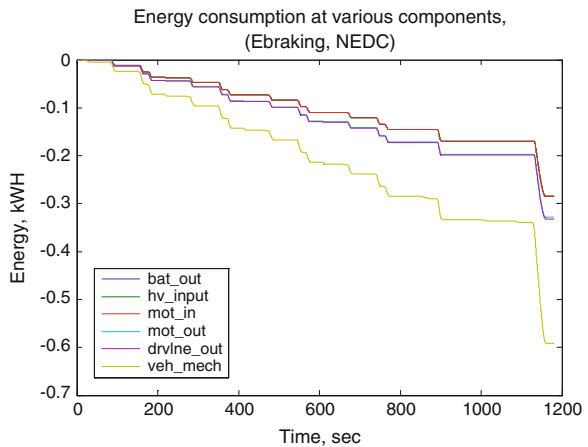


Figure 8 illustrates energy consumptions of different components with respect to time during e-braking. Since the low voltage e-loads and high voltage e-loads are disabled, the regenerated energy from motor/generator nearly all goes into the battery. It is shown that about 50 % of the total vehicle mechanical energy (i.e., kinetic energy) can be recovered through the e-braking approach. However, the energy loss of the motor/generator is larger than the loss during acceleration.

The operation points of the motor/generator in the simulation are illustrated in Fig. 9. Considering the effectiveness of braking performance and the safety of

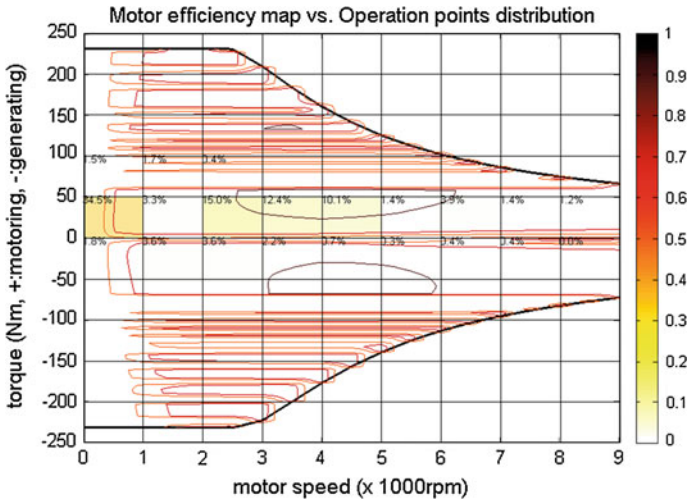


Fig. 9 Operation points distribution of motor during e-braking

vehicle, the e-braking torque is limited to less than 50 N m. During e-braking, the speed of most operation points is less than 4,000 rpm, and efficiency of the motor/generator of this area is about 70–90 %.

4 Conclusions

An efficient, effective, complete and accurate simulation model of EVs, focusing on energy flow, has been developed in this work. The mechanism and structure of the energy simulation model has been analysed and discussed. The model has been validated using the NEDC (New European Driving Cycle) and other driving scenarios with the case study of Nissan Leaf. A general platform that could be revised for other analysis in the future has been established, and different EV topologies are implemented and evaluated using this simulation. Future works in EV design and optimization can be conducted using the developed model.

References

1. Tate ED, Harpster MO, Savagian PJ (2008) The electrification of the automobile: from conventional hybrid, to plug-in hybrids, to extended-range electric vehicles [C]. SAE 2008-01-0458
2. Chan CC, Wong YS (2004) Electric vehicles charge forward. IEEE Power Energy Mag 2(6):24–33
3. Larminie J, Lowry J (2003) Electric vehicle technology explained [M]. Wiley, New York

4. Ehsani M, Gao Y, Gay SE, Emadi A (2005) Modern electric, hybrid electric, and fuel cell vehicles—fundamentals, theory and design. CRC, Boca Raton, FL
5. Markel T, Brooker A, Hendricks T, Johnson V, Kelly K, Kramer B, O’Keefe M, Sprik S, Wipke K (2002) ADVISOR: a systems analysis tool for advanced vehicle modelling. *J Power Sources* 110(2):255–266
6. Johnson VH (2002) Battery performance models in ADVISOR. *J Power Sources* 110: 321–329
7. Flohr GR (2002) Performance considerations of a bi-directional DC/DC converter for fuel cell power vehicles [C]. SAE 2002-01-1902
8. Dwiggin BH (2001) Automotive air conditioning, 8th edn [M]. Delmar cengage learning, NY
9. Pesaran A, Johnson V (2002) Battery thermal models for hybrid vehicle simulations. *J Power Sources* 110:377–382
10. Kiencke U, Nielsen L (2000) Automotive control system [M]. Springer, Berlin
11. Nissan Motor Company (2011) The new car: features and specifications. <http://www.nissanusa.com/leaf-electric-car/specs-features/index#/leaf-electric-car/specs-features/index>. 2011
12. SAE International (2011) Nissan leaf specifications. *Veh Electrification* 14–14
13. Nissan Motor Company (2011) Your nissan leaf is built to go 100 miles on a single charge. <http://www.nissanusa.com/leaf-electric-car/index#/leaf-electric-car/index>. 2011
14. Whitefoot JW, Ahn K, Papalambros PY (2010) The case for urban vehicles powertrain optimization of a power-split hybrid for fuel economy on multiple drive cycles [C]. Proceedings of the ASME 2010 international design engineering technical conferences & Computers and information in engineering conference, Aug 2010
15. Liu J, Peng H (2008) Modelling and control of a power-split hybrid vehicle [M]. *IEEE Trans Control Syst Technol* 16(6):1242–1251

Design of Auxiliary Electric Driving System in Rear Wheels of Vehicles

Hongzan Xu, Quan Sun, Xufeng Wu, Qiqian Jin,
Yi You and Fuquan Zhao

Abstract To find a proper method in the limited interior space to propel the vehicle by a power-assisted way and to improve the vehicle performance, a catamaran car concept is introduced in this paper to apply power-assisted drive on rear wheels and to achieve the energy sharing. The model is constructed in the GT-suit simulation condition to perform the simulation and the results are also analyzed. The results indicate that acceleration and gradeability can be significantly improved by utilizing catamaran car method to apply power-assisted drive on rear wheels, thereby verifying the feasibility of this design solution.

Keywords Catamaran car · Electric vehicle · Power-assisted drive · Simulation

1 Introduction

As a rash of global developments such as traffic congestion, climate change, the dwindling availability of resources, the electric vehicle plays an important role in the development strategies of many countries around the world. Some electric vehicles have poor performance in acceleration, uphill ability and range, owing to the limited battery capacity and ultra-compact space. “Pure Electric Passenger Car Technology (GB/T 28382-2012)” has been released, and it’s become extremely urgent to improve EV’s vehicle performance. The catamaran car concept was the

F2012-B03-015

H. Xu (✉) · Q. Sun · X. Wu · Q. Jin · Y. You · F. Zhao
Zhejiang Geely Automobile Research Institute Co., LTD, Hangzhou, China
e-mail: jkdxhz@126.com

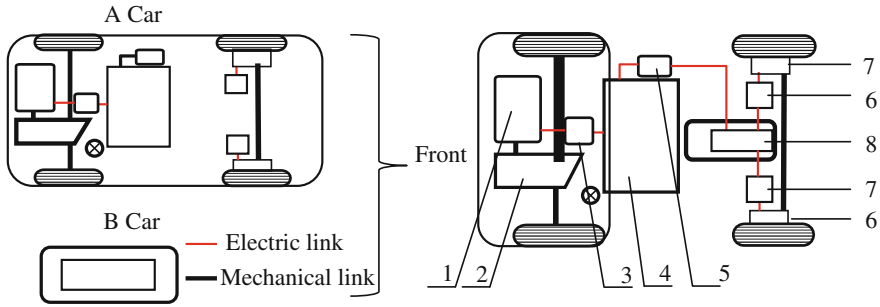


Fig. 1 Configuration of catamaran car. 1 main traction motor a, 2 mechanical transmission, 3 inverter, 4 power battery a, 5 DC converter, 6 motor controller, 7 hub traction motor b, 8 power battery b

first introduced as an efficient solution in the paper, through a small car auxiliary propelling the catamaran car, to achieve sharing of energy. The design's feasibility was validated through simulation, and also it lays the foundation for future control strategy study of auxiliary electric propelling vehicle.

2 Catamaran Car Concept

2.1 Configurations and Operation Principle

In Fig. 1, the catamaran car drive train is conceptually illustrated. The drive train shows it is a 4WD electric vehicle, and it consists of A car (EV) and B car (electric motorcycle). The A car subsystem is comprised main traction motor a, mechanical transmission, inverter, power battery a, DC converter, hub motor b and its motor controller. The B car subsystem involves power battery b and hub motor (not shown in Figure).

In general driving, the power battery a provides power to main traction motor to drive catamaran car. While the main traction motor can't meet the vehicle's demand, the power battery b will provide power for hub motor b to supply auxiliary drive, and ensure the improvement of vehicle performance. In this design, both the A car and B car are independent, so it allows the two energy resources separated and combined freely to achieve energy sharing.

2.2 Vehicle Performance Target

The catamaran car is design for traffic demand of Urban and suburban, according to requirements in "Pure Electric Passenger Car Technology", general electric vehicle performance needs to meet that in following Table 1.

Table 1 Vehicle performance of EV [1]

Performance	Unit	Value	Remarks
Maximum speed	km/h	80	In 30 min
Acceleration	s	15	50–80 km/h
Gradeability	%	20	/
Rang	km	80	/

Based on the parameters in Table 1 and the location, some specifications of the catamaran car can be shown in Table 2. The basic parameters of power battery a can be designed according to the layout space. And the battery capacity has been defined according to the requirement of B car, its vehicle performance calculation would not be involved in following simulation.

3 Model

3.1 Traction Motor Model

There are two operation patterns in general driving, including constant velocity and acceleration pattern. In the constant velocity driving, it needs less power from traction motor, whereas it has longer rang, contrary to that it needs more output power from traction motor and has shorter rang [2]. So it is important to estimate the rated and peak power of traction motor firstly [3].

At the beginning, according vehicle acceleration performance, motor characteristics, and transmission characteristics, the dive motor’s rated power can be estimated using the following equation [4].

$$P_t = \frac{\delta M}{2t_a}(V_f^2 + V_b^2) + \frac{2}{3}Mgf_r V_f + \frac{1}{5}\rho_a C_D A_f V_f^3 \tag{1}$$

where, M (kg)—the total vehicle mass, t_a (s)—the expected acceleration time, V_b (m/s)—the vehicle speed, V_f (m/s)—the final speed of the vehicle during acceleration, g (9.80 m/s²)—the gravity acceleration in, f_r —the tire rolling resistance coefficient, ρ_a (1.202 kg/m³)—the air density, A_f (m²)—the front area of the vehicle, C_D —the aerodynamic drag coefficient.

The torque of traction motor also can be calculated after its rated power is defined. Then, the speed–torque and speed–power profiles of the traction motor can be obtained.

3.2 Battery Model

Due to ultra-compact space for power battery pack, the battery energy and capacity are relative limited. The battery power output can be expressed as Eq. 2 [4],

Table 2 Specification of vehicle

Overall dimension	3,750 × 1,700 × 1,550	Tire	175/65R14
Curb mass of A car	1150 kg	Curb mass of catamaran car	1190 kg
Maximum speed	>110 km/h	Gradeability	>25 %
Acceleration (0–100 km/h)	<15 s	Driving cycle range	>80 km

according to load power that consists of the resistance power and power losses in the transmission and motor drive, including power losses in the electronics.

$$P_{out} = \frac{V}{\eta_t \eta_m} \left(Mg(f_r + k) + \frac{1}{2} \rho_a C_D A_f V^2 + M\delta \frac{dV}{dt} \right) \tag{2}$$

where, η_t —the power losses efficiencies in transmission, η_m —the power losses efficiencies in traction motor, k —road grade, $\frac{dV}{dt}$ (m/s²)—vehicle acceleration. If assume α ($0 < \alpha < 1$) is the percentage of the total braking energy P_{in} can be regenerated, so the regenerated power can be expressed as following equipment:

$$P_{in} = \alpha P_{out} \tag{3}$$

So the net energy consumption from the batteries is [3]:

$$E_{out} = \int P_{out} dt + \int P_{in} dt \tag{4}$$

3.3 Vehicle Model

According to Newton’s second law, vehicle acceleration can be written as following equipment:

$$M \frac{dV}{dt} = \sum F_t - \sum F_r = (F_{tf} + F_{tr}) - (F_{rf} + F_{rr} + F_w + F_g) \tag{5}$$

where, M —the total mass of the vehicle, V —vehicle speed, F_t —the total tractive effort, F_r —the total resistance, F_{tf} —the tractive effort of the front tires, F_{tr} —tractive effort of the rear tires, F_{rf} —rolling resistance of the front tires, F_{rr} —the rolling resistance of the rear tires, F_w = aerodynamic drag, F_g —climbing resistance. In the catamaran car, if it is only the main traction motor working as a front-wheel-driven vehicle, F_{tr} is zero.

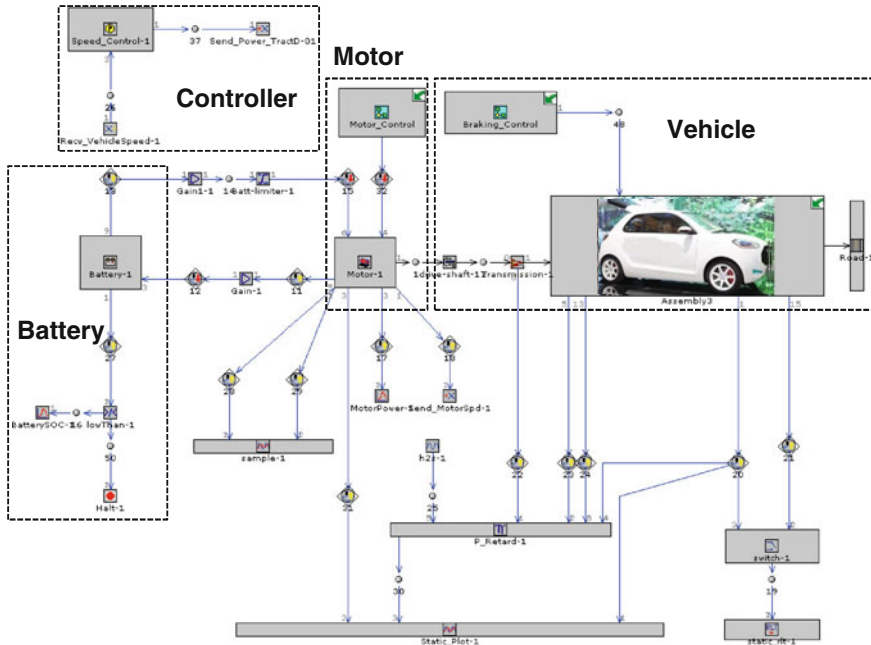


Fig. 2 Illustration of simulation model

4 Simulation and Analysis

4.1 Simulation Model

Firstly, the selection of traction motor mainly depends on a number of factors, including the driver’s expectation, vehicle constraints, and energy source, and at the beginning, some parameters as power, torque, rotate speed and ratio would be assessed. Here we choose permanent magnet synchronous motor for main traction motor a and DC brushless motor for hub traction motor b.

Secondly, according to above vehicle model, simulation model was established in GT-suit [5], including motor module, battery module, vehicle module, vehicle controller module and so on, and it is shown in Fig. 2. In the battery module, it involves the calculation of SOC (state of charge) [6], and in the motor module, it involves motor controller, and the regenerated module is in the vehicle module.

4.2 Simulation Result

Through the simulation model, it can simulate every operation pattern [7], mainly includes three operation as the following: main traction motor a-alone traction A car

Fig. 3 Acceleration performance

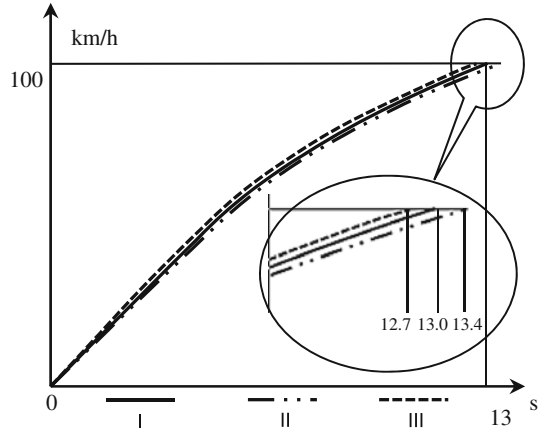
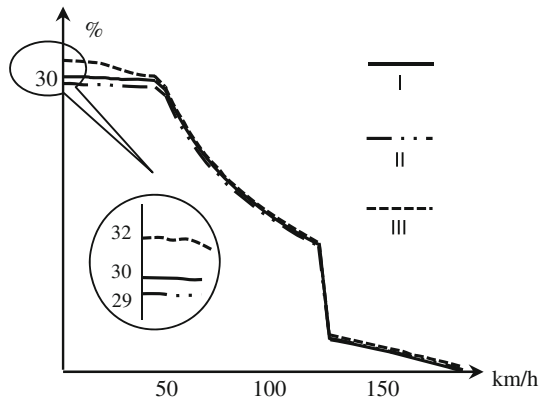


Fig. 4 Gradeability performance



(Pattern I), main traction motor a-alone traction catamaran car (Pattern II), hybrid traction catamaran car by main traction motor a and hub traction motor b (Pattern III).

Figure 3 shows the acceleration performance of every operation pattern, in which it also shows that the Pattern III advances 5.2 % of Pattern II.

In Fig. 4, it shows the contrast of uphill ability in three different operation patterns. It shows that the improvement of Pattern III for vehicle performance is considerable, from 29 till to 32 %.

In Fig. 5, it shows the maximum speed performance. According to the following equipment, the maximum vehicle speed depends on the rotate speed of motor. Due to the hub traction motor b’s rotate speed is slower than main traction a’s, it can’t contribute to the maximum speed.

$$U_a = 0.377 \frac{rn}{i_0 i_g} \tag{6}$$

Here, U_a (km/h)—vehicle speed, r (m)—the radius of the tire, i_0 —the gear ratio of the final drive. i_g —gear ratio of the transmission, n (r/min)—rotate speed of traction motor.

Fig. 5 Maximum speed

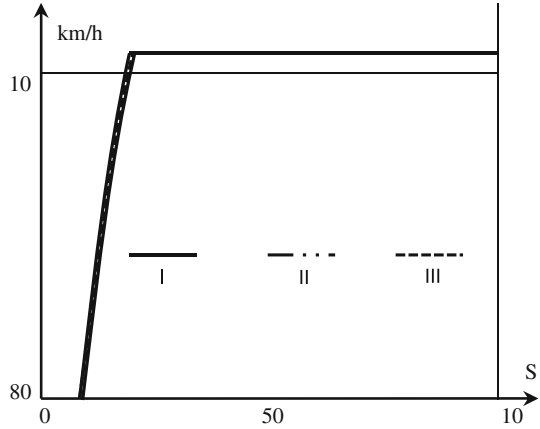


Table 3 The range in NEDC driving cycle

Operation pattern	Range/ km	Remarks
Pattern I	98	Main traction motor a-alone traction A car
Pattern II	96	Main traction motor a-alone traction catamaran
Pattern III	98	Hybrid traction catamaran car by main traction motor a and hub traction motor b

Table 4 Contrast of different operation patterns

Performance	Pattern I (%)	Pattern II (%)	Pattern III
Acceleration	2.3	5.2	12.7 s
Gradeability (%)	6.7	10.3	32
Maximum speed	0	0	122 km/h
NEDC range	0.3	2	98 km

In Table 3, it shows rang in NEDC driving cycle. The rang increases a little in operation Pattern III, but not obvious.

The vehicle performance differences of every operation pattern are listed in Table 4, it shows that the catamaran car concept can satisfy the target of design. And in the aspects of acceleration and uphill ability, the auxiliary system can improve the vehicle performance. The effect is not obvious, it only advances a little for the limited to the small capacity of power battery b in B car.

5 Conclusion

1. The Catamaran car concept is first introduced to design the electric auxiliary propulsion system and achieve the energy sharing between the large car (A car) and small car (B car). As a first attempt, the simulation proves the effectiveness

of the concept and it will also benefit the next study of the strategies of vehicle control;

2. Although it may not contribute much to the maximum speed and cruising range for the limited power of battery b and the hub traction motor's performance, the acceleration and uphill ability of the catamaran car are improved effectively in the auxiliary propelling operation pattern.
3. The simulation's precision would be influenced by the estimation of some vehicle specification. However, it provides reference for the forecast and analysis of vehicle performance and it also is an inspiration for some EV's engineers.

References

1. GB/T 28382-2012 Pure electric passenger car technology
2. Mehrdad E, Yimin G, Ali E (2010) Modern electric, hybrid electric, and fuel cell vehicles fundamentals, theory, and design, 2nd edn. CRC Press, Florida
3. Hor Y (2004) Future vehicle driven by electricity and control—research on four-wheel-motored “UOT electric march II”. *IEEE Trans Ind Electron* 51(5)
4. Grewe TM, Conlon BM, HA G (2007) Defining the general motors 2-mode hybrid transmission, SAE
5. Conlon B (2005) Comparative analysis of single and combined hybrid electrically variable transmission operating modes. SAE technical paper series, 2005-01-1162
6. Musardo C, Rizzoni G (2005) A-ECMS: An adaptive algorithm for hybrid electric vehicle energy management. In: Proceedings of the 44th IEEE conference on decision and control, and the european control conference 2005 Seville, Spain, 12–15 Dec 2005
7. Liu Q, Guo K (2003) Impacts on the performance of pure electric vehicles in the choices of dynamic parameter. *Nat Sci J Hunan Univ* 30(3):62–64 (in Chinese)

Study on the Relationship Between EV Cost and Performance

Pupeng Wan, Zhiqiang Du, Qiqian Jin, Yi You and Fuquan Zhao

Abstract This paper aims at studying the relationship between Electric Vehicle and its performance in the perspective of technology and economy. First, GT software is used to simulate vehicle performance. Second, cost is analyzed by technology condition and price, and then the relationship between performance and cost is discussed. Performance and cost are mutually affected by battery energy. In the aspect of performance, Vehicle performance increases initially and then decreases with increase of battery energy and there is a turning point. With respect to cost analysis, cost keeps increasing with cumulating of battery energy. Namely, cost is positively proportional to battery energy. There are two intersection points between performance and cost. In designing vehicles, the location of performance and cost properties should be restricted inside the region formed by those two intersection points as much as possible.

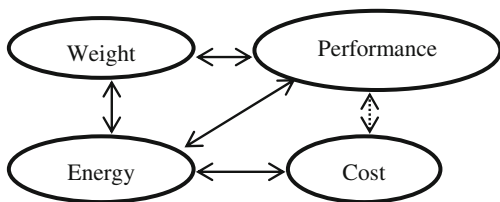
Keywords Electric vehicles · Vehicle performance · Cost analysis · Simulation · Vehicle weight

Recently, Ministry of Science and Technology published the “National Twelfth Five-Year Special Planning for Electric Vehicle Technology Development” and clearly set ‘Electric Driving’ as the strategy direction of vehicle power source. Considering of current technology level, the energy density of battery is not comparable to that of fossil fuel and short driving range of EVs has become the

F2012-B03-018

P. Wan (✉) · Z. Du · Q. Jin · Y. You · F. Zhao
Zhejiang Geely Automobile Research Institute Co., LTD, Hangzhou, China
e-mail: wanpp@rd.geely.com

Fig. 1 The interrelation of energy, weight, performance and cost



bottleneck of EV development [1]. In order to extend the driving range, increasing of battery pack energy is regarded as a general approach under current technology level [2]. In the condition of maintaining other components unchanged, battery pack energy is proportional to vehicle weight and manufacture cost. Improving of battery pack energy will increase vehicle manufacture cost and vehicle weight and thus affect its overall performance. The interrelation of energy, weight, performance and cost are presented in Fig. 1. The relationship of above four factors is analyzed in the perspective of technology and economy in this paper.

1 Performance Analysis

Vehicle performance is simulated by software—GT in this paper and the study subject is an Electric Vehicle. The power system is consisted of battery package, e-motor and transmission system of which the parameters are listed in following Table 1. By disregarding of space arrangement limits and the limits of national standards to battery weight, the battery energy and vehicle weight are gained respectively during the simulation based on a certain pattern. The vehicle performance is then calculated with respect to different battery energy.

The influence of battery energy to vehicle performance is displayed in Fig. 2. Initially, battery discharging power is insufficient, which results in long accelerating time and low climbing speed. With increase of battery energy, e-motor driving ability is sufficiently utilized although vehicle weight is increased as well. As a consequence, accelerating time is minimized and climbing speed is maximized. After e-motor reaches its maximum driving ability, increasing of vehicle weight starts to affect vehicle performance gradually. Acceleration time is then extended and climbing speed is reduced. Overall, accelerating time and climbing speed both experience a process from increasing to decreasing. So there are some advantages for both acceleration and climbing performance due to increase of battery energy initially, however, it turns into disadvantages later because of excessive battery weight. This indicates that, for a certain vehicle model, there is an optimum battery energy choice of which the vehicle performance is optimized. Figure 3 depicts the relation between battery energy and driving range. Battery energy increases linearly with increase of battery weight, which is computed by the ratio of battery weight to battery energy. Corresponding vehicle weight also increases linearly in condition of remaining other components unchanged. Driving

Table 1 E-motor and transmission system parameters

Vehicle parameters	
Kerb mass (kg)	1250
Fully loaded mass (kg)	1514
Wheel base (m)	2.34
Front area (m ²)	1.87
Drag coefficient	0.42
Dynamic rolling radius (m)	0.275
Rolling resistance coefficient	0.13
Ratio	9.34
E-motor parameters	
Peak/rated power (kW)	70/35
Peak/rated torque (Nm)	220/60
Max. Speed (rpm)	12000

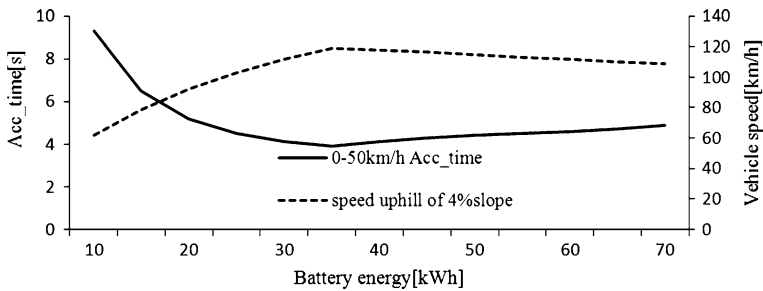


Fig. 2 The influence of battery energy to vehicle performance

range is extended because of increase of battery energy, however, due to increased weight, the changing rate of driving range (i.e. the slope of driving range curve) declines gradually. According to this trend, it could be estimated that driving range would increase to a particular value and then hold steady or decline. It can also be discovered from the figure that vehicle energy consumption rate (i.e. energy consumed per unit distance) increases gradually. After increasing of battery energy, the influence of battery weight to driving range becomes more apparent. There even exists a circumstance where battery weight is larger than that of other vehicle components. The driving range determined by battery energy should base on market demands when designing vehicles. It is not always good to have too large driving range. According to above analysis, the relationship between battery energy and vehicle performance could be abstracted as the one shown in Fig. 4. Vehicle performance trends to be better at the first place and turns to be worse later on which can be described as a parabola.

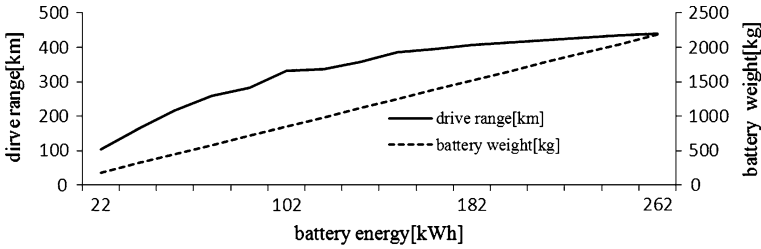


Fig. 3 The relation between battery energy and driving range

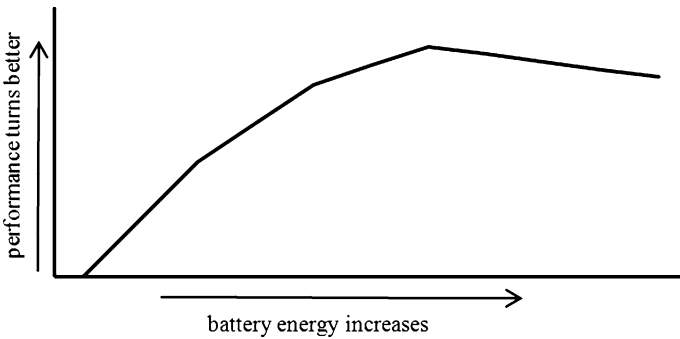


Fig. 4 The relationship between battery energy and vehicle performance

2 Cost Analysis

The analysis subject is lithium ion battery of which the actual performance target and market average price are listed in Table 2. According to current technology and market price [3], the cost of taking 1 kWh energy out of the battery (i.e. battery use cost) can be estimated. Assumptions have been made as follows: (1) Charger efficiency is 0.95 (2) Electrical cost from national grid is 0.58 Yuan/kwh (ignore on-peak or off-peak electricity) (3) Charging and discharging efficiency is 0.9. It can be deduced from Table 2 that lithium ion battery use cost is 0.75 Yuan when 1 kWh of electricity is taken from the battery (charged by national grid). In accordance with the simulation results in Fig. 3 vehicle energy consumption rate can be obtained. By combining battery use cost and energy consumption rate, the actual cost of vehicle running for a certain distance can be determined as shown in Fig. 5. The overall trend is that more distances vehicle travelled will result in more use cost. This can be explained by combination of Fig. 2 that increase of use cost is a result of gradual increased energy consumption rate. When driving range increases, demanded battery energy will increase accordingly. The increase of battery cost can be calculated based on battery market price. In the condition of maintaining other components unchanged, increase of battery cost can reflect the increase of vehicle cost

Table 2 The actual battery performance

Battery type	Lithium ion battery
Specific energy (Wh/kg)	120
Market average price (Yuan/kWh)	4000
Battery use cost (Yuan/kWh)	0.75

(i.e. vehicle acquisition cost). As can be seen from the figure, energy consumption rate will increase 0.37 kWh/100 km when driving range increases for every 10 km due to increased battery weight. By consideration of battery price, the use cost will be added for 0.26/100 km which is relatively low. The acquisition cost, however, will increase 10,000 Yuan which is considerable. Above all, the relationship between the battery energy and cost can be abstracted as shown in Fig. 6. The cost will increase linearly when battery energy increases.

3 Technological and Economic Analysis

The article above discusses the relationship between vehicle performance and battery energy and also the relationship between cost and battery energy respectively. As shown in Fig. 1 battery energy is treated as a bond for yielding the relationship between vehicle performance and cost. Consequently, the relationship between performance and battery can be described as depicted in Fig. 7. Main part of the cost is acquisition cost. This can be verified from Fig. 5 that the use cost is insignificant compared with acquisition cost and it can be neglected. Specific relationship between vehicle performance and cost depends on vehicle technology level and battery technology level as well as its prices. For certain vehicle technology level, battery unit price has to be decreased so as to reduce vehicle cost. For certain vehicle cost, increase of battery energy density can result in reduction of vehicle weight and make contribution to improvement of vehicle performance [4]. There are two intersection points in the curve of performance and cost. In front of the first intersection, vehicle cost is quite low but vehicle performance is undesired which cannot even satisfy the national standards. This should be abandoned. Only by increasing of battery energy in this phase, vehicle performance could be improved. After passing the second intersection point, vehicle performance is inversely proportional to cost. Increase of cost will lead to decrease of performance, which is also unacceptable. By reduction of battery energy could pull the second intersection point back a little. Therefore, designed vehicle should be placed in the region constructed by those two intersection points. Specific vehicle performance should be determined by the market.

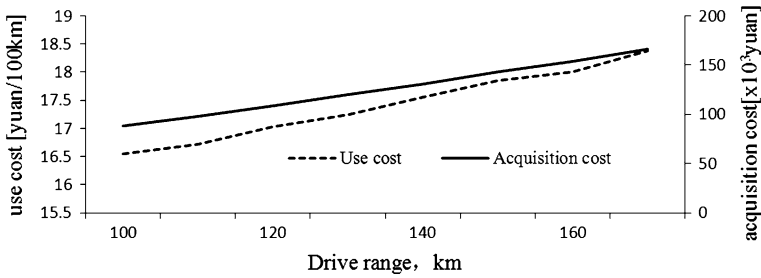


Fig. 5 The relationship between drive range and cost

Fig. 6 The relationship between the battery energy and cost

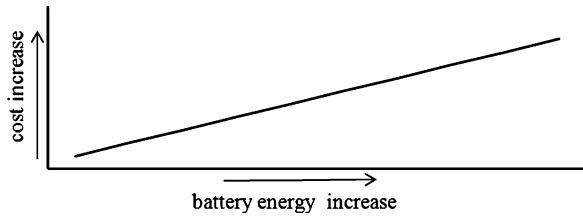
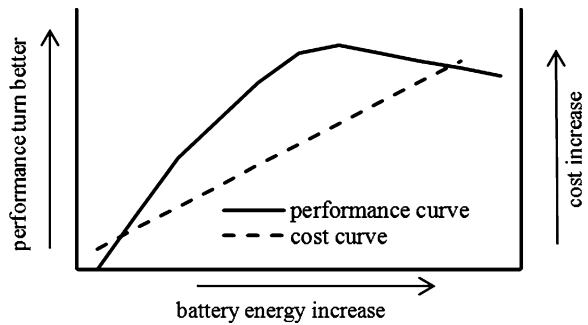


Fig. 7 The relationship between performance and battery



4 Conclusion

This paper analyzes the relationship between performance and cost of electric vehicles in the aspect of technology and economy. Performance and cost affects each other through battery energy. By consideration of vehicle performance, it increases first and then decreases with increase of battery energy and there is a turning point. As a consequence, it is not always good to have much battery energy. By taking account of cost, vehicle cost keeps increasing with increase of battery energy and the correlation is positive linear. There are two intersection points between vehicle performance and cost. Beyond the region constructed by these two points, the design is not acceptable. Therefore design of vehicles should maintain inside this region. Specific vehicle performance and cost should be determined by the market.

References

1. Zhen-po W, Feng- chun SUN (2004) Analysis of energy consumption distribution and factors of influence in electric vehicles. *Trans Beijing Inst Technol* 24(4)
2. Rand DAJ, Woods R, Dell RM (1988) Batteries for electric vehicles. Society of Automotive Engineer, Warren dale
3. Ehsani M, Gao Y, Emadi A (2010) Modern electric, hybrid electric and fuel cell vehicles- fundamentals, theory, and design second edition. China Machine Press, Beijing
4. Chan CC, Chau CC (2001) Modern electric vehicle. Technologies Oxford University Press, Oxford

Hil Validation of Extended-Range Electric Vehicle Control Unit Based on Orthogonal Test

Haibo He, Qiqian Jin, Tingting Dong and Fuquan Zhao

Abstract The control unit of a plug-in hybrid electric vehicle is taken as a test object in this paper. Based on HIL test definition of functional decomposition and establishment of test cases, the representative and typical test points are selected from a large number of test points to achieve a reasonable design of test solution by introducing the orthogonal principle in combination with a vehicle control strategy. The real-time HIL test platform is constructed based on test definition. Furthermore, the TESIS DYNAware simulation model is integrated to simulate the controlled object and environment, and carry out a whole performance test of vehicle control unit. The test results indicate that adoption of orthogonal design method can significantly reduce the number of test cases and improve test efficiency under the condition of full coverage of validation tests.

Keywords Vehicle control unit · HIL validation · Orthogonal test

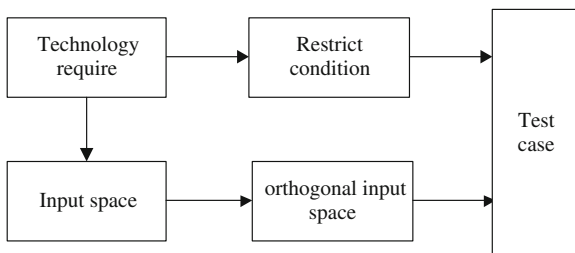
1 Foreword

Hardware-in-loop validation is the key way to test vehicle control unit currently [1]. By construction of virtual vehicle environment and application of real vehicle control unit, one loop of exciting signal and excited signal can be established. The function of control unit can then be verified.

F2012-B03-022

H. He (✉) · Q. Jin · T. Dong · F. Zhao
Zhejiang Geely Automobile Research Institute Co. Ltd, Hangzhou, China
e-mail: robot198411@yahoo.com.cn

Fig. 1 Test case design process



The vehicle control unit in electrical vehicle works as a multiple power source and needs to deal with massive signals. Therefore lots of function points have to be tested in the control unit. This can be reflected by the number of test cases from actual test. The orthogonal test can cope with factors properly to reduce test quantity and analyze the influence of factors on test purpose. It is suitable for VCU performance test with large numbers of test items and factors [2].

2 VCU Hardware-In-Loop Validation Orthogonal Design

2.1 Design Process

The orthogonal test is an optimized design method and suitable for massive experiments. It can ensure that the probability of all factors of VCU performance is equal. Test projects are made by use of orthogonal Table [3]. Those test projects are representative and orderly, and can cover all test content.

The main work is to test output parameters value in VCU validation. To ensure sufficiency and rationality, it must be tested under all kinds of inputs combination efficiency. According to vehicle control strategy and structure of test case, the whole design process is shown focusing on test case purpose in Fig. 1.

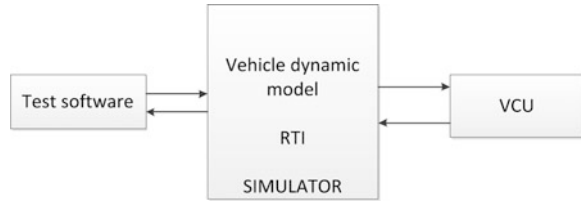
Firstly, according to technology requirement, it is found that all input space and restricted condition are related to current test function point. That can decompose ineffective, incompatible or impossible input combination to improve test efficiency. Then all valid input space can be turned into input combination in orthogonal test. It mainly focuses on continuous input parameters in orthogonal process, while it does not need to deal with switch input parameters. On one side, the continuous input parameters have two input states: valid and invalid. On the other side, it must consider that the input value in verge can spring software easily. The whole test case frame can be obtained finally.

There are lots of function points in VCU validation. They are related to each other in function definition. To reduce the complexity of test case design, firstly the test case of single function point is designed, and then the test case of multi-functions is designed.

Table 1 Test case orthogonal table of entry of drive mode(√ means constrain is effective, × means constrain is noneffective)

Number	1	2	3	4	5	6	7	8	9	10	11	12	13	14	15	16
Input condition	√	√	√	√	√	√	√	√	×	×	×	×	×	×	×	×
Key state ACC	×	×	×	×	×	×	×	×	√	√	√	√	√	√	√	√
Key state ON	√	√	×	×	×	×	×	×	×	×	×	×	×	×	×	×
High relay switch open	×	×	×	×	×	×	×	×	×	×	×	×	×	×	×	×
High relay switch close	×	×	√	√	√	√	√	√	×	×	×	×	×	×	×	×
Brake pedal position ≥25 %	×	√	√	×	×	×	×	×	×	×	×	×	×	×	×	×
Brake pedal position <25 %	√	×	×	√	×	×	√	×	×	√	×	×	√	×	×	√
D	×	√	×	√	×	√	×	√	×	√	×	√	×	√	×	√
N	√	×	√	×	√	×	√	×	√	×	√	×	√	×	√	×
Design rationality	×	×	×	√	×	×	×	√	×	√	×	√	×	√	×	√

Fig. 2 VCU Hardware-in-loop validation system



2.2 Single Function Test Case Design

The vehicle will be in driving mode. The paper takes it as an example and illuminates it with orthogonal theory and design process in Sect. 2.1.

According to vehicle control strategy, when the key position is ON, the high relay switch is closed; the shift is D, the current brake pedal position is more than 25 %, then the vehicle can enter driving mode effectively. In practice, there are two states of key when the vehicle has low power: (1) ON; (2) ACC. The shift has two states: (1) D; (2) N. The high relay switch has two states: (1) close; (2) open. The brake pedal position has two states: (1) $\geq 25\%$; (2) $< 25\%$.

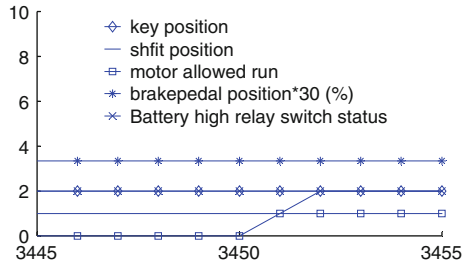
With orthogonalization of above input parameters, the orthogonal test table can be obtained in Table 1. When it is carrying out orthogonalization of continuous input parameters, the limited values of those will not be selected but ones between invalid and valid input [4]. Each enable condition of restrict constrains must be effective in design. For example, when the shift is turned into D, this shift state must be effective. There are lots of restrict constrains in all, so it will not specify anymore. It takes the rationality of test case as criterion of orthogonal test result in this paper.

After orthogonalization of input parameters in Table 1, there are 16 groups of combination in total No “2, 6”, the high relay switch cannot be closed when the key state is ACC. Therefore, these two test cases are irrational No “1, 3, 5, 7, 9, 11, 13, 15”, the shift state is not D, which does not accord with practice. It obtains 6 rational test cases finally.

2.3 Multi-Function Test Case Design

The design process in Sect. 2.1 is still applied to design multi-function test case, but it has different with single function test case in the emphases and restrict condition. It considers that it satisfies technique requirement in single function test, so all kinds of inputs must be considered. In multi-function test, it not only considers technique requirement, but also considers if there is overlap function test. So it only considers effective inputs. For example, the vehicle must enter driving mode and the battery power must be enough when it tests the function of motor max viable output torque. That means it can leave out the function test case of entry of driving mode.

Fig. 3 Entry of drive mode test case



There are 9 factors that have effect on VCU performance. Each factor has some kinds of states. For example, SOC has three states: low, moderate, high. There are 47 function points in total and 24,064 test cases in theory. With specification of test case design above, it gets 908 test cases effective finally.

3 Test System Build

It shows the hardware-in-loop validation system based on dSPACE/SIMULATOR in Fig. 2. It uses vehicle dynamic model in TESIS DYNAware software. It inputs test data of components into models and configures those with I/O. The off-line vehicle model can be turned into real time one with auto code building and transmitting. The SIMULATOR equipment inspirits signals of models in real time, which communicates with signals from VCU. It can monitor and modify test parameter value in Control desk software. The test result can be recorded and analyzed

4 Application

With application of the complete hardware-in-loop test platform and test case, it can carry out VCU hardware-in-loop test. Due to lots of functions in vehicle control unit, some representative test cases are selected to specify in paper.

In Fig. 3, the power battery high relay switch is closed after the key state is turned into “ON”. When the brake pedal position is greater than 25 % and the drive shift state is “D”, the vehicle enters driving mode. The result shows that the function of entry of drive mode is right.

In Fig. 4, as soon as the motor is allowed to run and the accelerator pedal position is 0 %, the vehicle is driving at idle and the output torque of motor is 7 Nm stably. During 683–689 s, the output torque of motor is increasing when the accelerator pedal position is increasing. During 690–695 s, the output torque of motor is stable when the accelerator pedal position is stable. It shows that the output torque of motor is greatly according with accelerator pedal position, and this function is right.

Fig. 4 Vehicle drive require torque calculation test case

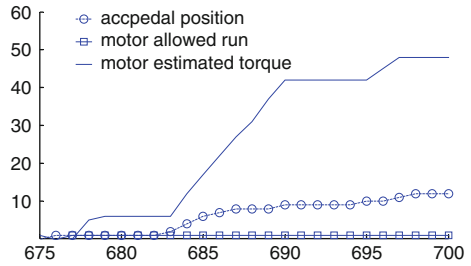
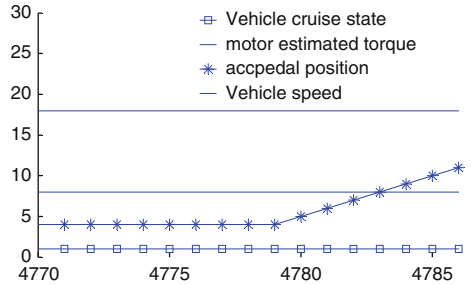


Fig. 5 Vehicle cruise mode exit test case



In Fig. 5, the vehicle is driving in cruise mode before 4,778 s. It keeps cruising mode while the accelerator pedal position starts to increase at 4,779 s. According to vehicle control strategy, if the accelerator pedal position is greater than it which is the accelerator pedal position when the vehicle is entering cruise mode, or the cruise button is closed, the vehicle will exit cruise mode. The test result is not according with design control strategy, which shows that there are some problems with this function.

5 Conclusion

1. The VCU is the main control unit in multi- power system and has lots of function points. They are complicated, so it is necessary to process hardware-in-loop test in project research;
2. It can reduce the number of test cases and improve test efficiency based on orthogonal optimization design, which has guiding significance in project.

References

1. Chen Q, Zhu J, Tian G (2002) Advanced electrical vehicle technology. Chemistry Press, Beijing
2. Jiang L, Hou W, Gu F (2011) Steady state circular performance simulation of automobile based on orthogonal test. J Beijing Univ aeronaut astronaut 37:969–972

3. Gao F, Zhang Q, Zhou J, Hewen A (2009) A study on the function logics test techniques for body control module. *Automot Eng* 31:966–970
4. Jiang H, Cai J, Cao D (2007) Development of a test bench for large-scale wind turbine controllers based on dspace. *Electric Machine & control application*

Development of a Control System of Hybrid Power System Based on the xPC Target for Electric Vehicles

Yaming Zhang and Rui Xiong

Abstract A rapid control prototyping design for hybrid power system has been proposed based on the real-time simulation test bench which constituted by double xPC Target system. A Topology structure is analyzed that the ultracapacitors are connected with power battery packs parallel after a bidirectional DC/DC converter. The ultracapacitor, power battery and the hybrid power system are modelled. For the electric vehicle (EV) application, the control strategy for the hybrid power system is proposed. The simulation results of the hybrid power system and battery-only power system is analyzed under the UDDS (Urban Dynamometer Driving Schedule) with the selective topology structure of hybrid power system. It was suggested that the ultracapacitor can significantly improve the efficiency of the hybrid power system, and the energy consumption of the power battery may decrease 8.97 %. Furthermore, the ultracapacitor can efficiency balance the output of the power battery, and the cycle life of the power battery is significantly improve through optimizing its working range.

Keywords xPC Target · Real-time simulation · Rapid control prototyping · Hybrid power system · Electric vehicle

F2012-B03-024

Y. Zhang (✉)

Electric Vehicle Research and Development Centre, China Automotive Engineering Research Institute, Mainland, China
e-mail: zhangyaming@evchina.org

R. Xiong

National Engineering Laboratory for Electric Vehicle, Beijing Institute of Technology, Mainland, China

1 Introduction

Battery with high energy density and high power density is expected for electric vehicles (EVs), but current Li-ion battery seldom possesses dual advantages. Thus, hybrid power system, comprised of ultracapacitor and Li-ion battery, is proposed to meet the expectations [1, 2].

Li-ion batteries are of high energy density and prefer slow charging-discharging, while ultracapacitors are of high power density and prefers fast charging-discharging. The characteristic difference is so great that the control system and control strategy are worthy of studying for hybrid power system application [3, 4].

A real-time control system for hybrid power system is developed in the article. Firstly, the hybrid power system is modeled based on Matlab/Simulink, and a real-time simulation test bench is built with xPC Target system, secondly a logic threshold control strategy is introduced, finally the control system and strategy are tested with results analyzed.

2 Hybrid Power System Modeling

2.1 Hybrid Power System

In this article, hybrid power system is comprised of LiFePO₄ Li-ion battery parallel with ultracapacitor, and the ultracapacitor is serially connected with a bidirectional DC/DC, as shown in Fig. 1. Li-ion battery provides vehicles the electric power, and ultracapacitor discharges aiding power while rapid accelerating/climbing and charges while regenerative braking. With the help of fast discharging and discharging of ultracapacitor, it is feasible for the Li-ion battery to work in optimized zones and be protected from over peak power/current [5, 6]. Thus, the cycle life of Li-ion battery can be prolonged and the efficiency of hybrid power system can be improved.

The Vehicle Control Unit monitors the vehicle velocity (v_{car}), battery SOC (State of Charge), ultracapacitor SOV [7] (State of Voltage), calculates the power requirement of driving motor (P_m^*) based on accelerator/brake pedal, decides requested discharging/charging power of the ultracapacitor (P_{uc}) based on the control strategy, and controls the output voltage/current of DC/DC to make ultracapacitor output P_{uc} , as shown in Fig. 2.

Power input of driving motor is provided by Li-ion battery together with ultracapacitor, as shown in (1), where P_m is the actual power input of the motor's inverter, τ_{car} is the equivalent time constant of the vehicle dynamic response, P_{DC} is the output power of the battery, P_{bat} is the output power of DC/DC, η_{DC} is the efficiency of DC/DC, λ represents the charging/discharging status of the ultracapacitor (1 means charging, -1 means discharging).

Fig. 1 The structure of vehicle control system using hybrid power system

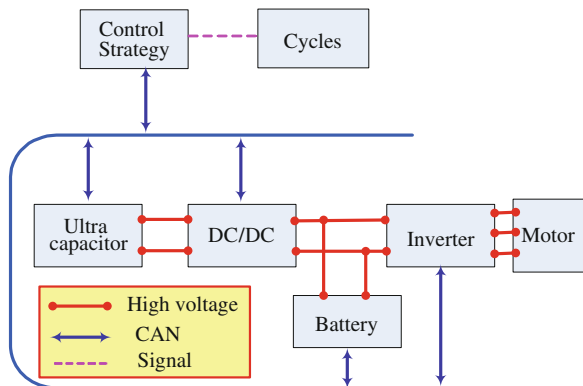
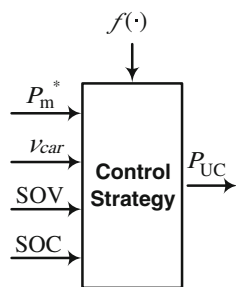


Fig. 2 The control structure of hybrid power system



$$\begin{cases} P_m = \frac{P_m^*}{1 + \tau_{car}s} \\ P_m = P_{DC} + P_{bat} = P_{UC}\eta_{DC}^2 + P_{bat} \end{cases} \quad (1)$$

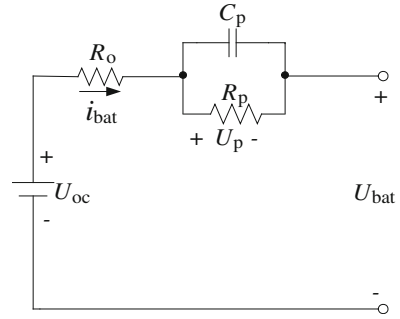
2.2 Li-ion Battery Modelling

Comparing to Rint model, RC model and PNGV model, Thevenin equivalent circuit model simulates dynamic character of Li-ion battery more precisely. Schematic of Thevenin battery model is shown in Fig. 3.

C_P is polarization capacitance is polarization voltage (U_P), caused by polarization resistance (R_P). R_O is ohmic resistance, U_{OC} is open circuit voltage, i_{bat} is the battery, U_{bat} is the battery terminal voltage. Above parameters are all variable with battery SOC and temperature. Temperature influence will be ignored because all the tests are done in an incubator. So Thevenin battery model can be described as formula (2)

$$\begin{cases} \dot{U}_P = \frac{i_{bat}}{C_P} - \frac{U_P}{R_P C_P} \\ U_{bat} = U_{OC} - U_P - i_{bat}R_O \end{cases} \quad (2)$$

Fig. 3 Schematic of Thevenin battery model



For parameter identification of U_{OC} , C_P , R_P , R_O , hybrid Pulse Power Characterization (HPPC) test of cells is executed with every 10 % SOC [8]. Here set that the current is positive while discharging and negative while charging, and the time constant is defined as $\tau = R_P C_P$, so (2) can be discredited as (3), Where i_p is the current through the polarization resistance (R_P).

$$\left\{ \begin{aligned} U_{bat,i} &= U_{OC} - R_O i_{bat,i} - R_P i_{p,i} \\ i_{p,i} &= \left\{ 1 - \frac{[1 - \exp(-\Delta t/\tau)]}{(\Delta t/\tau)} \right\} \times i_{bat,i} \\ &+ \left\{ \frac{[1 - \exp(-\Delta t/\tau)]}{(\Delta t/\tau)} - \exp(-\Delta t/\tau) \right\} \\ &\times i_{bat,i-1} + \exp(-\Delta t/\tau) \times i_{bat,i-1} \end{aligned} \right. \quad (3)$$

Parameter identification results are shown in Table 1 based on (3) with multiple linear regression method.

2.3 Ultracapacitor Modelling

RC circuit model is used for ultracapacitor modeling, as shown in Fig. 4. i_{uc} , U_{uc} , U_c respectively represents the load current, load voltage and ultracapacitor voltage. R_{PUC} is the self-discharge resistance, ESR is the equivalent internal resistance, C_U is the capacitance.

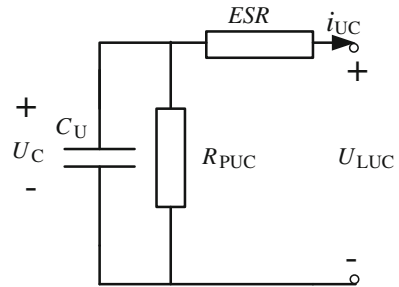
So ultracapacitor can be modelled as (4).With similar method as parameter identification of Li-ion battery, the capacitance C_U and the equivalent internal resistance ESR is achieved as shown in Tables 2, and 3.

$$\left\{ \begin{aligned} \dot{U}_C &= \frac{-U_C}{C_U \times R_{PUC}} + \frac{i_{UC}}{C_U} \\ U_{LUC} &= U_C - ESR \times i_{UC} \end{aligned} \right. \quad (4)$$

Table 1 The identification results of power battery

SOC	U_{OC}/V	C_p/F	$R_p/m\Omega$	$R_o/m\Omega$	τ_b/s
0.4	3.255	4083.6	5.17	3.32	21.1
0.5	3.278	4548.7	5.23	3.30	23.8
0.6	3.282	4906.8	5.32	3.28	26.1
0.7	3.285	4962.0	6.02	3.23	29.9
0.8	3.289	5304.8	7.73	3.28	41.1

Fig. 4 The model schematic for the ultracapacitor



3 Control System

3.1 Control Strategy Development

The principle of the control strategy is described as the following. Ultracapacitor is charged as fully as possible while regenerative braking. If the driving power is needed, the slowly changing power is given by the battery, and the abruptly changing one is given by the ultracapacitor.

A logic threshold control strategy is used in the article, whose scheme is shown in Fig. 5. The input variable is the input power of the motor’s inverter (P_m) and the ultracapacitor SOV. And the control strategy works with the following constraints.

$$f(\bullet) = \begin{cases} SOV_L \leq SOV \leq SOV_H \\ SOV \leq 100\% \\ P_{chg}(SOC) \leq P_{bat}^* \leq P_{bmax}(SOC) \end{cases} \quad (5)$$

where SOV_L and SOV_H is respectively the low and upper threshold of the ultracapacitor voltage, P_{bat}^* is the requested discharging power of battery, $P_{bmax}(>=0)$, $P_{chg}(< 0)$ is respectively the feasible maximum of battery discharging and charging power.

As shown in Fig. 5, P_a is a calibrated parameter and represents the average power requested by the inverters. The power request less than P_a is allocated to the Li-ion battery. P_m is the actual power of the inverters. $F(s)$ is the dynamic response of Li-ion battery for power calculation, described as (6).

Table 2 The identification results of the capacitance C_U

i_{UC}/A	C_U/F	i_{UC}/A	C_U/F
20	471.1	-20	486.7
50	468.9	-50	487.7
100	469	-100	487.1
150	467.3	-150	488.4
200	465.2	-200	486.6
250	464.3	-250	485.4

Table 3 The identification results of the equivalent internal resistance ESR

i_{UC}/A	ESR (m Ω)	i_{UC}/A	ESR (m Ω)
-2	2.41	2	2.36
-20	2.14	20	2.01
-50	1.96	50	1.96
-100	1.94	100	1.8
-150	1.84	150	1.76
-200	1.83	200	1.75
-250	1.82	250	1.72

$$F(s) = \begin{cases} \frac{1}{\tau_{bat} \cdot s + 1} & (P_m^* > 0, discharge) \\ \frac{1}{\tau_{uc} \cdot s + 1} & (P_m^* < 0, charge) \end{cases} \quad (6)$$

3.2 Simulation Test Bench Build

xPC-Target is a solution based on PC for product Rapid Control Prototyping (RCP) development, real-time system test[9]. The real-time simulation test bench in the article is constituted of one host PC and two xPC-Target PCs as shown in Fig. 6. Modelling of Control strategy and hybrid power system, model-in-loop simulation, real-time code compiling and test monitoring are executed on host PC [10]. Executable codes compiled by SIMULINK models on host PCs are downloaded to xPC-Target based on TCP/IP protocol through Ethernet Net Interface Card (NIC). Codes of control strategy and of hybrid power system are real-timely run on separate xPC-Target PC and the execution results can be uploaded to host PC.

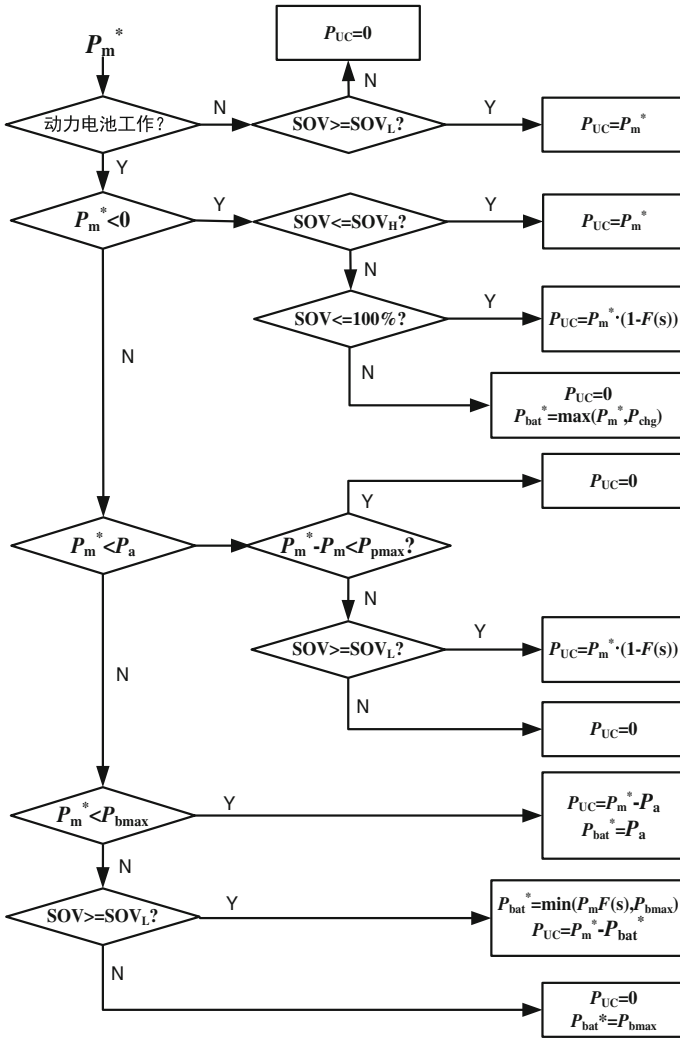


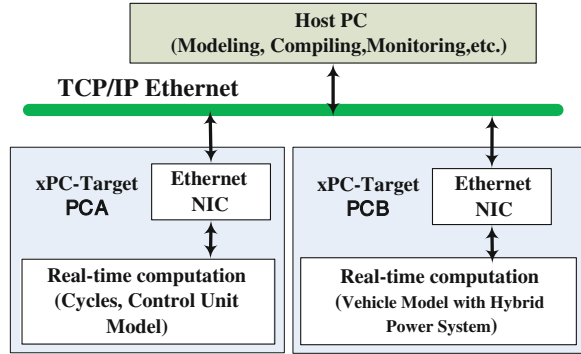
Fig. 5 Schematic of logic threshold control strategy

4 Real-Time Simulation Test of Control Strategy

4.1 Test Results

The simulation test is run based on UDDS and the vehicle parameters are set as Table 4. UDDC is an instantaneous changing cycle which is fit for validation of both hybrid power system modelling and real-time simulation test bench build up. Some results of real-time simulation based on xPC Target are shown in Fig. 7.

Fig. 6 Real-time simulation platform based on xPC Target



Battery current, ultracapacitor current, SOV, SOC and energy change during two UDDS cycles are shown in Fig. 8.

Figure 8a illustrates the battery current and ultracapacitor current. The battery current is mostly controlled to be no more than 1C, while the ultracapacitor discharges and charges high current, which is very good for battery cycle life and efficiency. The charging of battery is greatly less occasional than that of ultracapacitor. The charging efficiency of ultracapacitors, as known, is greatly higher than that of Li-ion battery, so more regenerative braking energy is recycled. At about second 200 and second 1,600, when peak power is requested by the motor's inverter, the ultracapacitor fast discharges to make peak power output of hybrid power system. And the battery discharges with greater current (48 A, 2 C) as the discharging power of ultracapacitor decreases because of limited energy capacity.

Figure 8b illustrates ultracapacitor SOV and battery SOC. The initial SOV and ultimate SOV is same. Figure 8c illustrates the requested driving energy, actual energy output of ultracapacitor and battery. When there is a peak energy request, the battery output energy can be kept slowly changing with the help of peak energy output of ultracapacitor.

4.2 Analysis and Discussion

If Li-ion battery is used as the only energy source, it should be designed as Table 5. The simulation comparison between the only-battery power system and the hybrid power system is shown in Fig. 9.

Figure 9a illustrates the battery current comparison. Battery usually discharges high current more than 2 C if it is the only energy source, which will shorten the cycle life and decrease the discharging efficiency. And the maximum charging current of the battery is much lower than that of the ultracapacitor (shown in Fig. 8a), so that much less regenerative braking energy is recycled.

Figure 9b illustrates the comparison of battery's energy output. Comparing to the battery-only power system, the energy provided by the battery of the hybrid

Table 4 The basic parameter of the EV

Vehicle	
Curb weight/kg	1320
Gross weight/kg	1845
Front Face Area/m ²	2.53
Air Friction Ratio	0.36
Diameter of tyre/m	0.299
Battery	
Type	LiFePO4 Li-ion battery
Cell voltage/V	3.2
Capacity/Ah	24
Number	105
Ultracapacitor	
Type	BMOD0500-16.2 V
Cell voltage/V	16
Capacity//F	500
Number	18

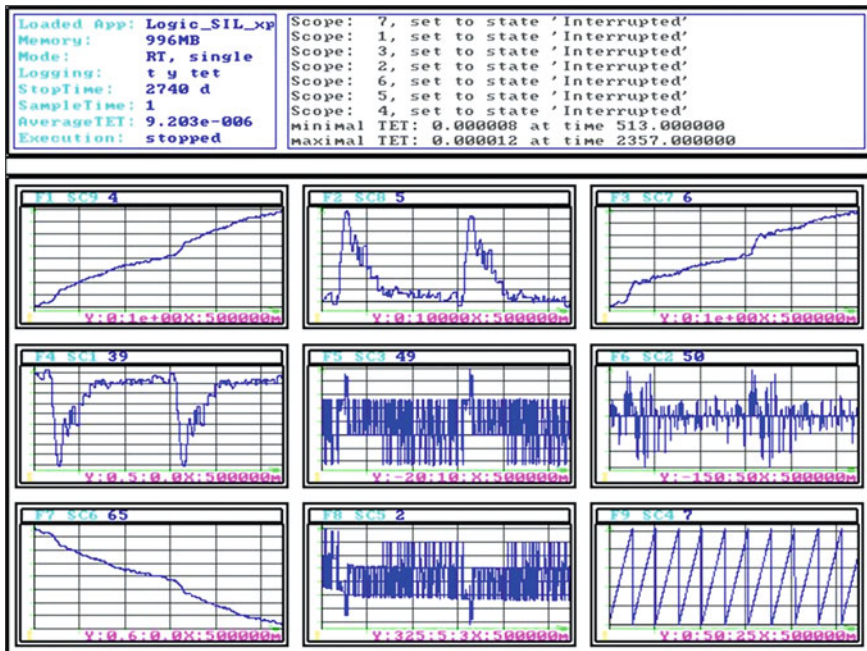


Fig. 7 Real-time simulation based on xPC target

system decreases by 8.97 %. The first reason is that the battery usually works in zones of high efficiency with the help of the ultracapacitor, and the second reason is that more regenerative braking energy is recycled with hybrid power system.

Fig. 8 Real-time simulation results **a** Battery current. **b** Ultracapcitor SOV and battery SOC. **c** Energy request and output

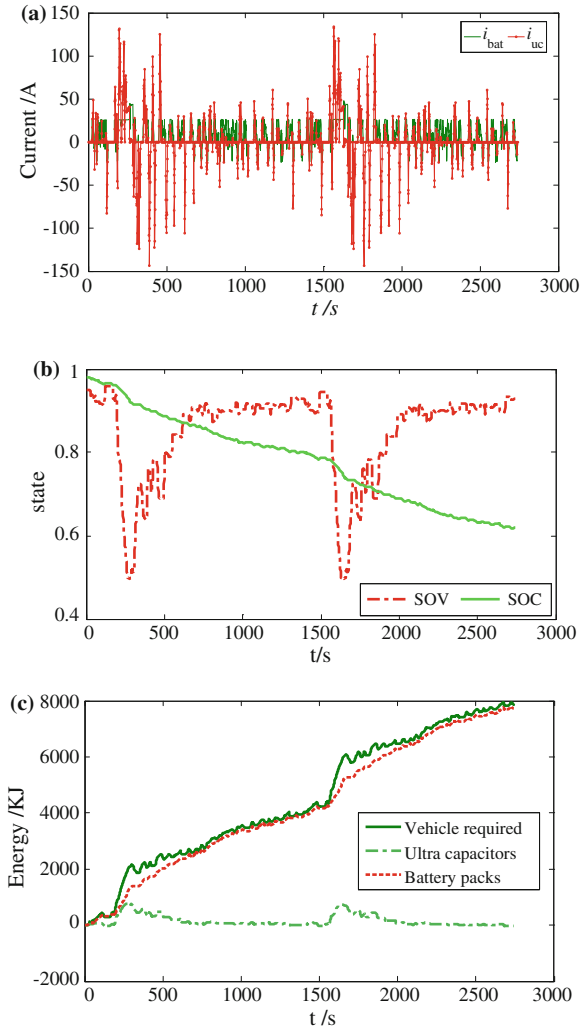
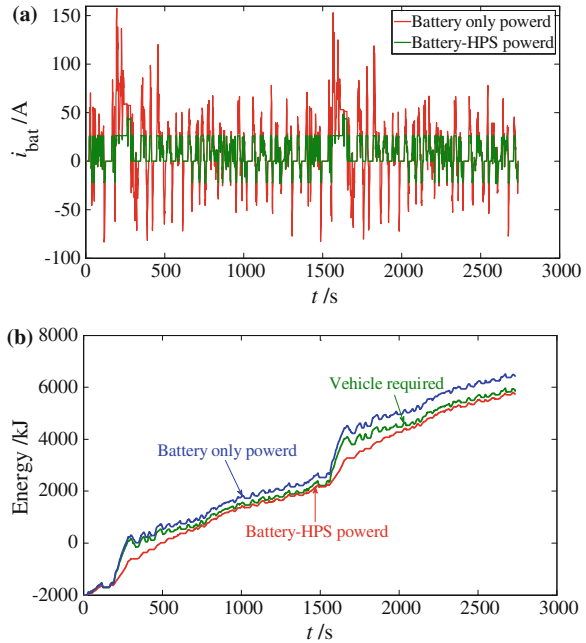


Table 5 Li-ion battery parameter

Type	LiFePO4 Li-ion battery
Cell voltage/V	3.2
Capacity/Ah	36
Serial number	105

Fig. 9 Compared simulation for battery-only power system and hybrid power system. **a** Battery current. **b** Energy request and output



5 Conclusions

A RCP designed based on xPC Target for hybrid power system is proposed. With the tests executed on the real-time simulation test bench, the following points are concluded.

- (1) Distributed simulation test bench comprised of two xPC-Target system with Communication Area Net (CAN) is helpful for real-time simulation.
- (2) Control strategy proposed in the article is tested to be able to control the hybrid power system well. The battery's current is controlled to be no higher than 2 C, so that the battery cycle life and efficiency will be improved.
- (3) Comparing to the batter-only power system, because the battery works more occasionally in zones of high efficiency and more regenerative braking energy is recycled, hybrid power system is more efficient with about 8.97 % output energy saving.

References

1. Dougal RA, Liu S, White RE (2002) Power and life extension of battery-ultracapacitor hybrids. *J IEEE Trans Compon Packag Technol* 25(1):120–131
2. Camara MB, Gualous H, Gustin F et al (2008) Design and new control of DC/DC converters to share energy between supercapacitors and batteries in hybrid vehicles. *J IEEE Trans Veh Technol* 57(5):2721–2735

3. Pay S, Baghzouz Y (2003) Effectiveness of battery-supercapacitor combination in electric vehicles. IEEE Bologna power tech conference proceedings, Bologna 1–6
4. Nan J, Wang J, Sun F (2005) Study of energy management system of electric vehicle. Trans Beijing Inst Technol 25(5):384–388 (in Chinese)
5. Gao L, Dougal RA, Liu S (2003) Active power sharing in hybrid battery/capacitor power sources. Eighteenth annual: IEEE applied power electronics conference and exposition (APEC) 497–503
6. Adam WS, Thomas S, Cyrus A (2006) An ultracapacitor circuit for reducing sulfation in lead acid batteries for mild hybrid electric vehicles. J Power Sources 156(2):755–762
7. Xiong R, He HW, Zhang XW et al. (2010) Simulation study on hybrid ultracapacitor-battery power system for PHEV. The 2010 international conference on future computer and communication (ICFCC 2010), Wuhan: IEEE 496–500
8. Xiong R (2010) Simulation study on the hybrid power system for plug-in hybrid electrical vehicles. Dissertation for master's degree, Beijing institute of technology
9. Luo J, Wang M, MA W (2010) Research on the simulation of on-orbit servicing spacecraft navigation system. J Astronautics 31(2):380–385
10. Yang Di, Li Li-tao, Yang Xu, et al. (2002) MATLAB/RTW and It's application. Tsinghua University press, Beijing 249–260

A Study on Effective Thermal-Shock Test Improvement of Battery Packs for PHEVs

Byoung-Hoon Kim, Hong-Jong Lee, Jin-Beom Jeong,
Baek-Haeng Lee, Dong-Hyun Shin, Hyun-Sik Song,
Tae-Hoon Kim and Ji-Yoon Yoo

Abstract While there are many test items to secure a vehicle's reliability, this study reviews the test method for Thermal-shock Test, one of climatic tests to evaluate the damage caused by thermal expansion coefficient differences of parts by rapid temperature change, and proposes more appropriate test method for test performance evaluation. The testing for automobile electronic parts is divided into two categories for reliability and for stability, and is varied in wide range. In this study, Thermal-shock Test, which performed to acquire durability life, one of the important factors of the automobile electronic part tests, is analyzed. The current Thermal-shock Test is conducted with higher than 500 cycles in case of automobile interior electronic parts, or higher than 1,000 cycles in case of the parts in the engine room or of the exterior or special area of automobile. And, according to installation area, the tests are performed in high temperature (75–115 °C) and in low temperature (−40 °C). And, test profile time is to evaluate battery's performance reduction by changing temperature for total one hour (high temperature, 30 min and low temperature 30 min). During and after the evaluation, any abnormality, such as venting, battery enclosure rupture, fire, or explosion, shouldn't be occurred to the tested battery. Also, the internal resistance should satisfy the preset range. Therefore, with Thermal-shock Standard Test, the Battery Pack for PHEV in development process is to be evaluated. And, the evaluation result is analyzed to verify if the evaluation can be performed with trust as the evaluation to other automobile electronic parts followed by a proposal of detailed

F2012-B03-025

B.-H. Kim (✉) · H.-S. Song · J.-Y. Yoo
Korea University, Seoul, Korea
e-mail: bhkim@katech.re.kr

H.-J. Lee · J.-B. Jeong · B.-H. Lee · D.-H. Shin · T.-H. Kim
Korea Automotive Technology Institute, Chonan Chugnam, Korea

test measure. Firstly the internal structure of the developed battery pack for PHEV is analyzed. Then, through the test method recently applied, the test procedure to measure the temperature distribution of battery pack is to be established. And, by analyzing the international thermal-shock test standard and conducting the test on the proposed profile, the detailed test method is drawn. After the verification process for the proposed test method, the reliability is to be secured.

Keywords Thermal-shock · PHEV · Battery pack · Energy storage system · Environmental test

1 Introduction

Recently, the interest on PHEV, which is the environment-friendly vehicle, is increasing, and various researches and developments are conducted in many nations. Also, several auto makers even sell PHEVs. Moreover, under the circumstance that the interest of users' stability and reliability security is increasing, the battery pack, an important component of existing vehicle parts, used to have simple structure in small volume but recently the size of battery pack are expanded to secure large capacity and high output in the complicated structure to equip electronic parts regarding the battery pack separately. Therefore, it is necessary to analyze if current evaluation method is suitable for the standard test for PHEV battery pack and to confront the analysis result.

The testing for automobile electronic parts is divided into two categories for reliability and for stability, and is varied in wide range. In this study, Thermal-shock Test, which performed to acquire durability life, one of the important factors of the automobile electronic part tests, is analyzed. The current Thermal-shock Test is conducted with higher than 500 cycles in case of automobile interior electronic parts, or higher than 1,000 cycles in case of the parts in the engine room or of the exterior or special area of automobile. And, according to installation area, the tests are performed in high temperature (75–115 °C) and in low temperature (−40 °C) [1, 2]. And, test profile time is to evaluate battery's performance reduction by changing temperature for total one hour (high temperature, 30 min and low temperature 30 min). During and after the evaluation, any abnormality, such as venting, battery enclosure rupture, fire, or explosion, shouldn't be occurred to the tested battery. Also, the internal resistance should satisfy the preset range. Therefore, with Thermal-shock Standard Test, the Battery Pack for PHEV in development process is to be evaluated. And, the evaluation result is analyzed to verify if the evaluation can be performed with trust as the evaluation to other automobile electronic parts followed by a proposal of detailed test measure.

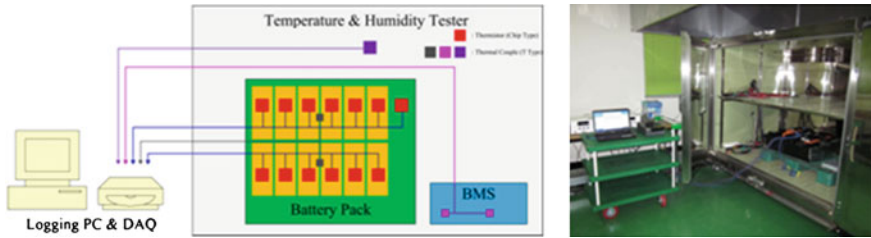


Fig. 1 A schematic diagram and a photo of the experimental environment for the temperature tests of the battery pack

2 Test Platform and Experiment Process

In this study, experiments were performed on the battery pack by applying temperature test items from the guidelines for testing electrical systems in conventional automobiles, and compared the variations in external temperature and the internal temperature according to the maintained temperature. The temperature steps test and the temperature cycling test specified in ISO 17650-4 were conducted [3, 4]. Comparative experiments were performed in the temperature range between -30 and 50 °C in order to protect the performance of the battery pack.

The temperature steps test involves varying the temperature in 5 °C steps in the -30 – 50 °C range, maintaining the specimen's temperature for a certain period at each step, and examining the mechanical and electrical performance of the specimen. For the temperature cycling test, temperature is increased, decreased, and maintained within the -30 – 50 °C range, and the performances of the specimen under rest and operating conditions are examined. Since experiments were conducted in this study to examine the temperature reaching performance of the specimen when the temperature was varied and maintained under rest condition, operation performances were not observed.

To conduct the temperature test of the vehicle battery pack and the BMS, each specimen was placed in a constant temperature and humidity chamber (3 °C/min), as shown in Fig. 1. A DAQ was used to measure data at 18 points, including the temperatures of each module, BMS, and the chamber's internal temperature. Thermistors were used to measure the temperature of each module of the battery pack. The temperatures of the 12 modules and at the entrance of the cooling air conditioner were recorded. The thermistor was placed at the center of each module of the battery pack. In addition, thermal couples were installed at 2 points on the PCB inside the case to measure the temperature of the BMS. Another thermal couple was installed to measure the ambient temperature inside the constant temperature and humidity chamber. Temperature data taken from 18 points were recorded using a DAQ and a logging PC.

In this study, temperature cycling, temperature characteristics, and thermal shock tests were performed to compare the test temperature and the internal temperature of the battery pack and to examine the temperature variation characteristics of the

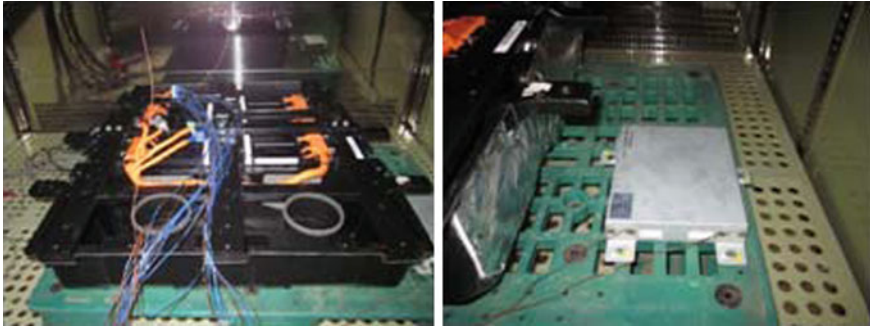


Fig. 2 Battery pack test

battery pack. A 6.9 kW battery pack shown in Fig. 2 was used for the experiment. The battery pack is an air-cooled system consisting of 12 modules, each module with 8 cells (96 cells total).

The comparative experiment was performed according to the temperature test pattern using the constant temperature and humidity chamber and the thermal shock tester shown in Figs. 3 and 4, respectively.

Figure 5 displays the temperature cycling test profile used in the experiment to examine the temperature variation characteristics. Temperature cycling test generally involves assessing the specimen's operation test performance and the state of parts and components while temperature is increased, decreased, and maintained. However, non-operation test was conducted for this study because our objective is to examine the variation characteristics of internal temperature. The test temperature range of the profile was between -30 and 50 °C, and the temperature was changed and maintained for 2 h.

Figure 6 displays the temperature characteristics test profile used in the experiment to examine the temperature variation characteristics. The temperature characteristics test was performed as a non-operation test. Starting at room temperature, the temperature was varied and maintained in 10 °C intervals. The test temperature range of the profile was between -30 and 50 °C, and the step interval was set at 10 °C. The temperature was varied for 10 min and maintained at each step for 1 h.

Figure 7 displays the thermal shock characteristics test profile used in the experiment to examine the temperature variation characteristics. The thermal shock test was performed as a non-operation test while temperature was increased, decreased, and maintained. It is a test for assessing damage caused by abrupt changes in temperature and the difference in the coefficients of thermal expansion between the parts in each specimen. The test temperature range of the profile was between -30 and 50 °C. The temperature was varied within 5 min and maintained at each level for 30 min.



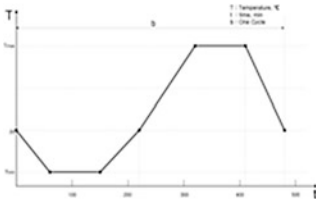
Dimension	2000(W) × 1500(H) × 1500(D)
Temp. Range	-40°C ~ 150°C
Humidity Range	30 ~ 98%

Fig. 3 Constant temperature and humidity chamber



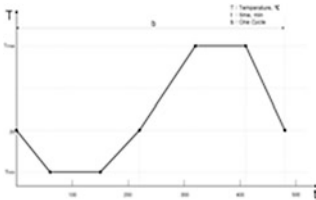
Dimension	2000(W) × 1500(H) × 1500(D)
Temp. Range	-40°C ~ 150°C
Temperature change time	> 5 [Min]

Fig. 4 Thermal shock tester



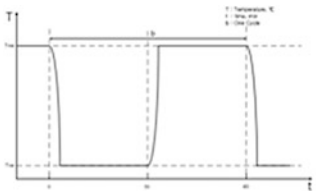
T_{max}	50[°C]
T_{min}	-30[°C]
Temperature change time	2 [Hour]
Temperature retention time	2 [Hour]

Fig. 5 Temperature cycling test profile



T_{max}	50[°C]
T_{min}	-30[°C]
Temperature change time	2 [Hour]
Temperature retention time	2 [Hour]

Fig. 6 Temperature characteristics test profile



T_{max}	50[°C]
T_{min}	-30[°C]
Temperature change time	> 5 [Min]
Temperature retention time	30 [Min]

Fig. 7 Thermal shock test profile

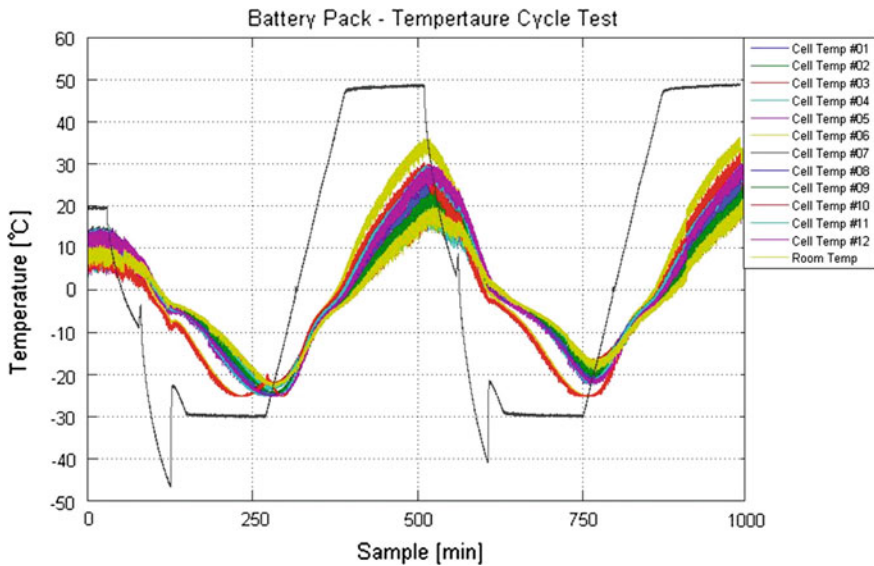


Fig. 8 Temperature cycling test result of the battery pack for PHEVs

3 Test Results

In this study, tests were performed according to the temperature cycling, temperature characteristics, and thermal shock test guidelines for electrical systems in conventional automobiles. Tests were conducted in non-operational state without taking into account the operational state between test temperatures. As explained earlier, temperatures were measured using thermistors, thermal couples, and DAQ. The test results of the battery pack are shown in graphs for comparison.

Figure 8 displays the results of the temperature cycling test, which was performed by maintaining room temperature (20 °C) for 5 h, followed by increasing, decreasing and maintaining the temperature for 2 h. Test results indicate that the temperature of the battery pack fell short by 5–15 °C during 2 h of temperature change and maintenance in the low temperature range. In the high temperature range, the discrepancy increased to 15–35 °C.

Figure 9 displays the results of the temperature characteristics test, which was performed by maintaining room temperature (20 °C) for 5 h, followed by decreasing and increasing the temperature. The temperature was varied in each step at the rate of 1 °C/min, and the temperature was maintained at each step for 1 h. Test results indicate that the BMS changed and maintained temperatures similar to the set levels. However, the internal temperature of the battery of the battery pack fell short of the set levels.

Figure 10 displays the results of the thermal shock test, which was performed starting at room temperature (20 °C) and the temperature was increased and decreased. The temperature was varied within 5 min and maintained at each level

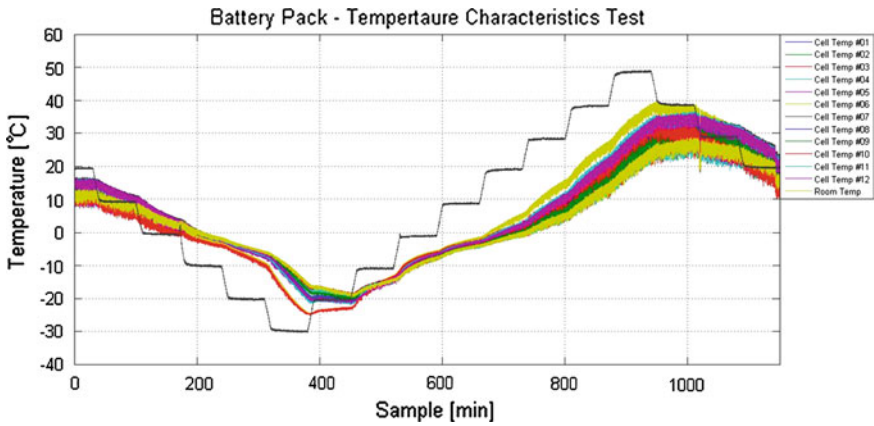


Fig. 9 Temperature characteristics test result of the battery pack for PHEVs

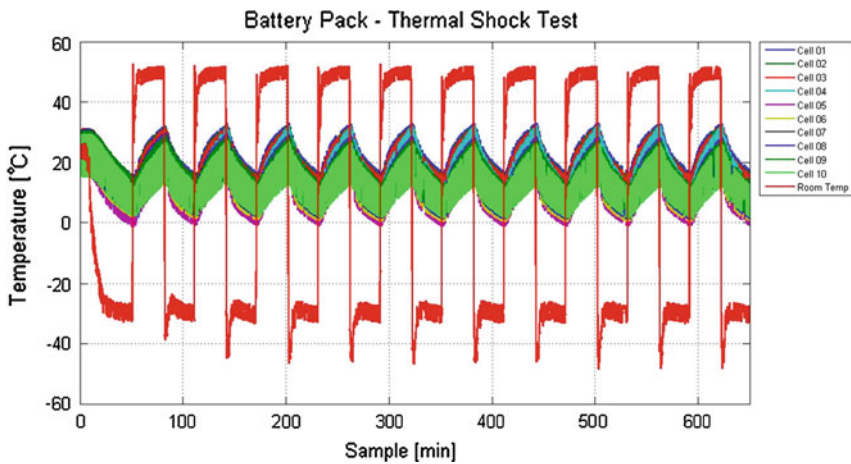


Fig. 10 Thermal shock test result (battery pack)

for 30 min. Test results indicate that it closely followed the set temperature levels. However, the internal temperature of the batter pack was only maintained within the 0–30 °C range, as shown in Fig. 10.

The results from the temperature step test and the temperature cycling test confirmed that the BMS reached the set temperatures within the corresponding time. However, the battery pack failed to reach the temperatures within the specified period.

4 Conclusion

In this study, thermistors (chip type) and thermal couples (T-type) were installed on a vehicle battery pack to conduct experiments to examine whether the temperature test items specified in the reliability evaluation test guidelines for electrical systems installed in conventional automobiles can be applied to battery packs. In the case of BMS installed in conventional automobiles, the temperature reached the experimental level within the corresponding time. However, it was confirmed that the temperature of the battery pack did not reach the level within the corresponding time. Therefore, it is necessary to extend the temperature maintenance time of the tests specified in the reliability evaluation standard of the electrical systems installed in conventional automobiles if the tests are to be applied to battery packs. Our future research plans include deriving temperature test durations suitable for battery packs by selecting temperature test items for battery packs based on repeated experiments over a substantial period. We hope the results of this study can serve as a useful reference for selecting test periods in temperature test items during reliability evaluation for high capacity battery packs.

Acknowledgments This work was supported by the human resources development of the Korea Institute of Energy Technology Evaluation and Planning (KETEP) grant funded by the Korea government ministry of knowledge economy (No. 20114010203010)

References

1. ISO 12405-1 (2011) Electrically propelled road vehicles—test specification for lithium-ion traction battery packs and systems—part 1: high-power applications
2. ISO/DIS 12405-2 (2010) Electrically propelled road vehicles—test specification for lithium-ion traction battery packs and systems—part 1: high energy application
3. ISO 16750-1 (2003) Road vehicles—environmental conditions and testing for electrical and electronic equipment—part 1: general
4. ISO 16750-4 (2003) Road vehicles—environmental conditions and testing for electrical and electronic equipment—part 4: climatic loads

Challenges in NVH for Electric Vehicles

Benjamin Meek, Herman Van der Auwear and Koen De Langhe

Abstract ERTRAC predictions currently show EV growing their market share to around 20 % of new vehicles sold by 2030, to meet these demands NVH engineers will be challenged to define and refine the sound, comfort and feel of tomorrow's automobile without hindering the drive for more efficient vehicles. Often though, improvements in efficiency such as those gained by weight reduction bring extra challenges to the NVH engineer as their concerns become secondary to performance and efficiency gains. This paper aims to show how NVH activities can positively aid efficiency gains for electric vehicles with examples of some recent simulation and test work carried out on electric vehicles. NVH Engineering takes on a new focus for Electric Vehicles with the removal of broadband internal combustion engine (ICE) noise, significant differences are found in the noise spectrum when comparing an Electric Vehicle (EV) with an ICE vehicle. EV noise is characterised by tonal harmonic noise related to the number of poles on the electric motor. Results from vehicle benchmarking tests together with analysis highlight the relative quietness in the low/mid frequency range (<1 kHz). An example of how this can offer opportunities for weight reduction is shown using NVH simulation tools to demonstrate that early application of NVH engineering can aid weight reduction while maintaining acceptable interior sound levels and quality. The choice of electric motor is often dictated by technical, financial and logistical limitations, increasingly in the automotive industry is researching alternative motor configurations that do not contain permanent magnets such as switched reluctance motors which do not contain magnetic materials which are expected to become increasingly expensive and scarce as demand grows. The drawback of

F2012-B03-029

B. Meek (✉) · H. Van der Auwear · K. De Langhe
LMS International, Leuven, Belgium
e-mail: ben.meek@lmsintl.com

SRM is increased noise and control complexity. A methodology using a combined 1D multi-physics approach and 3D finite element analysis approach is shown with initial results that can help optimize the mechanical design and controls of the SRM in parallel, maximising power without impairing the acoustic performance. Finally with a quieter powertrain a challenge facing vehicle manufacturers is how to alert vulnerable road users to the presence or movement of the electric vehicle, pedestrian warning systems are seen as the best solution but how can you optimize these systems, Fast Multipole BEM tools can help simulate the propagation so sound and the effect of the environment around it, results for such a study are presented to demonstrate its potential. This paper highlights the evolving NVH demands from the emergence of electric vehicles and demonstrates how NVH analysis methodologies can be applied to optimize key vehicle NVH attributes. Analysis of NVH benchmarking data for electric and ICE powered vehicles show the potential needs for NVH engineering focus on electric vehicles. Results of vibration and acoustic simulation tools applied to EV body weight, electric motor performance and warning sound are shown to demonstrate where NVH analysis can aid electric vehicle development without hindering the search for efficiency gains.

Keywords Electric vehicle · NVH · 1D · 3D · Multi-attribute

1 Introduction

Current ERTRAC predictions for the uptake of electric vehicles currently show they could account for >10 % of new vehicle sales by 2030, if one includes all hybrid configurations then this percentage further increases to 30 % [1]. This uptake in electric vehicles will be primarily being driven by legislation pressures, for example in Europe where the European Commission have proposed a new lower fleet average CO₂ limit of 95 g/km to come into effect in 2020 [2], meaning manufacturers will have to use electrification to meet the fleet targets. Alongside this consumers are going to have to be convinced that it meets their expectations. So ensuring that electric vehicles fulfill the cost, performance, feel and reliability needs remains the other top priority. Encompassed within the consumer expectations is the topic of NVH attributes, simple logic states that electric vehicles are by definition quieter than their ICE counterparts therefore NVH performance of these vehicles is better. If one looks beyond this principle and where will the focus for NVH engineer be on quieter electric vehicles [3, 4]?

- Minimizing tonal harmonic sound from the electric motor and power electronics
- Eliminating non-speed related noise sources (power steering, fuel pump, HVAC ...)
- Re-focus on road and wind generated noise as they become dominant sources in absence of broadband combustion engine noise.

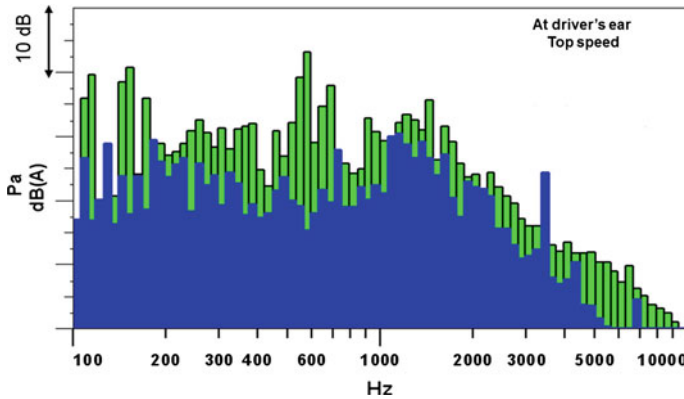


Fig. 1 Sound pressure level comparison of identical configured EV (blue) and Ice (green) powered equivalent

- Pedestrian warning system to relay vehicle operation to vulnerable road users

Using examples of work carried project work carried out on electric vehicles this sets out to demonstrate that focusing on NVH can have a positive influence on the strive for lower vehicle emissions and further vehicle efficiency gains.

2 Electrification Means Quieter Cars

The effect of replacing the internal combustion engine (ICE) with an electric motor fundamentally alters the balance of sound experience by vehicle occupants and other road users. Fundamentally Electric vehicles are quieter, Fig. 1 shows that on an identical vehicle configuration the overall sound power levels are reduced across the frequency spectrum for what is considered to be the worst case for an electric vehicle (EV), namely high driving (120 km/h) where motor rpm and torque requirements are both high. It highlights both the relative quietness of the electric vehicle, this is most pronounced in the frequency range 200–1,000 Hz where the electric motor has a distinct void in its frequency spectrum compared to the ICE equivalent; this potentially opens the door for body optimization or panel gauge reduction.

Also notable are the tonal peaks related to the motor design, these equate to 4x and 8x the number of poles in the electric motor, these are the tonal harmonics that give the electric motors its distinct whine under heavy load and high rpm, controlling these is important if occupants are not to be annoyed.

To make such analysis more objective one can turn to psychoacoustic measures such as sharpness, prominence ratio and tone to noise ratio. In the example shown in Fig. 2 the EV proved to have a sharper tone across the frequency spectrum then

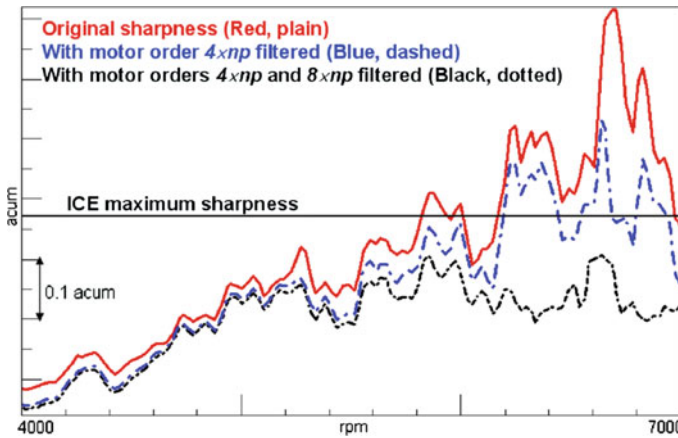


Fig. 2 Showing the effect of removing the electric motor tonal components on the EV sharpness

the ICE powered vehicle, particularly at the frequencies that tie in with the tonal motor components. Figure 2 also shows that with the tonal components filtered the sharpness result for the is reduced drastically.

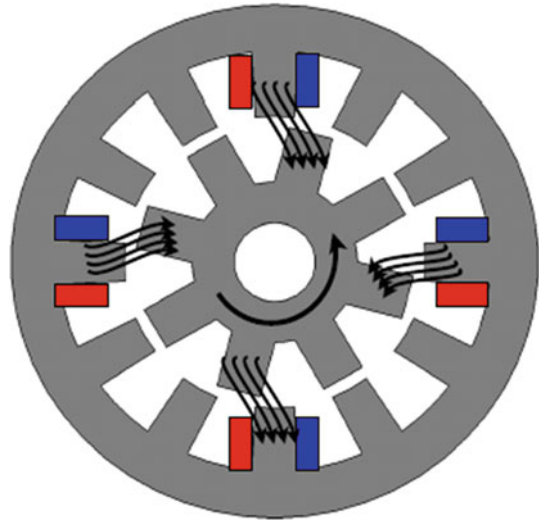
3 Body Weight Reduction

Knowing that the forcing function of the electric motor is less manufacturers can look to take advantage of this to reduce the body weight or down-gauge body panels to save weight. Studies have shown that body noise transfer functions (BNTF) for engine mounts can be reduced to 60 dB/N without compromising interior NVH performance [5]; however with road noise remaining unchanged on electric vehicle BNTF for suspension mounting points will have to remain at around 35 dB/N to achieve acceptable performance.

4 The Choice of Electric Motor

For automotive applications the choice of motors the industry is largely restricted by availability, cost and scalability, for this reason synchronous the permanent magnet motor is the current choice for the electric drive in automotive applications. From an NVH perspective these types of motors are more than capable of delivering the quiet performance expected from electric traction. Within the automotive industry there are fears that the increased demand for electric motors will drive up the cost and cause supply security issues in the future, this is fuelling a large amount of research into alternative motor technologies which do not

Fig. 3 Showing a section view of a SRM



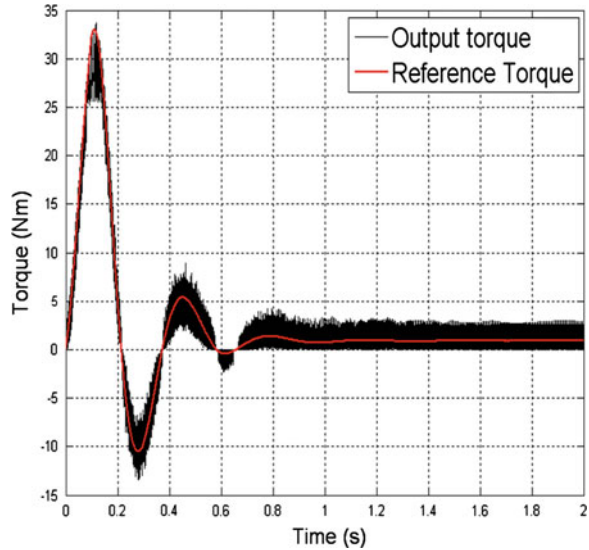
contain magnet materials; principally induction and reluctance motor configurations. Among these the reluctance motor, shown in Fig. 3 is thought within the industry to have the lowest potential cost from a material and manufacturability point of view. It works by switching the current between phased windings on the stator to pull the ferrous steel rotor around, producing the motion. The worry within the industry has been the propensity of such motors to be viewed as noisy.

The noise in a switched reluctance motor is generated by the switching on and off of current in the stator poles, creating the moving electromagnetic field that drives the motor. The switching on and off of the current causes a torque ripple within the motor, Fig. 4 shows such a ripple as a function of torque against time compared to the reference torque required by the control unit.

LMS is developing a process to optimize the design and performance of an SRM motor using a combined multi-physics 1D and 3D approach [6]. This approach allows the effect of the mechanical and controls design to be optimized in a single process. Figure 5 shows the outline of the process:

- A 2D magnetic finite element simulation is used to produce look up tables of torque and magnetic flux as a function of voltage and current.
- Using LMS Imagine.Lab a 1D multi-physics model of the SRM and electric vehicle is constructed to allow simulation of the mechanical, control and vehicle variables that determine motor performance.
- A 2D magnetic finite element simulation is then run for each time step on the motor operation to calculate the forces acting on the stator, by performing a Fast Fourier transfer the time domain results are converted to the frequency domain for further analysis
- A 3D acoustic BEM simulation is carried out to analyze the noise performance. Alternatively results can be left in the time domain and analyzed using a time

Fig. 4 Showing the torque ripple as function of time



domain BEM solver to allow replay of the simulated sound of the motor for psychoacoustic analysis.

The results of such a process allow optimization of the noise performance in through mechanical or controls means, Fig. 6 shows how such an optimization can take place for a SRM running at a constant speed equivalent to 90 km/h in the vehicle model by reducing the firing angles between the motors phases, and the torque ripple this created. The results are the highest noise peak at 1750 Hz is reduced.

5 Pedestrian Warning Systems

The other main NVH challenge arising from Electric vehicles is how to make the movement of electric vehicles clear to vulnerable road users. Current thinking focuses of the use of external warning devices, with the first systems introduces on EV's such as the Nissan Leaf. Such systems have a complex set of scenarios to be able to cope with, being audible above urban background noise but quiet enough to avoid nuisance, adaptive devices have been put forward as a method of achieving this balance satisfactorily but there are a lot of hurdles to overcome before this is a reality

What sounds effectively portrait the movement of the vehicle?

What happens when you put multiple vehicles with adaptive systems alongside each other?

How should the sound be directed from the vehicle to be most effective?

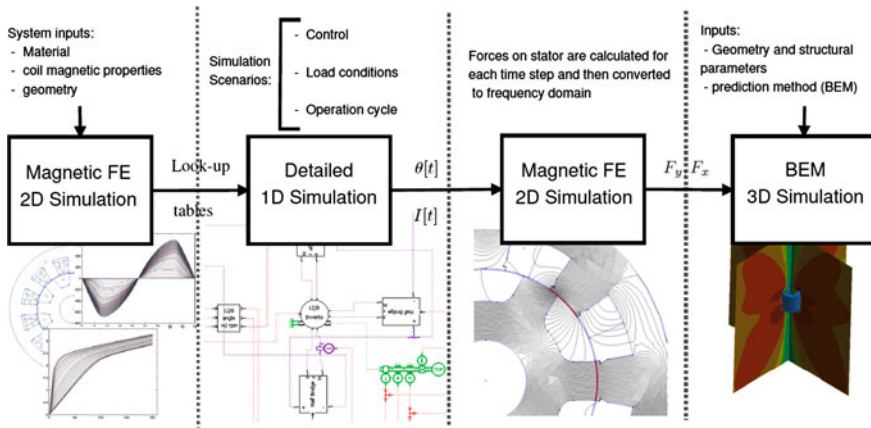
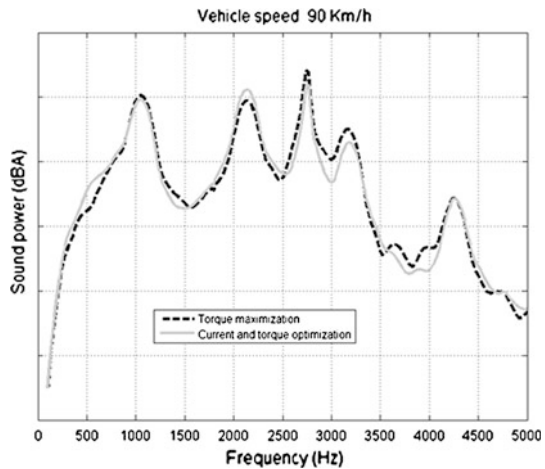


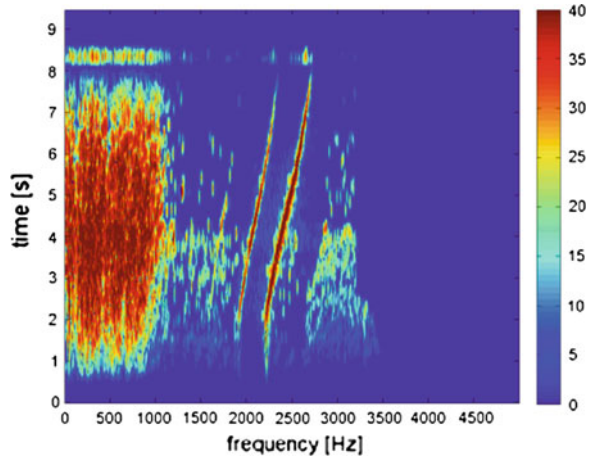
Fig. 5 Showing the acoustic optimization process for an SRM

Fig. 6 Showing the effect of torque and current optimization on the motor noise spectrum



How the vehicle should sound it much influences by the manufacturer and the brand identity it wishes to promote, contrast the different sounds of the Nissan Leaf and Audi R8 e-tron; both electric vehicles but with fundamentally different external noise signatures at low speeds, what is in common is the mix of broadband and harmonic components to both re-assure and alert VRU in the vicinity, in Fig. 7 the spectral map of the noise measured on an EV, attributed to the Nissan Leaf, showing these separate components clearly, broad band noise in the lower frequency and high frequency tonal components with modulation. The combination of these noises offers both awareness and directional movement feedback to VRU alerting them to the vehicles presence and trajectory.

Fig. 7 Low-speed drive-by signal analysis (YouTube source)



6 Propagation of Pedestrian Warning Sound

The prediction of the propagation of the generated sound to the location of the listener is an important challenge alongside the makeup of the sound itself. This propagation is frequency and space dependent, varying with the vehicle geometry, the location of the source on the vehicle, the road environment (sound obstacles and shaping profiles). Furthermore, masking effects of other traffic and ambient noise sources (wind, machinery etc.) have an impact on the pedestrian's perception of the sound. Approaches such as the Multipole BEM frequency and time domain methods and the Ray Tracing method can be used to simulate the directivity of the source and the level of noise in the car's surrounding, allowing an optimal source configuration and derivation of component and sound system specifications.

In a study carried out by LMS, the sound emitted by sources at 6 different positions on a representative car was calculated for two frequencies, 650 and 2,500 Hz, which according to [7] are within the most audible frequency ranges by human beings. A Boundary Element Modeling (BEM) approach was used using:

- 2D elements for discretizing the scattering surface of the vehicle.
- A high density microphone array was defined in front of the car as response grid.
- A symmetry plane was used to account for the road surface reflection.

As source model, monopole with unity amplitude corresponding to a power of about 101 dB was used (of course all results are fully scalable in level). Due to the size of the acoustic mesh, an advanced BEM solver, Fast Multipole BEM (or FMBEM), was used. The computation time was 3.5 h per frequency for 6 load cases on a 48 GB RAM dual-quad core windows 64 bit machine.

Some typical results for 3 sound source positions (bumper center, bumper extreme right, wheel housing right) are shown in Fig. 5 (650 Hz) and 6

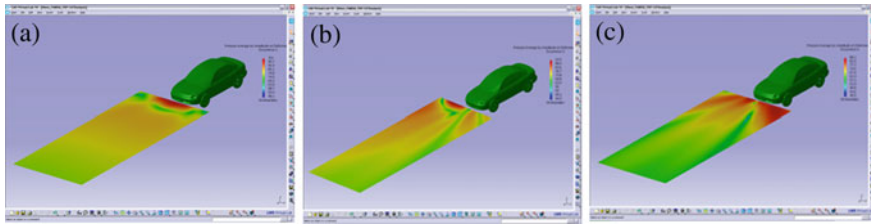


Fig. 8 Warning sound field 2500 Hz **a** Bumper center. **b** Bumper right. **c** Wheel housing

Table 1 Listener response values (dB)

Point	A	B	C	D	E	F
1	81	97	70	80	88	82
2	73	84	78	80	80	78
3	79	71	60	73	64	69
4	79	80	62	73	69	59
5	84	85	67	72	70	70

A = bumper center 650 Hz
 B = firewall 650 Hz
 C = wheel housing 650 Hz
 D = bumper center 2500 Hz
 E = firewall 2500 Hz
 F = wheel housing 250 Hz

(2,500 Hz). More simulations were conducted for sources at other positions allowing an optimization design (Fig. 8).

Table 1 and Fig. 9 summarize a number of acoustic response values at different locations.

These methodologies, which have proven their usefulness in pass-by-noise simulation, are shown to be instrumental for a proper configuration design of the sound source(s) to reach maximal warning effect in the danger zone with minimal annoyance for the environment or other traffic users. They also allow investigation of the noise propagation, the impact of the road and infrastructure objects, for example allowing optimization of the system design for perception by roadside listeners shielded by parked cars. Figure 10 shows an example of the impact of parked cars on the sound propagation cases of Fig. 11.

In order to perform the study of the actual sound perception, the sound simulation has to be linked to the source signal design and interpreted in terms of subjective perception and alert/warning level by actual listening tests. To realize this, the frequency domain BEM propagation results can be transformed into time domain filters as is applicable also in pass-by-noise testing. This approach is actually a time domain equivalent of the source contribution analysis methodology derived from Transfer Path analysis [8–10].

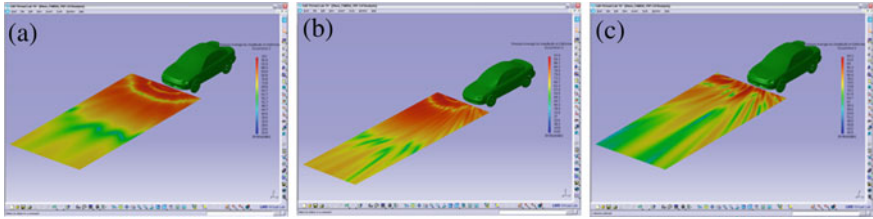


Fig. 9 Listener locations

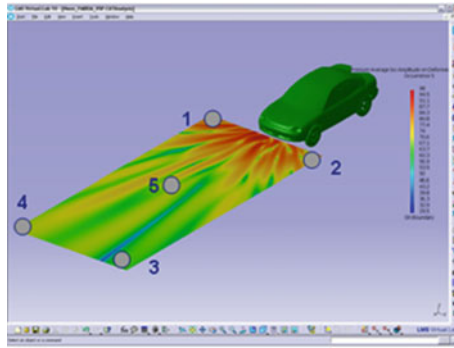


Fig. 10 Warning sound propagation in the presence of parked cars, 650 Hz **a** Bumper center. **b** Bumper right. **c** Wheel housing

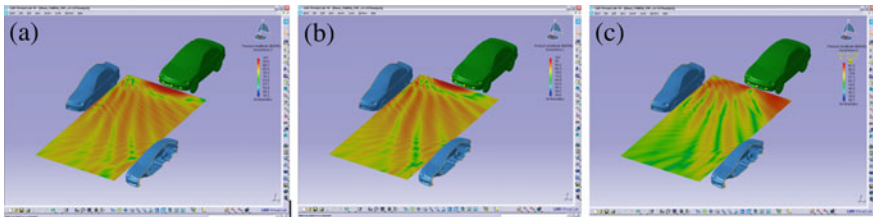


Fig. 11 Warning sound field 650 Hz **a** Bumper center. **b** Bumper right. **c** Wheel housing

Finally, in addition to the perceived sound emitted by the loudspeakers also the masking effect of the ambient sound is important. An interesting test that can be performed using the LMS tools is the synthesis of a number of internal combustion engines located next to the VRU in order to have a measurement of the masking effect of the ambient sounds. It is also possible to use recorded ambient sounds to simulate the passage of an electric vehicle in a pre-defined environment, i.e. an industrial district where the ambient sound can be complex and loud.

7 Conclusion

The paper has highlighted three key areas where Electric vehicle pose challenges in NVH. Comparisons of EV an ICE equivalents show the major differences between the vehicles and how these might be addressed or exploited with the goal of weight reduction; though ultimately road noise becomes the limiting factor. The choice of electric motor is currently limited but upcoming technology solutions to eliminate the need for expensive raw materials such as magnetic materials from motor design are maturing, the process discussed for mechanical and controls optimization of a SRM motor shows how 1D and 3D simulation tools can contribute effectively to this development for automotive applications. Finally the issue of sound propagation is addressed using 3D acoustic fast multi-pole BEM solvers to accurately predict the propagation and perception of warning sounds.

References

1. ERTRAC working group on Energy and Environment, European roadmap—future light-duty powertrain technologies and fuels science, version 30, August 2011
2. http://ec.europa.eu/clima/policies/transport/vehicles/cars/index_en.htm
3. Eisele G, Genender P, Wollf K, Schurmann G, Electric vehicle sound design—just wishful thinking? Proceedings of Aachen acoustics colloquium, Aachen (D), 22–24 Nov 2010
4. Le Nindre B, Guyader G (2010) EV-sound quality: customer expectations and fears—crucial NVH stakes, Proc Journée d'étude: NVH of hybrid and electric vehicles, Saint-Ouen (F), 4 Feb 2010
5. Florentin J, Durieux F, Kuriyama Y, Yamamoto T (2011) Electric motor noise in a lightweight steel vehicle. SAE 2011-01-1724
6. Santos F, Anthonis J, Van der Auweraer H (2012) Multi-physics NVH modeling: integrated simulation of a switched reluctance motor for an electric vehicle. IEEE Trans Industr Electron April 2012
7. Tabata T, Konet H, Kanuma T (2010) Development of nissan approaching vehicle sound for pedestrians, EVS-25 Shenzhen, China, 5–9 Nov 2010
8. Hallez R, De Langhe K (2009) Solving large industrial acoustic models with the fast multipole method, Proceedings of ICSV 16, Krakow (Poland)
9. Janssens K, Gajdatsy P, Gielen L, Mas P, Britte L, Desmet W, Van der Auweraer H, OPAX: a new transfer path analysis method using parametric load models, Mechanical systems and signal processing (MSSP), 25, No. 4, May 2011
10. Janssens K, Aarnoutse P, Gajdatsy P, Britte L, Deblauwe F, Van der Auweraer H (2011) Time-domain source contribution analysis method for in-room pass-by noise, SAE paper 2011-01-1609, Proceedings of SAE noise and vibration conference, Grand Rapids, Michigan, USA, 17–19 May 2011

Study on New Concept Powertrain for Range-Extended Electric Vehicles

Minghui Liu, Ziliang Zhao, Xingwang Yang, Chuan Li and Guopeng Luo

Abstract Range Extended Electric Vehicle (REEV) can extend driving range of EV by engine when battery SOC reaches its lower limit. But usual REEV powertrain is serial, fuel consumption of which is high in high speed driving condition when vehicle works in Range Extended mode. With the problem, a new concept powertrain for REEV is presented in this paper. It has better driving condition adaption, as it can work in serial or in parallel according to driving condition. Firstly, the configuration of new Range-Extended Electric Vehicle powertrain is proposed, which contains engine, BSG motor, clutch, traction motor and two-speed DCT. In Range Extended mode, it can work in serial or parallel. Two-speed DCT can adjust operating points of engine and traction motor. In addition, engine, BSG motor and traction motor can be downsized due to the use of clutch and DCT. Secondly, component parameters are designed according to vehicle requirements. Thirdly, control strategy of REEV based on the new concept powertrain is designed. Moreover, detail design for an A0 car is presented, and advantages of the new concept powertrain are evaluated by simulation. Evaluated by simulation, the new concept powertrain can meet requirements of Range Extended Electric Vehicle, and fuel economy of new concept powertrain is good in various driving cycles when vehicle works in Range Extended mode.

Keywords Range-extended electric vehicle (REEV) · Powertrain · Control strategy · Range-extended mode fuel economy · Driving condition adaption

F2012-B03-032

M. Liu (✉) · Z. Zhao · X. Yang · C. Li · G. Luo
China FAW CO., Ltd. R&D Centre, Changchun, China
e-mail: luogp05@gmail.com

1 Introduction

With the aggravation of oil crisis and environment crisis, it is more and more important to develop energy-saving and clean vehicles. Electric Vehicle is an effective way. Electric Vehicle can use electric energy to replace oil. And motor, the power source of Electric Vehicle, is in good accordance with ideal vehicle power source requirements. But due to the technology of battery, driving range of Electric Vehicle is limited, which restricts its development. In order to replace oil and ensure vehicle performance, it is necessary to develop Range Extended Electric Vehicle (REEV), which can use engine to extend driving range when battery SOC reaches its low limit [1].

Nowadays, the common approach is serial powertrain, which means adding an engine-generator which will work in serial in Range Extended Mode [2, 3]. But in high speed condition, the energy transfer efficiency of series driving is lower than that of direct engine driving. In order to improve fuel economy of Range Extended mode in various driving cycles, a new concept powertrain of Range Extended Electric Vehicle is proposed in this paper.

2 Powertrain Structure

The new concept powertrain is shown in Fig. 1. It contains an engine, a BSG motor, a traction motor, a Dual Clutch Transmission (DCT), a clutch and a battery. DCT is placed after traction motor. Engine is connected with traction motor by clutch. And BSG motor is connected with engine by belt. Traction motor is used to meet vehicle dynamic performance requirements. Engine is used to meet maximum speed requirement in Range Extended mode. BSG motor is used to meet energy requirement in low speed driving condition in Range Extended mode. DCT has two sets of gears. High speed gears are used to meet requirements of direct engine driving. Low speed gears are used to meet dynamic performance requirements.

When battery SOC is normal, the new concept powertrain works in pure electric driving condition. When battery SOC is low, the new concept powertrain can work in serial or in parallel. If vehicle speed or desired torque is low, it works in serial. Engine and BSG motor work in their optimal point. If vehicle speed is high, it works in parallel. Because engine is small in REEV, desired torque is in engine economic zone in high speed.

Comparison of different powertrains of REEV is shown in Table 1.

As shown in Table 1, in Range Extended mode, if vehicle speed is low, serial powertrain and the new concept powertrain can work in serial, fuel economy of which is better than that of direct engine driving. If vehicle speed is high, parallel powertrain and the new concept powertrain can work in parallel, fuel economy of which is better than that of series driving. As there is a generator in serial

Fig. 1 New concept powertrain of range extended electric vehicle

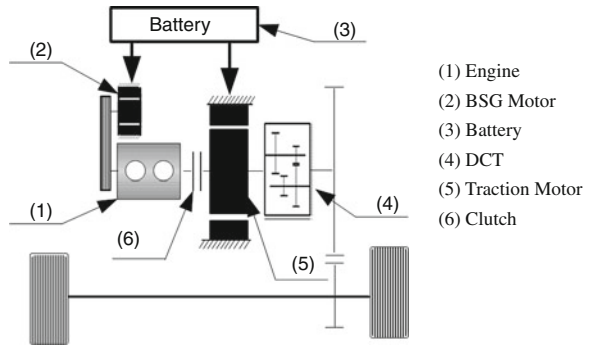


Table 1 Comparison of different powertrains of REEV

Powertrain		Serial powertrain	Parallel powertrain	New concept powertrain
Structure				
Fuel economy in range extended mode	Low speed conditions	Good	Bad	Good
	High speed conditions	Bad	Good	Good
Driving performance in range extended mode	Electric accessory usage	Not limited	Limited	Not limited
	Electric start	Always	Sometimes	Always
Component requirements	Power interrupt	No	Serious	Slight
	Traction motor maximum torque	High	Low	Medium
	Traction motor maximum speed	High	Low	Medium
	Engine	Big	Small	Small
	Generator	Big	No	Small
	Gearbox	No	Multi- speed	Two-speed

powertrain and the new concept powertrain, vehicle can always be started by motor and electric accessories usage is not limited. In parallel powertrain, vehicle must be directly driven by engine in total speed range. So multi-speed gearbox is necessary, which leads to serious power interrupt. The new concept powertrain only needs a two-speed gearbox because engine only drive vehicle directly in high speed, so power interrupt is slight.

Table 2 A0 Car performance indexes

Performance index	Requirement
Maximum speed in electric driving	>140 km/h
Maximum speed in range extended mode	>140 km/h
Maximum gradeability	30 %
0 ~ 100 km/h acceleration time	<13.5 s
Electric driving range	>60 km

Due to the role of gearbox, requirements of maximum torque and maximum speed of traction motor in parallel powertrain and the new concept powertrain is lower than those in serial powertrain. Engine is used to meet maximum speed in Range Extended mode. Because energy transfer efficiency is lower in serial powertrain, engine in serial powertrain must be bigger than that in parallel powertrain and new concept powertrain. In serial powertrain, generator must meet the maximum speed power demand while in new concept powertrain generator (BSG motor) only need to meet driving power demand in low speed condition. Motor performance is in good accordance with vehicle power requirements, so serial powertrain doesn't need a gearbox.

According to analysis above, the new concept powertrain has more advantages than serial powertrain and parallel powertrain. New concept powertrain has good fuel economy in various driving conditions, good driving performance and more balanced component matching.

2.1 Component Parameters Matching

In this paper, an A0 car with new concept powertrain is designed. Table 2 shows the performance requirements of the car.

Table 3 shows component parameters matching principles of the new concept powertrain.

(1) Traction Motor

The speed profile of vehicle acceleration can be formulated as expression (1).

$$v = v_m \left(\frac{t}{t_a} \right)^x \tag{1}$$

In the expression, v_m means final speed of acceleration, t_a means acceleration time, x represents speed profile characteristics. In normal situations, x is 0.5.

The maximum desired power occurs in final stage of acceleration. So the maximum power of traction motor can be got by expression (2).

Table 3 Component parameter matching principles

Component	Parameter	Design principles
Traction motor	Maximum power	Vehicle acceleration performance
	Maximum speed	Vehicle maximum speed
	Maximum torque	Vehicle gradeability
Engine	Maximum power	Vehicle maximum speed in range extended mode Accessories power
	Maximum speed	Vehicle maximum speed
BSG Motor	Rated power	Vehicle average driving power Accessories Power Engine fuel economy map
	Maximum speed	Engine maximum speed
	Low-speed gear ratio	Vehicle dynamic performance
DCT	High-speed gear ratio	Engine directly driving
	Capacity	Electric driving range
Battery	Maximum power	Maximum power of traction motor

$$P_{Max} \geq \frac{1}{\eta} v_m \left(\delta m \frac{v_m}{2t_a} + \frac{1}{2} C_d A \rho v^2 + mgf \right) \tag{2}$$

In the expression, η means vehicle transmission efficiency, δ means vehicle correction coefficient of rotating mass, m means vehicle mass, C_d means drag coefficient, A means frontal area, ρ means air density, f means rolling resistance coefficient.

So the maximum power of traction motor is determined as 75 kW.

Because vehicle maximum speed in Range Extended mode is the same as that in electric driving mode, maximum speeds of traction motor and engine are similar. Maximum speed of traction motor is defined as 6,000 rpm.

Permanent magnet motor is chosen as traction motor, whose ratio of maximum speed to rated speed is 2 ~ 3. So traction motor rated speed is defined as 2,400 rpm, and its maximum torque is 300 Nm.

(2) Engine

Engine power is designed to meet the demand of maximum speed cruise in Range Extended mode and accessories power. It can be determined as expression (3).

$$P_e \geq \frac{1}{\eta_1} v \bullet \left(mgf + \frac{C_D A}{2} \rho v^2 \right) + \frac{1}{\eta_2} P_{acc} \tag{3}$$

So, Engine power is determined as 43 kW.

(3) BSG Motor

BSG motor is used to meet the demand of average driving power and accessories power in low speed situation, as shown in expression (4). And engine fuel economy when BSG works is also considered.

$$P_{BSG} \geq \frac{1}{\eta_M \eta_0} \frac{\int_{P>0} (\delta m a + mgf + \frac{1}{2} C_D A v^2) v dt + P_{acc}}{t_{P>0}} \quad (4)$$

So, BSG motor rated power is set as 12 kW.

(4) DCT

Engine maximum power speed is appropriately 5,000 rpm. According to the relationship between vehicle speed and engine speed, high-speed gear ratio of DCT can be got by expression (5).

$$i_h = \frac{n_{Max}/60/i_0}{v_{Max}/2\pi r} = 0.96 \quad (5)$$

So, high-speed gear ratio can be set as 1 because of high transmission efficiency of direct gear. Low-speed gear ratio of DCT need to meet gradeability and acceleration time requirements, as expression (6) and (7).

$$i_l T_{Max} \geq \frac{(mgf + mgi)r}{\eta i_0} \quad (6)$$

$$\delta m \frac{dv}{dt} = T_m \left(\frac{v}{2\pi r} i_0 i_l \right) \eta i_0 i_l / r - mgf - \frac{1}{2} C_D A \rho v^2 \quad (7)$$

So low-speed gearratio can be set as 1.85.

(5) Battery

The capacity of battery is determined by electric driving range requirement, as expression (8).

$$E \geq \frac{1}{\eta \Delta SOC} \frac{P_{avr0} \cdot t_{P>0}}{\int v dt} s_0 \quad (8)$$

So battery energy is 12 kWh.

2.2 Control Strategy

The control strategy frame is shown as Figure 2.

As Figure 2 shows, the control strategy of REEV consists of EV mode and Range-Extended (RE) mode. When SOC is high, REEV works in EV mode. In EV mode, Engine and BSG motor don't work and the driving energy comes totally from battery. When SOC is low, REEV works in Range-Extended mode, which is the main task of this paper. In RE mode, there are two energy paths. If vehicle speed or required torque is low, REEV works in serial path, in which engine and BSG works in their optimal point. Serial path contains two states, serial driving and electric driving, determined by SOC. If vehicle speed is high and required

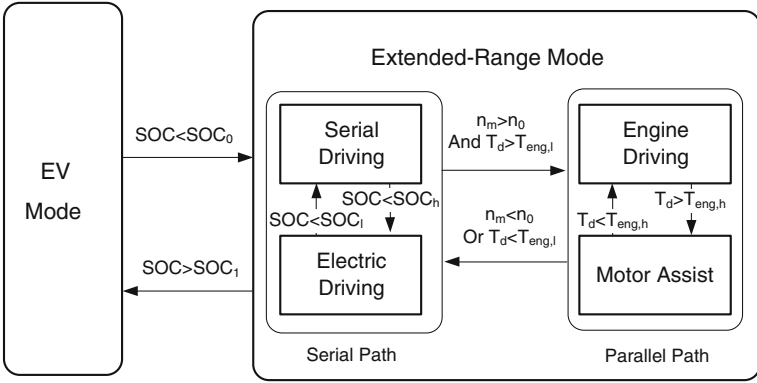


Fig. 2 Control strategy frame

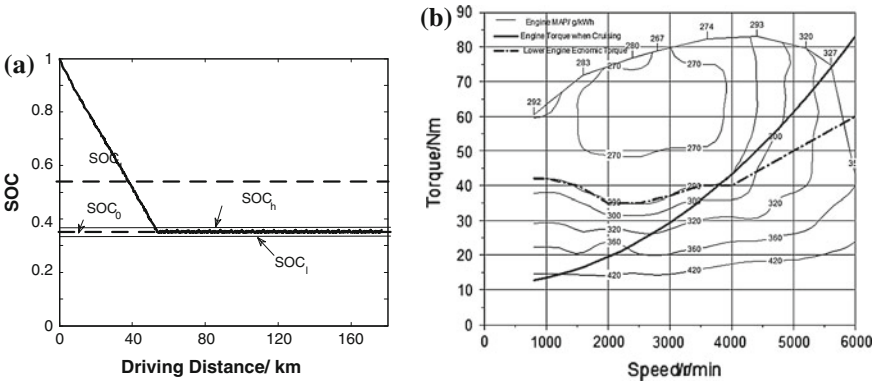


Fig. 3 Control strategy of range-extended mode

torque is in engine economic zone, REEV works in parallel path, and the fuel economy is good.

Figure 3 shows details of RE mode control strategy. In RE mode, SOC is sustained between SOC_1 and SOC_h , and engine works between lower limit of its economic zone and its maximum limit, in which fuel economy of engine is good. As engine is downsizing in RE powertrain, required driving torque is always in engine’s economic zone in comparison with conventional cars.

In engine driving state, engine torque is determined as expression (9).

$$T_e = \begin{cases} \text{Max}[\text{Min}(T_{eng,h}, T_{eng,opt} + f_{SOC}(SOC)), T_{eng,l}] & SOC < SOC_h \\ T_d & SOC \geq SOC_h \end{cases} \quad (9)$$

In motor assist state, engine torque is determined as expression (10).

Table 4 Simulation Performance of REEV based on new concept powertrain

Performance index	Serial powertrain	New concept powertrain	Comparison
Maximum speed/km/h	>140	>140	-
0-100 km/h acceleration time/s	12.93	13.05	-
Gradeability/ %	32	32	-
EUDC electric distance/km(70 % SOC)	64	64	-
Fuel consumption in RE mode (NEDC)/L/100 km	6.91	6.23	-9.8 %
Fuel consumption in RE mode (ECE)/L/100 km	5.56	5.6	+0.7 %
Fuel consumption in RE mode (EUDC)/L/100 km	7.28	6.0	-17.6 %

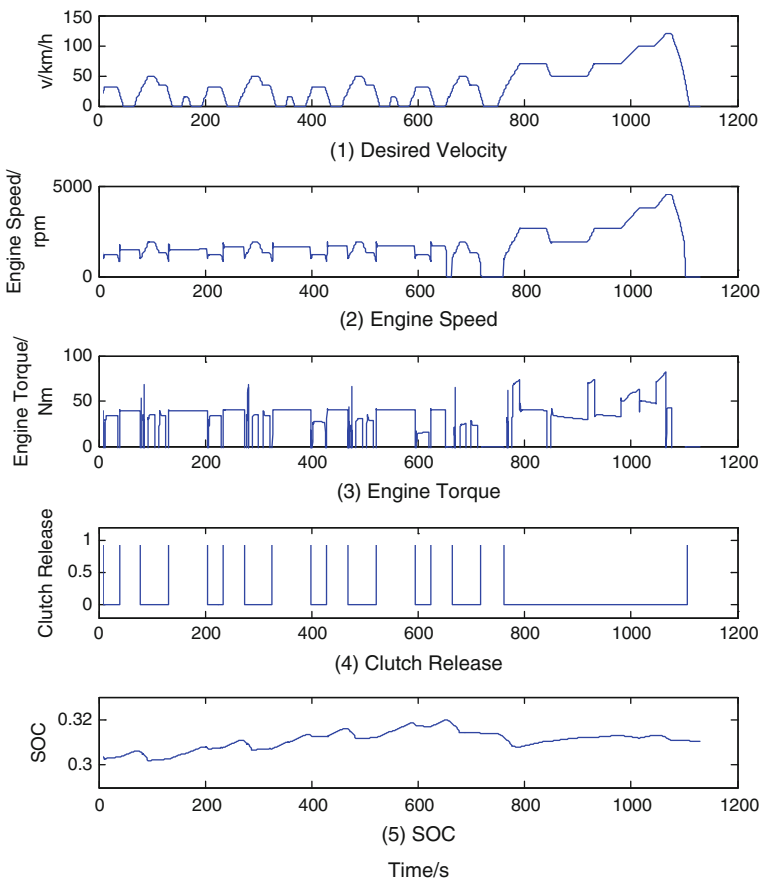


Fig. 4 NEDC driving curves of new concept powertrain

$$T_e = \begin{cases} T_{eng,opt} & SOC > SOC_0 \\ T_{eng,Max} & SOC \leq SOC_0 \end{cases} \quad (10)$$

2.3 Simulation Results

Table 4 shows simulation performance of designed REEV based on new concept powertrain by Cruise and Simulink.

Simulation results show that fuel economy of REEV based on new concept powertrain is better than that based on serial powertrain, and the dynamic performance can be ensured. In ECE cycle, new concept powertrain has similar fuel economy with serial powertrain, as they both work in serial path. In EUDC cycle, fuel economy of new concept powertrain is improved by 17.6 %, as the system efficiency of parallel path is higher than that of serial path. In EUDC cycle, which combined low speed and high speed driving, fuel consumption of new concept powertrain is 9.8 % less than that of serial powertrain.

Figure 4 shows the RE mode profiles of new concept powertrain in NEDC cycle.

Figure 4 shows in low speed situation, clutch is disengaged, and REEV works in serial path, while in high speed situation, clutch is engaged, and REEV works in parallel path. Engine speed and engine torque curves are also in accordance with design principles.

3 Conclusion

From this paper, there are two conclusions we may get.

- (1) New concept powertrain of Range Extended Electric Vehicle designed in this paper is able to meet requirements of Range Extended Electric Vehicle.
- (2) In Range-Extended Mode, new concept powertrain can get good fuel economy in various driving cycles.

References

1. Christian B, Matthias K (2011) Electric vehicle with or without range extender who is the driver—technology, customer or legislation? Internationales Wiener motorensymposium 2011
2. Ping H, Joerg S, Hao Z (2009) Strategy of range extending electric vehicle based on user's approval. The 25th world battery, hybrid and fuel cell electric vehicle symposium and exhibition, 2009
3. Zhou S, Niu J, Chen F (2011) A study on powertrain design and simulation for range-extended electric vehicle. *Automot Eng* 33(11):2011

Parameters Optimization of PHEV Based on Cost-Effectiveness from Life Cycle View in China

Jiuyu Du, Hewu Wang and Mingguo Ouyang

Abstract Plug-in hybrid electric vehicle (PHEV) technology combining the merits of Battery electric vehicle (BEV) and Hybrid electric vehicle (HEV), has the potential to reduce greenhouse gas (GHG) emissions, and petroleum consumption in the transportation sector. However, the cost-benefit of PHEVs mainly determined by battery technology, optimal powertrain design, and vehicle kilometers daily traveled and charging habits. Targeting to cost-benefit, the optimal design method was presented, taking battery cycle life Vs DOD data, driving data, battery performance data into consideration. The method provided optimal vehicle designs to realize minimum life cycle cost, and maximum petroleum consumption under different scenarios. For A-segment equivalent PHEV (similar to a F3DM), under Shanghai urban driving conditions, it can be find that while PHEVs with present traction battery technology, 30 km AER was most life cycle cost-effective to obtain maximum petroleum displacement based on Shanghai driving data. Large capacity battery lead to petroleum displacement not so much as cost increased. At China electricity price off peak, Li-ion battery pack costs must fall below $\text{€}2.0/\text{Wh}$ to be cost competitive with equivalent internal combustion engine vehicles (ICEs).

Keywords Plug-in hybrid · Cost-benefit · Parameters optimization · All electric range · Vehicle kilometers daily traveled

F2012-B03-037

J. Du (✉) · H. Wang · M. Ouyang (✉)

State Key Laboratory of Automotive Safety and Energy, Tsinghua University,
Beijing 100084, China

e-mail: dujiuyu@tsinghua.edu.cn

M. Ouyang

e-mail: cerc-cvc@tsinghua.edu.cn

J. Du · H. Wang · M. Ouyang

China Automotive Energy Research Center (CAERC), Beijing, China

1 Introduction

With rapid development of economy and urbanization, production and stock of vehicle increased sharply. By the end of 2011, the automotive production has been increased to 18.505 M [1], which aggravated the issues of energy security and environmental pollution of urban area became more seriously. Accordingly, the crude oil dependence of China has reached to 56.5 % [2]. The GHG emission mainly comes from vehicles' tailpipe in urban area [3].

Electric powertrain has been considered as solution to energy consumption and emission of GHG in urban area. Electric vehicles (including hybrid electric vehicle, plug-in hybrid electric vehicle, battery electric vehicle, fuel-cell electric vehicle) can effectively reduce fuel consumption and exhaust emission, and developing electric powertrain technologies has been chose as national sustainable transportation strategy. Pure electric vehicle can realize 100 % alternative to crude oil. However, subjecting to the key technologies limitation, electric powertrain vehicles is less competitive to conventional vehicles.

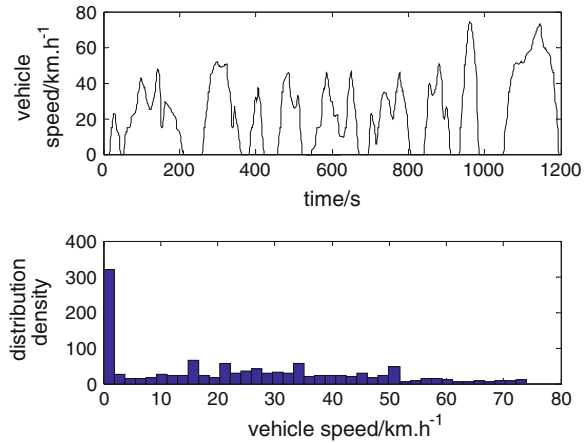
A PHEV has been defined by SAE [4] as: "A hybrid vehicle with the ability to store and use off-board electrical energy in the RESS." These systems are, in effect, an incremental improvement over the HEV, with the addition of a large battery with greater energy storage capability, a charger, and modified controls.

So PHEV technology integrated the advantages of BEV and HEV, will be the best choice of transit powertrain technology to all electric driving stage, and it is considered a potential near-term approach to addressing global warming and dependency on foreign oil in the transportation sector of China, as the cost, size, and weight of batteries are reduced.

To design a PHEV powertrain, more battery capacity will lead to more displacement of fuel, in other words, increased AER will result in a larger portion of travel propelled by electrical energy instead of gasoline, however, higher cost and lower system energy efficiency. Distance the vehicle is driven between charges plays an important role in determining the PHEVs advantage: Vehicles that are charged frequently can drive most of their miles on electric power, even with a relatively small battery pack, while vehicles that are charged infrequently require larger battery packs to cover longer distances with electric power. Meanwhile, at present, the PHEV testing standards is version translated from that of EU. Because the driving cycle and personal daily kilometer traveled in China is totally different from EU's, so how to design powertrain parameters optimized based on the AER, maximum speed, driving cycle is challenging problem.

The potential for PHEVs to displace fleet petroleum consumption derives from several factors [5, 6], including duty cycle, daily kilometer distribution, electric powertrain technology and components optimal sizing, etc.

Fig. 1 City duty cycle of passenger car in China



2 Duty Cycle of Passenger Car in China

To design electric vehicle more cost-benefit, parameter associated with dynamic performance of electric car should be designed economical based on the operating condition such as duty cycle of electric car in urban area of China.

From Fig. 1, it can be seen that the maximum speed is no more than 80 km/h.

3 Driver Behavior

To accurately calculate fuel costs for selected vehicles it is important to know how a user drives and how much of the vehicle's total mileage is driven using each fuel type. This is especially important for plug-in hybrid vehicles, which operate using both gasoline and electricity from the grid. In this study, we used data of vehicle kilometers daily traveled in Shanghai to investigate the optimization method of PHEV targeting cost-benefit. The characteristics of daily kilometers driven distribution in Shanghai was shown in Fig. 2.

4 Components Sizing

Based on the driving cycle shown in Fig. 1, the parameters of traction motor could be determined, thereby the power of traction battery was known. The parameters of prototype electric sedan chose to analyze were shown in Table 1.

Fig. 2 VKDT of Shanghai

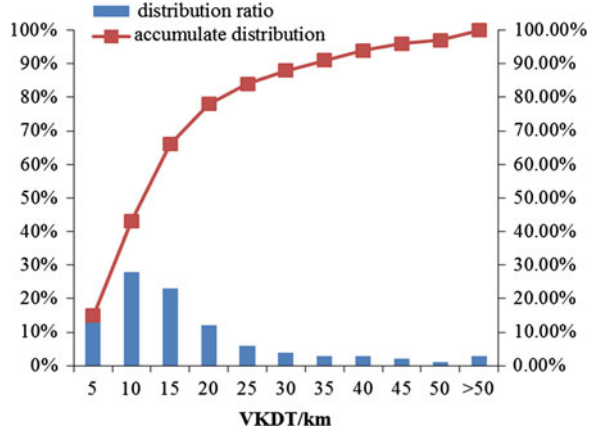


Table 1 Electric sedan parameters assumptions

Items	Values
Glider mass, kg	900
Curb mass, kg	1,350
Gross vehicle mass, kg	1,800
C_D	0.35
A	2
f	0.012
Acceleration time, s	0–50 km/h: 9(CD) 50–100 km/h: 12(CS)
Gradeability, %	20

5 Electric Motor

Based on the vehicle dynamic theory, the motor power is

$$P_m = \frac{1}{\eta_T} \frac{1}{\eta_B} \frac{1}{\eta_G} \left(\frac{1}{3600} \left(mgfu_a + mgiu_a + m\delta u_a \frac{du_a}{dt} \right) + \frac{C_D A u_a^3}{76140} \right) \quad (1)$$

Where η_T is efficiency of transmission system, η_B is charging efficiency of traction battery, η_G is efficiency of electric motor; A is frontal area, m^2 ; m is curb weight of electric car, kg; u_a is speed of vehicle, $km \cdot h^{-1}$; g is gravity acceleration, $m \cdot s^{-2}$; C_D is drag coefficient; f is rolling resistance coefficient; i is gradeability; δ is rotary inertia conversion factors.

6 Traction Battery

The capacity of traction battery is:

$$E_b = \frac{\frac{m_{\text{glider}} g S_{\text{AER}}}{3600 \eta_{u_a}} \left(f u_a + i u_a + \delta \frac{u_a}{g} \frac{d u_a}{d t} \right) + \frac{S_{\text{AER}}}{\eta_{u_a}} \frac{C_D A u_a^3}{76140}}{1 - \frac{g S_{\text{AER}}}{3600 \Delta E (1 - \text{SOC}_{\text{Min}}) \eta_{u_a}} \left(f u_a + i u_a + \delta \frac{u_a}{g} \frac{d u_a}{d t} \right)} \quad (2)$$

Electricity consumption is:

$$E_{\text{ele}} = \frac{1}{\eta_{\text{ep}} \eta_{\text{lm}}} \int_0^T P_{\text{m}} dt - \eta_{\text{B}} \eta_{\text{G}} \eta_{\text{T}} \int_0^T P_{\text{reg}} dt \quad (3)$$

Where P_{reg} is regenerative power, kW; η_{ep} is efficiency of power electronics.

7 Ownership Cost Analysis

For the calculations lifecycle ownership cost of PHEV, each driving type is further broken down into kilometers on electricity and kilometers on gasoline. The user may select one of three recharging schedules for normal daily use driving—twice per day, once per day, or every other day. When fully charged, the PHEV is capable of operating on grid-derived electricity for a limited number of kilometers. The potential average daily kilometers driven on electricity is set at AER times the number of recharges per day (RPD). If the normal daily driving mileage is greater than the potential daily miles on electricity (as defined by RPD times AER), the PHEV uses electrical power until the batteries are depleted, and gasoline is used for the remainder of the daily miles. The city-highway mileage split is assumed to be the same for the miles on electricity and the miles on gasoline. If the value of RPD times AER exceeds the normal daily mileage, only electric power is required for normal daily driving.

The ownership cost composed of energy consumption, battery displacement, maintenance, tires, insurance, license, and registration. Because the cost of maintenance, tires, insurance are relatively fixed and low [7] (as Fig. 3), so this study, they are not taken into consideration.

The lifecycle ownership cost was

$$C_{\text{oc}} = C_{\text{ele}} + C_{\text{gas}} + C_{\text{bat_chg}} \quad (1)$$

Because of the limitation of traction battery cycle life, during the PHEV operation life, the battery replacement is required. The cost of that was

$$C_{\text{bat_chg}} = \frac{\delta_{\text{bat}} E_b S_{\text{VKDT}}}{L_{\text{cyc}} (\text{DOD}\%) S_{\text{AER}}} \quad (2)$$

The calculation of electricity consumption in CD mode was divide into two scenarios.

If $S_{\text{AER}} \geq S_{\text{VKDT}}$, the cost functions are

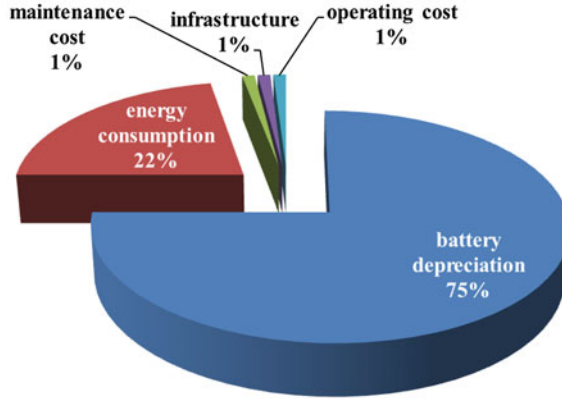


Fig. 3 Cost structure of some typical PHEV

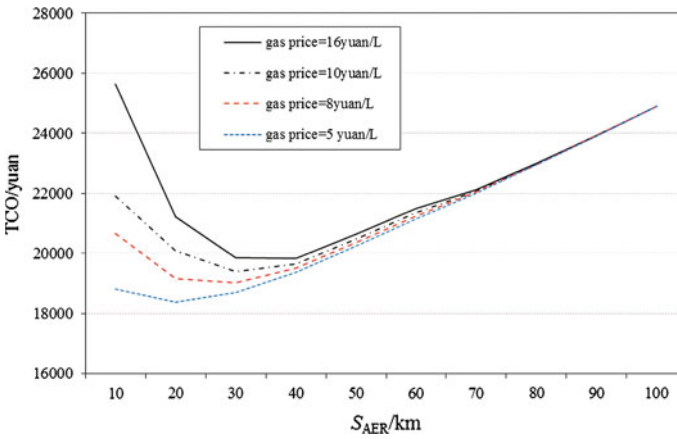


Fig. 4 TCO of PHEV under gasoline price scenario

$$C_{ele} = nNS_{KDT}E_E P_{elec} \quad (C_{gas} = 0) \tag{3}$$

$$C_{bat_chg} = \frac{\delta_{bat} E_b S_{VKDT}}{L_{cyc}(DOD\%)S_{AER}} \tag{4}$$

If $S_{AER} < S_{VKDT}$, the cost functions are

$$C_{ele} = nNS_{AER}E_E P_{ele} \tag{5}$$

$$C_{gas} = nN(S_{VKDT} - S_{AER})FE_{gas}P_{gas} \tag{6}$$

$$C_{bat_chg} = \frac{\delta_{spb} E_b}{L_{cyc}(100\%DOD)} \tag{7}$$

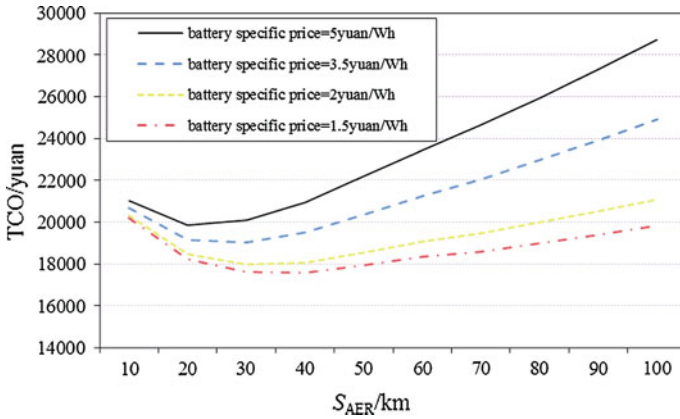


Fig. 5 TCO of PHEV under battery specific price scenario

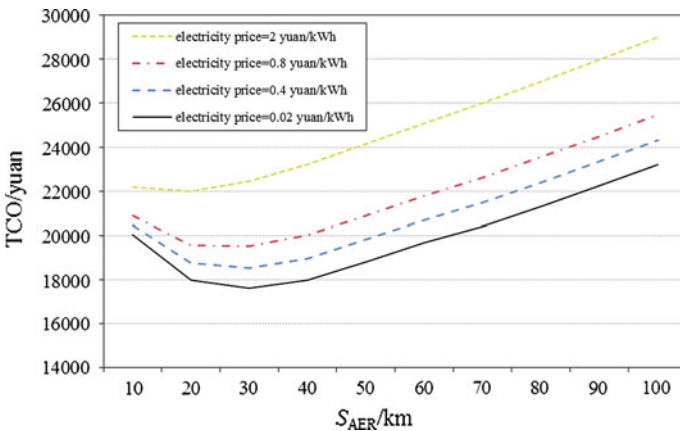


Fig. 6 TCO of PHEV under electricity price scenario

Where C_{oc} is the ownership cost of the EV in operating life, C_{ele} is the cost of electricity consumption, C_{bat_chg} is the cost of traction battery replacement, Yuan/pack; S_{AER} is all electric range of EV, km; δ_{bat} is the specific price of traction battery, Yuan/Wh; n is operating days in a year, $n = 360$; N is the operating life in years of PHEV, $N = 15$ years; C_{cpis} capital price of PHEV, yuan; δ_{spb} is specific price of traction battery, yuan/kWh; E_E is electricity consumption ratio, kWh/100 km; P_{ele} is price of electricity, Yuan/kWh; r is general discount rate; $L_{cyc}(DOD\%)$ is function of cycle life associated with DOD (Depth of Discharging); FE_{gas} is fuel economy of CS mode of PHEV, L/100 km; P_{gas} is price of gasoline, yuan/L; S_{VKDT} is vehicle traveled distance daily in kilometers, km.

8 Conclusions

Based on the VKDT of Shanghai city and passenger car city cycle, the TCOs of PHEV subjected to different parameter of AER under different scenarios were performed (Figs. 4, 5, 6).

From above analysis, it could be concluded:

- 1) Gasoline price affects TCO greatly, and lower price corresponds to lower optimal value of AER.
- 2) When gasoline price was 8 yuan/L, the optimal AER would be 25 km targeting to cost-benefit, and when gasoline price increased to 16 yuan/L, accordingly the optimal AER would be 30 km.

Traction battery specific and cycle life is the most important affective factors to TCO of PHEV.

When the specific cost of battery was decreased to 1.5 yuan/Wh, the trend almost was that more AER leads to better cost-benefit. At present level, the AER 28 was recommended.

- 3) The electricity price has minimum impact on TCO of PHEV

From the price of commercial use electricity to off-peak electricity price, the optimal AER were 25–30 km.

Acknowledgments Thanks to the subsidy of International S&T Cooperation Program of China (ISTCP):2010DFA72760

References

1. CAAM. The automotive industry production and sales by the end of 2011 [EB/OL], 2012-01-10/2012-07-18. <http://www.caam.org.cn/zhengche/20120112/1605066964.htm>
2. Sina. Import of crude oil increased by 6% and oil dependence increased to 56.5% in 2011[EB/OL], 2012-01-13/ 2012-07-20. <http://finance.sina.com.cn/chanjing/cywx/20120113/023011191685.shtml>
3. MEP. China Vehicle Pollution Prevention Annual Report (2010) (English abstract in Chinese) [R], Beijing: MET, 2010.
4. SAE J1715. Hybrid Electric Vehicle (HEV) & Electric Vehicle (EV) Terminology [S]. U.S.SAE 2008
5. Simpson A (2006) Cost-benefit analysis of plug-in hybrid electric vehicle technology [z]. Yokohama, Japan
6. Kloess M (2009) The role of plug-in-hybrids as bridging technology towards pure electric cars: an economic assessment [z]. Shenzhe, China
7. DAE of THU. Survey of industry of electric vehicle in China [R]. Beijing. 2010.

Approach of Gasoline Hybrid Technology for “95G CO₂/KM” Emissions Regulation

Jun Li, Ziliang Zhao, Yihong Zheng, Minghui Liu and Heqi Liang

Abstract In order to meet the increasingly strict regulations of CO₂ emissions limits, gasoline hybrid technology for “95 g CO₂/km” emissions regulation was analyzed in this paper. Study of energy-efficient technology shows that full hybrid technology, combined with lower rolling resistance and reducing drag technology is still difficult to achieve “95 g CO₂/km” emissions target. Plug-in hybrid technology is a better way to achieve this target. In this paper, aimed at “95 g CO₂/km” emissions target, appropriate motor and battery were chosen, the control strategy under CD mode was studied to develop a more reasonable powertrain system, and finally the purchase cost and daily using cost of vehicle were analyzed.

Keywords “95 g CO₂/km” Emissions · FAW-TMHTM System · Plug-In · Powertrain optimization · Cost analysis

1 Introduction

Currently Chinese automobile industry is facing a series of challenges such as large amount of cars, shortage of oil, and increasingly strict emissions regulations. Regulations of CO₂ emissions limits at different stages in Europe and China are

F2012-B03-038

J. Li (✉) · Z. Zhao · Y. Zheng · M. Liu · H. Liang
China FAW Co., Ltd R&D Center, Chengdu, China
e-mail: lj_qy@faw.com.cn

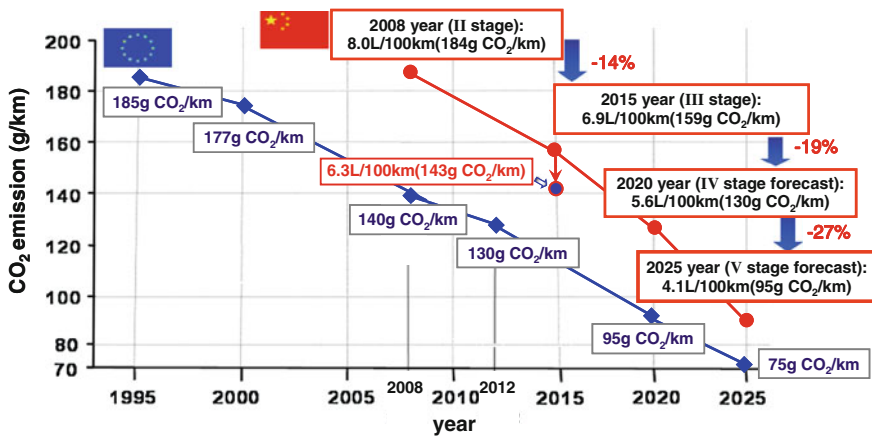


Fig. 1 China and Europe emissions regulations

shown in Fig. 1 [1], among which emissions limit is expected to be 95 g CO₂/km in Europe in 2020, and it is expected to implement the regulation in 2025 in China.

All these challenges and government's support promoted the development of electric vehicles. However, currently battery electric vehicle and fuel cell electric vehicle are not mature enough, and the gasoline engine is still the main development trend in China. In this paper, the powertrain topology is based on FAW-TMHTM (Twin-Motor Hybrid) system, and the vehicle is based on FAW existing A-class platform. From the perspective of energy, system efficiency, control strategies and costs, the approach of gasoline hybrid technology to meet "95 g CO₂/km" emissions regulation is introduced.

2 Technical Approach Analysis

2.1 Vehicle Topology and Parameters Input

Figure 2 shows FAW-TMHTM (Twin-Motor Hybrid) configuration, which has obtained invention patent in both China and United States. It has all hybrid functions such as start/stop, electric driving, series driving, boost, engine load shift and regenerative braking. The fuel-efficiency is equivalent to that of a few configurations which have been widely applied in the world, e.g. Toyota's THS.

Table 1 shows parameters of the baseline HEV. Based on this vehicle, gasoline hybrid technology for "95 g CO₂/km" emission target was analyzed in this paper. The curb weight of this vehicle is 1260 kg, so the fuel consumption target is 3.8 L/100 km according to "95 g CO₂/km" emissions regulation, as shown in Fig. 3.

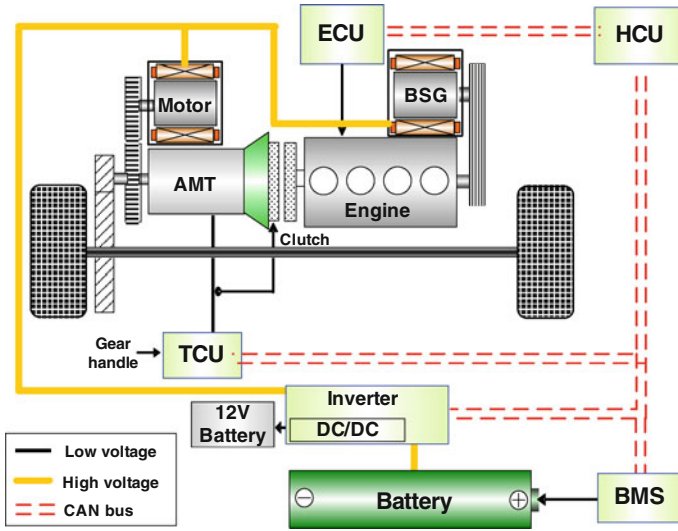


Fig. 2 FAW-TMH™ full hybrid configuration

Table 1 Basic parameters of the baseline HEV

Item		Baseline HEV
Vehicle	Curb weight, kg	1,260
	Frontal area, m ²	2.1
	Drag coefficient	0.33
	Rolling radius, mm	280
Engine	Type and displacement	2 cylinders 1.0T-GDI
	Nominal power, kW/rpm	72/5,500
	Nominal torque, Nm/rpm	140/2,000 ~ 4,500
Transmission	Gearbox type	Five-speed AMT
Drive motor	Motor type	Permanent magnet synchronous
	Power/torque, kW/Nm	20/220
	Maximum speed, rpm	8,300
BSG motor	Motor type	Permanent magnet synchronous
	Power/Torque, kW/Nm	10/50
Battery package	Battery type	Ni-MH
	Capacity, Ah	6
	Nominal voltage, V	288
	Mass of battery system, kg	70

2.2 Preliminary Analysis of Fuel Consumption Target

Figure 4 shows the power demand for vehicle driving in NEDC cycle. The positive areas represent energy required to propel vehicle, and the negative areas represent

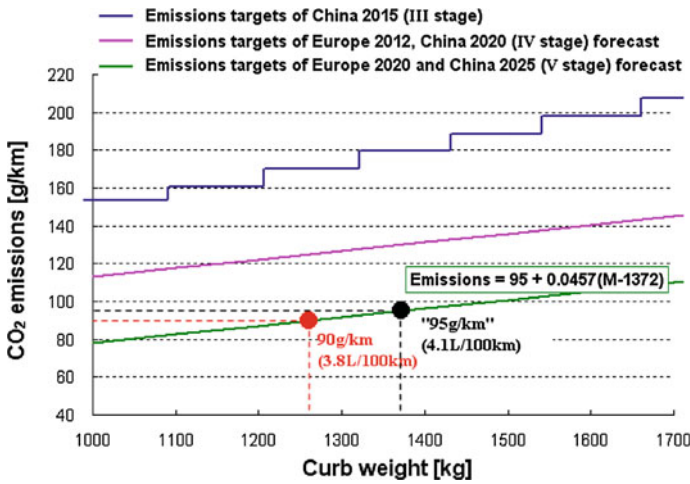


Fig. 3 Emissions regulations and fuel consumption target

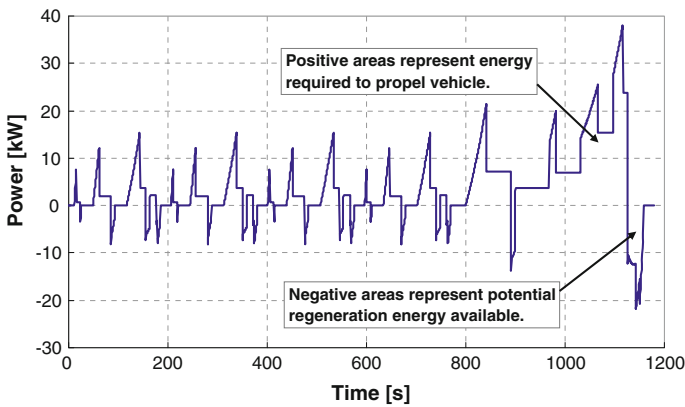


Fig. 4 Power demand curve in NEDC cycle

potential regeneration energy available when braking. As we know the average fuel density of 93 # gasoline is 0.725 kg/L, and the average calorific value is 43.5 MJ/kg. Required driving energy in NEDC cycle is 5265 kJ, and potentially regeneration energy is 1041 kJ, so in order to achieve the 3.8L/100 km target, the needed average fuel consumption of engine is 206 g/kWh if there is no recovery of braking energy (thermal conversion efficiency is about 40.2 %), and the needed average fuel consumption of engine is 256 g/kWh if the potential braking energy is fully recovered (thermal conversion efficiency is about 32.3 %). The conversion efficiency of electric drive systems was not considered in above calculation. Obviously it is difficult to achieve 3.8L/100 km target with hybrid technology because of the thermal conversion efficiency of the existing gasoline engines.

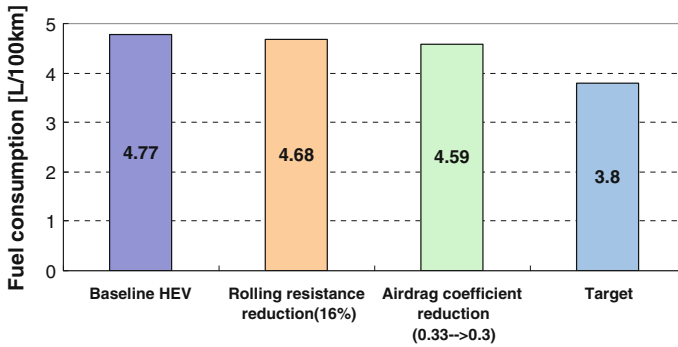


Fig. 5 Fuel consumption simulation results

Table 2 Three selected batteries for PHEV

Battery parameters	Battery 1 (PHEV1)	Battery 2 (PHEV2)	Battery 3 (PHEV3)
Battery energy, kWh	3	6	10
Battery weight, kg	70	100	160
SOC range under CD mode, %	50	60	60

Reducing rolling resistance and air drag coefficient are commonly used in conventional vehicles to save energy, which also applies to HEV. Figure 5 shows the simulation results of fuel consumption. Apparently on the basis of Baseline HEV, by reducing rolling resistance coefficient and drag coefficient, fuel consumption can be reduced to a certain degree, but there is still a long way to achieve 3.8L/100 km target. Besides, low rolling resistance tires will degrade other performance of vehicle, such as braking performance, and reshaping vehicle body needs a large sum of time and money. Therefore, on the basis of Baseline HEV, we can use the advanced lithium-ion battery to replace Ni-MH battery, and increase battery energy to achieve a plug-in hybrid, motor parameters should also be optimized in order to enhance the pure electric driving capability, this is a better way to achieve “95 g of CO₂/km” target.

3 Powertrain System Design

3.1 Battery Parameters Analysis

Based on three selected batteries shown in Table 2, and three different control strategies under CD mode are put forward. After comprehensive analysis of ECE R101 fuel consumption and the real fuel consumption, a reasonable battery is selected and the reasonable control strategy under CD mode is developed.

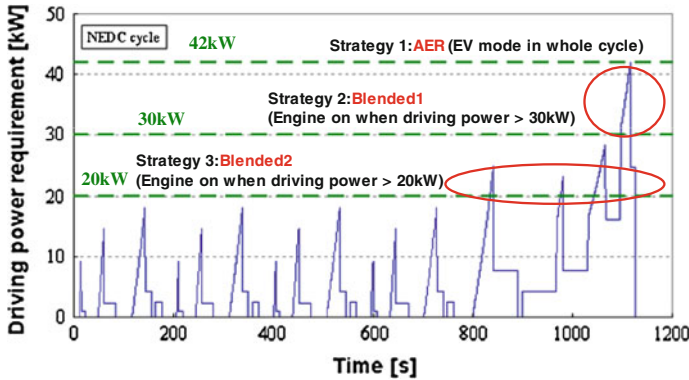


Fig. 6 Control strategies under CD mode in NEDC cycle

Table 3 Simulation results of the AER control strategy

Simulation results	PHEV1	PHEV2	PHEV3
Fuel consumption (NEDC), L/100 km	3.31	2.34	1.81
Electric consumption(NEDC), kWh/100 km	4.16	7.03	8.87

Three different control strategies of PHEV under CD mode in NEDC cycle are shown in Fig. 6. Horizontal axis represents running time and vertical axis is required driving power in NEDC cycle. The control strategies are described as below:

- (1) Strategy 1: Assuming that the motor power is large enough, the engine starting threshold power is more than 42 kW, AER (pure electric) driving is achieved in NEDC cycle. Mark strategy 1 as AER.
- (2) Strategy 2: Limit the engine starting threshold power to 30 kW, driving under Blended1 control mode in NEDC cycle (as shown in the red circle, when the required power is more than 30 kW, start engine to drive vehicles). Mark strategy 2 as Blended1.
- (3) Strategy 3: Limit the engine starting threshold power to 20 kW, driving under Blended2 control mode in NEDC cycle (as shown in the red circle, when the required power is more than 20 kW, start engine to drive vehicles).Mark strategy 3 as Blended2.

3.1.1 Regulation Fuel Consumption

The simulation results of different batteries and different control strategies under CD mode were shown in Tables 3, 4, 5. The fuel consumption and electric

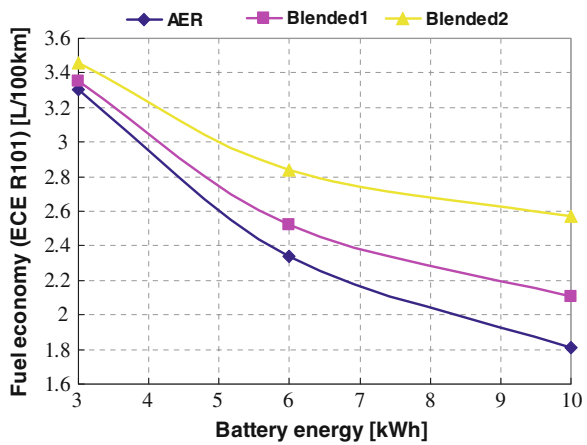
Table 4 Simulation results of the Blended1 control strategy

Simulation results	PHEV1	PHEV2	PHEV3
Fuel consumption (NEDC), L/100 km	3.35	2.52	2.11
Electric consumption(NEDC), kWh/100 km	3.88	6.27	7.73

Table 5 Simulation results of the Blended2 control strategy

Simulation results	PHEV1	PHEV2	PHEV3
Fuel consumption (NEDC), L/100 km	3.46	2.84	2.58
Electric consumption(NEDC), kWh/100 km	3.44	5.20	6.17

Fig. 7 NEDC fuel consumption (according to ECE R101 regulation) of different control strategies



consumption in the following table are calculated according to the formulas in ECE R101 regulation [2] (Note: PHEV consumption test regulation in China is also made reference to ECE R101 regulation). In the process of simulation under CS mode, keep the battery SOC a balance before and after simulation.

The NEDC fuel consumptions of different batteries and different control strategies can draw into a chart shown in Fig. 7, from which we can conclude that:

- (1) Adapting plug-in technology based on the baseline HEV, it can achieve 3.8L/100 km fuel consumption targets using the above three batteries.
- (2) In the same battery energy condition, the larger the engine starting threshold power is set, the lower the NEDC fuel consumption will be; the bigger the battery energy is, the greater the difference of fuel consumption will be.

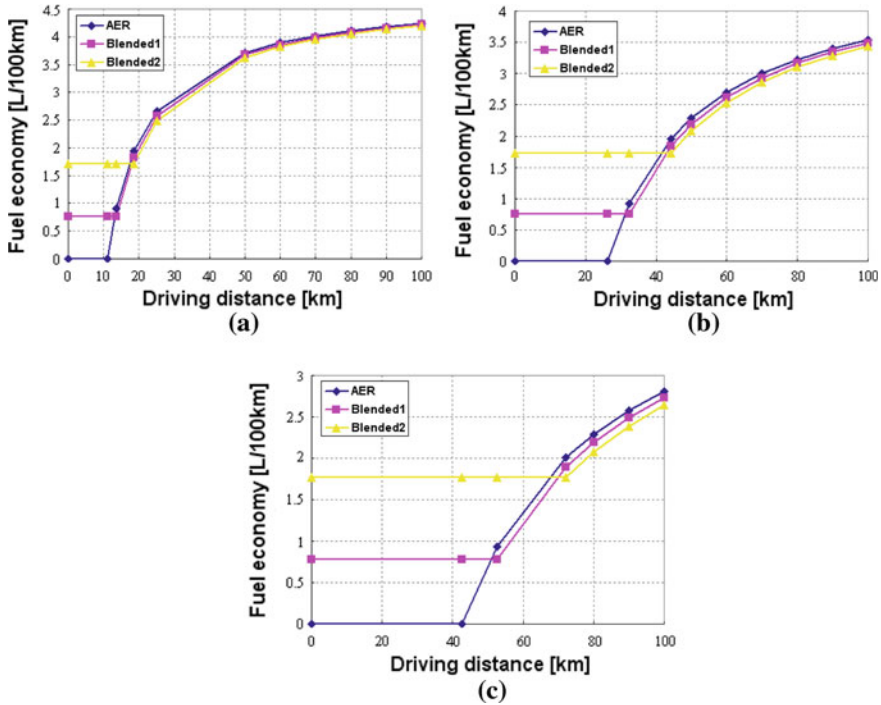


Fig. 8 Fuel consumption with different daily driving range. **a** Simulation results with Battery 1. **b** Simulation results with Battery 2. **c** Simulation results with Battery 3

3.1.2 Fuel Consumption with Different Daily Driving Distance

The fuel consumption compared above is based on ECE R101 regulation, and it cannot fully reflect the real fuel consumption. In fact, for PHEV, the fuel consumption is different in different daily driving distance. As the simulation results shown in Fig. 8:

- (1) In the same battery energy condition, if the daily driving distance is short, it is more fuel-efficient using AER control strategy in CD mode, and if the daily driving distance is long, it is more fuel-efficient using Blended2 control strategy. (This is because the blended control strategy can make the CD mode distance longer, and the engine load and efficiency in CD mode is higher than that of CS mode.)
- (2) The greater the battery energy, the bigger the difference of fuel consumption between different control strategies in CD mode is.

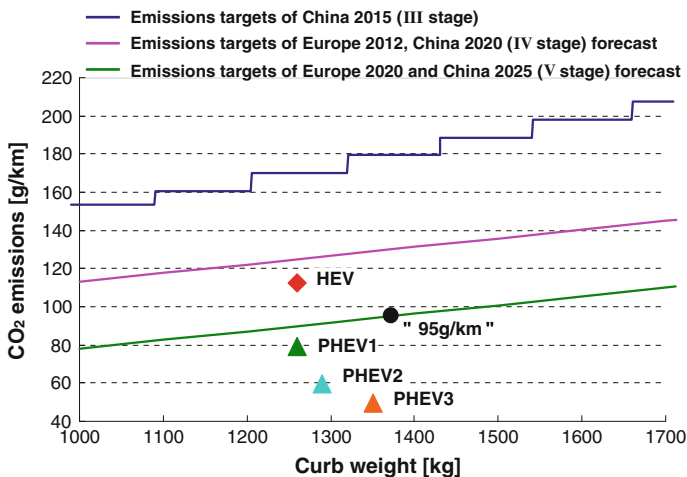
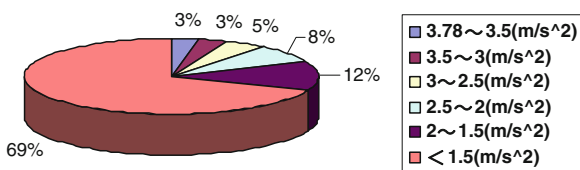


Fig. 9 Emissions regulations limits and comparison of different vehicles

Fig. 10 Launch acceleration in typical urban cycles



3.1.3 Results Analysis

- (1) From the above comparison between different control strategies in CD mode it can be concluded: Blended1 control strategy ensures not only a lower fuel consumption according to ECE R101 regulation, but also a higher fuel-efficiency with different daily driving distance, and only 30 kW of motor power can meet the requirements, the system cost is reduced, so it is a relatively compromise control strategy in CD mode.
- (2) From comparative analysis of different batteries it can be known: the “95 g CO₂/km” emissions target can be easily reached by using 3kWh lithium-ion battery to replace Ni-MH and adapting plug-in technology based on the baseline HEV, as shown in Fig. 9.

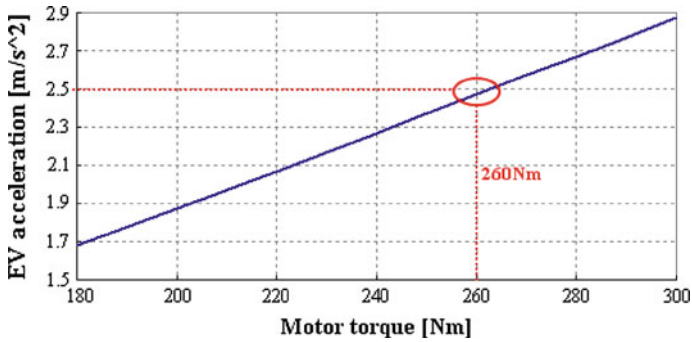


Fig. 11 Simulation results of pure electric launch acceleration

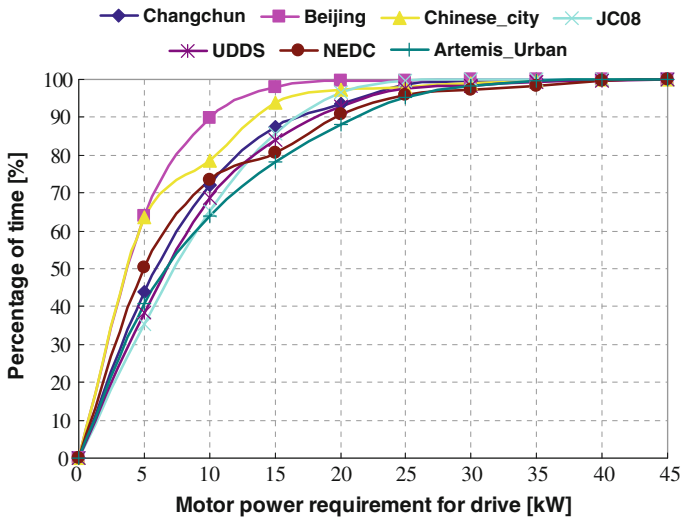


Fig. 12 Required motor power of pure electric driving

3.2 Motor Parameters Analysis

3.2.1 Motor Torque

As a kind of full hybrid vehicle, PHEV is required to launch under EV mode in most cases. Therefore, it is necessary to do a statistics of the vehicle launch acceleration in typical urban cycles in the world, which include China, United States, Europe and Japan. The result is shown in Fig. 10. About 81 % of the starting acceleration is less than $2 m/s^2$, and 89 % is less than $2.5 m/s^2$. Therefore,

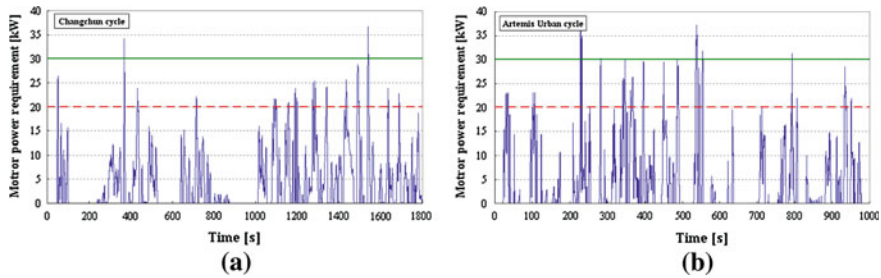


Fig. 13 Required driving power in two of typical cycles. **a** Changchun cycle. **b** Artemis Urban cycle

if the maximum pure electric launch acceleration of PHEV can reach 2.5 m/s^2 , the vehicle can launch under EV mode in most cases.

If the transmission system and other parameters remain unchanged, the motor torque directly determines the pure electric launch acceleration of the vehicle [3]. The simulation results of pure electric launch acceleration with different motor torque are shown in Fig. 11. When the motor torque is 260Nm, the pure electric launch acceleration can reach 2.5 m/s^2 , which can meet about 89 % of the launch demand. If the launch acceleration demand is more than 2.5 m/s^2 , the engine can be started to drive the vehicle.

3.2.2 Motor Power

In the second part of this paper the motor power demand in NEDC cycle has been analyzed. When the motor power is 30 kW, the vehicle can drive with Blended1 control strategy in CD mode. But analysis of pure electric driving power requirements in other typical cycles is also needed, as shown in Fig. 12. Visibly, when the motor power is 20 kW, it can meet more than 88 % of the driving power demand in typical cycles.

Furthermore, the engine starting frequency and corresponding minimum vehicle speed in typical cycles are analyzed and shown in Fig. 13 and Table 6. Although 20 kW motor can meet more than 88 % of the driving power demand in typical cycles, it will cause frequent starting of the engine, and the corresponding vehicle speed is not so high, which will not live up to the driver’s expectations of pure electric driving capability of PHEV.

It is suggested to choose a 30 kW motor, which can meet 97 % of the driving power demand, greatly reduce engine starting frequency and increase the corresponding vehicle speed when the engine is started. The conclusion of this part is in accordance with part 2 of this paper.

Table 6 Engine starting frequency and the corresponding vehicle speed

Cycles	20 kW motor		30 kW motor	
	Engine starting frequency (times/hour)	Vehicle speed when engine started (km/h)	Engine starting frequency (times/hour)	Vehicle speed when engine started (km/h)
Changchun	28	23	2	35
Beijing	6	57	3	60
Chinese typical city	9	26	3	38
JC08	21	22	0	–
UDDS	39	24	10	36
NEDC	12	58	3	100
Artemis urban	58	16	15	22

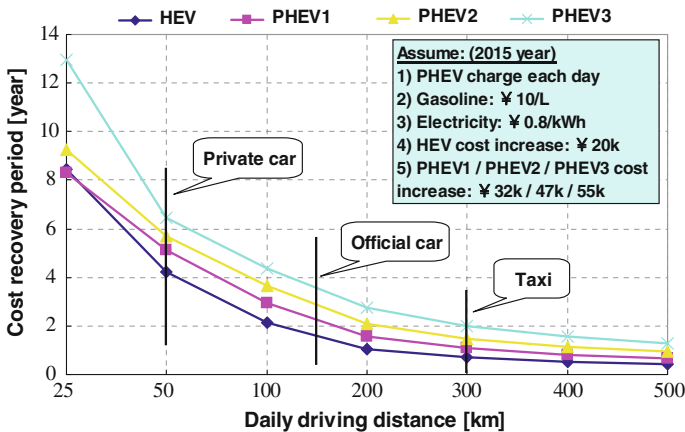


Fig. 14 Cost recovery periods analysis

4 Cost Analysis

After analyzing of HEV and PHEV, if the annual output is 10,000, the total cost of HEV is ϕ 20,000 more than conventional vehicle, and the figure for three kinds of PHEV are ϕ 32,000, ϕ 47,000 and ϕ 55,000 respectively. Assuming that oil price is ϕ 10/L and electricity price is ϕ 0.8/kWh in China by 2015. For three types of customers (Assuming that private car 50 km/day, official car 150 km/day and taxi 300 km/day), cost recovery periods of HEV and PHEV compared with conventional vehicle are shown in Fig. 14 (known that HEV is 35.2 % more fuel-efficient than conventional vehicle). Obviously, the longer the daily driving distance, the shorter the cost recovery period will be. The greater the battery energy, the higher the battery cost and the longer the cost recovery period will be.

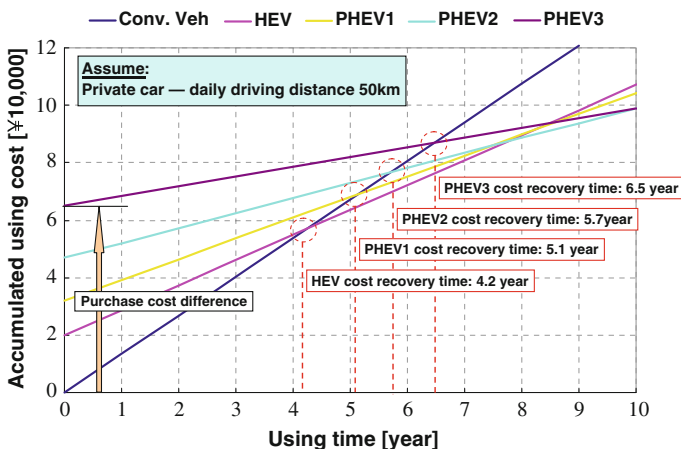


Fig. 15 Accumulated using cost of private cars

The accumulated using cost of private cars is shown in Fig. 15 (assuming daily driving distance is 50 km). For private car, cost recovery period of HEV is about 4.2 years, and the years for three kinds of PHEV are 5.1, 5.7 and 6.5 respectively. With the increase of using time, it is more cost-saving to use PHEV than HEV. As for private car, only when the using time is more than eight years, the order of the total benefits will achieve: PHEV3 > PHEV2 > PHEV1 > HEV. If considering the government incentive policy, the cost recovery period will be shorter.

5 Conclusion

- (1) For the current gasoline engines, on the basis of HEV, it is still difficult to achieve “95 g CO₂/km” emission goal by reducing rolling resistance coefficient and drag coefficient.
- (2) Comparative study of PHEV different control strategies in CD mode shows that: in CD mode, AER control strategy achieves lower regulation fuel consumption, but it needs a high power motor; in short daily driving distance condition, AER control strategy can also achieve lower fuel consumption, but when the daily driving distance is long, the blended control strategy will be more fuel-efficient. Blended1 control strategy ensures not only a lower fuel consumption according to ECE R101 regulation, but also a higher fuel-efficiency with different daily driving distance, and only 30 kW of motor power can meet the requirements, so it is a relatively compromise control strategy in CD mode.
- (3) On the basis of baseline HEV, the “95 g CO₂/km” emissions target can be easily reached by using 3kWh lithium-ion battery to replace Ni-MH, increasing the motor parameters to 30 kW/260Nm and adapting plug-in

technology. The vehicle curb weight is equalized to baseline HEV because of the higher energy density of Li-Ion battery, and the vehicle cost increase is acceptable, this technical approach is worthy of further research.

References

1. Laue T, Goede M, Schroeter O (2009) Optimization of light weight design and energy efficiency for sustainable CO₂-emissions, Aachener Kolloquium Fahrzeug- und Motorentechnik
2. ECE Regulation No. 101, Revision 2—Amendment 2, Nov 2009
3. Ehsani M, Gao Y, Emadi A (2009) Modern electric, hybrid electric, and fuel cell vehicles fundamentals, theory, and design, second edition, New York